Philipps Universität Marburg

Modellsysteme organischer Halbleiter: Präparation, Charakterisierung und Interpretation

Dissertation
zur
Erlangung des Doktorgrades
der Naturwissenschaften
(Dr. rer. nat.)

dem

Fachbereich Physik
der Philipps Universität Marburg

vorgelegt von

M.Sc. Michael Klues

aus

Lünne

Marburg, 2016

Vom Fachbereich Physik der Philipps-Universität als Dissertation angenommen am:	26.01.2017
Erstgutachter:	Prof. Dr. G. Witte
Zweitgutachter:	Prof. Dr. R. Berger
Tag der mündlichen Prüfung:	24.02.2017
Hochschulkennziffer:	1180

Große Teile dieser Dissertation wurden bereits in Fachzeitschriften veröffentlicht, weshalb die vorliegende Arbeit kumulativ verfasst ist. Die Darstellung der Ergebnisse beschränkt sich daher auf zentrale Aspekte und erfolgt teilweise anhand von modifizierten Grafiken aus den Veröffentlichungen. Für die Details sei auf die folgenden Artikel bzw. Kapitel in dieser Arbeit verwiesen:

- Jonas Schwaben, Niels Münster, Tobias Breuer, Michael Klues, Klaus Harms, Gregor Witte and Ulrich Koert: Synthesis and Solid-State Structures of 6,13-Bis(trifluoromethyl)- and 6,13-Dialkoxypentacene, *European Journal of Organic Chemistry* **2013**, 1639-1643; Kapitel: 5.1

- Michael Klues, Klaus Hermann and Gregor Witte: Analysis of the near-edge X-ray-absorption fine-structure of anthracene: A combined theoretical and experimental study, *The Journal of Chemical Physics* **2014**, 140, 014302; Kapitel: 5.7

- Jonas Schwaben, Niels Münster, Michael Klues, Tobias Breuer, Philipp Hofmann, Klaus Harms, Gregor Witte and Ulrich Koert: Efficient Syntheses of Novel Fluoro-Substituted Pentacenes and Azapentacenes: Molecular and Solid-State Properties, *Chemistry A European Journal* **2015**, 21, 13758-13771; Kapitel: 5.2

- André Pick, Michael Klues, Andre Rinn, Klaus Harms, Sangam Chatterjee and Gregor Witte: Polymorph-Selective Preparation and Structural Characterization of Perylene Single Crystals, *Crystal Growth & Design* **2015**, 15, 5495-5504; Kapitel: 5.3

- Tobias Breuer, Michael Klues and Gregor Witte: Characterization of orientational order in π-conjugated molecular thin films by NEXAFS, *Journal of Electron Spectroscopy and Related Phenomena* **2015**, 204, 102-115; Kapitel: 5.6

- F. Anger, T. Breuer, A. Ruff, M. Klues, A. Gerlach, R. Scholz, S. Ludwigs, G. Witte and F. Schreiber: Enhanced Stability of Rubrene against Oxidation by Partial and Complete Fluorination, *The Journal of Physical Chemistry C* **2016**, 120, 5515-5522; Kapitel: 5.4

- M. Klues, P. Jerabek, T. Breuer, M. Oehzelt, K. Hermann, R. Berger and G. Witte: Understanding the F 1s NEXAFS Dichroism in Fluorinated Organic Semiconductors, *The Journal of Physical Chemistry C* **2016**, 120, 12693-12705; Kapitel: 5.8

- Tobias Breuer, Michael Klues, Pauline Liesfeld, Andreas Viertel, Matthias Conrad, Stefan Hecht and Gregor Witte: Self-assembly of partially fluorinated hexabenzocoronene derivatives in the solid state, **Just accepted**, *Physical Chemistry Chemical Physics*; Kapitel: 5.5

- Michael Klues and Gregor Witte: Crystalline Packing Motifs in Pentacen-like Organic Semiconductors, In Vorbereitung zur Veröffentlichung in *CrystEngComm*; Kapitel: 5.9

Inhaltsverzeichnis

1. Einführung

1.1 Betrachtungen zu Werkzeugen

Werkzeuge zu nutzen zeichnet den Menschen von jeher aus. Sie stellen das Bindeglied zwischen dem außergewöhnlichsten Merkmal des Menschen, seiner Intelligenz, und der materiellen Welt dar. Ganz im Sinne des Werbeslogans eines bekannten Autoherstellers -„Vorsprung durch Technik"- war es dem Menschen so schon vor Jahrtausenden möglich mit Hilfe von Speeren und Bögen schnellere und stärkere Tiere zu erlegen, sowie mit Äxten und Hämmern ganze Landstriche zu gestalten und monumentale Bauwerke zu errichten. Auch heute noch assoziieren wir mit dem Begriff „Werkzeug" zunächst einmal unwillkürlich Geräte, die mechanisch auf die Welt einwirken. Auf den zweiten Blick liefert die mechanische Wirkung eines Gegenstandes jedoch keine gute Definition, denn auch einen Zollstock würden die meisten in einem gut sortierten Werkzeugkoffer erwarten. Mit einem Zollstock wird aber nichts Materielles bewegt oder verformt. Was für eine Art von Werkzeug ist das also? Tatsächlich reicht es nicht, sich Werkzeuge als Ausführungshilfen des Verstandes in der Welt vorzustellen. Es gibt auch solche, die umgekehrt auf den Verstand wirken. Zugegeben, der Gedanke, ein Zollstock könne ein Instrument sein, mit dem Menschen ihr Bild von der Welt formen, erscheint ein wenig abstrakt, aber genau das ist die Eigenschaft von Messinstrumenten. Indem wir etwas messen wird es quantifiziert und unsere Vorstellung davon wird konkreter. Es gibt noch eine dritte Kategorie von Werkzeugen, die häufig bei den Messinstrumenten verortet werden. Die Rede ist von solchen Geräten, die die Sinne des Menschen verstärken oder erweitern. Auch diese Instrumente wirken auf unsere Vorstellung der Welt, aber nicht, indem sie unser Bild der Welt präzisieren, sondern indem sie Bereiche erschließen, von denen es vorher gar keine Vorstellung gab, weil sie unserer Wahrnehmung schlicht nicht zugänglich waren. Der vielleicht prominenteste Vertreter dieser Kategorie von Werkzeugen ist das Mikroskop.[1] Als die ersten Mikroskope im 17. Jahrhundert aufkamen, gab es noch keine Begriffe für heute selbstverständliche Dinge, wie z.B. Zellen oder Bakterien, und folgerichtig auch keinerlei Vorstellung davon, wie das Leben auf dieser Ebene funktionieren könnte, bzw. dass es überhaupt Leben auf dieser Ebene gibt. Tatsächlich basiert unsere Auffassung von der

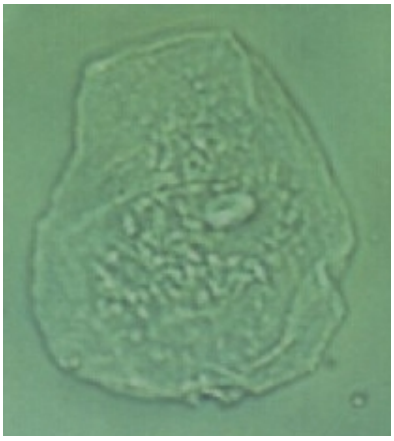

Abbildung 1.1: Zelle der Mundschleimhaut des Autors. Gut zu erkennen ist der eiförmige Zellkern nahe der Bildmitte.

[1] Wäre dies nicht eine Arbeit aus dem Bereich der Nanotechnologie, sondern der Astronomie, würde hier mit gleicher Berechtigung das Teleskop angeführt.

Welt - vom Weltall bis in den Mikrokosmos - maßgeblich auf Wahrnehmungen, die wir nur mit Hilfe von Werkzeugen machen können. Instrumente zu entwickeln, die die Grenze des Wahrnehmbaren weiter in den Bereich des noch nie Beobachteten verschieben, stellt dabei eine Frontlinie der experimentellen Naturwissenschaften dar.

Ein Mikroskop kann als ein Verstärker für den Sehsinn aufgefasst werden. Ein Blick durchs Okular offenbart eine fremdartige Welt, aber immerhin sehen wir Bilder, die sich unmittelbar interpretieren lassen, indem Ideen aus der normalen Erfahrungswelt angewandt werden. Betrachtet man die Namensgebung einiger Objekte, die damals unter dem Mikroskop zum ersten Mal sichtbar wurden, wird dies deutlich. Der Begriff „Zelle“ z.B. bezeichnet abseits der Biologie einen kleinen Raum ohne ständige Öffnung und ist damit ein sehr treffender Begriff für diesen Baustein des Lebens, wie er in Abb. 1.1 zu sehen ist. Deutlich schwieriger wird die Interpretation, wenn uns Instrumente physikalische Effekte zugänglich machen, für deren Wahrnehmung wir normalerweise über keinerlei Sinn verfügen. Insbesondere gilt dies für alle Formen von Spektrometern. *Spectrum* lässt sich aus dem Lateinischen unter anderem mit *Erscheinung* oder *Gespenst* übersetzen, was schon auf mögliche Probleme hindeutet. Jedes Spektrum ist immer eine Projektion des eigentlichen Phänomens in eine für Menschen wahrnehmbare Darstellungsform und bedarf deshalb stets einer aufwändigeren Deutung, die in der Regel viel zusätzliches Wissen aus anderen Quellen erfordert. So wird ein Infrarotspektroskopiker z.B. eine C-N Streckschwingung in einem Spektrum entdecken, aber diese Deutung ist bei weitem weniger unmittelbar, als z.B. die Analyse der Schwingungen eines Musikinstrumentes mit Hilfe einer hochauflösenden Zeitlupenaufnahme. Nur leider gibt es keine Kameras, die stark genug vergrößern und gleichzeitig auch noch schnell genug sind um Moleküle direkt beim Schwingen zu beobachten, sodass Infrarotspektren hier das Mittel der Wahl sind. Wenn es aber nie jemand gesehen hat, wieso kann der Experte dann ein bestimmtes Signal als C-N Streckschwingung identifizieren? Solch eine Deutung erfordert in der Regel ein theoretisches Modell. Schon die Vorstellung, dass molekulare Schwingungen für die Signaturen im Spektrum verantwortlich sein könnten, ergibt sich nicht aus der Messung selbst und welche Schwingung genau vorliegt, erfordert oft detailliertere theoretische Betrachtungen. So ließe sich z.B. ein IR-Spektrum des Anilin anhand des berechneten Spektrums aus Abb. 1.2 genauer analysieren und so die Position der C-N Streckschwingung im Spektrum finden. Bisweilen ist es möglich, geschickte Experimente durchzuführen, um eine Deutung rein experimentell zu überprüfen, was wiederum für die theoretische Modellierung von großem Wert ist, da diese Ergebnisse als Maßstab für die theoretischen Methoden fungieren können.[1] Im Allgemeinen ist dies aber nicht praktikabel und erst eine theoretische Modellierung macht eine abstrakte Messmethode zu einem leistungsfähigen „Sinneswerkzeug“. Damit ist eine gute Modellbildung sowie die Entwicklung von - heutzutage meist computergestützten -

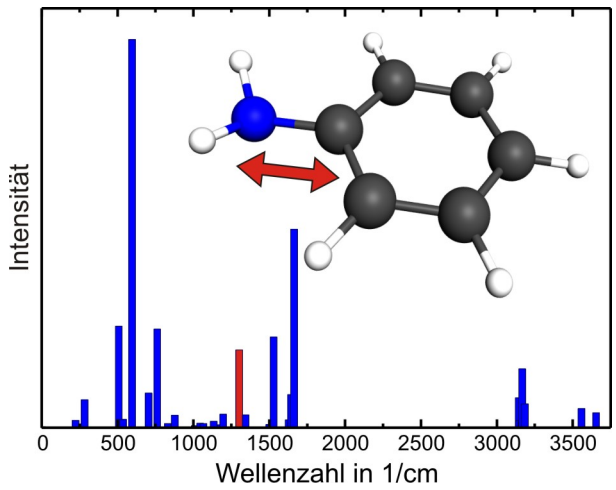

Abbildung 1.2: Berechnetes IR-Spektrums des Anilins. Die C-N Streckschwingung (rote Linie) kann anhand der Rechnung im Spektrum identifiziert werden.

Methoden zur Deutung abstrakter Daten wiederum eine Frontlinie der theoretischen Naturwissenschaften. Moderne Messinstrumente dienen sowohl der Sinneserweiterung, als auch der Quantifizierung. Damit sie jedoch ihr volles Potential als Werkzeuge, mit denen wir auf bisher Unentdecktes schauen und unser Bild von der Welt erweitern können, entfalten, müssen Experiment und Theorie Hand in Hand gehen. Diese Idee soll in der vorliegenden Arbeit verfolgt werden, indem verschiedene quantenchemische Programmpakete genutzt werden, um Daten zu analysieren, die ihrerseits aus Experimenten stammen, die die Deutung begünstigen oder überhaupt erst ermöglichen.

1.2 Das Forschungsgebiet

Auf welchem Gebiet wird nun der Blick auf bisher Unerforschtes geworfen? Im Folgenden geht es um organische Halbleiter. Die Klasse der Halbleitermaterialien hat im Laufe des 20. Jahrhunderts große technologische Bedeutung gewonnen. Ursache hierfür ist die Entwicklung des Transistors, der ohne Halbleiter nicht denkbar ist. Auf Basis des Transistors wiederum hat die Elektronik die wohlbekannten, rasanten Fortschritte der vergangenen Jahrzehnte gemacht. Dies beruht jedoch auf anorganischen Materialien - allen voran Silizium. Auch wenn viele grundlegende Experimente rund um organische Halbleiter, wie z.B. solche zur Leitfähigkeit organischer Kristalle [2], parallel zum Siegeszug der anorganischen Verwandten stattfanden, zog dieses Forschungsgebiet erst in den letzten beiden Jahrzehnten verstärkte Aufmerksamkeit auf sich. Als Beispiel für diese Verzögerung kann der Nobelpreis für Chemie dienen, den A.J. Heeger, A. MacDiarmid und H. Shirakawa 2000 für ihre Entdeckung leitender Polymere erhielten.[2] Die entsprechenden Arbeiten gehen aber schon auf die 1970er Jahre zurück [3]. Selbst die Weltrekordhalter unter den organischen Halbleitern erreichen in der Ladungsträgermobilität „nur“ das Niveau polykristallinen Siliziums [4] und werden damit niemals zum nächsten Leistungssprung in der Computertechnik führen. Was also macht diese Stoffklasse dennoch interessant? Bei weitem nicht für jede Anwendung ist eine Hochleistungs-CPU nötig. Überall dort, wo einfache elektronische Lösungen realisiert werden müssen, kann Organik eine kostengünstige und ökologische Alternative sein, da die Rohstoffe erheblich günstiger und die Produktionstechniken deutlich weniger energieintensiv sind. Zudem werden für die Prozessierung anorganischer Halbleiter in lithografischen Verfahren oft große Mengen von Gefahrstoffen, wie z.B. Säuren benötigt, was entsprechende Umwelt- und Sicherheitsstandards vorausgesetzt, wiederum mehr Aufwand und Kosten bedeutet. Für einfache Schaltkreise wird deshalb an Verfahren gearbeitet, die es erlauben, organische Elektronik in großer Stückzahl zu drucken (Ink-Jet Printing), aus der Gasphase aufzudampfen (Organic Vapour-Phase Deposition) oder direkt an der Oberfläche zu strukturieren, indem z.B. Stempelverfahren genutzt werden (Micro/Nanopatterning). [5] Insbesondere die Gasphasendeposition findet schon seit einigen Jahren industrielle Anwendung bei der Herstellung von Displays. Tatsächlich sind OLEDs (Organic Light Emitting Diods) in Form von Smartphonedisplays und inzwischen auch größeren Bildschirmen der bislang größte kommerzielle Anwendungsbereich organischer Elektronik, wobei hier ein weiterer inhärenter Vorteil zum Tragen kommt: Farbe ist in gewisser Weise eine fundamentale Eigenschaft organischer Halbleiter. Definitionsgemäß besitzt ein Halbleiter eine Bandlücke von höchstens einigen

[2]Hier geht es um leitende organische Materialien, womit die Nobelpreisträger sich nicht direkt mit Halbleitern beschäftigt haben. Die Modelle zum Ladungstransport, die unter anderem durch ihre Arbeit angestoßen oder verfeinert wurden, sind aber grundsätzlich für organische Elektronik und damit für das ganze Forschungsgebiet relevant.

eV. Auf die Situation molekularer Bausteine übertragen bedeutet dies einen entsprechenden energetischen Abstand der höchsten besetzten (Highest Occupied Molecular Orbital = HOMO) und tiefsten unbesetzten Orbitale (Lowest Unoccupied Molecular Orbital = LUMO). Da sichtbares Licht Photonenenergien von ca. 1,5 eV bis 3,0 eV besitzt, sind organische Halbleiter oft auch Farbstoffe. Umgekehrt ist der Gedanke aber noch wegweisender: Praktisch jeder Stoff, der in der Chemie als Farbstoff gilt, ist auch ein potentieller Halbleiter und kann in einer OLED zum Leuchten gebracht werden. Da es eine nahezu unbeschränkte Vielfalt an chemischen Verbindungen gibt, die zudem gezielt modifiziert werden können, ist es vergleichsweise einfach, Materialien zu finden, die Licht einer bestimmten Wellenlänge emittieren. Natürlich gibt es in der Praxis noch viele Parameter, die die Auswahl einschränken, dennoch stellt die große Palette möglicher Verbindungen einen Vorteil gegenüber der Anorganik dar, weil hier Veränderungen der Bandlücke über vergleichsweise aufwändige Schichtsysteme und Dotierungen erreicht werden müssen. Im Zusammenhang mit OLED-Displays wird gelegentlich eine Eigenschaft des organischen Materials spektakulär in Szene gesetzt, die im Kontext einer weiteren technischen Anwendung, der Solarzelle, noch viel wichtiger sein dürfte: Flexibilität. Die Organik kann auf dünne und flexible Substrate, wie z.B. Plastikfolien, aufgebracht werden und verliert bei Verformungen nicht ihre Funktion, was unter anderem zur Herstellung aufrollbarer Bildschirme führen kann. Den Prozess der Lichterzeugung aus Strom in gewisser Weise umkehrend, können aber auch organische Solarzellen gebaut werden. Diese werden auf absehbare Zeit nicht die Effizienz ihrer siliziumbasierten Pendants erreichen. Durch die Flexibilität ergeben sich jedoch völlig neue Designmöglichkeiten, sodass in Verbindung mit einer kostengünstigen Fertigung zukünftig an Stellen Strom erzeugt werden kann, an denen das bisher unattraktiv war. Grundsätzlich sind z.B. beschichtete Fenster denkbar. Da die organischen Schichten selbst äußerst dünn sein können ist es möglich, dass sie teiltransparent bleiben, sodass stromerzeugende Glasfassaden möglich werden. Solarzellen, OLEDs und druckbare Elektronik stellen die technologischen Paradebeispiele dieses Forschungsgebietes dar und finden teilweise schon heute milliardenschwere kommerzielle Anwendung. Aufgrund ihrer praktischen Bedeutung dürfen jene Beispiele in einer Einleitung wie dieser nicht fehlen. Dennoch ist es vorstellbar, dass zukünftige Generationen unserer heutigen Forschung attestieren werden, die tatsächliche Tragweite des Themengebietes anhand der unmittelbaren Anwendungen vollkommen unterschätzt zu haben. Was sich langfristig aus Grundlagenforschung ergibt ist schließlich nicht immer absehbar. In diesem Sinne sei hier noch ein Beispiel angeführt, das seltener im Zusammenhang mit organischen Halbleitern genannt wird, aber zweifellos eine faszinierende Zukunftsvision beinhaltet. In der Neurologie gibt es zunehmende Erfolge, die Kommunikation von Nervenzellen zu entschlüsseln. Insbesondere für die Prothetik ist dies hoch interessant, weil damit grundsätzlich die unmittelbare Steuerung von Prothesen, sowie das Einspeisen von Daten künstlicher Sinnesorgane möglich werden sollte. Dazu ist jedoch eine biologisch verträgliche Schnittstelle zwischen Nervenzelle und Maschine notwendig. Eine echte Herausforderung, da die Zellen zu einem gezielten Verwachsen mit den Kontakten animiert werden müssen, während viele der technischen Materialien für die Zellen, bzw. den Körper im Allgemeinen, unverträglich sind oder gar aktiv angegriffen werden. [6] Wie bereits erwähnt ist die Fülle möglicher organischer Halbleiter jedoch gewaltig und unter ihnen finden sich auch Biomoleküle ...

1.3 Die Herausforderung

OLEDs, Solarzellen und Feldeffekttransistoren lassen sich aus organischen Halbleitern herstellen. Wenn diese Dinge aber schon funktionieren, was soll dann noch erforscht werden? Welche Fragen bleiben auf diesem Gebiet bislang offen? Ein wichtiger Punkt wird unmittelbar deutlich, wenn ein Blick auf die grundlegenden Funktionsprinzipien dieser Bauteile geworfen wird. In Abb. 1.3 sind Energieniveauschemata für alle drei Anwendungen zu sehen. Hierbei handelt es sich um eine stark vereinfachte Darstellung der Funktionsweise und dennoch fällt ein Punkt sofort auf: Offensichtlich ist die relative Lage von Ferminiveaus der Kontaktmaterialien, sowie HOMO- bzw. LUMO-Energien der organischen Schichten zueinander von großer Bedeutung. Genau hier liegen einige der größten Herausforderungen. Allgemein ist in diesem Zusammenhang oft die Rede vom Aufklären der elektronischen Eigenschaften eines Moleküls, Materials, einer Grenzschicht oder einer Heterostruktur. So verbergen sich beispielsweise in Abb. 1.3a) schon einige kritische Bereiche, die Gegenstand aktueller Forschung sind. Der Übergang im Zentrum der Abbildung, der letztendlich zur Entstehung von Licht führt, findet z.B. gar nicht direkt zwischen HOMO- und LUMO-Niveaus statt, sondern wird über die Bildung eines Exzitons, das dann zerstrahlt, vermittelt. [7] Wie genau solche Exzitonen entstehen, welche Eigenschaften sie besitzen, über welche Mechanismen sie zerfallen, welche Bindungsenergien sie aufweisen und wie all diese Parameter einerseits von den Molekülen und andererseits von der Kristallstruktur, also von der Struktur des Festkörpers, abhängen, ist nach wie vor Gegenstand aktueller Forschung. Zudem sind insbesondere die Grenzflächen kritisch, da es hier zu einem Ladungsträgeraustausch kommen kann, was wiederum zu *band bending* führt[8–10]. Der tatsächliche Verlauf der Energieniveaus ist also insbesondere an den Grenzflächen wesentlich komplexer, als hier vereinfacht dargestellt. Um möglichst günstige Übergänge zu erhalten, ist deshalb die Kontrolle der Austrittsarbeiten wichtig [11], was durch monomolekulare Beschichtungen erreicht werden kann. Ansätze unter Verwendung organischer Materialien sind hier z.B. dipolbehaftete Moleküle in SAMs (Self-Assembled Monolayers) aufzubringen [12] oder den bereits erwähnten Ladungstransfer zu nutzen, indem Akzeptor- oder Donormoleküle an der Grenzschicht aufgebracht werden [13]. Viele Details sind also nach wie vor schwer zu kontrollieren und oft auch noch unverstanden, aber auch für einige der fundamentalen Vorgänge ist die theoretische Beschreibung im

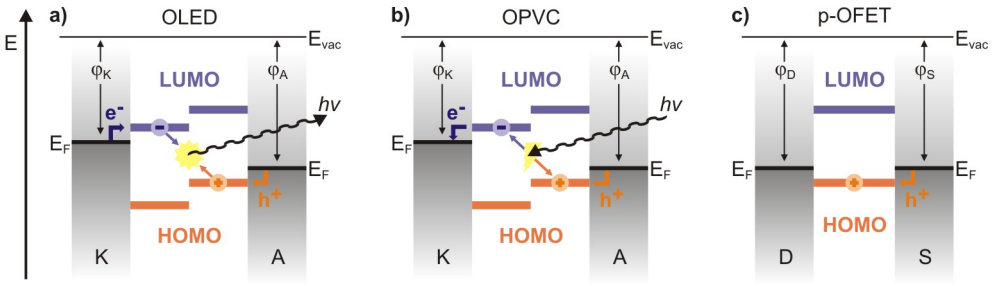

Abbildung 1.3: Vereinfachte Energieniveauschemata der wichtigsten elektronischen Bauteile. Eingezeichnet sind neben den HOMO- und LUMO-Niveaus der organischen Komponenten die Ferminiveaus (E_F) der Anoden-, Kathoden-, bzw. Drain- und Sourcekontakte, sowie die zugehörigen Austrittsarbeiten φ. Zudem sind die Flüsse von Elektronen (e^-) und Löchern (h^+) eingezeichnet. a) OLED b) Organische Solarzelle (Organic Photovoltaic Cell) c) p-typ OFET (Organic Field Effect Transistor)

Fall der Organik noch nicht abgeschlossen. Ein Beispiel hierfür ist der Ladungstransport. Im Rahmen des Blochtheorems lassen sich die elektronischen Eigenschaften der anorganischen Materialien sehr gut in einem Bändermodell beschreiben. Prinzipiell lässt sich das Blochtheorem auch auf Organik anwenden, da die entscheidende Grundbedingung Periodizität, also Kristallinität der Materialien, ist. In der Praxis gelingt diese Übertragung aber nicht reibungslos. Ursache hierfür ist ein Unterschied, der im Fall der Organik, die auch gerne als *soft matter* (weiche Materie) bezeichnet wird, namensgebend ist. Den starken kovalenten Bindungen in anorganischen Kristallen stehen in molekularen Materialien viel schwächere intermolekulare Wechselwirkungen, wie die van-der-Waals-Kräfte gegenüber. Zunächst einmal führt das in vielen Fällen zu einer verminderten Kristallinität in den organischen Festkörpern, da Fehlstellen, höherdimensionale Gitterfehler oder sogar das gleichzeitige Auftreten verschiedener Polymorphismen wahrscheinlicher werden und sich grundsätzlich nicht im gleichen Maße vermeiden lassen, wie das z.B. für Silizium möglich ist. In solchen Systemen liefert ein Hopping-Modell oft bessere Ergebnisse als eine Betrachtung von Bändern. [14] Noch fundamentaler ist jedoch die Verschiebung der Energieregime. Kovalente Bindungen gehen mit Energiegewinnen von einigen eV einher. Die elektronische Struktur lässt sich deshalb sehr gut separat von anderen Phänomenen behandeln, die dann mit einem störungstheoretischen Ansatz in das Modell eingefügt werden können. Insbesondere für phononische Effekte, die energetisch ca. zwei Größenordnungen kleiner ausfallen als die elektronischen Vorgänge, funktioniert das gut. Im Fall der Organik liegen die Energien der Vibrationen aber in der selben Größenordnung wie die der intermolekularen Bindungen, sodass sich diese Phänomene nicht ohne Weiteres entkoppeln lassen und z.B. als Polaron zusammen behandelt werden müssen. Deshalb steht die theoretische Beschreibung organischer Kristalle bzw. ihrer elektronischen Eigenschaften vor einigen fundamentalen Herausforderungen, an denen nach wie vor gearbeitet wird. [15, 16] Neben der Beschäftigung mit den elektronischen Phänomenen erfordert aber auch die tatsächliche Beschaffenheit der organischen Schichten verstärkte Aufmerksamkeit. In Abb.1.4a) ist das Schichtsystem einer OLED schematisch dargestellt, so wie es in vielen Artikeln oder Lehrbüchern zu finden ist. Tatsächlich sieht die Realität aber selten so geordnet aus, wie es ein solches Schema suggeriert. In Teilbild b) sind eine Reihe von Phänomenen angedeutet, die im Experiment oder der Produktion den Aufbau der OLED stören können. Hier ein paar Beispiele: Durch Chemisorption kann es gerade an der Grenze zum Metallkontakt zu starken Wechselwirkungen kommen, sodass vor allem die erste Schicht Moleküle einer deutlichen Veränderung unterliegt. Dieser Effekt kann gewollt sein,

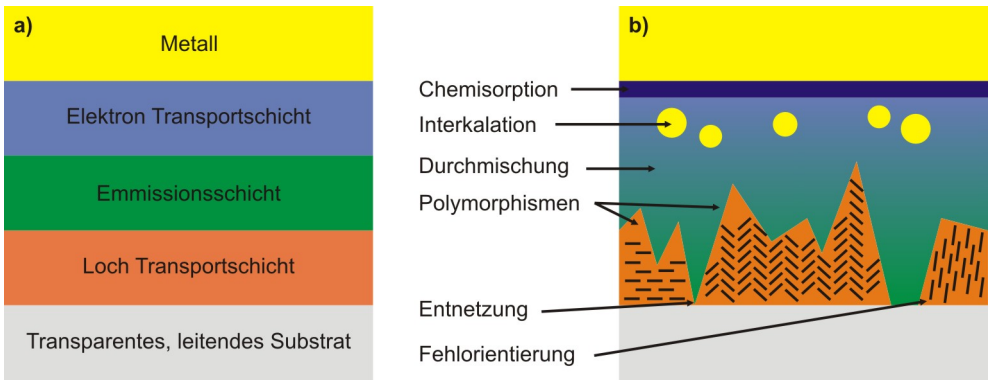

Abbildung 1.4: a) Exemplarischer Aufbau einer OLED. b) Beispiele für Probleme, die unter realen Bedingungen das Schichtsystem beeinflussen können.

wie z.B. im bereits erwähnten Fall der gezielten Modifikation von Austrittsarbeiten [13]. Oft verlieren die Moleküle jedoch die gewünschten Eigenschaften oder es kommt sogar zu Reaktionen, die die Moleküle zerstören. Der Zerfall des organischen Halbleiters Perfluoropentacen beim Kontakt mit Münzmetallen wie Silber und Kupfer ist ein Beispiel für solch einen unerwarteten Effekt [17]. Je nach Präparation kann es mit den Metallkontakten zu einem weiteren Problem kommen. Sollen Topkontakte hergestellt werden, muss das Metall auf die Organik aufgebracht werden, wobei es zu Interkalation von Metall kommen kann, wie Dürr *et al.* gezeigt haben [18]. Aber auch die Organik-Organik Grenzschichten lassen sich nicht immer komplikationslos herstellen. Auch hier kann es zu Durchmischungen oder sogar Reaktionen kommen. So haben Breuer *et al.* mit einer NEXAFS basierten Studie z.B. eine Diels-Alder-Reaktion zwischen Pentacen und Buckminster Fulleren (C_{60}) nachweisen können, die bereits bei Raumtemperatur an der Grenzfläche abläuft [19]. Zudem ist das Frank-van-der-Merwe-Wachstum, wie es in Abb.1.4a) durch die glatten Schichten angedeutet wird, nicht der Regelfall. Anstelle von geschlossenen Schichten, die sukzessive angelagert werden, kommt es häufig zu Entnetzung im Sinne eines Stranski-Krastanow- oder Volmer-Weber-Wachstums. Beispiele hierfür sind das Inselwachstum von Pentacen auf Siliziumdioxid (SiO_2) [20] oder die Kantendekoration von C_{60} auf Pentacen [21]. In der orangen Loch-Transportschicht von Teilbild b) sind durch kurze Striche mögliche Molekülorientierungen angedeutet. Fehlorientierung weist in diesem Zusammenhang auf ein weiteres fundamentales Merkmal der organischen Materialien hin: Die Eigenschaften der Moleküle sind stark richtungsabhängig und die zugehörigen Kristalle damit anisotrop. Eigenschaften wie das Absorptionsvermögen, thermische Ausdehnungskoeffizienten oder auch Leitfähigkeiten können mit der Richtung drastisch variieren. [22–24] Damit ist offensichtlich, dass die konkrete Orientierung der Domänen und damit der Moleküle ausschlaggebend sein kann. Tatsächlich sind schon kleine Veränderungen an den Grenzflächen entscheidend für die Ausrichtung. So nimmt Perfluoropentacen auf Graphen z.B. eine liegende Orientierung an. In Bereichen mit Fehlern der Graphenschicht, die sich z.B. durch Ionenbeschuss auch gezielt erzeugen lassen, stellt sich jedoch ein aufrechtes Wachstum ein [25]. Tatsächlich ändert sich im erwähnten Beispiel nicht nur die Orientierung der Moleküle, sondern auch der Polymorphismus, in dem sie sich anordnen. Da sich mit dem Polymorphismus wiederum Festkörpereigenschaften ändern können, selbst dann, wenn die Strukturen sich augenscheinlich kaum in der molekularen Anordnung unterscheiden, ist das kontrollierte Wachstum eines Polymorphismus für die späteren Bauteile ebenfalls von Bedeutung.

Die hier aufgeführten Beispiele sollen zeigen, dass viel Entwicklungsarbeit, aber auch viele physikalische Fragestellungen in den Details der Schichtsysteme liegen. Das Wachstumsverhalten aller beteiligten Komponenten, sowie ihre Wechselwirkungen untereinander zu kennen und gezielt kontrollieren zu können, ist der Schlüssel zu leistungsfähigen und vor allem reproduzierbaren Bauteilen. Aber nicht nur für die industrielle Fertigung sind diese Fähigkeiten entscheidend. Wie zu Beginn dieser Arbeit ausgeführt, lassen sich viele Experimente nur im Zusammenspiel mit einer theoretischen Modellierung interpretieren. Dafür ist es wichtig, dass das Modell die Realität möglichst gut abbildet. Schon aus Gründen der Rechenkapazität verwenden die meisten Modelle jedoch Ansätze, die der Komplexität von Abb.1.4a) entsprechen. Um einen sinnvollen Vergleich gewährleisten zu können, muss deshalb von experimenteller Seite dafür Sorge getragen werden, dass die Proben möglichst nah an das Ideal heranreichen. Deshalb ist die Untersuchung von Modellsystemen unverzichtbar, wie es in Abb. 1.5 in Form einer Mindmap zusammengefasst ist. Auch wenn das Modellsystem für die konkreten Messungen letztendlich realisiert werden muss, ist

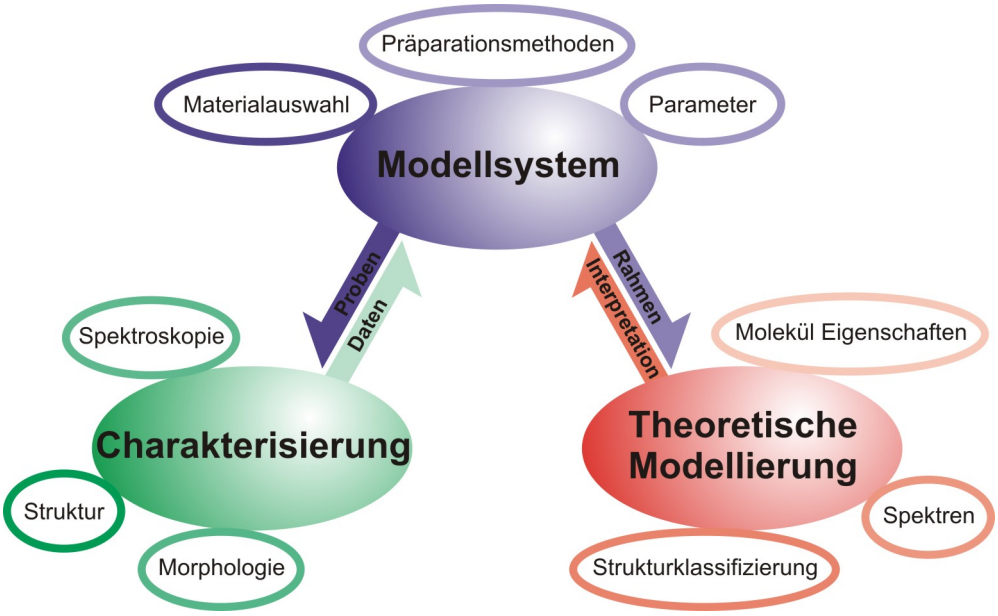

Abbildung 1.5: Modellsysteme als verbindendes Element zwischen experimentellen und theoretischen Ansätzen. Themengebiete dieser Arbeit sind mit den Hauptbegriffen verknüpft.

es mehr als die physisch greifbare Probe. Vielmehr ist es, im Rahmen einer physikalischen Fragestellung, ein Konzept, mit dem komplexe Zusammenhänge für Experiment und Theorie gleicher Maßen vereinfacht werden können, um Einblicke in die zu Grunde liegenden Phänomene zu erhalten. Der Idee von Modellsystemen soll in der vorliegenden Arbeit gefolgt werden, indem die einzelnen Projekte jeweils Aspekte der drei Hauptkategorien aus Abb. 1.5 miteinander verbinden. Die konkreten Fragestellungen entfallen dabei auf die Unterkategorien in den Nebenblasen.

Im ersten Teil der Arbeit wird es darum gehen die Auswahl an organischen Halbleitern, die sich als Basis für Modellsysteme eignen könnten, zu erweitern. Ausgangspunkt sind dabei polyaromatische Kohlenwasserstoffe, von denen bereits bekannt ist, dass sie viele vorteilhafte Eigenschaften besitzen. Durch Kollegen aus der Chemie wurden auf Basis dieser Verbindungen neue Moleküle synthetisiert, mit der Hoffnung die positiven Eigenschaften erhalten und ergänzen zu können. In dieser Arbeit werden Versuche unternommen die Substanzen zu Dünnfilmen zu prozessieren und in erster Linie mit Hilfe von Röntgenbeugung, sowie absorptionsspektroskopischen Methoden die Struktur und Eigenschaften der Filme aufzuklären. Dabei zeigt sich, dass die neuen Systeme oft die Vorteile der Ausgangssysteme verlieren, oder stark veränderte Eigenschaften aufweisen. Ursache für diese Modifikationen ist oft eine vollkommen geänderte Kristallstruktur. Es wird deutlich, dass die gezielte Kontrolle molekularer Eigenschaften bisher kaum auf Festkörpereigenschaften übertragen werden kann. Dadurch inspiriert, wird mittels Hirshfeldanalyse an einer Klassifizierung der Kristallstrukturen und ihrer zugrundeliegenden Wechselwirkungen gearbeitet. Ziel dieser Untersuchung ist es qualitative Zusammenhänge zwischen molekularen Eigenschaften und den intermolekularen Wechselwirkungen im Kristall zu identifizieren. Diese Erkenntnisse sind die Basis für Leitlinien zur Entwicklung neuer organischer Halbleiter mit Hinblick auf ihre Kristallstrukturen und Festkörpereigenschaften.

Im zweiten Teil dieser Arbeit geht es um die Anwendung von Modellsystemen im Bereich NEXAFS-Spektroskopie. Dabei wird ein besonders geeignetes System, basierend auf Perfluoropentacen, genutzt, um anhand von winkelaufgelösten Messungen, sowie einer

detaillierten theoretischen Modellierung der Spektren, Aufschluss über die Entstehung der Signatur im Bereich der Fluor-1s Absorptionskante zu erhalten. Die so gewonnenen Erkenntnisse sind genereller Natur und lassen sich auch auf andere fluorierte Moleküle übertragen. Vor dem Hintergrund des ersten Teils der Arbeit ist dies besonders wichtig, da Fluorierung wiederum eine der gängigen Strategien zur chemischen Modifikation von Halbleitermolekülen ist.

2. Moleküle und Methoden

Ziel dieses Methodenteils ist es, dem Leser die Grundkonzepte der verwendeten Messtechniken und Programme an die Hand zu geben. Keiner der folgenden Abschnitte hat den Anspruch, eine vollständige Darstellung des jeweiligen Themas zu liefern. Vielmehr geht es darum, ein Verständnis der im Verlauf dieser Arbeit gezeigten Ergebnisse zu ermöglichen, auch ohne dass spezielle Vorkenntnisse mitgebracht werden. Lediglich stellenweise werden Teilaspekte, die sich im Laufe der Arbeit als oftmals kritisch für das Verständnis herausgestellt haben, etwas genauer betrachtet. Ausnahmen von dieser Regel stellen der zweite Teil des NEXAFS-Abschnittes dar, in dem anhand einer speziellen Darstellung von Ergebnissen besonders aufschlussreich die grundlegenden physikalischen Prozesse erläutert werden, sowie das Kapitel über die Hirshfeldanalyse, da davon ausgegangen wird, dass diese Methode einer etwas ausführlicheren Darstellung bedarf, um die gezeigten Ergebnisse nachvollziehbar zu machen.

2.1 Molekülauswahl

Wie in der Einleitung ausgeführt, gibt es eine große Anzahl potentieller Halbleitermoleküle. Nicht jedes davon bringt jedoch die nötige Kombination günstiger Eigenschaften mit, um für weitergehende Untersuchungen oder gar großtechnische Anwendung geeignet zu sein. Im Rahmen dieser Arbeit werden Moleküle aus der Klasse der polyzyklischen

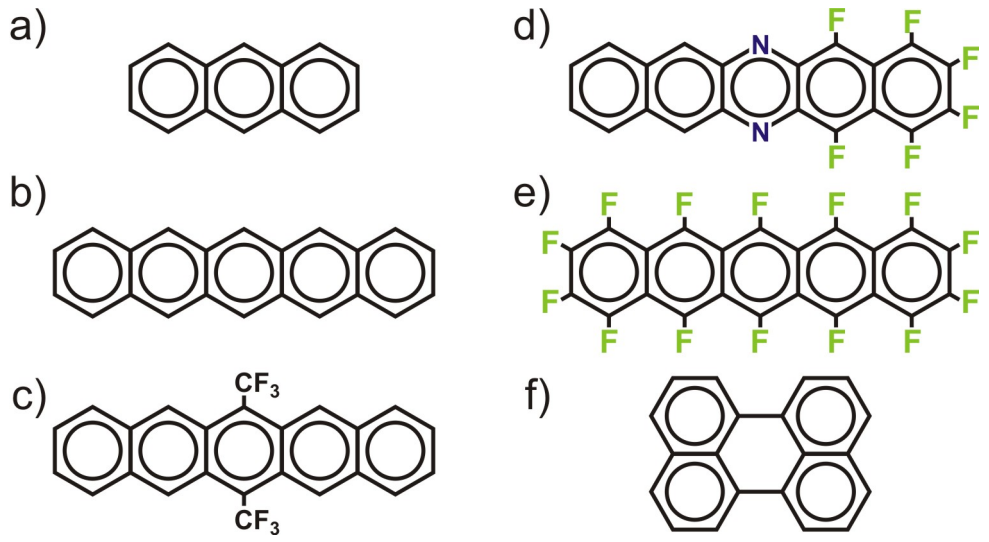

Abbildung 2.1: Beispiele polyzyklischer aromatischer Kohlenwasserstoffe: a) Anthracen ($C_{14}H_{10}$), b) Pentacen ($C_{22}H_{14}$), c) Bistrifluoromethylpentacene ($C_{24}F_6H_{12}$), d) Hexafluorodiazapentacen ($C_{20}N_2F_6H_6$), e) Perfluoropentacen ($C_{22}F_{14}$), f) Perylen ($C_{20}H_{12}$).

aromatischen Kohlenwasserstoffe (PAK) betrachtet, für die in Abb. 2.1 einige in dieser Arbeit relevante Beispiele gezeigt sind. Wie der Name andeutet, geht es um Moleküle, die mehrere aromatische Ringsysteme enthalten. Laut Definition müssen die Ringe des Weiteren so miteinander verbunden sein, dass mindestens zwei der Atome eines Zyklus an jeweils zwei Ringen beteiligt sind. Diese Randbedingung führt dazu, dass die Moleküle konjugiert sind und über ein delokalisiertes π-System verfügen, das sich über ihre gesamte Größe erstreckt. Dieser Punkt ist in mehrerlei Hinsicht entscheidend. Viele der höchsten Ladungsträgermobilitäten unter den organischen Verbindungen werden von PAK-Molekülen bzw. ihren Kristallen gehalten. Dafür wird unter anderem das ausgedehnte π-System verantwortlich gemacht, durch das der Ladungstransport innerhalb des Moleküls sehr effizient abläuft. Ein weiterer Effekt der Konjugation ist eine stets planare Molekülgeometrie. Diese führt zu vergleichsweise einfachen Kristallstrukturen, die von den Molekülen auch leichter angenommen werden. Deshalb führen viele dieser Stoffe leichter oder überhaupt erst zu geordneten, hoch kristallinen Dünnfilmen. Dieser Punkt wird auch dadurch begünstigt, dass sich unter den PAKs Vertreter mit einer passenden Sublimationsenthalpie finden um mittels OMBD (*Organic-Molecular-Beam-Deposition*) unter Vakuumbedingungen prozessiert zu werden. Bei dieser Technik, mit der sich das Wachstum kristalliner Dünnfilme besonders gut kontrollieren lässt, werden die Moleküle im Vakuum sublimiert und resublimieren auf dem gewünschten Substrat. Während dieses Prozesses können die Substrattemperatur, sowie die Rate, sehr genau gesteuert werden um optimale Wachstumsbedingungen zu schaffen. Deshalb sind Materialien von Vorteil, die bei Raumtemperatur einerseits im Vakuum fest vorliegen, sich andererseits jedoch mit moderaten Temperaturen sublimieren lassen, ohne das es zu thermisch angeregter Zersetzung kommt. So sublimieren z.B. alle Moleküle aus Abb. 2.1 im Ultrahochvakuum bei Temperaturen von weniger als 200°C. Das gutmütige Wachstumsverhalten, die hochgeordneten Schichten, sowie die außergewöhnlichen Transporteigenschaften machen viele PAKs zu vielversprechenden Halbleitermolekülen für weiterführende Untersuchungen. Tatsächlich ist Pentacen[1] (Strukur b) genau aus diesen Gründen eines der bestuntersuchten Halbleitermoleküle überhaupt [61, 62]. Deshalb dient es oft als Ausgangspunkt chemischer Modifikationen, die das Spektrum an Eigenschaften verbessern und erweitern sollen. Dies führt zu Derivaten, wie sie in Abb. 2.1 gezeigt sind. Ein solcher Ansatz wird auch in Teilen dieser Arbeit verfolgt. Neben dem Interesse an den Eigenschaften der Einzelmoleküle erlaubt aber gerade auch die gute Kenntnislage zu den Kristallstrukturen und ihrem Wachstum tiefer gehende Experimente. So sind mit der Campbell-Phase [63], der Siegrist-Phase [64] und der Dünnfilm-Phase [65] gleich drei Polymorphismen des Pentacens vollständig bekannt und für Perfluoropentacen sind es mit der *bulk-phase* [66] und der *π-stacked-phase* [67] immer noch zwei. Da hier nicht nur die Strukturen bekannt sind, sondern auch noch Möglichkeiten mit Hilfe des Substrates den Polymorphismus sowie teilweise auch Wachstumsrichtungen gezielt zu wählen [25], liefern diese Moleküle ideale Modellsysteme zur Untersuchung orientierungsabhängiger Eigenschaften, was in Abschnitt 5.8 genutzt wird.

[1] Acene sind lineare, aromatische Multiringmoleküle. Sie bilden damit einer Teilmenge der PAK.

2.2 Strukturanalyse

Die Strukturanalyse erfolgt hier in erster Linie mittels Röntgenbeugung, die oft mit der englischen Abkürzung XRD *X-Ray Diffraction* bezeichnet wird. Allgemein können sich hinter diesem Kürzel verschiedene Techniken verbergen, die auf Röntgenbeugung basieren. Im Zusammenhang mit dieser Arbeit wird aber vor allem Beugung in der grundlegenden Bragg-Brentano-Geometrie betrieben. In Abb.2.2b) ist ein Schema für solch einen Aufbau gezeigt. Die Probe wird unter einem Winkel Θ relativ zu den Netzebenen (blaue Ebenen) mit monochromatischer Röntgenstrahlung der Wellenlänge λ beleuchtet. Falls die Braggbedingung (siehe Gleichung 2.1) erfüllt ist, kann wiederum unter dem gleichen Winkel ein konstruktives Interferenzsignal detektiert werden. Relativ zum einfallenden Strahl steht der Detektor also unter einem Winkel 2Θ. Für eine Messung werden deshalb die Winkel Θ und 2Θ synchron variiert, sodass stets die Regel „Einfallswinkel gleich Ausfallswinkel“ erfüllt ist. Eine solche Θ-2Θ-Kopplung wird durch ein Goniometer realisiert, das im Fall des hier verwendeten Bruker D8 Discover die Probe und den Detektor mit mechanischen Abweichungen kleiner als 0.0001° um die entsprechenden Winkel bewegt. In der Praxis liegt die experimentelle Herausforderung in der Einjustage der Probe, mit der sichergestellt wird, dass die Netzebenen senkrecht zur φ-Achse liegen. Da die Kenntnis dieses Vorgehens aber zum Verständnis der Ergebnisse nicht nötig ist, wird hier auf die entsprechenden Details verzichtet. Ebenso sollen hier nicht alle in Abb.2.2a) im Strahlengang des Gerätes gezeigten Komponenten erläutert werden. Nur so viel sei erwähnt: Die besondere Herausforderung an die Technik liegt im Fall der organischen Dünnfilme in einem sehr kleinen Streuvolumen, sowie einem generell geringen Streuvermögen. Deshalb wird ein empfindliches Detektionssystem, in diesem Fall ein Si-Halbleiterdetektor, benötigt, in dem ein eindimensionales Array von Sensoren das Integrieren über einen größeren Winkelbereich erlaubt und so die Sensitivität steigert. Zudem wird der Röntgenstrahlung durch einen Göbelspiegel fokussiert. Hinzu kommt, dass zur Einjustage der Proben mehr Freiheitsgrade am Goniometer benötigt werden, als dies z.B. für die Pulverdiffraktometrie der Fall ist. Die hier beschriebene Θ-2Θ-Messung ist eine Messung in *Out-of-Plane*-Geometrie. Anordnungen, die in diese Kategorie gehören, zeichnen sich dadurch aus, dass die Dünnfilmebene bzw. die zugehörige Substratoberfläche senkrecht zur Strahlebene stehen. In dieser Geometrie können also ausschließlich Reflexe von Netzebenen detektiert werden, die parallel zur Substratoberfläche liegen. Obwohl dies wie eine starke Einschränkung

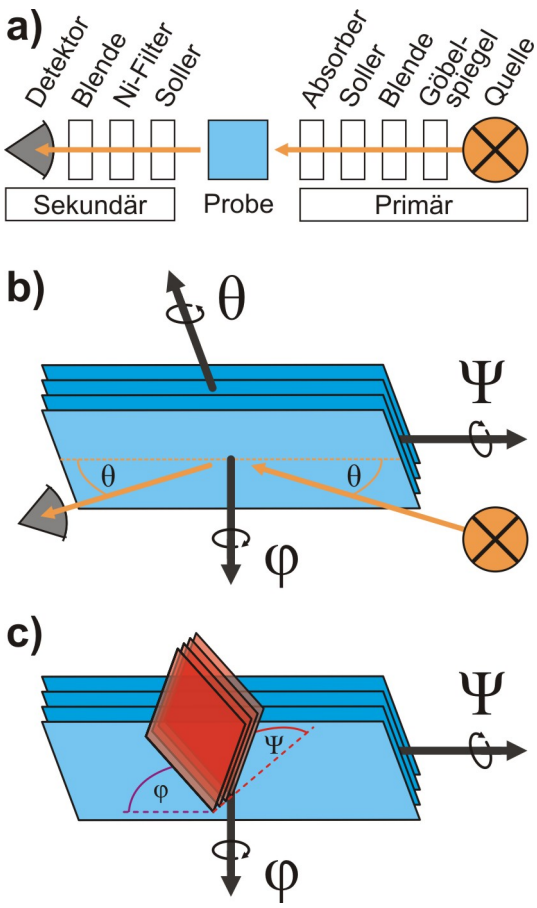

Abbildung 2.2: a) Komponenten im Strahlengang des Diffraktometers. b) Schema zur Bragg-Beugung. Zusätzlich sind relevante Achsen für *In-Plane*-Messungen eingezeichnet. c) Winkel für die Einjustage auf einen *In-Plane*-Reflex.

klingt, liefern diese Messungen bereits viele Informationen. So lässt sich beurteilen, ob kristallines Wachstum vorliegt und anhand von Peakbreiten lassen sich z.B. auch Aussagen über Kristallinität und Mosaizität treffen. Zudem kann, eine bekannte Kristallstruktur des Materials vorausgesetzt, direkt auf die Netzebene geschlossen werden, entlang derer sich die Moleküle auf dem Substrat anlagern. Damit ist, vom azemuthalen Freiheitsgrad abgesehen, auch die Orientierung der Moleküle relativ zum Substrat bekannt und nicht zuletzt können mittels der genauen Reflexposition Polymorphismen sicher unterschieden werden. Sollte die Struktur nicht bekannt sein, kann zumindest der Netzebenenabstand d der Hauptwachstumsrichtung mithilfe der Braggleichung bestimmt werden, wobei m eine natürliche Zahl ist und die Ordnung des Reflexes angibt:

$$m \cdot \lambda = 2 \cdot d \cdot \sin \Theta \tag{2.1}$$

Will man darüber hinaus auch noch azimuthale Informationen gewinnen, muss die *Out-of-Plane*-Geometrie verlassen werden, was in Abb.2.2b) einer Rotation um die Ψ-Achse entspricht und zu sogenannten *In-Plane*-Messungen führt. Obwohl sich die Beugung in solch einem Experiment wiederum vollständig durch die Braggbedingung interpretieren lässt, sind Messungen dieser Kategorie aus zwei systematischen Gründen signifikant schwieriger zu realisieren. Zum einen wird die Probe nun je nach Wahl von Ψ von der schmalen Seite bestrahlt, was das Streuvolumen weiter einschränkt, und zudem tragen im Fall einer polykristallinen Probe nicht mehr alle Domänen zum Signal bei, sodass die Reflexe nochmals deutlich schwächer werden. Zum anderen kommen mit Ψ und ϕ zwei Freiheitsgrade hinzu, sodass Reflexe zusammen mit Θ in einem dreidimensionalen Raum gesucht werden müssen, was die Einjustage nochmals erschwert. In Abb.2.1c) ist die Ausgangssituation für eine *In-Plane*-Messung schematisch gezeigt. Voraussetzung ist eine korrekte Einjustage auf die blauen Ebenen. Nun wird der Reflex der roten Ebenen gesucht. Dazu muss die Probe so gedreht werden, dass für die roten Ebenen die Braggbedingung gilt. Dazu muss um ϕ so weit gedreht werden, dass die Schnittgeraden der blauen und roten Ebenen parallel zur Ψ-Achse liegen und Ψ muss gerade um den Winkel zwischen den Ebenen verstellt werden. Um in der Praxis Aufschluss über die azimutale Ordnung einer Probe zu bekommen, werden der Ψ-Winkel sowie der Θ-Winkel aus der bekannten Kristallstruktur berechnet, das Diffraktometer entsprechend verfahren und anschließend ein ϕ-Scan gemacht, bei dem die Probe einmal um 360° gedreht werden kann. Für den Fall eines Einkristalls, wie es in Teilbild c) angedeutet ist, tritt dann im Allgemeinen nur ein Reflex auf. Sollte die Probe jedoch mehrere einkristalline Domänen besitzen, die sich epitaktisch am Substrat orientieren, spiegelt der ϕ-Scan die Symmetrie der Substratoberfläche wieder und polykristallines Wachstum würde zu einem konstanten Signal führen.
Durch ihre hohe Eindringtiefe und die notwendige Voraussetzung der Kristallinität liefert die Röntgenbeugung Informationen über die langreichweitige Ordnung eines Systems. Zudem erlaubt diese Technik die genaue Anordnung von Molekülen in einer Struktur mit hoher Präzision zu bestimmen. Ist das Streuvolumen jedoch zu klein oder ist die Probe amorph ist XRD „blind“ und es bedarf einer komplementären Technik. Insbesondere für Monolagen an Grenzschichten ist dies wichtig. Für solche Systeme kann die molekulare Orientierung mit Hilfe der NEXAFS-Spektroskopie untersucht werden, die im übernächsten Abschnitt vorgestellt wird.

2.3 Photoelektronenspektroskopie

Die Röntgen Photoelektronenspektroskopie XPS (englisch: *X-ray Photoelectron Spectroscopy*) ist vermutlich die fundamentalste aller Röntgenabsorptionstechniken und besitzt einen einfach zu skizzierenden Aufbau, der in Abb. 2.3a) gezeigt ist. Die Probe wird mit monochromatischem Röntgenlicht bestrahlt und die austretenden Elektronen energieaufgelöst detektiert. Dass dieser Aufbau vergleichsweise einfach aussieht, liegt daran, dass sich ein Großteil des technischen Aufwandes hinter dem Begriff „Analysator“ verbirgt. Dabei sind kommerziell erhältliche Halbkugelenergieanalysatoren, wie auch hier einer angedeutet ist, der derzeitige Standard für verschiedene Elektronenspektroskopiemethoden. Zum Verständnis der später präsentierten Ergebnisse ist die genaue Funktionsweise des Analysators jedoch nicht entscheidend, sodass hier der Fokus auf die grundlegenden Prozesse rund um die gemessenen Elektronen gelegt wird. In Abb. 2.3c) sind die beiden wichtigsten Effekte schematisch dargestellt. Ist die Photonenenergie größer als das Ionisationspotential des absorbierenden Elektrons, kommt es zum Photoeffekt und das Elektron wird aus dem Atom geschlagen. Für die leichten Elemente der Organik werden Röntgenphotonen überwiegend von Elektronen der K-Schale, also 1s-Elektronen, absorbiert. Der zweite Prozess ist der Augereffekt. Dabei handelt es sich um einen Folgeeffekt der Ionisation. Um Energie abzubauen relaxiert ein Elektron aus einer höheren Schale in das frei gewordene Loch. Die Energiedifferenz der beiden beteiligten Niveaus wird dabei an ein Nachbarelektron übertragen, das seinerseits aus dem Atom geschlagen wird. Für die Interpretation der Spektren ist wichtig, dass sich Elektronen aus diesen beiden Prozessen durch eine Variation der Anregungsenergie unterscheiden lassen. Augerelektronen stammen aus einem Schalenübergang und haben damit unabhängig von der Photonenenergie immer die selbe charakteristische kinetische Energie, während sie sich für Photoelektronen ändert. Welche Informationen lassen sich mit XPS gewinnen? Aufgrund der geringen freien Weglänge der Elektronen im Festkörper ist XPS eine oberflächensensitive Technik. Dies kann durch Variation des Austrittswinkels der Elektronen, also durch Drehen der Probe, noch verstärkt werden, sodass eine Tiefenprofilierung möglich ist. Durch das Auftreten charakteristischer Peaks können Elemente nachgewiesen werden. So lässt sich z.B. die Reinheit von Substratoberflächen oder das erfolgreiche Aufbringen von Molekülen prüfen. Das 1s-Niveau wird durch chemische Bindungen je nach Bindungspartner leicht verschoben. Dieser Effekt wird *chemical shift* genannt. Indem die Bindungsenergien genau bestimmt werden, können

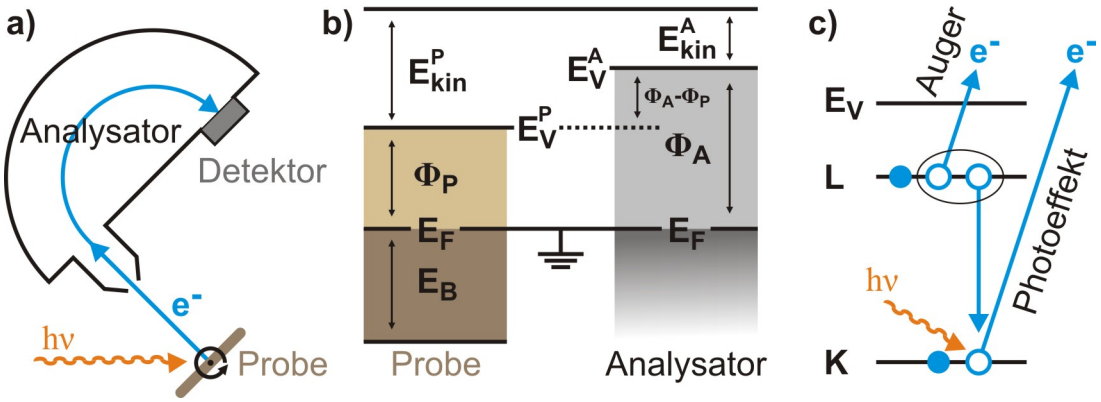

Abbildung 2.3: a) Schematischer XPS-Aufbau. b) Energieniveausschema zur Kalibrierung der XP-Messung. c) Elektronenbesetzung für Auger- und Photoeffekt.

auch Erkenntnisse über die Bindungssituation gewonnen werden. So lässt sich an einer Grenzschicht z.B. die Ankerung eines chemisch gebundenen Moleküls untersuchen [38]. Um die Bindungsenergie genau bestimmen zu können, benötigt man die Grundgleichung der Photoelektronenspektroskopie, in der die kinetische Energie der Elektronen E_{kin}, die Photonenenergie $h\nu$, die Bindungsenergie E_B und die Austrittsarbeit des Analysators Φ_A in einer Energiebilanz zusammengebracht werden:

$$E_{kin} = h\nu - E_B - \Phi_A \tag{2.2}$$

Da es bisweilen zu Irritation darüber kommt, dass die Austrittsarbeit der Probe Φ_P nicht benötigt wird, folgt hier noch ein Blick auf die Herleitung. Betrachtet man in Abb. 2.3b) nur die linke Seite des Schemas, wird der Ursprung des Problems deutlich. Allerdings misst der Anlaysator nicht E^P_{kin}, sondern E^A_{kin}. Ursache hierfür ist, dass sich experimentell kein gemeinsames Vakuumniveau E_V für Probe und Analysator einstellen lässt. Lediglich das Ferminiveau kann durch eine gemeinsame Erdung angeglichen werden. Für die kinetische Energie gilt also:

$$\begin{aligned} E_{kin} &= E^A_{kin} \\ &= E^P_{kin} - (\Phi_A - \Phi_P) \\ &= h\nu - E_B - \Phi_P - (\Phi_A - \Phi_P) \\ &= h\nu - E_B - \Phi_A \end{aligned}$$

2.4 Röntgenabsorptionspektroskopie nahe der Kante

Die Abkürzung NEXAFS steht streng genommen nicht für die Messtechnik, sondern für das Phänomen, das mit ihr vermessen werden soll, da NEXAFS in voller Länge *Near Edge X-ray Absorption Fine Structure* bedeutet. Es ist also korrekter, von Nah-Kanten-Röntgen-Absorbtions-Fein-Struktur-Spektroskopie zu sprechen, was in der Praxis aber nicht geläufig ist, sodass NEXAFS synonym für Technik und Signatur verwendet wird. Bei der Feinstruktur handelt es sich um jene Resonanzen, die im Spektrum in direkter Nachbarschaft zu einer Röntgenabsorptionskante auftreten und damit unter anderem Informationen über unbesetzte Zustände enthalten. Wie genau diese Spektren gewonnen werden, soll im Folgenden aus zwei Gründen nur kurz zusammen gefasst werden. Der erste Grund ist, dass es zu diesem Thema bereits sehr ausführliche Abhandlungen gibt. Mit dem Buch von J. Stöhr [39] existiert ein Standardwerk zu dieser Technik und Artikel, wie z.B. der von Watts *et al.* [40], schildern detailliert das Vorgehen zur Datenauswertung. Zudem hat C. Schmidt in seiner Dissertation unter anderem einige Eigenheiten der HE-SGM Beamline, die im Rahmen der vorliegenden Arbeit überwiegend zum Einsatz gekommen ist, untersucht. So beschreibt er z.B. das Hystereseverhalten des Monochromators im Bereich der F1s-Bindungsenergien [41]. Der zweite Grund ist, dass die in Abschnitt 5.6 vorgestellte Veröffentlichung [42] eine umfassende Darstellung der Messtechnik und ihrer Nutzung für die Orientierungsbestimmung von Molekülen beinhaltet, sodass hier eine Doppelung vermieden werden soll. Deshalb folgt hier auf eine kurze Darstellung des Grundkonzeptes ein Abschnitt, indem anhand einer speziellen zweidimensionalen Darstellung von Ergebnissen die Fülle an physikalischen Prozessen, die für diese Messtechnik relevant sind, aufgezeigt wird.

2.4.1 Das Grundkonzept

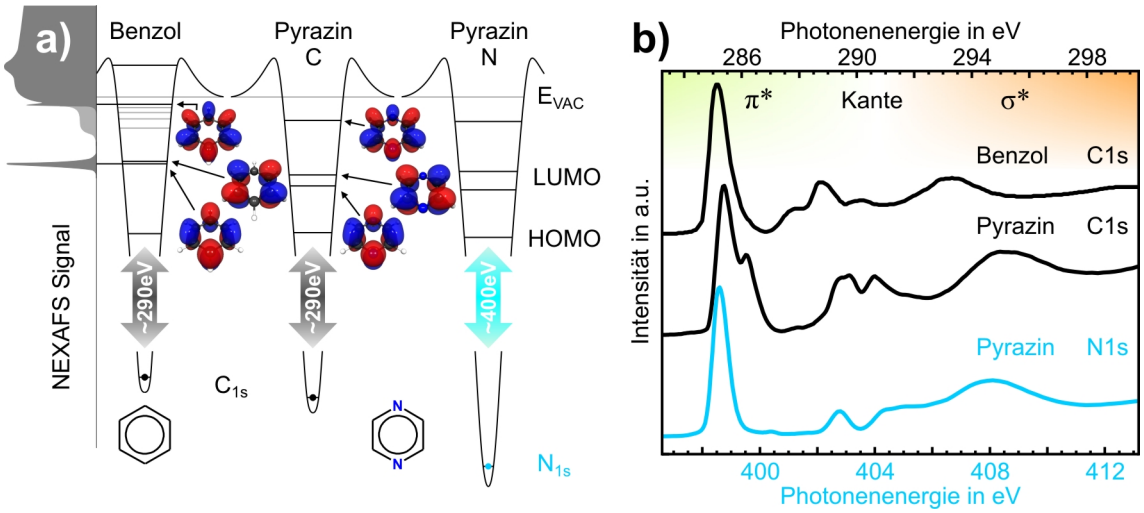

Abbildung 2.4: a) Schema zur Entstehung der NEXAFS-Signatur von Benzol und Pyrazin. Wesentliche Energieniveaus der Moleküle sind mit zugehörigen Orbitalen dargestellt und werden mit dem Beispielspektrum auf der linken Seite in Korrelation gebracht. b) Spektren für die drei Beispielszenarien aus a). Die C1s- und N1s-Energieskalen sind um die Differenz der 1s-Bindungsenergien gegeneinander verschoben [43]. Das Benzolspektrum stammt aus [44]. Abbildungen wurde leicht modifiziert aus [42] übernommen.

Die Grundidee der Messtechnik ist eine Anregung kernnaher Elektronen in unbesetzte Zustände, die zur Absorption eines Photons mit der entsprechenden Übergangsenergie führt. Im Grunde soll also eine Absorptionsmessung analog zu Techniken wie UV-Vis durchgeführt werden, mit dem Unterschied, dass Röntgenstrahlung verwendet wird. Technisch bringt dies jedoch erhebliche Probleme mit sich: Zum einen wird eine starke Röntgenquelle mit kontinuierlichem Spektrum benötigt und zum anderen erfordert die Detektion von Röntgenquanten mehr Aufwand. Das erste Problem lässt sich mit Synchrotronstrahlung lösen. Elektronenspeicherringe wie BESSY II in Berlin stellen die erforderliche Strahlung zur Verfügung, sodass die Photonenenergie für die Messung mit Hilfe eines Monochromators variiert werden kann. Das zweite Problem wird geschickt umgangen, indem nicht die Abschwächung des Primärsignals direkt, sondern Sekundäreffekte in Form von Elektronen, die aus der Probe gelöst werden, gemessen werden. Die Idee dabei ist, dass die Absorption zu einem angeregten Zustand führt, der im Fall leichter Elemente vor allem durch Augerprozesse relaxiert. Die Augerelektronen verlassen die Probe und können als Strom detektiert werden. Unter der Annahme, dass die Anzahl von Augerprozessen proportional zur Anzahl der ursprünglichen Anregungen ist und diese wiederum proportional vom Absorptionsvermögen abhängt, ist der gemessene Strom ein Maß für Letzteres. Anstelle der Intensität von Röntgenstrahlung kann also im einfachsten Fall ein Probenstrom im pA-Bereich gemessen werden, sodass lediglich ein entsprechender Verstärker benötigt wird. Ein solcher Messmodus wird *Total Electron Yield* (TEY) genannt. Weitere Messmodi sind der *Partial Electron Yield* (PEY) bei dem mit Hilfe eines Channeltrondetektors und einem elektrischen Gegenfeld nur Elektronen mit einer kinetischen Mindestenergie detektiert werden, sowie der *Auger Electron Yield*(AEY) bei dem ein Energieanalysator benötigt wird, um nur Elektronen mit einer definierten kinetischen Energie zu berücksichtigen. Der Vergleich von Daten aus unterschiedlichen Messmodi kann zur Tiefenpro-

filierung genutzt werden (siehe Abschnitt 5.6). In Abb.2.4a) ist schematisch dargestellt, wie das Spektrum eines Moleküls wie Benzol interpretiert werden kann: C1s-Elektronen können in die LUMOs des Moleküls angeregt werden, was zu Peaks im Spektrum führt, wobei die Signatur konjugierter Moleküle im Bereich vor der Kante von π^*-Resonanzen dominiert wird. Die Kante selbst entsteht durch direkte Anregung der 1s-Elektronen in das Kontinuum oberhalb der Vakuumenergie. Im Spektrum wird die Kante als eine Stufe sichtbar, die ihrerseits aber von diskreten Anregungen überlagert sein kann, wie in Teilbild a) auf der linken Seite angedeutet. Der Kante direkt vorgelagert findet sich häufig eine Serie σ-artiger Zustände, die als Rydbergzustände bekannt sind und sich oft nicht auflösen lassen (hier als hellgraue Stufe im Spektrum eingezeichnet), während oberhalb der Kante die eigentlichen σ^*-Resonanzen liegen, die sich durch eine größere Halbwertsbreite aufgrund kürzerer Lebensdauern der zugehörigen angeregten Zustände auszeichnen. Durch die großen Unterschiede in der Bindungsenergie der 1s-Zustände ist NEXAFS eine elementspezifische Technik. So können, wie in Teilbild b) gezeigt, für das Pyrazinmolekül zwei verschiedene Spektren aufgenommen werden: Eines an der C1s- und eines an der N1s-Kante. Obwohl die Zielzustände die selben sind und der Startzustand lediglich energetisch tiefer liegt, ergeben sich jedoch zwei unterschiedliche Signaturen. Erklärt werden kann dies anhand der in a) gezeigten Orbitale. Durch die geringere Symmetrie des Pyrazins gegenüber dem Benzol wird die Entartung der beiden LUMOs aufgehoben, wodurch die beiden führenden Resonanzen im C1s-Spektrum entstehen. Im N1s-Spektrum erscheint die Zweite jedoch nicht, da das entsprechende Orbital an den N-Positionen eine Knotenebene hat, sodass das Überlappintegral zwischen N1s und LUMO+1 den Wert 0 annimmt und eine Anregung nicht möglich ist. An dieser Stelle wird deutlich, wie sehr die Interpretation der NEXAFS-Spektren von einer theoretischen Modellierung der Systeme profitieren kann und es ist leicht vorstellbar, dass die Spektren komplexerer Systeme sich andernfalls gar nicht mehr deuten lassen. Als letzter Punkt sei in diesem Abschnitt noch die Dichroismusmessung erwähnt. NEXAFS ist aufgrund der geringen Ausdringtiefen der Elektronen äußerst oberflächensensitiv, sodass es möglich ist, Informationen über Mono- oder sogar Submonolagen von Molekülen zu bekommen. Dabei wird gerne genutzt, dass sich die Synchrotronstrahlung auch im Röntgenbereich linear polarisiert erzeugen lässt. Übergangsdipolmomente sind vektorielle Größen und die zugehörige Absorption ist maximal, wenn E-Feldvektor und Übergangsdipolmoment parallel sind. Falls die Moleküle an der Oberfläche eine Vorzugsorientierung besitzen, führt Drehen der Probe relativ zum E-Feldvektor zu einem winkelabhängigen Intensitätsverlauf der Resonanzen, aus dem die Orientierung des Übergangsdipolmomentes und damit ggf. auch die Orientierung des Moleküls bestimmt werden kann. Insbesondere ist dies auch für Schichten möglich, die für eine Untersuchung mittels Röntgenbeugung zu dünn sind. Zudem sind auch Effekte zugänglich, bei denen sich nur die Moleküle in unmittelbarem Kontakt zu einer Grenzschicht anders verhalten als benachbarte Schichten. Da dieses Verfahren Kerninhalt der in Abschnitt 5.6 präsentierten Veröffenlichung ist, sei für weitere Details auf die dortigen Ausführungen verwiesen.

2.4.2 Anregungsenergieabhängige Photoelektronenspektroskopie

Durch kontinuierliche Verbesserungen der Messsoftware an der HE-SGM Beamline, an denen ich beteiligt war, die aber insbesondere durch Tobias Breuer voran getrieben wurden, ist es dort inzwischen möglich, in allen drei oben beschriebenen Messmodi Spektren aufzunehmen. Insbesondere die Nutzung des Energieanalysators erweist sich in diesem Zu-

sammenhang als nützlich, da er die Wahl eines beliebigen Messbereichs erlaubt, während die anderen Methoden stets integrierte Spektren liefern. NEXAFS-Spektren lassen sich mit dem Analysator auf zwei Wegen gewinnen: Entweder man nutzt ihn direkt, indem die Zählrate während der Variation der Photonenenergie aufgezeichnet wird, oder es werden XP-Spektren für eine Serie von Anregungsenergien aufgezeichnet, aneinander gereiht und die NEXAFS-Spektren indirekt als vertikale Schnitte der so gewonnenen zweidimensionalen Darstellung extrahiert. (siehe Abb.2.5) Die Aufnahme solch einer Serie ist jedoch nur problemlos möglich, wenn die Synchrotronquelle über längere Zeiträume hinweg (einige Stunden) konstante Intensitäten bereitstellt. Am BESSY II ist dies in jüngerer Zeit durch die Einführung des sogenannten *Top Up Mode*, bei dem der Ringstrom konstant gehalten

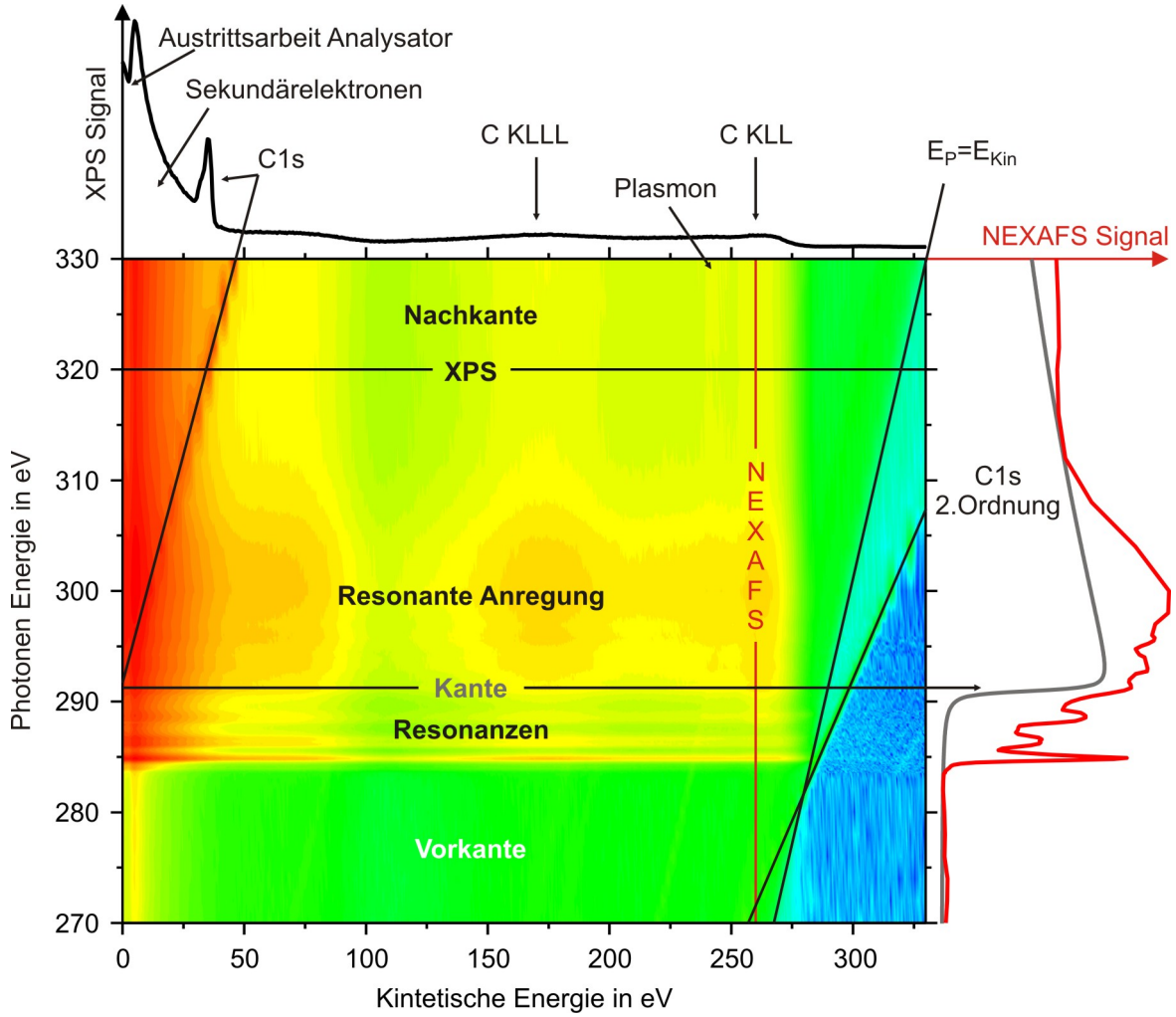

Abbildung 2.5: Die dargestellte Falschfarbendarstellung entsteht durch Aneinanderreihung einer Serie von XPS-Messungen mit Anregungsenergien von 270 eV bis 330 eV. Die Zählraten sind logarithmisch aufgetragen, wobei blau für geringe und rot für hohe Raten steht. Entlang der mit „XPS“ bzw. „NEXAFS“ beschrifteten Linien wurden die oben und rechts dargestellten Schnitte extrahiert. Von der Photonenenergie abhängige Merkmale sind durch schräge Linien markiert, während typische Bereiche eines NEXAFS-Spektrums im Plot beschriftet sind. Merkmale, die im Plot vertikal verlaufen, sind an der oberen Seite beschriftet. Das NEXAFS-Spektrum ist mit einem typischen Intensitätsverlauf der Kante in grau unterlegt. Die Probe ist ein Schichtsystem aus einer Monolage C_{60} auf einer Pentacenmultilage auf SiO_2.

wird, möglich geworden. Die in Abb. 2.5 gezeigte Messung wurde an einem Schichtsystem aus einer Monolage C_{60} auf einer Pentacenmultilage auf SiO_2 durchgeführt, wobei im Folgenden entscheidend ist, dass die Probe praktisch nur aus Kohlenstoff besteht, da die Organik zu dick ist um Signale vom Substrat durchzulassen und Wasserstoff in diesem Energiebereich nicht von Bedeutung ist[2]. Die hier gezeigte Falschfarbengrafik, in der der Farbcode die logarithmischen Zählraten widerspiegelt, verdeutlicht den Zusammenhang zwischen XP- und NEXAFS-Spektroskopie und macht zudem einige spektrale Merkmale eindrucksvoll sichtbar, die hier kurz vorgestellt werden. Jeder horizontale Schnitt entspricht einem XP-Spektrum, wobei der generelle Trend gilt, dass für kleine E_{kin} aufgrund von Sekundärelektronen hohe Raten beobachtet werden, während am anderen Ende des Spektrums immer weniger Elektronen detektiert werden. Der Intensitätssprung entlang der Geraden $E_P = E_{Kin}$, der durch Elektronen mit maximal möglicher kinetischer Energie entsteht, ist gut zu erkennen. Obwohl es unterhalb dieser Geraden keine Photoelektronen geben sollte, ist eine zweite Linie mit kleinerer Steigung zu erkennen. Hierbei handelt es sich um C1s-Elektronen, die mit Photonen aus der 2.Beugungsordnung des Monochromators, also mit doppelt so hoher Energie wie eigentlich vorgesehen, aus ihren Atomen gelöst wurden. Aufgrund des *Spherical Grating Monochromators* liegt die Intensität der 2.Ordnung an der HESGM Beamline aber nur bei 2% der 1.Ordnung und ist damit in vielen Fällen vernachlässigbar klein. Die regulären C1s-Elektronen sind hingegen links oben als schräge Linie zu erkennen. Bedenkt man, dass NEXAFS-Spektren sich hier als vertikale Schnitte ergeben, wird deutlich, dass Photoelektronen mit steigender Photonenenergie in ein Spektrum „hinein schieben“ können, was im Falle von TEY oder PEY zu einer Kante führt und im AEY einen artifiziellen Peak erzeugen kann. Besonders wenn weitere Elemente im Spiel sind, ist es deshalb wichtig, auf eine günstige Wahl von Gegenfeldern für den PEY bzw. kinetischen Energien für den AEY zu achten. Im oben gezeigten XP-Spektrum scheint es ganz links einen weiteren Peak zu geben. Dies ist jedoch ein Artefakt, da die kinetische Energie mit der Austrittsarbeit des Detektors kalibriert ist, sodass die Werte direkt über die Photonenenergie in Bindungsenergien übersetzt werden können (siehe Gl. 2.2). Bedenkt man wiederum, dass die NEXAFS-Spektren vertikalen Schnitten entsprechen, wird in diesem Zusammenhang deutlich, dass die Spektren weitestgehend unempfindlich gegen ein Verschieben der kinetischen Energieachse sind, da die genaue kinetische Energie der Elektronen für NEXAFS (abgesehen von der Tiefenprofilierung) weitestgehend unwichtig ist. Es zählt nur die Gesamtzahl. Deshalb ist NEXAFS bis zu einem gewissen Grad unempfindlich gegen eine Aufladung der Probe, die in einem XP-Spektrum unmittelbar zu verschobenen Signalen führt. In der Mitte des Plots sind einige charakteristische Bereiche eines NEXAFS-Spektrums benannt, die sich in Verbindung mit dem Beispielspektrum auf der rechten Seite oft selbst erklären. Besonders wichtig ist hier die namensgebende Kante, in deren Bereich der Photoeffekt zu einem stufenartigen Anstieg der Intensität führt. Zur Illustration ist auf der rechten Seite ein theoretischer Verlauf unterlegt, wie er auch in den Abschnitten 5.6 und 5.7 verwendet wurde. Gut zu sehen ist, dass das Absorptionsvermögen, welches auf dem Photoeffekt basiert, mit zunehmendem energetischem Abstand von der Kante abnimmt. In der Nähe der Kante ist das Absorptionsvermögen wegen des Photoeffekts und unbesetzter Zielzustände der Moleküle also besonders hoch. Abschließend soll hier ein Blick auf spektrale Merkmale geworfen werden, die sich im Plot durch vertikale Linien oder vielmehr Bereiche zeigen.

[2]Die Spektren in Fig. 6 zum Thema Tiefenprofilierung in Abschnitt 5.6 sind Ausschnitte der hier gezeigten Messung. Das Schichtsystem wurde ursprünglich zur Demonstration des Tiefeneffektes ausgewählt.

Diese beruhen auf Augerprozessen, da die Energien der Elektronen unabhängig von den Anregungsenergien sind. Für den AEY sind diese Bereiche besonders interessant, da hier Spektren mit Elektronen aufgenommen werden können, die aus einem bestimmten Prozess stammen. Indem ungestörte Augerelektronen detektiert werden erreicht man z.B. die höchste Oberflächensensitivität. Insgesamt fallen drei Merkmale auf. Im Bereich von $E_{Kin} = 260\,\text{eV}$ liegt die Kohlenstoff KLL-Linie. Dieser Bereich ist damit die native Wahl um im AEY zu messen, sodass das Beispielspektrum auch an dieser Stelle entnommen wurde. Weiter links tritt eine weitere Linie auf, die auf die Anregung eines Plasmons zurückzuführen ist und somit zur KLL-Linie gehört. Ein Merkmal, dass tatsächlich erst durch diese 2D-Darstellung ins Bewusstsein gerückt ist, da Kohlenstoff in den Standardtabellenwerken keine weiteren nennenswerten Augerübergänge hat und die leichte Welle im XP-Spektrum kaum als Signal zu erkennen ist, tritt zwischen 150 eV und 190 eV auf. Hierbei dürfte es sich um Elektronen aus einem Doppel-Augerprozess handeln, bei dem zwei Elektronen zeitgleich aus dem Atom geschlagen werden, die sich die Energie des Primärübergangs teilen. So entsteht eine kontinuierliche Energieverteilung, in der aber Aufteilungen, in denen ein Partner nahezu die gesamte Energie trägt, wahrscheinlicher sind. Dies erklärt die große Breite der „Linie“. Obwohl Doppel-Augerprozesse je nach Element und Bindungszustand mit einem deutlichen zweistelligen Prozentsatz an der Gesamtheit der Augerprozesse beteiligt sind, finden sich aufgrund der hohen experimentellen Anforderungen diesen Übergang selektiv nachzuweisen jedoch nur wenige Daten in der Literatur, besonders dann, wenn es um Elemente abseits der achten Hauptgruppe geht. Eine Veröffentlichung aus dem Jahr 2015 bestätigt jedoch, dass mit Elektronen aus diesem Prozess in dem hier beobachteten Energiebereich zu rechnen ist. [46]

2.5 GAMESS

GAMESS steht für *General Atomic and Molecular Electronic Structure System* und ist ein für akademische Anwendung frei erhältliches Programmpaket. [47, 48] Von seinem Funktionsumfang her ist es vergleichbar mit dem weitverbreiteten, kommerziellen Gaussian-Code. Im Gegensatz zu den anderen hier vorgestellten Programmen ist GAMESS-US nicht auf eine spezielle Anwendung ausgerichtet, sondern stellt eine Fülle von Methoden zur Verfügung, die für verschiedene Fragestellungen genutzt werden können. Wie umfangreich die Möglichkeiten sind, wird anhand der Dokumentation der Input-Befehle deutlich. In diesem recht knapp zusammengefassten, über 500 Seiten starken Dokument finden sich ca. 160 Input-Gruppen für verschiedene Methoden, die ihrerseits viele Unterbefehle haben, die wiederum unterschiedliche Parameter übernehmen können [49]. Von dieser Fülle an Optionen wird hier jedoch nur ein kleiner Teil benötigt. Folgende Eigenschaften wurden im Rahmen dieser Arbeit mit GAMESS behandelt: Molekülgeometrie, Energieniveaus (HOMO-LUMO-Energien), Dipol- sowie Quadrupolmomente und α-Polarisierbarkeiten. Zudem basiert die Visualisierung von Orbitalen, Elektronendichteverteilungen und Elektrostatischen Konturen in vielen Fällen auf Ergebnissen der GAMESS-Rechnungen. Analog zu den Erläuterungen der experimentellen Methoden wird hier ein Überblick über die verwendeten Methoden gegeben werden, um die später gezeigten Ergebnisse nachvollziehbar zu machen. Für Details zu den theoretischen Grundlagen sei hier auf entsprechende Literatur verwiesen [50].
Ergebnisse der in dieser Arbeit zusammengefassten Veröffentlichungen wurden überwiegend mit DFT-Rechnungen unter Verwendung des B3LYP Funktionals und einem 6-311G(d,p) Basissatz gewonnen. Dabei fiel die Wahl aus zwei Gründen auf das B3LYP

Funktional: Zum einen liefert es für die hier betrachteten Eigenschaften vergleichsweise zuverlässige Ergebnisse, zum anderen ist es äußerst populär, sodass Vergleiche mit anderen Arbeiten erleichtert werden [51]. Für den Basissatz gilt eine ähnliche Überlegung. Er stellt einen guten Kompromiss zwischen Genauigkeit und Rechenaufwand dar und ist ebenso wie das Funktional für die hier relevanten Anwendungen weit verbreitet. Da die DFT-Rechnungen hier in erster Linie unterstützend bei der Interpretation helfen sollten, lag das Augenmerk vor allem auf einer möglichst „robusten“ Auswahl, die Vergleiche ermöglicht, auch wenn es für viele Detailfragen jeweils leistungsfähigere Funktionale gibt [51].
Viele der Rechnungen lassen sich mit den Defaulteinstellungen von GAMESS realisieren, sodass im Folgenden auf Abweichungen hiervon eingegangen werden soll. Für sämtliche Rechnungen ist jeweils eine Strukturoptimierung des Moleküls Ausgangspunkt. Dabei wird stets die Molekülsymmetrie berücksichtigt. Das spart nicht nur Rechenzeit, sondern stellt auch sicher, dass die Moleküle innerhalb der Rechnungen entlang der Koordinatenachsen orientiert sind, sodass sich insbesondere die tensoriellen Größen leichter vergleichen lassen, da die entsprechenden Hauptachsen aufgrund der hohen Molekülsymmetrie oft mit den Koordinatenachsen zusammenfallen. Bisweilen ist es problematisch für den ersten Schritt der Optimierung Konvergenz im SCF-Prozess zu erreichen. Dieses Problem wird auch in der Dokumentation für Multi-Ring-Moleküle erwähnt und kann durch ein Anheben des Grenzwertes für lineare Abhängigkeit (QMTTOL)[3] behoben werden [49]. Dipolmomente werden standardmäßig ausgegeben, während Quadrupolmomente gesonderd angefordert werden müssen (IEMOM). Allerdings bringen sie, im Gegensatz zur Polarisierbarkeit (FFIELD) keine zusätzlichen Anforderungen an die Rechnung mit sich. Für letztere muss die Genauigkeit, mit der die Wellenfunktion bestimmt wird, erhöht werden, sodass kleinere Konvergenzkriterien (CONV), sowie kleinere Schwellwerte, bis zu denen Integrale und Basisfunktionen ausgewertete werden (ICUT, ITOL), Anwendung finden. Für besonders genaue Ergebnisse werden in diesem Zusammenhang auch größere Basissätze empfohlen [49], sodass die hier gezeigten Ergebnisse vor allem in einem qualitativen Sinne genutzt werden, um Trends herauszuarbeiten. Sowohl zum Erstellen der Input-Dateien, als auch für die Darstellung der Ergebnisse, liefert wxMacMolPlt ein leistungsfähiges, grafisches Benutzerinterface, mit dem in vielen Fällen die Orbitalvisualisierung vorgenommen wurde [52]. Dieses Programm ist auch in der Lage elektrostatische Konturplots zu erzeugen. Aufgrund der ansprechenderen Darstellung wurde zu diesem Zweck aber auf Molekel zurückgegriffen [53].

2.6 StoBe

StoBe steht für Stockholm-Berlin, was den Wirkungsstätten der beiden Hauptautoren des Codes - L.G.M. Pettersson und K.Hermann - entspricht [54]. Dabei handelt es sich um einen DFT-Code, der speziell dazu entwickelt wurde Übergänge, in denen kernnahe Elektronen involviert sind, zu modellieren. Damit lassen sich insbesondere Prozesse der Röntgenabsorption berechnen, was im Rahmen dieser Arbeit speziell NEXAFS-Spektren betrifft. Ähnlich wie im Fall der NEXAFS-Technik selbst, soll die Darstellung hier kurz gehalten werden, da eine grobe Betrachtung des Programms bereits in meiner Masterar-

[3] Die etwas kryptischen Abkürzungen in diesem Abschnitt sind die entsprechenden GAMESS-Befehle für die im Text erwähnten Modifikationen. Sie sollen es ggf. erleichtern die entsprechenden Stellen in den Input-Dateien, bzw. in der Dokumentation zu finden.

beit erfolgt ist [55], vor allem aber im Abschnitt 5.7 ein Artikel vorgestellt wird, der sich detailliert mit der Berechnung der NEXAFS-Spektren beschäftigt [45]. Am einfachsten lassen sich die Schritte der StoBe-Rechnung anhand einer Grafik aus der genannten Veröffentlichung, die in Abb. 2.6 zu sehen ist, nachvollziehen. Ausgangspunkt ist in jedem Fall eine Optimierung der Molekülestruktur unter Verwendung des RPBE-Funktionals und eines TZVP Basissatzes. Die hier gewonnene Struktur wird in allen weiteren Schritten verwendet[4]. Als nächstes folgen Grundzustandsrechnungen für alle nicht symmetrieäquivalenten Anregungszentren C_i.[5] An dieser Stelle ist ein entscheidender Kunstgriff nötig, um die 1s-Elektronen unterscheidbar zu machen. Hintergrund ist, dass die Ausgangszustände der NEXAFS-Übergänge offenbar stark lokalisiert sind, was z.B. an experimentellen Daten wie in Abb. 2.4b) deutlich wird. Beim Aufbau der Wellenfunktion des Moleküls im Rahmen des LCAO-Ansatzes (*Linear Combination of Atomic Orbitals*) werden jedoch auch Kombinationen aus den 1s-Orbitalen gebildet, die in Abb. 2.7 gezeigt sind. Darunter finden sich die sechs wohlbekannten π-Orbitale des Benzol, die sich aus der Symmetrisierung der zugehörigen p-Orbitale ergeben. Obwohl die 1s-Orbitale keinerlei Bindung ausbilden, sind die aus ihnen gebildeten σ-Orbitale im Sinne der Elektronenverteilung jedoch genauso delokalisiert wie die π-Orbitale. Insbesondere könnte keiner der sechs Ausgangszustände einem bestimmten Atom als Anregungszentrum zugeordnet werden. Deshalb wird nur noch das Anregungszentrum mit einem vollen Basissatz, der alle Elektronen des Atoms repräsentiert modelliert. Tatsächlich kommt hier ein IGLO-III Basissatz zum Einsatz, um die kernnahe Elektronendichte besser abzubilden [57]. Die 1s-Elektronen aller anderen Atome des selben Elementes im Molekül werden durch Effektive-Kernpotentiale (ECPs) repräsentiert [58], sodass für diese Atome jeweils ein entsprechend verkleinerter Basissatz verwendet wird. Da das 1s-Orbital nun nicht mehr mischen kann, ist es gleich dem entsprechenden Molekülorbital und kann als lokalisierter Ausgangszustand fungieren. Allerdings müssen nun alle Anregungszentren jeweils in getrennten Rechnungen berücksichtigt werden. Im nächsten Schritt wird für jedes Zentrum der einfach ionisierte Zustand, in dem ein 1s-Elektron fehlt, konvergiert. Aus der Differenz der Gesamtenergien des Grundzustandes E_{GS} und ionisierten Zustandes E_{IS} ergibt sich das Ionisationspotential für jedes Anregungszentrum. Um nun Spektren zu berechnen, wird die *Slater-Transition-State*-Methode verwendet. Slater hat gezeigt, dass

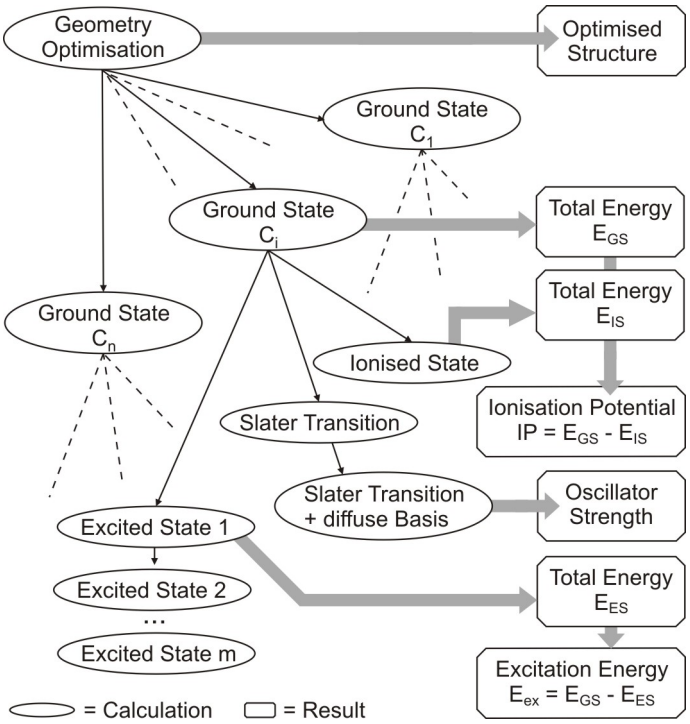

Abbildung 2.6: Vorgehen zur Berechnung eines C1s-NEXAFS-Spektrums mit StoBe. Grafik aus [45] übernommen.

[4]Die Rechnungen berücksichtigen also keine Veränderungen der Struktur aufgrund der Anregungen

[5]Abb. 2.6 nimmt das Beispiel eines C-Kanten Spektrums an, sodass die Kohlenstoffatome betrachtet werden. Für jedes andere Element gilt ein analoges Vorgehen.

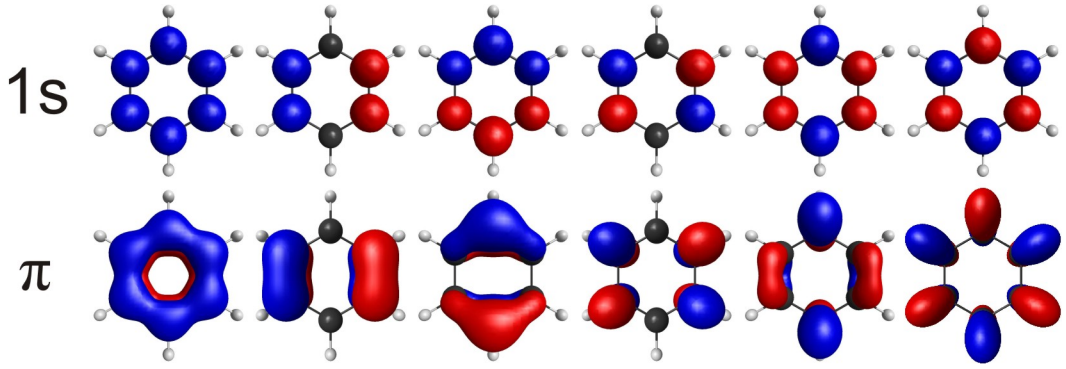

Abbildung 2.7: Obere Reihe: Die sechs energetisch tiefst liegenden Orbitale des Benzol. Untere Reihe: Entsprechende π-Orbitale des Benzol.

sich angeregte Zustände näherungsweise abbilden lassen, wenn mit der Besetzung von einem halben Elektron im Ausgangszustand gearbeitet wird [59]. Durch diese Näherung lassen sich sehr kostengünstig Oszillatorstärken und Anregungsenergien gewinnen. Indem der Basissatz am Anregungszentrum noch um diffuse Funktionen ergänzt wird, kann in einem weiteren Schritt die Genauigkeit noch verbessert werden, da diffusere LUMOs besser repräsentiert werden. Durch die vergleichsweise grobe Näherung durch die *Transition-State*-Methode liegen die Anregungsenergien systematisch zu hoch, was auch für das so berechnetet Ionisationspotential gilt. Durch einen Vergleich dieses Wertes mit dem zuvor beschriebenen Ergebnis aus Grundzustand und ionisiertem Zustand, können die Spektren an einem internen Standard kalibriert werden. Hinzu kommt noch ein Shift von 0.4 eV, der sich aus der fehlenden Berücksichtigung relativistischer Effekte ergibt [60]. Die Rechnungen liefern also für jedes Anregungszentrum ein partielles NEXAFS-Spektrum, was einer hypothetischen experimentellen Messung entspricht, bei der nur ein Atom von Strahlung getroffen wird. Das Gesamtspektrum ergibt sich als Summe der Teilspektren unter Berücksichtigung der Multiplizität der Anregungszentren im Molekül. Um eine bessere Vergleichbarkeit zum Experiment herzustellen, wird das Spektrum mit Gausskurven an den Positionen der Anregungen überlagert, deren Amplitude durch die Oszillatorstärke gegeben ist. Bis hier her ist die Halbwertsbreite der Gausskurven der einzige freie Parameter! Dieser wird so gewählt, dass sich gute Übereinstimmung mit dem Experiment ergibt, wobei π-artige Zustände mit 0.5 eV kleinere Werte zeigen als σ-artige Zustände mit 0.7 eV.

Für noch präzisere Ergebnisse ist deutlich mehr Aufwand erforderlich, da nicht mehr auf die *Transition-State*-Methode zurückgegriffen werden kann: Jeder angeregte Zustand muss nun für jedes Anregungszentrum einzeln konvergiert werden, um aus der Differenz der Gesamtenergien des angeregten Zustandes E_{ES} und des Grundzustandes E_{GS} die Anregungsenergie direkt zu bestimmen. Auch hier ist die Nachjustage aufgrund fehlender relativistischer Effekte nötig. Ansonsten können die Werte jedoch direkt verwendet werden, da mit dem angeregten Einzelzustand Relaxation in Folge der Anregung möglichst vollständig berücksichtigt wird. Bis jetzt erlaubt StoBe allerdings nicht für den angeregten Zustand auch eine zugehörige Oszillatorstärke zu berechnen, sodass durch einen Vergleich der Zielorbitale hier auf die Werte aus der *Transition-State*-Rechnung zurückgegriffen werden muss.

2.7 Hirshfeldanalyse

Wie in der Einleitung erläutert, hängen viele der interessanten Festkörpereigenschaften molekularer Materialien stark von der zugrundeliegenden Kristallstruktur ab. Kristallstrukturen vergleichen und klassifizieren zu können ist daher ein grundsätzlich sinnvoll erscheinendes Ziel. Tatsächlich ist dieses Vorhaben aber nicht leicht zu realisieren, da eine Klassifizierung der Struktur möglichst unabhängig von der Geometrie der Moleküle sein sollte. Damit ist klar, dass die bloße Betrachtung von Atompositionen und Kontaktpunkten im Sinne von *close contacts* diesem Anspruch kaum gerecht werden kann und andere Methoden gefunden werden müssen. CrystalExplorer ist ein für akademische Zwecke frei erhältliches Programm [26], mit dem sich eine mögliche Antwort auf dieses Problem erarbeiten lässt, weshalb es hier kurz vorgestellt wird. CrystalExplorer ist dazu ausgelegt Hirshfeldoberflächen von Molekülen in gegebenen Kristallstrukturen zu berechnen. Um die Ergebnisse dieser Rechnungen sinnvoll diskutieren zu können, muss also zunächst geklärt werden, was eine Hirshfeldanalyse ist.

2.7.1 Grundlagen der Hirshfeldanalyse

Hinter einer Hirshfeldanalyse verbirgt sich letztlich die Frage nach der Größe bzw. dem Volumen eines Moleküls in einem Kristall. Dieses zunächst trivial erscheinende Problem entpuppt sich bei genauerem Hinsehen jedoch als anspruchsvoll und findet seine theoretischen Wurzeln in der Frage nach dem Volumen eines bestimmten Atoms innerhalb eines Moleküls. Verschiedene Konzepte lassen sich verfolgen, um sich diesem Problem zu nähern. Ein vergleichsweise einfacher geometrischer Ansatz ist der der Voronoizelle: Analog zur Definition der Wigner-Seitz-Zelle ist das Atomvolumen begrenzt durch senkrechte Ebenen durch die Mittelpunkte aller Verbindungslinien zu den nächsten Nachbaratomen. Dieser Ansatz berücksichtigt jedoch nicht, dass Atome je nach Kernladungszahl unterschiedlich groß sein können. Um diesem Umstand Rechnung zu tragen, muss die Elektronendichte betrachtet werden[6]. Am anderen Ende der Komplexitätsskala findet sich mit der Bader Ladungsanalyse eine Methode, die ausschließlich die Elektronendichte nutzt, um eine Raumaufteilung zu erreichen. Hier wird das Atomvolumen durch eine „Nullfluss“ Oberfläche begrenzt. Diese ist gegeben durch ein Minimum der Elektronendichte senkrecht zur Oberfläche. Die Berechnung solch einer Fläche erfordert die Betrachtung des Gradientenfeldes der Elektronendichte bzw. der Trajektorien dieses Feldes. Die Baderanalyse macht sich so die intuitive Überlegung zunutze, dass zwischen den Atomen jeweils ein Minimum der Elektronendichte liegen muss, da diese für jedes Atom vom Kern aus gesehen exponentiell abnimmt. Die Hirshfeldanalyse basiert ebenfalls auf dieser Überlegung, nutzt aber eine etwas anschaulichere Herangehensweise: Das Hirshfeldvolumen ist definiert als der Bereich um ein Atom, in dem die Elektrondichte in jedem Punkt mindestens zur Hälfte durch Elektronen des Atoms gegeben ist. Die zugehörige Hirshfeldfläche ist die Oberfläche dieses Volumens und setzt sich aus allen Punkten, für die der Elektronendichteanteil genau 0.5 beträgt, zusammen. Übersetzt man diesen Gedankengang in eine Gleichung, ergibt sich eine Gewichtungsfunktion $w_a(\boldsymbol{r})$, die jedem Punkt im Raum den Anteil des untersuchten Atoms an der dortigen Gesamtelektronendichte zuordnet, die sich

[6] Um auf Basis dieser Partitionierung sinnvolle Aussagen über Ladungen treffen zu können, muss wiederum die Elektronendichte berücksichtigt werden. Hierbei wird der Fluss von Ladung aus den Partitionen im Vergleich zu ungebundenen Atomen betrachtet, was zur *Voronoi deformation density* führt. [27]

als Summe der Elektronendichten ρ_i der Einzelatome des Moleküls ergibt:

$$w_a(\boldsymbol{r}) = \frac{\rho_a(\boldsymbol{r})}{\sum\limits_{i \in Mol} \rho_i(\boldsymbol{r})} \tag{2.3}$$

Für die Gewichtungsfunktion gilt also: $0 \leq w_a(\boldsymbol{r}) \leq 1$. Die beschriebene Hirshfeldfläche ist entsprechend die Isofläche der Gewichtungsfunktion mit dem Wert 0.5. Auch wenn diese Definition vergleichsweise anschaulich ist, ist sie nicht unproblematisch, da Elektronen quantenmechanisch betrachtet grundsätzlich ununterscheidbar sind. Die Methode, mit der die Elektronendichte modelliert wird, muss es also erlauben, diese künstlich nach Quellen aufzuschlüsseln. Eine solche Methode einmal vorausgesetzt ist es jedoch einfach, das Konzept auf Moleküle in Kristallen zu erweitern, indem in Gleichung 2.3 ρ_a durch ρ_{Mol} und $i \in Mol$ durch $i \in Kristall$ ersetzt wird. Es wird also nach dem Raumvolumen gesucht, innerhalb dessen die Elektronendichte für jeden Punkt mindestens zur Hälfte durch ein bestimmtes Molekül gegeben ist. Für ein genaueres Studium der Hirshfeldanalyse eignet sich als Einstieg ein Artikel von M.A. Spackman und D. Jayatilaka [28], an den diese Kurzeinleitung angelehnt ist, sowie selbstverständlich die Originalveröffentlichung von F.L. Hirshfeld [29]. Um diesen Abschnitt abzurunden wird noch ein Blick auf einige Eigenschaften von Hirshfeldvolumina geworfen, die in Abb. 2.8 verdeutlicht sind. Im Gegensatz zu den beiden anderen oben erwähnten Partitionierungsverfahren sind Hirshfeldvolumina nicht raumfüllend. Grenzen zwei Moleküle unmittelbar aneinander, grenzen auch die Hirschfeldflächen lückenlos aneinander. In Raumbereichen, an die drei oder mehr Moleküle angrenzen, kann es jedoch sein, dass keines der Moleküle die Elektronendichte dominiert, sodass dieser Bereich nach der Definition zu keiner der Hirshfeldvolumina gehört. Der rot umrandete, karierte Bereich zwischen den abgebildeten Pentacenmolekülen ist ein Beispiel für solch eine Zone. Für die Kristallstrukturen der im Rahmen dieser Arbeit betrachteten Stoffe ergeben sich typische Raumfüllungen von ca. 98%. In diesem Zusammenhang ist es lohnend, einen Blick auf den Fall eines echten Loches in der Kristallstruktur zu werfen. Rechts unten in Abb. 2.8 ist ein solcher Bereich durch vergleichsweise weit entfernte Nachbarmoleküle angedeutet. Die Gewichtungsfunktion für das orange hinterlegte Mo-

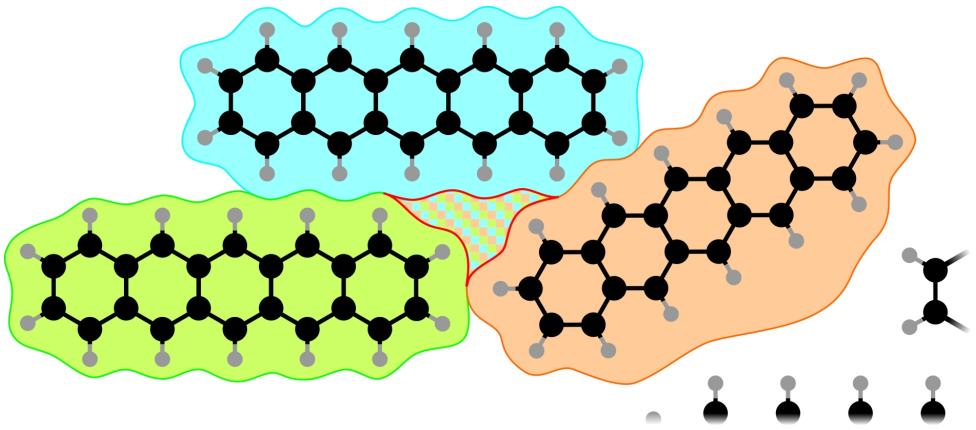

Abbildung 2.8: Schematische Darstellung von Hirshfeldvolumina (blaue, grüne, orange Flächen) dreier Pentacenmoleküle. Hirshfeldvolumina sind nicht zwingend raumfüllend (karierter Bereich) und können untypische Verformungen zeigen, wenn die Struktur Löcher enthält (Ausbuchtung im orangefarbenen Bereich rechts unten).

lekül ist jedoch im ganzen Raum definiert und kann auch für sehr kleine absolute Werte der Elektronendichte Werte größer 0.5 annehmen. Das Loch in der Kristallstruktur führt deshalb zu einem unverhältnismäßig großen Hirshfeldvolumen, hier durch eine Ausbuchtung in dem orangen Volumen angedeutet. Grundsätzlich sollte das Hirshfeldvolumen eines Moleküls im Kristall eine gewisse Ähnlichkeit zu Isoflächen der Elektronendichte dieses Moleküls im Grundzustand haben[7]. Dies liegt daran, dass im Falle einer dichten Packung Zonen geringer Elektronendichte schon in den Einflussbereich des Nachbarmoleküls fallen und das Hirshfeldvolumen damit vor allem den Großteil der Elektronendichte des Moleküls selbst abdeckt. Untypische Ausbuchtungen des Volumens, wie im hier gezeigten Beispiel, sind deshalb Indikatoren für eine nicht optimale Packung, da die dichteste Packung in der Regel die energetisch günstigste ist. Eine alternative Erklärung wäre, dass in der Kristallstruktur eine Komponente fehlt. Ein naheliegendes Beispiel wären kleine Lösungsmittelmoleküle, die im Kristall eingelagert sind, bei der Strukturaufklärung aber nicht berücksichtigt wurden. Tatsächlich ist die Identifikation solcher Problemstellen in einer Kristallstruktur ein mögliches Anwendungsgebiet der Hirshfeldanalyse [31].

2.7.2 Realisierung der Hirshfeldanalyse mittels CrystalExplorer

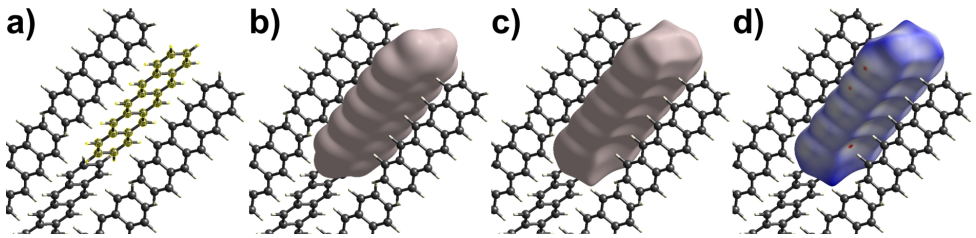

Abbildung 2.9: Arbeitsschritte zur Erzeugung einer Hirshfeldoberfläche mit CrystalExplorer am Beispiel der Pentacen Campbellphase. a) Darstellung der Struktur mit einem markierten Molekül. b) Promolekül Elektronendichte des ausgewählten Moleküls mit Isowert 0.002 au. c) Hirshfeldoberfläche d) Hirshfeldoberfläche aus c) entsprechend der d_{norm} eingefärbt.

Als Ausgangspunkt benötigt CrystalExplorer eine Kristallstruktur in Form einer CIF-Datei[8]. Für die späteren Ergebnisse ist die Qualität der Strukturdaten entscheidend. Ein systematisches Problem sind dabei die Positionen der Wasserstoffatome, da sie mit röntgenbasierten Methoden kaum bestimmt werden können. Deshalb setzt CrystalExplorer die Bindungslängen der Wasserstoffatome auf typische Werte, die mittels der Neutronenstreuung bestimmt wurden[9]. Mit Hilfe einer grafischen Oberfläche, in der die Struktur visualisiert wird, kann nun ein bestimmtes Fragment oder Molekül wie in Abb. 2.9a) ausgewählt werden, für das eine Oberfläche berechnet werden soll. Wie oben beschrieben muss zu diesem Zweck die Elektronendichte modelliert werden, wobei es wichtig ist, dass die Dichte stets nach ihren Ursprungsatomen aufgeschlüsselt werden kann. Dazu bietet

[7] Tatsächlich kann die Größe eines Moleküls im Kristall durch eine Isofläche der Elektronendichte mit dem Wert 0.002 au abgeschätzt werden, wie Bader *et al.* gezeigt haben. [30]

[8] Praktische Anmerkung: Viele CIF-Dateien sind nicht nach einheitlichen Standards formatiert, was beim Laden in CrystalExplorer zu Schwierigkeiten führen kann. Solche Dateien zunächst mit Mercury [32] zu öffnen und erneut zu speichern kann dieses Problem lösen, da Mercury viele der Formatierungsprobleme abfängt und selber Dateien in der Standardformatierung erzeugt.

[9] X-H Bindungslängen, wie sie von CrystalExplorer verwendet werden [26]: C-H: 1.083 Å, N-H: 1.009 Å, O-H: 0.983 Å, B-H: 1.180 Å

sich ein LCAO Ansatz an, da dieses Vorgehen über die Komponenten der Wellenfunktion, die mit bestimmten Atomen assoziiert sind, automatisch eine solche Zuordnung liefert. Dieser Vorteil wird mit der Notwendigkeit, einen größeren Cluster zu berechnen, erkauft. Schließlich muss nicht nur die Elektronendichte des ausgewählten Fragmentes, sondern auch die seiner Umgebung berücksichtigt werden. Offensichtlich ergibt sich so schnell eine große Anzahl von Atomen, sodass Rechnungen mit Basissätzen und Funktionalen, wie sie in vorangegangenen Abschnitten diskutiert wurden, nur noch mit großem Aufwand zu realisieren wären. Deshalb wird die Elektronendichte mit der drastischen Vereinfachung des „Promoleküls“ bestimmt. Dieser Ansatz basiert auf der Erkenntnis, dass die Absolutverteilung der Elektronendichte eines Atoms im Wesentlichen sphärisch ist, da sich Anisotropien durch gerichtete Orbitale herausmitteln. Jedes Atom kann also durch eine sphärische Verteilungsfunktion, deren Abklingverhalten mit zunehmendem Abstand vom Kern elementspezifisch ist, repräsentiert werden. [33] Die Gesamtelektronendichte des Clusters sowie des Moleküls wird dann einfach durch Summation der jeweiligen Einzelfunktionen, die in diesem Fall durch Basissätze von Thakkar *et al.* [34] realisiert werden, gewonnen. In Abb. 2.9b) ist eine solche Promoleküldichte beispielhaft für Pentacene gezeigt. Liegen die Elektronendichten einmal vor, kann daraus die oben beschriebene Gewichtungsfunktion bestimmt werden, womit sich wiederum die Hirshfeldoberfläche wie in c) ergibt. Im letzten Teilbild ist diese Oberfläche entsprechend der d_{norm} eingefärbt. Wie diese definiert ist und wie die Hirshfeldoberfläche genutzt werden kann um die Kristallstruktur zu charakterisieren, ist Inhalt des folgenden Abschnittes.

2.7.3 Fingerprints, d_{norm} und Kristallstrukturen

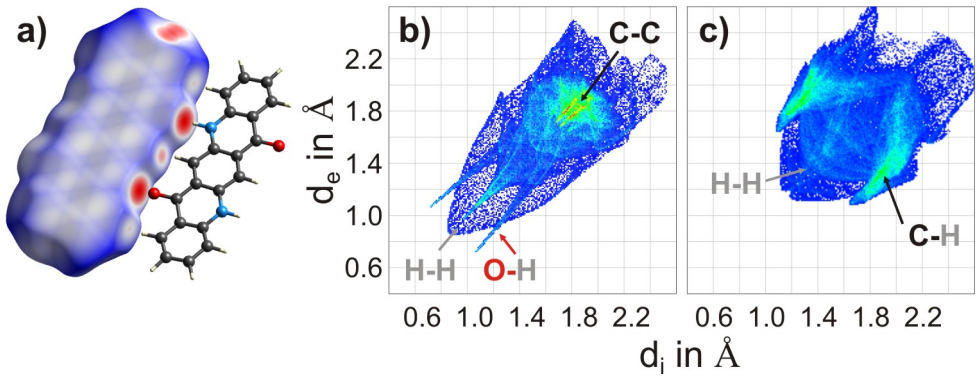

Abbildung 2.10: a) Hirshfeldfläche des Chinacridons im α-Polymorphismus mit d_{norm}. Gut zu sehen: Große, rote Bereiche zeigen Wasserstoffbrücken an. b) Fingerprintplot zur nebenstehenden Fläche. c) Fingerprintplot zur Campbellphase des Pentacens passend zu Abb. 2.9d). In beiden Fingerprintplots sind Merkmale mit den Kontaktpaaren, auf die sie zurückgehen, markiert.

Die Hirshfeldflächen alleine liefern noch keine Charakterisierung der Kristallstruktur. Allerdings können mit wenigen zusätzlichen Informationen mittels einiger bestechend einfacher Methoden interessante Aussagen getroffen werden. Eine dieser Methoden ist das Einfärben der Fläche nach den Werten der d_{norm}, die sich nach folgender Formel bestimmen lassen:

$$d_{norm} = \frac{d_i - r_i^{vdW}}{r_i^{vdW}} + \frac{d_e - r_e^{vdW}}{r_e^{vdW}} \tag{2.4}$$

Damit wird der Wert der d_{norm} für jeden Punkt der Hirshfeldoberfläche einzeln bestimmt,

wobei d_i und d_e für den Abstand dieses Punktes zum nächsten Atom innerhalb des durch die Fläche umschlossenen Volumens (interior) bzw. für den Abstand zum nächst gelegenen Atom außerhalb (exterior) steht. r_i^{vdW} bzw. r_e^{vdW} bezeichnen jeweils den van der Waals Radius des entsprechenden Nachbaratoms[10]. Der Standardfarbcode färbt Bereiche, für die $d_{norm} = 0$ gilt weiß, während Bereiche mit negativen Werten rot und solche mit positiven blau markiert werden. Betrachtet man die Summe der vdW-Radien zweier Atome als den Standardabstand unter dem sie sich annähern, zeigen rote Zonen der Oberfläche also Kontaktpunkte an, in denen sich benachbarte Atome untypisch nahe kommen, während blaue Bereiche einen vergleichsweise großen Abstand bedeuten. Damit werden auf der Hirshfeldfläche sozusagen auf einen Blick alle *close contacts* sichtbar, wobei elementspezifische Abstandsunterschiede direkt berücksichtigt sind. Eine solche Darstellung macht es also einfach, nach den Kontaktstellen zu suchen, die für die Vermittlung der Kristallstruktur von besonderer Bedeutung sind. Ein Beispiel hierfür ist in Abb. 2.10a) anhand der α-Phase des Chinacridons [37] gegeben. Das Molekül innerhalb der Hirshfeldfläche liegt parallel zu der gezeigten benachbarten Struktur, sodass N-H Gruppen und Sauerstoffatome benachbart sind, die Wasserstoffbrücken ausbilden. Diese starke Wechselwirkung zwischen den Molekülen lässt sie näher zusammenrücken und führt zu den großen, roten Bereichen an der Flanke der Hirshfeldfläche. Vergleicht man dieses Bild mit der Situation für Pentacen in Abb. 2.9d) wird sofort deutlich, dass Pentacen über keine derart starken intermolekularen Wechselwirkungen verfügt. Damit wird schon angedeutet, in welche Richtung eine Charakterisierung der Strukturen gehen muss. Entscheidender als die Geometrie der Moleküle sind die Wechselwirkungen, die sie untereinander eingehen. Zwei Strukturen unterschiedlicher Moleküle können als vergleichbar gelten, wenn die Mechanismen, nach denen sich die Struktur ausbildet, die selben sind. Ein Mittel, um einen solchen Vergleich ziehen zu können, sind die sogenannten „Fingerprintplots“. Solch ein Plot entsteht, indem die bereits erwähnten d_i und d_e Werte gegeneinander aufgetragen werden und die Punkte im Plot nach der Häufigkeit, mit der eine Abstandspaarung auftritt, eingefärbt werden. In der Praxis besitzt solch ein Plot eine begrenzte Auflösung, sodass ein Pixel im Plot jeweils einen Abstandsbereich abdeckt, ebenso wie die Hirshfeldfläche im Rechner durch Vertices repräsentiert wird, sodass der Farbcode für die Pixel sich aus dem Flächenanteil ergibt, den die Vertices mit einer entsprechenden Abstandspaarung an der Gesamtfläche haben. Blau bedeutet ein seltenes Auftreten, während rote Pixel auf einen Anteil von mindestens 0.1% der Gesamtfläche zurückgehen. Durch diese relative Definition des Farbcodes können Fingerprints unabhängig von der Molekülgröße verglichen werden. Es bleibt aber noch die Frage, wieso der Vergleich dieser Plots überhaupt relevant sein sollte. Die Grundidee ist, dass Bindungslängen indirekt Informationen über die zugrundeliegenden Wechselwirkungen enthalten. Die Fingerprintplots enthalten wiederum alle Bindungslängen, die zwischen einem Molekül bzw. seinen Atomen und seiner Umgebung vorliegen. Treten bestimmte Abstände nun gehäuft auf, deutet dies auf das Vorliegen einer bestimmten Wechselwirkung hin. So erlauben die Plots es, Kristallstrukturen nach ihren vorherrschenden Wechselwirkungen zu klassifizieren, ohne mit extrem aufwändigen Rechnungen die genaue Natur dieser Kräfte aufklären zu müssen. In Abb. 2.10b) ist ein Beispiel dafür gezeigt, wie die bereits beschriebenen Wasserstoffbrücken des Chinacridon zu typischen „Nadeln“ im Bereich kleiner d_i- und d_e-Werte führt, während in Teilbild c) die für Pentacen dominante, elektrostatisch getriebene C-H-Wechselwirkung als „Flügel“

[10] Van-der-Waals-Radien können je nach Bestimmungsmethode stark schwanken, sodass die jeweiligen Werte auf ihre Tauglichkeit für das Anwendungsgebiet geprüft werden müssen. CrystalExplorer verwendet folgende Werte [35, 36]: H: 1.09 Å, C: 1.70 Å, N: 1.55 Å, O: 1.52 Å, F: 1.47 Å.

sichtbar wird.

3. Ergebnisse

Die folgenden Projekte lassen sich grob in zwei Gruppen einteilen. Zum einen geht es um die explorative Suche bzw. die Entwicklung neuer Modellsysteme. Zum anderen geht es um die gezielte Nutzung passender Modellsysteme, um tiefer gehende Untersuchungen zu ermöglichen. Im Sinne der Einleitung entspricht die erste Gruppe damit Arbeiten, die von ihrer Ausrichtung her im linken Teil der Mindmap in Abb. 1.5 verortet sind. Hier geht es vor allem um neue Substanzen, die Art ihrer Verarbeitung und die Eigenschaften, die insbesondere ihre Dünnfilme besitzen. Im Idealfall ermöglicht das so erworbene Wissen über Präparation und Eigenschaften eine Nutzung dieser Systeme für weitergehende Untersuchungen. In der zweiten Gruppe geht es um genau solche Betrachtungen. Hier werden Systeme aufgrund ihrer spezifischen Eigenschaften ausgewählt, um Fragestellungen bearbeiten zu können, die über das System selbst hinaus gehen. Hier wird also im engeren Sinne mit Modellsystemen gearbeitet und es kommen alle drei Teilbereiche aus Abb. 1.5 gleichberechtigt zum Tragen. Erst durch ein passendes Modell wird eine tiefer gehende Untersuchung erst möglich, in der sich experimentelle Ergebnisse und theoretische Modellierung zu Erkenntnissen über einen, auch für andere Gebiete relevanten, Aspekt des Modellsystems ergänzen.

3.1 Neue Verbindungen

Innerhalb dieser Arbeit wurden Derivate verschiedener organischer Halbleitermoleküle untersucht. In Abschnitt 2.1 wurde bereits das Pentacen vorgestellt, das sich durch außergewöhnliche Leitungseigenschaften und eine vergleichsweise einfache Handhabung auszeichnet und deshalb als Ausgangspunkt für chemische Modifikationen gewählt wurde. Hinzu kommen Derivate des Rubren und des Hexa-peri-hexabenzocoronen (HBC), deren Derivate aufgrund einer ähnlichen Ausgangslage wie beim Pentacen von Interesse sind. Vor diesem Hintergrund fällt eine Studie zum Perylen hier scheinbar aus dem Rahmen, da dieses Molekül schon lange bekannt ist und in vielerlei Hinsicht untersucht wurde. Die hier vorgestellten Ergebnisse ermöglichen es jedoch, Perylenkristalle für weitergehende, richtungsaufgelöste, optische Messungen zu nutzen und erschließen sie damit als Modellsystem für diese Art von Experimenten.

3.1.1 Pentacenderivate mit statischem Dipolmoment

Im Rahmen der Arbeiten „*Synthesis and Solid-State Structures of 6,13-Bis(trifluoromethyl)- and 6,13-Dialkoxypentacene*“ (siehe Abschnitt 5.1) und „*Efficient Syntheses of Novel Fluoro-Substituted Pentacenes and Azapentacenes: Molecular and Solid-State Properties*“ (siehe Abschnitt 5.2) wurden 6,13-substituierte, sowie teilfluorierte Pentacene untersucht. Die Substitution verfolgt verschiedene Ziele. Pentacen weist eine geringe Löslich-

keit auf, die sich durch Seitengruppen leicht erhöhen lässt, um die Anwendbarkeit in lösungsbasierten Verfahren zu verbessern. Zudem ist eine der größten Schwächen des Pentacens seine chemische Instabilität unter Normalbedingungen. Unter Lichteinfluss oxidiert das Molekül an den zentralen Kohlenstoffatomen, also an den 6,13-Positionen, zu Pentacenquinon. Diesem Problem kann mit Seitengruppen begegnet werden, die entweder durch sterische Effekte Reaktionen erschweren, oder durch ein Absenken der HOMO- und LUMO-Niveaus das Molekül energetisch stabilisieren. Neben diesen Aspekten können Seitengruppen je nach ihrer Elektronenaffinität aber auch zu einer Polarisierung des Moleküls führen und damit ein statisches Dipolmoment etablieren. Entsprechend dieser Leitlinien haben die Kollegen aus der Arbeitsgruppe von Professor Koert in zwei Schritten neue Derivate synthetisiert, deren Strukturen in Abb. 3.1 gezeigt sind. Dabei wurden zunächst die Verbindungen **1** und **2** erzeugt, in denen die Trifluormethylgruppe elektronenaffin ist und die Energieniveaus dadurch absenkt, während für die Methoxygruppe das Gegenteil gilt. Darauf aufbauend folgten dann Moleküle, in denen einer affinen Gruppe (-CF_3) eine Gruppe mit Elektronenüberschuss entgegengesetzt wurde, wodurch ein statisches Dipolmoment entlang der schmalen Achse der Pentacenmoleküle entsteht. Die Stärke des Momentes kann durch die Wahl der Seitengruppen eingestellt werden. Zudem wurden durch Teilfluorierung zunächst Diazatetracene (z.B. **4**) und darauf aufbauend Hexafluorodiazapentacen **3** mit einem statischen Dipolmoment entlang der Längsachse realisiert. Für all diese Verbindungen wurden Versuche unternommen, mit Hilfe von OMBD Dünnfilme auf verschiedenen Substraten zu erzeugen. Dabei zeigt sich eine sehr unterschiedliche Prozessierbarkeit der Substanzen. Während sich **1**, **3** und **5** ähnlich wie Pentacen selbst verarbeiten lassen, zeigen die übrigen Verbindungen Degradationserscheinungen. So sind z.B. Farbveränderungen des Reservoirs nach dem Erhitzen für die Bedampfung zu

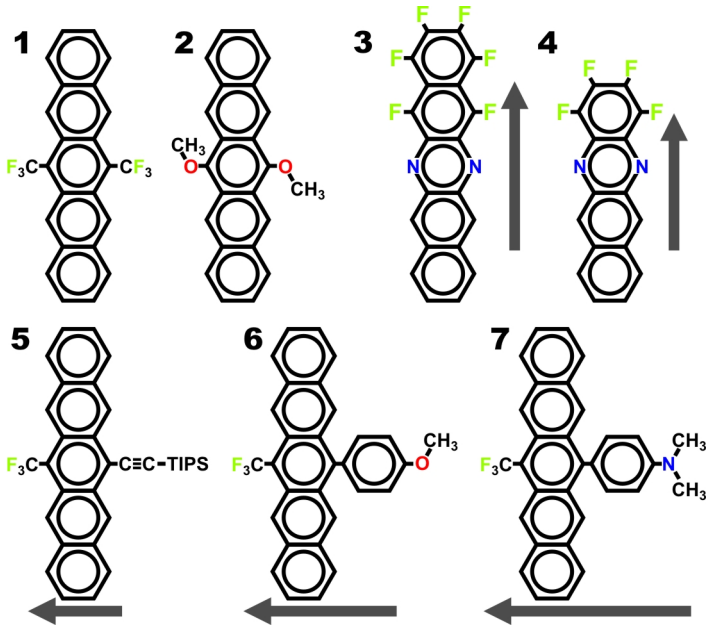

Abbildung 3.1: Strukturen neu synthetisierter Pentacenderivate: **1**) 6,13-Bistrifluoromethylpentacene, **2**) 6,13-Dimethoxypentacen, **3**) Hexafluorodiazapentecen, **4**) Tetrafluorodiazatetracen **5**) 6-Trifluoromethyl-13-triisopropylsilylethynylpentacen, **6**) 6-Trifluoromethyl-13-anilinpentacen, **7**) 6-Trifluoromethyl-13-anisolpentacen. Graue Pfeile deuten das statische Dipolmoment des jeweiligen Moleküls an. Die Pfeillängen stehen im Verhältnis zu den Stärken der Dipolmomente.

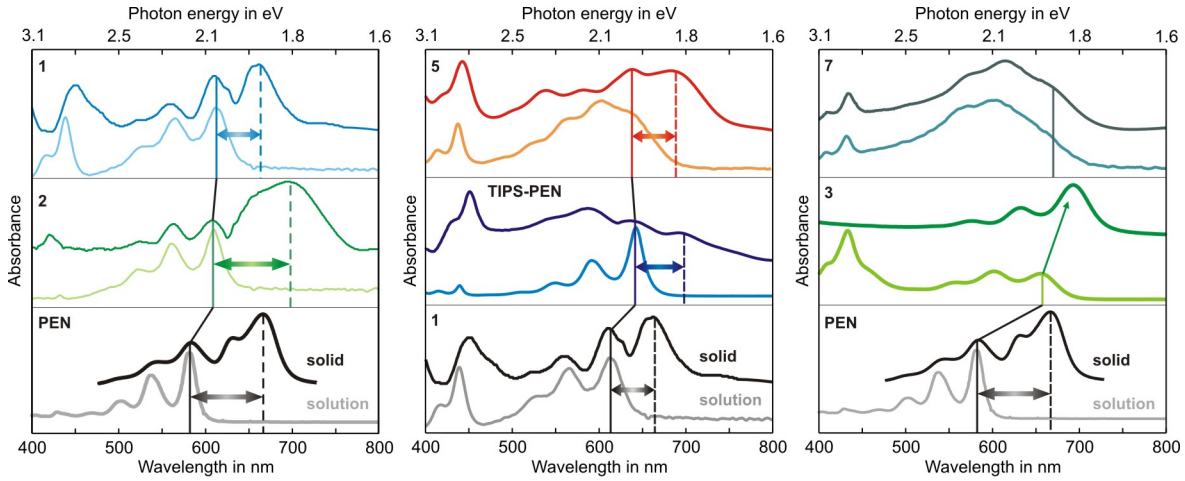

Abbildung 3.2: UV-Vis-Spektren verschiedener neu synthetisierter Pentacenderivate [68, 69] in Lösung und als Dünnfilm im Vergleich mit Pentacen (PEN) und TIPS-PEN [70]. Durchgezogene senkrechte Linien zeigen HOMO-LUMO-Übergänge an, während gestrichelte Linien die Position von excitonischen Signalen verdeutlichen. Horizontale Doppelpfeile markieren die Excitonenbindungsenergie.

beobachten, oder die Dünnfilme weisen bei XRD-Messungen keinerlei Kristallinität auf. In Abb.3.2 sind UV-Vis-Spektren der verschiedenen Verbindungen in Lösung und als Dünnfilm, also im Festkörper, gezeigt, soweit sie sich gewinnen ließen. Von besonderem Interesse sind hier die Unterschiede zwischen den Lösungs- und Festkörperspektren. Insbesondere kann es in den Festkörperspektren zur Ausbildung zusätzlicher Signale bei größeren Wellenlängen kommen, die der primären Anregung (in der Regel ein HOMO-LUMO-Übergang) vorgelagert sind. Diese Signaturen werden Excitonen zugeordnet und stellen damit einen reinen Festkörpereffekt dar, der durch die Wechselwirkung der Nachbarmoleküle miteinander entsteht. In Abschnitt 5.2 wird ein Vergleich zwischen experimentellen und theoretisch abgeschätzten Excitonenbindungsenergien vorgestellt. Erstere werden dabei als Abstand der primären zur excitonischen Anregung in den UV-Vis-Spektren ermittelt (Horizontale Doppelpfeile in Abb. 3.2), während sich Letztere aus einer einfachen dipolbasierten Abschätzung ergeben [71]. In diese Abschätzung gehen die α-Polarisierbarkeit des Moleküls, sowie die Abstände zu seinen nächsten Nachbarn ein. Diese Abschätzung liegen einige grobe Näherungen zu Grunde, weshalb nur der Trend betrachtet werden soll. Dabei zeigt sich jedoch deutlich, dass die Bindungsenergien von den Abständen zu den Nachbarn dominiert werden, während die Polarisierbarkeit eine untergeordnete Rolle spielt. Die Kristallstruktur ist hier also wichtiger als die Eigenschaften des Einzelmoleküls.

Für die Untersuchung der UV-Vis-Spektren wurden lediglich transparente Substrate benötigt, um in Transmission arbeiten zu können. Darüber hinaus haben Untersuchungen unter anderem an Perfluoropentacen gezeigt, dass die Wahl des Substrates auch die molekulare Orientierung beeinflusst, was z.B. richtungsabhängige Untersuchungen ermöglicht [1, 22]. Um zu prüfen in wie weit dies auch für die neuen Verbindungen möglich ist, wurde der C1s NEXAFS-Dichroismus von Verbindung **1** und **3** auf HOPG und SiO_2 untersucht. Die Ergebnisse sind in Abb. 3.3a)-d) zu sehen. Mit einer nahezu liegenden Orientierung auf HOPG und stehenden Molekülen auf SiO_2 zeigen die Verbindungen damit das selbe Verhalten wie z.B. Perfluoropentacen. In den Teilbildern innerhalb der Diagramme ist die Molekülorientierung jeweils angedeutet, wobei in den unteren beiden Bildern ein

stehendes und ein seitlich liegendes Molekül gezeigt sind. Diese beiden Fälle können von der NEXAFS-Messung nicht unterschieden werden. In den Teilbildern e) und f) ist eine entsprechende Messung für **4** gezeigt, wobei hier eine dramatische Veränderung der NEXAFS-Signatur für SiO_2 als Substrat auffällt[1] und sich auch kein Dichroismus mehr zeigt. Dies deutet auf starke Schäden hin, die vermutlich durch Sekundärelektronen, die wiederum von Photoelektronen aus den Siliziumatomen des Substrates erzeugt werden, entstehen. Auch wenn Strahlenschäden organischer Verbindungen bei Untersuchungen mit Röntgenstrahlung grundsätzlich ein bekanntes Phänomen sind, fällt die Reaktion hier außergewöhnlich stark aus. Neben Fragen zur Orientierung und chemischen Unversehrtheit kann NEXAFS auch Antworten zur elektronischen Struktur liefern. In Abb. 3.3g) sind Ausschnitte aus den Spektren der Verbindungen **1**, **3**, Pentacen und Perfluoropentacen gezeigt. Senkrechte Linien befinden sich jeweils an der mit StoBe berechneten Position des zugehörigen Ionisationspotentials. Dabei wird jeweils nur das Ionisationspotential betrachtet, das zu dem Anregungszentrum gehört, welches für die führende Resonanz in den Spektren verantwortlich ist. Diese kann direkt mit dem LUMO-Zustand des Moleküls in Verbindung gebracht werden. Indem in h) für alle Spektren der Wert des Ionisationspotentials auf Null gesetzt wird, lässt sich die relative Position der LUMOs ablesen. Vergleicht man die so gewonnenen Ergebnisse mit Werten aus der Cyclovoltametrie, die mit Lösungen arbeitet, zeigen sich vergleichbare Werte. Im Gegensatz zu den Excitonenbindungsenergien, die stark vom Festkörper abhängen, sind die LUMO-Zustände selbst also kaum von der Molekülumgebung betroffen.
Ohne hier jedes Einzelspektrum der beiden Veröffentlichungen diskutiert zu haben, lassen sich dennoch folgende Kernaussagen aus den Ergebnissen ableiten:

- Es können gezielt Pentacenderivate mit statischen Dipolmomenten oder modifizierten Energieniveaus erzeugt werden.
- Die Derivate zeigen äußerst unterschiedliches Verhalten in der Prozessierbarkeit. Sie „erben“ also nicht auf triviale Weise die positiven Eigenschaften des Pentacens.
- Dennoch ist auch für die neuen Moleküle eine gezielte Beeinflussung der Orientierung durch die Wahl des Substrates möglich.
- Festkörpereigenschaften, wie z.B. Excitonenbindungsenergien, ändern sich dramatisch mit der Kristallstruktur, die sich wiederum unvorhersehbar mit den Substituenten ändert. Eine bessere Vorhersage der Struktur erscheint daher sinnvoll für die Auswahl der chemischen Modifikationen.
- Von den hier vorgestellten Molekülen sind die Verbindungen **1**, **3** und **5** aufgrund ihrer vergleichsweise hohen Stabilität und guten Prozessierbarkeit die beste Wahl für weitere Experimente.

Abschließend sei hier noch ein bemerkenswertes Detail zu den Packungsmotiven der neuen Moleküle angemerkt: Grundsätzlich zeigt keine der Substanzen ein Heringbonemotiv, wie es für reines Pentacen typisch ist. Vielmehr ergeben sich parallele Anordnungen des Pentacenrückrades. Für die Verbindungen **6** und **7** konnten zunächst nur Kristallstrukturen, in die Lösungsmittelmoleküle inkorporiert sind, bestimmt werden. Möglicherweise ist dies ein

[1] Anhand der Signatur des reinen Tetracens lässt sich abschätzen, wie die Signatur für **4** aussehen müsste. Für die Spektren in e) ist dieser Vergleich sinnvoll, sodass eine Veränderung in f) vermutet werden kann.

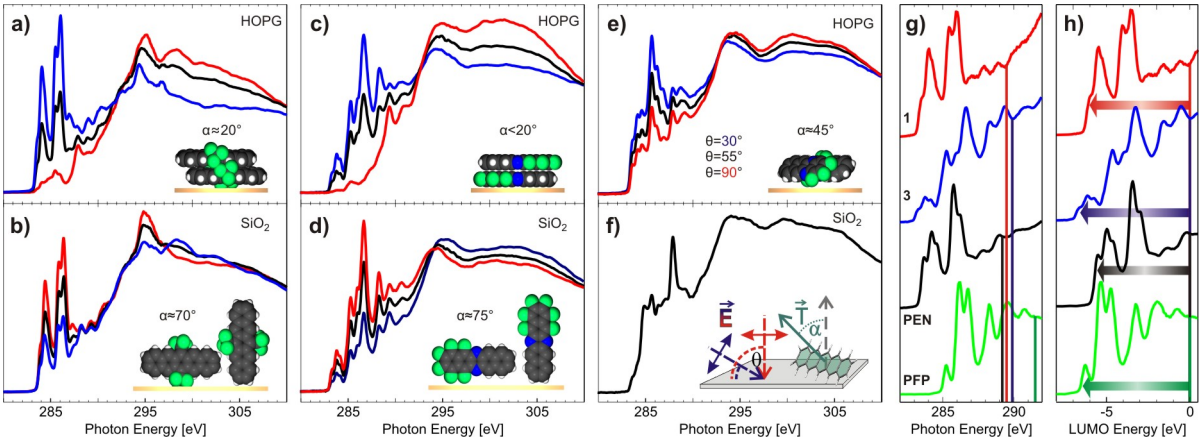

Abbildung 3.3: a)-f) Dichroismen der Verbindungen **1**, **3** und **4** auf HOPG (obere Reihe) und SiO_2 (untere Reihe). Teilbilder in den Diagrammen veranschaulichen die Molekülorientierung auf den Substraten. f) Teilbild veranschaulicht den Tiltwinkel α der Moleküle, sowie den Einfallswinkel θ der linear polarisierten Röntgenstrahlung. g) Vergrößerung der C1s NEXAFS-Signatur von **1**, **3**, Pentacen (PEN) und Perfluoropentacen (PFP) im Bereich der Absorptionskante. Senkrechte Linien markieren berechnete Ionisationspotenziale. h) Spektren aus g) nach Verschieben der Ionisationspotentiale auf den Wert Null. An führenden Resonanzen kann die relative Lage der LUMO-Niveaus abgelesen werden.

Hinweis darauf, dass die großen Seitengruppen zu sterischen Problemen führen und eine dichte Packung erschweren. Dennoch ist es für **7** durch Sublimation gelungen, reine Kristalle ohne Lösungsmittel zu erzeugen, für die eine Kristallstrukturbestimmung möglich war. Während fast alle anderen dipolbehafteten Moleküle Strukturen zeigen, in denen je zwei Moleküle sich entsprechend ihrem Dipolmoment antiparallel anordnen, ergibt sich in der lösungsmittelfreien Struktur von **7** eine parallele Anordnung der nächsten Nachbarn. Dies zeigt, dass andere Beiträge, wie z.B. die van-der-Waals-Kräfte, die elektrostatische Dipol-Dipol-Wechselwirkung überwiegen können. Ein Effekt, der in Abschnitt 3.1.3 bzw. 5.5 detaillierter thematisiert wird.

3.1.2 Fluoriertes Rubren

Die Veröffentlichung „*Enhanced Stability of Rubrene against Oxidation by Partial and Complete Fluorination*“ behandelt fluorierte Rubrene. Rubren selbst zählt zu den prominentesten organischen Halbleitermolekülen, da es zu den Weltrekordhaltern auf dem Gebiet der Ladungsträgermobilität gehört [72]. Ebenso wie Pentacen ist Rubren unter Raumbedingungen jedoch empfindlich gegen Oxidation, was seine Anwendung außerhalb des Labors erschwert [73]. Eine grundsätzliche Strategie, ein Molekül gegen Oxidation zu stabilisieren, ist Fluorierung, die hier für Rubren Anwendung findet. Dazu wurden ein teilfluoriertes Rubrenmolekül ($C_{42}F_{14}H_{14}$ = F_{14}-RUB) sowie die perfluorierte Variante ($C_{42}F_{28}$ = PF-RUB) untersucht. Dabei konnte von den Kollegen mit verschiedenen Techniken eine Zunahme des Oxidationspotentials mit steigendem Grad der Fluorierung nachgewiesen werden, was eine höhere chemische Stabilität mit sich bringt. Von T. Breuer und mir wurde diese Studie mit einer NEXAFS Untersuchung an Dünnfilmen unterstützt, deren Ergebnisse hier genauer betrachtet werden.
In Abbildung 3.4 sind C1s-Dichroismusdaten von F_{14}-RUB und PF-RUB-Dünnfilmen im Vergleich zu einem Spektrum des reinen Rubrens gezeigt. Das Fehlen einer Winkelabhängig-

keit deutet auf eine isotrope Anordnung der Moleküle hin. Eine Zunahme der Intensität von Resonanzen im Bereich von 288 eV mit zunehmender Fluorierung lässt sich auf den *chemical shift* durch benachbarte Fluoratome zurückführen. Aufgrund der geringen Menge an Material konnten für die NEXAFS-Studie keine neuen Dünnfilme in situ hergestellt werden, sodass bereits vorhandene Dünnfilme vermessen wurden, die einige Tage Luftkontakt hatten. Die hohe Ähnlichkeit der Signaturen zu der des reinen Rubren unter Berücksichtigung der Änderungen durch die Fluorierung ist ein Indiz für die höhere chemische Stabilität der neuen Verbindungen. Diese These wird durch StoBe-Rechnungen zu den Spektren weiter erhärtet. In Abb. 3.5a) und b) ist ein Vergleich der PF-RUB-Signatur mit dem zugehörigen berechneten Spektrum gezeigt. Auch hier deutet die hohe Vergleichbarkeit auf ein stabiles Molekül hin, da Oxidation durch das Aufheben von Konjugation im Ringsystem zu erheblich veränderten Spektren führen würde. Des Weiteren dienen die berechneten Spektren zur Aufklärung zweier zusätzlicher Fragestellungen: Die C1s-NEXAFS-Signatur des Rubren lässt sich nach dem sogenannten *building-block*-Prinzip sehr gut als Superposition der Tetracen- und Benzolsignaturen beschreiben, was eine Entkopplung der elektronischen Systeme des Tetracens und der Phenylgruppen bedeutet. Lässt sich das elektronische System des PF-RUB auch so beschreiben? In Abb. 3.5a) ist zu sehen, dass die Superposition der experimentellen Spektren offenbar eine gute Näherung liefert. Innerhalb der StoBe-Rechnungen ist es jedoch besonders einfach, Teilspektren für Untereinheiten eines Moleküls zu berechnen, da die Teilspektren der entsprechenden Anregungszentren aufaddiert werden können. In Abb. 3.4d) sind die symmetrieinäquivalenten Kohlenstoffatome durchnummeriert, wobei 1-6 zum Tetracen gehören und 7-11 zur Phenylgruppe. In Abb.3.5b) sind die Spektren der jeweiligen Untereinheiten gezeigt. Auffällig ist, dass das Tetracenteilspektrum signifikante Intensität bei 288 eV zeigt, was auf die teilweise Fluorierung zurückzuführen ist und im experimentellen Referenzspektrum nicht auftritt. Umgekehrt zeigt die Phenylgruppe in der Rechnung eine Resonanz bei 266.5 eV, die in den Spektren des Perfluorobenzols nicht auftritt. Aufgrund der starken *chemical shifts* durch die Fluorsubstituierung lässt sich das Gesamtspektrum des PF-RUB nicht mehr so leicht als Superposition eines Tetracen- und Perfluorobenzolspektrums beschreiben und bedarf deshalb einer detaillierteren Analyse. Dennoch zerfällt das elektronische System des Moleküls analog zum Rubren in das Tetracenrückrad und die Phenylflügel, wie in der Mitte von Abb. 3.5 gut zu sehen ist. Die Orbitale der Zielzustände zu den Resonanzen in Teilbild b) zeigen lokalisierte Elektronendichten im Bereich der entsprechenden Moleküluntereinheiten. Die zweite Frage an die Rechnungen betrifft die Molekülkonformation. Es ist bekannt, dass PF-RUB in einer planaren Form

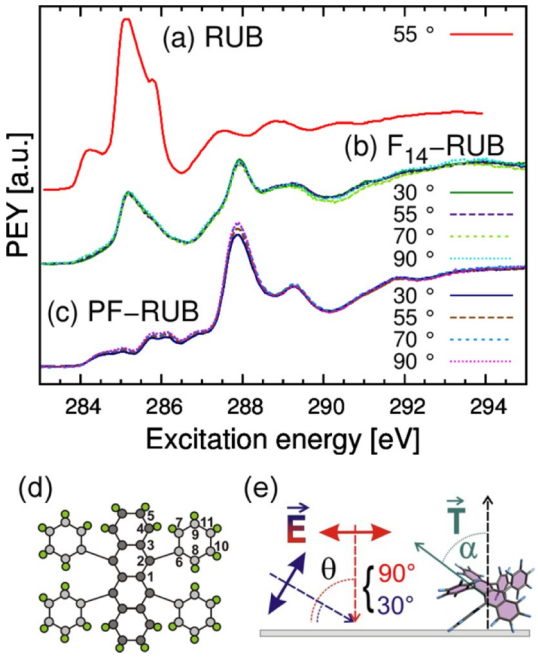

Abbildung 3.4: a) Rubrenreferenz aus [74], b) C1s-Dichroismus des teilfluorierten Rubrens, c) C1s-Dichroismus des perfluorierten Rubrens, d) Struktur des perfluorierten Rubren mit nummerierten Anregungszentren für StoBe-Rechnungen, e) Visualisierung des Einfallswinkels θ der polarisierten Röntgenstrahlung und der Molekülorientierung α.

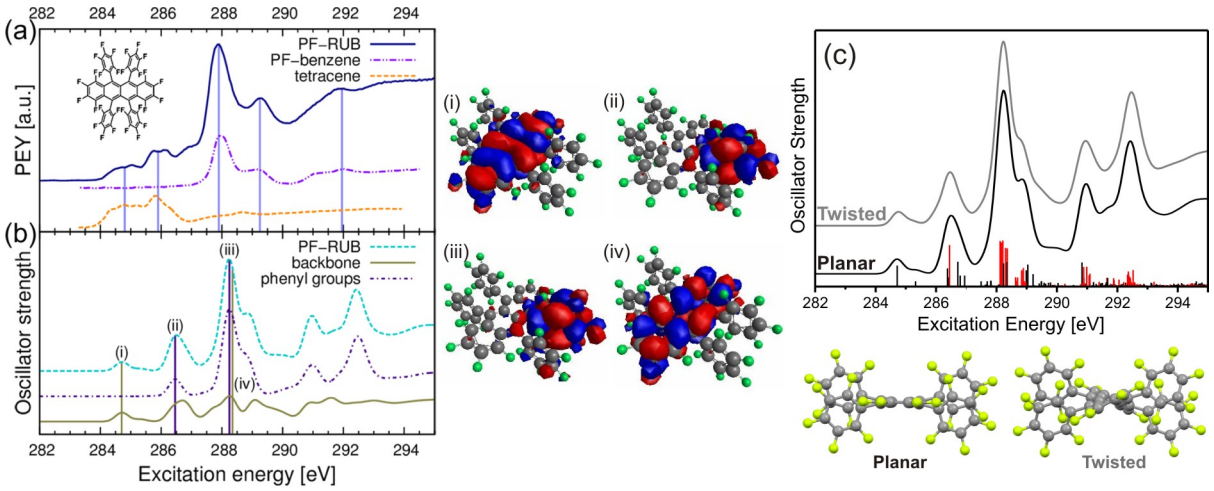

Abbildung 3.5: a) C1s NEXAFS-Spektren des perfluorierten Rubren (PF-RUB), sowie von Perfluorobenzol (PF-benzene) aus [75] und Tetracen aus [74]. Oben links: Struktur des PF-RUB. b) Mit StoBe berechnetes Spektrum des PF-RUB, sowie Teilspektren, die sich ausschließlich aus Beiträgen der Phenylgruppen bzw. des Tetracengerüstes (backbone) ergeben. Mitte: Orbitale zu den in b) markierten Resonanzen. c) Vergleich der berechneten C1s-NEXAFS-Signaturen für PF-RUB mit planarer C_{2h}- bzw. verdrillter D_2-Symmetrie. Das unterlegte Balkendiagramm markiert die Position und Stärke einzelner Resonanzen. Schwarz steht für Anregungszentren im Tetracenrückrad, während rot Zentren in den Phenylgruppen anzeigt.

mit C_{2h}-Symmetrie oder in einer verdrillten Form mit D_2-Symmetrie in Dünnfilmen vorliegen kann [76]. Lassen sich diese Konformationen anhand der Spektren unterscheiden? In Abb. 3.5c) sind berechnete Spektren für beide Symmetrien gezeigt und es ist zu sehen, dass sich nur ein minimaler Unterschied ergibt. Deshalb ist davon auszugehen, dass sich die Konformationen mit NEXAFS nicht unterscheiden lassen.

3.1.3 Der Einfluss von Fluorierung auf Packungsmotive

Ein weiteres Molekül, das als Modellsystem Aufmerksamkeit auf sich gezogen hat, ist Hexabenzocoronen[2] (HBC). Aufgrund seiner Struktur und Eigenschaften gilt es als eine verkleinerte Ausgabe des Graphen [77]. Verglichen mit Pentacen oder Rubren ist es chemisch stabil und aufgrund einer hohen Desorptionsenthalpie sind auch die Dünnfilme sehr stabil. Während in den vorangegangenen Arbeiten chemische Modifikationen betrachtet wurden, die in erster Linie Moleküleigenschaften beeinflussen sollen, geht es in der Veröffentlichung „*Self-assembly of partially fluorinated hexabenzocoronene derivatives in the solid state*“ (siehe Abschnitt 5.5) primär um den Einfluss auf die Kristallstruktur. Ebenso wie im Fall des Rubrens werden teilfluorierte HBC-Moleküle untersucht, die zwei (F_2HBC), vier (F_4HBC) und sechs (F_6HBC) Fluoratome tragen. Die Strukturen sind in Abb. 3.6a) zu sehen, während b) den Einfluss der Fluorierung auf das elektronische System der Moleküle in Form elektrostatischer Konturen zeigt. HBC besitzt einen Elektronenüberschuss im Bereich des Kohlenstoffgerüstes und ein entsprechendes Defizit im Randbereich. Für F_6HBC ist die Lage nahezu invertiert. Allerdings ist hervorzu-

[2]Chemisch korrekt müsste es Hexa-peri-benzocoronen heißen. Je nach Anlagerung der sechs Bezolringe an das zentrale Coronen sind zwei unterschiedliche Strukturen denkbar, die aber auch in der Literatur oft synonym mit Hexabenzocoronen bezeichnet werden. Um sicher zu gehen, worüber gesprochen wird, ist deshalb immer ein Blick auf die Struktur sinnvoll.

heben, dass F_6HBC nicht perfluoriert ist. D.h. am Rand des Moleküls finden sich immer noch elektronendefizitäte Wasserstoffe. Durch die asymmetrische Ladungsverteilung in F_2HBC und F_4HBC stellt sich analog zu den teilfluorierten Acenen in Abschnitt 3.1.1 ein statisches Dipolmoment ein. Mit Blick auf die Packungsmotive ist davon auszugehen, dass die Dipolmomente sich ausrichten und eine parallele Anordnung der Moleküle begünstigen. Während HBC ein Herringbone-Motiv zeigt, ist hier also eher ein sogenanntes π-*stacked*-Motiv zu erwarten, wie es auch beim F_6HBC auftritt (siehe Abb 3.6) und allgemein für verschiedene fluorierte, planare Moleküle beobachtet wird. Eine vollständige Aufklärung der Kristallstrukturen war leider nicht möglich. Allerdings konnten anhand von Pulverdiffraktogrammen die Einheitszellen bestimmt werden und es zeigt sich, dass alle drei teilfluorierten Moleküle nahezu identische Einheitszellen, sowie vergleichbare Diffraktogramme besitzen. Auch ohne in jedem Fall sämtliche Atompositionen bestimmen zu können, ist deshalb davon auszugehen, dass alle drei Strukturen nahezu identische Packungsmotive und damit das π-*stacked*-Motiv des F_6HBC besitzen. Was für die dipolbehafteten Moleküle plausibel erscheint, ist jedoch bei genauerer Betrachtung für F_6HBC nicht zu erwarten. Hier liegt kein Dipol vor und eine Invertierung der elektrostatischen Vorzeichen ändert nichts an der Ausbildung eines Herringbone-Motivs. Offenbar ändert sich mit der Fluorierung nicht nur die Elektrostatik des Gesamtmoleküls. Eine Hirshfeldanalyse bietet hier eine anschauliche Möglichkeit, Einblicke in die herrschenden intermolekularen Wechselwirkungen zu bekommen. In Abb. 3.6d) sind die Ergebnisse einer Analyse des F_6HBC, bzw. seiner Struktur [79], gezeigt. Im *Fingerprintplot* fallen zwei charakteristische Merkmale auf, die sich jeweils auf ein spezielles Kontaktpaar zurückführen lassen: C-C-Kontakte führen zu einer Häufung in der Plotmitte, während F-H-Kontakte nadelartige Fortsätz im Bereich kleiner Abstände bilden. Diese Merkmale können selektiv dargestellt werden, indem sowohl im *Fingerprintplot*, als auch bei der Einfärbung der Hirshfeldfläche mit der d_{norm} nur Bereiche berücksichtigt wer-

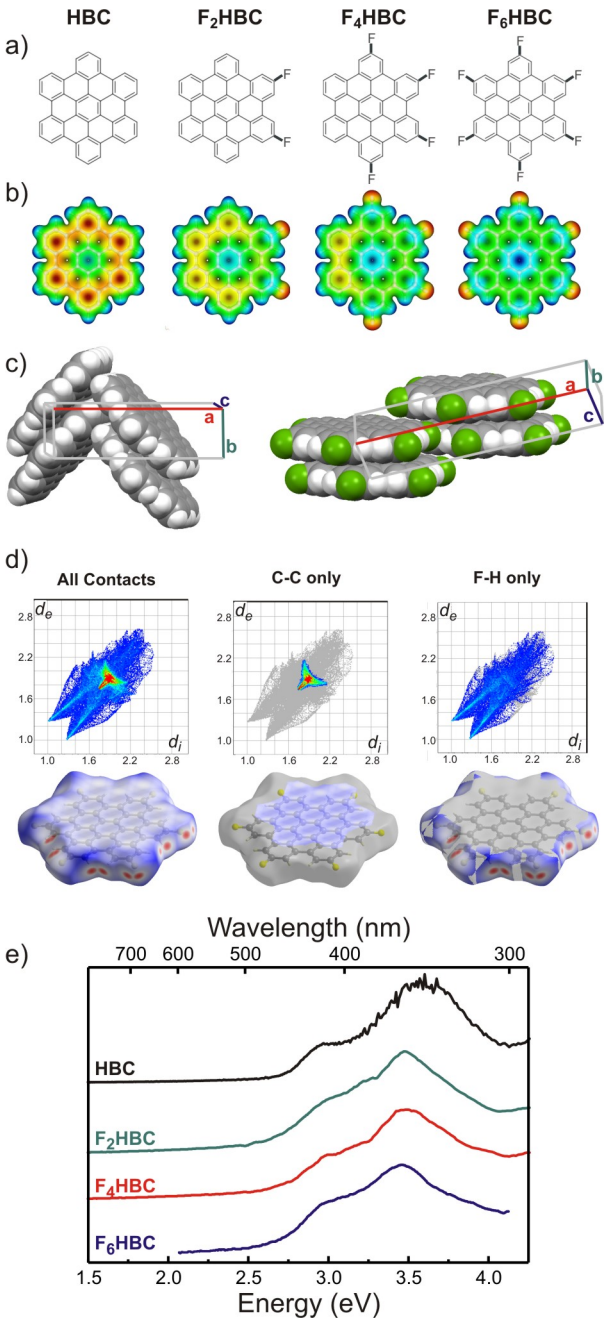

Abbildung 3.6: a) Strukturen aller teilfluorierten HBC-Moleküle, b) elektrostatische Konturplots, c) Packungsmotive von HBC [78] und F_6HBC [79], d) Hirshfeldanalyse des F_6HBC, e) UV-Vis-Spektren von Dünnfilmen aller Moleküle.

den, die auf die entsprechenden Kontaktpaare zurückgehen. So wird deutlich, dass die verstärkten C-C-Kontakte Ausdruck des π-*stackings* sind. Besonders interessant sind jedoch die F-H-Kontakte. Sie werden ausschließlich im Randbereich des Moleküls als starke Kontaktpunkte sichtbar. Dies und die vergleichsweise geringen F-H-Abstände deuten auf die Ausbildung moderater Wasserstoffbrücken zwischen den freien Elektronenpaaren der Fluoratome und den elektronendefizitären Wasserstoffatomen hin. Offenbar überwiegt dieser attraktive Beitrag den Einfluss der Elektrostatik und begünstigt so ein π-*stacked*-Motiv an Stelle des Herringbone-Motivs. Da in organischen Kristallen verschiedene Wechselwirkungen, wie z.B. elektrostatische Beiträge oder van-der-Waals-Kräfte, mit vergleichbarer Stärke zur Ausbildung einer Struktur beitragen, ist es denkbar, das bereits ein einzelnes Fluoratom durch die Ausbildung eines Dipolmomentes und von Wasserstoffbrückenbindungen das Packungsmotiv von Herringbone auf π-*stacked* ändern könnte. Besonders bemerkenswert ist dies vor dem Hintergrund ansonsten kaum veränderter Moleküleigenschaften. In Abb. 3.6e) sind UV-Vis-Spektren von Dünnfilmen aller Moleküle zu sehen, die kaum Veränderungen aufgrund der Fluorierung aufweisen. Der HOMO-LUMO-Abstand bleibt also nahezu konstant, auch wenn Rechnungen zeigen, dass die Absolutniveaus der Zustände abgesenkt werden. Damit sind zumindest die optischen Eigenschaften kaum beeinflusst. Während chemische Modifikationen bislang vor allem der gezielten Justage von Moleküleigenschaften dienten, aber zu unvorhersehbaren Änderungen der Kristallstruktur führten, zeichnet sich hier umgekehrt ein Ansatz zur Kontrolle der Kristallstruktur bei gleichzeitig möglichst kleiner Einflussnahme auf die Moleküleigenschaften ab.

3.1.4 Perylenkristalle

Bereits an mehreren Stellen dieser Arbeit wurde angemerkt, dass es nützlich sein kann, die Molekülorientierung genau zu kennen und ggf. sogar kontrollieren zu können. Insbesondere für optische Untersuchungen ist dies im Zusammenhang mit Dünnfilmen relevant. Kristalle von ausreichender Größe zu züchten ist für viele organische Materialien ohnehin schwierig. Gelingt es dennoch, sind z.B. Absorptionsmessung zumindest in Transmission trotzdem nicht möglich, weil viele organische Materialien so stark absorbieren, dass die Kristalle oft zu dick sind. Dünnfilme bieten hier einen Ausweg. Gelingt es zudem noch, ausreichend große Domänen wachsen zu lassen, können in einem fokussierten optischen Aufbau Einkristallmessungen vorgenommen werden. Wenn es dann auch noch möglich ist, die Ausrichtung der Domäne zu bestimmen, können die gemessenen Daten direkt mit kristallographischen Richtungen korreliert werden und im Falle einer vollständig bekannten Kristallstruktur ist dies sogar für die Ausrichtung der einzelnen Moleküle möglich. Die Arbeit „*Polymorph-Selective Preparation and Structural Characterization of Perylene Single Crystals*“ (siehe Abschnitt 5.3) schafft die nötigen Grundlagen für derartige Untersuchungen am Halbleitermolekül Perylen. André Pick ist es gelungen, auf Basis verschiedener Präparationsmethoden Perylenkristalle von außergewöhnlicher Qualität polymorphselektiv zu züchten, die in dieser Veröffentlichung detailliert vorgestellt werden. Im Folgenden wird es hier um die Ergebnisse der Röntgenbeugungsexperimente an diesen Kristallen gehen. Für Perylen sind zwei Polymorphismen bekannt, die mit α und β bezeichnet werden [80]. *Out-of-plane*-Messungen an aufgedampften bzw. durch mehrfache Resublimation von Perylenpulver hergestellte Perylendünnfilme zeigen jedoch Hinweise auf einen dritten Polymorphismus. In Abb. 3.7a) sind entsprechende Diffraktogramme zu sehen. Gut zu erkennen ist, dass mit zunehmender Anzahl von Resublimationszyklen fast ausschließlich Kristalle der α-Phase wachsen. Bei kleineren Winkeln ist jedoch zunächst

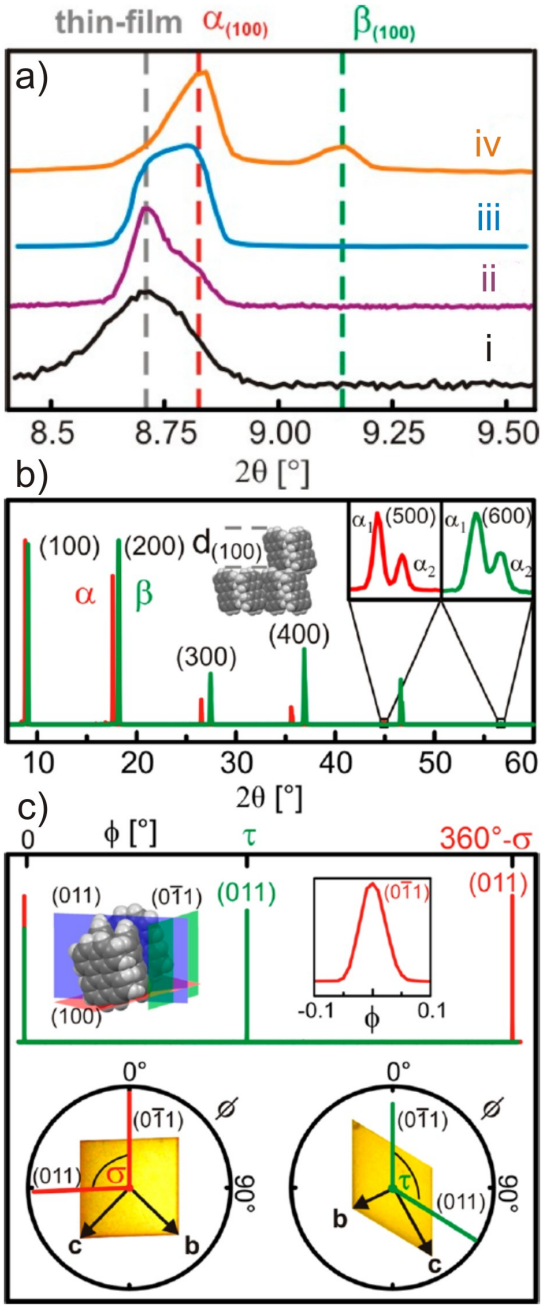

Abbildung 3.7: a) *Out-of-plane*-Diffraktogramme verschieden präparierter Dünnfilme, i) 30 nm Perylen mittels OMBD bei 270 K aufgedampft, ii) Perylenpulver zwischen zwei Platten einmal resublimiert, iii) nach drei Resublimationszyklen, iv) nach fünffacher Resublimation, b) *Out-of-plane*-Diffraktogramme makroskopischer Peryleneinkristalle. Insets zeigen Feinstrukturaufspaltung in fünfter bzw. sechster Ordnung, c) *In-plane*-Messungen an den Kristallen aus b). (011)- und (0$\bar{1}$1)-Ebenen können unmittelbar mit den Seitenflächen der Kristalle korreliert werden.

ein weiterer Reflex zu sehen, dessen Intensität in der Serie abnimmt. Dieser Reflex ist vermutlich auf einen substratvermittelten Polymorphismus zurückzuführen, wie er z.B. auch für Pentacen bekannt ist [65], sodass er analog als *thin-film-phase* bezeichnet wird. Neben der selektiven Zucht von α-Kristallen zeigen die Beugungsdaten außerdem, dass die Kristalle auf dem SiO_2-Substrat in (100)-Orientierung vorliegen.
Für weitergehende optische Untersuchungen, wie sie oben beschrieben sind, kann nun anhand zweier einfacher Kriterien, nämlich dem Habitus und der Fluoreszenz, der Polymorphismus sicher unterschieden werden. In der α-Phase wachsen die Kristalle nahezu quadratisch, während die β-Phase rautenförmig erscheint. Mikroskopaufnahmen gelber Perylenkristalle sind in Abb. 3.7c) den Polarplots hinterlegt. Sollte dieses Kriterium nicht ausreichen, lassen sich die Polymorphismen eindeutig anhand ihrer Fluoreszenz zuordnen. α-Kristalle leuchten rot, während β-Kristalle grünes Licht aussenden. Neben der Nützlichkeit für die Unterscheidung ist dies zudem ein gutes Beispiel für den Einfluss der Kristallstruktur auf festkörperphysikalische Eigenschaften. Der Polymorph eines Kristalls kann also eindeutig bestimmt werden. Um zudem vom Habitus auf kristallographische Richtungen schließen zu können, wurden makroskopische Kristalle beider Polymorphismen einer *in-plane*-Messung unterzogen. Für diese Messung ist zunächst eine Einjustage in *out-of-plane*-Geometrie nötig, deren Ergebnisse in Abb. 3.7b) zu sehen sind. Dass Reflexe bis zur sechsten Ordnung auftreten und die Feinstrukturaufspaltung der Röntgenstrahlung aufgelöst werden kann, zeigt die außergewöhnliche Qualität der Perylenkristalle. In Teilbild c) sind die Ergebnisse der eigentlichen *in-plane*-Messung gezeigt, die belegen, dass Seitenflächen der Kristalle jeweils der (011)- bzw. der (0$\bar{1}$1)-Ebene entsprechen, womit die $\vec{\mathbf{b}}$- und $\vec{\mathbf{c}}$-Vektoren der Einheitszellen jeweils auf die Ecken der

Kristalle weisen. Anhand dieser Ergebnisse ist es also nicht nur möglich, hochwertige Kristalle des Perylen zu züchten, sie können über dies auch noch auf einfache Weise nach Polymorphismen sortiert werden und die Orientierung der Kristalle lässt sich mit einem Blick durchs Mikroskop genau bestimmen.

3.2 Modellsysteme in der Anwendung

Bis hierher ging es vor allem darum, neue Verbindungen auf ihre Tauglichkeit als Modellsysteme für weitere Untersuchungen zu testen. Dabei wurden viele Informationen über die Moleküle selbst bzw. ihre Kristalle gesammelt, aber nur wenige der Ergebnisse liefern Erkenntnisse, die über das Molekül selbst hinaus gehen und allgemeinere Gültigkeit besitzen. Eine Ausnahme stellt hier die Charakterisierung der teilfluorierten Hexabenzocoronene dar, bei der bereits das Potential eines guten Modellsystems für tiefere Erkenntnisse deutlich wurde. Die hier festgestellten Zusammenhänge zwischen Fluorierung und Packungsmotiven sind nicht nur für HBC gültig. Im zweiten Abschnitt dieses Ergebnisteils sollen Untersuchungen vorgestellt werden, bei denen ein bewusst gewähltes Modellsystem tiefere Einblicke gewährt. Hier finden sich Beispiele, die im Sinne der Einleitung zeigen, wie Experiment und computergestützte Modellierung bei der Untersuchung eines geeigneten Modellsystems Hand in Hand gehen können und dabei neue Einsichten liefern.

3.2.1 Backsteinmoleküle für die Hirshfeldanalyse

Viele Festkörpereigenschaften, die insbesondere auch für die Funktion elektronischer Bauteile wichtig sind, hängen unmittelbar von der Kristallstruktur ab. In den vorangegangenen Abschnitten hat sich gezeigt, wie kritisch diese wiederum durch teilweise geringfügig erscheinende chemische Modifikationen der molekularen Bausteine beeinflusst wird. Um diesen Zusammenhang aufzuklären und langfristig womöglich gezielt kontrollieren zu können, wird in der noch unveröffentlichten Arbeit „*Crystalline Packing Motifs in Pentacen-like Organic Semiconductors*“(siehe Abschnitt 5.9) eine vergleichende Studie der Kristallstrukturen pentacenartiger Halbleitermolküle auf Basis der Hirshfeldanalyse vorgestellt. Die entscheidende Idee dieses Vergleichs liegt in der Auswahl der betrachteten Moleküle, die in Abb. 3.8 gezeigt ist. Sämtliche Moleküle haben nahezu identische geometrische Abmessungen. Vernachlässigt man die genaue chemische Struktur, können alle Moleküle im Sinne der Packung durch einfache, gleichgroße „Backsteine“ genähert werden. Von einem rein

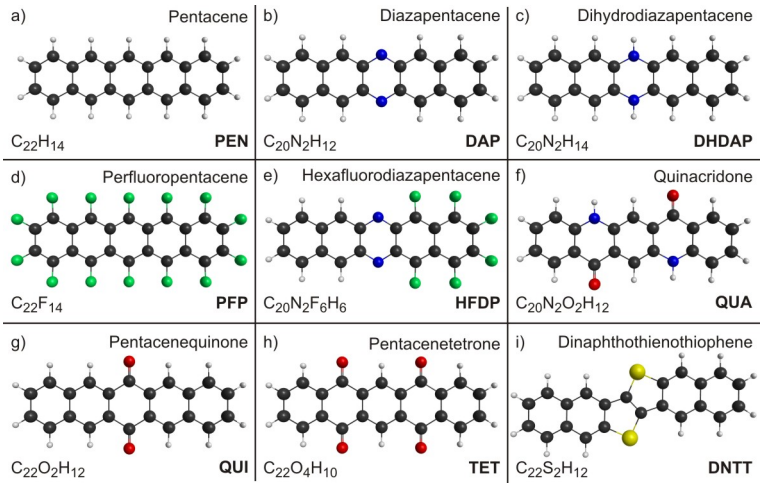

Abbildung 3.8: Zusammenstellung pentacenartiger Halbleitermoleküle für die vergleichende Hirshfeldanalyse. Neben der Summenformel ist jeweils auch eine Abkürzung für das Molekül angegeben.

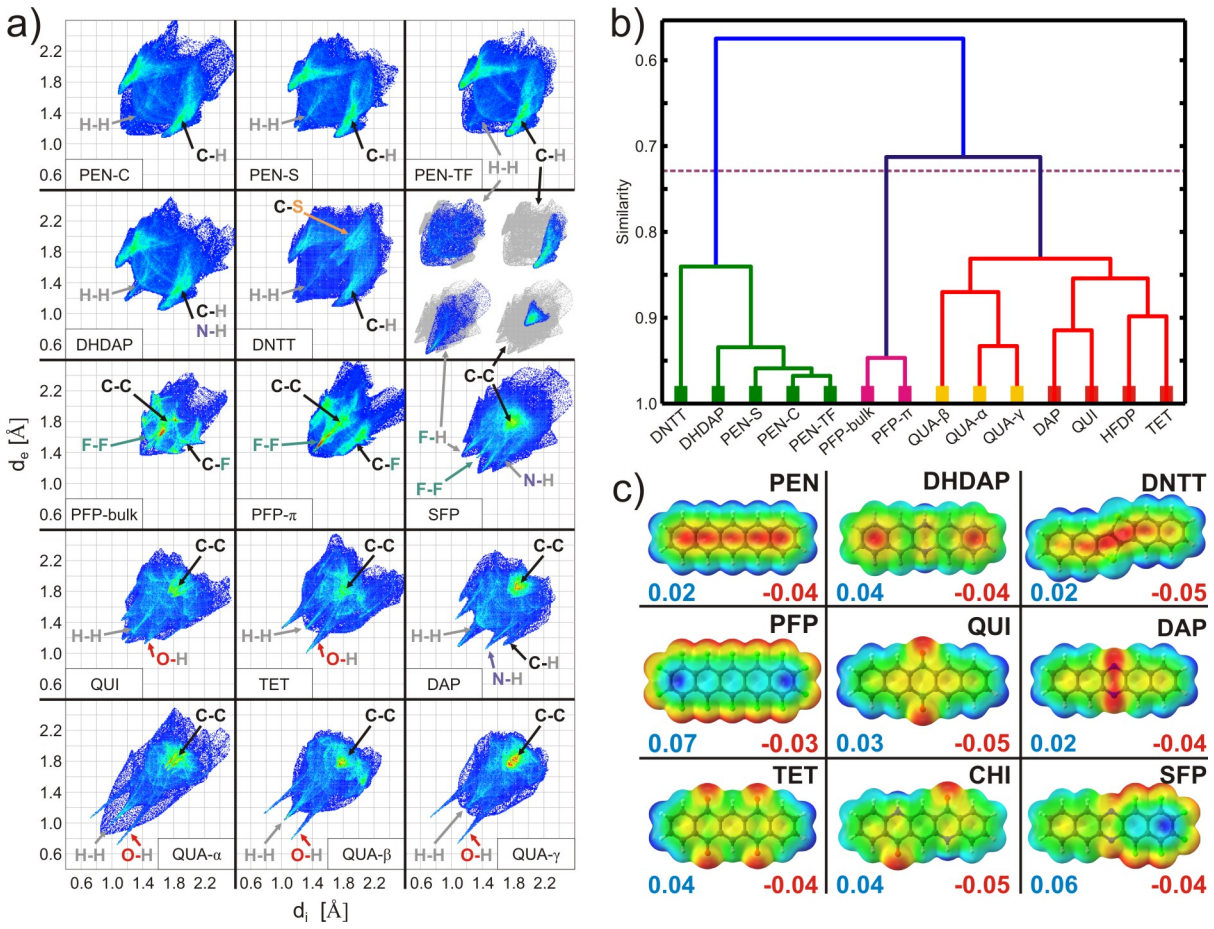

Abbildung 3.9: a) Fingerprintplots aller Strukturen. Charakteristische Merkmale sind mit den entsprechenden Kontaktpaaren markiert, b) Korrelationen der Fingerprintplots aus a) als Baumdiagramm dargestellt. Ähnliche Strukturen sind durch Farben in Gruppen zusammengefasst, c) Elektrostatische Konturplots aller Moleküle.

geometrischen Standpunkt aus betrachtet sollten also alle Moleküle das selbe Packungsmotiv zeigen. Da dies nicht der Fall ist, können Unterschiede unmittelbar auf verschiedene Wechselwirkungen zurückgeführt werden. Damit sind sterische Effekte, wie sie z.B. in Abschnitt 3.1.1 erwähnt wurden, ausgeschlossen und die Interpretation der Packungsmotive, sowie der zugrunde liegenden Kräfte, somit deutlich erleichtert. Zudem finden sich in der Auswahl viele außergewöhnlich leistungsfähige organische Halbleiter, was die Zusammenstellung für dieses Gebiet besonders interessant macht. Die im Folgenden gezeigten Ergebnisse der Hirshfeldanalyse sind ausschließlich am Computer entstanden. Eingangs wurde jedoch eine Studie angekündigt, die sowohl auf experimentellen, als auch auf theoretischen Betrachtungen basiert. Der vermeintliche Widerspruch löst sich auf, wenn die Kristallstrukturdaten berücksichtigt werden. Die Hirshfeldanalyse ist ein Werkzeug zur Interpretation der Kristallstrukturen, kann aber nur so zuverlässig sein, wie es die Bestimmung der Strukturen ist, auf denen sie aufbaut.
In Abb. 3.9a) sind Fingerprintplots für alle Moleküle gezeigt, wobei einige Vertreter mehr als eine bekannte Kristallstruktur besitzen[3]. Wie in Abschnitt 2.7 ausgeführt wurde, kann

[3]Einige der Strukturen weisen mehrere Moleküle pro Einheitszelle auf, die nicht aus Symmetriegründen äquivalent sind. In diesen Fällen wurde eine Superposition aller unterschiedlichen Fingerprintplots dieser Strukturen gebildet. Für Details siehe Abschnitt 5.9

anhand der Plots die intermolekulare Bindungssituation beurteilt werden. So lassen sich charakteristische Merkmale in den Plots z.B. bestimmten Kontaktpaaren zuordnen. Anhand dieser Merkmale können die Fingerprintplots nach ihrer Ähnlichkeit sortiert werden, was einer Einteilung nach den vorherrschenden Wechselwirkungen entspricht. Eine solche Zuordnung kann quantifiziert werden, indem Korrelationen zwischen den Fingerprintplots berechnet und in einem Baumdiagramm visualisiert werden[4] [81]. Nach diesem Vorgehen lassen sich drei Gruppen im Diagramm ausmachen: Strukturen mit Herringbone-Motiven finden sich in der grünen Gruppe, die beiden Strukturen des Perfluoropentacens haben in der pinken Gruppe eine Sonderstellung und in der roten Gruppe finden sich Strukturen, die durch gerichtete, lokale Wechselwirkungen einzelner Atome im Molekül bestimmt werden. Innerhalb dieser Gruppe bilden die drei Strukturen des Chinacridon (gelbe Blätter) eine Untereinheit, in der vergleichsweise starke Wasserstoffbrückenbindungen dominieren. Ein weiterer Vorteil der gezielten Molekülauswahl ist, dass die Unterschiede der Gruppen anhand von elektrostatischen Konturplots (MEPs) der Moleküle qualitativ beschrieben werden können, wie sie in Abb. 3.9c) gezeigt sind. Hintergrund hierfür ist, dass die London-Dispersion durch eine Näherung, in die die α-Polarisierbarkeit der Moleküle quadratisch eingeht, abgeschätzt werden kann [82]. Die Polarisierbarkeit wiederum hängt stark von der Geometrie der Moleküle ab, die in diesem Fall für alle Moleküle vergleichbar ist, sodass dieser Wert überall ähnlich ausfällt. Damit lassen sich Unterschiede in den Packungsmotiven kaum auf unterschiedliche Dispersionskräfte zurückführen und die elektrostatischen Anteile bleiben als treibende Kraft übrig, da die Debye-Wechselwirkung generell schwächer ausfällt [83]. Aus der Betrachtung der MEPs lässt sich direkt eine einfache Regel für die Ausbildung eines Herringbone-Motivs ableiten. Für dieses Packungsmotiv muss das Potential der Moleküle im Randbereich durchgehend das selbe Vorzeichen aufweisen. Bereits zwei Störungen, wie z.B. im Fall des Diazapentacens (DAP), führen zu einem völlig anderen Packungsmotiv. Der Erhalt des elektronischen Systems des Kohlenstoffrückrades ist also irrelevant, da DAP isoelektronisch zu Pentacen ist, während Dihydrodiazapentacen es nicht ist und trotzdem das bekannte Herringbone-Motiv zeigt. Diese Beobachtung stimmt mit den Ergebnissen aus Abschnitt 3.1.3 überein, da die Fluorierung dort auch als Störung des Randpotentials betrachtet werden kann. Perfluoropentacen (PFP) stellt mit seinen Strukturen eine Sonderrolle dar. Anhand der obigen Regel sollte PFP ebenfalls ein Herringbone-Motiv ausbilden, was mit der PFP-*bulk* Struktur auch der Fall ist. Die Fingerprintplots zeigen mit starken F-F-Kontakten jedoch ein Merkmal, für das es mit den H-H-Kontakten ansonsten kein entsprechend ausgeprägtes Analogon gibt. Hierfür kann eine einfache geometrische Erklärung gefunden werden. Der vdW-Radius von Fluor ist größer als der von Wasserstoff. Bei ansonsten gleicher Struktur kommt es über die F-F-Kontakte daher verstärkt zu Paulirepulsion, sodass diese Kontakte in den Fingerprintplots mit einem typischen Gleichgewichtsabstand sichtbar werden. Zudem sind die vdW-Radien von Kohlenstoff und Fluor fast identisch, sodass PFP der „Backstein-

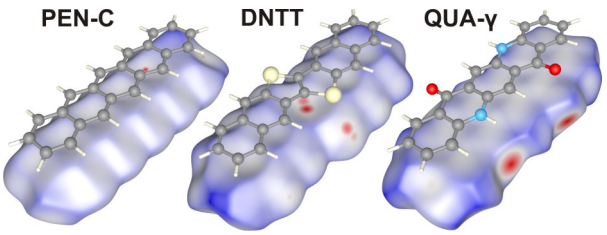

Abbildung 3.10: Hirshfeldoberflächen des Pentacens, DNTTs und Chinacridons entsprechend der d_{norm} eingefärbt. Auffällig sind die roten Kontaktpunkte des DNTT.

[4]Die Korrelation wurde als ein Mittel aus Spearman- und Pearsonkoeffizienten bestimmt und im Baumdiagramm nach der UPGMA-Methode aufgetragen.

form“ am nächsten kommt. Eine möglichst dichte, raumfüllende Packung dieser Quader erfordert eine rechtwinklige oder parallele Anordnung, was den beiden Strukturen des PFP entspricht. Die dritte Gruppe ist durch starke lokale Wechselwirkungen geprägt. Diese werden in den Fingerprintplots durch nadelartige Fortsätze im linken, unteren Bildteil sichtbar. Kleinere Abstände bedeuten stärkere Wechselwirkungen. Neben der elektrostatischen Argumentation kann hier ein zusätzlicher kovalenter Beitrag in Form von Wasserstoffbrückenbindungen von Bedeutung sein. Dies wird deutlich, wenn man berücksichtigt, dass die „Nadelmerkmale“ stets auf O-H-, N-H- oder F-H-Kontakte zurückgehen. Sobald also Heteroatome, die freie Elektronenpaare zur Verfügung stellen, sowie Wasserstoffatome vorhanden sind, kommen Wasserstoffbrücken als zusätzliche attraktive Kraft hinzu.
Eine Ausnahme in der Auswahl bildet Dinaphthothienothiophen (DNTT). Auch wenn dieses Molekül die geometrische Bedingung für seine Form in guter Näherung erfüllt, ist das Molekül chemisch betrachtet kein Derivat des Pentacen. Dennoch ist es für diese Auswahl besonders interessant, da seine Kristalle eine außergewöhnlich hohe Ladungsträgermobilität zeigen [84]. Allgemein finden sich unter den Molekülen, die ein Herringbone-Motiv ausbilden, viele performante Halbleiter, was im Widerspruch zur landläufigen Auffassung steht, dass π-π-Kontakte ein entscheidendes Kriterium für besonders hohe Mobilitäten sind. Für die Ursache der höheren Mobilität im DNTT verglichen zum Pentacen könnte Abb. 3.10 einen Hinweis geben. Während die Hirshfeldoberfläche des Pentacen nahezu keine Kontaktpunkte in der d_{norm} aufweist, sind beim DNTT entsprechende Bereiche zu erkennen. Eine genauere Betrachtung zeigt, dass es sich um C-S-Kontakte handelt, die hier auffallen. Um die Stärke des Kontaktes besser einschätzen zu können, ist nebenstehend auch noch die Wasserstoffbrückenbindung des Chinacridons gezeigt. Möglicherweise erzeugt das vergleichsweise große Schwefelatom, welches selber Teil des konjugierten Systems ist und im DNTT eine randständige Position einnimmt, einen signifikanten Überlapp mit dem π-System des Nachbarmoleküls und erleichtert so den Ladungstransport. Eine weitere Strategie zur Optimierung organischer Halbleiter könnte also der gezielte Einbau großer Atome wie Schwefel oder Selen sein, die den Kontakt zu den Nachbarmolekülen über einzelne Kontaktstellen verbessern, anstatt die Moleküle insgesamt näher zu bringen, wie dies im Fall des π-π-*stacking* versucht wird.

3.2.2 Das Anthracen C1s NEXAFS-Spektrum im Detail

Bis hierher ging es vor allem um die Eigenschaften bestimmter Halbleitermoleküle oder ihrer Kristalle. In diesem und den folgenden Abschnitten wird es jedoch verstärkt um eine Messtechnik sowie die Modellierung ihrer Ergebnisse mit Hilfe von DFT-Rechnungen gehen. Die Rede ist von NEXAFS. Die Veröffentlichung „*Analysis of the near-edge X-ray-absorption fine-structure of anthracene: A combined theoretical and experimental study*“ (siehe Abschnitt 5.7) behandelt in diesem Zusammenhang die NEXAFS-Signatur des Anthracen. Ziel der Studie ist, neben einem detaillierten Verständnis des Spektrums die Möglichkeiten des StoBe-Codes anhand eines Modellsystems, das für die Forschung im Bereich der organischen Halbleiter relevant ist, zu erproben. Die Wahl fiel aus mehreren Gründen auf den linearen, polyzyklischen, aromatischen Kohlenwasserstoff Anthracen (siehe Abb. 3.12a)). Viele theoretische Studien werden mit möglichst einfachen Systemen, wie z.B. Benzol, durchgeführt. Die meisten Moleküle, die im Bereich der organischen Elektronik genutzt werden können, sind jedoch wesentlich größer, alleine schon weil kleinere Vertreter zu flüchtig sind und unter normalen Bedingungen keine Festkörper ausbilden.

Anthracen bildet in dieser Hinsicht einen guten Kompromiss. Als naher Verwandter des Pentacens besitzt es die selbe Symmetrie und weist Kohlenstoffatome in allen Koordinationen auf, die sich auch im größeren Molekül finden[5]. Gleichzeitig ist es aber kleiner und lässt sich deshalb im Rahmen der Rechnung einfacher handhaben. Zudem war die Signatur des reinen Anthracen bis dato nicht literaturbekannt, sodass hier mit dem entsprechenden Spektrum eine Lücke in der Reihe der Acene geschlossen werden konnte. In Abb. 3.11a) ist das C1s-NEXAFS-Spektrum mit abgezogener Kante zu sehen. Bereits das Modellieren der Kante ist nur mit den berechneten Ionisationspotentialen möglich, da sie im Experiment von Molekülresonanzen überlagert wird und ihre genaue Position deshalb unbekannt ist. In Teilbild b) wird dieses Spektrum mit dem Ergebnis einer StoBe-Rechnung mittels der Slater-Transition-Methode verglichen, wobei sämtliche Rechnungen, die hier Erwähnung finden, wie in Abschnitt 2.6 beschrieben durchgeführt wurden. Zu sehen ist, dass diese Näherung bereits ein gutes Ergebnis liefert, anhand dessen eine Zuordnung der Resonanzen möglich ist. Allerding überschätzt dieser Ansatz systematisch die Anregungsenergien, da Relaxationseffekte nicht berücksichtigt werden. In Teilbild c) ist der Vorkantenbereich des Spektrums im Vergleich mit berechneten Spektren auf Basis der Slater-Transition-Methode, sowie vollständig relaxierter, angeregter Zustände zu sehen. Offensichtlich führt dieser zusätzliche Aufwand zu Anregungsenergien, die bis auf wenige 100 meV mit dem Experiment übereinstimmen. Zudem wird auch die Signatur besser abgebildet, da nicht alle Resonanzen gleichermaßen durch die Berücksichtigung der Relaxation verschoben werden. Die genauen Positionen der Resonanzen können dem Balkendiagramm unterhalb des Spektrums entnommen werden,

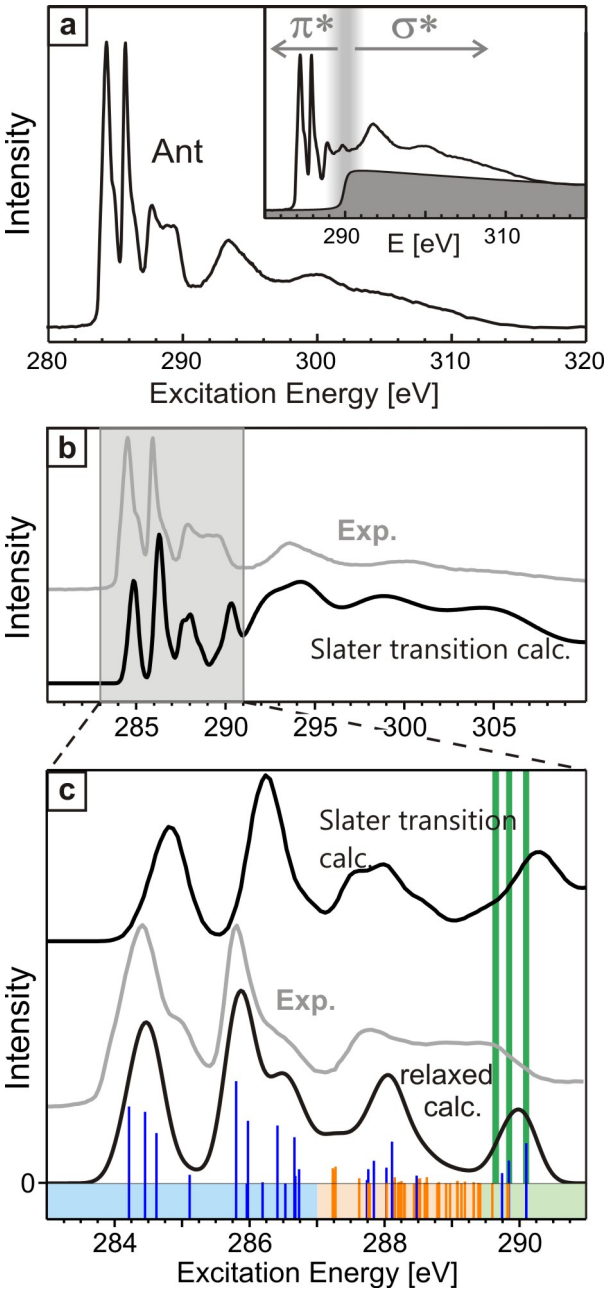

Abbildung 3.11: a) Experimentelles Anthracen-C1s-NEXAFS-Spektrum nach Abzug einer Kante. Die Rohdaten mit der Kante sind im Teilbild gezeigt. b) Vergleich von a) mit Ergebnis einer Slater-Transition-Rechnung. c) Zusätzlicher Vergleich mit einem berechneten Spektrum auf Basis relaxierter Zustände im Bereich der Vorkante. Grüne Linien markieren Ionisationspotentiale, blaue Linien zeigen π^*-Zielzustände an, während orange für σ^*-Zustände steht.

[5]Die C1s-Signatur des Pentacens wurde zudem bereits detailliert von Alagia *et al.* analysiert [85]. Diese Analyse basiert jedoch nicht auf StoBe.

wobei die Höhen proportional zur berechneten Oszillatorstärke sind. Besonders interessant für die spätere Interpretation von winkelabhängigen Messungen ist der Charakter der Resonanzen, der hier anhand der Farbe abgelesen werden kann. Blau steht für π^*-Zustände, während orange σ^*-Zustände anzeigt. Innerhalb des farbigen Streifens am unteren Rand des Diagramms sind zudem auch Resonanzen eingezeichnet, deren Oszillatorstärke sehr gering ist. Diese tragen nicht zum Spektrum bei, können aber für die Interpretation wichtig sein. In Abb. 3.12b)-e) sind die Teilspektren gezeigt, aus denen das zuvor diskutierte Gesamtspektrum durch Superposition berechnet wird, während nebenstehend beispielhaft die relaxierten Orbitale des angeregten LUMO+1 gezeigt sind. Verschiedene Details können den Teilspektren entnommen werden. In c) fällt z.B. das höhere Ionisationspotential für das Anregungszentrum C_2 auf. Dies ist ein Beispiel für einen *chemical shift* und liegt an der Koordination des C_2-Atoms im Molekül, welches als einziges drei Kohlenstoff-

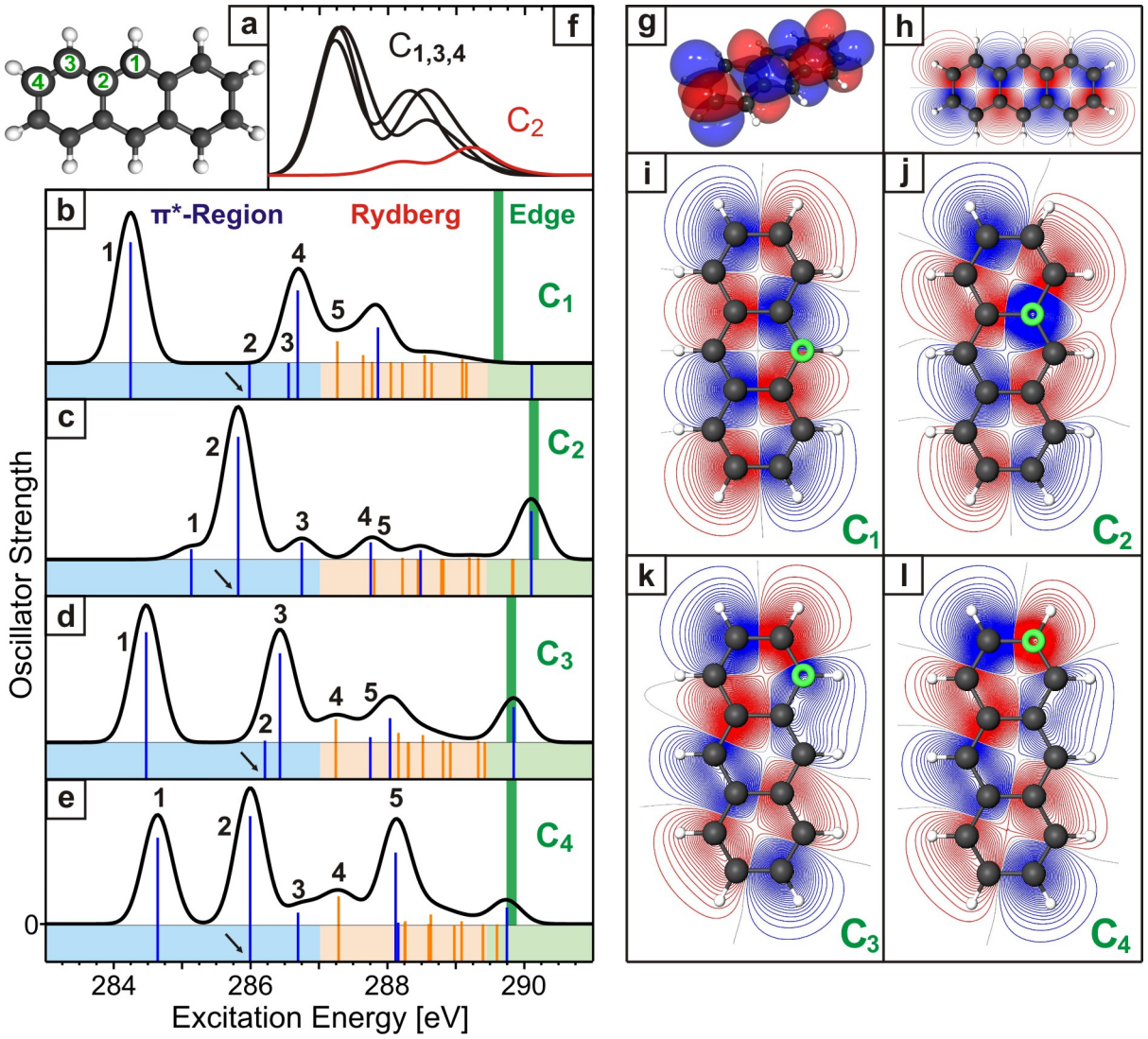

Abbildung 3.12: a) Anthracenstruktur mit nummerierten Anregungszentren. b)-e) Berechnete Teilspektren für die vier Anregungszentren. Farblogik wie in Abb. 3.11c). f) Teilspektren auf Basis von σ^*-Zuständen. g) LUMO+1 im Grundzustand. h) Schnitt durch das Orbital aus g) 0.5 Å unterhalb der Molekülebene. i)-l) Schnitte wie in h) für das angeregte LUMO+1 (Pfeile in a)-e)). Grüne Ringe markieren das jeweilige Anregungszentrum.

nachbarn hat. In diesem Zusammenhang wird die Bedeutung einer detaillierten Betrachtung der Ergebnisse ersichtlich: In diesem Beispiel fällt der *chemical shift* sehr gering aus. Elektronegative Substituenten, wie z.B. Fluor, können aber zu Verschiebungen von über 2 eV führen. Am Fall der hier gezeigten Teilspektren würde die erste Resonanz damit in den Bereich der dritten Resonanz für nicht substituierte Anregungszentren schieben. LUMO und LUMO+2 Zustände würden im Spektrum folglich mischen. Genau dieser Effekt führte im Fall der Fluorierung des Rubrens in Abschnitt 3.1.2 zu den stark veränderten Signaturen. In solch einem Fall kann das Spektrum nur anhand einer theoretischen Modellierung, wie sie hier gezeigt ist, exakt analysiert werden. Dieses Beispiel zeigt auch, dass in einem NEXAFS-Spektrum Resonanzen nicht unbedingt eindeutig einem Zielzustand zugeordnet werden können. Während z.B. die führende Resonanz im Gesamtspektrum ausschließlich auf LUMO-Zustände zurück zu führen ist, überlagern sich im Bereich von ca. 287 eV Beiträge der dritten und vierten Resonanzen. Noch fundamentaler ist, dass die Zustände unterschiedlich stark schieben. Je nach Anregungszentrum kann sich dadurch die Reihenfolge der Zustände ändern. So ist Resonanz vier in b) und c) z.B. π-artig, während sie in d) und e) σ-artig ist. Begriffe wie LUMO+2 oder LUMO+3 sind an dieser Stelle also gar nicht eindeutig definiert, da jeweils eine Mischung unterschiedlicher Zielzustände vorliegt. Abschließend sei noch ein Blick auf die σ^*-Zustände geworfen. Diese Zustände werden im Bereich der Vorkante oft auch als Rydbergzustände bezeichnet. Im Fall von Kohlenwasserstoffen sind sie mit antibindenden C-H-Orbitalen assoziiert. Dies wird in Teilbild f) deutlich. Hier sind alle vier Teilspektren gezeigt, jedoch wurden jeweils nur σ-Zustände berücksichtigt. Gut zu sehen ist, dass von C_2 aus kaum in diese Zustände angeregt werden kann, da dieses Kohlenstoffatom keine Bindung zu einem Wasserstoffatom besitzt und sich deshalb kaum Überlapp zu den entsprechenden Orbitalen ergibt.
Insgesamt liefert diese Studie also tiefe Einsichten in die Entstehung der C1s-NEXAFS-Signatur des Anthracen. Dabei zeigt sie durch den Vergleich mit dem Experiment, dass StoBe im Bereich der Kohlenstoffkante Anregungsenergien mit einer Genauigkeit von besser als 300 meV liefert, wenn man bereit ist, die aufwendige Berechnung einzelner angeregter Zustände in Kauf zu nehmen. Allerdings liefert auch schon die Slater-Transition-Methode gute Ergebnisse und die systematische Überschätzung der Energien kann entsprechend berücksichtigt werden. Darüber hinaus wird insbesondere anhand der Teilspektren deutlich, dass eine zu einfache Interpretation von NEXAFS-Spektren in die Irre führen kann, da verschiedene Zielzustände durch *chemical shifts* und Relaxationseffekte zur selben Resonanz beitragen können. Kommt es also auf die genauen Beiträge in einem Spektrum an, ist eine Analyse wie sie hier gezeigt ist das Mittel der Wahl.

3.2.3 NEXAFS-Dichroismus planarer, konjugierter Kohlenwasserstoffe

Die Veröffentlichung „*Characterization of orientational order in π-conjugated molecular thin films by NEXAFS*“ stellt in der Reihe der hier vorgestellten Artikel eine Ausnahme dar, weil es sich um einen reviewartigen Beitrag zu einer Sonderausgabe des *Journal of Electron Spectroscopy and Related Phenomena* handelt. Dabei wird im Detail beleuchtet, wie NEXAFS zur Orientierungsbestimmung konjugierter Moleküle genutzt werden kann. Dies geschieht anhand ausgewählter Beispiele und Grafiken, die die physikalischen Zusammenhänge so anschaulich wie möglich vermitteln sollen. Im Folgenden wird die Entstehung des Dichroismus mit Blick auf Abschnitt 3.2.4, für den dies von besonderer Bedeutung ist, genauer dargestellt.

Für die Intensität I_v einer vektorartigen Anregung in Abhängigkeit ihres Winkels zur Oberflächennormalen α sowie des Einfallswinkels θ der linear polarisierten Röntgenstrahlung gilt für Proben mit dreizähliger oder höherer Symmetrie folgende Beziehung:

$$I_v \propto P\cos^2\theta\left(\cos^2\alpha + \frac{1}{2P}\tan^2\theta\sin^2\alpha\right) \tag{3.1}$$

P bezeichnet dabei den Polarisationsgrad der Strahlung. Mit Hilfe dieser Gleichung kann anhand des winkelabhängigen Intensitätsverlaufes einer Resonanz auf die Orientierung des Moleküls geschlossen werden. Dazu muss jedoch bekannt sein, wie das entsprechende Übergangsdipolmoment (TDM für *Transition Dipole Moment*) im Molekül orientiert ist. Dies ist ebenfalls eine Information, die z.B. aus einer Analyse wie in Abschnitt 3.2.2, gewonnen werden kann. Für die führenden Resonanzen planarer, konjugierter Moleküle ist die Zuordnung jedoch einfach. Hier liegen stets π^*-Resonanzen vor, deren TDM senkrecht zur Molekülebene liegt. In der Praxis werden mehrere Spektren bei verschiedenen Winkeln aufgenommen und der Intensitätsverlauf einer bestimmten Resonanz ausgewertet. An die so gewonnenen Stützpunkte wird dann mit Gleichung 3.1 der passende Winkel α gefittet. Ein Beispiel für solch eine Messung ist zusammen mit einer Darstellung der relevanten Winkel in Abb. 3.13a) zu sehen. Um diesen Zusammenhang zu verdeutlichen wurde für die Veröffentlichung ein Datensatz mit besonders kleinschrittigen Winkelveränderungen erhoben. Aneinander gereiht liefern diese Messungen an einer Pentacen/SiO_2-Probe eine quasikontinuierliche Darstellung des Dichroismus. In Abb. 3.1b) ist das Ergebnis zu sehen. Pentacenmoleküle nehmen auf SiO_2 eine stehende Orientierung ein, sodass die führenden π^*-Resonanzen für große Winkel θ maximale Intensität zeigen, die zusammen mit dem Winkel abnimmt. Dahingegen sind bei höheren Energien Resonanzen zu sehen, die einen gegenläufigen Dichroismus zeigen. Dieses Verhalten geht auf σ^2_{top}-Resonanzen zurück. Horizontale Schnitte durch die zweidimensionale Falschfarbendarstellung liefern die gewohnten

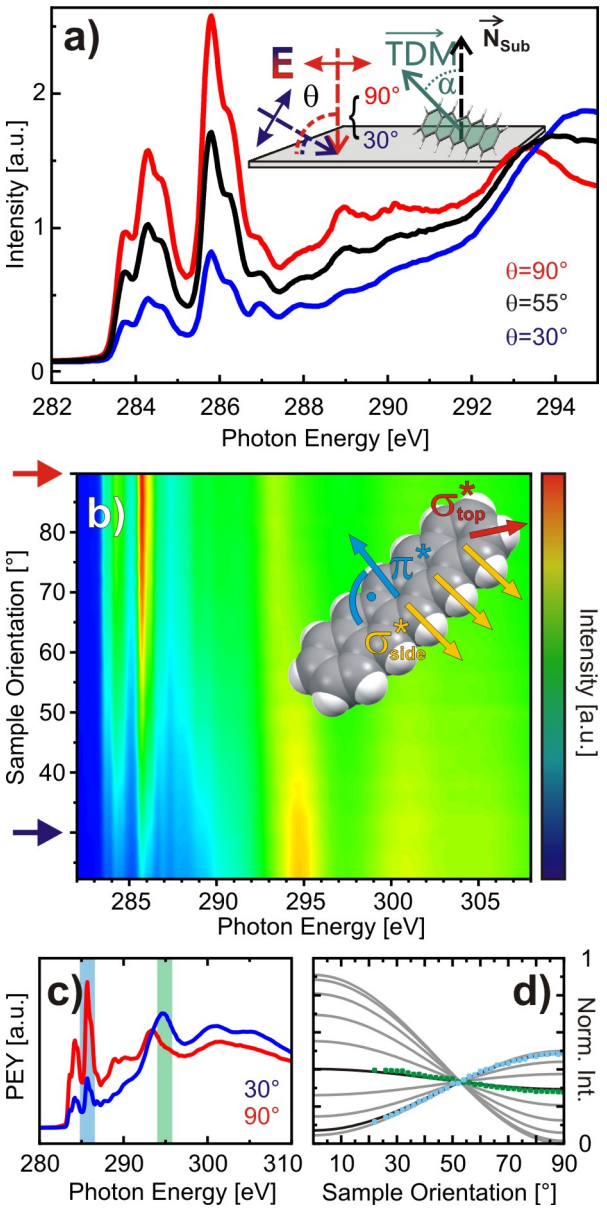

Abbildung 3.13: a) Typischer Dichroismus führender π^*-Resonanzen. Teilbild zeigt die Winkelbeziehungen schematisch b) Quasikontinuierliche Dichroismusmessung einer PEN/SiO_2-Probe. c) Horizontale Schnitte aus b). d) Vertikale Schnitte an markierten Positionen aus c).

NEXAFS-Spektren, die in Teilbild c) gezeigt sind. Nimmt man stattdessen an den in c) farbig markierten Stellen vertikale Schnitte, erhält man den eigentlichen Dichroismus, wie er in d) zu sehen ist. Grau hinterlegt sind theoretische Kurven nach Gleichung 3.1 für verschiedene α. Zu den experimentellen Daten passt aber jeweils nur ein Verlauf, der in schwarz dargestellt ist.

Mit Hilfe von Abb. 3.13b) wird ein verbreiteter Denkfehler im Zusammenhang mit Dichroismen nachvollziehbar. Oft wird der Dichroismus von π^*- und σ^*-Resonanzen als grundsätzlich gegenläufig angenommen, da die zugehörigen TDMs in planaren Molekülen stets einen 90° Winkel einschließen. Elementare geometrische Überlegungen zeigen jedoch, dass dieser Schluss zu einfach ist und nur in einigen Spezialfällen zutrifft. Dies kann anhand von Abb. 3.14 verdeutlicht werden. In a) ist ein liegendes Acenmolekül als Quader dargestellt zusammen mit drei Pfeilen, die die Richtungen der entscheidenden Übergangsdipolmomente anzeigen. Blau zeigt hierbei eine π^*-Resonanz an, während orange für eine seitliche und rot für eine σ^*-Resonanz am Kopfende des Moleküls steht. Nebenstehend sind exemplarisch berechnete Dichroismen für die drei TDMs, sowie die Summe der beiden σ^*-Verläufe gezeigt. Da die σ^*-Resonanzen oft auf ähnliche Bindungssituationen zurück gehen, liegen sie in den Spektren bei der selben Anregungsenergie, sodass im Experiment

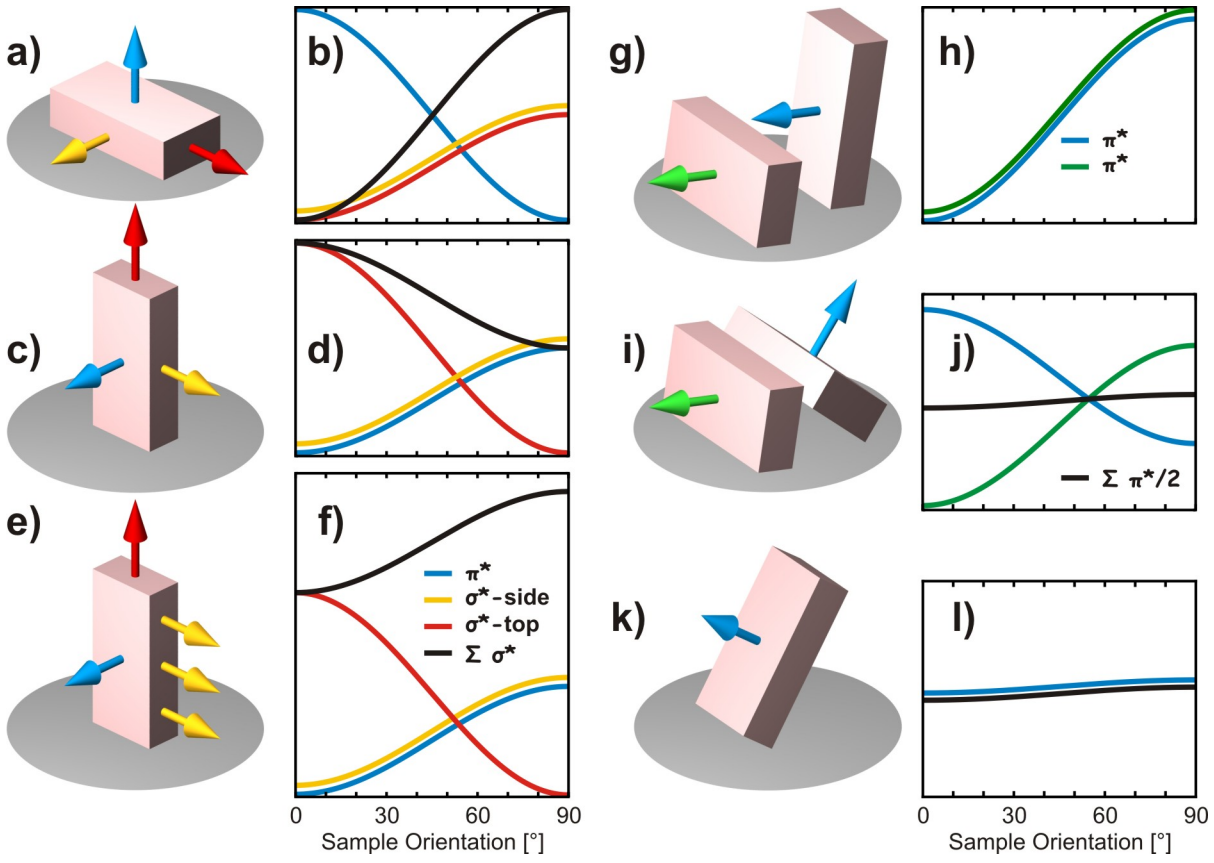

Abbildung 3.14: a) Schematische Darstellung eines Acenmoleküls als Quader. Pfeile zeigen Übergangsdipolmomente an: blau steht für π^*-Resonanzen, während orange und rot für σ^*-Übergänge stehen. a,c,e) Beispiele für verschiedene Orientierungen und Moleküllängen. b,d,f) Jeweilige Dichroismusverläufe der einzelnen Resonanzen nach Gleichung 3.1. g,h) Anhand von π^*-Resonanzen ununterscheidbare Orientierungen. i,j) Einfluss des Packungsmotivs auf den Dichroismus. k,l) Von i) ununterscheidbare Molekülorientierung. Identische Kurven sind leicht gegeneinander verschoben, um beide sichtbar zu machen.

stets die Summe der Intensitäten betrachtet wird (siehe z.B. Abb. 3.12f)). Für den liegenden Fall in a) gilt tatsächlich, dass π^* und σ^* gegenläufige Abhängigkeiten zeigen. Auch für den stehenden Fall in c) gilt dies, jedoch ist die Situation schon nicht mehr so eindeutig, denn π^* und σ^*_{side} zeigen den selben Dichroismus. Nur weil σ^*_{side} aufgrund der azemuthalen Mittlung die Hälfte seiner maximalen Intensität gegenüber σ^*_{top} einbüßt, wird der Gesamtverlauf durch σ^*_{top} dominiert. Für stehende Moleküle, wie im Pentacenbeispiel aus Abb. 3.11b), kann also nur eine σ^*_{top}-Resonanz einen zu π^* gegenläufigen Dichroismus zeigen. In Teilbild e) ist der realitätsnahe Fall eines langen Acens gezeigt, indem σ^*_{side}-Resonanzen die σ^*_{top}-Beiträge zahlenmäßig überbieten. Hier gibt es überhaupt keinen gegenläufigen Dichroismus solange die σ^*-Resonanzen energetisch überlappen und ähnliche Intensitäten besitzen. Hier wird deutlich, dass die bereits mehrfach erwähnte Kontrolle der Molekülorientierung zusätzliche Erkenntnisse ermöglicht. Durch den Vergleich des Dichroismus bei verschiedenen Molekülorientierungen kann anhand der hier gezeigten Überlegungen eine experimentelle Aussage über den Charakter einer Resonanz getroffen werden. Diese Information ist ansonsten oft nur theoretisch zugänglich.
Neben einer zu einfachen Betrachtung des Dichroimus gibt es aber noch einige Fälle, die im Rahmen einer NEXAFS-Messung ununterscheidbar sind und deshalb leicht zu Fehlinterpretationen führen können. Diese sind im zweiten Teil von Abb. 3.14 dargestellt. In Teilbild g) bzw. h) ist zu sehen, dass eine stehende und eine aufrecht liegende Orientierung nicht anhand der π^*-Resonanzen allein unterschieden werden können, da primär eben nicht die Molekül-, sondern die TDM-Orientierung bestimmt wird. Ein weiteres Problem können Kristallstrukturen mit mehreren Molekülen in der Einheitszelle sein. In i) ist der Fall eines Herringbone-Motivs dargestellt. Hier mittelt die Messung über die Anteile beider Moleküle, sodass ein α bestimmt wird, das zu keinem der beiden Moleküle passt. Zudem kann dieser Fall nicht ohne Weiteres von einer Molekülorientierung mit genau dem gemittelten Winkel unterschieden werden, wie es in den Teilbildern k) und l) zu sehen ist. Die Betrachtung zusätzlicher Resonanzen kann helfen, manche dieser Fälle zu unterscheiden, was in der Praxis jedoch oft schwierig ist, da sich abseits der führenden π^*-Resonanzen viele Signale überlagern. Deshalb sind in der Praxis komplementäre Daten, z.B. aus der Röntgenbeugung, nötig, um gesicherte Aussagen zu komplexen Systemen machen zu können.

3.2.4 Dichroismus an der F1s-Kante

NEXAFS-Messungen können elementspezifisch durchgeführt werden, indem die Anregungsenergien im Bereich einer entsprechenden Absorptionskante gewählt werden. In der Veröffentlichung „*Understanding the F 1s NEXAFS Dichroism in Fluorinated Organic Semiconductors*“ (siehe Abschnitt 5.8) geht es speziell um Dichroismusmessungen an der Fluor 1s-Kante. Grundsätzlich erwartet man hier die selbe Winkelabhängigkeit wie an der zugehörigen C1s-Kante, da die beiden 1s-Anfangszustände die selbe Symmetrie besitzen und die Zielzustände unverändert bleiben, wodurch die entsprechenden Übergangsdipolmomente die selbe Richtung haben. Lediglich die Intensitäten der Resonanzen sollten sich mit dem Kantenwechsel ändern können, so wie es in Abschnitt 2.4 am Beispiel des Pyrazins vorgestellt wurde. Aufgrund dieser Überlegung würde man für fluorierte Kohlenwasserstoffe, wie sie in dieser Arbeit schon mehrfach diskutiert wurden, für die führenden Signale π^*-Resonanzen mit dem entsprechenden Dichroismus in den F1s-Spektren erwarten. Tatsächlich passen die Ergebnisse aber oft nicht zu dieser Annahme und entsprechende Winkelauswertungen führen zu anderen Werten als an der C1s-Kante. Oteyza *et al.*

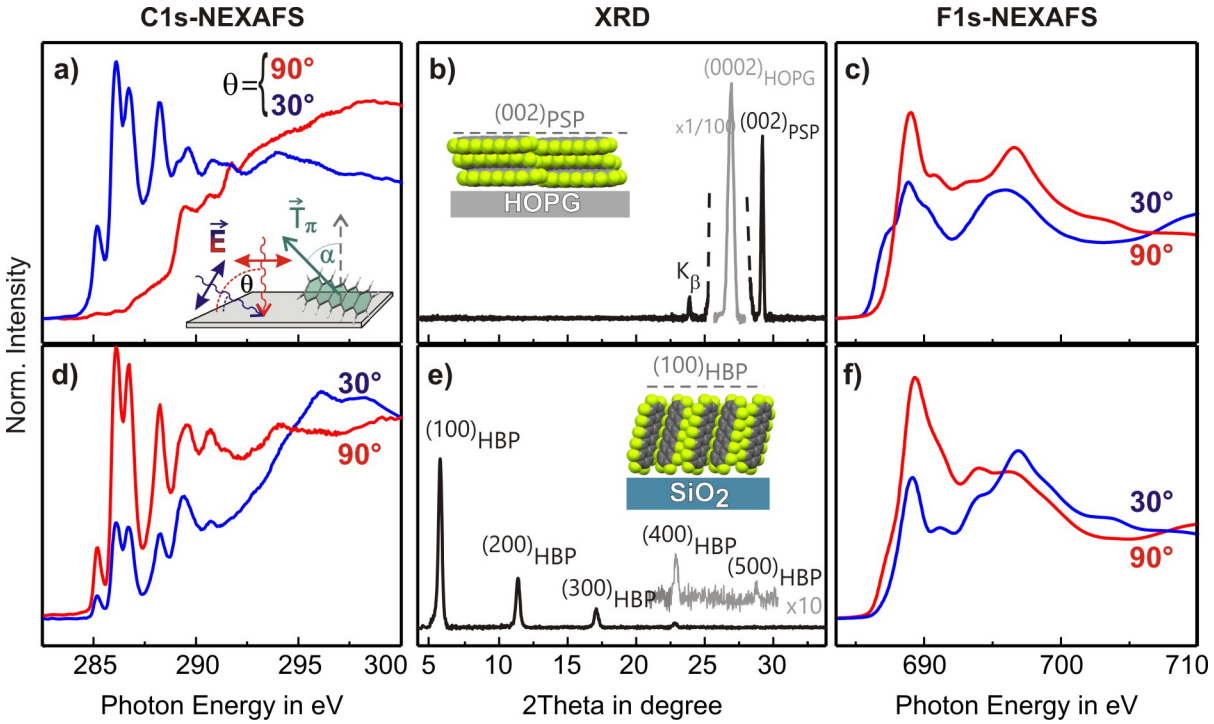

Abbildung 3.15: Vergleich der C1s-NEXAFS-Dichroismen von Perfluoropentacen auf HOPG und SiO_2 (a,d) mit den entsprechenden Spektren der F1s-Kante (c,f). b,e) zeigen XRD Daten der Dünnfilme.

konnten im Rahmen einer theoretischen Modellierung der F1s-Spektren von Kupferphthalocyanin zeigen, dass sich an der Fluorkante π- und σ-artige Beiträge für die führenden Resonanzen mischen, was die Abweichungen erklärt. Allerdings wird nicht erläutert, wieso es zu diesem unerwarteten Verhalten kommt und zudem wird von einem stets invertierten Dichroismus an der F1s-Kante im Vergleich zur C1s-Kante ausgegangen. Dass solch eine Annahme problematisch ist, wurde im vorangegangen Abschnitt diskutiert. Aufgrund dieser Ausgangslage wurde nach einem Modellsystem gesucht, das die grundlegende Aufklärung des Dichroismus fluorierter Moleküle an der F1s-Kante erlaubt. Hier fiel die Wahl auf Perfluoropentacen (PFP), weil sich aus diesem Material Dünnfilme mit einer exklusiven kristallinen Ausrichtung herstellen lassen und zudem die Molekülorientierung über das Substrat kontrolliert werden kann. Auf HOPG (Highly Ordered Pyrolytic Graphene) liegen die Moleküle [67], während sie auf SiO_2 stehen [87]. In Abb. 3.15 sind die NEXAFS-Spektren der C1s- und F1s-Kante für die unterschiedlichen Proben vergleichend dargestellt. Zudem finden sich in Teilbild b) und e) die zugehörigen XRD-Daten, die belegen, dass die Dünnfilme exklusiv in der gewünschten kristallinen Orientierung vorliegen. Vergleicht man die Diagramme a) und c), ist der postulierte, invertierte Dichroismus zu sehen, während d) und f) zumindest qualitativ das selbe Verhalten zeigen. Um diesen Widerspruch aufzuklären wurde das F1s-Spektrum mit StoBe simuliert. Dabei wurde für die führenden Resonanzen analog zur Anthracen-Studie in Abschnitt 3.2.2 vorgegangen, nur mit dem Unterschied, dass die in Abb. 3.16a) nummerierten Fluoratome als Anregungszentren dienen. Wie in Abschnitt 2.6 erläutert, lassen sich mit StoBe jedoch keine Oszillatorstärken berechnen, wenn die angeregten Zustände einzeln konvergiert werden, weshalb hier die Ergebnisse der Slater-Transition-Rechnung manuell zugeordnet werden. Für PFP war dies jedoch teilweise aufgrund stark verzerrter Orbitale kaum möglich und zudem zeichneten

sich starke Relaxationseffekte ab, die sich auch auf die Oszillatorstärken auswirken könnten. Aus diesem Grund wurden die entsprechenden Matrixelemente zwischen der Grundzustandskonfiguration und den angeregten Zuständen von Paul Jerabek und Robert Berger auf der Basis von Löwdin Regeln berechnet [88]. In Abb. 3.16b) sind die Ergebnisse dieser Rechnungen mit dem aus Abschnitt 3.2.2 bekannten Farbcode dargestellt. Auffällig ist, dass die führenden Resonanzen tatsächlich π-artig sind, ihre Oszillatorstärken im Vergleich zu den σ^*-Resonanzen jedoch gering ausfallen. Zudem liegen letztere bei deutlich tieferen Energien als man erwarten würde, wodurch es zur Mischung unterschiedlicher Resonanztypen kommt. Verantwortlich hierfür ist eine starke Verschiebung der σ^*-Resonanzen aufgrund der Relaxation, die wiederum durch die hohe Elektronegativität der Fluoratome verstärkt wird. Starke Verschiebungen in den Spektren aufgrund von Fluorierung wurden schon früher beobachtet und dort als „Perfluoroeffekt“ bezeichnet [89]. In Abb. 3.16c) sind Teilspektren für das F1-Zentrum gezeigt, die auf der Slater-Transition-Methode und der Rechnung mit angeregten Konfigurationen beruhen. Zusätzlich sind jeweils eine π^*-

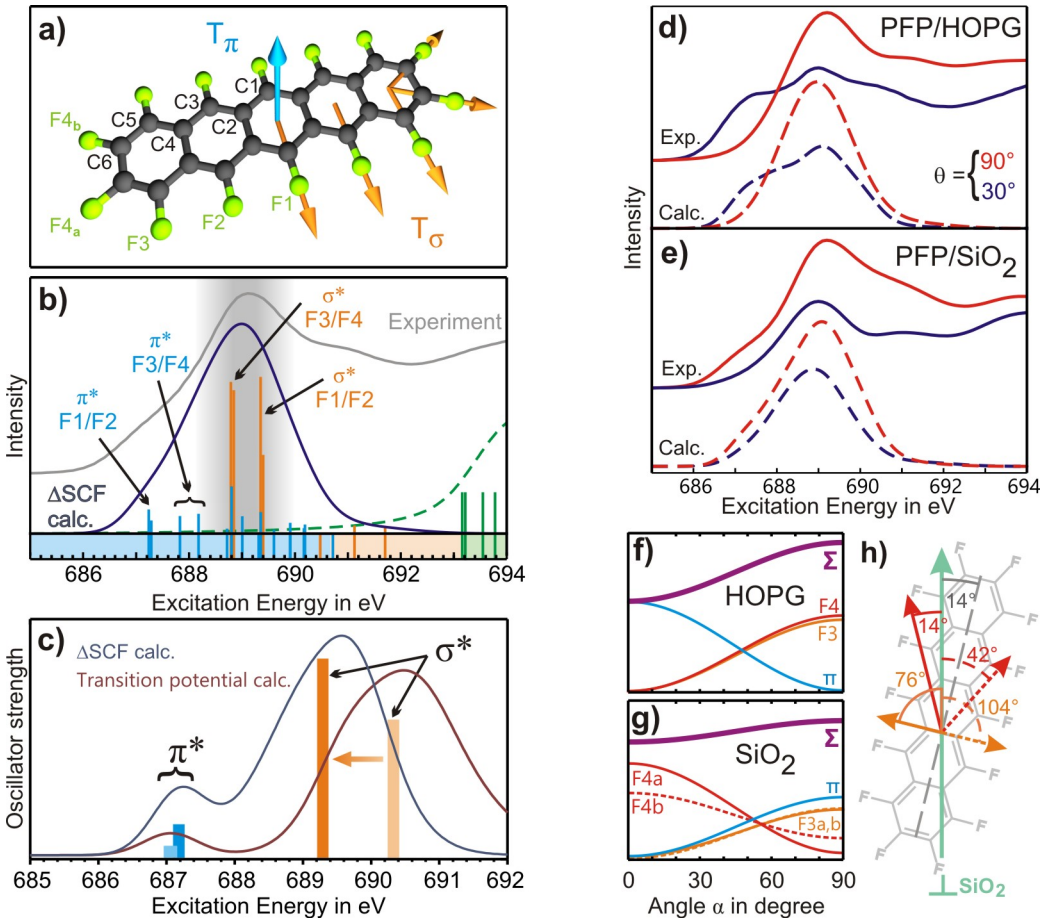

Abbildung 3.16: a) PFP-Struktur mit nummerierten Anregungszentren. Pfeile zeigen Richtungen relevanter TDMs an. b) Berechnetes PFP-F1s-NEXAFS-Spektrum im Vergleich mit dem Experiment. Blaue Linien zeigen π^*-, orange Linien σ^*-Resonanzen an. Ionisationspotentiale sind grün dargestellt. c) Starke Verschiebung von σ^*-Resonanzen durch Relaxation. d,e) Vergleich berechneter und experimenteller winkelabhängiger Spektren für PFP/HOPG und PFP/SiO_2. f,g) Berechnete Dichroismen einzelner Resonanzen im Bereich des Hauptsignals bei ca. 689 eV für die jeweils bekannte Molekülorientierung. h) Visualisierung der Orientierung verschiedener σ^*-TDMs des PFP auf SiO_2.

und eine σ^*-Resonanz eingezeichnet. Auffällig ist, dass nur letztere auf die Berücksichtigung der Relaxation reagiert. Hintergrund ist, dass σ-Orbitale sich überwiegend aus s-Anteilen zusammensetzen, die wiederum stärker auf die veränderten elektrostatischen Bedingungen reagieren, als p-Anteile, sodass der Energiegewinn hier größer ist. Neben den Oszillatorstärken und Energien liefern die Rechnungen auch die genaue Orientierung der TDMs, welche in Teilbild a) als Pfeile eingezeichnet sind. Dies erlaubt, den Dichroismus gegen zu rechnen, da die genaue Orientierung der Moleküle in den Dünnfilmen aufgrund der Kristallstruktur- und XRD-Daten exakt bekannt ist. Es kann also für jede Anregung ein Winkel α bestimmt werden und mit Gleichung 3.1 die Intensität für einen gegebenen Winkel θ bestimmt werden. Das Ergebnis dieser Rechnungen ist in Abb. 3.16d) und e) im Vergleich zu den experimentellen Daten zu sehen. Offensichtlich wird eine sehr gute Übereinstimmung erreicht. Dadurch, dass hier nun auch Winkelabhängigkeiten einfließen, kann auch die Qualität der berechneten Intensitäten beurteilt werden. Würde das Verhältnis zwischen π- und σ-Intensitäten nicht stimmen, könnte bestenfalls einer der berechneten Dichroismen mit dem Experiment übereinstimmen, nicht aber beide. Analysiert man die Winkelabhängigkeit noch genauer, gelangt man zu Teilbild f) bzw. g). Hier sind die Dichroismen verschiedener Resonanzen im Bereich des Hauptsignals bei ca. 689 eV gezeigt. Dieser Bereich ist besonderes interessant, da der Gesamtdichroismus bei dieser Energie für beide Molekülorientierungen nahezu identisch ist. Tatsächlich entspricht die Situation in f) sehr genau dem vereinfachten Schema in Abb. 3.14a), während g) sehr gut durch Abb. 3.14e) beschrieben wird. Auffällig ist jedoch, dass die Kurven für die σ-TDMs F4a und F4b im Fall von PFP auf SiO_2 nicht identisch sind. Ursache hierfür ist, dass das PFP-Molekül nicht exakt aufrecht steht, was in Teilbild h) genauer gezeigt ist. Dadurch ist die Symmetrie des Kristalls kleiner als die des Moleküls und die beiden genannten TDMs nicht mehr symmetrieäquivalent, wenn es um die Bestimmung des Dichroismus geht. Bleibt abschließend noch die Frage zu klären, wieso die σ^*-Resonanzen an der F1s-Kante so viel stärker ausfallen als an der C1s-Kante, wo normalerweise π^*-Resonanzen dominieren. Die Antwort liefert ein MO-Diagramm, das die

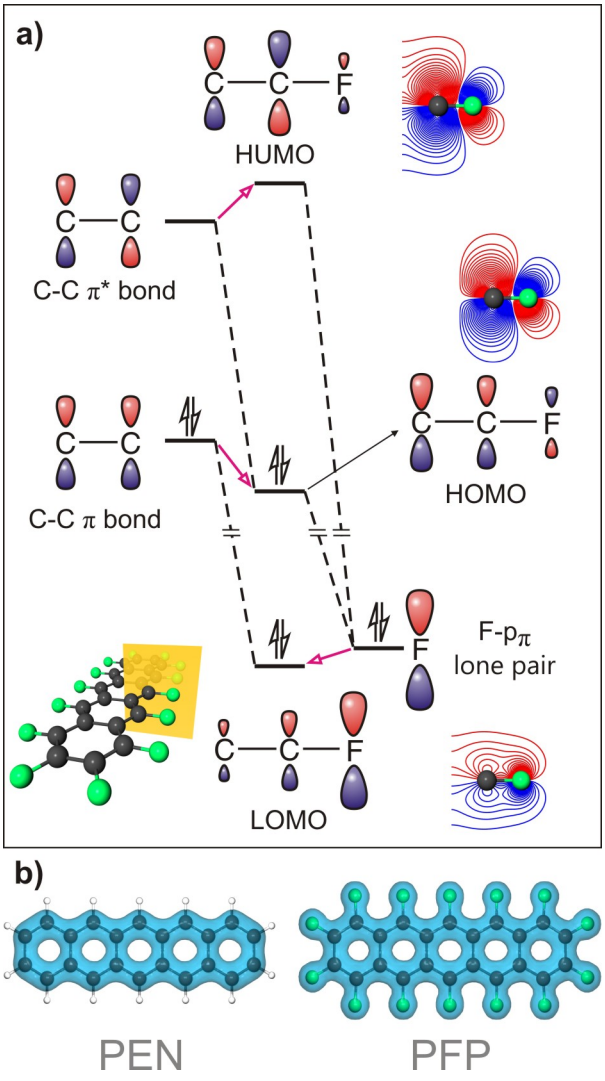

Abbildung 3.17: a) MO-Diagramm der π-Wechselwirkung eines Fluoratoms mit einem konjugierten Kohlenstoffgerüst. Rechts sind Schnitte der entsprechenden Orbitale aus DFT-Rechnungen gezeigt. Die gelbe Fläche links unten zeigt die Lage der Schnittebene an. b) Kumulierte Elektronendichte aller π-Orbitale des Pentacens bzw. Perfluoropentacens.

π-Bindung der Fluoratome an das konjugierte Kohlenstoffgerüst des PFP beschreibt. Die Ausgangsniveaus der Bindungspartner liegen energetisch weit auseinander, wodurch das entstehende Orbital im gebundenen Zustand durch den energetisch näher liegenden Bindungspartner dominiert wird. Die energetisch hoch liegenden LUMO-Orbitale, die für die NEXAFS-Spektroskopie relevant sind, werden deshalb von p-Orbitalen der Kohlenstoffatome bestimmt, während die Elektronendichte am Fluor gering ausfällt. Dies führt unmittelbar zu einem kleineren Überlappintegral für eine Anregung von F1s-Elektronen in diesen Zielzustand als bei C1s-Anregungen. Die σ^*-Resonanzen an der F1s-Kante sind also nicht viel stärker, sondern die π^*-Resonanzen sind erheblich schwächer, als man es von der C1s-Kante für konjugierte Moleküle gewohnt ist.
Aus der Betrachtung des MO-Schemas ergibt sich eine weitere Konsequenz, die im Zusammenhang mit fluorierten Systemen selten zur Sprache kommt: Die Fluoratome beteiligen sich mit ihren p-Orbitalen am π-System des Moleküls, auch wenn zwischen Fluor und Kohlenstoff keine π-Bindung im engeren Sinne vorliegt. Damit ist das delokalisierte π-System in fluorierten Molekülen erheblich größer als in den reinen Kohlenwasserstoffen. In Abb. 3.17b) wird dies anhand der kumulierten Elektronendichte aller π-Orbitale des Pentacens im Vergleich zu der des PFP verdeutlicht. Damit kann auch Fluorierung zu einer Verbesserung des π-π-Überlapps im Sinne des Ladungstransportes in molekularen Kristallen beitragen.

4. Zusammenfassung und Ausblick

In dieser Arbeit wurden die Eigenschaften verschiedener molekularer Materialien im Hinblick auf ihre Eignung als nützliche Modellsysteme für weiterführende Experimente untersucht. In diesem Zusammenhang wurden neu synthetisierte Pentacenderivate mit permanentem Dipol betrachtet. Dazu wurden Dünnfilme dieser Materialien mittels OMBD hergestellt und durch Röntgenbeugung, UV-Vis- sowie teilweise auch NEXAFS-Spektroskopie untersucht. Obwohl die verschiedenen Moleküle ein systematisch zunehmendes Dipolmoment aufweisen, zeigen sie stark variierende Festkörpereigenschaften. Insbesondere sind einige der Moleküle aufgrund chemischer Instabilität schwer prozessierbar oder bilden teilweise keine kristallinen Dünnfilme aus. Die Hoffnung, die positiven festkörperphysikalischen Eigenschaften des Ausgangsmoleküls zu bewahren und die Moleküle mit zusätzlicher Funktionalität auszustatten, hat sich hier nicht erfüllt. Hauptgrund für die Probleme ist der unvorhersehbare Einfluss chemischer Modifikationen auf die Kristallstruktur. Dies wurde insbesondere anhand der Excitonenbindungsenergien, die aus UV-Vis-Spektren bestimmt wurden, deutlich, da die Änderung mittlerer Molekülabstände und damit der Kristallstruktur für diese Werte stärker ins Gewicht fällt als veränderte intrinsische Moleküleigenschaften in Form der Polarisierbarkeit. Dennoch haben sich Bistrifluormethylpentacen, Trifluormethyl-TIPS-pentacen und Hexafluorodiazapentacen als vielversprechende Kandidaten für weitere Studien erwiesen. Besonders günstig ist hier der Umstand, dass NEXAFS-Messungen an Dünnfilmen auf verschiedenen Substraten gezeigt haben, dass diese Moleküle sich analog zu Pentacen oder Perfluoropentacen durch die Wahl des Substrates in ihrer Orientierung beeinflussen lassen, was richtungsaufgelöste spektroskopische Untersuchungen ermöglicht.
In weiteren Studien stand die Fluorierung als gezielte chemische Modifikation im Vordergrund. Unter anderem durch NEXAFS-Messungen konnte gezeigt werden, dass die Steigerung des Oxidationspotentials durch Fluorierung zu einer deutlichen Stabilisierung des Moleküls gegen Oxidation führt. Berechnete NEXAFS Spektren des perfluorierten Rubrens haben gezeigt, dass unterschiedliche Konformationen des Moleküls anhand der Spektren nicht unterschieden werden können. Dafür war auf Basis der berechneten Daten eine detaillierte Analyse möglich, die gezeigt hat, dass die elektronischen Systeme der Phenylringe sowie des Tetracenrückrades weitestgehend elektronisch entkoppelt sind und getrennt voneinander betrachtet werden können. Die Rechnungen haben jedoch auch gezeigt, dass ein Verständnis der NEXAFS-Signatur als Superposition einer Perfluorobenzol- und einer Tetracensignatur dennoch nicht möglich ist, da starke *chemical shifts* zu einer komplizierteren Situation führen, die nur im Rahmen einer vollständigen Analyse des Spektrums zuverlässig erfasst werden kann.
Während im Fall des Rubrens mit der chemischen Stabilität eine Moleküleigenschaft im Fokus stand, wurde im Fall des HBCs der Einfluss von Fluorierung auf das Packungsmotiv genauer betrachtet. Beugungsexperimente konnten für alle teilfluorierten Varianten parallele Anordnungen der Moleküle nachweisen. Eine Hirshfeldanalyse legt nahe, dass für

die Bevorzugung dieser Packung gegenüber dem Herringbonemotiv weniger die statischen Dipolmomente der Moleküle, als in erster Linie Wasserstoffbrückenbindungen zwischen Fluor- und Wasserstoffatomen im Randbereich der Moleküle verantwortlich sind.
In einer weiteren Arbeit, die sich mit der genauen Struktur eines Modellsystems befasst, wurden Kristalle des Perylen untersucht. Dabei ist es mit Hilfe von *In-plane*-Messungen gelungen, den typischen Habitus von Kristallen beider bekannter Polymorphismen des Perylens mit kristallographischen Richtungen zu korrelieren. Dadurch ist es zukünftig möglich, diese Kristalle unter dem Mikroskop gezielt auszurichten, ohne dass weitere Techniken benötigt werden. Zudem wurde im Rahmen der Beugungsexperimente die Existenz einer Dünnfilmphase des Perylens nachgewiesen.
Inspiriert durch die Erfolge bei der Beschreibung der Kristallstrukturen teilfluorierter HBC-Moleküle wurde mittels der Hirshfeldanalyse eine vergleichende Studie der Packungsmotive pentacenartiger Moleküle durchgeführt. Indem die Auswahl der Moleküle auf solche mit vergleichbarer Geometrie beschränkt wurde, konnte die Komplexität des Problems deutlich verringert werden. Sterische Effekte spielen keine Rolle und der Einfluss der London Dispersion kann für alle Moleküle als vergleichbar angenommen werden. So lassen sich Unterschiede der Packungsmotive auf Atomgrößen und elektrostatische Eigenschaften der Moleküle zurückführen, die durch MEPs visualisiert werden können. Aus dem Vergleich ergibt sich, dass für ein Herringbonemotiv ein einheitliches Vorzeichen des Potentials im Randbereich der Moleküle vorliegen muss. Eine Verletzung dieses Kriteriums führt bereits bei wenigen Heteroatomen zu anderen Packungsmotiven, wobei die elektrostatischen Wechselwirkungen oft durch lokale Wasserstoffbrücken ergänzt werden. Anhand der Hirshfeldfläche des DNTT kann zudem die Vermutung aufgestellt werden, dass im Sinne ihrer vdW-Radien große Atome wie Schwefel oder Selen, die in das Kohlenstoffgerüst des Moleküls integriert sind, zu starkem, lokalem Orbitalüberlapp zwischen benachbarten Molekülen führen und so den Ladungstransport verbessern. Solche Kontaktpunkte gezielt zu erzeugen könnte eine mögliche Strategie zur Entwicklung neuer organischer Halbleitermaterialien sein.
Neben den teilweise explorativen Studien an verschiedenen organischen Halbleitern, die jeweils einen Kanon verschiedener experimenteller Methoden erfordern, wurden einige vertiefende Arbeiten rund um die NEXAFS-Technik und die theoretische Modellierung ihrer Spektren mit Hilfe des StoBe-Codes durchgeführt. In einer dieser Studien wurde das C1s-NEXAFS-Spektrum des Anthracen gemessen und mit Hilfe der StoBe-Rechnungen im Detail analysiert. Dabei zeigt sich, dass der StoBe-Code in der Lage ist, die Anregungsenergien der NEXAFS-Resonanzen im Bereich der C1s-Kante mit Abweichungen, die unter 300 meV liegen, vorherzusagen. Aufgrund dieser hohen Präzision ist es z.B. auch möglich, mit Hilfe berechneter Ionisationspotentiale den Kantenverlauf zu modellieren und von experimentellen Daten abzuziehen, wodurch eine bessere Vergleichbarkeit zwischen Experiment und Rechnung erreicht wird. Allerdings wird diese hohe Genauigkeit nur im Rahmen einer sehr aufwendigen Betrachtung einzelner angeregter Zustände erreicht. Der Vergleich zeigt, dass bereits Rechnungen auf Basis der Slater-Transition-Methode sehr gute Ergebnisse liefern und oft ausreichend sind, wenn nicht gerade die Betrachtung von Relaxationseffekten im Vordergrund steht. Bei der genaueren Aufschlüsselung der Teilspektren wurde des weiteren deutlich, dass *chemical Shifts* und Relaxationseffekte die Reihenfolge der Zielzustände für verschiedene Anregungszentren ändern oder zu Beiträgen unterschiedlicher Zustände bei der selben Anregungsenergie führen können. Damit ist eine Zuordnung einzelner experimenteller NEXAFS-Resonanzen zu LUMOs des Grundzustandes streng genommen aus prinzipiellen Gründen nicht möglich und muss im Einzelfall

durch eine theoretische Analyse des Spektrums, wie sie hier für Anthracen vorgestellt wurde, untermauert werden.
Neben der theoretischen Analyse der NEXAFS-Spektren wurde in einem weiteren review-artigen Artikel besonderes Augenmerk auf den Dichroismus gelegt. Hier wurde möglichst anschaulich die Entstehung der Winkelabhängigkeit der Intensität bestimmter Anregungen erläutert, um die Quellen möglicher Fehlinterpretationen aufzuzeigen. Insbesondere wurde dabei das Wechselspiel von π^*- und σ^*-Resonanzen in den Dichroismen planarer aromatischer Kohlenwasserstoffe beleuchtet. Dabei stellt sich heraus, dass der einfache Leitsatz „π^*- und σ^*-Resonanzen besitzen eine gegenläufige Winkelabhängigkeit.“ nur für Spezialfälle gilt. Im Allgemeinen können auch leicht Gegenbeispiele gefunden werden, sodass eine genaue Betrachtung der einzelnen Resonanzen für eine vollständige Interpretation nötig ist. Zudem wurden Situationen verdeutlicht, in denen die Dichroismusauswertung aus prinzipiellen Gründen keine eindeutigen Ergebnisse liefert. Diese Beispiele zeigen, dass in bestimmten Fällen der Einsatz zusätzlicher, komplementärer Techniken unabdingbar ist, um ein vollständiges Bild der Struktur zu erhalten.
Viele der bis hierher vorgestellten Ergebnisse wurden in der Untersuchung des F1s-Dichroismus fluorierter, konjugierter Moleküle genutzt. Dazu dienten Dünnfilme des Perfluoropentacens auf HOPG bzw. SiO_2, auf denen die Moleküle exklusiv in liegender bzw. stehender Orientierung vorliegen, als Modellsystem für eine tiefgehende Untersuchung der Winkelabhängigkeit. Da aufgrund von Beugungsexperimenten die Orientierung der Moleküle exakt bekannt ist, konnten mit Hilfe von StoBe-Rechnungen nicht nur die F1s-Spektren reproduziert und analysiert, sondern auch der zu erwartende Dichroismus untersucht werden. Die Analyse zeigt, dass durch den sogenannten „Perfluoroeffekt“ σ^*-Zustände stark relaxieren, während π^* unbetroffen sind. Dies führt zu einer Mischung von σ^*- und π^*-Zuständen bei unerwartet niedrigen Anregungsenergien. Zudem besitzen die σ^*-Resonanzen eine vergleichsweise hohe Intensität und dominieren das F1s-Spektrum im Bereich der Vorkante. Eine Betrachtung der C-F-Bindungssituation zeigt, dass dies an einer geringen Elektronendichte der π-Orbitale im Bereich der Fluoratome liegt, was zu einem kleinen Überlapp mit dem F1s-Orbital führt. Es zeigt sich also, dass σ^*-Resonanzen dominieren, weil π^*-Resonanzen an der F1s-Kante aus systematischen Gründen schwächer ausfallen. Darüber hinaus belegt der Vergleich des experimentellen und berechneten Dichroismus, dass nicht nur die Energien, sondern auch die Oszillatorstärken der Anregungen mit hoher Genauigkeit von den Rechnungen vorhergesagt werden. Durch die detaillierte Analyse der Winkelabhängigkeiten einzelner Resonanzen im Spektrum wird damit für zukünftige Experimente grundsätzlich auch die Fluorkante für Untersuchungen der Molekülorientierung zugänglich. Damit ist diese Studie im Sinne der Einleitung ein Paradebeispiel für das Zusammenspiel von Modellsystem, Experiment und theoretischer Modellierung und zeigt, wie das „Werkzeug“ NEXAFS-Messung erst durch das Ineinandergreifen all dieser Aspekte sein volles Potential entfaltet.

An den hier untersuchten Fragestellungen sowie den vorgestellten Ergebnissen lassen sich die grundsätzliche Richtung, aber auch die fundamentalen Probleme der Forschung an organischen Halbleitern erkennen. In Abb. 4.1 wurde versucht, dies schematisch darzustellen. Das Diagramm zeigt entlang der Achsen die beiden Aspekte, die auch in dieser Arbeit oftmals getrennt voneinander untersucht wurden. Auf der horizontalen Achse geht es um die einzelnen Bausteine, also die Moleküle. Entwicklung auf dieser Achse ist zumeist Forschung, die eng mit der Chemie verknüpft ist. Auf der vertikalen Achse geht es um die Festkörperphysik. Entwicklung in dieser Richtung entspricht der „klassischen“

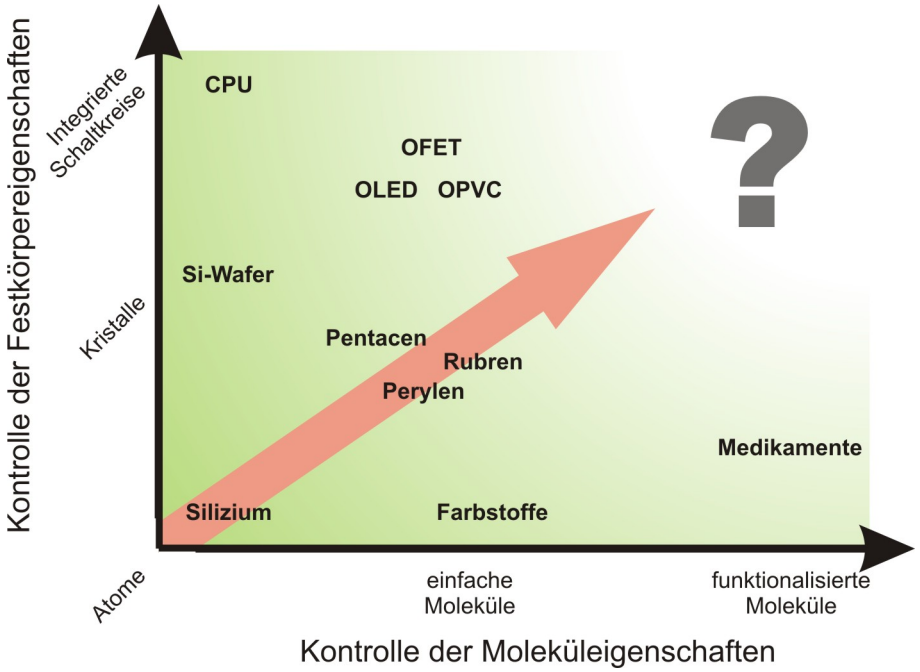

Abbildung 4.1: Das Diagramm zeigt die Entwicklung rund um organische Halbleiter, die einerseits stark durch die Substanzen, mit denen gearbeitet wird, geprägt ist (horizontale Achse) und andererseits auch die Wechselwirkungen der molekularen Bausteine untereinander berücksichtigen muss (vertikale Achse). Beide Aspekte sowohl in der praktischen Anwendung, als auch in der theoretischen Beschreibung zu vereinen, ist bisher nicht gelungen und stellt das Fernziel dar.

Festkörperphysik und beschäftigte sich bis dato vor allem mit anorganischen Materialien. Reine Entwicklung entlang einer dieser beiden Richtungen wird jedoch kaum zu einem Fortschritt auf dem Gebiet der organischen Halbleiter führen, da hier beide Aspekte berücksichtigt werden müssen. Genau aus diesem Grund sind Arbeiten an diesem Thema oft interdisziplinär und erfordern Kooperationen zwischen Chemie und Physik. In der „Zweidimensionalität“ der Entwicklung liegt aber auch das größte Problem. Ein Fortschritt in eine der beiden Richtungen ist nicht unbedingt ein Fortschritt auf dem Gebiet der organischen Halbleiter. Auch in dieser Arbeit können dafür Beispiele gefunden werden, da die Funktionalisierung des Pentacens zwar erfolgreich war, die Nutzbarkeit der Materialien im Hinblick auf festkörperphysikalische Untersuchungen aber zu wünschen übrig lässt. Vor diesem Hintergrund erscheint die systematische Erforschung des Zusammenhangs von Moleküleigenschaften und Kristallstruktur von zentraler Bedeutung. Experimente wie die Fluorierung des HBC lassen sich auch mit anderen funktionalen Gruppen und Molekülklassen durchführen, um die jeweilige Veränderung der Kristallstruktur zu analysieren und den Mechanismus für die Veränderung zu identifizieren. In diese Richtung weist auch die vorgestellte Hirshfeldstudie. Die Hirshfeldanalyse ist in der pharmazeutischen Forschung verbreitet, findet in der Physik bisher aber kaum Anwendung. Dies mag an einer zu starken Fixierung auf einige wenige Moleküle liegen, die im Detail erforscht werden. Weitere vergleichende Studien für andere Molekülklassen, die durch eine geschickte Auswahl versuchen, das komplexe Problem der Strukturbildung zu vereinfachen, könnten jedoch den gewaltigen Fundus an bekannten Substanzen und ihrer Strukturen erschließen und es erlauben, grundlegende Prinzipien der Strukturbildung herauszuarbeiten. Mittelfristiges Ziel ist also die Entwicklung von Regeln, die es erlauben,

Moleküle mit Blick auf die Festkörpereigenschaften ihrer Kristalle zu funktionalisieren. Abseits dieser allgemeineren Zukunftsvision bieten sich verschiedene Folgeuntersuchungen auf Basis der hier vorgestellten Ergebnisse an. So müssen die hier untersuchten, funktionalisierten Materialien in Folgeexperimenten auf ihre elektronischen Festkörpereigenschaften untersucht werden. Dies ist besonders für das perfluorierte Rubren von Interesse. Behält es die hohe Ladungsträgermobilität des Rubren bei, wäre die Fluorierung tatsächlich ein kleiner Schritt entlang des roten Pfeils in Abb. 4.1. Ebenso sind polymorphselektive, richtungsaufgelöste, optische Untersuchungen an Perylenkristallen ein naheliegender nächster Schritt, um tiefere Einblicke in das Zusammenspiel von Kristallstruktur und optischen Eigenschaften organischer Materialien zu erhalten. Darüber hinaus wurde die Leistungsfähigkeit des StoBe-Codes zur Analyse von NEXAFS-Signaturen organischer Halbleitermoleküle gezeigt. Zusammen mit diesem Analysewerkzeug können NEXAFS-Messungen tiefe Einblicke in die elektronische Struktur verschiedener Halbleitermoleküle gewähren. Zudem kann die detaillierte Analyse auch Dichroismusauswertungen ermöglichen, die über die Betrachtung einzelner, separierter Resonanzen hinaus geht. So ist es nun z.B. denkbar, F1s-Spektren des Perfluoropentacens für eine Orientierungsbestimmung der Moleküle heranzuziehen. Insbesondere für Mischsysteme verschiedener Moleküle könnte dies interessant sein. Enthält nur eine der Komponenten ein bestimmtes Element, kann praktisch ein molekülselektiver Dichroismus aufgenommen und ausgewertet werden. Wie im Fall der Fluorkante erfordert dies jedoch unter Umständen eine detaillierte Analyse der Signatur. Als letzter Punkt in diesem Ausblick sei hier noch auf den Begriff „Mischsysteme“ eingegangen. Bisher werden auf dem Gebiet der organischen Halbleiter vor allem einzelne Substanzen gezielt untersucht. Langfristig müssen aber auch Grenzflächen und Mischungen unterschiedlicher Materialien in Betracht gezogen werden. Schon heute bestehen z.B. OLEDs aus mehreren organischen Komponenten und das Konzept der Dotierung ist in der anorganischen Halbleitertechnik entscheidend für den Fortschritt gewesen. Es ist also gut möglich, dass der weiße Fleck mit dem Fragezeichen in Abb. 4.1 eines Tages durch ein Heterosystem unterschiedlicher organischer Halbleiter gefüllt wird, zu dessen Entwicklung und Erforschung auch diese Arbeit, z.B. in Form einer genauen NEXAFS-Analyse, einen kleinen Beitrag geleistet hat.

5. Veröffentlichungen

In diesem Kapitel finden sich alle Artikel, die im Laufe der Doktorarbeit entstanden sind, und in denen die zuvor diskutierten Ergebnisse veröffentlicht wurden. Im Vorfeld zu jedem Artikel wird die eigene Beteiligung an den Veröffentlichungen kurz zusammen gefasst. Einige der Veröffentlichungen wurden um zusätzliche Informationen im Rahmen einer *Supporting Information* ergänzt. Diese Dokumente enthalten teilweise eine große Anzahl von Abbildungen und Daten, sodass sich bei vollständiger Einbindung in die vorliegende Arbeit eine unverhältnismäßig hohe Anzahl von Seiten ergeben würde. Deshalb wird die Darstellung besonders umfangreicher *Supporting Information* hier auf jene Seiten beschränkt, die unmittelbar mit der Eigenleistung, bzw. den entsprechenden Abschnitten im Artikel verknüpft sind.

5.1 Synthesis and Solid-State Structures of 6,13-Bis (trifluoromethyl)- and 6,13-Dialkoxypentacene

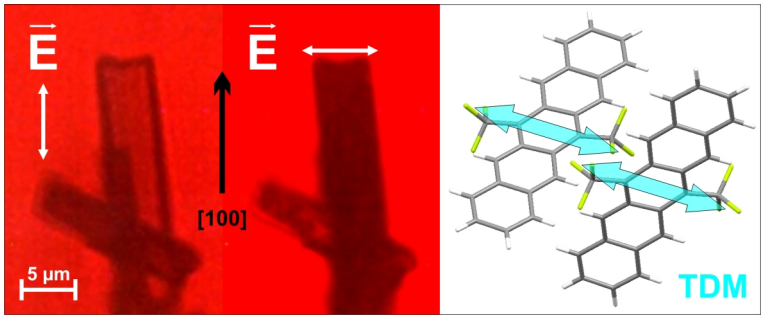

5.1.1 Inhaltsangabe

6,13-Disubstituted pentacenes were synthesized. Their electrochemical and optical properties, in addition to their packing motifs in the solid state, were determined. Treatment of pentacenequinone with $TMSCF_3$ (Ruppert's reagent) and deprotection led to 6,13-bis (trifluoromethyl)pentacene-6,13-diol, which was aromatized to 6,13 bis(trifluoromethyl) pentacene by using PBr_3. 6,13-Dialkoxypentacenes were accessible by alkylation of the corresponding hydroquinopentacenes by using dialkyl sulfates. 6,13-Bis(trifluoromethyl)-pentacene and 6,13-dimethoxypentacene exhibit slipped face-to-face π stacking in the solid state, whereas 6,13-diethoxypentacene forms pairs of π-stacking molecules in the solid state.

5.1.2 Eigenleistung

Die Planung der UV-Vis-Experimente an Dünnfilmen, ebenso wie die Aufnahme polarisationsabhängiger Mikroskopaufnahmen kristalliner Domänen basiert auf Ideen von Tobias Breuer und wurde in Zusammenarbeit mit ihm entwickelt. Die Präparation von Dünnfilmen aus neu synthetisierten Materialien, sowie die Durchführung der erwähnten Experimente wurde von mir vorgenommen. Alle unterstützenden DFT-Rechnungen wurden von mir durchgeführt und ausgewertet. Die grafische Aufbereitung der Ergebnisse erfolgte durch mich, ebenso wie der Entwurf von Textbausteinen zu den präsentierten Daten. Gregor Witte half bei der Interpretation der Daten, sowie der Ausarbeitung des Textes. Der festkörperphysikalische Teil des Artikels wurde von Tobias Breuer verfasst und von Jonas Schwaben in den Gesamtartikel eingefügt.

EurJOC European Journal of Organic Chemistry

SHORT COMMUNICATION

DOI: 10.1002/ejoc.201201714

Synthesis and Solid-State Structures of 6,13-Bis(trifluoromethyl)- and 6,13-Dialkoxypentacene

Jonas Schwaben,[a] Niels Münster,[a] Tobias Breuer,[b] Michael Klues,[b] Klaus Harms,[a] Gregor Witte,[b] and Ulrich Koert*[a]

Keywords: Synthesis design / Fused-ring systems / Polycycles / Acenes / Solid-state structures / Fluorine

6,13-Disubstituted pentacenes were synthesized. Their electrochemical and optical properties, in addition to their packing motifs in the solid state, were determined. Treatment of pentacenequinone with $TMSCF_3$ (Ruppert's reagent) and deprotection led to 6,13-bis(trifluoromethyl)pentacene-6,13-diol, which was aromatized to 6,13-bis(trifluoromethyl)pentacene by using PBr_3. 6,13-Dialkoxypentacenes were accessible by alkylation of the corresponding hydroquinopentacenes by using dialkyl sulfates. 6,13-Bis(trifluoromethyl)-pentacene and 6,13-dimethoxypentacene exhibit slipped face-to-face π stacking in the solid state, whereas 6,13-diethoxypentacene forms pairs of π-stacking molecules in the solid state.

Introduction

The synthesis of molecular building blocks such as acenes for electronic functional materials, for example, organic field-effect transistors (OFET) and organic photovoltaics (OPVs), represents an important research area with significant application potential.[1] On the basis of its electronic properties, pentacene is a suitable OFET and OPV material.[2] Its low solubility and chemical instability causes problems, which can be overcome by introduction of substituents, in particular at the 6,13-positions. Stability problems can arise, for example, from reactions with $^1O_2$ (6,13-endoperoxide formation).[3] Electron-withdrawing substituents in the 6,13-positions lead to a low LUMO level, which is necessary for efficient n-type semiconducting materials.[4] Yamada achieved the introduction of cyano substituents,[5] Zhu reported on 6,13-dichloropentacene,[6] and 6,13-difluoropentacene is patented.[7] Electron-donating substituents in the 6,13-positions lead to a high HOMO level, and the synthesis of 6,13-bis(alkylthio)pentacenes was reported by Kobayashi.[8] Here we report novel routes to 6,13-disubstituted pentacenes. Alkoxy groups were chosen as prototypes for electron-donating groups and the trifluoromethyl group was chosen as a well-known electron-withdrawing and stabilizing[9] substituent. Solid-state structures of the novel pentacenes are reported because the packing motif determines the electronic properties of the semiconducting materials.

Pentacenequinone (**1**) is a suitable starting point for the synthesis of 6,13-disubstituted pentacene derivatives (Scheme 1). Anthony introduced an efficient route to bis(alkynyl)pentacenes by addition of acetylides to produce the corresponding diol, which could be aromatized to desired bis(alkynyl)pentacenes **2**.[10] This strategy was successfully applied in the synthesis of conjugated pentacene dimers and oligomers by Tykwinski.[11]

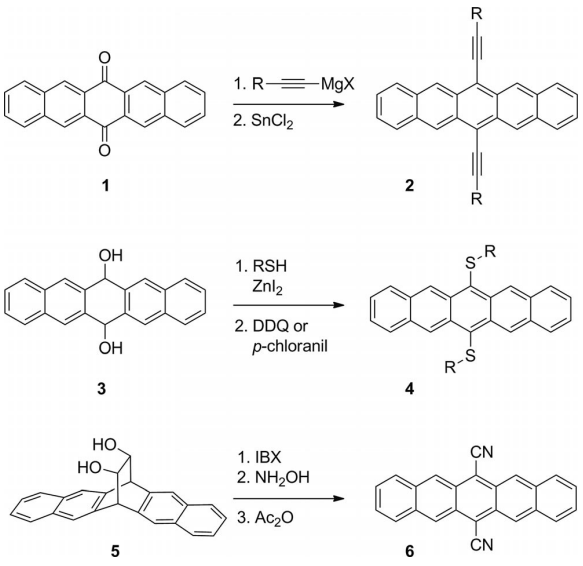

Scheme 1. Synthetic routes to 6,13-disubstituted pentacenes.

[a] Fachbereich Chemie, Philipps-Universität Marburg, Hans-Meerwein-Straße 4, 35043 Marburg, Germany
Fax: +49-6421-2825677
E-mail: koert@chemie.uni-marburg.de
Homepage: http://www.uni-marburg.de/fb-15/ag-koert
[b] Fachbereich Physik, Philipps-Universität Marburg, Renthof 7, 35032 Marburg, Germany
Fax: +49-6421-2821380
E-mail: gregor.witte@physik.uni-marburg.de

Supporting information for this article is available on the WWW under http://dx.doi.org/10.1002/ejoc.201201714.

A synthetic route to 6,13-bis(alkylthio)pentacenes **4** was devised by Kobayashi.[8] Diol **3**, which can be prepared by $NaBH_4$ reduction of quinone **1**,[12] was transformed into the corresponding bisthioethers by treatment with zinc iodide and alkyl or aryl thiols. Subsequent aromatization with DDQ or *p*-chloranil led to bis(alkylthio)pentacenes **4**. Yamada's route to 6,13-dicyanopentacene proceeded through oxidative cleavage of diol **5**[13] and subsequent conversion via the dioxime into 6,13-dicyanopentacene (**6**). Convergent, multistep assembly of the pentacene structure was used by Takahashi to synthesize 6,13-bis(trimethylsilyl)-pentacene.[14]

Results and Discussion

The synthesis of 6,13-bis(trifluoromethyl)pentacene (**9**) started with the fluoride-mediated addition of Ruppert's reagent ($TMSCF_3$) to pentacenequinone (**1**, Scheme 2). Resulting bis(trimethyl)siloxypentacene **7** could be converted into diol **8**. Different conditions for the aromatization of **8** to desired pentacene **9** were examined (Table 1). Tin(II)-mediated reduction[10] of diol **8** under various conditions or NaI/NaH_2PO_2[15] did not afford pentacene **9**. Treatment of diol with PBr_3 gave desired pentacene **9** in good yield. The rearrangement of an sp^3 substituent at C6 into an sp^2 atom, which is known for the methyl case (i.e., **10**→**11**)[16a,16b] and the propyl case,[16c] was not observed for the trifluoromethyl case (i.e., **9**→**12**).

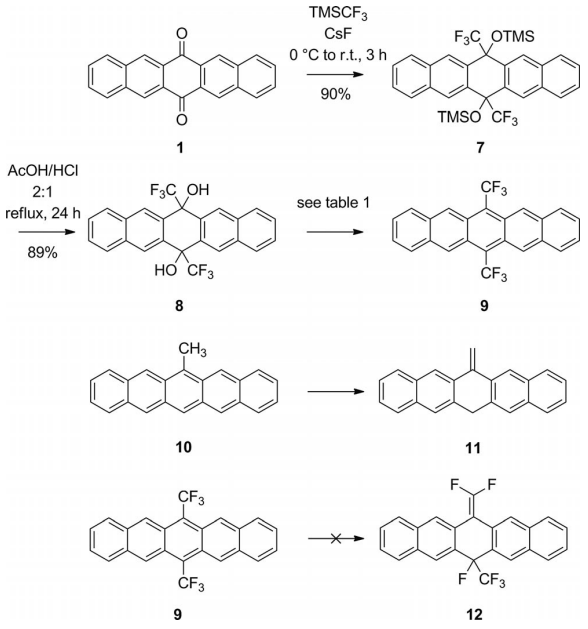

Scheme 2. Synthesis of 6,13-bis(trifluoromethyl)pentacene (**9**).

Two routes for the synthesis of 6,13-dialkoxypentacenes were evaluated (Scheme 3). First, dihydropentacenediol **3** was converted into dimethyl ether **13**, but attempts to oxidize this compound into pentacene **14** by using DDQ or *p*-chloranil failed. An alternative more successful route involved the reduction of quinone **1** to hydroquinone **15**, which is in equilibrium with tautomer **16**. Dithionite reduction of **1** gave a mixture of **15** and **16**, which could be alkylated in situ with dialkyl sulfates to the corresponding dialkoxypentacenes **14** and **17**. In these reductions, over-reduction products **18** (10–21%), as well as unreacted starting materials (10–15%), were obtained. The alkoxy substituents in the 6,13-positions direct over-reduction, which is in contrast to Clar's rule not to 6,13-dihydropentacene but to 5,14-dihydro compound **18**.[16a,17] Treatment of isolated pentacene **17** with an excess amount of dithionite gave dihydropentacene **18b** in 70% yield.

Table 1. Conversion of diol **8** into pentacene **9**.

Entry	Reagent	Conditions	% Yield
1	$SnCl_2{\cdot}2H_2O$	THF, reflux 2 d	–
2	$SnCl_2{\cdot}2H_2O$	AcOH/HCl, reflux, 24 h	–
3	NaI, NaH_2PO_2	AcOH, reflux 2 d	–
4	Zn	AcOH, reflux, 24 h	–
5	SmI_2	THF, reflux	–
6	PBr_3	THF, 50 °C, 21 h	70

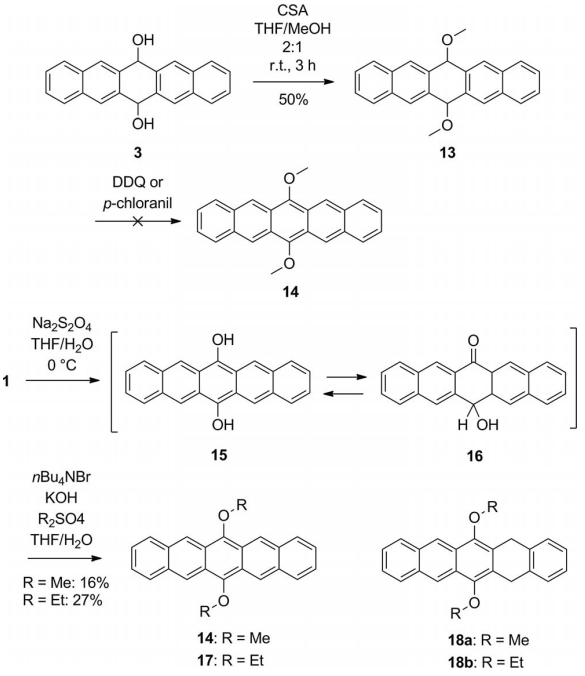

Scheme 3. Synthesis of 6,13-dialkoxypentacenes **17**.

In contrast to unsubstituted pentacene, compounds **9**, **14**, and **17** show a pronounced increased solubility in organic solvents (CH_2Cl_2, $CHCl_3$, and THF). As a result of the instability of **9**, **14**, and **17** under an oxygen atmosphere and in sun light, these compounds should be stored under an argon atmosphere with the exclusion of light; they are stable under these conditions for weeks. The redox behaviors of **9** and **14** were investigated by cyclic voltammetry (Figure 1, Table 2). One reversible oxidation peak and two quasireversible reduction peaks were observed for pent-

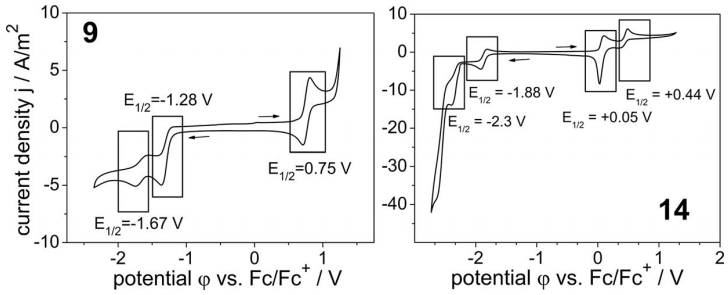

Figure 1. Cyclic voltammograms of pentacenes **9** and **14** in CH_2Cl_2 (1 mM) with $TBAPF_6$ (100 mM) at a scan rate of 100 mV s^{-1}. Potentials are plotted against the ferrocene/ferrocenium redox couple (Fc/Fc+). Arrows indicate the scan direction.

acene **9** (0.75, –1.28, –1.67 V). The cyclic voltammogram of pentacene **14** shows one irreversible oxidation peak (0.05 V), one quasireversible oxidation peak (0.44 V), one reversible reduction peak (–1.88 V), and one irreversible reduction peak (–2.30 V).

Table 2. Electrochemical and optical properties of **9** and **14**.

	E_G^{opt} [eV][a]	$E_{1/2}$[ox] [V][b]	$E_{1/2}$[red] [V][b]	$E_G^{electro.}$ [eV]	$E_G^{calcd.}$ [eV][c]
9	2.02	0.75	–1.28	2.03	2.04
14	2.04	0.05	–1.88	1.93	2.12
PEN[d]	2.13				2.20

[a] Optical HOMO–LUMO gaps determined from the maximum of the lowest energy visible absorption band. [b] Recorded $E^{1/2}$ values vs. F_c/F_c^+ in CH_2Cl_2 with $TBAPF_6$ as supporting electrolyte. All potentials represent a one-electron reduction or oxidation event. [c] B3LYP/6-311+G**//PM3. [d] PEN = pentacene.

The electronic structures of **9** and **14** were also analyzed theoretically in the frame of DFT calculations. In each case, the structure of the individual molecules (i.e., gas phase) was optimized by using C_{2h} symmetry. Because this symmetry constraint hampers rotation of the trifluoromethyl groups around the C–C-bond in **9**, a slightly different structure than that derived for the crystalline phase results. Therefore, the energies of the HOMO and LUMO were also calculated for an individual molecule by adopting the structure obtained from X-ray structural analysis. This leads only to small energy differences (Table S3, Supporting Information), which indicates that the symmetry of the side group has only a minor influence on the electronic structure. Thus, the energies are essentially determined by the π-conjugated backbone. This is also corroborated by comparison of the energy levels calculated for pentacene, which shows that these side groups do not alter the conjugation of the backbone and, therefore, exhibit only a small influence on the optical gap of the molecules. The experimentally determined band gaps of compounds **9** and **14** are in accordance with the calculated ones and those in the literature.[4a,9]

The UV/Vis spectra of **9** and **14** in solution reveal the lowest energy excitation at around 610 nm, which is attributed to the HOMO–LUMO transition, as well as higher energy excitations around 430 nm (Figure 2). Relative to those of unsubstituted pentacene (PEN), the HOMO–LUMO gaps are only slightly redshifted. In contrast to the solution spectra, additional excitations appear at lower energies for solid molecular films that were evaporated onto transparent KCl substrates, and these are attributed to excitonic excitations (dashed line in Figure 2). Interestingly, **14** exhibits an energetic difference between the HOMO–LUMO peak and the lowest exciton component that is essentially the same as that in PEN (0.26 eV), whereas a distinctly smaller exciton binding energy is found for **9** (ΔE = 0.16 eV). This demonstrates that the HOMO–LUMO gap of the individual molecules is given by the π-conjugated backbone, whereas in the crystalline phase, the excitonic energies are determined by the polarizability of the entire molecule, which is expected to be lower for acenes with trifluoromethyl side groups.

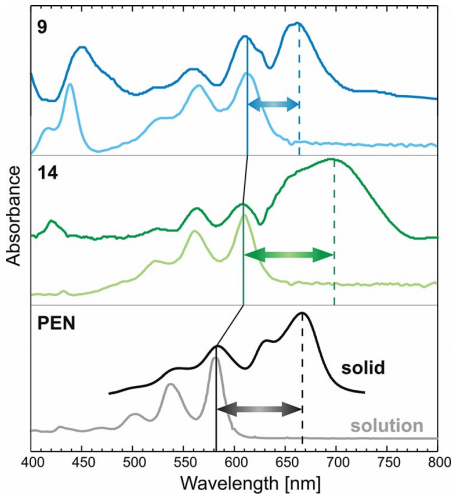

Figure 2. UV/Vis spectra of pentacene, **9**, and **14** in CH_2Cl_2 (50 μM) and for solid films evaporated onto KCl substrates. For comparison, data are also shown for PEN dissolved in CH_2Cl_2[18a] and for crystalline films grown on ZnO (0001).[18b]

X-ray crystallographic analysis of pentacenes **9**, **14**, and **17** shows a distinct packing for each compound (Figure 3).[19] A common motif for **9** and **14** is slipped cofacial π stacking along the *a* axis to form a 2D-network sheet. The distances between the parallel mean planes of the pentacenes in these columns are 3.38 (**9**) and 3.43 Å (**14**). The

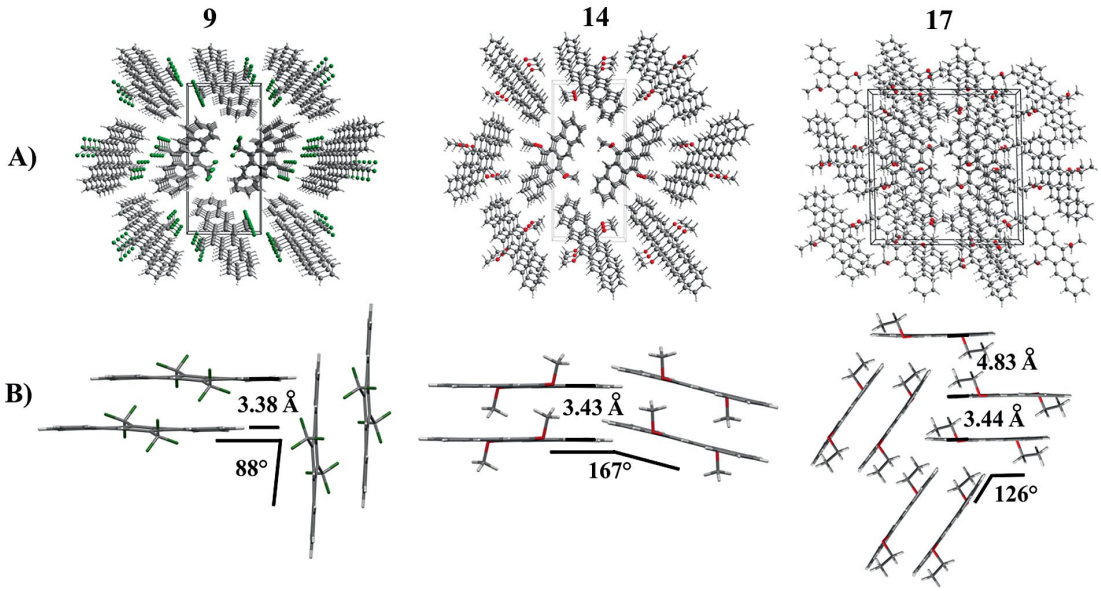

Figure 3. (a) 3D packing structures of **9**, **14**, and **17** in the crystal structure; perspective views looking down the *a* axis. (b) π stacking arrangements of **9**, **14**, and **17**; parallel projections looking along the pentacene planes.

slippage is 3.55 Å for **9** and 2.49 Å for **14** with components for both the longest and the shortest molecular axis. Neighboring columns of the 2D sheets form a contact angle of 88° for **9** and 167° for **14**. This results in a hitherto unknown tight face-to-face π stacking for **14**, whereas the packing of **9** is quite similar to that of the S–Me derivative.[8] The trifluoromethyl group in **9** is slightly bent out of the pentacene plane and participates in F–HC hydrogen bonds in the planes of the 2D-network sheets and in C–F–C contacts to the neighboring columns. The packing of **17** is different. No 2D-network sheets are present. In the packing, there are pairs of π-stacked pentacene molecules with a plane-to-plane distance of 3.48 Å. The slippage here is only 1.78 Å. Parallel-orientated pairs show a stairlike arrangement with a principal plane-to-plane distance of 4.83 Å and a large offset, so that only C–H ring contacts of the Me groups of the ethoxy substituents are present. Neighboring pairs form an angle of 126° and are involved in additional C–H ring interactions. The uniform recumbent molecular tilting in the crystalline phase and the orientation of the transition dipole moment of the HOMO–LUMO excitation along the molecular M axis causes a pronounced polarization contrast of the crystalline fibers for illuminating E-fields oriented along or perpendicular to the fiber axis (Figure 4).

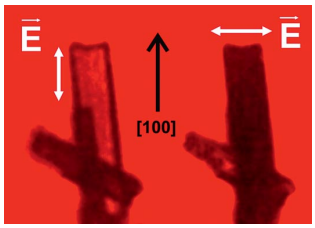

Figure 4. Linearly polarized optical micrograph of spicular crystallites of **9** observed in transmission geometry by using red-filtered light with an electrical field vector **E** (a) parallel and (b) perpendicular to the [100]-oriented crystal axis.

Conclusions

In summary, the syntheses of three novel 6,13-disubstituted pentacenes were achieved. Trifluoromethyl substituents were chosen to generate an electron-deficient pentacene derivative, and alkoxy groups were chosen to generate an electron-rich pentacene derivative. 6,13-Bis(trifluoromethyl)pentacene and 6,13-dimethoxypentacene exhibit slipped face-to-face π stacking, whereas 6,13-diethoxypentacene forms pairs of π-stacking molecules in the solid state. The present work forms the basis for potential applications of these novel pentacenes in molecular electronics.

Experimental Section

6,13-Bis(trifluoromethyl)pentacene (9): To a solution of diol **8** (100 mg, 0.22 mmol, 1.00 equiv.) in THF (1.0 mL) at room temperature in the dark was dropwise added PBr_3 (242 mg, 0.89 mmol, 4.00 equiv.). After stirring for 30 min at room temperature, the mixture was heated to 50 °C for 21 h in the dark, and the solvent was slowly evaporated. Workup and purification were carried out in air but without room light. After cooling to room temperature, the mixture was diluted with CH_2Cl_2 (10 mL) and washed with a solution of 5% $NaHCO_3$ in H_2O (5 mL) and brine (5 mL). The organic layer was dried with Mg_2SO_4, and the solvent was removed under reduced pressure. The remaining crude product was purified by column chromatography on silica (*n*-pentane) to give pentacene **9**

(65 mg, 0.16 mmol, 70%) as a dark green solid. R_f (silica) = 0.46 (*n*-pentane); m.p. 216 °C (decomp., $CHCl_3$). UV/Vis (CH_2Cl_2) λ_{max} (ε): 302 (45000), 439 (6300), 528 (3800), 566 (5800), 611 (6500) nm. ^{1}H NMR (500 MHz, [D$_8$]THF): δ = 7.47 (dd, J = 3.1, 6.7 Hz, 4 H), 8.04 (dd, J = 3.2, 6.6 Hz, 4 H), 9.17 (s, 4 H) ppm. ^{19}F NMR (471 MHz, [D$_8$]THF): δ = –49.0 ppm. ^{13}C NMR (126 MHz, [D$_8$]-THF): δ = 124.2 (m, CH), 125.8 (q, J = 28.4 Hz, C), 127.5 (q, J = 276 Hz, CF_3), 128.3 (C), 128.6 (CH), 129.7 (CH), 133.4 (C) ppm. HRMS (EI, 70 eV): calcd. for $C_{24}H_{12}F_6$ $[M]^+$ 414.0845; found 414.0845.

Supporting Information (see footnote on the first page of this article): Experimental procedures and ^{1}H NMR and ^{13}C NMR spectroscopic data for all new compounds and UV/Vis, polarization microscopy, CV, and HOMO/LUMO calculations for compounds **9** and **14**.

Acknowledgments

The Deutsche Forschungsgemeinschaft (DFG) and the Fonds der Chemischen Industrie are gratefully acknowledged for financial support. C. Prinzisky, M.Sc., and M. Drüschler, Dipl. Chem., are thanked for support with the cyclic voltammograms. T. B. gratefully acknowledges financial support from the Friedrich-Ebert-Stiftung.

[1] C. Wöll (Ed.), *Physical and Chemical Aspects of Molecular Electronics*, Wiley-VCH, Weinheim, Germany, **2009**.

[2] a) J. E. Anthony, *Angew. Chem.* **2008**, *120*, 460; *Angew. Chem. Int. Ed.* **2008**, *47*, 452–483; b) J. E. Anthony, *Chem. Rev.* **2006**, *106*, 5028–5048; c) D. J. Gundlach, Y. Y. Lin, T. N. Jackson, S. F. Nelson, D. G. Schlom, *IEEE Electron Device Lett.* **1997**, *18*, 87–89.

[3] W. Fudickar, T. Linker, *J. Am. Chem. Soc.* **2012**, *134*, 15071–15082.

[4] a) B. M. Medina, J. E. Anthony, J. Girschner, *ChemPhysChem* **2008**, *9*, 1519–1523; b) I. Kaur, W. Jia, R. P. Kopreski, S. Selvarasah, M. R. Dokmeci, C. Pramanik, N. E. McGruer, G. P. Miller, *J. Am. Chem. Soc.* **2008**, *130*, 16274–16286.

[5] S. Katsuta, D. Miyagi, H. Yamada, T. Okujima, S. Mori, K. Nakayama, H. Uno, *Org. Lett.* **2011**, *13*, 1454–1457.

[6] J. Li, M. Wang, S. Ren, X. Gao, W. Hong, H. Li, D. Zhu, *J. Mater. Chem.* **2012**, *22*, 10496–10500.

[7] M. Kobayashi, O. Omae, K. Ohkubo, Y. Gao, PCT Int. Appl., **2005**, WO 2005042445 A2 20050512.

[8] K. Kobayashi, R. Shimaoka, M. Kawahata, M. Yamanaka, K. Yamaguchi, *Org. Lett.* **2006**, *8*, 2385–2388.

[9] A. Putta, M. Billion, H. Sun, *J. Phys. Chem. A* **2012**, *116*, 8015–8022.

[10] J. E. Anthony, D. L. Eaton, S. R. Parkin, *Org. Lett.* **2002**, *4*, 15–18.

[11] D. Lehnherr, J. Gao, F. A. Hegmann, R. R. Tykwinski, *Org. Lett.* **2008**, *10*, 4779–4782.

[12] N. Vets, M. Smet, W. Dehaen, *Tetrahedron Lett.* **2004**, *45*, 7287–7289.

[13] H. Yamada, Y. Yamashita, M. Kikuchi, H. Watanabe, T. Okujima, H. Uno, T. Ogawa, K. Ohara, N. Ono, *Chem. Eur. J.* **2005**, *11*, 6212–6220.

[14] Z. Jia, S. Li, K. Nakajima, K. Kanno, T. Takahashi, *J. Org. Chem.* **2011**, *76*, 293–296.

[15] N. Vets, M. Smet, W. Dehaen, *Synlett* **2005**, 217–222.

[16] a) E. Clar, J. W. Wright, *Nature* **1949**, *163*, 921; b) J. E. Norton, B. H. Northrop, C. Nuckolls, K. N. Houk, *Org. Lett.* **2006**, *8*, 4915–4918; c) T. Takahashi, K. Kashima, S. Li, K. Nakajima, K. Kanno, *J. Am. Chem. Soc.* **2007**, *129*, 15752–15753.

[17] a) E. Clar, *Chem. Ber.* **1949**, *82*, 495–514; b) J. I. Wu, C. S. Wannere, Y. Mo, P. von Ragué Schleyer, U. H. F. Bunz, *J. Org. Chem.* **2009**, *74*, 4343–4349.

[18] a) A. Hinderhofer, U. Heinemeyer, A. Gerlach, S. Kowarik, R. M. J. Jacobs, Y. Sakamoto, T. Suzuki, F. Schreiber, *J. Chem. Phys.* **2007**, *127*, 194705; b) J. Helzel, S. Jankowski, M. El Helou, G. Witte, W. Heimbrodt, *Appl. Phys. Lett.* **2011**, *99*, 211102.

[19] CCDC-916473 (for **9**), -916474 (for **14**), and -916475 (for **17**) contain the supplementary crystallographic data for this paper. These data can be obtained free of charge from The Cambridge Crystallographic Data Centre via www.ccdc.cam.ac.uk/data_request/cif.

Received: December 19, 2012
Published Online: February 1, 2013

Auszüge aus den *Supporting Information* zum Artikel:

J. Schwaben, N. Münster, T. Breuer, M. Klues, K. Harms, G. Witte und U. Koert, Eur. J. Org. Chem. (2013), 1639-1643. DOI: 10.1002/ejoc.201201714

UV-vis Spectra

Typical UV-vis spectra of compounds **9**, **14** and **17** dissolved in CH_2Cl_2 (DCM) or C_4H_8O (THF) with concentration of 50 μM are shown in Fig. S1. All excitations were found to be shifted by less than 5 nm in both solvents. Additional measurements that were carried out for different concentrations revealed no noticeable peak shift and thus indicate a negligible solvatorchromism. The different compounds reveal rather similar UV-vis spectra comprising in each case a low energy excitation, E_1, around 610 nm followed by some vibrational replica separated by ΔE_{vib} = 171 meV as well as a higher energetic excitation, E_2, around 442 nm. For **14** and **17** a further excitation, E_3, at 352 nm was found. According to our theoretical analysis E_1 is attributed to a HOMO-LUMO excitation.

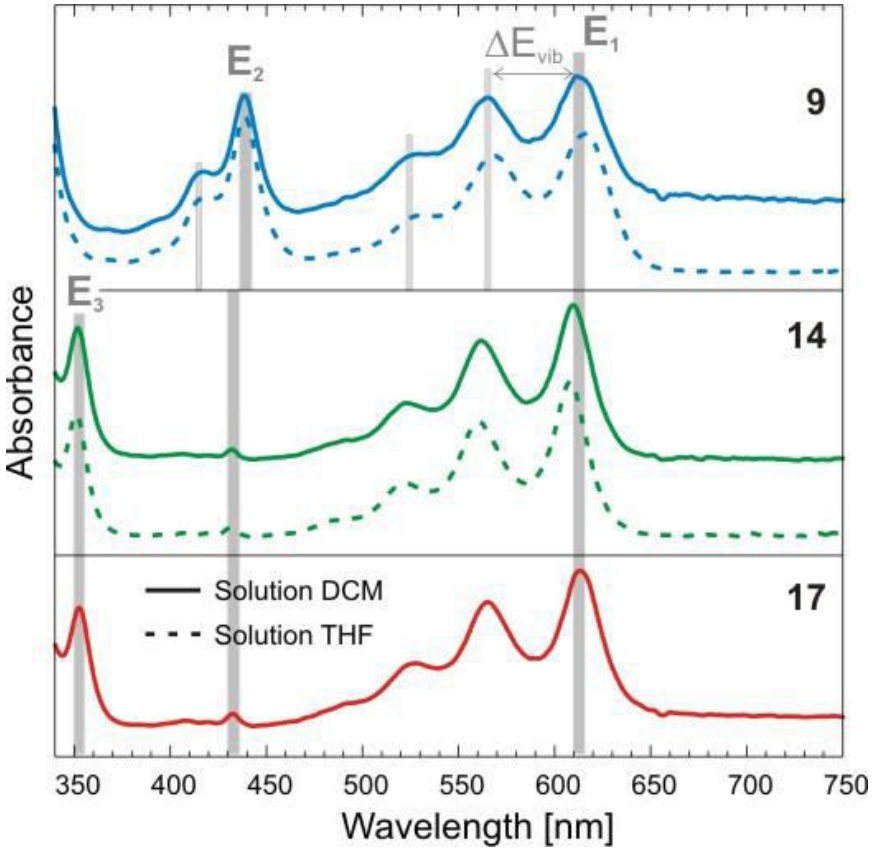

Figure S1: UV-vis spectra of **9** , and **14** and **17** dissolved in CH_2Cl_2 or C_4H_8O (50 μM).

Compared to the unsubstituted pentacene (PEN) the HOMO-LUMO gap of the newly synthesized compounds appears only slightly red-shifted. By contrast additional excitations occur at lower energies for solid molecular films, that were evaporated onto transparent KCl(001) substrates KCl, and are attributed to excitonic excitations (dashed line in Fig. 1). As demonstrated in a previous study for the case

of pentacene on ZnO these excitations exhibit two Davydov sub-components due to their non-primitive crystalline structure.[3] Though a Davydov splitting is not resolved for the films of **9** and **14** the broad absorption peak at large wavelength suggests the presence of two sub-resonances.

Table S1: Peak positions of UV-vis spectra of **9, 14** and **17** in CH_2Cl_2.

Compd.	E_1[a] (nm)	E_1 (eV)	E_2 (nm)	E_2 (eV)	E_3 (nm)	E_3 (eV)
9	614.5	2.018	438.8	2.826	-	-
14	608.6	2.037	431.7	2.872	351.5	3.528
17	613.3	2.022	432.8	2.826	352.7	3.516

[a] E_1 is equivalent to $E_G^{opt.}$ (Manuscript).

(3) Helzel, J; Jankowski, S; El Helou M.; Witte G.; Heimbrodt, W. *Appl. Phys. Lett.* **2011**, *99*, 211102.

Polarization Microscopy

Rotary evaporation of **9** yields spicular crystallites that are oriented along the [100]-direction and exhibit a distinct polarization contrast in transmission geometry. As depicted in Figure S2 a distinct absorption occurs if the electrical field vector $\vec{\mathbf{E}}$ of the incident linearly polarized light is oriented perpendicular to the crystal axis while the fibers appear almost transparent if E is aligned along the [100] axis. This polarization contrast can be well understood if one looks at the molecular packing of both molecules within the unit cell (as shown in Fig. S2c) and considers that the transition dipole moment of the HOMO-LUMO excitation of acenes is oriented along the molecular M-direction.

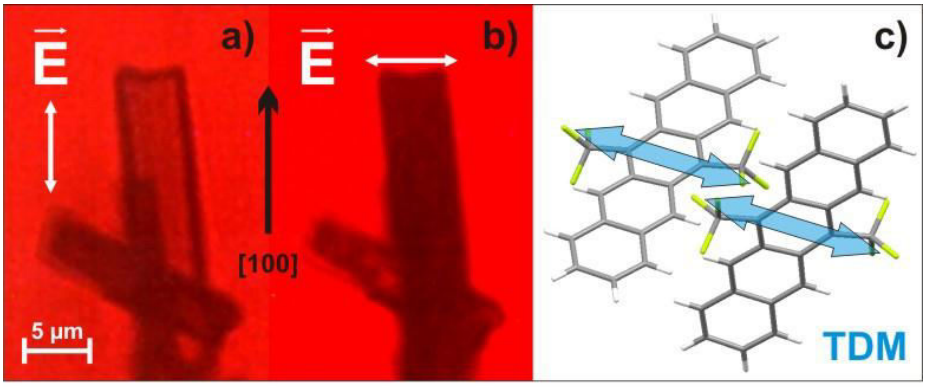

Figure S2: Linearly polarized optical micrograph of spicular crystallites of **9** observed in transmission geometry using red-filtered light with electrical field vector E a) parallel and b) perpendicular to the [100]-oriented crystal axis. Panel c) shows the molecular packing projected onto the bc-plane together with the orientation of the transition dipole moment (TDM) of the HOMO-LUMO excitation.

Quantum Chemical Calculations

The electronic structure of **9** and **14** have also been analyzed theoretically in the frame of DFT-calculations carried out with a 6-311G(d,p) basis-set, using the B3LYP functional as implemented in the US GAMESS-code.[4] In each case the structure of the individual molecules (i.e. gas phase) was optimized by using C_{2h}-symmetry. Since this symmetry constrain hampers a rotation of the trifluoromethyl groups around the C-C-bond in **9** it results in a slightly different structure than derived for the crystalline phase. Therefore, HOMO- and LUMO-energies were also calculated for an individual molecule adopting the structure received from the x-ray structural analysis. As listed below this leads only to small energetic differences, thus indicating that the symmetry of the side groups have only minor influence on the electronic structure which is essentially determined by the π-conjugated backbone. This is also corroborated by a comparison with the energy levels calculated for pentacene showing that these side groups do not alter the conjugation of the backbone and therefore exhibit only small influence on the optical gap of the molecules. This can also be visualized by the HOMO and LUMO orbitals that are essentially are localized at the pentacene backbone and reveal only a small distortion at the central ring.

Table S3: Calculated HOMO and LUMO energies of compounds **14** and **9.**

Compound	E_{HOMO} (eV)	E_{LUMO} (eV)	E_G (eV)
9 (C2h)	-5.279	-3.238	2.041
9 (crystal structure)	-5.279	-3.184	2.095
14	-4.653	-2.531	2.122
PEN	-4.762	-2.558	2.204

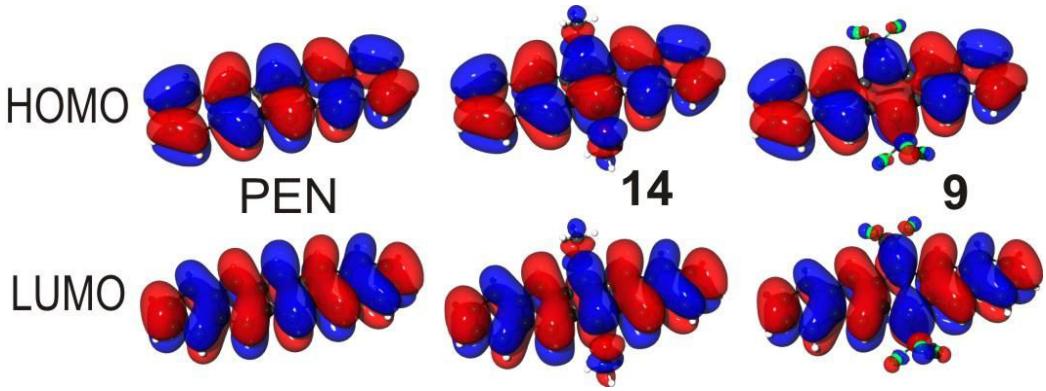

Figure S4: Visualization of HOMO and LUMO orbital of PEN, and compounds **14** and **9**.

(4) Schmidt, M. W.; Baldridge, K. K.; Boatz, J. A.; Elbert, S. T.; Gordon, M. S.; Jensen, J. H.; Koseki, S.; Matsunaga, N.; Nguyen, K. A.; Su, S. J.; Windus, T. L.; Dupuis, M.; Montgomery, J. A. *J. Comput. Chem.* **1993**, *14*, 1347-1363.

5.2 Efficient Syntheses of Novel Fluoro-Substituted Pentacenes and Azapentacenes: Molecular and Solid-State Properties

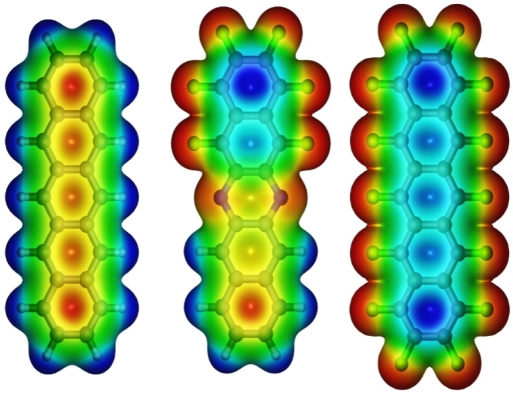

5.2.1 Inhaltsangabe

Non-symmetrical 6,13-disubstituted pentacenes bearing trifluoromethyl and aryl substituents have been synthesized starting from pentacenequinone. Diazapentacenes with a variety of fluorine substituents were prepared either via a Hartwig–Buchwald aryl amination route or by a S_NAr strategy. As a result of a non-symmetric substitution pattern containing electron-donating substituents in combination with electron-accepting fluorine substituents, the synthesized compounds feature distinct molecular dipoles. All compounds are analyzed regarding their optoelectronic properties in solution with special focus on the frontier orbital energies as well as their molecular packing in the crystal structures. The analyses of isolated molecules are complemented by thin-film studies to examine their solid-state properties. A precise comparison between these and the molecular properties gave detailed insights into the exciton binding energies of these compounds, which are explained by means of a simple model considering the molecular packing and polarizabilities.

5.2.2 Eigenleistung

Sämtliche Experimente und Rechnungen, die im Abschnitt „*Thin-film studies* “ des vorliegenden Artikels vorgestellt werden, wurden von mir in Zusammenarbeit mit Tobias Breuer und Gregor Witte geplant. Alle DFT-basierten Rechnungen wurden vollständig von mir durchgeführt und ausgewertet. Ebenso wurden die Dünnfilme aus den neuen Substanzen von mir hergestellt und mit UV-Vis vermessen. Außerdem wurden die durch Resublimation gewonnenen Kristalle des Trifluoromethyl-Anisol-Pentacens von mir hergestellt.

Während der Messzeiten am Synchrotron (NEXAFS-Messungen) wurde ich durch Tobias Breuer bei der *in situ* Präparation der Proben, sowie den Messungen unterstützt. Ebenso ist die Abschätzung der Excitonbindungsenergien nach dem Bässler-Model eine Gemeinschaftsleistung. Die sonstige Auswertung sowie die grafische Aufbereitung der Ergebnisse erfolgte durch mich. Zu den jeweiligen Inhalten wurden von mir Textpassagen verfasst, die durch Tobias Breuer zusammengefasst und ergänzt wurden. Gregor Witte wirkte unterstützend bei der Interpretation der Daten, sowie der Textarbeit. Der so entstandene Abschnitt wurde von Jonas Schwaben in das Gesamtmanuskript integriert.

ChemPubSoc Europe

DOI: 10.1002/chem.201501399

CHEMISTRY
A European Journal
Full Paper

Organic Solids |*Hot Paper*|

Efficient Syntheses of Novel Fluoro-Substituted Pentacenes and Azapentacenes: Molecular and Solid-State Properties

Jonas Schwaben,[a] Niels Münster,[a] Michael Klues,[b] Tobias Breuer,[b] Philipp Hofmann,[a] Klaus Harms,[a] Gregor Witte,*[b] and Ulrich Koert*[a]

Abstract: Non-symmetrical 6,13-disubstituted pentacenes bearing trifluoromethyl and aryl substituents have been synthesized starting from pentacenequinone. Diazapentacenes with a variety of fluorine substituents were prepared either via a Hartwig–Buchwald aryl amination route or by a S_NAr strategy. As a result of a non-symmetric substitution pattern containing electron-donating substituents in combination with electron-accepting fluorine substituents, the synthesized compounds feature distinct molecular dipoles. All compounds are analyzed regarding their optoelectronic properties in solution with special focus on the frontier orbital energies as well as their molecular packing in the crystal structures. The analyses of isolated molecules are complemented by thin-film studies to examine their solid-state properties. A precise comparison between these and the molecular properties gave detailed insights into the exciton binding energies of these compounds, which are explained by means of a simple model considering the molecular packing and polarizabilities.

Introduction

Polycyclic aromatic and heteroaromatic molecules are versatile building blocks for organoelectronic devices, such as organic-light-emitting diodes (OLEDs), organic field-effect transistors (OFETs) and organic photovoltaics (OPVs).[1] Besides oligo-thiophenes[2] and perylenes,[3] especially pentacenes (PEN) are of particular interest because they form highly-ordered crystalline phases, which exhibit large carrier mobility, and thus have been considered as prototypical materials in many conceptual studies.[4] To mitigate unfavorable properties of longer acenes, such as their low threshold for photodegradation and poor solubility, various pentacene derivatives have been developed by introducing either electronegative heteroatoms (e.g., azapentacenes[4c]) or side groups such as silylethynyl (e.g., 6,13-bis(triisopropylsilylethynyl)pentacene[5]). In addition, the optoelectronic properties of such molecular materials like the HOMO–LUMO gap can also be modulated by the proper choice of substituents.[6]

[a] *J. Schwaben, N. Münster, P. Hofmann, Dr. K. Harms, Prof. Dr. U. Koert*
Fachbereich Chemie, Philipps-Universität Marburg
Hans-Meerwein-Straße 4, 35043 Marburg (Germany)
Fax: (+49) 6421-2825677
E-mail: koert@chemie.uni-marburg.de
Homepage: http://www.uni-marburg.de/fb15/ag-koert

[b] *M. Klues, Dr. T. Breuer, Prof. Dr. G. Witte*
Fachbereich Physik, Philipps-Universität Marburg
Renthof 7, 35032 Marburg (Germany)
Fax: (+49) 6421-2821384
E-mail: gregor.witte@physik.uni-marburg.de
Homepage: http://www.uni-marburg.de/fb13/molfk

Supporting information for this article is available on the WWW under http://dx.doi.org/10.1002/chem.201501399.

Among many substituents that affect the properties of acene-based organic semiconductors, fluorine and perfluoroalkyl groups possess strong electron-withdrawing ability, enhanced hydrophobicity as well as lipophobicity and yield excellent chemical and photochemical stabilities. Owing to its ultimate electronegativity, fluorine forms highly polar and strong C–F bonds (ca. 480 kJ mol^{-1}), which causes an inverted charge density distribution within the fluorinated aromatic compounds (cf. Figure 2a, c).[7] Direct ring fluorination and the introduction of trifluoromethyl groups have been employed to stabilize acene-based organic semiconductors.[7,8] In the last decade a few fluoropentacenes and fluoroazapentacenes have already been synthesized.[9] Fluoro-substituted pentacene derivatives are accessible by either aldol condensation or Diels–Alder reaction.[9b–f,10a] Fluoro-substituted *N*-hetero acenes can be synthesized by means of condensations and S_NAr reaction.[9i,j] To our knowledge, fluoroalkyl substituents are less commonly used.[9c,g] Relevant examples for fluorinated pentacenes are perfluoropentacene (PFP),[9a] compounds **1**[9b] and **2**[9d] (cf. Figure 1). 6,13-Difluoropentacene has been patented.[9h] Also trifluoromethylated pentacenes, like **3**,[9g] and fluorinated azapentacenes, like **4**,[9j] are known.

As a result of the introduction of polar groups or heteroatoms with high electronegativity (e.g., fluorine and perfluoroalkyl groups), the interplay between attractive and repulsive forces, such as quadrupolar stabilization, is altered for each compound. This affects not only the molecular packing motifs and resulting crystal structures but also has an impact on the optoelectronic solid-state properties, which is of great importance for device performance.[10] A striking example of this effect is provided by a comparison of the optoelectronic properties of crystalline PEN and its perfluorinated counterpart

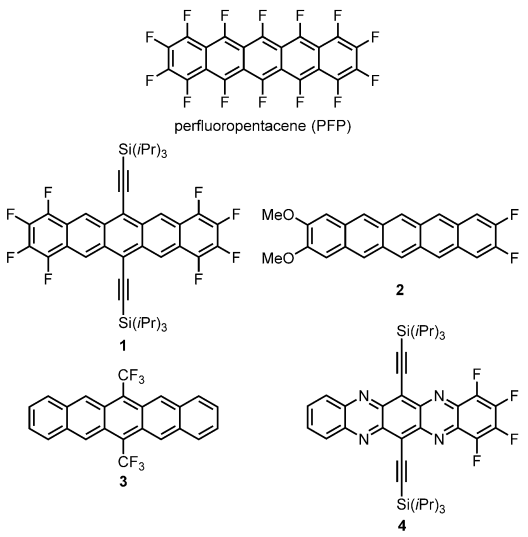

Figure 1. Structures of known fluoro- and trifluoromethyl-substituted pentacene derivatives prepared by Suzuki (PFP),[9a] Anthony (**1**),[9b] Bettinger (**2**),[9d] Koert (**3**)[9g] and Bunz (**4**).[9j]

PFP.[9a] The crystalline phase of both materials exhibits a layered structure, where all molecules within the layer are uprightly-oriented and adopt a face-on-edge arrangement. In the case of PEN,[11] the herringbone angle between neighboring aromatic planes amounts to about 55°, while for PFP an almost perpendicular herringbone packing occurs. Moreover, the PFP molecules are slightly displaced within the layer yielding an anisotropic stacking with perfect contrast between slip–stack and zig–zag packing along the two high symmetry azimuth directions. By contrast, PEN exhibits a packing motif with reduced anisotropy within the layers. As a consequence of the slightly different packing motifs, both molecular materials exhibit distinctly different physical properties. Especially the anisotropic packing within the PFP layers causes an anisotropic optical absorption,[12] which can be related to the formation of a one-dimensional band structure due to a pronounced π-stacking along the slip-stack packing direction[8d], which also favors the process of singlet exciton fission.[13]

Another interesting perspective arises in the case of non-symmetric substitutions, such as a partial fluorination, because this introduces a permanent dipole moment within the molecule (cf. Figure 2b) that in turn is expected to also affect the solid-state packing motifs. More generally, non-symmetric functionalized aromatic molecules comprising electron-rich and electron-poor moieties (also referred to as *push–pull* molecules) exhibit a smaller energy gap and enable efficient intramolecular charge transfer, which renders them interesting candidates for OPV applications.[10c,d]

Here, we report a combined experimental and computational study of various partially fluorinated pentacene and azapentacene derivatives. Besides the efficient syntheses of novel derivatives, their optoelectronic properties were characterized by means of UV/Vis absorption spectroscopy and cyclic voltammetry in solution and were further compared with absorption measurements on thin solid films in order to also determine their excitonic response. Computationally, the HOMO–LUMO energies, as well as dipole moments and polarizabilities, were calculated. Together with the determined crystal structure of the various compounds, this enables a detailed analysis of the scaling of optical gap and excitonic excitations. It is found that the solid-state packing rather than the molecular polarizability is decisive for the excitonic energy, hence emphasizing the importance to analyze solid-state optoelectronic properties in order to understand and optimize device applications. Moreover, since previous growth studies of pentacene and derivatives have demonstrated the control of the molecular orientation by the choice of the substrate,[12,14] we have also examined whether films with specific orientational order can be prepared by vapor deposition onto different substrates. By using X-ray absorption spectroscopy (NEXAFS), the processability by vacuum sublimation and the molecular orientation in thin films has been determined for various compounds. In combination with calculated NEXAFS spectra, these measurements also yielded important information on the relative energetics of the LUMO orbitals in solid films compared to those in solution.

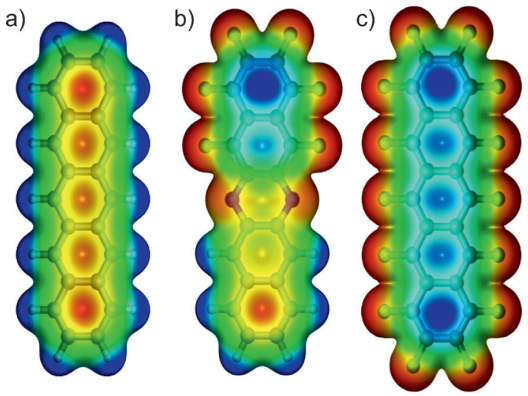

Figure 2. Electrostatic contour plots of a) PEN, b) a partially fluorinated diazapentacene which exhibits a permanent dipole moment and c) PFP (details in the Supporting Information, page S74).

Results and Discussion

Synthesis and Characterization

Retrosynthetic considerations towards non-symmetrical fluoroalkyl-substituted pentacenes and fluoro-substituted diazapentacenes are summarized in Scheme 1. The introduction of a trifluoromethyl group in the 6-position resulting in a substitution pattern outlined in **5**, was obtained by successive addition of substituents to quinone **6**. Diazapentacenes of type **7** should be accessible from a diamino precursor **8** and a fluoro-substituted bishalogenated precursor **9**, either by S_NAr reaction or by Pd-catalyzed aryl amination.

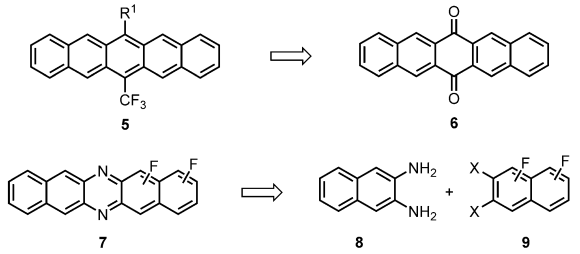

Scheme 1. Retrosynthetic strategies for the synthesis of non-symmetrical fluoroalkyl-substituted pentacenes and fluoro-substituted diazapentacenes.

Trifluoromethyl-substituted pentacenes

The starting point for the synthesis of 6-trifluoromethyl-substituted pentacenes was the pentacenequinone **6** (Scheme 2). CsF-mediated addition of Rupperts reagent gave the monoadduct **10** together with the bisadduct **11**, which were separated by silica gel chromatography. Desilylation of **10** provided alcohol **12**. The conversion of the bisadduct **11** via the diol **13** into 6,13-bistrifluoromethylpentacene (**3**) followed the previously described route,[9g] but used improved conditions for the aromatization step (**13**→**3**).

With ketones **10** and **12** in hand, the addition of various organolithium reagents was examined. The reaction of ketone **10** with TIPS-acetylene gave the two diastereomeric alcohols **14** and **15** in nearly equal amount (Scheme 3).[15]

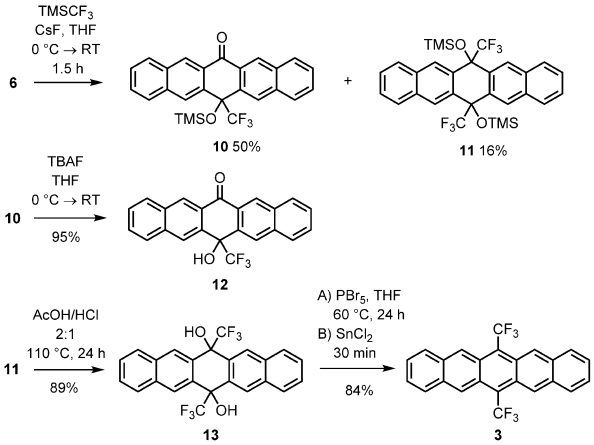

Scheme 2. Syntheses of ketones **10** and **12**.

In contrast, the addition of the same lithium acetylide to ketone **12** produced the *trans* alcohol **16** diastereoselectively. The free hydroxyl group in **12** can act as active volume to direct, via precomplexation of the organolithium reagent, the incoming nucleophile towards the *trans* product **16**. Interestingly, attempted synthesis of **16** via deprotection of **14** by means of one equivalent TBAF gave the completely desilylated compound. The aromatization of **16** using PBr_5 and $SnCl_2$ led

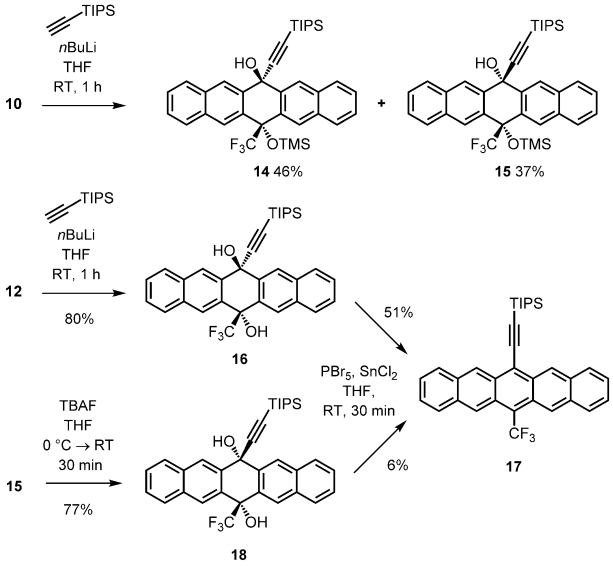

Scheme 3. Synthesis of the trifluoromethylpentacene **17**.

to the desired trifluoromethyl-substituted pentacene **17**. Attempts to aromatize the corresponding *cis* diol **18**, which was available from **15**, resulted in a low yield and mainly decomposition of the starting material. From a mechanistic point of view, the *trans* configuration of the diol can favor a concerted elimination via a phenylogous antiperiplanar transition state.

In order to obtain 6-trifluoromethyl-13-aryl-substituted pentacenes of type **21** and **24**, the addition of aryllithium reagents to ketones **10** and **12** was investigated (Scheme 4).

Addition of (4-(dimethylamino)phenyl)lithium gave the *trans*-trimethylsiloxy-alcohol **19** as sole stereoisomer. This result is surprising if one considers the trimethylsiloxy substituent as bulky passive volume, which should lead to the *cis* product. The *trans* product **20** was also accessible stereoselectively by addition of the aryllithium reagent to the ketone **12**.[15] As for the reaction **12**→**16**, the free hydroxyl group in **12** may direct the stereochemical outcome for the formation of **20**. Aromatization of the diol **20** to the pentacene **21** succeeded in moderate (47%) yield using $PBr_3/SnCl_2$. The use of $PBr_5/SnCl_2$ led to less than 20% yield due to a bromination side reaction at the electron rich aniline substructure. The addition of (4-methoxyphenyl)lithium to the ketones **10** and **12** showed similar results. The reaction of the TMSO-ketone **10** exclusively led to the *trans* product **22**, which could be deprotected to the *trans* diol **23**. The latter was also accessible stereoselectively from the hydroxyl-ketone **12**. The aromatization of the central pentacene ring was possible for **23** by means of $PBr_5/SnCl_2$ in 45% yield. The selective formation of the *trans* product in both cases (**10** and **12**) indicates an active role of the trifluoromethyl group in the addition of aryllithium reagents to such ketones. The strong dipole of the trifluoromethyl group could support the entrance of the incoming nucleophile from the *trans* side of the carbonyl group. The stereose-

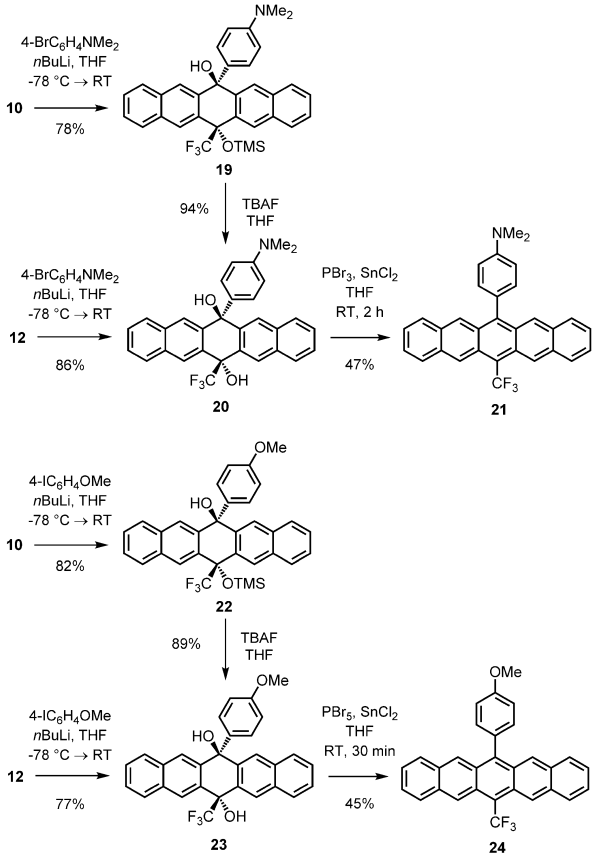

Scheme 4. Syntheses of the trifluoromethylpentacenes **21** and **24**.

lectivity observed here for the pentacene case is supported by related results for the anthracene series.[16] Detailed information about the aromatization steps is given in the Supporting Information (cf. Table S1).

As known for this class of substances, the resulting pentacenes **17**, **21** and **24** decompose in solution (50 μM, CH_2Cl_2) when exposed to ambient laboratory conditions within a few hours. To avoid photo-oxidation these compounds should therefore be stored as solids under argon atmosphere and exclusion of light. With respect to the poor solubility of PEN, derivatives **17**, **21** and **24** exhibit a clearly better solubility in organic solvents (CH_2Cl_2, $CHCl_3$ and THF), which is comparable to the solubility of **3** and of 6,13-bis(triisopropylsilylethynyl)pentacene (TIPS-PEN).

UV/Vis absorption spectra of **17**, **21** and **24** in CH_2Cl_2 differ only slightly in the low energy region (cf. Figure 3a), indicating a similar impact of the aryl and alkynyl substituents on the pentacene chromophore. Characteristic for the UV/Vis spectra of linear acenes, all spectra show vibronic fine structures. In contrast to the parent functionalized acene, 6,13-bis(trifluoromethyl)pentacene (**3**, λ_{max} = 611 nm), non-symmetrical substitution exhibits broadened bands and red-shifted λ_{max} values of 635 nm (**17**), 655 nm (**21**) and 637 nm (**24**). The corresponding optical HOMO–LUMO gaps are shown in Table 1.

Table 1. Summary of the optical band gaps ($E_G^{opt.}$), HOMO and LUMO energies, the electronical ($E_G^{elec.}$) and calculated gaps ($E_G^{calc.}$) and dipole moments.

Compound	$E_G^{opt.}$ [eV][a]	HOMO [eV][b]	LUMO [eV][b]	$E_G^{elec.}$ [eV][b]	$E_G^{calc.}$ [eV][c]	P [D][c]
17	1.95	−4.85	−2.89	1.96	2.01	2.95
3[9g]	2.02	−5.55	−3.52	2.03	2.04	0
TIPS-PEN	1.93	−5.34[18]	−3.32[18]	2.02[18]	2.01[6a]	0
21	1.89	−4.99	−2.85	2.14	2.15	6.49
24	1.95	−4.80	−2.75	2.05	2.15	4.76
PEN	2.13[19]	−5.02[9a],[d]	−2.93[9a],[d]	2.09[9a],[d]	2.20[9a]	0
PFP	1.99[19]	−5.59[9a],[d]	−3.67[9a],[d]	1.92[9a],[d]	2.02[9a]	0

[a] Optical HOMO–LUMO gaps are determined from the maximum of lowest-energy visible absorption band. Owing to the broad bands in the spectra of compound **21**, the lowest-energy shoulder was determined by means of a fit of three pseudo-voigt functions to the three major resonances. [b] Determined using CV. [c] Calculated with US-GAMESS using B3LYP/6-311G(d,p). [d] HOMO and LUMO energies were obtained using differential pulse voltammetry and 1,2-dichlorobenzene as solvent.

With respect to the aryl substituents in **21** and **24**, a reduced interaction between both π-systems is expected due to the hindered rotation about the aryl-pentacene C–C bond. In accordance with previous work,[17b] an almost orthogonal orientation of the aryl groups was also observed in the single crystal structures (vide infra and Supporting Information page S80). Therefore, the redshift of up to 44 nm for **21** (26 nm for **24**) compared to **3** could be attributed to the different auxochromes at the *para*-position of the benzene ring. In pentacene **17**, the extended conjugation through the TIPS-acetylene substituent could be considered as the reason for the red-shifted λ_{max} value. Regarding the observed broad band shapes, molecular aggregation in solution appears unlikely as explanation since the use of solvents with different polarity (CH_2Cl_2, THF) has not influenced the peak shapes (further details in the Supporting Information, page S81). Such a peak broadening was not observed for non-symmetrically bisalkynyl-substituted pentacenes,[17a] which can probably be ascribed to the weaker coupling of the auxochromes to the acene in that case.

Cyclic voltammetry was used to investigate the electronic properties in solution (cf. Figure 3b). The determined HOMO and LUMO energies, as well as the electronical band gaps ($E_G^{elec.}$), are summarized in Table 1 (details on evaluation presented in the Supporting Information, S4). Although, in congruence with the observations from the UV/Vis measurements, the HOMO–LUMO gaps remain relatively unchanged, the absolute HOMO and LUMO levels eminently depend on the substitution patterns. Pentacene **3** exhibits values comparable to PFP, an n-type organic semiconductor material.[9a] By contrast, replacing one of the trifluoromethyl groups in **21** and **24** increases the HOMO and LUMO levels drastically, even for the non-symmetrically substituted pentacene derivative **17**, where one of the trifluoromethyl groups is replaced by a TIPS-acetylene group. Compounds **17**, **21** and **24** show one reversible (black box), one irreversible (blue box) oxidation wave and up to two irreversible reduction waves (red and green box) within the scanned potential window. The electronic structures of the

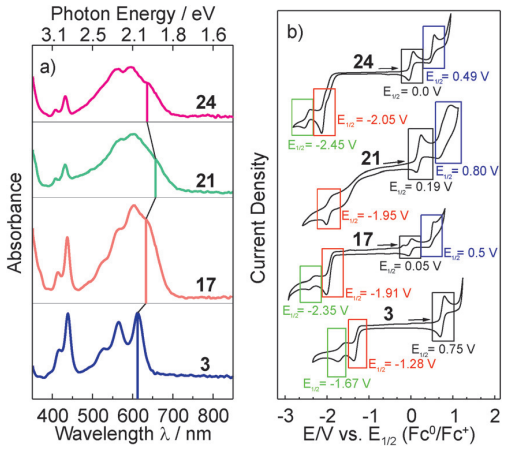

Figure 3. a) UV/Vis spectra of compounds **3**, **17**, **21** and **24** in solution (50 μM, CH_2Cl_2) in the low-energy region. b) Cyclic voltammograms of pentacene derivatives **3**, **17**, **21** and **24** in CH_2Cl_2 (1–2 mM) with $TBAPF_6$ (100 mM) at a scan rate of 100 mV s^{-1}. Potentials are referenced to ferrocene/ferrocenium redox couple (Fc/Fc^+). Arrows indicate the scan direction. For simplicity, the scale of current density is omitted. For exact current densities, the single cyclic voltammograms are provided in the Supporting Information (page S69).

acenes were also analyzed theoretically in the frame of DFT calculations (further details in the Supporting Information, pages S72–S74). As can be directly derived from Table 1, the computed gaps are in good agreement with the experimental ones, despite small overestimations of the energies.[20] Furthermore, the dipole moments of the molecules have also been calculated indicating that the inductive effect of the aryl substituents is significantly stronger than that of the TIPS group.

Fluoro-substituted diazaacenes

Two key reactions were studied for the construction of fluoro-substituted diazatetracenes and diazapentacenes: Pd-catalyzed aryl amination (Hartwig–Buchwald)[21] and nucleophilic aromatic substitution (S_NAr). Preliminary experiments revealed RuPhosPd G2 as precatalyst of choice for the Pd-catalyzed aryl amination strategy (cf. Figure 4).[22,23]

The aryl amination–oxidation sequence was elaborated for diazatetracenes first. Naphthalene-2,3-diamine (**8**) was allowed to react with different fluoro-substituted dibromobenzenes **25**, **27** and **29** (Scheme 5). Owing to the sensitivity towards oxidation of dihydrodiazaacenes,[24] a sequence without isolation

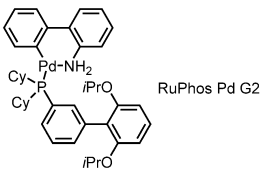

Figure 4. Structure of RuPhos Pd G2.

was applied. The optimization of the coupling conditions, as well as the subsequent dehydrogenation, was crucial in each case. For **25**, Cs_2CO_3 as base and $K_2Cr_2O_7$ as oxidizing agent provided the desired difluorodiazatetracene **26** in good yield. A fluorine substituent in *ortho*-position to the bromine caused problems, resulting in a moderate yield of 34% for diazatetracene **28** using LiO*t*Bu and chloranil. For **29** with two *ortho* fluorine substituents, the Pd-catalyzed aryl amination towards **30** failed. Application of the aryl amination conditions from the diazatetracene studies provided highly efficient routes to the diazapentacenes **33** and **36**. Pd-catalyzed reaction of diamine **8** with the dibromonaphthalene **31**[25] gave the dihydrodiazapentacene **32** in very good yield. The subsequent dehydrogenation, generating diazapentacene **33**, worked best with $K_2Cr_2O_7$ which was superior to MnO_2 or chloranil. Reaction of **8** and the dicyanonaphthalene dibromide **34**[26] led, via the dihydrodiazapentacene **35**, to the dicyanodiazapentacene **36**. The present cases demonstrate the double Hartwig–Buchwald aryl amination as a suitable synthetic route to azapentacenes even without solubilizing TIPS-acetylene substituents.[23]

The double nucleophilic aromatic substitution of the diamine **8** with perfluorinated benzene **37** or perfluoronaphtha-

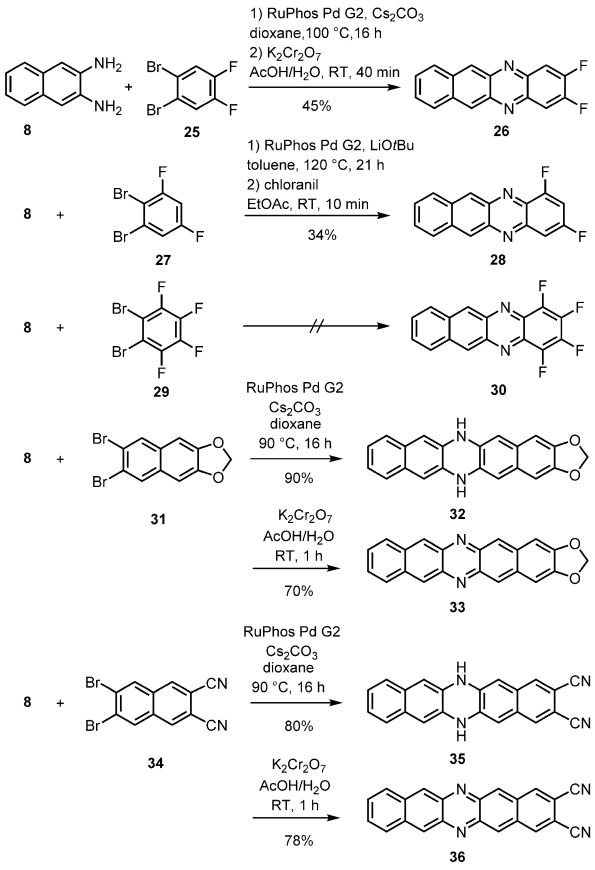

Scheme 5. Syntheses of diazatetracenes **26**, **28** and diazapentacenes **33**, **36** via Pd-catalyzed aryl amination.

lene (**39**) should provide rapid access to the fluoro-substituted diazatetracene **30** and diazapentacene **42** (Scheme 6). However, all attempts to form both C–N bonds in one operation failed. The use of several equivalents NaH at higher temperatures, such as reported for the synthesis of tetraazapentacene **4**[9j] resulted merely in decomposition and polymerization of the starting material. Whereas monoamination product **38** could be obtained within 1 h at 60 °C with poor yield, an optimization by reducing the temperature and extending the reaction time to 5 h at RT yielded **38** in 66%. The intramolecular cyclization of **38** required the use of a weak base, such as Hünig's base, in combination with higher temperatures. Stronger bases, such as NaH or NaHMDS, only led to decomposition. After dehydrogenation of the corresponding dihydro species, the tetrafluorodiazatetracene **30** was isolated in very good yield. These findings (stepwise amination and use of Hünig's base for the second step) could be transferred to the diazapentacene case. Monoamination of perfluoronaphthalene (**39**) provided compound **40** in good yield. The latter could be cyclized to the dihydrodiazapentacene **41** in nearly quantitative yield. Hexafluorodiazapentacene **42** was obtained after final dehydrogenation by $K_2Cr_2O_7$.

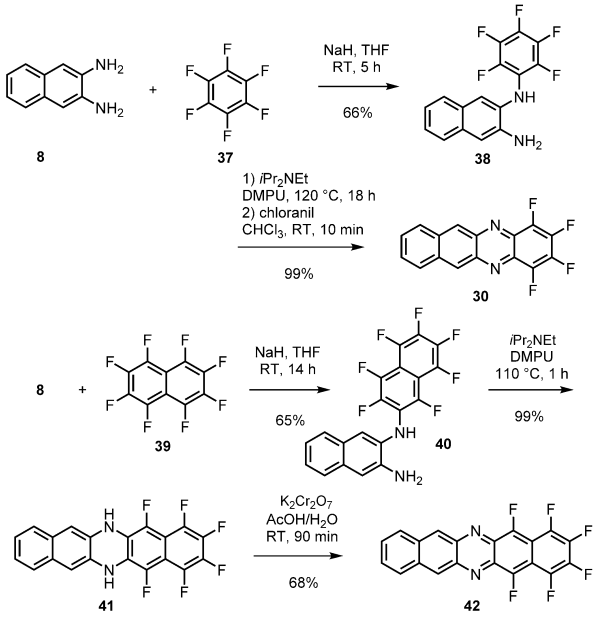

Scheme 6. Syntheses of the tetrafluorodiazatetracene **30** and the hexafluorodiazapentacene **42**.

Tetracenes **28** and **30** show satisfactory solubility in organic solvents (>1 mM in CH_2Cl_2 or $CHCl_3$), while compounds **26**, **33**, **36** and **42** exhibit a significantly lower solubility.[27] As solids, all synthesized diazaacenes show good stability. Under exclusion of light they are storable for several months at ambient temperature without decomposition. In solution (50 μM, CH_2Cl_2), they decompose within one week under ambient laboratory conditions. All synthesized diazatetracenes formed red-colored solutions; UV/Vis absorption spectra of which are shown in Figure 5a and b. The optical HOMO–LUMO gaps of the diazatetracenes decrease with the number of fluorine substituents. As expected, the smallest HOMO–LUMO gap among the modified tetracenes was found for the tetrafluorinated compound **30** (2.37 eV). Notable 1,3-difluorosubstitution in **28** causes a non-negligible redshift of the λ_{max} value compared to the isomeric 2,3-difluoro-substituted compound **26**. In comparison with the non-substituted benzo[*b*]phenazine, all fluorinated compounds exhibit a redshift in the low-energy region.[24] The enlargement of the fluorinated part of the aromatic system, shown in Figure 5b, leads to a pronounced lower HOMO–LUMO gap ($\Delta E_G^{Opt.} = 0.46$ eV). The spectrum of hexafluorodiazapentacene **42** displays a more distinct vibronic fine structure and the lowest optical band gap with λ_{max} at 650 nm. This λ_{max} value is significantly red-shifted compared to 6,13-diazapentacene (DAP) (615 nm).[28] The absolute HOMO and LUMO energies of **26**, **28**, **30** and **42** were determined by cyclic voltammetry (cf. Figure 5c and d) and are shown in Table 2. The redox behavior of the fluorinated diazaacenes are similar. They exhibit one irreversible oxidation wave (blue box), one reversible (black box) and one irreversible (red box) reduction wave in the scanned window.

Interestingly, the determined HOMO and LUMO levels of **42** are significantly lower than those of PFP, indicating that n-type behavior could be favorable following the prediction by Bao et al.[10a] Again, the gap energies, as well as the dipole moments, were calculated by DFT methods. In congruence with

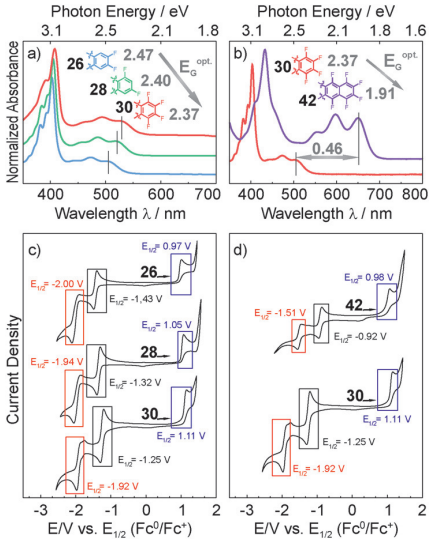

Figure 5. a) and b) UV/Vis spectra of compounds **26**, **28**, **30** and **42** in solution (50 μM, CH_2Cl_2) at the low-energy region. Optical HOMO–LUMO gaps are determined from the maximum of the lowest absorption band. c) and d) Cyclic voltammograms of diazatetracenes **26**, **28** and **30** and diazapentacene **42** in CH_2Cl_2 (1 ≤ mM) with $TBAPF_6$ (100 mM) at a scan rate of 100 mV s^{-1}. Potentials are referenced to ferrocene/ferrocenium redox couple (Fc/Fc^+). Arrows indicate the scan direction. For simplicity, the scale of current density is omitted. For exact current densities, the single cyclic voltammograms are provided in the Supporting Information (page S70).

Table 2. Summary of the optical band gaps ($E_G^{opt.}$), HOMO and LUMO energies, the electronical ($E_G^{elec.}$) and calculated gaps ($E_G^{calc.}$) and dipole moments.

Compound	$E_G^{opt.}$ [eV][a]	HOMO [eV][b]	LUMO [eV][b]	$E_G^{elec.}$ [eV][b]	$E_G^{calc.}$ [eV][c]	P [D][c]
26	2.47	−5.77	−3.34	2.43	2.75	3.16
28	2.40	−5.85	−3.48	2.37	2.69	2.47
30	2.37	−5.91	−3.55	2.36	2.64	4.31
42	1.91	−5.78	−3.88	1.90	2.04	5.27
DAP	2.02[28]	–	–	–	–	0
PEN	2.13[19]	−5.02[9a],[d]	−2.93[9a],[d]	2.09[9a],[d]	2.20[9a]	0
PFP	1.99[19]	−5.59[9a],[d]	−3.67[9a],[d]	1.92[9a],[d]	2.02[9a]	0

[a] Optical HOMO–LUMO gaps are determined from the maximum of lowest absorption band. [b] Determined using CV. [c] Calculated with US-GAMESS using B3LYP/aug-cc-pVTZ. [d] HOMO and LUMO energies were obtained using differential pulse voltammetry and 1,2-dichlorobenzene as solvent.

the before discussed results, the calculated gaps are slightly overestimated compared to the experimental values. The highest dipole moment is found for **42**; a result of the large number of fluorine atoms and the bigger size compared to **30**, which features the second highest dipole moment. Owing to the lower degree of fluorination, the values for the tetracene derivatives **26** and **28** are both lower than for **30**, whereas the 1,3-difluoro-substituted compound **28** possesses a slightly lower dipole moment compared to the 2,3-difluoro-substituted counterpart **26**.

Solid-State Studies

Molecular packing

X-ray crystallographic analysis of pentacenes **17**, **21**, and **24** reveals distinctly different packing for each compound, whereas a solvent-free structure of **24** could only be obtained by sublimation (see below).[29] As a consequence of replacing one trifluoromethyl group, the herringbone motif of the parent pentacene **3** is lost. In the crystal structures obtained from solution, the pentacene derivatives assemble in dimeric pairs realizing an antiparallel alignment of the molecules with regard to their dipole moment. The individual molecules are slightly bent, and no 2D brick-wall arrangement, as observed for TIPS-PEN, is present.

Pentacene **17** adopts a so-called sandwich-herringbone motif[30] (cf. Figure 6a, **17**). The angle between dimeric pairs amounts to 74°. This almost perpendicular arrangement of planes enables aryl-H-ring (edge-to-face) and aryl-H-acetylene contacts. Adjacent molecules of these pairs are slightly bent apart (11°) with an interplanar distance of 3.34 Å and moderate overlap (cf. Figure 6b, c; **17**). With respect to the packing motif, compound **17** displays a greater relationship to **3** than to TIPS-PEN. The structural motif of **17** features similarity to the herringbone motif, but in contrast to **3**, no F–H or F–C contacts exist, and the overlap is reduced. Changing to an aryl substituent in **21** results in a one-dimensional π-slipped stack motif of the dimeric pairs (cf. Figure 7a). The adjacent molecules are slightly bent towards each other (7.3°) with an interplanar distance of 3.43 Å, yielding an overlap of more than 3 aromatic rings of neighboring molecules (cf. Figure 7b and c). The interplanar distance of adjacent dimeric pairs is 3.6 Å. The aryl substituent and the pentacene core are twisted (69°). In the case of **21** (and **24**, see below), the trifluoromethyl group is disordered and exhibits several discrete arrangements, indicating, in accordance to previous observations,[31] a low rotational energy barrier. This finding is further supported by geometry calculations of isolated molecules of **21** (and **24**), where also several stable conformations are found. Notably, a significant bending from planarity of the molecular backbone (11° for **17**, 7.3° for **21**) was observed in the structural analysis of compounds **17** and **21**. Such a bending is also found in calculated single molecule structures when the geometry is constrained to C_s symmetry (6.7° for **17**, 7.0° for **21**, details on calculation provided in the Supporting Information, page S72).

While F–C and F–H contacts based on the trifluoromethyl group do not occur in the crystal structures of the non-symmetrically substituted pentacene derivatives, the fluoro-substituted diazaacenes exhibit F–C and F–H interactions at some points. The packing of compounds **28**, **30** and **42** is significantly influenced by fluorine based interactions and not only by π–π interactions. The corresponding crystal packings and π stacking arrangements are shown in Figure 8, where the investigated single crystals were obtained from solution.[32] Again, adjacent molecules realize an antiparallel alignment with regard to their dipole moment (head-to-tail, cf. Figure 8b). In compound **28**, the molecules form isolated, one-dimensional parallel columns along the crystallographic *b* axis with alternating stacking distances of 3.40 and 3.34 Å (cf. Figure 8a, **28**). The head-to-tail orientation results in strong π–π interactions, and the columns interact via F–H contacts (cf. Figure 8b, c; **28**). The increased amount of fluorine in compound **30** is reflected in the observation of strong F–H and F–C interactions within one stack as well as between the stacks (cf. Figure 8c, **30**). Diazatetracene **30** packs in a brick-wall motif of head-to-tail oriented dimeric pairs (cf. Figure 8a, b; **30**). The π-stacking distance between adjacent molecules is 3.35 Å and 3.38 Å to the next dimeric pair in the column. Neighboring brick-wall stacks are twisted relative to each other, with an angle of 68°. In contrast to **30**, the enlargement of the fluorinated part of the aromatic system in **42** results in a herringbone-like packing of the head-to-tail oriented dimeric pairs (cf. Figure 8a, b; **42**). Edge-to-face and face-to-face interactions within one 2D sheet are observed. The interplanar distance in one dimeric pair amounts to 3.41 Å, but to 3.34 Å to the next layered diazapentacene. In one 2D sheet of the crystal packing, the columns form a contact angle of 67°. With regard to the three fluorinated diazaacenes **28**, **30** and **42**, a stronger tendency of forming dimeric pairs is observed with increasing the dipole moment.

As mentioned before, crystal growth from solution has not yielded a solvent-free crystal structure of **24** yet. This is also the case for compound **26**. Surprisingly, single crystal structures of these compounds obtained by sublimation exhibit a parallel, or head-to-head, alignment of the molecules with regard to their dipole moment (cf. Figure 9).[33] Furthermore, no dimeric pairs as found for the other compounds are ob-

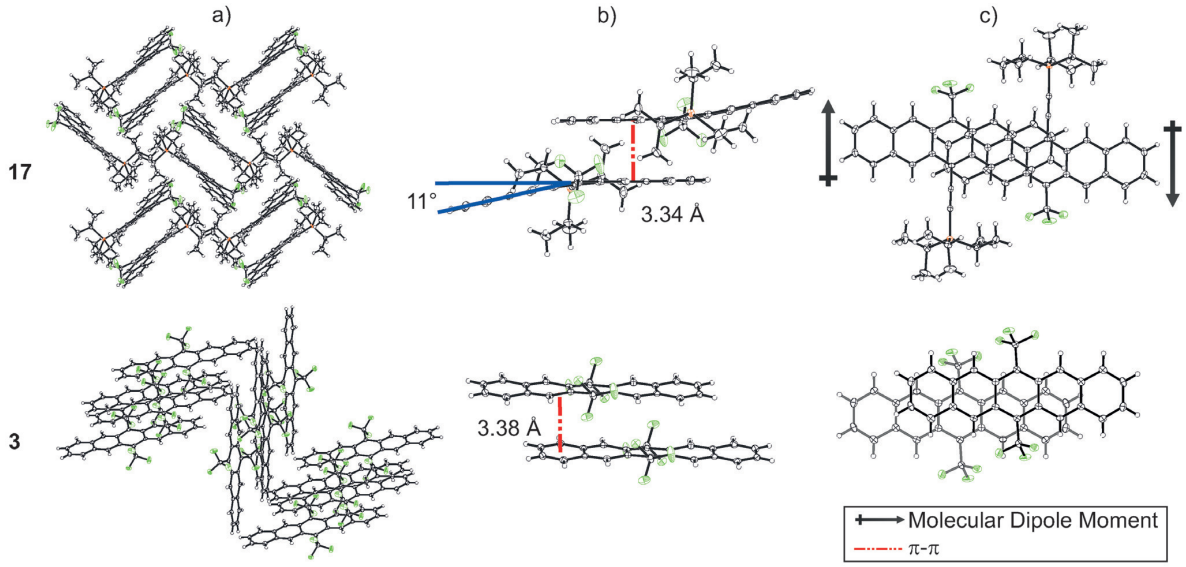

Figure 6. Single crystal structure of **17** compared to the parent pentacene derivative **3**. a) Packing arrangement; b) π stacking arrangement, viewing direction along the backbone; c) π stacking arrangement, viewing direction perpendicular to the backbone.

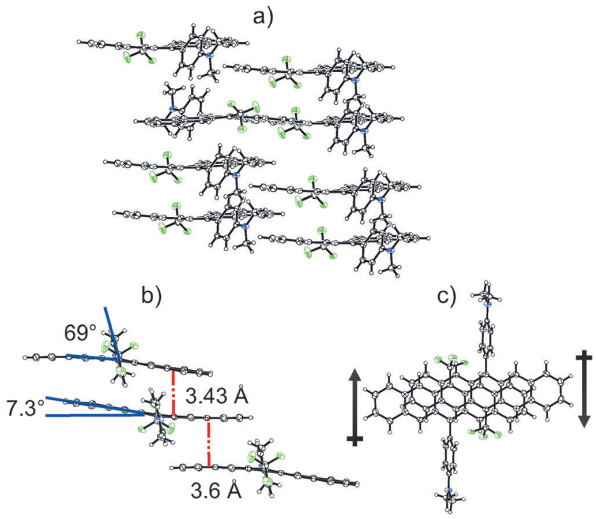

Figure 7. Single crystal structure of **21**. a) Packing arrangement; b) π stacking arrangement, viewing direction along the backbone; c) π stacking arrangement, viewing direction perpendicular to the backbone. Note that in the crystal structure, two discrete arrangements of the trifluoromethyl group are observed. For clarity, only one of these is depicted in this visualization.

served. Pentacene derivative **24** adopts slipped cofacial π-stacking along the crystallographic *b* axis. The interplanar distance between the parallel mean planes of the pentacene backbones in these columns amounts to 3.62 Å, whereas neighboring columns form a contact angle of 77°. The trifluoromethyl group is again disordered, which precludes a precise location (see above). In the crystal structure, compound **26** features certain similarity to **28**. The molecules form isolated columns along the *a* axis with an interplanar distance of 3.34 Å, whereas the columns again interact via F···H contacts. The finding that for **24** no solvent-free crystal structure could be obtained from solution suggests that solvent molecules compensate the strong electrostatic dipoles via solvation shells, which in turn affects the recrystallization dynamics and structure. Therefore, the crystalline phases resulting either from thermodynamically or kinetically controlled growth via solution-based recrystallization or sublimation can be rather different, which needs to be taken into account when analyzing the solid-state properties of these materials and using them in device applications.

Thin-film studies

To investigate the electronic properties of the acenes in their solid phase, thin films of compounds **17**, **21**, **24** and **42** were prepared by organic molecular beam-deposition (OMBD) under high vacuum conditions.[34] Upon deposition onto transparent supporting substrates (glass or potassium chloride crystals), UV/Vis absorption measurements in transmission were enabled. The achieved solid-state spectra are presented in Figure 10 as dark lines (top trace), while the corresponding solution spectra are provided for comparison in brighter color (lower trace). For **3**, TIPS-PEN and **17**, a typical behavior is observed; though modified in oscillator strength, the fundamental absorption bands of the molecules in solution are also observed in the solid state. At higher wavelength, an additional band is found which is attributed to a transition to an excitonic state. Owing to the additional correlation between electron and hole in this state, the energy spacing relative to the ground state is reduced compared to the fundamental HOMO–LUMO transition in the single molecule.[35]

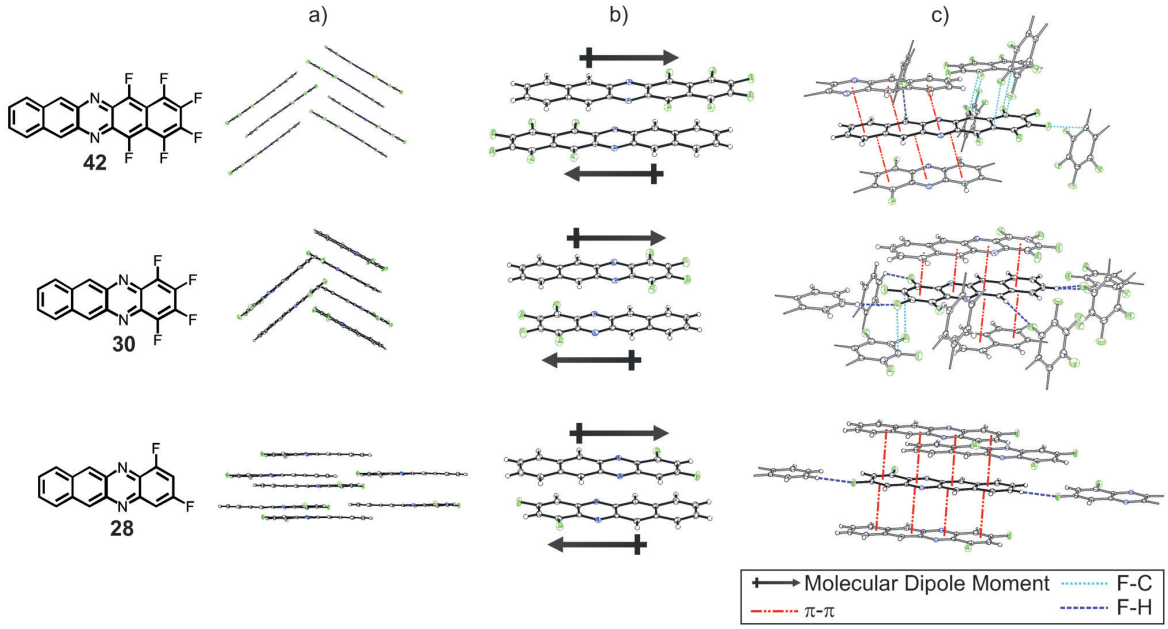

Figure 8. Crystal packing and π stacking arrangement of **28**, **30** and **42**. a) Viewing direction along the backbones; b) viewing direction onto the backbones; c) different types of interaction on basis of short contacts.

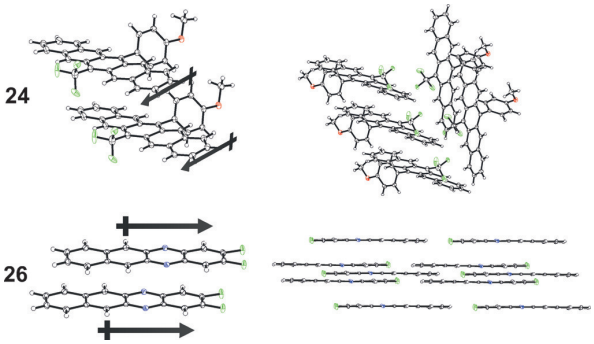

Figure 9. Crystal packing and π stacking arrangement of **24** and **26** obtained by sublimation. Note that in the crystal structure of **24** three discrete arrangements of the trifluoromethyl group are observed. For clarity, only one of these is depicted in this visualization.

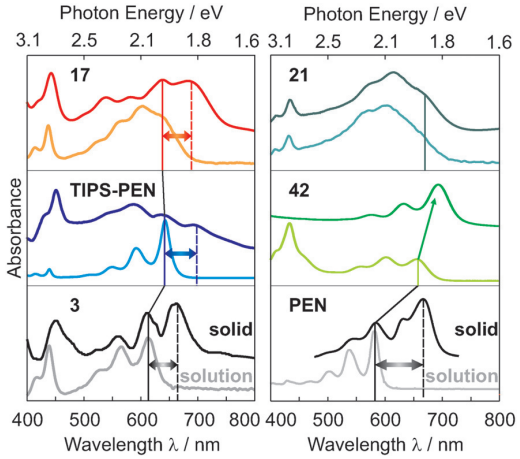

Figure 10. UV/Vis spectra of **3**, TIPS-PEN, **17**, PEN, **42** and **21** in solution (50 μM, CH_2Cl_2, lower trace) and for solid films evaporated onto transparent substrates (top trace) with labelled peak positions and exciton binding energies (arrow).

The difference between the HOMO–LUMO transition in the solution-spectra ($E_G^{solution}$) and the exciton-related transition (E_G^{solid}) allows quantifying the exciton binding energy (E_{ExcBin}). Interestingly, this value is clearly lower for all present acene compounds compared to pure pentacene (cf. Table 3).

The variation in exciton binding energy for different compounds is frequently explained by different molecular polarizabilities. In a simple model, Bässler has proposed a quantitative correlation between the polarizability and the exciton binding energy as given by Equation (1) in which α denotes the molecular polarizability and r_{ik} the intermolecular distances (calculated here as the distances between the center of the pentacene backbones) assuming that the response to the *E*-field generated by the exciton can be described within a dipole approach.[36]

$$E_{E,B,Cal} \propto \alpha \sum_{i \neq k} r_{ik}^{-6} \quad (1)$$

We note that such an approach is strictly correct only in the far-field approximation and does not perfectly hold true for dipoles with extensions comparable to intermolecular distances (as the case here). To test the validity of this quantification for

Table 3. Exciton binding energies (E_{ExcBin}) derived from the difference between the energies of the lowest excitation in the solid state (E_G^{solid}) and the solution spectra ($E_G^{solution}$).

Compound	$E_G^{solution}$ [eV][a]	E_G^{solid}[eV]	E_{ExcBin} [eV]
17	1.95	1.81	0.14
TIPS-PEN	1.93	1.78	0.15
3	2.02	1.87	0.15
21	1.89	(1.89)[b]	(–)[b]
42	1.91	(1.79)[b]	(0.12)[b]
PEN[19]	2.13	1.81	0.32
PFP[19]	1.99	1.78	0.21

[a] $E_G^{solution} = E_G^{opt.}$ in Tables 1 and 2. [b] The values for **21** and **42** cannot directly be compared to the other ones. Further details explained in the text.

the present case, we have computed the molecular polarizabilities for **3**, **17**, PEN and PFP and derived a lattice sum from the intermolecular spacings (further details in the Supporting Information, page S80). Despite deviations in the absolute values, which are attributed to the aforementioned approximations, the general trend is perfectly compatible with the experimental data for all compounds (cf. Table 4).

Table 4. Linear polarizabilities α computed for different acene derivatives along the long (α_L), medium (α_M) and normal axis (α_N) of the molecule and effective polarizabilities (α_{eff}), given in atomic units. Additionally, the lattice sums over r^{-6} for the compounds are presented (in 10^{-5} Å^{-6}) as well as the calculated exciton binding energies ($E_{EB,Cal}$).

Compound	α_L	α_M	α_N	α_{eff}[a]	$\Sigma\ 1/r_{ik}^6$	$E_{EB,Cal}$[b]
17	701	523	201	475	1.4	0.02
3	616	274	103	331	16	0.14
PEN	612	244	87	314	38	0.32
PFP	640	257	87	328	33	0.29

[a] Determined by calculating the average of the anisotropic polarizabilities. [b] Calculated using the Model by Bässler (see text) and normalized to the experimental E_{ExcBin} of PEN (0.32 eV) (details presented in the Supporting Information, page S80).

Interestingly, a direct correlation between the molecular polarizability and the exciton binding energy is not found. In fact, the compound with the highest polarizability (**17**) features the smallest E_{ExcBin}, while the highest binding energy is found for PEN, which exhibits lowest molecular polarizability. This can be understood, since not only the polarizability but also the molecular arrangement determines the actual energy balance. Indeed, this is also accounted for in the proposed model, since the dependence of $E_{EB,Cal}$ on the intermolecular distances is significantly stronger than that on the polarizability due to the rapid descent of the lattice sum.

For compounds **21** and **42**, a distinctly different behavior of the spectra is observed. For vacuum-evaporated films of **42**, again a shift of the lowest observed absorption band is found. In contrast to the aforementioned cases, however, no isolated additional band is observed. Instead, the complete spectrum, including the vibronic replica, appears shifted to higher wavelengths, as similarly reported for the case of diazapentacene.[28] Furthermore, the absorption band at about 430 nm is only found in the solution spectrum. This is probably due to preferential molecular orientation in the thin film. The molecules are arranged in an upright fashion, with their long molecular axis perpendicular to the sample surface (see below). In this case, the transverse electrical field cannot couple to excitations with transition dipole moment (TDM) oriented along the long axis of the molecules. This interpretation is supported by observations for the case of PFP, where it has been shown that an absorption band at a similar energy indeed features a TDM with according orientation.[12] For **21**, finally, the solid-state spectra are nearly equivalent to those of molecules in solution, and no indication of additional excitonic states is found. Although we cannot provide a definite explanation for this observation at this stage, we note that the prepared films did not exhibit any crystalline ordering. Based on this low structural order one might expect that the formation of the partially delocalized excitonic states is hampered, and, therefore, the oscillator strength of such excitations is reduced.[37] Such behavior has also been reported for thin films of TIPS-PEN, where films in amorphous configuration exhibit absorption spectra, which are equivalent to solution spectra, and in crystalline films only spectra are found similar to the one presented in this study.[38] In the present case, a detailed understanding is additionally complicated by the rather broad resonances in the spectrum of **21**.

In order to gain further insights into the electronic structure of the processed compounds and to analyze whether distinct molecular orientations can be achieved upon film preparation on different substrates, X-ray absorption spectroscopy (NEXAFS) was applied for thin films of selected compounds. In this method, the excitation of C1s core electrons into unoccupied molecular states is observed. The absorption intensity of the distinct resonances depends on the relative orientation between the electrical field vector (E) and the molecular TDM. Considering that the TDMs corresponding to excitations into π^* orbitals (typically found in the energetic range from 282 to 292 eV for aromatic hydrocarbons) are oriented perpendicular to the molecular backbone, the orientation of the molecules can be determined by comparing absorption spectra measured at different sample orientations.[39] For PEN,[40,41] PFP[42,43] and pentacene-5,7,12,14-tetrone (P-TET),[43] it has been reported that the molecular orientation is strongly influenced by the supporting substrate; the molecules adopt upright orientations on SiO_2 while they crystallize in lying configurations on graphite surfaces. Due to the high expenditure of time of the NEXAFS measurements and limited synchrotron beam time these analyses could only be performed for a limited number of compounds. For this purpose **3**, **30** and **42** have been chosen since they represent different types of substitution and the complementary experiments have verified their processability by vacuum sublimation. **3** stands for an acene with symmetrically attached fluorine-containing substituents at the short molecular axis, whereas **30** and **42** are representatives of asymmetrical fluorine substitution along the long molecular axis leading to permanent dipoles. In the latter case, the vari-

ous size of the parent acene (tetracene vs. pentacene) also results in different dipole strength, which renders these two compounds an interesting combination. Based on these reports, we have prepared multilayer thin films with nominal thicknesses of about 15 nm of **3**, **30**, and **42** on these two substrates and compared the NEXAFS dichroisms (in-situ measurements without contact to the ambient). As presented in Figure 11 a, strongest X-ray absorption is observed for grazing incidence (blue curve, $\theta = 30^\circ$, cf. experimental setup in Figure 11 f), while only very weak absorption is found under normal incidence (red curve). This behavior corresponds to lying molecules with an effective orientation of their aromatic backbone relative to the surface (α) of about 20°. For films deposited on SiO_2 substrates (cf. Figure 11 b), the analysis yields an inverse dichroism, which corresponds to $\alpha = 70^\circ$. Therefore, it can be concluded that, in agreement with the observations for PEN, PFP and P-TET, thin films of **3** are formed by uprightly-oriented molecules on SiO_2 and molecules in lying orientation on graphite. This trend is similarly observed for thin films of **42**, where molecular orientations of $\alpha = 75^\circ$ on SiO_2 and $\alpha < 20^\circ$ on graphite are determined. Interestingly, there is no crystalline arrangement in the bulk structure that could lead to such low values as found in the latter case. Owing to the herringbone arrangement of both molecules in the unit cell, the lowest value for α in this crystal structure amounts to 34°. Therefore, the clearly lower determined orientation indicates nucleation of **42** in a different polymorph with rather parallel arrangement of all molecules with respect to the graphite surface. Such a substrate-mediated polymorph has also been observed for PFP[44] and hexa-*peri*-hexabenzocoronene[45] thin films on graphite, and is attributed to lattice match between the molecular backbone and the graphite lattice. By contrast, a strikingly different situation occurs for thin films of the tetracene derivative **30**. The dichroism for thin films on graphite is strongly reduced compared to the other films, and the evaluation of the molecular orientation yields $\alpha = 45^\circ$. This value is compatible with the determined crystal structure and can be explained by molecules in rather recumbent orientation with slight tilt of the long axis relative to the substrate. Interestingly, no dichroism is observed for thin films of **30** prepared on SiO_2. There, the X-ray absorption is constant, independent of the sample orientation. Since all molecules, regardless whether in crystalline or amorphous state, contribute equally to the NEXAFS signal, it cannot directly be discriminated between a molecular arrangement where all molecules are equally tilted with an angle of 55° and a balanced co-existence of differently oriented molecules.[46] However, it can be clearly stated that no upright molecular orientation is found as in the other cases. Furthermore, a comparison between the signatures of the spectra on both substrates reveals clear differences. Most prominently, an additional resonance is found at 288 eV for films on SiO_2, while the resonances at 286 eV vanish. Since the spectral shape should be equivalent for thin films on both substrates, this indicates severe molecular decomposition, either introduced by secondary electrons from the surface or substrate-induced decomposition.[47]

In Figure 12, the X-ray absorption spectra for **3**, **42**, PEN and PFP are presented as magnifications in the region from 282 to 292 eV. As mentioned before, mostly resonances corresponding to excitations into π^* orbitals are found in this energetic range. These resonances are superimposed by a step-like increase of the absorption (so-called absorption edge), which corresponds to the ionization of core electrons into vacuum states. The spectral signature of PEN[48] and **3** is rather similar, indicating that the electronic structure is not strongly affected by the introduction of the trifluoromethyl side-groups. At higher energies well above the absorption edge, some additional resonances arising from these groups can be identified

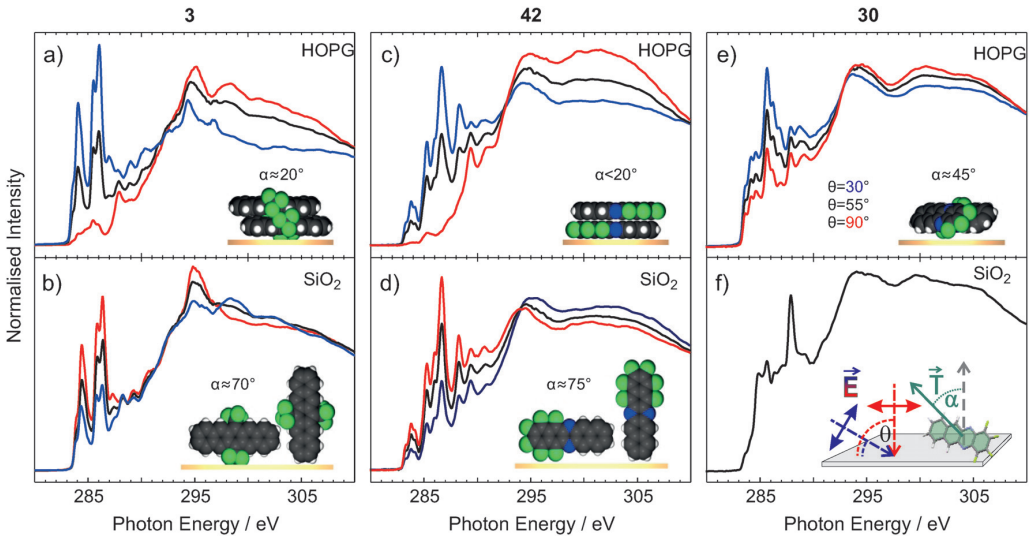

Figure 11. Dichroic NEXAFS measurements of compounds **3**, **42** and **30** (from left to right) on HOPG (top) and SiO_2 (bottom) substrates. Inset pictures illustrate schematically the derived molecular orientation. f) $\theta = 55^\circ$ spectrum for compound **30** on SiO_2. Inset indicates definition of different angles.

(cf. Figure 11 a, b), which are attributed to excitations into σ* orbitals. For PFP,[49] an overall shift of the resonances to higher photon energies was found, which results from the higher binding energy of the core electrons (chemical shift upon fluorination) and, therefore, an increased ionization potential. For the case of **42**, not the entire spectrum, but some resonances are shifted with respect to the PEN spectrum, which can be easily understood by considering that in this compound carbon atoms with different substituents (C–H, C–C and C–F) are present. Therefore, some of the initial states are similar to the case of PFP, while others correspond to PEN. Upon numerical calculation of the NEXAFS spectra by application of the StoBe code[50] (further details in the Supporting Information, page S72), the ionization potentials have been computed. We note that in a detailed description, the ionization potential is different for each excitation center, that is, individual carbon atom, due to the aforementioned different chemical surrounding. In the following, we will constrain the discussion to the ionization potential of the excitation center which corresponds to the lowest lying resonance. As expected, these values follow the afore discussed trend; the IP of **3**, **42** and PEN is rather equivalent, while it lies significantly higher for PFP. In Figure 12 b, the spectra are calibrated such that the different IP values are equalized, that is, IP is set to zero for all compounds.

This then allows to directly derive the differences between the ionization potential and the lowest resonance, which can be interpreted as LUMO energy. Clearly, the observed values are significantly lower than those determined by cyclic voltammetry as well as by computation (cf. Tables 1 and 2). This is not surprising since in NEXAFS spectroscopy, not the actual LUMO energies are determined, but the values for excited molecules. In this case, the relaxation of the molecule, due to the introduction of a core hole, also contributes to the energetic position of the resonances.[51] Assuming the effect of relaxation to be similar for all discussed molecules, which appears reasonable as they are isoelectronic in the aromatic backbone, the differences between the determined LUMO values, with respect to the value for PEN, can be analyzed, that is, the PEN LUMO energy as determined from NEXAFS (−5.58 eV) is subtracted from all values. As presented in Table 5, the relative differences in the LUMO levels (ΔE_{LUMO}^{NEXAFS}) correspond very well with those determined from the cyclovoltammetric measurements (ΔE_{LUMO}^{CV}), hence, indicating that the LUMO energies are rather similar for isolated molecules and the solid state.

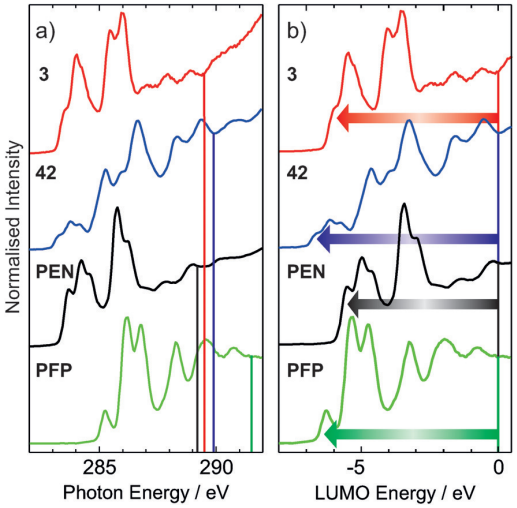

Figure 12. a) NEXAFS signature of compounds **3** and **42** compared to those of PEN and PFP in the C1 s edge region. Vertical lines indicate positions of calculated ionization potentials. b) Spectra like in a) aligned to the ionization potentials. Arrows pointing to corresponding LUMO resonances. Note that the energy scale is given relative to the ionization potentials.

Table 5. Comparison between absolute and relative (with respect to PEN) LUMO energies derived from cyclic voltammetry (E_{LUMO}^{CV}) and NEXAFS measurements (E_{LUMO}^{NEXAFS}).

Compound	E_{LUMO}^{CV} [eV]	E_{LUMO}^{NEXAFS} [eV]	ΔE_{LUMO}^{CV} [eV]	ΔE_{LUMO}^{NEXAFS} [eV]
3	−3.52	−6.05	−0.59	−0.47
42	−3.88	−6.66	−0.95	−1.08
PEN	−2.93[9a]	−5.58	0	0
PFP	−3.67[9a]	−6.30	−0.74	−0.72

Conclusion

In conclusion, efficient syntheses of non-symmetrical trifluoromethyl-substituted pentacenes and fluoro-substituted azapentacenes have been achieved. Key steps were the monoaddition of $TMSCF_3$ to pentacenequinone for the introduction of the trifluoromethyl group in the pentacene series and for the azapentacene syntheses a Hartwig–Buchwald aryl amination approach or sequential S_NAr reaction. Although the electronic properties of the new polyaromatic compounds differ significantly with respect to the absolute energy levels, the energy gap between the frontier orbitals remains rather similar compared to the parent acenes. The fluorine substituents induce strong molecular dipoles, causing distinct effects on the molecular packing in the crystalline state. Complementary thin-film studies show that the intermolecular distances, rather than the molecular polarizabilities, are the decisive factor determining the exciton binding energy. Furthermore, the effect of substrate–adsorbate interaction has been addressed by preparing thin films on different substrates yielding different distinct molecular orientations. The novel fluoro-substituted pentacenes and azapentacenes should be interesting candidates for various organoelectronic devices.

Experimental Section

Experimental conditions and detailed experimental procedures for Schemes 2–6 as well as ^{1}H, ^{13}C and ^{19}F NMR spectra, cyclic voltammograms, quantum chemical calculations and X-ray data are provided in the Supporting Information together with details on thin-film preparation, UV/Vis and NEXAFS measurements.

Acknowledgements

We acknowledge support by the Deutsche Forschungs-Gemeinschaft (Grant SFB 1083, TP A2 and A8) and the Helmholtz-Zentrum Berlin (electron storage ring BESSY II) for provision of synchrotron radiation at beamline HE-SGM. Jonas Schwaben gratefully acknowledges financial support by the Fonds der Chemischen Industrie. Dr. M. Drüschler is gratefully acknowledged for support with the CVs.

Keywords: acene · fluorinated compounds · optical properties · organic solids · synthesis

[1] For reviews see: a) H. Yamada, T. Okujiama, N. Ono, *Chem. Commun.* **2008**, 2957 – 2974; b) A. W. Hains, Z. Liang, M. A. Woodhouse, B. A. Gregg, *Chem. Rev.* **2010**, *110*, 6689 – 6735; c) J. E. Anthony, A. Facchetti, M. Heeney, S. R. Marder, X. Zhan, *Adv. Mater.* **2010**, *22*, 3876 – 3892; d) K. Zhou, H. Dong, H.-l. Zhang, W. Hu, *Phys. Chem. Chem. Phys.* **2014**, *16*, 22448 – 22457.

[2] a) *Organic Electronics: Materials, Manufacturing and Applications, Vol. 1* (Eds.: H. Klauk), Wiley-VCH, Weinheim **2006**, pp. 80 – 90; b) A. R. Murphy, J. M. J. Frechét, *Chem. Rev.* **2007**, *107*, 1066 – 1096.

[3] a) B. A. Jones, A. Facchetti, M. R. Wasielewski, T. J. Marks, *J. Am. Chem. Soc.* **2007**, *129*, 15259 – 15278; b) C. Li, H. Wonneberger, *Adv. Mater.* **2012**, *24*, 613 – 636.

[4] For reviews see: a) J. E. Anthony, *Chem. Rev.* **2006**, *106*, 5028 – 5048; b) J. E. Anthony, *Angew. Chem. Int. Ed.* **2008**, *47*, 452 – 483; *Angew. Chem.* **2008**, *120*, 460 – 492; c) U. H. F. Bunz, J. U. Engelhart, B. D. Lindner, M. Schaffroth, *Angew. Chem. Int. Ed.* **2013**, *52*, 3810 – 3821; *Angew. Chem.* **2013**, *125*, 3898 – 3910.

[5] a) J. E. Anthony, J. S. Brooks, D. L. Eaton, S. R. Parkin, *J. Am. Chem. Soc.* **2001**, *123*, 9482 – 9483; b) J. E. Anthony, D. L. Eaton, S. R. Parkin, *Org. Lett.* **2002**, *4*, 15 – 18; c) A. Maliakal, K. Raghavachari, H. Katz, E. Chandross, T. Siegrist, *Chem. Mater.* **2004**, *16*, 4980 – 4986; d) W. Fudickar, T. Linker, *J. Am. Chem. Soc.* **2012**, *134*, 15071 – 15082.

[6] a) I. Kaur, W. Jia, R. P. Kopreski, S. Selvarasah, M. R. Dokmeci, C. Pramanik, N. E. McGruer, G. P. Miller, *J. Am. Chem. Soc.* **2008**, *130*, 16274 – 16286; b) A. L. Appleton, S. M. Brombosz, S. Barlow, J. S. Sears, J.-L. Bredas, S. R. Marder, U. H. F. Bunz, *Nat. Commun.* **2010**, *1*, 91; c) S. Katsuta, D. Miyagi, H. Yamada, T. Okujima, S. Mori, K. Nakayama, H. Uno, *Org. Lett.* **2011**, *13*, 1454 – 1457.

[7] a) F. Babudri, G. M. Farinola, F. Naso, R. Ragni, *Chem. Commun.* **2007**, 1003 – 1022; b) M. L. Tang, Z. Bao, *Chem. Mater.* **2011**, *23*, 446 – 455.

[8] a) Y. Kim, T. M. Swager, *Chem. Commun.* **2005**, 372 – 374; b) C. Di, J. Li, G. Yu, Y. Xiao, Y. Guo, Y. Liu, X. Qian, D. Zhu, *Org. Lett.* **2008**, *10*, 3025 – 3028; c) X. Feng, Q. Li, J. Gu, F. A. Cotton, Y. Xie, H. F. Schaefer III, *J. Phys. Chem. A* **2009**, *113*, 887 – 894; d) M. C. R. Delgado, K. R. Pigg, D. A. da Silva Filho, N. E. Gruhn, Y. Sakamoto, T. Suzuki, R. M. Osuna, J. Casado, V. Hernández, J. T. L. Navarrete, N. G. Martinelli, J. Cornil, R. S. Sánchez-Carrera, V. Coropceanu, J.-L. Brédas, *J. Am. Chem. Soc.* **2009**, *131*, 1502 – 1512; e) E. Di Donato, R. P. Fornari, S. Di Motta, Y. Li, Z. Wang, F. Negri, *J. Phys. Chem. B* **2010**, *114*, 5327 – 5334; f) H. Sun, A. Putta, M. Billion, *J. Phys. Chem. A* **2012**, *116*, 8015 – 8022.

[9] For pentacenes see: a) Y. Sakamoto, T. Suzuki, M. Kobayashi, Y. Gao, Y. Fukai, Y. Inoue, F. Sato, S. Tokito, *J. Am. Chem. Soc.* **2004**, *126*, 8138 – 8140; b) C. R. Swartz, S. R. Parkin, J. E. Bullock, J. E. Anthony, A. C. Mayer, G. G. Malliaras, *Org. Lett.* **2005**, *7*, 3163 – 3166; c) Y. Shu, Y.-F. Lim, Z. Li, B. Purushothaman, R. Hallani, J. E. Kim, S. R. Parkin, G. G. Malliaras, J. E. Anthony, *Chem. Sci.* **2011**, *2*, 323 – 368; d) C. Tönshoff, H. F. Bettinger, *Chem. Eur. J.* **2012**, *18*, 1789 – 1799; e) C.-T. Chien, T.-C. Chiang, M. Watanabe, T.-H. Chao, Y. J. Chang, Y.-D. Lin, H.-K. Lee, C.-Y. Liu, C.-H. Tu, C.-H. Sun, T. J. Chow, *Tetrahedron Lett.* **2013**, *54*, 903 – 906; f) R. R. Bula, I. M. Oppel, H. F. Bettinger, *J. Org. Chem.* **2012**, *77*, 3538 – 3542; g) J. Schwaben, N. Münster, T. Breuer, M. Klues, K. Harms, G. Witte, U. Koert, *Eur. J. Org. Chem.* **2013**, 1639 – 1643; h) M. Kobayashi, O. Omae, K. Ohkubo, Y. Gao, PCT Int. Appl., **2005**, WO 2005042445A2 20050512; for azaacenes see: i) B. D. Lindner, J. U. Engelhart, M. Märken, O. Tverskoy, A. L. Appleton, F. Rominger, K. I. Hardcastle, M. Enders, U. H. F. Bunz, *Chem. Eur. J.* **2012**, *18*, 4627 – 4633; j) J. U. Engelhart, B. D. Linder, O. Tverskoy, F. Rominger, U. H. F. Bunz, *J. Org. Chem.* **2013**, *78*, 10832 – 10839.

[10] a) M. L. Tang, A. D. Reichardt, P. Wei, Z. Bao, *J. Am. Chem. Soc.* **2009**, *131*, 5264 – 5273; b) Y. Diao, K. M. Lenn, W.-Y. Wee, M. A. Bood-Forsythe, J. Xu, Y. Mao, Y. Kim, J. A. Reinspach, S. Park, A. Aspuru-Guzik, G. Xue, P. Clancy, Z. Bao, S. C. B. Mannsfeld, *J. Am. Chem. Soc.* **2014**, *136*, 17046 – 17057; c) S. Karak, F. Liu, T. P. Russell, V. V. Duzhko, *ACS Appl. Mater. Interfaces* **2014**, *6*, 20904 – 20912; d) Y. J. Kim, G. B. Lee, C. W. Jeon, Y. H. Kim, D. S. Chung, C. E. Park, *RSC Adv.* **2015**, *5*, 3435 – 3442.

[11] R. B. Campbell, J. M. Robertson, J. Trotter, *Acta Crystallogr.* **1962**, *15*, 289 – 290.

[12] T. Breuer, G. Witte, *Phys. Rev. B* **2011**, *83*, 155428.

[13] K. Kolata, T. Breuer, G. Witte, S. Chatterjee, *ACS Nano* **2014**, *8*, 7377 – 7383.

[14] G. Witte, C. Wöll, *J. Mater. Res.* **2004**, *19*, 1889 – 1916.

[15] Relative stereochemistry was assigned by X-ray structural analysis (see Supporting Information, page S78).

[16] S. Yamada, K. Kinoshita, S. Iwama, T. Yamazaki, T. Kubota, T. Yajima, *RSC Adv.* **2013**, *3*, 6803 – 6806.

[17] a) D. Lehnherr, R. McDonald, R. R. Tykwinski, *Org. Lett.* **2008**, *10*, 4163 – 4166; b) A. R. Waterloo, A.-C. Sale, D. Lehnherr, F. Hampel, R. R. Tykwinski, *Beilstein J. Org. Chem.* **2014**, *10*, 1692 – 1705.

[18] D. Lehnherr, A. H. Murray, R. McDonald, R. R. Tykwinski, *Angew. Chem. Int. Ed.* **2010**, *49*, 6190 – 6194; *Angew. Chem.* **2010**, *122*, 6326 – 6330.

[19] A. Hinderhofer, U. Heinemeyer, A. Gerlach, S. Kowarik, R. M. J. Jacobs, Y. Sakamoto, T. Suzuki, F. Schreiber, *J. Chem. Phys.* **2007**, *127*, 194705.

[20] Since screening effects due to defect-electrons are not considered in the calculation, the absolute values of unoccupied orbitals are known to be overestimated in DFT calculations.

[21] a) J. Louie, J. F. Hartwig, *Tetrahedron Lett.* **1995**, *36*, 3609 – 3612; b) A. S. Guram, R. A. Rennels, S. L. Buchwald, *Angew. Chem. Int. Ed. Engl.* **1995**, *34*, 1348 – 1350; *Angew. Chem.* **1995**, *107*, 1456 – 1459.

[22] D. S. Surry, S. L. Buchwald, *Chem. Sci.* **2011**, *2*, 27 – 50.

[23] J. U. Engelhart, B. D. Lindner, O. Tverskoy, F. Rominger, U. H. F. Bunz, *Chem. Eur. J.* **2013**, *19*, 15089 – 15092.

[24] M. Shaobin, S. M. Brombosz, P. v. R. Schleyer, J. I. Wu, S. Barlow, S. R. Marder, K. I. Hardcastle, U. H. F. Bunz, *J. Am. Chem. Soc.* **2008**, *130*, 7339 – 7344.

[25] Synthesis as described in the Supporting Information on page S29.

[26] T. V. Dubinina, A. V. Ivanov, N. E. Borisova, S. A. Trashin, S. I. Gurskiy, L. G. Tomilova, N. S. Zefirov, *Inorg. Chim. Acta* **2010**, *363*, 1869 – 1878.

[27] Compound **36** is almost insoluble in common organic solvents. Therefore no NMR or CV spectra were obtained.

[28] D. Liu, Z. Li, Z. He, J. Xu, Q. Miao, *J. Mater. Chem.* **2012**, *22*, 4396 – 4400.

[29] a) The crystal packing and dimeric pairs of **24**·thf are provided in the Supporting Information (page S80); b) CCDC 1051988 (for **17**), 1051990 (for **21**), and 1051991 (for **24**·thf) contain the supplementary crystallographic data for this paper. These data are provided free of charge by The Cambridge Crystallographic Data Centre.

[30] Y.-F. Lim, Y. Shu, S. R. Parkin, J. E. Anthony, G. G. Malliaras, *J. Mater. Chem.* **2009**, *19*, 3049 – 3056.

[31] X. Wang, F. B. Mallory, P. A. Beckmann, A. L. Rheingold, M. M. Francl, *J. Phys. Chem. A* **2006**, *110*, 3954 – 3960.

[32] CCDC 1051993 (for **28**), 1051995 (for **30**), and 1051997 (for **42**) contain the supplementary crystallographic data for this paper. These data are provided free of charge by The Cambridge Crystallographic Data Centre.

[33] CCDC 1051992 (for **24**) and 1051994 (for **26**) contain the supplementary crystallographic data for this paper. These data are provided free of charge by The Cambridge Crystallographic Data Centre.

[34] Upon equivalent preparation as for the other compounds, only colorless films of **24** have been obtained which revealed no absorption signals in the visible region, thus indicating that this compound experiences decomposition upon sublimation. Therefore, an analysis of the optical properties in the solid state has not been possible so far for **24**.

[35] S. Sharifzadeh, P. Darancet, L. Kronik, J. Neaton, *J. Phys. Chem. Lett.* **2013**, *4*, 2197 – 2201.

[36] H. Bässler, *Phys. Status Solidi B* **1981**, *107*, 9 – 54.

[37] Despite their frequent denotation as Frenckel excitons which reside on a single molecule, in many cases also for organic semiconductors ex-

tensions of the excitonic state wavefunctions over several molecules have been observed.[35]

[38] O. Ostroverkhova, S. Shcherbyna, D. G. Cooke, R. F. Egerton, F. A. Hegmann, R. R. Tykwinski, S. R. Parkin, J. E. Anthony, *J. Appl. Phys.* **2005**, *98*, 033701.

[39] NEXAFS Spectroscopy, Springer Series in Surface Sciences, Series Vol. 25 (Eds.: G. Ertl, R. Gomer, D. L. Mills, G. K. V. Lotsch), Springer, Berlin **1992**, pp. 276 – 291.

[40] I. P. M. Bouchoms, W. A. Schoonveld, J. Vrijmoeth, T. M. Klapwijk, *Synth. Met.* **1999**, *104*, 175 – 178.

[41] J. Götzen, D. Käfer, G. Witte, *Phys. Rev. B* **2010**, *81*, 85440.

[42] S. Kowarik, A. Gerlach, A. Hinderhofer, S. Milita, F. Borgatti, F. Zontone, T. Suzuki, F. Biscarini, F. Schreiber, *Phys. Status Solidi RRL* **2008**, *2*, 120 – 122.

[43] T. Breuer, I. Salzmann, J. Götzen, M. Oehzelt, A. Morherr, N. Koch, G. Witte, *Cryst. Growth Des.* **2011**, *11*, 4996 – 5001.

[44] I. Salzmann, A. Moser, M. Oehzelt, T. Breuer, X. Feng, Z.-Y. Juang, D. Nabok, R. G. Della Valle, S. Duhm, G. Heimel, A. Brillante, E. Venuti, I. Bilotti, C. Christodoulou, J. Frisch, P. Puschnig, C. Draxl, G. Witte, K. Müllen, N. Koch, *ACS Nano* **2012**, *6*, 10874 – 10883.

[45] P. Beyer, T. Breuer, S. Ndiaye, A. Zykov, A. Viertel, M. Gensler, J. P. Rabe, S. Hecht, G. Witte, S. Kowarik, *ACS Appl. Mater. Interfaces* **2014**, *6*, 21484 – 21493.

[46] As described in ref. [39], for molecular tilts of 55° the X-ray absorption is independent of the sample orientation.

[47] P. Feulner, T. Niedermayer, K. Eberle, R. Schneider, D. Menzel, A. Baumer, E. Schmich, A. Shaporenko, Y. Tai, M. Zharnikov, *Phys. Rev. Lett.* **2004**, *93*, 178302.

[48] M. Alagia, C. Baldacchini, M. G. Betti, F. Bussolotti, V. Carravetta, U. Ekström, C. Mariani, S. Stranges, *J. Chem. Phys.* **2005**, *122*, 124305.

[49] M. Marks, C. Schmidt, C. H. Schwalb, T. Breuer, G. Witte, U. Höfer, *J. Phys. Chem. C* **2012**, *116*, 1904 – 1911.

[50] K. Hermann, L. G. M. Pettersson, M. E. Casida, C. Daul, A. Goursot, A. Koester, E. Proynov, A. St-Amant, D. R. Salahub. Contributing authors: V. Carravetta, H. Duarte, C. Friedrich, N. Godbout, J. Guan, C. Jamorski, M. Leboeuf, M. Leetmaa, M. Nyberg, S. Patchkovskii, L. Pedocchi, F. Sim, L. Triguero, A. Vela. StoBe-deMon version 3.2 (**2013**).

[51] M. Klues, K. Hermann, G. Witte, *J. Chem. Phys.* **2014**, *140*, 014302.

Received: April 10, 2015
Published online on August 6, 2015

Auszüge aus den *Supporting Information* zum Artikel:

J. Schwaben, N. Münster, M. Klues, T. Breuer, P. Hofmann, K. Harms, G. Witte und U. Koert, Chem Eur. J. 21 (2015), 13758-13771. DOI: 10.1002/chem.201501399

Quantum Chemical Calculations

The electronic structures of **17**, **21** and **24** have been analyzed theoretically in the frame of DFT-calculations carried out with a 6-311G(d,p) basis-set, using the B3LYP functional as implemented in the US GAMESS-code.[9] To ensure comparability to Gaussian implementation we utilized 5 carthesian functions to represent the spherical harmonic d-functions. Due to the higher symmetry and smaller number of atoms in the case of **26**, **28**, **30**, **33**, **36** and **42** the bigger Dunning aug-cc-pVTZ basis set could be used to obtain more precise energy levels. In addition, these calculations have also allowed to determine the molecular dipole moments. By this approach, also the ionization potentials of the differently coordinated carbon atoms have been calculated, which allowed to determine the ionization potentials corresponding to the lowest transitions in the NEXAFS-spectra which have been derived from computations of the NEXAFS spectra using the StoBe code (further information[10]). Since rotation of the trifluoromethyl groups around the C-C-bond in **17**, **21** and **24** dramatically increases computational costs for structure optimizations, C_S-symmetry constraints were applied to hamper these rotations. Using this symmetry during optimization leads to bent structures like those found in the crystal structure (see manuscript), while a calculation without symmetry constraints for **17** leaves the pentacene backbone straight. Since no bending is found for calculations without symmetry restrictions, where CF_3-groups adopt different positions, the bending is assumed to be the result of intramolecular interaction between the pentacene backbone and the CF_3-group, while the rotational position of the side group within the crystal is effected by intermolecular interplay. Comparing the energies for this case shows that the absolute position of HOMO and LUMO energies is shifted due to the symmetry restrictions, while the gap is nearly unaffected, justifying the symmetry approach used in this work. As visualized in Figure S4, the substituents have only minor influence on the frontier orbitals for all present compounds, showing that the energy levels are mainly

[9] Schmidt, M. W.; Baldridge, K. K.; Boatz, J. A.; Elbert, S. T.; Gordon, M. S.; Jensen, J. H.; Koseki, S.; Matsunaga, N.; Nguyen, K. A.; Su, S. J.; Windus, T. L.; Dupuis, M.; Montgomery, J. A. *J. Comput. Chem.* **1993**, *14*, 1347-1363.

[10] Klues, M.; Hermann, K.; Witte, G. *J. Chem. Phys.* **2014**, *140*, 14302.

determined by the acene backbone. The orbital visualizations were realized employing the MacMolPlt package[11].

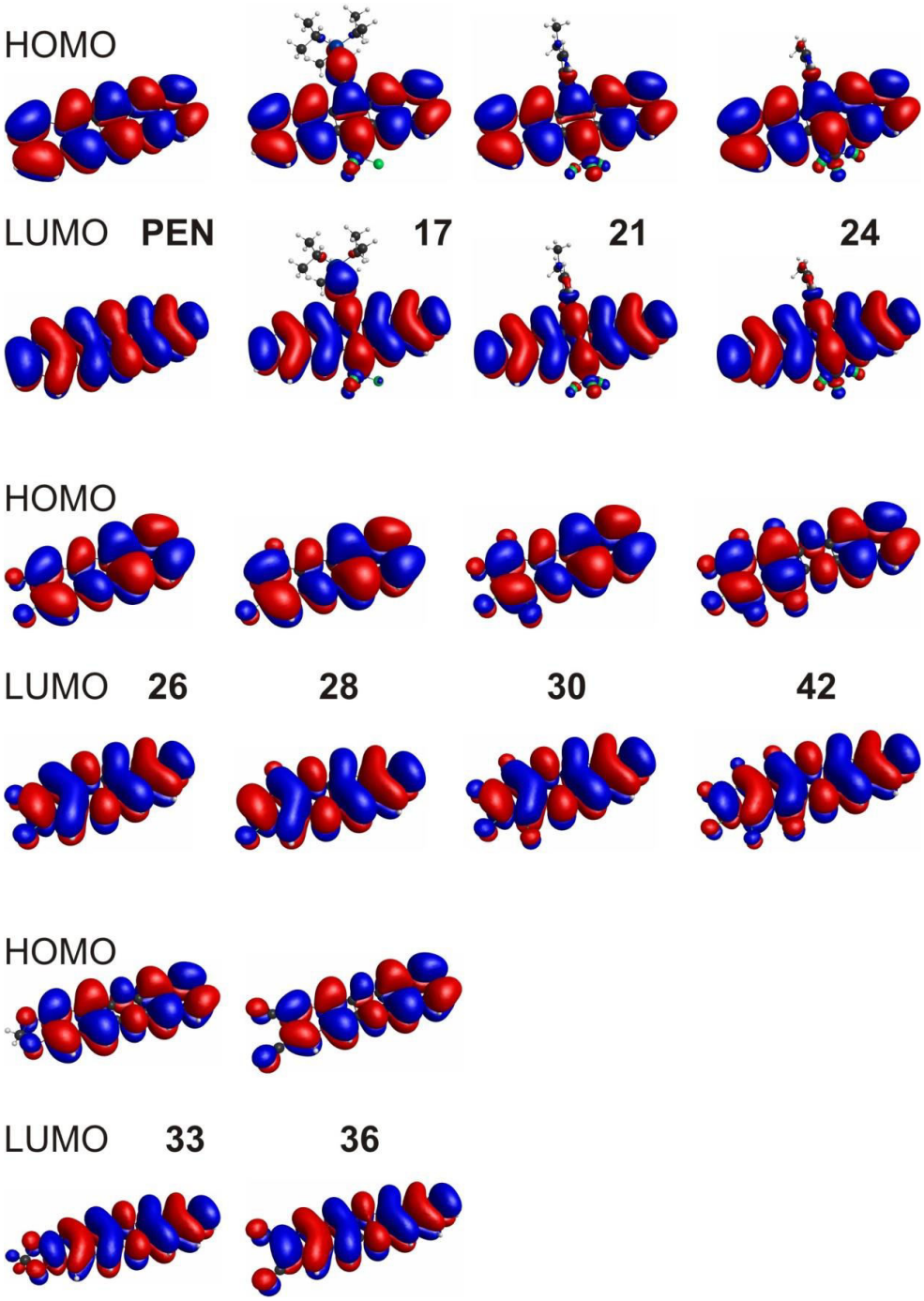

[11] Bode, B. M.; Gordon, M. S. *J. Mol. Graphics Mod.*, **1998**, *16*, 133-138.

Figure S4: Visualization of frontier orbitals for all discussed compounds.

Molecular electrostatic potentials, color-coded on electron density isosurfaces of pentacene, perfluoropentacene, **17** and **42** as shown in the manuscript were calculated using the Gabedit package[12], based on the output of the aforementioned DFT-calculations, using the partial charge method. The polarizabilities presented in the manuscript, were calculated by applying the finite field method as implemented in the US-GAMESS code[13] using a 6-311G(d,p) basis-set and the B3LYP functional for all compounds. For all molecules with high symmetry the resulting polarizability tensor is perfectly diagonal. For **17**, **21** and **24** the symmetry axes of the pentacene backbone were aligned along the coordinate axes, yielding off-diagonal elements of which values amount to less than a few percent of the principal diagonal values, hence only the three diagonal components were considered also in these cases.

[12] Allouche, A. R. *Journal of Computational Chemistry*, **2011**, *32,* 174-182.
[13] Kurzt, H. A.; Stewart, J. J. P.; Dieter, K. M. *J.Comput.Chem.*, **1990,** *11*, 82-87.

Crystal Packing and Dimeric Pairs of 24·thf

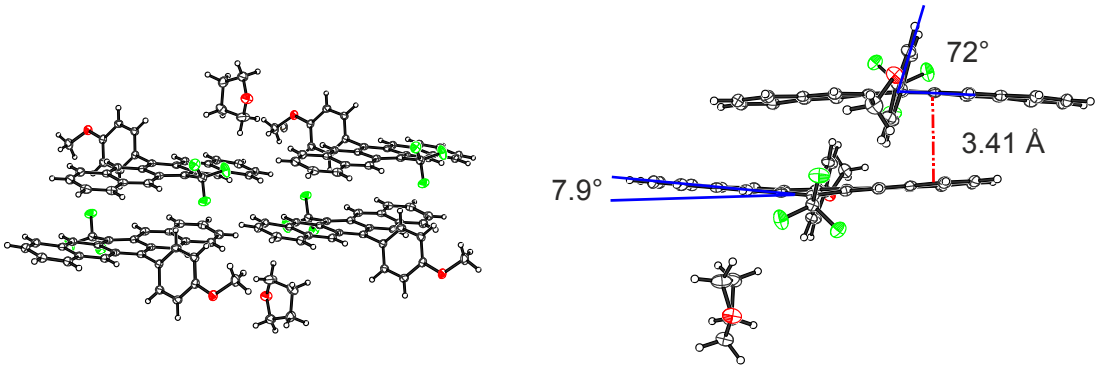

The dimeric pairs in the crystal structure of **24**·thf are separated by the anisole moieties and THF molecules. The adjacent molecules are slightly bent towards each other (7.9°) with an interplanar distance of 3.41 Å and nearly 4 of the aromatic pentacene rings overlap. The aryl substituent and the pentacene core are twisted (72°). Adjacent dimeric pairs are connected via F-H contacts.

Determination of Molecular Distances for Bässler-model

To approximate the exciton binding energies based on the model proposed by Bässler (see manuscript), the molecular polarizabilities α and the lattice sum $\sum_{i\neq k} r_{ik}^{-6}$ (r_{ik} denotes the molecular distances) have to be calculated.

The molecular distances were derived from the crystal structures of the compounds. Due to the strong descent of the r^{-6} term, only molecules with contributions > 0.008 compared to the strongest contribution have been considered. By this means, the deviation between the estimated and actual amount of the lattice sum can be estimated to not more than 2%.

5.3 Polymorph-Selective Preparation and Structural Characterization of Perylene Single Crystals

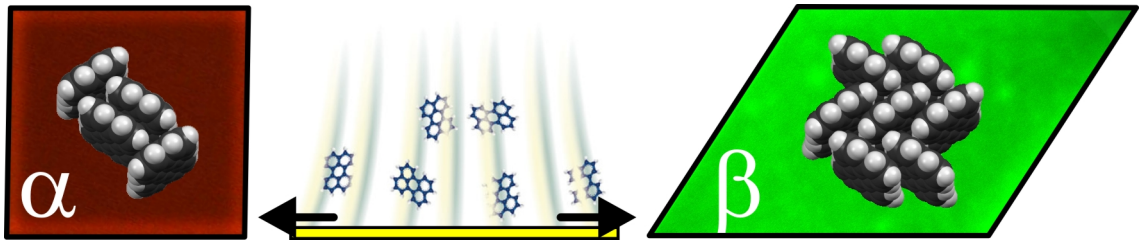

5.3.1 Inhaltsangabe

Organic semiconductors occurring in polymorphic structures represent excellent model systems for fundamental studies of optoelectronic excitations in different crystalline configurations. Perylene is an archetypal polycyclic aromatic hydrocarbon appearing in two polymorphs known as α- and β-phases which adopt different molecular packing motifs. However, the growth of high quality single crystals with appropriate sizes and polymorph selectivity remains challenging. In this study, we compare various approaches toward polymorph-selective perylene single-crystal growth. Though crystals of both polymorphs are obtained from toluene solution (either by cooling of a saturated solution or by evaporation of the solvents), they exhibit numerous defects and their size cannot be precisely controlled. Vapor deposition and resublimation favor the formation of α-crystals which can be rationalized by a newly identified thin-film phase that forms initially. Further, we demonstrate that organic molecular beam deposition onto silicone-oil-covered substrates enables the fabrication of high-quality crystals of both phases. The relative occurrence of the individual polymorphs is controlled by the actual deposition parameters. Combining the results of X-ray diffraction, atomic force microscopy, and fluorescence analysis enables an unambiguous polymorph identification solely based on the characteristic crystal shape. The morphological characterization reveals characteristic screw dislocations at crystals grown from solution or by resublimation while the liquid-mediated crystals exhibit exceptionally flat surfaces and enable detailed fluorescence studies without defect-related emission signals.

5.3.2 Eigenleistung

Die *In-Plane*-Messungen an Peryleneinkristallen wurden von mir vorgeschlagen, geplant und durchgeführt. Die Auswertung und graphische Aufbereitung der Ergebnisse erfolgte durch mich. Die Interpretation der Beugungsdaten im Hinblick auf den Zusammenhang von kristallographischen Ebenen und dem Habitus der Kristalle wurde in Zusammenarbeit mit Andrè Pick erarbeitet. Zudem wurden alle Beugungsexperimente an Dünnfilmen von

mir durchgeführt und aufbereitet. Inhaltlich habe ich zu den Textpassagen des Artikels beigetragen, die in Verbindung mit den von mir durchgeführten Experimenten stehen.

CRYSTAL GROWTH & DESIGN

Article

pubs.acs.org/crystal

Polymorph-Selective Preparation and Structural Characterization of Perylene Single Crystals

André Pick,[†] Michael Klues,[†] Andre Rinn,[†] Klaus Harms,[‡] Sangam Chatterjee,[†,§] and Gregor Witte*[,†,§]

[†]Faculty of Physics, [‡]Faculty of Chemistry, and [§]Material Sciences Center, Philipps-Universität Marburg, D-35032 Marburg, Germany

Supporting Information

ABSTRACT: Organic semiconductors occurring in polymorphic structures represent excellent model systems for fundamental studies of optoelectronic excitations in different crystalline configurations. Perylene is an archetypal polycyclic aromatic hydrocarbon appearing in two polymorphs known as α- and β-phases which adopt different molecular packing motifs. However, the growth of high quality single crystals with appropriate sizes and polymorph selectivity remains challenging. In this study, we compare various approaches toward polymorph-selective perylene single-crystal growth. Though crystals of both polymorphs are obtained from toluene solution (either by cooling of a saturated solution or by evaporation of the solvents), they exhibit numerous defects and their size cannot be precisely controlled. Vapor deposition and resublimation favor the formation of α-crystals which can be rationalized by a newly identified thin-film phase that forms initially. Further, we demonstrate that organic molecular beam deposition onto silicone-oil-covered substrates enables the fabrication of high-quality crystals of both phases. The relative occurrence of the individual polymorphs is controlled by the actual deposition parameters. Combining the results of X-ray diffraction, atomic force microscopy, and fluorescence analysis enables an unambiguous polymorph identification solely based on the characteristic crystal shape. The morphological characterization reveals characteristic screw dislocations at crystals grown from solution or by resublimation while the liquid-mediated crystals exhibit exceptionally flat surfaces and enable detailed fluorescence studies without defect-related emission signals.

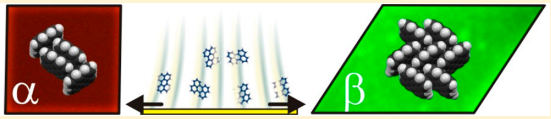

INTRODUCTION

Organic semiconductors and dye materials are presently receiving significant research interest because of their promising potential for the fabrication of future optoelectronic devices such as, e.g., organic light emitting diodes or organic photovoltaic cells.[1−3] Besides their advantages of low cost, high quantum yields, flexibility, and low temperature processing, organic materials conceptually allow a tuning of optoelectronic properties by chemical design,[4,5] while this task requires complex band structure engineering in the case of their inorganic counterparts. However, it should be noted that the optical and electronic properties as well as the dynamics of excited electronic states of molecular solids are distinctly different from that of single molecules (or solutions) due to intermolecular coupling.[6] Striking examples for such solid-state effects are the formation of exciton states or efficient charge-carrier transport. Well-defined model studies are mandatory to develop a microscopic understanding of the elementary excitations since intrinsic properties of molecular solids are frequently masked by impurities or structural defects. Studies on single crystalline samples are of particular interest along this direction of research as they enable the direct correlation between the molecular packing and the resulting electronic properties of solids.[7−10]

Apart from the difficulty of growing suitably sized single crystals allowing for optical or electronic measurements, an additional complexity arises from the fact that molecular materials can exist in different crystalline forms (so-called polymorphisms)[11] which affects the resulting optoelectronic and charge transport properties of the molecular solids.[12−16] Various strategies to control polymorphism in organic crystals have been reported including *inter alia* variation of thermodynamic growth conditions, seeding technique, use of surfactants, or crystallization under nanoscale confinement.[17−20] Despite significant research efforts, a rational approach of phase-selective crystallization, however, still remains challenging, and many attempts result in crystalline mixtures of various polymorphs.

In the present study we focus on the phase-selective crystallization of perylene ($C_{20}H_{12}$), a widely used dye molecule and also an organic semiconductor with notable charge-carrier mobility.[21,22] Perylene is of particular interest for optoelectronic case studies of organic solids as it crystallizes in two monoclinic phases, which both reveal $P2_1/c$ symmetry: the α-polymorph (a = 10.24 Å, b = 10.79 Å, c = 11.13 Å, α = 90°, β = 100.92°, and γ = 90°) contains four molecules per unit cell and is packed in a sandwich-herringbone motif (also considered as a dimeric structure), while the β-polymorph (a = 9.76 Å, b = 5.84 Å, c = 10.61 Å, α = 90°, β = 96.77°, and γ = 90°) has two molecules within the unit cell arranged in the so-called γ-type herringbone packing (monomeric structure).[23] Both are schematically depicted in Figure 1.

Received: August 6, 2015
Revised: September 29, 2015
Published: September 30, 2015

DOI: 10.1021/acs.cgd.5b01130
Cryst. Growth Des. 2015, 15, 5495−5504

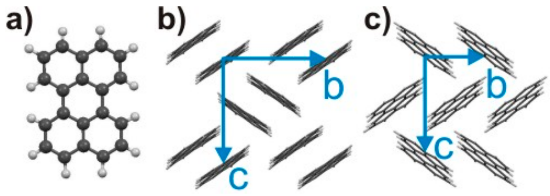

Figure 1. (a) Molecular structure of perylene and molecular arrangements adopted in the two polymorphs: (b) α-phase and (c) β-phase.[23] The viewing direction is perpendicular to the (bc)-plane (i.e., along a^*). The complete crystallographic structure data are listed in the Supporting Information.

As a consequence of the various molecular packing motifs and intermolecular couplings, both polymorphs exhibit different luminescence and absorption properties.[24−26] In addition, significant differences in the charge-carrier mobility are proposed for both phases.[27] Unfortunately, a direct experimental verification of this proposal as well as detailed optical measurements are, however, hampered by the lack of appropriate crystals of the β-polymorph. This problem is partly related to the fact that perylene crystals reveal an irreversible phase transition from the β-phase to the α-phase while the latter is stable up to the melting point.[23] So far, perylene crystal growth is reported either from solution[23,24,28] or by sublimation methods,[25,26,29,30] both resulting in a preferred crystallization of the α-phase. By pipetting saturated droplets of a perylene solution onto glass, followed by rapid cooling, Yago et al.[31,32] observe a preferential crystallization of the β-phase, hence indicating this process to be kinetically driven, rather than thermodynamically. Another route to control the phase of perylene is reported by Lei et al.,[33] who utilized cetyltrimethylammonium bromide (CTAB) as a surfactant upon crystallization. Though this yields individual crystals of both phases depending on the actual CTAB concentration, only micrometer-sized crystallites are obtained which still hamper detailed optical studies. More recently, Urbelis and Swift[34] reported a polymorph-selective crystallization of perylene from solution onto supports coated before by self-assembled monolayers of different chemical termination. So far, most optical studies of perylene samples were performed without any microscopic characterization of the crystals surface and morphology, thus neglecting the influence of defects. In addition, we note that the crystalline shapes (so-called *tracht*) of perylene crystals often have not been correctly described, so that belonging crystallographic directions were wrongly assigned.[25,29,33]

Here, we compare different crystallization procedures (including resublimation and solution growth) and demonstrate a reliable method allowing for a controlled preparation of well-defined perylene crystals of both polymorphs. By employing liquid-mediated growth[35] under high vacuum conditions and optimizing growth parameters, polymorph-selective crystallization is achieved yielding highly ordered, platelet-like perylene single crystals with lateral extensions of more than 100 μm. Combining X-ray diffraction (XRD) and atomic force microscopy (AFM) allowed an unambiguous correlation between crystallographic axes and the *tracht* of the respective single crystals. The exceptional quality of selected platelet-like crystals is also affirmed by AFM data showing virtually molecularly flat surfaces with very few monomolecular steps, while pyramidal crystals obtained from vapor deposition exhibit characteristic screw dislocations. Finally, the well-ordered crystallites were used for exemplary photoluminescence measurements to quantify the prevailing characteristic color impressions.

EXPERIMENTAL SECTION

Epi-ready silicon wafers coated with a native oxide (Siegert Wafer GmbH) or object glass slides are used as supporting substrates. Initially, all supports are cleaned in an ultrasonic bath by a mixture of ethanol and acetone and subsequently blown dry in a nitrogen stream. Films and crystallites of perylene (Sigma-Aldrich; purity, 99.9%) are grown under HV conditions ($<10^{-7}$ mbar) either by resublimation of pestled material placed between two substrate plates, which enables crystal growth at the bottom side of the cover plate, or by organic molecular beam deposition (OMBD) from an alumina crucible of a resistively heated Knudsen cell. The latter approach is utilized for polymorph-selective growth upon deposition onto thin films of silicone oil (VWR GmbH, 45 V 350 Rhodorsil) spin-coated onto the substrates. The incident flux of perylene is measured by means of a quartz crystal microbalance. Note that it is mandatory to utilize oil films of similar thickness to achieve reproducible crystal growth. Therefore, in all cases a (2 μL) droplet of oil was spin-coated at 2500 rpm for 1 min yielding a film thickness of about 25 μm. Complementary, macroscopic-sized single crystals with characteristic shapes were grown from toluene solution to enable detailed single-crystal analyses. α-phase crystals are obtained by cooling a supersaturated perylene solution in a water bath from 100 °C to room temperature, while β-phase crystals are grown within 2−3 days by slow solvent evaporation of a nonsaturated toluene solution at room temperature.

The morphology of perylene single crystals is characterized by means of atomic force microscopy using an SPM5500-AFM instrument (Agilent) operated in closed loop tapping mode at ambient conditions and using HQ:NSC15/AlBS cantilevers (MikroMasch; resonance frequency, 325 kHz). Furthermore, scanning electron micrographs are recorded using a scanning electron microscope JSM-7500F (Jeol) equipped with a cold field emitter. Here, Si-wafer substrates are used to avoid charging effects. The crystalline texture and orientation of the films are analyzed by X-ray diffraction (Bruker AXS Discover D8) using monochromatized Cu K_α radiation and a LynxEye silicon strip detector. In addition, a unit cell determination of the single crystals is performed with a Bruker D8 Quest single-crystal diffractometer equipped with a microfocus anode and a PHOTON 100 CMOS detector. To correlate photoluminescence and shape of the various crystalline perylene phases, confocal laser scanning fluorescence microscopy (CLSFM, Zeiss 510 Meta) is employed using a UV laser diode (405 nm) for illumination.

Furthermore, we performed photoluminescence experiments in a setup with high spatial resolution. It is implemented in reflection geometry using all-reflective optics to minimize chromatic aberrations. The samples are excited at 412 nm, 100 fs pulses—generated by a frequency-doubled Ti:sapphire oscillator at a repetition rate of 78 MHz. A 0.5 numerical aperture reflective microscope objective is used to focus the beam on the sample. The emission is detected by a deep-cooled charge-coupled device camera mounted on an imaging spectrometer yielding spectral resolution of 2 nm. The system's spectral responsivity is carefully calibrated using a traceable thermal source.

DOI: 10.1021/acs.cgd.5b01130
Cryst. Growth Des. 2015, 15, 5495−5504

RESULTS AND DISCUSSION

Preparation of Perylene Single Crystals by Sublimation Methods. First, perylene films are prepared by OMBD onto Si wafers covered with a native oxide. This preparation method yields well-oriented yet polycrystalline thin films on single crystalline metal substrates but also exhibits a pronounced postdeposition dewetting.[36] Figure 2 shows a

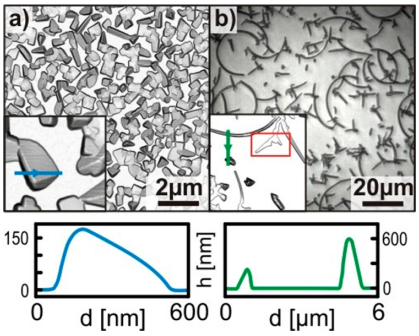

Figure 2. Micrographs showing the morphology of perylene films with a nominal thickness of 60 nm deposited with a growth rate of 5 Å/min onto oxidized Si wafers (a) at 270 K (displayed as derivative of the AFM topography) and (b) at 300 K (optical micrograph). Insets depict magnified AFM topography data with corresponding cross-sections below.

similar behavior also on the glass substrates and demonstrates that the resulting film morphology depends critically on the substrate temperature, T_S, during growth. Already at T_S = 270 K disjoined individual islands with lateral extensions up to 1 μm are formed that exhibit a cubic or tetrahedral shape. These islands reach a height of 100−150 nm, which exceeds the nominal film thickness of 60 nm and thus reflects a pronounced dewetting. This effect is even more pronounced when slightly raising the sample temperature during growth to 300 K. In the latter case, well-separated curved, narrow fibers form, which extend over 10−30 μm and adopt a height of nearly 300 nm, while individual tetrahedrons with a height of more than 500 nm occur. In addition characteristic branched islands are formed (cf. red box in Figure 2b) which are also reported for perylene films grown on Cu(110).[36] This growth mode is denoted as skeletal growth which is characteristic for diffusion limited growth.[37]

Because this approach did not yield sufficiently sized crystallites to allow for their individual optical characterization, we report an alternative approach essentially based on crystallization by repeated resublimation. For this purpose, perylene powder (typically 1 mg) is placed between two Si wafers or object slides. The sandwich is subsequently heated under HV conditions. The bottom plate of the sandwich was heated to 350 K, while the lid reached a somewhat lower temperature (347−348 K) as perylene multilayers significantly desorb at substrate temperatures above 350 K.[38] The material is completely transferred to the top plate after heating for several hours (typically 3 h). This process is repeated several times (typically 3−5) after exchanging the plates. As shown in Figure 3, this yields continued dilution (due to pumping of perylene vapor) and formation of individual crystallites. Extensive experiments show that the efficiency of crystallite formation critically depends on the initial amount of material, the

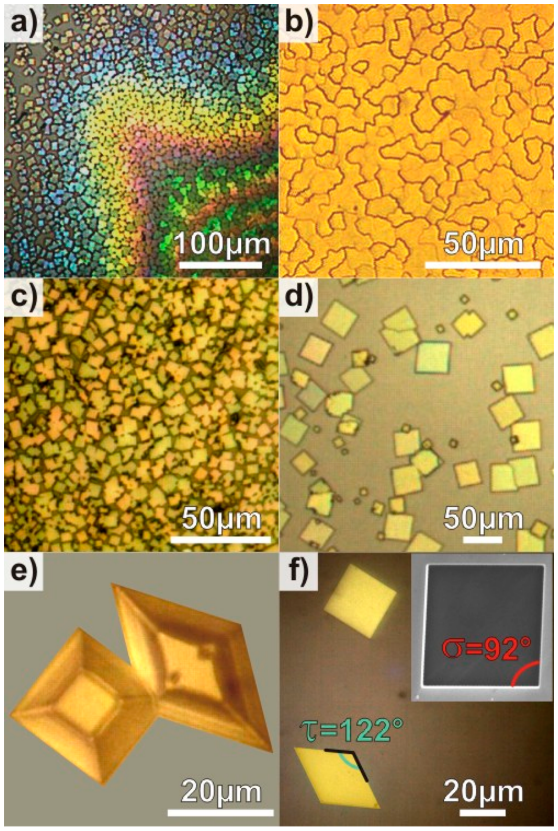

Figure 3. Optical micrographs showing the evolution of perylene crystallites upon repeated resublimation between two inert substrates (a−f). (a) The thickness variation gives rise to Newton rings and reveals a coexistence of discrete crystals and a dense film. With increasing number of resublimation cycles the film gets diluted (c) and individual crystallites are formed (d), which reveal different shapes (e, f) with characteristic angles of the base surface (f). To avoid image distortions upon imaging of the rectangular-shaped crystals, their angle was determined from a SEM micrograph (see inset in panel f).

substrate heating temperature, and the duration. Another important parameter is the homogeneity of the initially introduced powder, as lateral variations of the amount of perylene powder cause fluctuations of the local growth rate upon heating. The inhomogeneity of the films is recognized by characteristic Newton rings (cf. Figure 3a) and turns out to be beneficial and self-regulating, as it locally provides the proper growth conditions, while too small crystallites disappear. After repeated resublimation cycles individual crystallites are formed, which exhibit characteristic shapes as depicted in Figure 3e,f): truncated pyramid or platelet-shaped crystals reveal either an almost quadratic or rhombic base area with characteristic base-area angles of 92° and 122° based on AFM and SEM micrographs for the near rectangular and rhombic crystallites, respectively. These are identified as α- and β-polymorphs on the basis of XRD measurements as presented later. We note that crystals with a clear rhombic fashion in the platelet configuration are extremely rare, while the nearly rectangularly shaped platelets are clearly dominanting, indicating an enhanced thermodynamic stability of the latter species. In

DOI: 10.1021/acs.cgd.5b01130
Cryst. Growth Des. 2015, 15, 5495−5504

fact, a comparative thermal treatment of differently shaped platelet crystallites reveals a more rapid disappearance of rhombic (β-phase) crystals (see Figure S2, Supporting Information), hence confirming their lower thermal stability.

To analyze the crystalline phases of the differently prepared perylene films, XRD measurements in Bragg−Brentano geometry are performed and the diffractograms are compared with the positions of the (100)-reflexes expected for the known α- and β-phases.[23] Figure 4 summarizes the magnified region of

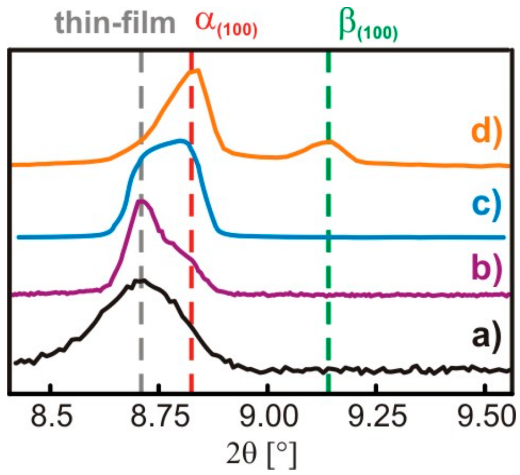

Figure 4. Comparison of XRD data of differently prepared perylene films: (a) 30 nm perylene deposited by OMBD at 270 K (rate 5 Å/min), (b) perylene powder resublimated once between two plates (cf. Figure 3b), (c) after triple resublimation (cf. Figure 3c), and (d) after 5-fold resublimation (cf. Figure S3, Supporting Information). The green, red, and gray dashed lines denote the positions of the (100) reflex of the β- and α-phase and a new thin-film phase, respectively.

this reflex for perylene films prepared by OMBD and after different cycles of resublimation. After five resublimation cycles, distinct diffraction peaks at 2θ angles of 8.80° and 9.12° are obtained (cf. Figure 4d). They are in excellent agreement with the positions expected for the α-phase (dashed red line at 8.79°) and the β-phase (dashed green line at 9.11°), respectively. The dominating intensity of the α-phase peak is in agreement with the majority of near rectangular islands found in the micrographs. For OMBD grown as well as only few times resublimated perylene films, the diffraction peak appears at a smaller angle around 2θ = 8.71° and no β-phase-related peak is observed. A shoulder evolves from the lower angle peak that occurs at the position of the α-phase with increasing number of resublimation cycles. The appearance of an additional diffraction peak at 8.71° reflects the initial formation of a new crystalline phase with slightly increased interlayer distance ($d_{(100)}$ = 10.15 Å) compared to the α-phase ($d_{(100)}$ = 10.06 Å). We note that a notable broadening of the (100)-peak is reported in a growth study of perylene films on amorphous Al_2O_3 substrates,[39] however, without explicit recognition of this new crystalline phase. We term this phase the "thin-film phase" of perylene. The presence of such thin-film phases of films with upright molecular orientation grown on inert substrates has been observed before for various π-conjugated molecular materials such as, e.g., pentacene,[40] perfluoropentacene,[41] sexithiophene,[42] *p*-sexiphenyl,[43] or the charge-transfer salt TTF-TCNQ.[44] As in the case of pentacene, this relaxation can be attributed to the slight vertical displacement of every second perylene molecule within the (100)-plane of the α-phase, which prevents direct contact with the supporting substrate. By slightly tilting further upright (and possibly lateral compression), all molecules of the unit cell can interact with the supporting substrate, which stabilizes this interface-mediated phase (cf. Figure S5a, Supporting Information). In a more elaborate description it has been shown for the case of pentacene that the thin-film phase in fact exhibits a lower surface free energy[45] while with increasing film thickness the total lattice energy of the bulk polymorph becomes energetically favorable.[46] The evolution of α-phase perylene crystallites from an initially formed thin-film phase upon vapor deposition or resublimation suggests that the latter acts similarly as structural precursor with nearly matching interlayer spacing, thus providing an explanation for the substantial absence of the β-phase. Additional optical micrographs for the rare case of β-phase crystallites (cf. Figure S13, Supporting Information) show that they actually nucleate at α-phase crystallites thus indicating crystallization without initial thin-film seed-layer formation. A pronounced 3D growth of perylene crystallites was also observed in previous work where impurities such as dust particles were found to act as nucleation centers and effectively suppress a homogeneous film growth from the surface of the support.[36]

We note further, that the outcome of the resublimation method depends critically on the exact heating treatment and frequently results in the formation of perylene fibers similar to those shown in Figure 2b). Therefore, this preparation procedure does not represent a rational approach for phase-selective crystallization since β-phase crystallites are obtained only very rarely. However, the occasional appearance of pyramidal and platelet crystallites of both polymorphs allows their morphological characterization by means of AFM.

As shown in Figure 5, the truncated pyramidal-shaped crystallites of both phases exhibit characteristic screw dislocations on their top surfaces, which can have different complexity. For better visualization of the molecular steps the magnified AFM images (cf. Figure 5c−e) are shown as the derivative of the topography and clearly reveal the existence of single and paired as well as 4-fold screw dislocations. The belonging topographical cross-sections reveal a total crystallite thickness of typically 1−2 μm and the presence of monomolecular steps of about 1 nm height for both polymorphs. In the same sample batch also platelet crystallites of both polymorphs were found that are distinctly thinner having a thickness of several 100 nm (cf. Figure 6). Interestingly, they exhibit no screw dislocations and possess remarkably flat surfaces; along the entire surface only one monomolecular step could be detected as shown in Figure 6d).

The formation of screw dislocations upon growth of molecular films has been observed before, e.g., for the case of pentacene or perylene.[47,48] Generally, such a defect-related growth is believed to occur when layer-by-layer growth imposes an energy barrier to nucleate new islands and therefore helps to overcome this limitation and enables a faster growth.[47] For the growth of perylene films on Al_2O_3 at large deposition rates (typically several angstroms per second), Beigmohamadi et al. observed an increasing density of screw dislocations with the deposition rate which they attributed to a strain release by spiral growth.[48] Similarly, we also observed a large density of screw dislocations after rapid resublimation by heating the stack

DOI: 10.1021/acs.cgd.5b01130
Cryst. Growth Des. 2015, 15, 5495−5504

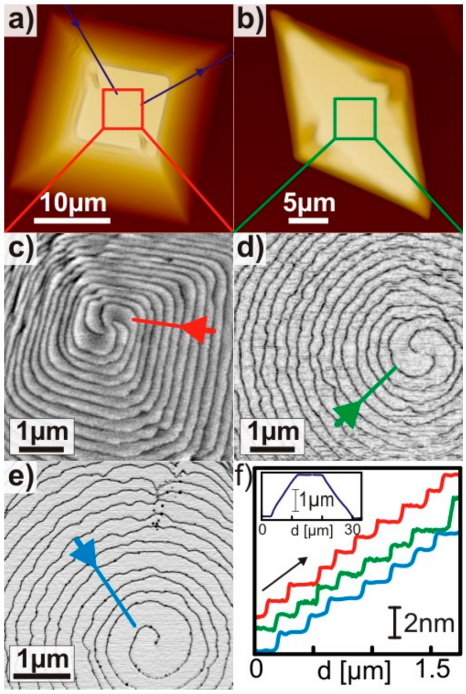

Figure 5. AFM data showing the morphology of truncated pyramidal perylene single crystals of (a) α-phase and (b) β-phase, together with magnified surface areas of the top surface of the crystals (c–e) (displayed as the derivative of the topography), which exhibit the presence of screw dislocations with different numbers of spiral arms. Panel (f) depicts the corresponding topographical cross-sections confirming the presence of monomolecular steps.

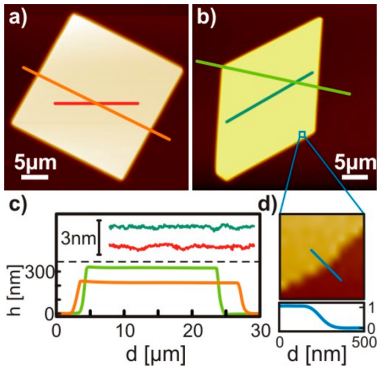

Figure 6. AFM data summarizing the topographies of platelet perylene crystallites (a) of α-polymorph (thickness ~ 200 nm) and (b) of β-polymorph (thickness ~ 325 nm). Corresponding line scans (c) exhibit the presence of remarkably flat surfaces. Only very occasionally, a monomolecular step is found (d).

from 300 to 400 K within less than 2 min (see Figure S7, Supporting Information), which yields a large effective deposition rate. By contrast, when applying a slow heating ramp (300–390 K within 1 h), virtually no dislocations were observed. Therefore, we attribute the large abundance of screw dislocations on pyramidal-shaped perylene crystals to the high effective deposition rates due to local material excess which constitutes a kinetically driven process. On the other hand, the platelet-shaped crystallites are grown at a much lower effective growth rate which seems to avoid spiral growth quite effectively.

Preparation of Perylene Single Crystals from Solution. Larger single crystals are mandatory to precisely identify the crystal structure of the differently shaped crystallites to correlate crystalline directions with their characteristic shapes. Therefore, we also tried to specifically grow them from toluene solution and observed a certain polymorph selectivity depending on the details of the applied growth procedure. While α-phase crystals preferentially grow upon cooling of a supersaturated solution from 100 °C to room temperature (cf. Figure 7a,b), rhombic crystallites of the β-phase occur when slowly

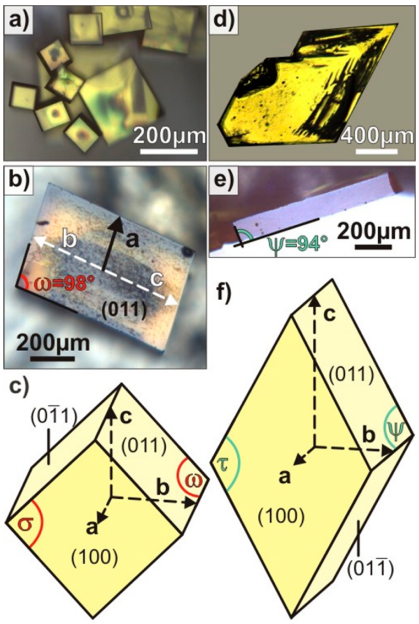

Figure 7. Summary of optical micrographs of perylene crystals of α-phase (left column) and of β-phase (right column) grown from toluene solution (for experimental details see text). Panels (a), (d) and (b), (e) show top views of the (100) face and the belonging side views, respectively, while the bottom row depicts the *tracht* of the various crystalline phases together with the unit cell axes and characteristic angles of the faces.

evaporating toluene of a nonsaturated solution at room temperature (see Figure 7d,e) over a period of 2–3 days. The resulting crystallites reach almost millimeter sizes laterally and thicknesses of 100–400 μm allowing for a detailed unit cell determination (which is listed in Table S2, Supporting Information) and confirms the presence of α- and β-phase crystals.

The extended thicknesses of these crystallites allow, in particular, to determine the characteristic angles of their side faces with respect to the base area (cf. Figure 7b,e). The *tracht* of crystallites of both phases is further characterized by additional X-ray diffraction measurements which are summarized in Figure 8. The high number of (n00)-diffraction peaks observed in the out-of-plane X-ray diffraction scans for single

DOI: 10.1021/acs.cgd.5b01130
Cryst. Growth Des. 2015, 15, 5495–5504

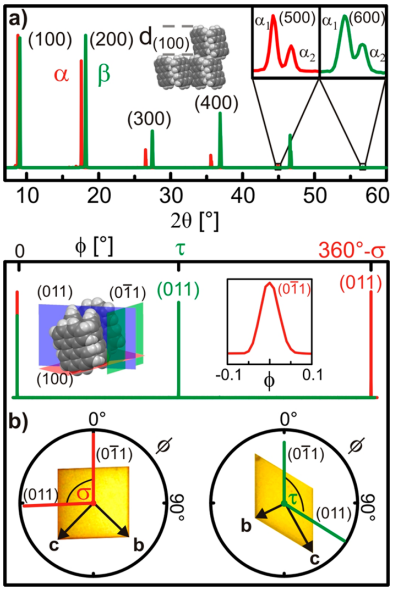

Figure 8. XRD analysis of perylene single crystals: (a) θ–2θ scans resolving the different interlayer spacings $d_{(100)}$ for the α- (red) and β-phase (green). The inset shows a peak splitting due to the fine structure of the X-ray light. (b) Azimuthal in-plane scans of the {011} perylene reflexes depicted as linear and polar plots together with the belonging orientation of the perylene single crystallites indicating the location of the unit cell vectors relative to the crystal habitus.

crystallites of both polymorphs reflects their excellent crystallinity and allows a reliable distinction of the polymorphs on the basis of their slightly different interlayer spacing $d_{(100)}$ (cf. Figure 8a). The high perfection of crystals is also corroborated by a distinct splitting of the higher order (n00)-peaks due to the $K_{\alpha1,\alpha2}$ fine structure of the X-ray beam that is only visible for rather perfect lattices.

In-plane diffraction measurements reveal the azimuthal orientation of crystalline planes within the top faces, which allows one to correlate the molecular orientation in such planes with respect to the characteristic crystalline shapes. Therefore, the crystallites are tilted such that the (011) reflection of the perylene lattices can be detected, and the azimuthal distribution is measured by azimuthal ϕ-scans (cf. the inset in Figure 8b and the scheme shown in Figure S4, Supporting Information). The corresponding ϕ-scans are shown as linear and as polar plots for both polymorphs in Figure 8b. Note that only two symmetry-equivalent diffraction signals appear within a full circle due to the monoclinic nature of both perylene phases. They enclose angles of $\sigma = 92°$ and $\tau = 122°$ for the α- and β-phases, respectively. Optical micrographs of the appropriate sample orientation are superimposed onto the polar scans to clarify the azimuth directions with respect to the crystalline shape. In particular, this reveals that the unit cell vectors **b** and **c** are pointing toward the corners of the crystal, with the **b** vector toward the greater crystal angle.

The characteristic trachts of platelet crystals of both polymorphs are shown together with the unit cell vectors and an assignment of the crystallographic faces in the bottom row of Figure 7. The tracht is modeled by calculating low-index surfaces using the KRISTALL 2000 program,[49] while the angles between the low-indexed side faces are obtained from the Mercury visualization program[50] for both bulk polymorphs. This analysis yields angles of $\sigma = 90.76°$ (between the (011) and (01$\bar{1}$) or (0$\bar{1}$1) and (0$\bar{1}$1) faces) and $\omega = 97.65°$ (between the (100) and all {011} faces) for the α-phase, and values of $\tau = 121.97°$ (between the (011) and (01$\bar{1}$) or (0$\bar{1}$1) and (0$\bar{1}$1) faces) and $\psi = 93.28°$ (between (100) and all {011} faces) which are in close agreement with the experimentally observed angles. The corresponding molecular packing motifs in the respective surfaces are provided in Figure S5 of the Supporting Information.

We note further that attempts to also model the habit of the pyramidal crystals are not successful. This suggests that their side faces do not represent low-indexed surfaces. A closer inspection of the morphology yields different slopes for the side faces (cf. the inset in Figure 5f) and further shows the presence of characteristic kinks (cf. Figure S6, Supporting Information) which indicates that such crystallites are actually composed of stacked plates and that their side faces do not represent low-indexed crystal planes. This characteristic is also supported by a notable emission of fluorescence light on such kinked side faces as presented later.

Polymorph-Selective Preparation of Perylene Crystallites by Liquid-Mediated Growth. Previous studies have demonstrated the successful preparation of individual mesoscopic-sized molecular single crystallites by liquid-assisted vacuum deposition using the liquids as crystallization solvents.[35,51,52] Also, deposition of perylene into liquid substrates consisting of spin-coated films of silicone oil was studied by Liu et al.[53] Depending on the actual perylene concentration in the oil various crystal shapes were observed: while the formation of nearly square-shaped platelets occurred at low concentration, increasing concentration favored a needle growth and finally the formation of branched needles yielding dendritic crystals. Liu et al. attribute this behavior to limited diffusion which causes preferential crystalline growth directions. Moreover, after interrupting and continuing the perylene deposition, the formation of characteristic creases at the edge of platelet-shaped crystals was observed[54] which relaxed after some time. Regarding the crystallization process, the authors claim that nucleation of perylene crystallites always takes place at the oil–vacuum interface upon deposition. To test this hypothesis, we have carefully deposited an amount of perylene into a silicone-oil film so that just no crystallization occurs. Afterward, the film is scratched by a needle which causes a spontaneous nucleation of small crystallites (see Figure S9, Supporting Information). This behavior reflects the supersaturated character of the oil and suggests that nucleation not necessarily takes place at the surface. Based on the findings reported by Liu et al.,[53] we use rather slow deposition rates of a few angstroms per minute in order to guarantee platelet crystal growth. These are a factor of 20–30 smaller than those applied in their study. In addition, we investigate the influence of the substrate temperature as is expected to have a notable impact on molecular diffusion and viscosity of the oil. On the other hand, great care is taken to prepare all oil films reproducibly and uniformly (cf. Experimental Section) to ensure comparable thicknesses of the oil films, since the dimensions of the oil film were shown to determine the diffusion field of the molecules.[35] By systematically optimizing the deposition conditions, we obtain the formation of well-defined single crystallites of both polymorphs as depicted in Figure 9. When keeping the oil substrate at 310 K and using a low deposition rate of 4 Å/min,

DOI: 10.1021/acs.cgd.5b01130
Cryst. Growth Des. 2015, 15, 5495–5504

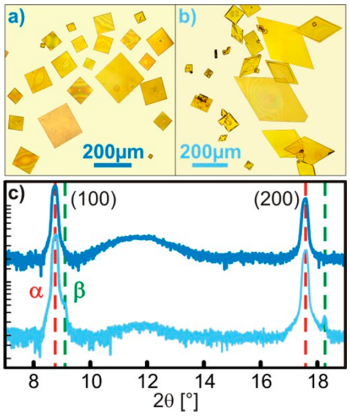

Figure 9. Optical micrographs of (a) selectively grown α-polymorph perylene platelets (preparation conditions: 310 K; 4 Å/min; 35 nm) and (b) a mixture of α- and β-phase crystals grown at 290 K, 2 Å, and ~235 nm. (c) XRD out-of-plane measurements revealing the absence and presence of the β-phase, depending on the preparation conditions. The modulation of the background intensity in the spectra is tentatively attributed to a microscopic short-range order of the silicone oil.

an exclusive formation of α-phase platelets is observed. Figure 9a shows an optical micrograph after deposition of nominal 35 nm which yields well-ordered platelet crystals with lateral extensions of more than 200 μm. Slight variation of the flux and the nominal thickness not necessarily leads to a formation of more extended crystals, but rather increases the nucleation density (cf. Figure S10, Supporting Information) and yields small crystallites which limit the size of usable isolated crystals.

By reducing the oil temperature upon growth to 290−295 K, a notable portion of β-crystals occurs as depicted in Figure 9b for an overall deposition time of 12−18 h. The corresponding XRD data presented in Figure 9c confirmed the polymorph selectivity. We note that in the case of a mixture of both phases the intensity of the belonging diffraction peaks does not directly reflect the actual quantity of α- and β-crystals because β-crystals often appear tilted with their (100)-plane with respect to the substrate. One reason is a frequently found twinning with other crystallites which causes also a tilted orientation (cf. Figure S11, Supporting Information). Despite systematic variation of the growth parameters, it was not possible to prepare solely β-crystals. However, we find that β-phase crystallites are also formed when depositing perylene at high rates of 30−60 Å/min and a substrate temperature of 325 K (see Figure S11, Supporting Information), hence indicating a rather complex interplay of nucleation and diffusion that governs the formed polymorph. Notably, the latter growth regime yields some β-crystals that exhibit a hexagonal shape. Such crystal shapes have also been reported for solution grown crystallites on monolayer templates.[34] They can be constructed by truncation of rhombic crystals and replacing a corner of the rhombic crystals by an additional plane which can be seen in the micrographs shown in Figures 6b and 7d. Branched needle-shaped crystallites of the α-polymorph form when further increasing the deposition rate (cf. Figure S12, Supporting Information). These are similar to those reported by Liu et al.[53] Finally, we note that the crystallites grown in silicon oil are completely covered by oil in most cases. This hampers their analysis by AFM. However, we observe a gradual dewetting of the platelet crystallites over a time scale of several months so that their surface morphology could still be analyzed by AFM. This reveals extremely flat surfaces and thus corroborates their excellent quality (cf. Figure, S8, Supporting Information).

Polymorphism is a commonly observed phenomenon in the crystallization of π-conjugated molecules. A prominent example is pentacene which exhibits two bulk polymorphs (denoted as the Campbell and Siegrist phase). Interestingly, the phase with the somewhat lower packing density is observed by crystallization from solution, while the more densely packed phase is formed by vapor transport growth, although the relative difference in the respective molecular volume amounts to 1% only. Though frequently an incorporation of solvent molecules into the crystal lattice is found to stabilize specific polymorphs, this scenario can be excluded for pentacene as well as for perylene. Therefore, it is conceivable that solvent molecules might assist the outermost layer formation upon crystallization (like a partial salvation shell), yielding a lower packing density.

Interestingly, when growing pentacene films on inert substrates such as glass, initially a thin-film phase is formed while the less dense Campbell phase is adopted with increasing film thicknesses. A similar scenario is presently observed for perylene growth by vapor deposition or resublimation. It suggests that the initial thin-film seed layer serves as precursor for the subsequent α-phase crystal growth. In contrast, the relative difference in the molecular volume of both perylene phases is less than 0.4% and thus shows a rather similar packing density for both polymorphs. We further note that perylene crystals of both polymorphs can be grown from toluene solution which indicates that purely energetic reasons for the polymorphs selectivity appear unlikely. The present study shows that β-phase crystals are obtained either by liquid-mediated deposition at low temperatures or by crystallization from solution by evaporation of solvents which essentially proceeds at room temperature. On the other hand, liquid-mediated deposition at elevated temperature as well as crystallization by cooling of a saturated solution (where nucleation actually proceeds well above room temperature) only leads to formation of α-crystals, hence suggesting that their growth is kinetically controlled. However, at even higher temperatures another regime is found where again the formation of β-crystals during liquid-mediated deposition is favored which challenges a simple kinetically controlled growth scenario.

Photoluminescence Properties of α- and β-Phase Perylene Crystals. To spectroscopically characterize the crystals grown in this study, we performed confocal laser scanning fluorescence microscopy (CLSFM) with crystals grown in oil as well as sublimed samples without the presence of oil. For crystals grown in silicone oil one has to consider also the fluorescence of the liquid which cross-fades the fluorescence of the crystals (cf. Figure S12, Supporting Information). Nevertheless, it is possible to obtain micrographs of individual crystals a few months after preparation, as the oil film dewets with time, thus leaving some crystals surrounded by a negligible amount of oil. Thereby, for one α-crystal we even were able to perform AFM analysis which is shown in Figure S8 of the Supporting Information, confirming a molecular flat (100)-surface and a thickness which is similar to that of sublimed platelets. Parts a and b of Figure 10 show the CLSF micrographs of platelets grown in oil. While the α-phase

DOI: 10.1021/acs.cgd.5b01130
Cryst. Growth Des. 2015, 15, 5495−5504

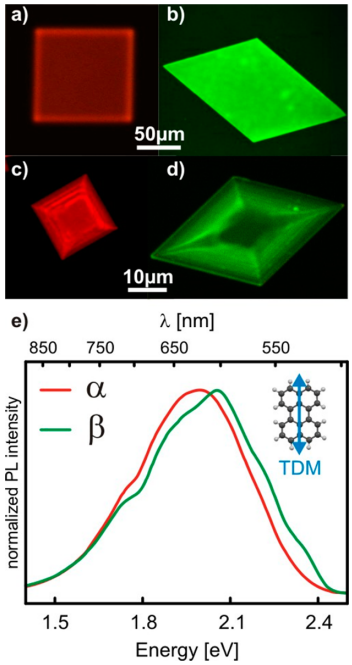

Figure 10. Confocal laser scanning fluorescence micrographs of (a) α-phase and (b) β-phase platelets grown in silicone oil as well as (c) α-phase and (d) β-phase pyramidal crystals by resublimation between wafers. Note that in the case of pyramids, apart from the presence of defects, additional crystalline faces can influence optical data when illuminating the (100)-plane yielding bright side faces. (e) Photoluminescence spectra of α- and β-platelets obtained under consideration of the spectral sensitivity of the detection system and transforming the data to the energy scale according to a Jacobian transformation. The inset depicts the belonging orientation of the transition dipole moment of the low energetic optical transition.

appears red, the β-phase is fluorescing green. These color impressions enable a straightforward method of identification besides the characteristic crystal shapes by the bare eye, which is in line with previous reports.[28] Interestingly, the emission appears brighter toward the edges of the single crystals. This effect is tentatively attributed to wave guiding as the orientation of the transition dipoles (cf. inset Figure 10e) favors the emission within the crystal slab planes, and hence, the light will predominantly leak out of the edges. Bright emission is also found at side faces of the pyramidal crystallites which actually consist of microfacets which do not represent low-indexed crystalline planes (cf. Figure S6, Supporting Information). We note further that intensity and spectral shape of the emission also depends on sample tilting as well as the position of observation (cf. Figure S14, Supporting Information). Therefore, ensemble measurements and polycrystalline samples may yield misleading results and make a conclusive interpretation challenging. Nevertheless, the clear differences in color impression of the different crystalline phases when inspected by the bare eye yield a straightforward yet conclusive identification mechanism. Still, carefully quantifying the emission spectra by considering the spectral sensitivity of the detection system and transforming the data to the energy scale according to a Jacobian transformation[55] (cf. Figure S15, Supporting Information) yields only a slight shift of the spectral weight to higher energies for the β-crystal compared to the α-crystal as shown in Figure 10e. These comparatively small spectral changes render the large change in color due to the limited infrared response of the human eye and accordingly adopted optical camera systems which have to be taken into account for theoretical analyzes. In addition, both phases display signatures of vibronic replicas in their emission spectra.

SUMMARY

In this work, we compare various strategies to grow perylene crystals with a special emphasis on polymorph-selective crystallization. While crystallization by resublimation of powder primarily yields crystals in the α-phase, β-phase crystals only very rarely form. In addition, a new thin-film phase is identified for the initial stage of film growth by vapor deposition. Its interlayer spacing matches that of the α-phase and it thus can be considered as a seed layer for the crystallization. Though crystals of both polymorphs are obtained from toluene solution (either by cooling of a saturated solution or by evaporation of solvents), the resulting crystallites exhibit a number of structural defects and the thickness of these crystallites cannot be easily controlled. A more rational approach for polymorph-selective crystal growth is achieved by means of liquid-mediated molecular beam deposition. Depending on the temperature of the supporting oil and growth rate, the relative occurrence of both crystalline phases is largely adjusted and yields an increased occurrence of β-phase crystal formation at low oil temperature and deposition rates. Although this behavior suggests that polymorph selectivity is mainly kinetically driven, we note that another regime of β-phase formation is found at distinctly higher temperatures which challenge this simple explanation. The crystals of both polymorphs exhibit characteristic base areas (rhombic vs near rectangular). They are comparatively characterized by means of AFM, XRD, and optical microscopy, therefore allowing an unambiguous distinction solely based on their crystalline shape. The liquid-mediated-grown perylene crystals of both polymorphs are disc-shaped with a thickness of less than 350 nm and exhibit almost atomically flat surfaces. By contrast, pyramidal-shaped crystals grown by repeated resublimation or from solution are substantially thicker and frequently exhibit defects such as screw dislocations or steps and microfacets.

Finally, we examine also the fluorescence signature of the various crystals. Though the different color impression of both polymorphs enables their easy distinction, the fluorescence emission is spatially rather than anisotropically. In addition parasitic emission at defects is found which also affects their spectral signature. Moreover, we show that consideration of the spectral sensitivity of the detection system is important as it distinctly affects the true fluorescence spectrum. The exceptionally high quality of platelet crystals in combination with their low thickness makes them semitransparent and enables, in particular, optical studies in transmission geometry without the disturbing influence of defects. Previous work has shown that this approach can provide detailed information on the excitation dynamics in crystalline organic semiconductors[10] and will be applied also to the various polymorphs of perylene in future studies.

ASSOCIATED CONTENT

Supporting Information

The Supporting Information is available free of charge on the ACS Publications website at DOI: 10.1021/acs.cgd.5b01130.

DOI: 10.1021/acs.cgd.5b01130
Cryst. Growth Des. 2015, 15, 5495−5504

Additional data on crystal characterization, microscopy, and XRD analyses (PDF)

AUTHOR INFORMATION

Corresponding Author

*E-mail: gregor.witte@physik.uni-marburg.de.

Notes

The authors declare no competing financial interest.

ACKNOWLEDGMENTS

We gratefully acknowledge support from the German Research Foundation (DFG) in the framework of the RTG1782 "Functionalization of Semiconductors" and W. Parak (University Marburg) for providing access to the confocal laser scanning microscope.

REFERENCES

(1) Hung, L. S.; Chen, C. H. Recent progress of molecular organic electroluminescent materials and devices. *Mater. Sci. Eng., R* **2002**, *39*, 143−222.

(2) Peumans, P.; Yakimov, A.; Forrest, S. R. Small molecular weight organic thin-film photodetectors and solar cells. *J. Appl. Phys.* **2003**, *93*, 3693−3723.

(3) Hoppe, H.; Sariciftci, N. S. Organic solar cells: An overview. *J. Mater. Res.* **2004**, *19*, 1924−1945.

(4) Anthony, J. E. The larger acenes: Versatile organic semiconductors. *Angew. Chem., Int. Ed.* **2008**, *47*, 452−483.

(5) Katz, H. E.; Huang, J. Thin-Film Organic Electronic Devices. *Annu. Rev. Mater. Res.* **2009**, *39*, 71−92.

(6) Sharifzadeh, S.; Biller, A.; Kronik, L.; Neaton, J. B. Quasiparticle and optical spectroscopy of the organic semiconductors pentacene and PTCDA from first principles. *Phys. Rev. B: Condens. Matter Mater. Phys.* **2012**, *85*, 125307.

(7) de Boer, R. W. I.; Gershenson, M. E.; Morpurgo, A. F.; Podzorov, V. Organic single-crystal field-effect transistors. *Phys. Status Solidi A* **2004**, *201*, 1302−1331.

(8) Gershenson, M. E.; Podzorov, V.; Morpurgo, A. F. *Colloquium*: Electronic transport in single-crystal organic transistors. *Rev. Mod. Phys.* **2006**, *78*, 973−989.

(9) Amimoto, K.; Kawato, T. Photochromism of organic compounds in the crystal state. *J. Photochem. Photobiol., C* **2005**, *6*, 207−226.

(10) Kolata, K.; Breuer, T.; Witte, G.; Chatterjee, S. Molecular Packing Determines Singlet Exciton Fission in Organic Solids. *ACS Nano* **2014**, *8*, 7377−7383.

(11) Desiraju, G. R. Polymorphism: The Same and Not Quite the Same. *Cryst. Growth Des.* **2008**, *8* (1), 3−5 (see also other contributions within this special issue).

(12) Brinkmann, M.; Gadret, G.; Muccini, M.; Taliani, C.; Masciocchi, N.; Sironi, A. Correlation between Molecular Packing and Optical Properties in Different Crystalline Polymorphs and Amorphous Thin Films of *mer*-Tris(8-hydroxyquinoline)aluminum-(III). *J. Am. Chem. Soc.* **2000**, *122*, 5147−5157.

(13) Huang, L.; Liao, Q.; Shi, Q.; Fu, H.; Ma, J.; Yao, J. Rubrene micro-crystals from solution routes: their crystallography, morphology and optical properties. *J. Mater. Chem.* **2010**, *20*, 159−166.

(14) Sharp, J. H.; Lardon, M. Spectroscopic characterization of a new polymorph of metal-free phthalocyanine. *J. Phys. Chem.* **1968**, *72* (9), 3230−3235.

(15) Ambrosch-Draxl, C.; Nabok, D.; Puschnig, P.; Meisenbichler, C. The role of polymorphism in organic thin films: oligoacenes investigated from first principles. *New J. Phys.* **2009**, *11*, 125010.

(16) Jurchescu, O. D.; Mourey, D. A.; Subramanian, S.; Parkin, S. R.; Vogel, B. M.; Anthony, A. E.; Jackson, T. N.; Gundlach, D. J. Effects of polymorphism on charge transport in organic semiconductors. *Phys. Rev. B: Condens. Matter Mater. Phys.* **2009**, *80*, 085201.

(17) Beckmann, W. Seeding the Desired Polymorph: Background, Possibilities, Limitations and Case Studies. *Org. Process Res. Dev.* **2000**, *4* (5), 372−383.

(18) Mangin, D.; Puel, F.; Veesler, S. Polymorphism in Processes of Crystallization in Solution: A Practical Review. *Org. Process Res. Dev.* **2009**, *13*, 1241.

(19) Braga, D.; Grepioni, F.; Maini, L. The growing world of crystal forms. *Chem. Commun.* **2010**, *46*, 6232−3242.

(20) Jiang, Q.; Ward, M. D. Crystallization under nanoscale confinement. *Chem. Soc. Rev.* **2014**, *43*, 2066−2079.

(21) Karl, N. Organic Semiconductors. In *Landolt−Börnstein: Numerical Data and Functional Relationships in Science and Technology*, New Series Vol. *17i*; Madelung, O., Schulz, M., Weiss, H., Eds.; Springer: Heidelberg, Germany, 1985; p 106.

(22) Kotani, M.; Kakinuma, K.; Yoshimura, M.; Ishii, K.; Yamazaki, S.; Kobori, T.; Okuyama, H.; Kobayashi, H.; Tada, H. Charge carrier transport in high purity perylene single crystals studied by time-of-flight measurements and through field effect transistor characteristics. *Chem. Phys.* **2006**, *325*, 160−169.

(23) Botoshansky, M.; Herbstein, F. H.; Kapon, M. Towards a Complete Description of a Polymorphic Crystal: The Example of Perylene; Redetermination of the Structures of the (Z = 2 and 4) Polymorphs. *Helv. Chim. Acta* **2003**, *86*, 1113−1128.

(24) Fuke, K.; Kaya, K.; Kajiwara, T.; Nagakura, S. The Polarized Reflection and Absorption Spectra of Perylene Crystals in Monomeric and Dimeric Forms. *J. Mol. Spectrosc.* **1976**, *63*, 98−107.

(25) Hochstrasser, R. M. The Crystal Spectrum of Perylene. *Can. J. Chem.* **1961**, *39*, 451−458.

(26) Hochstrasser, R. M.; Nyi, C. A. Dynamical effects from resonance Raman and fluorescence studies of the molecular exciton system perylene. *J. Chem. Phys.* **1980**, *72*, 2591−2600.

(27) Datta, A.; Mohakud, S.; Pati, S. K. Comparing the electron and hole mobilities in the α and β phases of perylene: role of π-stacking. *J. Mater. Chem.* **2007**, *17*, 1933−1938.

(28) Tanaka, J. The electronic spectra of aromatic molecular crystals. 2. The crystal structure and spectra of perylene. *Bull. Chem. Soc. Jpn.* **1963**, *36*, 1237−1249.

(29) Hochstrasser, R. M. Spectral Effects of Strong Exciton Coupling in the Lowest Electronic Transition of Perylene. *J. Chem. Phys.* **1964**, *40*, 2559−2564.

(30) Iemura, M.; Matsui, A. Crystal growth of α- and β-perylene by a vacuum sublimation method. *Mem. Konan Univ., Sci. Ser.* **1981**, *27*, 7−12.

(31) Yago, T.; Tamaki, Y.; Furube, A.; Katoh, R. Growth of β-Perylene Crystal. *Chem. Lett.* **2007**, *36*, 370−371.

(32) Yago, T.; Tamaki, Y.; Furube, A.; Katoh, R. Self-trapping limited exciton diffusion in a monomeric perylene crystal as revealed by femtosecond transient absorption microscopy. *Phys. Chem. Chem. Phys.* **2008**, *10*, 4435−4441.

(33) Lei, Y.; Liao, Q.; Fu, H.; Yao, J. Phase- and Shape-Controlled Synthesis of Single Crystalline Perylene Nanosheets and Its Optical Properties. *J. Phys. Chem. C* **2009**, *113*, 10038−10043.

(34) Urbelis, J. H.; Swift, J. A. Phase-Selective Crystallization of Perylene on Monolayer Templates. *Cryst. Growth Des.* **2014**, *14* (10), 5244−5251.

(35) Voigt, M.; Dorsfeld, S.; Volz, A.; Sokolowski, M. Nucleation and Growth of Molecular Organic Crystals in a Liquid Film under Vapor Deposition. *Phys. Rev. Lett.* **2003**, *91* (2), 026103.

(36) Witte, G.; Hänel, K.; Söhnchen, S.; Wöll, C. Growth and morphology of thin films of aromatic molecules on metals; the case of perylene. *Appl. Phys. A: Mater. Sci. Process.* **2006**, *82*, 447−455.

(37) Chernov, A. A. *Modern Crystallography III: Crystal Growth*, Springer Series in Solid-State Science, Vol. *36*; Springer Science & Business Media: Berlin, 2012.

(38) Söhnchen, S.; Hänel, K.; Birkner, A.; Witte, G.; Wöll, C. Molecular Beam Deposition of Perylene on Copper: Formation of Ordered Phases. *Chem. Mater.* **2005**, *17*, 5297−5304.

(39) Beigmohamadi, M.; Niyamakom, P.; Farahzadi, A.; Effertz, C.; Kremers, S.; Brueggemann, D.; Wuttig, M. Structure and morphology

DOI: 10.1021/acs.cgd.5b01130
Cryst. Growth Des. 2015, 15, 5495−5504

of perylene films grown on different substrates. *J. Appl. Phys.* **2008**, *104*, 013505.
(40) Dimitrakopoulos, C. D.; Brown, A. R.; Pomp, A. Molecular beam deposited thin films of pentacene for organic field effect transistor applications. *J. Appl. Phys.* **1996**, *80* (4), 2501−2508.
(41) Salzmann, I.; Duhm, S.; Heimel, G.; Rabe, J. P.; Koch, N.; Oehzelt, M.; Sakamoto, Y.; Suzuki, T. Structural Order in Perfluoropentacene Thin Films and Heterostructures with Pentacene. *Langmuir* **2008**, *24*, 7294−7298.
(42) Wittmann, J. C.; Straupe, C.; Meyer, S.; Lotz, B.; Lang, P.; Horowitz, G.; Garnier, F. Sexithiophene thin films epitaxially oriented on polytetrauoroethylene substrates: Structure and morphology. *Thin Solid Films* **1997**, *311*, 317−322.
(43) Resel, R. Surface induced crystallographic order in sexiphenyl thin films. *J. Phys.: Condens. Matter* **2008**, *20*, 184009.
(44) Mänz, A.; Breuer, T.; Witte, G. Epitaxial Tetrathiafulvalene-Tetracyanoquinodimethane Thin Films on KCl(100): New Preparation Methods and Observation of Interface-Mediated Thin Film Polymorph. *Cryst. Growth Des.* **2015**, *15*, 395−403.
(45) Ambrosch-Draxl, C.; Nabok, N.; Puschnig, P.; Meisenbichler, C. The role of polymorphism in organic thin films: oligoacenes investigated from first principles. *New J. Phys.* **2009**, *11*, 125010.
(46) Drummy, L. F.; Martin, D. C. Thickness-Driven Orthorhombic to Triclinic Phase Transformation in Pentacene Thin Films. *Adv. Mater.* **2005**, *17*, 903.
(47) Ruiz, R.; Choudhary, D.; Nickel, B.; Toccoli, T.; Chang, K. C.; Mayer, A. C.; Clancy, P.; Blakely, J. M.; Headrick, R. L.; Iannotta, S.; Malliaras, G. G. Pentacene Thin Film Growth. *Chem. Mater.* **2004**, *16*, 4497.
(48) Beigmohamadi, M.; Niyamakom, P.; Farahzadi, A.; Kremers, S.; Michely, T.; Wuttig, M. Evolution of dislocations in perylene films with thickness and deposition rate. *Phys. Status Solidi RRL* **2008**, *2* (1), 1−3.
(49) www.kristall2000.de.
(50) http://www.ccdc.cam.ac.uk/mercury/.
(51) Takeyama, Y.; Maruyama, S.; Matsumoto, Y. Growth of Single-Crystal Phase Pentacene in Ionic Liquids by Vacuum Deposition. *Cryst. Growth Des.* **2011**, *11*, 2273.
(52) Takeyama, Y.; Maruyama, S.; Taniguchi, H.; Itoh, M.; Ueno, K.; Matsumoto, Y. Ionic liquid-mediated epitaxy of high-quality C_{60} crystallites in a vacuum. *CrystEngComm* **2012**, *14*, 4939.
(53) Liu, X.; Kaiser, V.; Wuttig, M.; Michely, T. Unidirectional anisotropies in perylene crystal growth on a liquid surface. *J. Cryst. Growth* **2004**, *269*, 542−549.
(54) Liu, X.; Wuttig, M. Inherent features in the growth of perylene crystals on an oil substrate. *Phys. Rev. B: Condens. Matter Mater. Phys.* **2006**, *73*, 033405.
(55) Mooney, J.; Kambhampati, P. Get the Basics Right: Jacobian Conversion of Wavelength and Energy Scales for Quantitative Analysis of Emission Spectra. *J. Phys. Chem. Lett.* **2013**, *4* (19), 3316−3318.

DOI: 10.1021/acs.cgd.5b01130
Cryst. Growth Des. 2015, 15, 5495−5504

Auszüge aus den *Supporting Information* zum Artikel:

A. Pick, M. Klues, A. Rinn, K. Harms, S. Chatterjee und G. Witte, Cryst. Growth Des. 15 (2015), 5495-5504. DOI: 10.1021/acs.cgd.5b01130

I. The crystal structures of perylene

The two polymorphs of perylene, which are denoted as α- and β-phases, are both of monoclinic type. The crystal structures are shown in Fig. S1, where in a) and c) the unit cells of the α- and β-phases are sketched. The α-phase contains four molecules per unit cell, which are arranged in a sandwich herringbone motif (cf. Fig. S1 b)), while the β-polymorph contains two molecules per unit cell that are arranged in a γ-type motif (cf. Fig. S1 d)).

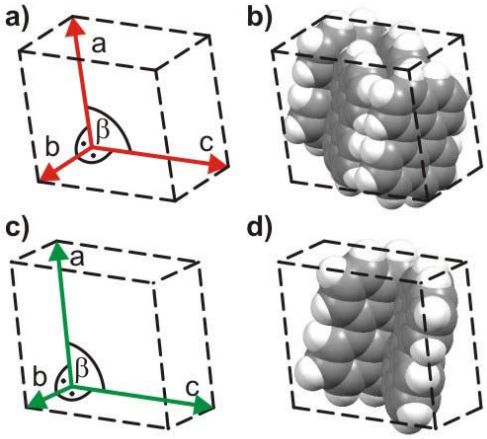

Figure S1: Unit cell and molecular packing motifs of perylene crystals in (a,b) the α-phase and (c,d) the β-phase.

	α-phase	β-phase
Z	4	2
a	10.24 Å	9.76 Å
b	10.79 Å	5.84 Å
c	11.13 Å	10.61 Å
α	90°	90°
β	100.92°	96.77°
γ	90°	90°
V/Z	301.8 $Å^3$	300.5 $Å^3$

Table S1: Unit cell parameters of both perylene polymorphs reported in [23].

To verify the presence of the known polymorphs and to enable a clear correlation with their crystallographic shape, the unit cells of perylene crystals of both phases grown from toluene solution were also determined in this study at 100K. As presented in Tab. S2 they are in excellent agreement with the literature data [23] listed in Tab. S1 that were taken at 150K (α-phase) and 200K (β-phase).

	α-phase	β-phase
a	10.21 Å	9.77 Å
b	10.77 Å	5.82 Å
c	11.06 Å	10.55 Å
α	90°	90°
β	101.13°	96.92°
γ	90°	90°

Table S2: Unit cell parameters determined in this study for solution grown perylene crystals.

Crystals of the α-phase are known to be stable up to their melting point, while the β-phase irreversibly transforms into the α-phase at about 373K [23]. In Fig. S2 single-crystals of perylene are shown, which were prepared by re-sublimation between two substrates. Here, the sample was heated within 30 min from 300K to 400K. Postdeposition heating at ambient conditions confirms, that the β-phase is thermically less stable, as the crystal in b) is nearly sublimed at 165°C, while the α-phase appears stable, apart from some changes in reflectivity.

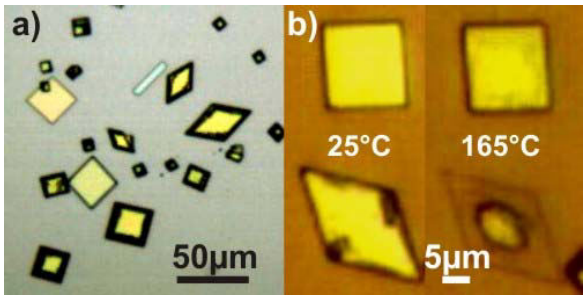

Figure S2: (a) Single crystals of α- and β- perylene observed upon re-sublimation. (b) Comparison of the thermal stability of crystallites of both polymoprhs upon heating at ambient conditions, indicating a lower thermal stability of the β- polymorph (lower row).

Apart from the two known polymorphs, we observed also an interface mediated thin film phase (cf. Fig. 4). It especially occurs when depositing perylene by OMBD on an oxidized Si-wafer, while an increasing number of cycles of re-sublimation between two substrates leads to a increasing α-phase-signal. The diffractogram in Fig. 4 d) has been obtained for a sample, which is presented in Fig. S3, where also pyramidal crystallites of the β-phase are present.

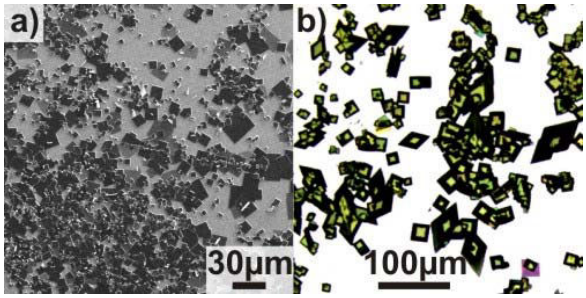

Figure S3: (a) SEM micrograph of accumulated α-crystals and (b) optical migrograph of preferentially formed pyramidal crystallites of the β-phase on the same sample. Re-sublimation was performed by applying a heating ramp from 300K to 385K within 1h.

For polarization resolved spectroscopic studies it is crucial to know the exact azimuthal orientations within the (100) top-faces. Therefore, in-plane measurements were performed to identify specific azimuth directions and thus the relative orientation of unit cell vectors with respect to the characteristic shape of the crystallites. For this purpose the (011) reflex was used which was obtained by tilting the sample at the angles ω and ψ for the α- and β-phase respectively (angles between (100) and {011} planes) such that the Bragg-reflex of the (011) planes was observed and subsequently rotating the samples around the a* axis as shown schematically in Fig. S4. Here, the

exact orientation of the single-crystals is crucial: the (0-11) reflex is thus calibrated to 0°. Although opposing planes are parallel, only one reflex appears. This is due to the monoclinic nature of both crystal structures: As the sample rotates, e.g. the (011) plane encloses a cone, so that there is only one position for a reflex. Altogether we obtain two reflexes, the second one belongs to the (0-11) or the (01-1) plane. Those enclose angles, which correspond to the angles σ and τ, which are those when looking ontop of the (100) plane of a crystal.

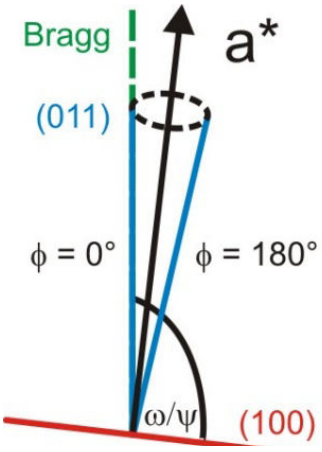

Figure S4: Scheme for the in-plane scan geometry.

In summary, the {011} planes are indeed the occuring side faces of the single-crystals, which is visualized in Fig. S5 where top views of such planes are shown for both phases.

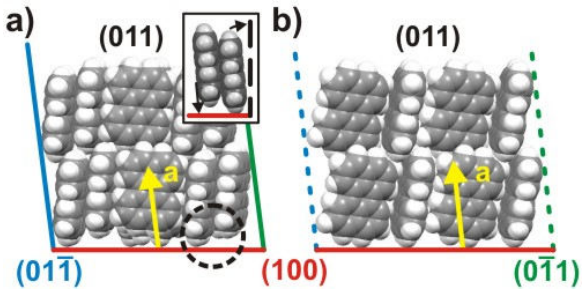

Figure S5: Top views of the (011) planes together with the belonging molecular packing motifs of both polymorphs of perylene. (a) For the α-phase the (01-1) (blue) and (0-11) (green) side faces are oriented nearly perpendicular (angle σ=92°) with respect to the drawing plane, while for the β-phase they form an angle of τ=122°. Therefore, the projection of the side faces are shown as dashed lines in (b). The inset in (a) explains the formation of a thin-film-phase: one of the sandwiched molecules in the α-phase is vertically slightly shifted, so that only every second molecule is in contact with a supporting substrate. By contrast in the substrate-mediated thin film phase the (100)-interlayer spacing is somewhat increased. This can be attributed to a levelling of all molecules within the layer which enables contact with the substrate and in turn causes a more upright tilting of the molecules.

5.4 Enhanced Stability of Rubrene against Oxidation by Partial and Complete Fluorination

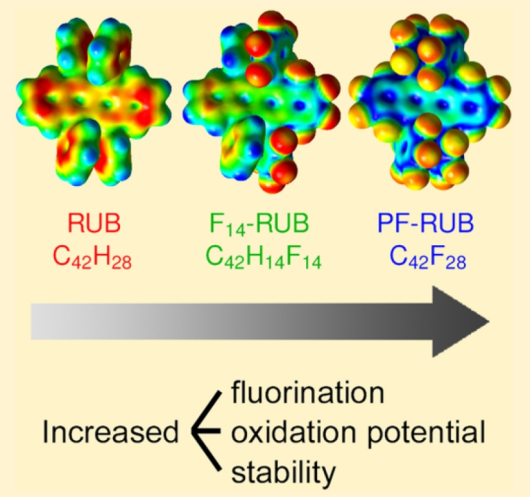

5.4.1 Inhaltsangabe

We report on the oxidation potential of partially fluorinated ($C_{42}F_{14}H_{14}$, F_{14}-RUB) and perfluorinated rubrene ($C_{42}F_{28}$, PF-RUB) studied by cyclic voltammetry (CV) in solution as well as by spectroscopic ellipsometry and near edge X-ray absorption fine structure (NEXAFS) spectroscopy in thin films in combination with density functional theory computations. Due to their different electronic structure, the fluorinated derivatives have a higher oxidation potential and are more stable than rubrene ($C_{42}H_{28}$, RUB).

5.4.2 Eigenleistung

Mein Hauptbeitrag zu dieser Studie besteht in der Klärung des Einflusses von Konformationsänderungen auf die NEXAFS-Signatur. Zu diesem Zweck wurde eine aufwändige Berechnung der entsprechenden Spektren von mir geplant und durchgeführt. Zudem basiert die allgemeine Analyse der Signatur im Artikel auf diesen Ergebnissen. Die graphische und inhaltliche Aufbereitung dieser Ergebnisse erfolgte in Zusammenarbeit mit Tobias Breuer. Ebenso war ich an der Durchführung der NEXAFS-Messungen beteiligt war.

THE JOURNAL OF PHYSICAL CHEMISTRY C

Article

pubs.acs.org/JPCC

Enhanced Stability of Rubrene against Oxidation by Partial and Complete Fluorination

F. Anger,[†] T. Breuer,[‡] A. Ruff,[§,⊥] M. Klues,[‡] A. Gerlach,[†] R. Scholz,[∥] S. Ludwigs,[§] G. Witte,[‡] and F. Schreiber*[,†]

[†]Institut für Angewandte Physik, Universität Tübingen, Auf der Morgenstelle 10, 72076 Tübingen, Germany

[‡]Fachbereich Physik, Universität Marburg, Renthof 7, 35032 Marburg, Germany

[§]Institut für Polymerchemie (IPOC), Universität Stuttgart, Pfaffenwaldring 55, 70569 Stuttgart, Germany

[∥]Institut für Angewandte Photophysik, TU Dresden, George-Bähr-Straße 1, 01069 Dresden, Germany

Supporting Information

ABSTRACT: We report on the oxidation potential of partially fluorinated ($C_{42}F_{14}H_{14}$, F_{14}-RUB) and perfluorinated rubrene ($C_{42}F_{28}$, PF-RUB) studied by cyclic voltammetry (CV) in solution as well as by spectroscopic ellipsometry and near edge X-ray absorption fine structure (NEXAFS) spectroscopy in thin films in combination with density functional theory computations. Due to their different electronic structure, the fluorinated derivatives have a higher oxidation potential and are more stable than rubrene ($C_{42}H_{28}$, RUB).

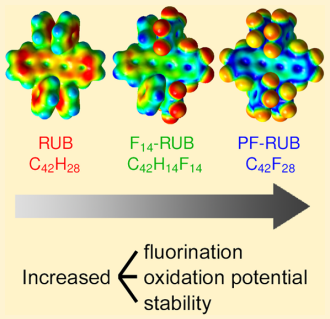

INTRODUCTION

Rubrene (5,6,11,12-tetraphenyltetracene, $C_{42}H_{28}$, RUB) is among the most promising materials for applications based on organic semiconductors,[1] at least due to its high charge carrier mobility.[2−5] One of the challenges in organic and hybrid electronics concerns the stability against exposure to ambient gases, including in particular oxygen.[6,7] This is especially relevant for thin films, which are easier to produce than single crystals and thus more attractive for applications, but can often exhibit a more grainy morphology which allows oxygen to penetrate into the material.[8−11] A possibility to address this issue is to modify the rubrene molecule by substitution with different elements or side groups in order to reduce its susceptibility to oxidation.[12−16] Partial or complete fluorination is a typical strategy in this context, since the large electronegativity of fluorine is expected to hinder oxidation very effectively.[17,18] Furthermore, fluorination will also change the electronic and optical properties of a material,[19,20] which also is of relevance for the interface between organic compounds in applications.[21−23]

In this study, we examine to which extent rubrene can be stabilized by (per)fluorination and how this chemical modification affects the desirable optical as well as electronic spectra. For this purpose, the newly synthesized perfluoro-5,6,11,12-tetraphenyltetracene ($C_{42}F_{28}$, PF-RUB) and 1,2,3,4-tetrafluoro-5,12-bis(2,3,4,5,6-pentafluorophenyl)-6,11-diphenyltetracene ($C_{42}F_{14}H_{14}$, F_{14}-RUB) shown in Figure 1, both excellent candidates for a systematic investigation, are studied using cyclic voltammetry (CV), spectroscopic ellipsometry, and near edge X-ray absorption fine structure (NEXAFS). Together with density functional theory (DFT), we evaluate the experimental results of the fluorinated compounds in solution and thin films with unsubstituted rubrene itself. A comparison of the experimental and DFT results obtained for the fluorinated compounds in solution and thin films provides a consistent picture of the stabilization mechanism.

EXPERIMENTAL SECTION

Pristine RUB was purchased from Acros, while the fluorinated rubrenes were synthesized by Sakamoto and Suzuki.[25] All materials were purified by temperature gradient sublimation.

Cyclic voltammograms were recorded with a PGSTAT101 potentiostat from Metrohm (Filderstadt, Germany) under argon atmosphere in a gastight three electrode cell. The working electrode consisted of a Pt disk (nominal diameter d = 1 mm) sealed in glass. A Pt wire was used as the counter electrode. An Ag wire coated with an AgCl-layer which was directly immersed into the electrolyte solution served as (pseudo)reference electrode. All potentials are given versus the formal potential of the redox couple Fc/Fc^+ (ferrocene/ferrocenium).[26] Fc was used as internal standard (added after substrate measurements). Voltammograms were recorded in deaerated (argon bubbling) CH_2Cl_2 containing NBu_4PF_6 acting as the supporting electrolyte

Received: December 15, 2015
Revised: February 2, 2016
Published: March 3, 2016

DOI: 10.1021/acs.jpcc.5b12293
J. Phys. Chem. C 2016, 120, 5515−5522

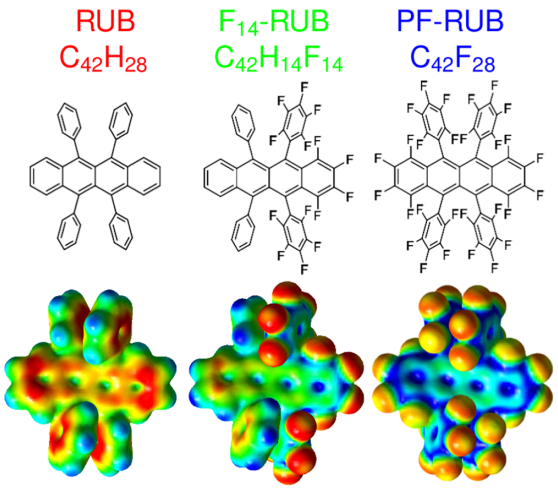

Figure 1. Chemical structure and molecular electrostatic potential (MEP) plot of the compounds investigated (from left to right) rubrene (RUB, $C_{42}H_{28}$), partially fluorinated rubrene (F_{14}-RUB, $C_{42}F_{14}H_{14}$), and perfluorinated rubrene (PF-RUB, $C_{42}F_{28}$).[24]

(0.1 M). CH_2Cl_2 was dried prior to use with activated Al_2O_3 (dried at 80 °C for several days in an oven). Cyclic voltammograms were not background corrected. For the estimation of half wave potentials voltammograms recorded with 100 mV/s were used. Half wave potentials $E_{1/2}$ of the redox couple were calculated from the peak potentials of the oxidation E_p^{ox} and reduction E_p^{red} as $E_{1/2} = (E_p^{ox} + E_p^{ox})/2$. Substrate concentrations were 2.6 mM in the case of RUB and 1.4 mM for F_{14}-RUB and PF-RUB.

The ionization potential (IP) and electron affinity (EA) of the RUB, F_{14}-RUB, and PF-RUB molecules in solution were computed with the B3LYP functional and triple-ζ valence plus polarization (TZVP) basis set using Turbomole 6.4.[27] The values for IP and EA of the RUB and PF-RUB (F_{14}-RUB) molecules in D_2 (C_2) symmetry were estimated from the energies of the ionized species under the consideration of the polarization energy of the solvent (CH_2Cl_2).

Thin films of the three materials were deposited at room temperature under high vacuum conditions on silicon wafers covered by a native oxide layer. By keeping the molecular flux at a constant rate of 1.1 Å/min monitored by a quartz crystal microbalance (QCM), films with thicknesses of 20 nm were prepared. Under these conditions RUB, F_{14}-RUB, and PF-RUB are known to form amorphous thin films.[24] About 90 min after thin film deposition, air was leaked into the UHV chamber up to a pressure of 50 mbar. Real-time data of the oxidation process were obtained using spectroscopic ellipsometry with a broad band Xe lamp (75 W, 250−1000 nm), while the samples were exposed to air.[28] The ellipsometer (Wollam M-2000 SE) was equipped with a rotating compensator for accurate measurement of the polarization and a CCD camera enabling simultaneous detection of all wavelengths, which allows minimization of the acquisition time (t = 1 min). In order to measure the samples in situ, the ellipsometer was mounted on the vacuum system with strain free quartz windows resulting in a fixed angle of incidence of ~61°. Data acquisition started directly with the partial venting process of the vacuum system until after 4−10 min a pressure of 50 mbar was reached, which then was kept constant.

Near edge X-ray absorption fine structure (NEXAFS) spectra were obtained from thin films of F_{14}-RUB and PF-RUB that were deposited in ultrahigh vacuum with similar growth parameters as above. Prior to the measurements, the thin films had been exposed to air for several days as the low amount of available material did not allow for the in situ preparation of an additional batch of samples. The measurements were performed at the HE-SGM dipole beamline of the synchrotron BESSY II in Berlin (Germany) providing linearly polarized light (polarization factor = 0.91) and an energy resolution at the carbon K-edge of about 300 meV. All NEXAFS spectra were recorded in partial electron-yield mode using a channel-plate detector with a retarding field of −150 V. For the calibration of the absolute energy scale, the photocurrent from a carbon-coated gold grid in the incident beam (absorption maximum = 284.9 eV) was recorded simultaneously. In order to determine the average molecular orientation relative to the sample surface, NEXAFS spectra were recorded at different angles of incidence (θ = 30°, 55°, 70°, and 90°). The observed dichroism was analyzed after flux normalization and considering the transmission of the monochromator.

Computations of C 1s NEXAFS spectra were performed on the Slater transition state level by optimizing the molecular geometry using the gradient-corrected revised Perdew−Burke−Ernzerhof (RPBE) functional and all-electron TZVP basis sets. Subsequently, the excited states for each nonsymmetry equivalent excitation center, i.e., carbon atom, were calculated separately. In this step, the excitation center is modeled using an IGLO-III basis set which allows the description of inner shell relaxation effects, while the other carbon centers are described by effective core potentials (ECPs). Further details on the computations can be found in previous work.[29,30]

RESULTS

Electrochemical Properties in Solution. Electrochemical methods such as CV allow for the investigation of the general electrochemical properties of a redox-active compound. Both, oxidation and reduction processes at the electrode interface can be examined by means of the same method, including the determination of redox potentials.[31] Moreover, from the potential values of the corresponding oxidative or reductive processes, values for the energy levels of the highest occupied molecular orbital (HOMO) and the lowest unoccupied molecular orbital (LUMO) can be estimated.[32]

The redox behavior, including the determination of the redox potentials, of RUB, F_{14}-RUB, and PF-RUB in solution and the absence of oxygen was studied by means of CV in 0.1 M NBu_4PF_6/CH_2Cl_2 at a Pt disk electrode under planar diffusion conditions. Cyclic voltammograms of RUB (Figure 2a) show a first chemically reversible oxidation (solid line, cation formation) and a chemically reversible reduction (dashed line, anion formation) with peak potentials for the oxidation (E_p^{ox}) and the reduction (E_p^{red}) of +0.39 and −2.16 V, respectively. The half wave potentials of the anodic and cathodic redox couple are found at +0.33 ($E_{1/2}^{ox}$, oxidation) and −2.09 V ($E_{1/2}^{red}$, reduction). Both values are in good agreement with previously reported data.[12,16,17,33] At higher potentials, a second chemically irreversible oxidation (formation of the dication) wave located at around +1.0 V[16] is observed (see the Supporting Information).

The anodic and cathodic I−E curves of the partially fluorinated F_{14}-RUB (Figure 2b) show a chemically reversible oxidation (solid line, cation formation) and a chemically reversible reduction (dashed line, anion formation) with half wave potentials of $E_{1/2}^{ox}$ = +0.91 V and $E_{1/2}^{red}$ = −1.55 V. At lower

DOI: 10.1021/acs.jpcc.5b12293
J. Phys. Chem. C 2016, 120, 5515−5522

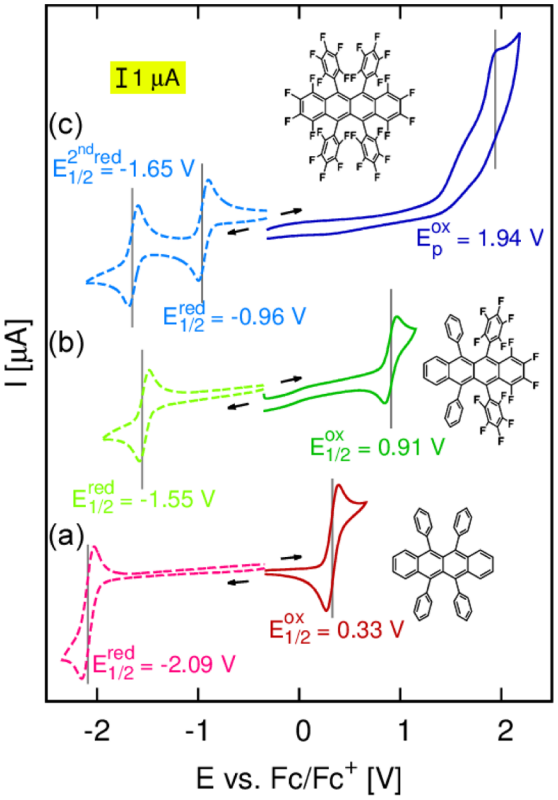

Figure 2. Anodic (solid lines) and cathodic (dashed lines) cyclic voltammograms of RUB (a), c = 2.3 mM, F_{14}-RUB (b), c = 1.4 mM, and PF-RUB (c), c = 1.4 mM, in 0.1 M NBu_4PF_6/CH_2Cl_2 at Pt recorded with a scan rate of ν = 100 mV s^{-1}. Arrows indicate scan direction, anodic and cathodic I–E curves were recorded separately, voltammograms were not background corrected. The shoulder in (c) located at around +1.6 V is attributed to impurities in the electrolyte (revealed by measuring the background current in the absence of substrate).

potentials a chemically irreversible redox wave at around −2.15 V is visible, which becomes chemically reversible for fast scan rates. This process relies on a decomposition within the time scale of the experiment (see the Supporting Information).

Cyclic voltammograms of PF-RUB (Figure 2c) show two chemically reversible reduction processes with half wave potentials of −0.96 V and −1.65 V. We attribute the two redox processes to the stepwise formation of the dianion via an anionic species. In contrast to F_{14}-RUB, the dianionic species formed during the second reduction of PF-RUB (−1.65 V) seems to be more stable within the time scale of the voltammetric experiment. The second electron transfer process is chemically reversible even at slow scan rates ($\nu \leq$ 200 mV s^{-1}). A chemically irreversible oxidation wave at considerably high potentials (close to the limit of the potential window of the electrolyte, Figure 2c, solid line) is revealed by the anodic potential cycle of PF-RUB. The peak potential of the oxidation is +1.94 V (ν = 100 mV s^{-1}).

An increase in the degree of fluorination leads to an increase of the oxidation potentials of +1.6 V when going from RUB (+0.33 V) via F_{14}-RUB (+0.91 V) to PF-RUB (+1.94 V), because of the electron withdrawing effect of the fluorine atoms that are attached to the RUB core. Simultaneously, the reduction potential increases by about +1.1 V from −2.09 V (RUB) to −0.96 V (PF-RUB) for the same reason. The systematic tuning of the molecular energy levels by different degrees of fluorination has also been shown for other small molecule organic semiconductors, such as phtalocyanines.[34] Indeed, the perfluorinated compound PF-RUB is thermodynamically more stable against oxidation (high oxidation potential, low HOMO level) than F_{14}-RUB and much more stable than RUB, but is readily reduced (high reduction potential, low LUMO level).

Under the assumption that the redox couple Fc/Fc^+ (redox potential standard[26]) is located at −5.1 eV in the Fermi energy scale,[32] the HOMO (E_{HOMO}^{exp}) and LUMO (E_{LUMO}^{exp}) energy values of RUB, F_{14}-RUB and PF-RUB can be estimated from the half wave potentials of the oxidation and the first reduction according to

$$E_{HOMO}^{exp} = -(E_{1/2}^{ox} + 5.1)[eV] \quad (1)$$

$$E_{LUMO}^{exp} = -(E_{1/2}^{red} + 5.1)[eV] \quad (2)$$

As follows from the redox potentials, PF-RUB has the lowest HOMO (−7.0 eV) and lowest LUMO (−4.1 eV) level whereas RUB exhibits the highest HOMO (−5.4 eV) and highest LUMO (−3.0 eV) level. Note that the HOMO of PF-RUB may be slightly overestimated since the peak potential was used instead of the half wave potential. The energy level of the partially fluorinated compound F_{14}-RUB is located between the values for the other two compounds, at E_{HOMO}^{exp} = −6.0 eV and E_{LUMO}^{exp} = −3.6 eV, which is in good agreement with recent observations obtained with photoelectron spectroscopy in the solid state.[35] Hence, we find for both fluorinated compounds, F_{14}-RUB and PF-RUB, that the oxidation potentials lie above the ionization potentials (IPs) of most other RUB derivatives studied so far.[12,14−16]

Optical Absorption of Thin Films. Figure 3 shows real-time absorption spectra (ε_2) that were obtained during exposure to air using spectroscopic ellipsometry from thin films of RUB, F_{14}-RUB, and PF-RUB with a thickness of 20 nm, each. The ellipsometric raw data consisting of the parameters Ψ and Δ was converted into the dielectric function $\varepsilon_1 + i\varepsilon_2$ using a commercial software package (WVASE32). The data was modeled with an isotropic layer accounting for the organic thin film deposited on the native silicon wafer, which in each case is represented by a silicon and a dioxide layer, respectively. The spectra shown in Figure 3a–c were acquired in intervals of 100 min beginning with the exposure to air at a pressure of 50 mbar into the vacuum chamber. The time resolution of the experiment was determined by their integration time of 1 min.

At t = 0 min (still under vacuum conditions) we observe the HOMO–LUMO transition of the unoxidized RUB, F_{14}-RUB, and PF-RUB thin films at 2.34, 2.30, and 2.33 eV, respectively, which is in good agreement with previously reported values for the optical gap.[35] All compounds show a pronounced vibronic progression of the HOMO–LUMO transition that can be well fitted with a spacing of ∼0.16 eV.[24] For RUB, we find an additional peak at 4.03 eV[28] that essentially relies on the HOMO-(LUMO+1) transition. For the fluorinated materials F_{14}-RUB and PF-RUB, we find analogous transitions at 3.95 and 4.03 eV, respectively.

These observations clearly show that the relative energy alignment of the three materials is remarkably similar, merely the optical transitions of F_{14}-RUB are slightly red-shifted by 0.05 eV compared to PF-RUB and RUB.[24] This evidences that the optical properties of the compounds do not change fundamentally with

DOI: 10.1021/acs.jpcc.5b12293
J. Phys. Chem. C 2016, 120, 5515−5522

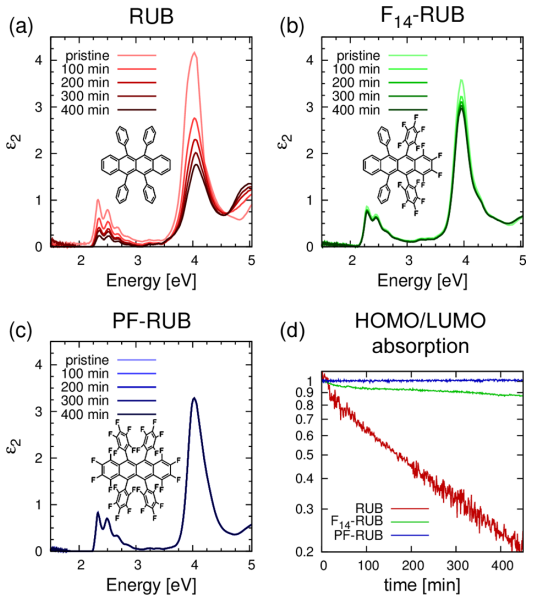

Figure 3. Real-time observation of the optical properties (ε_2) of (a) RUB, (b) F_{14}-RUB, and (c) PF-RUB thin films using spectroscopic ellipsometry. 90 min after deposition (20 nm), the thin films were exposed to air (50 mbar). (d) Time dependent intensity of the HOMO-LUMO transition of the thin films shown in (a–c). The respective intensities are normalized to the value before exposure to oxygen at $t = 0$ min. While the intensity of RUB decreases exponentially to almost 20% after 400 min[13,28] (strong oxidation effects resulting in bleaching), there is almost 90% of the initial intensity observed for F_{14}-RUB. For PF-RUB no change can be measured within the time scale of the experiment.

the degree of fluorination, which is in contrast to perfluorinated acenes like pentacene or tetracene, where fluorination results in a notable redshift of the respective HOMO–LUMO transition.[19,36] However, the ionization potential of thin films of the fluorinated rubrenes was shown to differ by ~0.9 eV and ~1.7 eV from RUB to F_{14}-RUB and PF-RUB, respectively.[35]

It is well-known that RUB becomes transparent in the visible spectral region upon exposure to light and oxygen since photooxidation leads to the formation of transparent rubrene-endoxide or -peroxide.[7,13,28,37] In good agreement with this expectation, we observe an exponential distinct decrease in intensity of the HOMO–LUMO transition of RUB when permitting air to enter the vacuum system (Figure 3d). Simultaneously, the transition at ~4 eV is getting weaker, and a new transition at ~5 eV related to photooxidized RUB exhibits increased intensity.[28]

For F_{14}-RUB, the observed change in the absorption spectra is qualitatively similar to that observed for RUB; however, it is considerably less pronounced. The intensity decrease of the HOMO–LUMO transition and also of the transition at ~4.03 eV is clearly less pronounced than for RUB. As a result, the residual absorption signal after 400 min is still stronger than that which is found only after 100 min for RUB with respect to the initial signals, indicating a reduced susceptibility to oxygen. In contrast to these two cases, we do not observe any changes in the optical spectra of PF-RUB upon exposure to air within the duration of the experiment.

Similarly to RUB, thin films of fluorinated rubrene have been shown to grow disordered on silicon,[24,38] which allows oxygen to penetrate all films. Thus, a stabilizing mechanism due to molecular ordering as it occurs particularly in the bulk of RUB single crystals, where it leads to a reduction of the susceptibility to oxidation due to sterical hindrance,[10] can be neglected. Note, however, that thin films of fluorinated rubrene indeed can dewet during storage, but a possible molecular reordering occurs on a time scale that is expected to be significantly longer than the oxidation process. This demonstrates that F_{14}-RUB is considerably and PF-RUB far more stable against oxidation in comparison to RUB.

Computation of Ionized Molecules. For a more quantitative analysis of the ionization energies of the three compounds, we performed density functional theory (DFT) computations (B3LYP/TZVP) with the quantum chemistry program package Turbomole 6.4.[27] Relying on the ionization potential and electron affinity of the free (gas phase) molecules of the three materials with twisted tetracene backbone,[35] the ionization potential (IP_+^{sol}) and electron affinity (EA_-^{sol}) of the ionized species in solution were estimated via[39,40]

$$IP_+^{sol} = IP_+^{gas} - P_+ \quad \text{and} \quad EA_-^{sol} = EA_-^{gas} + P_- \tag{3}$$

P_+ and P_- designate the polarization energies arising from the embedding into a medium with dielectric constant differing from one. The polarization energies in dichloromethane with dielectric constant $\varepsilon_{Solvent} = 9.08$ is calculated by[41]

$$P_+ = \frac{e^2}{4\pi\varepsilon_0}\frac{1}{2r_{Ion}}\left(1 - \frac{1}{\varepsilon_{Solvent}}\right) \tag{4}$$

where r_{Ion} is the radius of the ionized molecules. For an effective ion radius $r_{Ion} = r_+ = r_- = 7.0$ Å[33] for both cation and anion of all three compounds, eq 4 yields a polarization energy of $P_+ = P_- = 0.92$ eV for the simply ionized molecules. Table 1 summarizes the characteristic potential values and orbital energies of RUB, F_{14}-RUB and PF-RUB derived from cyclic voltammetric experiments and DFT computations. From the experimental E_{HOMO}^{exp} and E_{LUMO}^{exp} values the electrochemical HOMO–LUMO gap was obtained from $E_{gap,CV}^{exp} = E_{LUMO}^{exp} - E_{HOMO}^{exp}$. The comparison of the values for computed potentials with the experimental electrochemical gaps reveals particularly for PF-RUB a very good agreement. For RUB and F_{14}-RUB, the computed gap $E_{gap,CV}^{DFT}$ overestimates $E_{gap,CV}^{exp}$ slightly, which suggests a smaller radius r_{Ion} of the ionized molecules (and hence larger polarization energies) for these two materials compared to PF-RUB. The electrochemical gap $E_{gap,CV}^{exp}$ increases when going from RUB (2.4 eV) to PF-RUB (2.9 eV), which lies slightly above the optical gap $E_{gap,opt}^{exp}$.[24] The high value of PF-RUB is a result of the nonlinear increase of the redox potentials with increasing F-content within the RUB core.

NEXAFS of Thin Films. In order to investigate the electronic structure of the fluorinated rubrenes with respect to their unoccupied states in the processed thin films, X-ray absorption spectroscopy at the carbon K-edge (C 1s-NEXAFS) was applied. Comparing the X-ray absorption spectra detected in partial electron yield (PEY) at different sample orientation (dichroism) also allows us to determine the effective molecular orientation with respect to the surface normal.[44] Figure 4 shows NEXAFS spectra of PF-RUB and F_{14}-RUB that were acquired at different angles of incidence. The observed equal absorption signals at all angles for the F_{14}-RUB and PF-RUB films indicate that the molecules do not exhibit a distinct orientation but are disordered

DOI: 10.1021/acs.jpcc.5b12293
J. Phys. Chem. C 2016, 120, 5515–5522

Table 1. Comparison of Experimental and Computed Orbital and Gap Energies[a]

	RUB	F_{14}-RUB	PF-RUB	
Cyclic voltammetry				
$E_{1/2}^{\text{2nd red}}$		-2.14 ± 0.01[b]	-1.65 ± 0.01	[V]
$E_{1/2}^{\text{red}}$	-2.09 ± 0.01	-1.55 ± 0.01	-0.96 ± 0.03	[V]
$E_{1/2}^{\text{ox}}$	$+0.33 \pm 0.01$	$+0.91 \pm 0.01$	$+1.94$[c]	[V]
$E_{1/2}^{\text{2nd ox}}$	$+1.00 \pm 0.01$	$+1.43 \pm 0.01$		[V]
HOMO and LUMO energies (exp.)				
$E_{\text{LUMO}}^{\text{exp}}$	-3.0	-3.6	-4.1	[eV]
$E_{\text{HOMO}}^{\text{exp}}$	-5.4	-6.0	-7.0[c]	[eV]
Electron affinities and ionization potential (DFT)				
EA_{2-}^{sol}		-2.6	-3.5	[eV]
EA_{-}^{sol}	-2.1	-3.1	-3.9	[eV]
IP_{+}^{sol}	-5.1	-6.0	-6.9	[eV]
IP_{2+}^{sol}	-5.7	-6.5		[eV]
Gap energies				
$E_{\text{gap, CV}}^{\text{exp}}$	2.4	2.4	2.9[c]	[eV]
$E_{\text{gap, CV}}^{\text{DFT}}$	3.0	2.9	3.0	[eV]
$E_{\text{gap, opt}}^{\text{exp}}$	2.3	2.3	2.3	[eV]

[a]Half wave potential values $E_{1/2}^{\text{ox}}$ and $E_{1/2}^{\text{red}}$ derived from cyclic voltammetric experiments in 0.1 M NBu_4PF_6/CH_2Cl_2 at a Pt electrode (ν = 100 mV s^{-1}). All $E_{1/2}$ are vs Fc/Fc^+ and are mean values over several cycles. The resulting $E_{\text{HOMO}}^{\text{exp}}$, $E_{\text{LUMO}}^{\text{exp}}$, and the electrochemical HOMO-LUMO gap $E_{\text{gap,CV}}^{\text{exp}}$ ($= E_{\text{LUMO}}^{\text{exp}} - E_{\text{HOMO}}^{\text{exp}}$) for the three compounds are compared with computed DFT (TZVP/B3LYP) values (see text). For the estimation of the computed LUMO−1 level, a polarization energy $P_{2-} = 4P_{-}$ was used. Values for the optical gap ($E_{\text{gap,opt}}^{\text{exp}}$) obtained from molecules diluted in CH_2Cl_2 are taken from ref 24. [b]Estimated from voltammograms recorded with $\nu \geq 500$ mV s^{-1}. [c]Value of E_{p}^{ox} is used, since the oxidation is chemically irreversible.

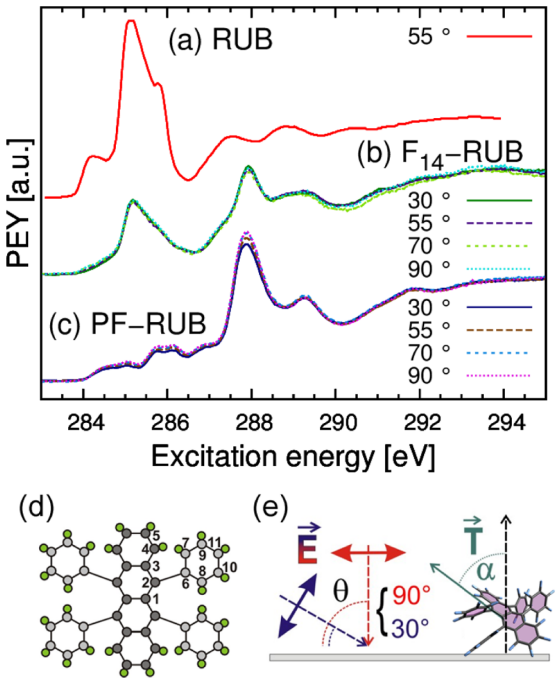

Figure 4. C 1s NEXAFS spectra of (a) RUB, (b) F_{14}-RUB, and (c) PF-RUB taken at different angles of the incident light after several days of exposure to air. The uniformity of the signal intensities at all angles proves the isotropic orientation of the fluorinated molecules in the samples (see text). The data of the unsubstituted RUB was taken from ref 42. (c) Sketch of PF-RUB with indices showing differently coordinated carbon atoms and (d) sketch of experimental setup for the NEXAFS measurements.

or polycrystalline within the film. This is in good agreement with previous results from PF-RUB and F_{14}-RUB thin films.[24,38]

In general, in the absence of a distinct dichroism it cannot directly be discriminated between statistically oriented molecules and molecules with a uniform orientation of 55°,[45] which represents the so-called magic angle where the dichroism disappears.[44] However, since the tetracene backbone and the phenyl side groups exhibit relative twists between each other and both of them yield resonances with different transition dipole moment (TDM) orientation, this allows their individual orientation analysis.[46] Hence, the assumption of a uniform orientation of 55° with respect to the TDM of the tetracene-related excitations would result in a different and distinct dichroism of the phenyl groups. Since, however, constant X-ray absorption is found over the entire energy range, such a situation can safely be ruled out, and the molecules are reliably determined to have no preferential orientation.

In the case of pristine RUB, the NEXAFS spectra were found to be well described by superpositions of the NEXAFS signatures of benzene and tetracene, hence indicating that the electronic system of RUB can be separated into the backbone and side group.[42] Due to the stability of PF-RUB against oxidation, the corresponding spectra can also be analyzed in this form. The NEXAFS resonances at low energies can be correlated to excitations found in pure tetracene, while those at higher energies correspond well to the signature of perfluorobenzene (PF-benzene), cf. Figure 5a.[43] Although the F_{14}-RUB films are only slightly susceptible to oxidation as observed in the optical measurements, a corresponding decomposition of the NEXAFS spectra for F_{14}-RUB is more complicated, since some of the molecules could be significantly modified as it is throughout the case for RUB.[42,47] Indeed, strong modifications of the RUB NEXAFS spectra are observed upon oxidation of corresponding thin films.[48] In particular, the resonances at 284.2 and 285.8 eV (cf. Figure 4a) vanish, leaving behind a major resonance at 285.1 eV.

Upon closer inspection, however, the successful decomposition of PF-RUB into parts resulting from tetracene and perfluorobenzene is surprising. In fact, tetracene is not an ideal choice to be compared to the PF-RUB spectra, since the acene backbone in PF-RUB is significantly altered with respect to pure tetracene. Not only are the carbon atoms at the center position modified in their chemical surrounding due to the attached phenyl side groups (carbon atom 2 and symmetric equivalents in Figure 4), but furthermore is the chemical environment of the carbon atoms 4 and 5 (and the symmetry equivalents) severely changed as a result of the fluorination. The strong electronegativity of the fluorine neighbors leads to an increased ionization potential of the core electrons in these atoms by about 2 eV as it has been found in previous measurements.[35] Following a similar line of argument, also the contributions of the phenyl side groups are expected to differ from pure PF-benzene, which applies particularly to the carbon atoms linked to the tetracene backbone without direct fluorine neighbors. In order to verify these considerations and gain further insights into the actual nature of the signature of the PF-RUB NEXAFS resonances, we performed DFT-computations using the StoBe package,[29] which

DOI: 10.1021/acs.jpcc.5b12293
J. Phys. Chem. C 2016, 120, 5515−5522

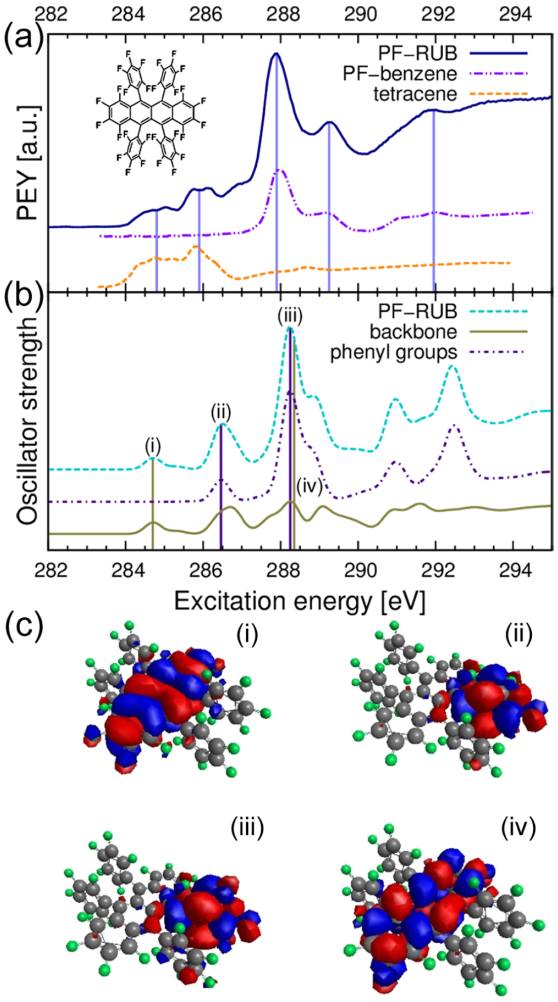

Figure 5. (a) Comparison of the experimental C 1s NEXAFS spectra of PF-RUB, perfluorobenzene (PF-benzene, data taken from ref 43) and tetracene (data taken from ref 42). The spectrum of PF-RUB can be interpreted as a superposition of the latter two. (b) Comparison of the computed spectrum of PF-RUB with separation into the computed contributions from the phenyl groups ((ii) and (iii)) and the tetracene backbone ((i) and (vi)). (c) Visualization of the excited states (i–iv) depicted in (b) showing that the electronic systems of the phenyl groups and the tetracene backbone are strictly separated.

allows the reliable simulation of polycyclic aromatic hydrocarbons and their derivatives.[30] Since in mature PF-RUB thin films molecules with both planar and twisted tetracene backbones may occur,[38] isomers in both D_2 (twisted) and C_{2h} (planar) symmetry[10,42] were considered for the computations. As these results show that the computed spectra of the different species are virtually identical (for details see the Supporting Information), we do not distinguish between the different conformations in the following.

As presented in Figure 5b, the computed spectrum (cyan dashed curve) corresponds nicely to the experiment in Figure 5a. Since oxidation of RUB was shown to significantly modify the NEXAFS signature,[42,48] the remarkably good agreement between experiment and theory supports our finding that the PF-RUB films are stable against oxidation.

Since the computed spectrum represents the sum of all 11 partial NEXAFS spectra for the inequivalent individual excitation centers (i.e., carbon atoms), this data can be easily separated into one spectrum representing the contributions from carbon atoms in the phenyl rings (purple dashed curve) and another one with the peaks corresponding to excitation centers in the tetracene backbone (olive curve). This analysis shows that the resonances at lowest energy (284.5–285 eV) indeed result from excitations of carbon atoms in the tetracene backbone. Also the electron density in the corresponding final states is almost completely localized in the tetracene backbone while no appreciable density is found in the phenyl groups (cf. Figure 5c (i)). In the region of the second-lowest peak, however, not only contributions from excitations of tetracene core electrons but also from the innermost carbon atom of the phenyl side groups (carbon atom 6) are found. Moreover, even the strongest resonance at about 288.2 eV embraces individual resonances from both, the phenyl groups and the tetracene backbone (cf. Figure 5c (iii, iv) and Supporting Information), showing that the afore discussed very simple interpretation of the resonances based on isolated tetracene and PF-benzene spectra is not sufficient. Interestingly, the excitations of the carbon atoms in the phenyl groups at 286.3 and 288.2 eV end up in an equivalent final molecular orbital as visualized in Figure 5c (ii), (iii), hence demonstrating that the energetic difference between both resonances directly results from the aforementioned chemical shift between the carbon atoms 6 and 7–11. As shown exemplarily for the excited states presented in Figure 5c, the electron density is strictly limited to either the backbone or the phenyl groups depending on the respective excitation centers, demonstrating that the electronic systems of the molecular subunits are indeed decoupled from each other.

CONCLUSION

In summary, we have investigated partially fluorinated (F_{14}-RUB) and perfluorinated rubrene (PF-RUB) in thin films and solution with respect to their stability against oxidation. As we observe by real-time absorption experiments of thin films that were exposed to air for several hours, both the partially fluorinated F_{14}-RUB and the fully fluorinated PF-RUB are much more stable against oxygen than unsubstituted rubrene. Moreover, using NEXAFS spectroscopy combined with DFT computations we have analyzed the electronic structure and thin film orientation particularly of PF-RUB and we show that the molecules have not undergone a chemical reaction with oxygen. While oxidation of the thin films through oxygen has been investigated in the solid state, the electrochemical behavior (oxidation/reduction) in solution has been examined by cyclic voltammetric measurements. In addition, we further investigated the reduction and oxidation potentials of the three compounds in solution by comparison with DFT calculations. Both, experiments in the solid state and in solution show that the fully fluorinated PF-RUB is much more and the partially fluorinated F_{14}-RUB is considerably more stable than RUB, due to an increased oxidation potential. A systematic tunability of the oxidation potential depending on the degree of fluorination is in good agreement with observations from other rubrene derivatives with less fluorine.[16,17]

As a consequence, we believe that both fluorinated rubrene derivatives are promising candidates as an alternative to unsubstituted rubrene (RUB) in terms of stability against

DOI: 10.1021/acs.jpcc.5b12293
J. Phys. Chem. C 2016, 120, 5515–5522

photooxidation processes in organic electronics, since both F_{14}-RUB and PF-RUB have sterical and optical properties that are very similar to RUB. Hence, it would be vitally important to measure the transport properties of the fluoriated rubrenes in order to investigate whether these new compounds show similarly high charge carrier mobilities.[2,3] By now, it can be speculated that, due to their reduced susceptibility to oxygen, devices made of fluorinated rubrene would require less protection against ambient influence than common RUB devices.

■ ASSOCIATED CONTENT

Supporting Information

The Supporting Information is available free of charge on the ACS Publications website at DOI: 10.1021/acs.jpcc.5b12293.

Anodic cyclic voltammograms of RUB recorded with different scan rates (potential window of −0.34 to +1.26 V); cathodic cyclic voltammograms of F_{14}-RUB recorded with different scan rates (potential window of −0.35 to −2.45 V); computed NEXAFS spectra of PF-RUB for twisted and planar configuration; individual resonances of the spectrum computed for the planar geometry (PDF)

■ AUTHOR INFORMATION

Corresponding Author

*E-mail: Frank.Schreiber@uni-tuebingen.de.

Present Address

⊥Analytische Chemie, Ruhr-Universität-Bochum, Universitätsstr. 150, 44780 Bochum, Germany.

Notes

The authors declare no competing financial interest.

■ ACKNOWLEDGMENTS

We thank T. Suzuki for providing the material (F_{14}-RUB and PF-RUB). We gratefully thank the bwGRiD project[49] for the computational resources. We acknowledge the Helmholtz-Zentrum Berlin - Electron storage ring BESSY II for provision of synchrotron radiation at beamline HE-SGM. Furthermore, the DFG is acknowledged for funding within the Emmy Noether program.

■ REFERENCES

(1) Briseno, A. L.; Mannsfeld, S. C. B.; Ling, M. M.; Liu, S.; Tseng, R. J.; Reese, C.; Roberts, M. E.; Yang, Y.; Wudl, F.; Bao, Z. Patterning Organic Single-crystal Transistor Arrays. *Nature* **2006**, *444*, 913−917.

(2) Podzorov, V.; Menard, E.; Borissov, A.; Kiryukhin, V.; Rogers, J. A.; Gershenson, M. E. Intrinsic Charge Transport on the Surface of Organic Semiconductors. *Phys. Rev. Lett.* **2004**, *93*, 086602.

(3) Sundar, V. C.; Zaumseil, J.; Podzorov, V.; Menard, E.; Willett, R. L.; Someya, T.; Gershenson, M. E.; Rogers, J. A. Elastomeric Transistor Stamps: Reversible Probing of Charge Transport in Organic Crystals. *Science* **2004**, *303*, 1644−1646.

(4) Takeya, J.; Yamagishi, M.; Tominari, Y.; Hirahara, R.; Nakazawa, Y.; Nishikawa, T.; Kawase, T.; Shimoda, T.; Ogawa, S. Very High-Mobility Organic Single-Crystal Transistors with in-Crystal Conduction Channels. *Appl. Phys. Lett.* **2007**, *90*, 102120.

(5) Takeya, J.; Kato, J.; Hara, K.; Yamagishi, M.; Hirahara, R.; Yamada, K.; Nakazawa, Y.; Ikehata, S.; Tsukagoshi, K.; Aoyagi, Y.; et al. In-Crystal and Surface Charge Transport of Electric-Field-Induced Carriers in Organic Single-Crystal Semiconductors. *Phys. Rev. Lett.* **2007**, *98*, 196804.

(6) Podzorov, V.; Menard, E.; Pereversev, S.; Yakshinsky, B.; Madey, T.; Rogers, J. A.; Gershenson, M. E. Interaction of Organic Surfaces with Active Species in the High-vacuum Environment. *Appl. Phys. Lett.* **2005**, *87*, 093505.

(7) Bowen, E. J.; Steadman, F. 233. The Photo-oxidation of Rubrene. *J. Chem. Soc.* **1934**, 1098−1101.

(8) Nakayama, Y.; Machida, S.; Minari, T.; Tsukagishi, K.; Noguchi, Y.; Ishii, H. Direct Observation of the Electronic States of Single Crystalline Rubrene under Ambient Condition by Photoelectron Yield Spectroscopy. *Appl. Phys. Lett.* **2008**, *93*, 173305.

(9) Helou, M. E.; Medenbach, O.; Witte, G. Rubrene Microcrystals: A Route to Investigate Surface Morphology and Bulk Anisotropies of Organic Semiconductors. *Cryst. Growth Des.* **2010**, *10*, 3496−3501.

(10) Käfer, D.; Witte, G. Growth of Crystalline Rubrene Films with Enhanced Stability. *Phys. Chem. Chem. Phys.* **2005**, *7*, 2850−2853.

(11) Kowarik, S.; Gerlach, A.; Sellner, S.; Schreiber, F.; Pflaum, J.; Cavalcanti, L.; Konovalov, O. Anomalous Roughness Evolution of Rubrene Thin Films Observed in Real Time during Growth. *Phys. Chem. Chem. Phys.* **2006**, *8*, 1834−1836.

(12) McGarry, K. A.; Xie, W.; Sutton, C.; Risko, C.; Wu, Y.; Young, V. G.; Brédas, J.-L.; Frisbie, C. D.; Douglas, C. J. Rubrene-Based Single-Crystal Organic Semiconductors: Synthesis, Electronic Structure, and Charge-Transport Properties. *Chem. Mater.* **2013**, *25*, 2254−2263.

(13) Mamada, M.; Katagiri, H.; Sakanoue, T.; Tokito, S. Characterization of New Rubrene Analogues with Heteroaryl Substituents. *Cryst. Growth Des.* **2015**, *15*, 442−448.

(14) Uttiya, S.; Miozzo, L.; Fumagalli, E. M.; Bergantin, S.; Ruffo, R.; Parravicini, M.; Papagni, A.; Moret, M.; Sassella, A. Connecting Molecule Oxidation to Single Crystal Structural and Charge Transport Properties in Rubrene Derivatives. *J. Mater. Chem. C* **2014**, *2*, 4147−4155.

(15) Zhang, X.; Sørensen, J. K.; Fu, X.; Zhen, Y.; Zhao, G.; Jiang, L.; Dong, H.; Liu, J.; Shuai, Z.; Geng, H.; et al. Rubrene Analogues with the Aggregation-induced Emission Enhancement Behaviour. *J. Mater. Chem. C* **2014**, *2*, 884−890.

(16) Paraskar, A. S.; Reddy, A. R.; Patra, A.; Wijsboom, Y. H.; Gidron, O.; Shimon, L. J. W.; Leitus, G.; Bendikov, M. Rubrenes Planar and Twisted. *Chem. - Eur. J.* **2008**, *14*, 10639−10647.

(17) Uttiya, S.; Raimondo, L.; Campione, M.; Miozzo, L.; Yassar, A.; Moret, M.; Fumagalli, E.; Borghesi, A.; Sassella, A. Stability to Photo-Oxidation of Rubrene and Fluorine-Substituted Rubrene. *Synth. Met.* **2012**, *161*, 2603−2606.

(18) Mullenbach, T. K.; McGarry, K. A.; Luhman, W. A.; Douglas, C. J.; Holmes, R. J. Connecting Molecular Structure and Exciton Diffusion Length in Rubrene Derivatives. *Adv. Mater.* **2013**, *25*, 3689−3693.

(19) Hinderhofer, A.; Heinemeyer, U.; Gerlach, A.; Kowarik, S.; Jacobs, R. M. J.; Sakamoto, Y.; Suzuki, T.; Schreiber, F. Optical Properties of Pentacene and Perfluoropentacene Thin Films. *J. Chem. Phys.* **2007**, *127*, 194705.

(20) Kowarik, S.; Gerlach, A.; Hinderhofer, A.; Milita, S.; Borgatti, F.; Zontone, F.; Suzuki, T.; Biscarini, F.; Schreiber, F. Structure, Morphology, and Growth Dynamics of Perfluoro-pentacene Thin Films. *Phys. Status Solidi RRL* **2008**, *2*, 120−122.

(21) Duhm, S.; Hosoumi, S.; Salzmann, I.; Gerlach, A.; Oehzelt, M.; Wedl, B.; Lee, T.-L.; Schreiber, F.; Koch, N.; Ueno, N.; et al. Influence of Intramolecular Polar Bonds on Interface Energetics in Perfluoropentacene on Ag(111). *Phys. Rev. B: Condens. Matter Mater. Phys.* **2010**, *81*, 045418.

(22) Koch, N.; Gerlach, A.; Duhm, S.; Glowatzki, H.; Heimel, G.; Vollmer, A.; Sakamoto, Y.; Suzuki, T.; Zegenhagen, J.; Rabe, J. P.; et al. Adsorption Induced Intramolecular Dipole: Correlating Molecular Conformation and Interface Electronic Structure. *J. Am. Chem. Soc.* **2008**, *130*, 7300−7304.

(23) Anger, F.; Ossó, J. O.; Heinemeyer, U.; Broch, K.; Scholz, R.; Gerlach, A.; Schreiber, F. Photoluminescence Spectroscopy of Pure Pentacene, Perfluoropentacene, and Mixed Thin Films. *J. Chem. Phys.* **2012**, *136*, 054701.

(24) Anger, F.; Scholz, R.; Adamski, E.; Broch, K.; Gerlach, A.; Sakamoto, Y.; Suzuki, T.; Schreiber, F. Optical Properties of Fully and Partially Fluorinated Rubrene in Films and Solution. *Appl. Phys. Lett.* **2013**, *102*, 013308.

DOI: 10.1021/acs.jpcc.5b12293
J. Phys. Chem. C 2016, 120, 5515−5522

(25) Suzuki, T.; Sakamoto, Y. *Development of Organic Semiconductors for Molecular Thin-Film Devices*; Institute for Molecular Science: Myodaiji, Japan, 2013; pp 84−85.
(26) Gritzner, G.; Kůta, J. Recommendations on Reporting Electrode Potentials in Nonaqueous Solvents (Recommendations 1983). *Pure Appl. Chem.* **1984**, *56*, 461−466.
(27) TURBOMOLE V6.4 2012, a development of University of Karlsruhe and Forschungszentrum Karlsruhe GmbH, 1989−2007, TURBOMOLE GmbH, since 2007; available from http://www.turbomole.com.
(28) Kytka, M.; Gerlach, A.; Kováč, J.; Schreiber, F. Real-time Observation of Oxidation and Photo-oxidation of Rubrene Thin Films by Spectroscopic Ellipsometry. *Appl. Phys. Lett.* **2007**, *90*, 131911.
(29) Hermann, K., Pettersson, L. G. M., Casida, M. E., Daul, C., Goursot, A., Koester, A., Proynov, E., St-Amant, A., Salahub, D. R. Contributing authors: Carravetta, V., Duarte, H., Friedrich, C., Godbout, N., Guan, J., Jamorski, C., Leboeuf, M., Leetmaa, M., Nyberg, M., Patchkovskii, S., Pedocchi, L., Sim, F., Triguero, L., Vela, A. StoBe-deMon version 3.2, 2013.
(30) Klues, M.; Hermann, K.; Witte, G. Analysis of the Near-edge X-ray-absorption Fine-structure of Anthracene: A Combined Theoretical and Experimental Study. *J. Chem. Phys.* **2014**, *140*, 014302.
(31) Heinze, J. Cyclic Voltammetry-"Electrochemical Spectroscopy". *Angew. Chem., Int. Ed. Engl.* **1984**, *23*, 831−847.
(32) Cardona, C. M.; Li, W.; Kaifer, A. E.; Stockdale, D.; Bazan, G. C. Electrochemical Considerations for Determining Absolute Frontier Orbital Energy Levels of Conjugated Polymers for Solar Cell Applications. *Adv. Mater.* **2011**, *23*, 2367−2371.
(33) Kapturkiewicz, A. Solvent and Temperature Control of the Reaction Mechanism and Efficiency in the Electrogenerated Chemiluminescence of Rubrene. *J. Electroanal. Chem.* **1994**, *372*, 101−116.
(34) Yamaguchi, Y. Effects of Fluorination on Electronic and Excited States of Fused Zinc Oligoporphyrins. *J. Chem. Phys.* **2005**, *122*, 184702.
(35) Anger, F.; Glowatzki, H.; Franco-Cañellas, A.; Bürker, C.; Gerlach, A.; Scholz, R.; Sakamoto, Y.; Suzuki, T.; Koch, N.; Schreiber, F. Interface Dipole and Growth Mode of Partially and Fully Fluorinated Rubrene on Au(111) and Ag(111). *J. Phys. Chem. C* **2015**, *119*, 6769−6776.
(36) Sakamoto, Y.; Suzuki, T.; Kobayashi, M.; Gao, Y.; Inoue, Y.; Tokito, S. Perfluoropentacene and Perfluorotetracene: Syntheses, Crystal Structures, and FET Characteristics. *Mol. Cryst. Liq. Cryst.* **2006**, *444*, 225−232.
(37) Harada, Y.; Takahashi, T.; Fujisawa, S.; Kajiwara, T. Application of Photoelectron Spectroscopy to the Study of Photochemical Reactions of Solids. Photooxidation of Rubrene (5,6,11,12-tetraphenylnaphthacene). *Chem. Phys. Lett.* **1979**, *62*, 283−286.
(38) Anger, F.; Scholz, R.; Gerlach, A.; Schreiber, F. Vibrational Modes and Changing Molecular Conformation of Perfluororubrene in Thin Films and Solution. *J. Chem. Phys.* **2015**, *142*, 224703.
(39) Hill, I. G.; Kahn, A.; Soos, Z. G.; Pascal, R. A., Jr. Charge-separation Energy in Films of π-conjugated Organic Molecules. *Chem. Phys. Lett.* **2000**, *327*, 181−188.
(40) Scholz, R.; Luschtinetz, R.; Seifert, G.; Jägeler-Hoheisel, T.; Körner, C.; Leo, K.; Rapacioli, M. Quantifying Charge Transfer Energies at Donor-acceptor Interfaces in Small-molecule Solar Cells with Constrained DFTB and Spectroscopic Methods. *J. Phys.: Condens. Matter* **2013**, *25*, 473201.
(41) Hofmann, S.; Hummert, M.; Scholz, R.; Luschtinetz, R.; Murawski, C.; Will, P.-A.; Hintschich, S. I.; Alex, J.; Jankus, V.; Monkman, A. P.; et al. Engineering Blue Fluorescent Bulk Emitters for OLEDs: Triplet Harvesting by Green Phosphors. *Chem. Mater.* **2014**, *26*, 2414−2426.
(42) Käfer, D.; Ruppel, L.; Witte, G.; Wöll, C. Role of Molecular Conformations in Rubrene Thin Film Growth. *Phys. Rev. Lett.* **2005**, *95*, 166602.
(43) Vijayalakshmi, S.; Föhlisch, A.; Kirchmann, P.; Hennies, F.; Pietzsch, A.; Nagasono, M.; Wurth, W. Bond Polarization and Image-potential Screening in Adsorbed C_6F_6 on Cu(111). *Surf. Sci.* **2006**, *600*, 4972−4977.
(44) Breuer, T.; Klues, M.; Witte, G. Characterization of Orientational Order in π-conjugated Molecular Thin Films by NEXAFS. *J. Electron Spectrosc. Relat. Phenom.* **2015**, *204*, 102−115.
(45) Stöhr, J., Ed.; *NEXAFS Spectroscopy*; Springer-Verlag: Berlin, 1992.
(46) Wang, L.; Chen, S.; Liu, L.; Qi, D.; Gao, X.; Subbiah, J.; Swaminathan, S.; Wee, A. T. S. Conformational Degree and Molecular Orientation in Rubrene Film by in Situ X-ray Absorption Spectroscopy. *J. Appl. Phys.* **2007**, *102*, 063504.
(47) Song, X.; Wang, L.; Fan, Q.; Wu, Y.; Wang, H.; Liu, C.; Liu, N.; Zhu, J.; Qi, D.; Gao, X.; et al. Role of Oxygen Incorporation in Electronic Properties of Rubrene Films. *Appl. Phys. Lett.* **2010**, *97*, 032106.
(48) Sinha, S.; Wang, C.-H.; Mukherjee, M.; Mukherjee, T.; Yang, Y.-W. Oxidation of Rubrene Thin Films: An Electronic Structure Study. *Langmuir* **2014**, *30*, 15433−15441.
(49) bwGRiD (http://www.bw-grid.de), member of the German D-Grid initiative, funded by the Ministry for Education and Research (Bundesministerium für Bildung und Forschung) and the Ministry for Science, Research and Arts Baden-Württemberg (Ministerium für Wissenschaft, Forschung und Kunst Baden-Württemberg).

DOI: 10.1021/acs.jpcc.5b12293
J. Phys. Chem. C 2016, 120, 5515−5522

Supporting Information

Enhanced Stability of Rubrene against Oxidation by Partial and Complete Fluorination

F. Anger,[1] T. Breuer,[2] A. Ruff,[3,4] M. Klues,[2] A. Gerlach,[1] R. Scholz,[5] S. Ludwigs,[3] G. Witte,[2] and F. Schreiber[1]

[1] *Institut für Angewandte Physik, Universität Tübingen, 72076 Tübingen, Germany*
[2] *Fachbereich Physik, Universität Marburg, 35032 Marburg, Germany*
[3] *Institut für Polymerchemie (IPOC), Universität Stuttgart, 70569 Stuttgart, Germany*
[4] *present address: Analytische Chemie, Ruhr-Universität-Bochum, 44780 Bochum, Germany*
[5] *Institut für Angewandte Photophysik, TU Dresden, 01069 Dresden, Germany*

(Dated: February 1, 2016)

I. CYCLIC VOLTAMMETRY

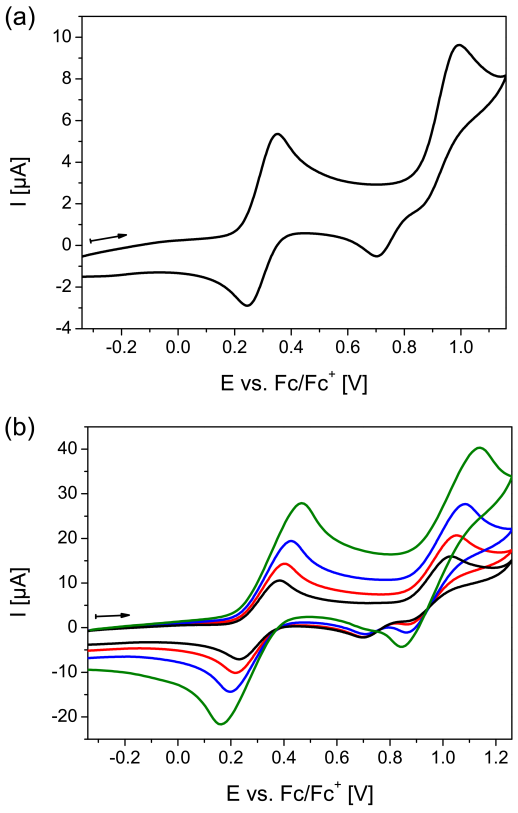

Figure S1. Anodic cyclic voltammograms of RUB (c = 2.6 mM) in 0.1 M NBu_4PF_6/CH_2Cl_2 at Pt recorded with different scan rates in a potential window of −0.34 to +1.26 V. (a) black line = 100 mV s^{-1}. (b) black line = 500 mV s^{-1}, red line = 1000 mV s^{-1}, blue line = 2000 mV s^{-1} and green line = 5000 mV s^{-1}. The voltammograms are not background corrected.

At potentials above 0.5 V, a second chemically irreversible oxidation wave located at around +1.0 V is observed for RUB (Fig. S1a). In the backward scan a weak reduction signal at ∼ +0.7 V appears. We attribute this peak to the reduction of products formed in follow up reactions that are coupled to the second oxidation. At higher scan rates ($v \geq 1000$ mV s^{-1}) the peak current of the signal at +0.7 V decreases and the second oxidation becomes chemically reversible (Fig. S1b). Thus, the follow up reactions seem to be slow and within the time scale of the cyclic voltammetric experiment.

For F_{14}-RUB the electron transfer reaction at −2.15 V becomes chemically reversible for scan rates $v \geq$ 500 mV s^{-1} (Fig. S2). Nevertheless, the corresponding peak current of the re-oxidation peak in the backward scan remains low. We observe a weak oxidation wave at around −1.2 V which indicates products from follow up reactions that are coupled to the second reduction.

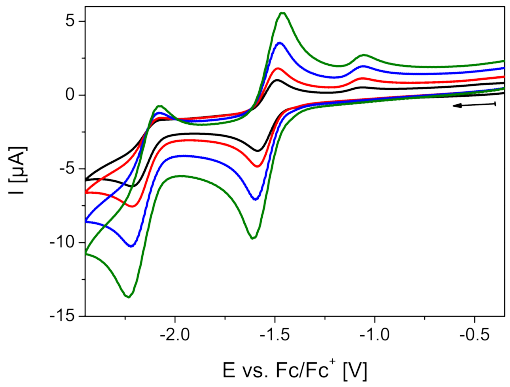

Figure S2. Cathodic cyclic voltammograms of F_{14}-RUB (c = 1.4 mM) in 0.1 M NBu_4PF_6/CH_2Cl_2 at Pt recorded in a potential window of −0.35 to −2.45 V with different scan rates. Black line = 100 mV s^{-1}, red line = 200 mV s^{-1}, blue line = 500 mV s^{-1} and green line = 1000 mV s^{-1}. The voltammograms are not background corrected

II. NEXAFS

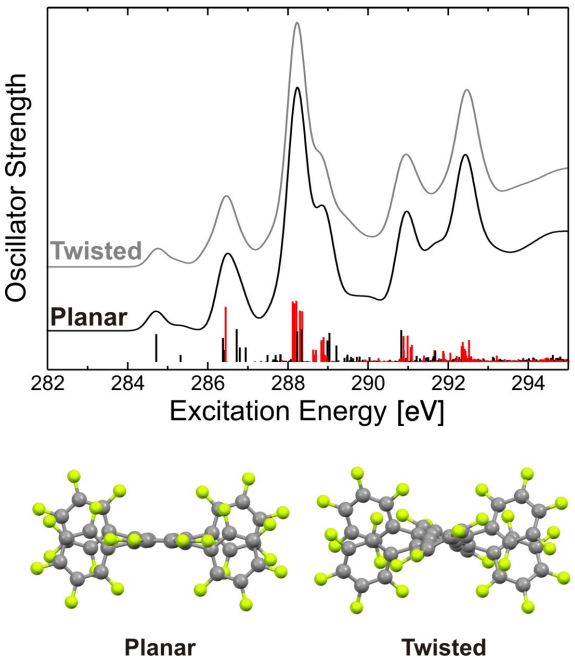

Figure S3. Computed NEXAFS spectra of PF-RUB for twisted and planar configuration of the tetracene backbone (visualized in bottom panel). In the top panel additionally all individual resonances of the spectrum computed for the planar geometry are presented (black: excitation center in the tetracene backbone, red: in the phenyl rings)

For the unsubstituted rubrene it has been observed that the molecules exhibit significant twist in the gas phase and in amorphous thin films, while the backbone is planarized in the crystalline phase [1,2]. As reported recently, in contrast to RUB for PF-RUB thin film phases with both planar and twisted tetracene backbone are possible [3]. Hence PF-RUB molecules in twisted D_2 and planar C_{2h} symmteries have been considered for the NEXFAS computations. However, as it turns out the spectra of the two different isomers with planar and twisted backbone are virtually identical (Fig. S3). In addition, a visualization of all contributing NEXAFS resonances combined with the origin of their respective excitation centers (either tetracene backbone or phenyl rings) is presented in this figure as vertical bars.

[1] Käfer, D.; Ruppel, L.; Witte, G.; Wöll, C. Role of Molecular Conformations in Rubrene Thin Film Growth. *Phys. Rev. Lett.* **2005**, *95*, 166602.

[2] Käfer, D.; Witte, G. Growth of Crystalline Rubrene Films with Enhanced Stability. *Phys. Chem. Chem. Phys.* **2005**, *7*, 2850.

[3] Anger, F.; Scholz, R.; Gerlach, A.; Schreiber, F. Vibrational Modes and Changing Molecular Conformation of Perfluororubrene in Thin Films and Solution. *J. Chem. Phys.* **2015**, *142*, 224703.

5.5 Self-assembly of partially fluorinated hexabenzocoronene derivatives in the solid state

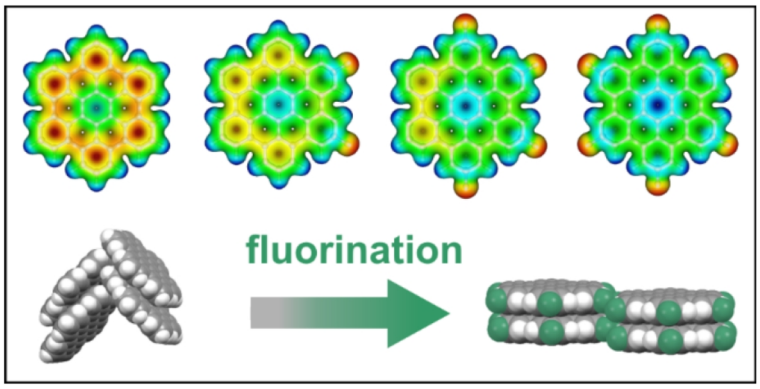

Artikel hat zum Zeitpunkt des Drucks den Status „Just Accepted“ im Journal *Physical Chemistry Chemical Physics*.

5.5.1 Inhaltsangabe

We report on the synthesis and structural characterization of novel, partially fluorinated hexabenzocoronene (HBC) derivatives. Fluorination of polycyclic aromatic hydrocarbons (PAHs) is a well-established method to enhance the stability of organic semiconductors (OSCs) and render them n-type. For HBC it has been observed that fluorination leads to a modification of the molecular packing motif from a herringbone arrangement to a parallel-packed motif. Here, we study whether this transformation of the molecular packing is also found for the partially fluorinated HBCs 2,5-difluoro-hexaperi-hexabenzocoronene (F_2HBC) and 2,5,8,11-tetrafluoro-peri-hexabenzocoronene (F_4HBC). Combining powder diffraction and NEXAFS dichroism measurements, we reveal that indeed all partially fluorinated compounds adopt a parallel molecular packing, hence maximizing the intermolecular contact area. We identify fluorine-hydrogen bonds as mediating driving force to specifically stabilize this molecular arrangement and direct self-assembly. Furthermore, we show that the relative orientation of the HBCs on the underlying surface can be precisely controlled by varying substrate materials. Finally, the energetic states of the compounds are analyzed by photoelectron spectroscopy, optical spectroscopy and density functional theory to identify the effects of fluorination on these fundamental electronic characteristics.

5.5.2 Eigenleistung

Die Berechnung der elektrostatischen Konturen, Dipolmomente und Energieniveaus, ebenso wie die Hirshfeldanalyse wurden von mir vorgenommen. Im Rahmen der Interpretation dieser Daten wurde die Bedeutung der H-F-Kontakte für die Bildung planarer Packungsmotive von mir herausgearbeitet, womit ich eine der Kernaussagen des Artikels beigetragen habe. Zudem war ich an der Durchführung der NEXAFS-Experimente in Form von Probenpräparation und Messung beteiligt. Die graphische Aufbereitung der Ergebnisse,

sowie das Verfassen der zugehörigen Textpassagen erfolgte in Zusammenarbeit mit Tobias Breuer und Gregor Witte, die die entsprechenden Inhalte in den Gesamtkontext des Artikels eingefügt haben.

PCCP

ARTICLE

Self-assembly of partially fluorinated hexabenzocoronene derivatives in the solid state

Received 00th January 20xx,
Accepted 00th January 20xx

DOI: 10.1039/x0xx00000x

www.rsc.org/

Tobias Breuer*[a], Michael Klues[a], Pauline Liesfeld[b], Andreas Viertel[b], Matthias Conrad[c], Stefan Hecht[b] and Gregor Witte[a]

We report on the synthesis and structural characterization of novel, partially fluorinated hexabenzocoronene (HBC) derivatives. Fluorination of polycyclic aromatic hydrocarbons (PAHs) is a well-established method to enhance the stability of organic semiconductors (OSCs) and render them n-type. For HBC it has been observed that fluorination leads to a modification of the molecular packing motif from a herringbone arrangement to a parallel-packed motif. Here, we study whether this transformation of the molecular packing is also found for the partially fluorinated HBCs 2,5-difluoro-hexa-peri-hexabenzocoronene (F_2HBC) and 2,5,8,11-tetrafluoro-peri-hexabenzocoronene (F_4HBC). Combining powder diffraction and NEXAFS dichroism measurements, we reveal that indeed all partially fluorinated compounds adopt a parallel molecular packing, hence maximizing the intermolecular contact area. We identify fluorine-hydrogen bonds as mediating driving force to specifically stabilize this molecular arrangement and direct self-assembly. Furthermore, we show that the relative orientation of the HBCs on the underlying surface can be precisely controlled by varying substrate materials. Finally, the energetic states of the compounds are analyzed by photoelectron spectroscopy, optical spectroscopy and density functional theory to identify the effects of fluorination on these fundamental electronic characteristics.

1 Introduction

Due to their promising potential for low-cost and tuneable future optoelectronic devices like light emitting diodes (OLED)[1,2] and solar cells (OPV)[3-5] as well as OFETs,[6,7] the investigation of organic semiconductors (OSC) and dyes has strongly gained attention over the last decade.[8,9] While organic synthesis has allowed developing new compounds, numerous studies have focused on the synthesis and characterization of a wide variety of OSCs to correlate their structures with their electronic properties.

One very important relationship is the dependence of the electronic transport characteristics on the structural packing motif of an OSC in the solid state.[10] This is because the relative overlap of the molecular orbitals, as quantified by the electronic transfer integrals, is directly determined by the relative arrangement and distance between neighbouring molecules. Therefore, different packing motifs, e.g. (slip-stacked) parallel, "π-stacked" arrangements on the one hand side and staggered, "herringbone-like" arrangements on the other hand side may yield largely different charge carrier mobilities[11,12] and optoelectronic coupling.[13]

This complicated and hardly predictable interplay also explains why the virtually straightforward functionalization of OSCs is frequently not as effective as expected. The adopted packing motifs of an initial compound may strongly differ from that of the functionalized derivative, hence complicating their reliable comparison.[14]

Among the OSCs, extended planar aromatic hydrocarbons (PAHs) play an important role. An interesting example is hexa-peri-hexabenzocoronene (HBC, $C_{42}H_{18}$) which can be viewed as a molecular version of graphene, therefore commonly denoted as nanographene.[15-18] This compound provides a rather large charge carrier mobility combined with high thermal and

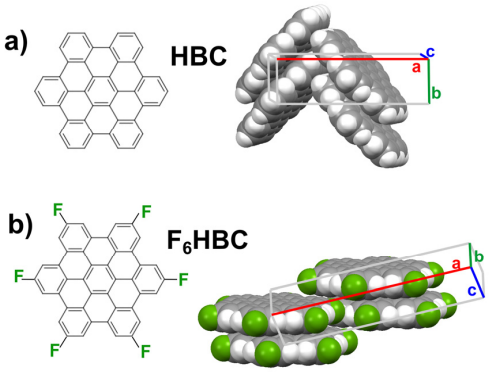

Fig. 1 Comparison of packing motifs in the crystal structures of a) HBC[19] and b) F_6HBC[20].

[a] Fachbereich Physik, Universität Marburg, Renthof 7, 35032 Marburg, Germany. *E-Mail: tobias.breuer@physik.uni-marburg.de
[b] Department of Chemistry, Humboldt-Universität zu Berlin, 12489 Berlin, Germany
[c] Fachbereich Chemie, Universität Marburg, Renthof 7, 35032 Marburg, Germany

† Electronic Supplementary Information (ESI) available: Additional information on the synthesis and supporting measurements (full sets of all NEXAFS measurements). See DOI: 10.1039/x0xx00000x

chemical stability as well as a high threshold for radiation damage, hence rendering it an interesting candidate for the precise investigation of fundamental properties of organic semiconductor physics and the potential application in devices.[21] In solid form, HBC crystallizes in a herringbone-like arrangement, where the molecules are staggered nearly orthogonally (cf. Fig. 1a).[19] By introducing side-groups like alkyl chains, this interlaced molecular arrangement can, however, be modified and columnar molecular packing is achieved.[15,22] These columnar alignments also show evidence for band-like transport along the stacking direction.[23,24] Yet, this approach of controlling the molecular packing is accompanied by the presence of rather large isolating spacer units between the HBC cores, which decrease the intercolumnar packing density.

To also change the major carrier type of OSCs, fluorination is a widely applied method allowing for the conversion of a p-type OSC into an n-type semiconductor.[25] In fact, symmetrical fluorination of HBC has been reported and yields a stable PAH, denoted as F_6HBC (2,5,8,11,14,17-hexafluoro-hexa-peri-hexabenzocoronene), which indeed shows considerable electron transport.[20,26,27] Interestingly, this electronic modification also changes the crystalline packing motif: the former herringbone-like packing motif of HBC is transformed into a parallel stacking in F_6HBC crystals (cf. Fig. 1b).[20] The absence of insulating spacer chains in this case also yields a dense intercolumnar packing.

In this study we investigate whether this approach is also successful for reduced degrees of fluorination of the HBC core. Therefore, we present the synthesis and structural characterization of HBC derivatives with fluorination degrees between that of HBC and F_6HBC. In particular, we have processed 2,5-difluoro-hexa-peri-hexabenzocoronene (F_2HBC) and 2,5,8,11-tetrafluoro-peri-hexabenzocoronene (F_4HBC). To provide a complementary picture, not only the crystal structures, but also the fundamental electronic characteristics, regarding both, the unoccupied electronic levels as well as transitions between the frontier orbitals are compared. Since the structure of processed organic thin films, as required in potential device applications, also strongly depends on the choice of the supporting substrate, thin films have been prepared on different substrates. For this purpose, we have compared films grown on oxidized silicon wafers and graphene substrates, on which the parent HBC has been shown to adopt different molecular orientations.[28]

2 Experimental

The previously unknown partially fluorinated HBC derivatives F_2HBC and F_4HBC were prepared adopting known literature procedures.[29] Synthetic details and compounds characterization data are provided in the Electronic Supplementary Information.†

All thin films have been prepared by organic molecular beam deposition under high vacuum conditions onto oxidized silicon wafers and transparent, graphene-coated quartz substrates (Graphenea, Spain) which enable also optical studies in transmission geometry. The film growth rates were monitored by a quartz crystal microbalance and the films were processed at rates of about 6 Å min^{-1} to a total thickness of 20 nm, if not otherwise stated.

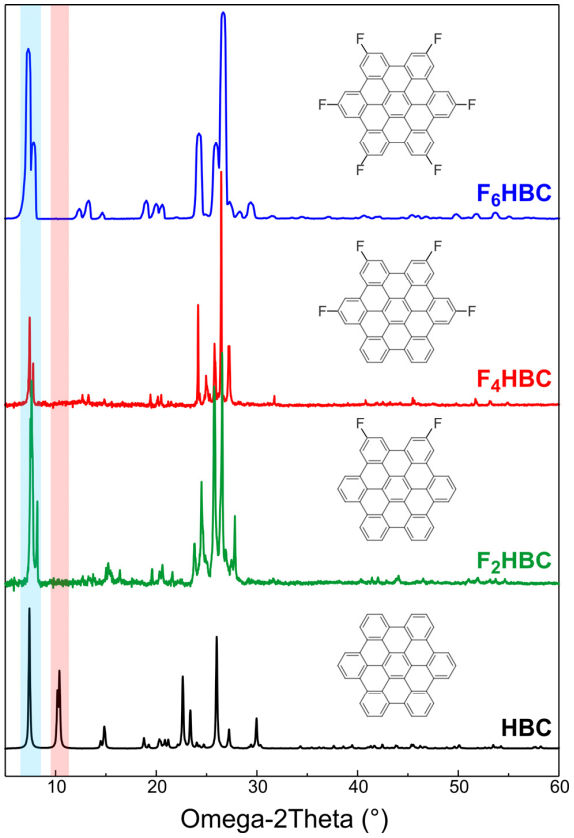

Fig. 2 Powder diffractograms of F_6HBC[20], F_4HBC, F_2HBC, and HBC[19]. All diffractograms were acquired using Cu-Kα radiation. The high similarity between the F_2HBC, F_4HBC and F_6HBC diffractograms are in contrast to the distinctly different diffractogram of pure HBC (the strongest differences are found in the regions which are highlighted by the colored boxes).

X-ray diffraction was utilized to characterize crystalline structure of the thin films with a Bruker D8 Discovery diffractometer using Cu Kα radiation and a UV/Vis spectrophotometer (Agilent 8453) was employed to characterize the optical properties of the films. The unit cell parameters were derived from the XRD powder data using the winXPOW software package (version 3.07, STOE (Germany), 2015)

NEXAFS measurements were performed at the HE-SGM dipole beam line of the synchrotron storage ring BESSY II in Berlin (Germany) in partial electron-yield (PEY) mode using a retarding field of -150 V. Further information on the experimental details and data analysis are provided in Ref. 30.

DFT ground state calculations were carried out with the US Gamess code[31,32] using the B3LYP hybrid functional and a 6-311G(d,p) basis set. Molecular electrostatic potential (MEP) plots were visualized with Molekel[33] at an isovalue of 0.02au

for the electron density. Hirshfeld surface analyses were performed using the CrystalExplorer software package.[34, 35]

3 Results and Discussion

A Crystal Packing Motifs

In Fig. 2, powder diffractograms of the partially fluorinated HBCs are compared to that of the parent HBC and F_6HBC. Clearly, the powder patterns of all fluorinated compounds (F_2HBC, F_4HBC, F_6HBC) are qualitatively rather similar and in particular different from that of the non-fluorinated HBC (black curve). For example, two signals are found at low angles ($2\theta<10°$, blue-shaded area) for the fluorinated HBCs, but only one is present for the non-fluorinated one. In contrast, two reflexes are found for HBC slightly above $2\theta=10°$, while there is no corresponding intensity for the fluorinated compounds (red-shaded area). This similarity between the powder diffractograms of F_2HBC, F_4HBC, and F_6HBC indicates that also for F_2HBC and F_4HBC a parallel stacking motif of the molecules in the unit cell is present. This interpretation is verified by the unit cell parameters that have been derived from the powder diffraction patterns, which are presented in Table 1. The analysis shows that the unit cell parameters are rather similar for all fluorinated HBCs, while the geometry is significantly different for the parent HBC.

Table 1 Unit cell parameters of the parent HBC compared to the various partially fluorinated HBC derivatives.

	HBC[19]	F_2HBC	F_4HBC	F_6HBC[20]
a	18.43 Å	21.9 Å	22.95 Å	22.95 Å
b	5.12 Å	13.9 Å	13.96 Å	14.32 Å
c	12.93 Å	3.79 Å	3.72 Å	3.72 Å
α	90°	90°	90°	90°
β	112.57°	99.8°	98.0°	99.22°
γ	90°	90°	90°	90°
V	1126.4 Å³	1138 Å³	1179 Å³	1207 Å³

To rationalize why the parent HBC crystallizes in a herringbone structure, but all fluorinated compounds form parallel packed arrangements, we have analysed the charge distribution within the molecules. As shown in Fig. 3, the charge distribution is indeed strongly affected by the fluorination.

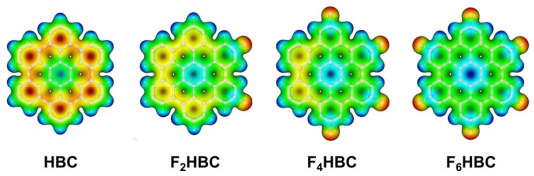

Fig. 3 DFT-based (B3LYP/6-311G(d,p)) computed charge distribution in HBC, F_2HBC, F_4HBC, and F_6HBC as visualized in molecular electrostatic potential plots (blue-green-yellow-red in ascending order).

As expected, the strongest differences are found between HBC and F_6HBC. The electron density is rather high within the molecular core for HBC while the molecular rim is electronically partially depleted. This situation is inverted for F_6HBC, yielding reduced electron density in the core and high density particularly at the strongly electronegative fluorine atoms. Despite these differences, one characteristic is similarly found for HBC and F_6HBC: the high symmetry of the molecule is directly transferred to the charge distribution in the molecule, therefore also being sixfold. This is not the case for the non-symmetrically functionalized HBCs. Here, the non-symmetrical fluorination leads to a symmetry break in the charge distribution and results in molecular net dipole moments, for which values of 3.48 (F_2HBC) and 3.45 (F_4HBC) Debye, respectively, have been computed. These significant molecular dipole moments may act as mediators in the crystal formation process since the antiparallel or shifted placement of both dipoles allows for an additional energy gain. This gain is, however, only possible if the molecules are packed in a parallel fashion, which is not the case for tilted molecular arrangements as found in the herringbone structures.[36] While this nicely allows understanding why F_2HBC and F_4HBC exhibit parallel packing in their bulk structure it does not explain why also a parallel configuration is adopted for F_6HBC which does not feature a dipole moment. To explain this, we have to consider also the non-negligible fluorine-hydrogen interaction for this compound. Obviously, a slight rotation of the molecules with respect to each other as well as a lateral shift enable several short-contacts between fluorine and hydrogen atoms, which, again, is most favoured in parallel stacking geometries. Therefore, the F-H interactions appear as suitable explanation for the observed absence of herringbone packing in the partially fluorinated HBCs. This interpretation can be further supported by conducting a Hirshfeld surface analysis[35] of F_6HBC, of which a full crystal structure has been solved before, hence enabling also to exactly derive the placement of the molecules within the unit cell.[20]

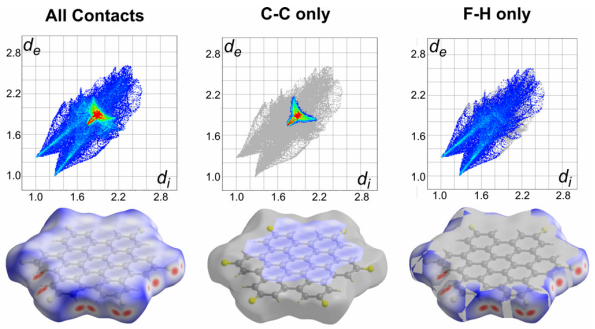

Fig. 4 Hirshfeld surface analysis of F_6HBC. The visualizations show the fingerprint plots for all contacts (left) and exclusively the C-C, and F-H contacts, respectively, in combination with the corresponding surface vertices.

In this analysis, the closest contact points are determined for the molecular Hirshfeld surfaces (which correspond to the molecular volume within the crystal structure, a detailed

description is provided in Ref. 35). Plotting the distances to the closest atoms in both directions (inside (*di)* and outside (*de*) of the Hirshfeld volume) yields the characteristic fingerprint plots which provide an objective and quantitative measure of the crystal packing situation (cf. top of Fig. 4). In the fingerprint plots for F_6HBC two prominent characteristics are observed. First, a large number of contact points with *di*=*de*=1.8-2.1 Å is present, which correspond to C-C bonds and result from contacts in-between the molecular centre. As second characteristic, two "wings" at low distances are found. An analysis of only the contacts between fluorine and hydrogen atoms reveals that these wings indeed represent the F-H contacts. The analysis furthermore shows that these contacts provide more than 40% of all determined contacts and therefore strongly contribute to the intermolecular binding. This becomes even clearer in an additional visualization. To that purpose, all closest contact distances are compared with the expected van-der-Waals distances for the respective combinations of contacted elements (e.g. carbon and hydrogen). By this means a colouring of this surface is achieved, where red colour corresponds to a smaller and blue to a larger distance than expected from the vdW distances. Hence, red points on these surfaces identify the positions where the decisive intermolecular bonds are formed. The corresponding results are presented in the bottom of Fig. 4. One can easily identify the contact points at the molecular rim. Evaluating this data such that only the F-H bonds are considered, we clearly see that in particular those contacts distinct the intermolecular bonds. Therefore, they indeed act as mediator for the parallel alignment of the molecules in their solid state as typically found for partially fluorinated organic compounds.[37] The observed molecular packing motif of the HBC-derivatives can be even more beneficial for the intermolecular coupling, since the π-systems of fluorinated PAHs were found to be considerably larger than those of their non-fluorinated analogues.[38] Interestingly, a rather similar situation is found also for partially fluorinated benzene. Regardless of the presence of a resulting dipole moment (i.e. fluorination at 1,2,3- or 1,3,5-positions) these molecules exhibit a planar stacking in the crystalline phase.[39,40] By contrast, the perfluorinated benzene still shows a herringbone packing like the non-fluorinated benzene.[41,42] Perfluorination of π-conjugated molecules on the other hand yields an inverted quadrupole moment but also stabilizes a herringbone packing as also found in the bulk crystal structure of larger fluorinated acenes such as perfluoro-pentacene.[43] We note that in contrast to C_6F_6 the F_6HBC has additional 12 hydrogen atoms at the rim and thus allow for F-H interactions which are absent in the former case.

B. Molecular Orientation in Crystalline Thin Films

For the non-fluorinated HBC, crystalline films in different molecular orientation were reported upon modification of the supporting substrate.[28] In particular, exclusive upright and horizontal molecular alignments were observed on SiO_2 and graphite surfaces, respectively. To investigate whether such crystalline growth and structural control is also achieved for the fluorinated HBCs, corresponding thin films of F_2HBC and F_4HBC have been prepared on these substrates.

To enlighten this issue in detail, the film structures were investigated by X-ray diffraction (XRD). As summarized in the specular scans presented in Fig. 5, indeed all thin films exhibit a crystalline texture. For thin films of F_2HBC and F_4HBC prepared on SiO_2 one distinct peak is observed at 2θ=7.32° and 7.22° respectively. These values correspond to lattice distances of 12.07 Å and 12.23 Å which closely resembles the value found for uprightly-oriented films of non-fluorinated HBC (11.94 Å), and are identified as (110)-reflexes based on the crystal structures derived before. On a graphite surface, in contrast, strong diffraction peaks at higher angles are

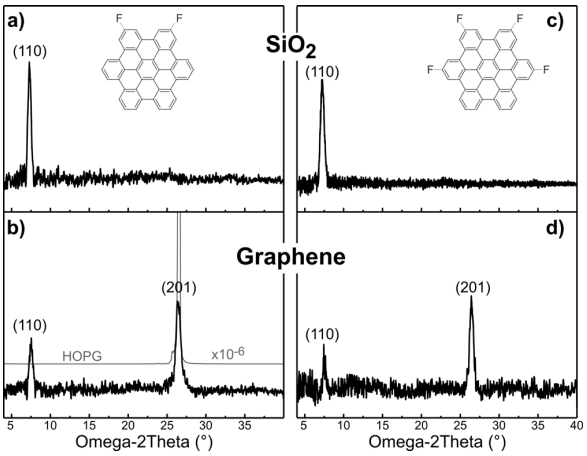

Fig. 5: Specular X-ray diffractograms of a,b) F_2HBC and c,d) F_4HBC on SiO_2 (a,c) and graphene (b,d) substrates. In panel b) additionally the strong $(0002)_C$ signal of an HOPG diffractogram is presented which masks the thin-film signals in conventional measurements.

observed (F_2HBC: 2θ=26.40°, F_4HBC: 2θ=26.48°). We note that in conventionally prepared films on highly ordered pyrolytic graphite (HOPG) these signals could not be detected since they were masked by the very intense substrate peaks of the HOPG support (2θ=26.54°, cf. scaled HOPG diffractogram in the background of Fig. 5b). This problem was prevented in our measurements by using graphene-coated quartz instead, where this substrate signal is not present. The close similarity to the peak position of graphite indicates that the molecules are arranged in parallel stacks without intermolecular tilts, resembling the geometry of graphite sheets. Again using the derived crystal structure, these signals are identified as (201)-reflections, which indeed correspond to a virtually perfectly flat-lying molecular arrangement. The slight (110)-related signals are attributed to surface defects, leading to an upright growth as observed before for non-fluorinated HBC as well as acenes.[28,44]

Since the assignment of the signals to the related packing motifs is based on the crystal structures which were derived from a powder analysis, one might argue that the reliability of these interpretations is not perfect. To dispel these doubts, we have additionally performed NEXAFS dichroism measurements of the discussed thin films, which independently allowed analysing the molecular orientations in these films.[30] In all cases, the derived molecular tilt angles are in very good agreement with the presented assignments, which therefore proves the correctness of our interpretations (exemplary data shown in Fig. 6, full data set and evaluation presented in the Supplementary Information†).

C. Effects of Fluorination on the Electronic Signatures

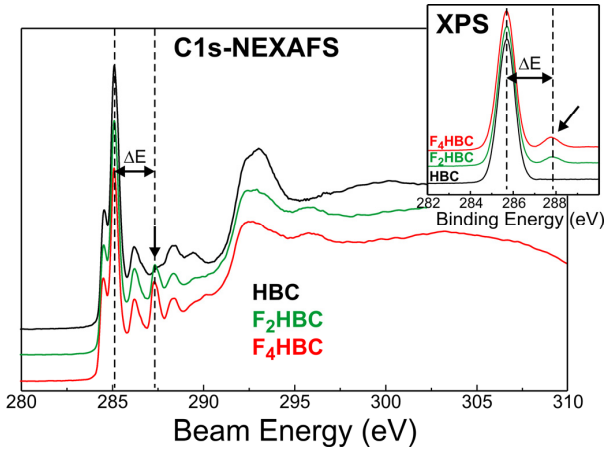

Fig. 6 Comparison of C1s X-ray photoelectron spectra (inset) and near edge X-ray absorption fine structure spectroscopy (NEXAFS) spectra of fluorinated and original HBCs.

While so far the structural characteristics of the fluorinated HBCs in the solid state were discussed, we will now focus on their fundamental electronic properties. In the inset of Fig. 6, the XPS spectra of the newly synthesized HBC derivatives are compared to that of pure HBC. In addition to the C1s photoelectron signals arising from the HBC core and the non-fluorinated rim (C-C and C-H species), a distinct peak that is shifted by 2.1 eV is observed which corresponds to the fluorine-bound carbon atoms. Clearly, the height of this signal scales accordingly with the degree of fluorination. While these measurements provide information about the carbon core levels of the compounds, NEXAFS analyses allow the investigation of the unoccupied molecular levels. As presented in Fig. 6, the NEXAFS signatures of all three HBCs are rather similar. However, a distinct signal at 287.7 eV is only found for the fluorinated compounds and experiences rising intensity with increasing fluorination (highlighted by black arrow in Fig. 6). This excitation is directly ascribed to the higher binding energy of the C1s core electron which therefore leads to increased energies of the respective transitions into the molecular π*-LUMO level. This interpretation is well supported by a comprehensive work on the nature of the HBC NEXAFS signature by Luo *et al.*. There, the authors have deduced that the carbon atoms with highest distance from the molecule centre are prominent excitation centres for the most intense absorption band at 285.6 eV.[45] Since this is the position of the atoms where the fluorine atoms are attached, the corresponding excitation is energetically shifted for the fluorinated compounds. Comparing the energetic shifts observed in the NEXAFS and XPS spectra (denoted as ΔE in Fig. 6) indeed reveals similar values of about 2 eV, hence supporting this assignment. The residual small deviations can be explained by slightly different relaxation shifts for the functionalized and parent HBCs.[30]

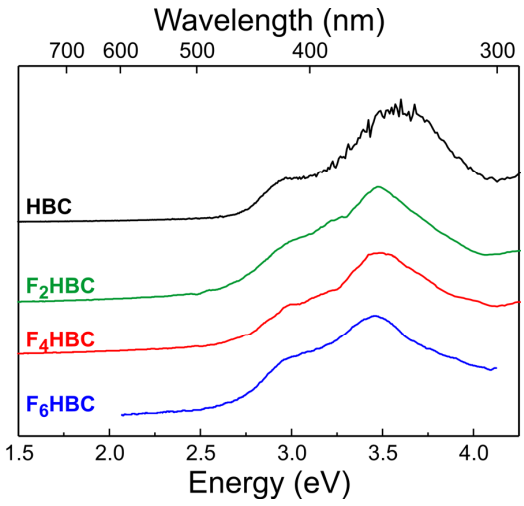

Fig. 7 Optical absorption spectra of F_6HBC, F_4HBC, F_2HBC and HBC thin films (from top to bottom). Data for F_6HBC and HBC taken from Ref. 27.

To examine potential modifications of the energy spacing between the HBC frontier orbitals upon fluorination, furthermore optical absorption measurements have been performed for thin films of the new compounds which are compared with that of F_6HBC and HBC in Fig. 7. Clearly, the signature of all HBCs is rather similar, featuring two strong absorption bands at about 2.9-3.0 eV and 3.4-3.6 eV. We note that using matrix-isolation spectroscopy the optical absorption of individual HBC molecules has been studied previously in great detail and revealed a number of sublevels[46] which are not resolved in the solid film spectra.

To further classify our observations, computational methods have been applied to calculate the energy levels of the molecular frontier orbitals. As presented in Table 2, the values from the corresponding DFT calculations are in good agreement with the experimentally obtained ones, suggesting that the higher energetic peak might be attributed to the optical gap. This assignment is corroborated by solution absorption data of HBC showing a distinct maximum around 3.5 eV.[47]

Table 2 Comparison of computed LUMO, HOMO and band gap energies.

[eV]	$HOMO^{DFT}$	$LUMO^{DFT}$	E_G^{DFT}
HBC	-5.42	-1.82	3.60
F_2HBC	-5.55	-2.07	3.48
F_4HBC	-5.71	-2.26	3.45
F_6HBC	-5.91	-2.40	3.51

The analysis shows that the absolute energies of the frontier orbitals are significantly different for the different degrees of fluorination, since their energies are reduced with increasing fluorination degree, as frequently found upon fluorination of PAHs.[48] Interestingly, however, the gaps are found to be equal for all compounds. A similar situation has been observed before for rubrene where the different degree of fluorination has not significantly affected the optical band gap, while the absolute energies of the involved frontier orbitals are systematically different.[49] For the prominent case of pentacene, a different situation is found since in this case perfluorination leads to a significant reduction of the excitation energies.[50,51] Apparently, the effect of fluorine substitution on the optical gap is not easily predictable and decisively depends on the number of fluorine substituents and their position within the molecule. As concluded by B. M. Medina et al. in an extensive study on this correlation, "the subtle interplay of the electron donating and withdrawing properties of fluorine with a given molecular backbone does not allow for an easy 'intuitive' insight into the overall effect" on the width of the HOMO-LUMO gap.[52]

4 Conclusions

We have prepared and investigated a series of novel, fluorinated HBC derivatives with varying degree of peripheral fluorination. We observe that in all cases the initial herringbone arrangement adopted in HBC crystals is transformed into parallel packing motifs for the fluorinated derivatives. This observation is attributed to fluorine-hydrogen bonds between the molecules which mediate a parallel alignment in the molecular crystals.

By preparing thin films of F_2HBC and F_4HBC on SiO_2 and graphene substrates we show that on both substrates crystalline thin films are formed. Moreover, these substrates enable the structural control of the crystallites since the HBCs adopt an upright molecular orientation on SiO_2 and exhibit horizontal alignment on graphene.

The optical linear absorption spectra of all compared HBCs in the solid state are rather similar, showing that the spacing of the molecular frontier orbitals is hardly affected by the fluorination. Nevertheless, the absolute energies of the involved orbitals are strongly modified, similarly to what has been observed upon introduction of endocyclic N-atoms into graphene nanoribbons.[53,54] This appears interesting for using molecular heterostructures based on HBC, since additional absorption channels like charge-transfer excitations might be beneficial for HBC-based OPV applications.[55]

Acknowledgements

We acknowledge support by the Deutsche Forschungsgemeinschaft (Grant SFB 1083, TP A2; SFB 951, TP Z1) and the Helmholtz-Zentrum Berlin (electron storage ring BESSY II) for provision of synchrotron radiation at beamline HE-SGM. We thank Matthias Zarg and Björn Kobin for support with the powder diffraction analysis.

Notes and references

1 Y. Shirota, *J. Mater. Chem.*, 2000, **10**, 1-25.
2 S. Reineke, F. Lindner, G. Schwarz, N. Seidler, K. Walzer, B. Lüssem and K. Leo, *Nature* 2009, **459**, 234-238.
3 B. Kippelen and J.-L. Brédas, *Energy Environ. Sci.*, 2009, **2**, 251-261.
4 S. R. Forrest, *Nature* 2004, **428**, 911-918.
5 D. J. Lipomi, H. Chong, M. Vosgueritchian, J. Mei and Z. Bao, *Sol. Energ. Mat. Sol. Cells*, 2012, **107**, 355-365.
6 S. Liu, W. M. Wang, A. L. Briseno, S. C. B. Mannsfeld and Z. Bao, *Adv. Mater.* 2009, **21**, 1217-1232.
7 C. D. Dimitrakopoulos and P. R. L. Malenfant, *Adv. Mater.* 2002, **14**, 99-117.
8 J. E. Anthony, *Angew. Chem. Int. Ed.*, 2008, **47**, 452-483.
9 W. Brütting *Physics of Organic Semiconductors*, Wiley-VCH Augsburg, Germany, 2005.
10 V. Coropceanu, J. Cornil, D. A. da Silva Filho, Y. Olivier, R. Silbey and J.-L. Brédas, *Chem. Rev.* 2007, **107**, 926-952.
11 G. Nan, Q. Shi, Z. Shuai and Z. Li, *Phys. Chem. Chem. Phys.*, 2011, **13**, 9736-9746.
12 A. Troisi and G. Orlandi, *J. Phys. Chem. B*, 2005, **109**, 1849-1856.
13 K. Kolata, T. Breuer, G. Witte and S. Chatterjee *ACS Nano*, 2014, **8**, 7377-7383.
14 J. E. Anthony, *Chem. Rev.* 2006, **106**, 5028-5048.
15 J. Wu, W. Pisula and K. Müllen, *Chem. Rev.*, 2007, **107**, 718-747.
16 K. Müllen and J. P. Rabe, *Acc. Chem. Res.*, 2008, **41**, 511−520.
17 A. C. Grimsdale and K. Müllen, *Angew. Chem. Int. Ed.*, 2005, **44**, 5592−5629.
18 H. Seyler, B. Purushothaman, D. J. Jones, A. B. Holmes and W. W. H. Wong, *Pure Appl. Chem.*, 2012, **84**, 1047−1067.
19 R. Goddard, M. W. Haenel, W. C. Herndon, C. Krueger and M. Zander, *J. Am. Chem. Soc.* 1995, **117**, 30-41.
20 K. Mukai, M. Harada, Y. Kikuzawa, T. Mori and J. Sugiyama, *Electrochem. Solid-State Lett*., 2011, **14**, A52-A55.
21 L. Schmidt-Mende, A. Fechtenkötter, K. Müllen, E. Moons, R. H. Friend and J. D. MacKenzie, *Science*, 2001, **293**, 1119-1122.
22 A. van de Craats, J. M. Warman, K. Müllen, Y. Geerts and J. D. Brand, *Adv. Mater.*, 1998, **10**, 36-38.
23 J. Kirkpatrick, V. Marcon, J. Nelson, K. Kremer and D. Andrienko, *Phys. Rev. Lett.*, 2007, **98**, 227402.
24 D. Käfer, A. Bashir, X. Dou, G. Witte, K. Müllen and C. Wöll, *Adv. Mater.*, 2010, **22**, 384-388.
25 M. L. Tang and Z. Bao, *Chem. Mat. Rev.* 2011, **23**, 446-455.
26 T. Mori, Y. Kikuzawa and H. Takeuchi, *Org. Electron.*, 2008, **328**, 328-332.
27 Y. Kikuzawa, T. Mori and H. Takeuchi, *Org. Lett.*, 2007, **9**, 4817-4820.
28 P. Beyer, T. Breuer, S. Ndiaye, A. Zykov, A. Viertel, M. Gensler, J. P. Rabe, S. Hecht, G. Witte and S. Kowarik, *ACS Appl. Mater. Interfaces*, 2014, **6**, 21484-21493.
29 A. Narita, X.-Y. Wang, X. Feng and K. Müllen, *Chem. Soc. Rev.*, 2015, **44**, 6616-6643.
30 T. Breuer, M. Klues and G. Witte, *J. Electron Spectrosc. Relat. Phenom.*, 2015, **204**, 102-115.

31 M. W. Schmidt, K. K. Baldridge, J. A. Boatz, S. T. Elbert, M. S. Gordon, J. H. Jensen, S. Koseki, N. Matsunaga, K. A. Nguyen, S. Su, T. L. Windus, M. Dupuis and J. A. Montgomery, *J. Comput. Chem*., 1993, **14**, 1347-1363.
32 M. S. Gordon and M. W. Schmidt in Theory and Applications of Computational Chemistry: the first forty years, ed. C.E. Dykstra, G. Frenking, K.S. Kim and G.E. Scuseria, Elsevier, Amsterdam, 2005, Advances in electronic structure theory: GAMESS a decade later, 1167-1189.
33 U. Varetto, Molekel 5.4
34 CrystalExplorer (Version 3.1), S.K. Wolff, D.J. Grimwood, J.J. McKin-non, M.J. Turner, D. Jayatilaka and M.A. Spackman, University of Western Australia, 2012.
35 M. A. Spackman and D. Jayatilaka, *CrystEngComm*, 2009, **11**, 19-32.
36 D. M. Cho, S. R. Parkin and M. D. Watson, *Org. Lett.*, 2005, **7**, 1067-1068.
37 K. Reichenbächer, H. I. Süss and J. Hulliger, *Chem. Soc. Rev.*, 2005, **34**, 22-30.
38 M. Klues, P. Jerabek, T. Breuer, M. Oehzelt, K. E. Hermann, R. Berger and G. Witte, *J. Phys. Chem. C*, 2016, **120**, 12693-12705.
39 V. R. Thalladi, H.-C. Weiss, D. Bläser, R. Boese, A. Nangia and G.R. Desiraju, *J. Am. Chem. Soc.*, 1998, **120**, 8702–8710.
40 M. T. Kirchner, D. Bläser, R. Boese, T.S. Thakur and G.R. Desiraju, *Acta Crystallogr., Sect. E: Struct. Rep. Online*, 2009, **65**, o2670.
41 H. Shorafa, D. Mollenhauer, B. Paulus and K. Seppelt, *Angew. Chem. Int. Ed.*, 2009, **48**, 5845–5847.
42 G.E.Bacon, N.A.Curry and S.A.Wilson, *Proc. R. Soc. A*, 1964, **279**, 98-110.
43 Y. Sakamoto, T. Suzuki, M. Kobayashi, Y. Gao, Y. Fukai, Y. Inoue, F. Sato and S. Tokito, *J. Am. Chem. Soc.*, 2004, **126**, 8138–8140.
44 T. Breuer, I. Salzmann, J. Götzen, M. Oehzelt, A. Morherr, N. Koch, G. Witte, *Cryst. Growth Des.* 2011, **11**, 4996-5001.
45 Y. Luo, H. Agren, M. Keil, R. Friedlein and W. R. A. Salaneck, *Chem. Phys. Lett.*, 2001, **337**, 176-180.
46 G. Rouille, M. Steglich, F. Huisken, T. Henning and K. Müllen, *J. Chem. Phys.*, 2009, **131**, 204311.
47 W. Hendel, Z. H. Khan and W. Schmidt *Tetrahedron*, 1986, **42**, 1127-1134.
48 M. L. Tang, A. D. Reichardt, P. Wie and Z. Bao, *J. Am. Chem. Soc.*, 2009, **131**, 5264-5273.
49 F. Anger, T. Breuer, A. Ruff, M. Klues, A. Gerlach, R. Scholz, S. Ludwigs, G. Witte and F. Schreiber, *J. Phys. Chem. C*, 2016, **120**, 5515-5522.
50 A. Hinderhofer, U. Heinemeyer, A. Gerlach, S. Kowarik, R. M. J. Jacobs, Y. Sakamoto, T. Suzuki and F. Schreiber, *J. Chem. Phys.*, 2007, **127**, 194705.
51 J. Schwaben, N. Münster, M. Klues, T. Breuer, P. Hofmann, K. Harms, G. Witte and U. Koert, *Chem. Eur. J.*, 2015, **21**, 13758-13771.
52 B.M. Medina, D. Beljonne, H.-J. Egelhaaf, J. Gierschner, *J. Chem. Phys.*, 2007, **126**,111101.
53 C. Bronner, S. Stremlau, D. M. Gille, F. Braußе, A. Haase, S. Hecht and P. Tegeder, *Angew. Chem. Int. Ed.*, 2013, **52**, 4422-4425.
54 J. Cai, C. A. Pignedoli, L. Talirz, P. Ruffieux, H. Söde, L. Liang, V. Meunier, R. Berger, R. Li, X. Feng, K. Müllen and R. Fasel, *Nat. Nanotech*, 2014, **9**, 896-900.
55 H. C. Hesse, C. Schaffer, C. Hundschell, A. Narita, X. Feng, K. Müllen, B. Nickel and L. Schmidt-Mende, *Phys. Stat. Sol. (a)*, 2012, **209**, 785-789.

Electronic Supplementary Information

Self-assembly of partially fluorinated hexabenzocoronene derivatives in the solid state

Tobias Breuer*[a], Michael Klues[a], Pauline Liesfeld[b], Andreas Viertel[b], Matthias Conrad[c], Stefan Hecht[b] and Gregor Witte[a]

[a] Fachbereich Physik, Universität Marburg, Renthof 7, 35032 Marburg, Germany

[b] Department of Chemistry, Humboldt-Universität zu Berlin, 12489 Berlin, Germany

[c] Fachbereich Chemie, Universität Marburg, Hans-Meerwein-Str. 4, 35032 Marburg,Germany

** Email: tobias.breuer@physik.uni-marburg.de*

Table of Contents

Synthesis and Characterization of F_2HBC and F_4HBC

General synthetic and analytical methods. Commercially available starting material (compound **1a**, **2**, and **4**) were handled as received. Solvent destillation was carried out prior to the application. In need of inert conditions the solvents were subjected to additional drying and degassing and the reactions were performed under a blanket of argon. For thin-layer chromatography silica gel 60 F_{254}-plates purchased from Merck were used. Silica gel (35-70 µm, 60 Å) by Acros was utilized for column chromatography. Analysis by means of NMR-spectroscopy were performed using a 300 MHz for ^{1}H-NMR (75 MHz for ^{13}C-NMR) Bruker AVANCE II 300 spectrometer at 25 °C. The received spectra were adjusted to the signals of the solvent (^{1}H: δ ($CDCl_3$) = 7.26 ppm and ^{13}C: δ ($CDCl_3$) = 77.16 ppm). The UPLC-MS-measurements were performed on an Acquity UPLC (Waters) equipped with a ESI-MS-Detector LCT Premier XE for HR-MS (Waters) and a Photo diode arraydetector 2996. MALDI-MS spectra were measured on a Bruker Autoflex III MALDI-mass spectrometer using a smartbeam laser with a wavelength of 355 nm, 200 Hz, and 20 kV acceleration voltage, calibrated with PEG 1000. Elemental analysis was performed using a EuroVector EuroEA 3000 CHNS elemental analyser.

The synthetic route to **F_2HBC** and **F_4HBC** is shown below (Scheme S1).

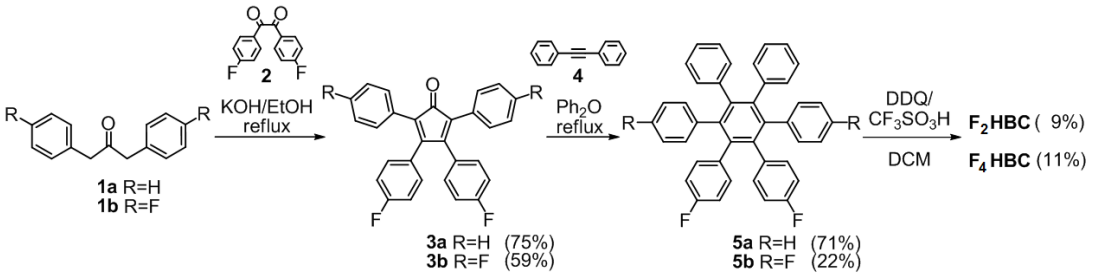

Scheme S1: Synthesis of partially fluorinated **F_2HBC** and **F_4HBC**.

1,3-Bis(4-fluorophenyl)propan-2-one ***1b***

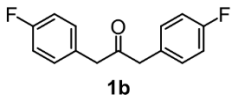

1b

The synthesis was adapted from a literature procedure.[1] 4-Fluorophenylacetic acid (0.62 g, 4.0 mmol) and 4-dimethylaminopyridine (0.61 g, 5.0 mmol) were dissolved in 10 mL of dichloromethane (DCM). Afterwards *N,N'*-dicyclohexylcarbodiimide (DCC, 0.83 g, 4.0 mmol) was added to the solution and stirred at room temperature for 40 h. DCM and water were added to the reaction mixture and the organic layer was washed with aqueous HCl and subsequently with saturated aqueous $NaHCO_3$ and afterwards was dried over $MgSO_4$.

After removal of the solvent column chromatogaphy (silica gel using petroleum ether/DCM = 2:1 as the eluent) gave **1b** as a solid in 35% yield (0.34 g, 1.38 mmol).

^{1}H-NMR (300 MHz, $CDCl_3$): δ = 7.07-7.14 (m, 4*H*), 6.97-7.05 (m, 4*H*), 3.70 (s, 4*H*). **^{13}C{^{1}H}-NMR (75 MHz, $CDCl_3$):** δ = 205.3, 162.1 (d), 131.1 (d), 129.6 (d), 115.7 (d), 48.3.

*3,4-Bis(p-fluorophenyl)-2,5-diphenylcyclopentadienone **3a***

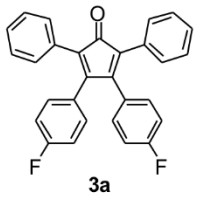

3a

The synthesis was adapted from a literature procedure.[1] A solution of 4,4'-difluorobenzil **2** (2.34 g, 9.5 mmol) and 1,3-diphenylacetone **1a** (2.00 g, 9.5 mmol) in 18 mL of ethanol was heated to reflux. A solution of KOH (0.3 g, 7.03 mmol) in 4 mL of ethanol was added. After 20 min the refluxing mixture was cooled to room temperature. The formed precipitate was washed with methanol affording cyclopentadienone **3a** as a dark purple solid in 75% yield (2.98 g, 6.87 mmol).

^{1}H-NMR (300 MHz, $CDCl_3$): δ = 6.73-6.92 (m, 10*H*), 6.9 (d, 8*H*). **^{13}C{^{1}H}-NMR** (75 MHz, $CDCl_3$): δ = 200.0, 162.9 (d), 131.5 (d), 153.1, 130.6, 130.2, 129.0 (d), 128.3, 127.8, 125.7, 115.6 (d). **MS** (ES+): *m/z* = 421.142 $[M+H]^+$.

*2,3,4,5-Tetrakis(4-fluorophenyl)cyclopentadienone **3b***

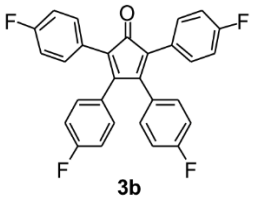

3b

Analogously to cyclopentadienone **3a**, the related tetrasubstituted derivate **3b** is obtained from 4,4'-difluorobenzil **2** (0.33 g, 1.35 mmol), 1,3-bis(4-fluorophenyl)propan-2-one **1b** (0.33 g, 1.35 mmol), and KOH (0.06 g, 1.00 mmol) in 3.2 mL of ethanol in 59% yield (0.34 g, 0.74 mmol).

^{1}H-NMR (300 MHz, $CDCl_3$): δ = 7.15-7.22 (m, 4*H*), 6.85-7.00 (m, 12*H*). **^{13}C{^{1}H}-NMR (75 MHz, $CDCl_3$):** δ = 199.9, 162.1 (2xd), 153.1, 132.0, 131.4 (d), 128.7, 126.5 (d), 124.7, 115.7 (d), 115.5 (d).

1,2-Bis(p-fluorophenyl)-3,4,5,6-tetraphenylbenzene ***5a***

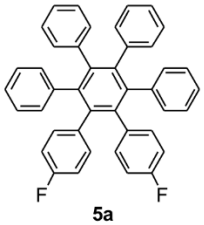

5a

Adopting a literature procedure[1] a suspension of cyclopentadienone **3a** (0.84 g, 2 mmol) and diphenylacetylene **4** (0.36 g, 2 mmol) in 8 mL of diphenylether was refluxed at 260 °C overnight. During the reaction the purple suspension turned into an orange solution. Addition of methanol induced precipitation of the crude product, which was purified by column chromatography (silica gel using petroleum ether/DCM = 3:1 as the eluent) to yield the desired hexaphenylbenzene **5a** as a white solid in 71% yield (0.8 g, 1.42 mmol).

^{1}H-NMR (300 MHz, $CDCl_3$): δ = 7.18-7.30 (m, 24*H*), 6.58 (tt, 8*H*). **^{13}C{^{1}H}-NMR** (75 MHz, $CDCl_3$): δ = 160.8 (d), 140.8, 140.7, 140.5, 140.5, 139.5, 136.6 (d), 132.9 (d), 131.4, 131.4, 126.9, 126.8, 125.5, 125.4, 113.9 (d).

MS (MALDI+, matrix: tetracyanoquinodimethane): *m/z* = 569.8 ($[C_{42}H_{28}F_2]^+$).

1,2,3,4-Tetrakis(p-fluorophenyl)-5,6-diphenylbenzene ***5b***

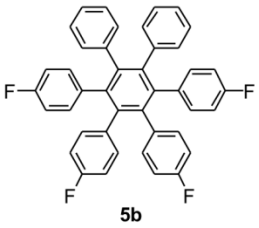

5b

Analogously to **4a**, the reaction of cyclopentadienone **3b** (0.33 g, 0.72 mmol) and diphenylacetylene **6** (0.13 g, 0.72 mmol) in 3 mL of diphenyl ether resulted in the desired hexaphenylbenzene **5b** after column chromatography (silica gel using petroleum ether/DCM = 3:1 as the eluent) in 22% yield (0.09 g, 0.16 mmol).

^{1}H-NMR (300 MHz, $CDCl_3$): δ = 6.84-6.92 (m, 6*H*), 6.70-6.82 (m, 12*H*), 6.59 (m, 8*H*). **^{13}C{^{1}H}-NMR (75 MHz, $CDCl_3$):** δ = 160.7 (2xd), 140.9, 140.1, 139.7, 139.6, 136.2 (d), 132.6 (d), 131.2, 126.8, 125.5, 114.0 (d), 113.8 (d). **MS** (MALDI+, matrix: tetracyanoquinodimethane): *m/z* = 605.957 ($[C_{42}H_{26}F_4]^+$).

2,5-Difluoro-hexa-peri-hexabenzocoronene ***F$_2$HBC***

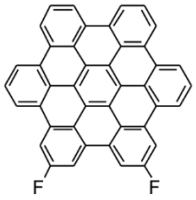

F$_2$HBC

Adopting a literature procedure[2] a dried Schlenk flask was charged with 100 mL of dry DCM. **5a** (0.71 g, 1.25 mmol) was added and the solution was degassed, put under Ar atmosphere, and cooled down to 0 °C. First 2,3-dichloro-5,6-dichlorobenzoquinone (DDQ, 1.92 g, 8.46 mmol) and afterwards trifluoromethanesulfonic acid (1.5 mL, 17.31 mmol) were added. The reaction mixture was stirred at ambient temperature for 3 h and then 100 mL of methanol were added. The precipitate was collected by filtration and washed with methanol and DCM. The crude product was purified via sublimation to afford the target **F$_2$HBC** as a bright yellow solid in 9% yield (60 mg, 0.11 mmol).

MS (MALDI+, matrix: tetracyanoquinodimethane, Fig. S1): *m/z* = 557.707 ($[C_{42}H_{16}F_2]^+$). **Elemental analysis**: found C: 88.80%, H: 2.82% (calc. C: 90.31%, H: 2.89%).

2,5,8,11-Tetrafluoro-hexa-peri-hexabenzocoronene ***F$_4$HBC***

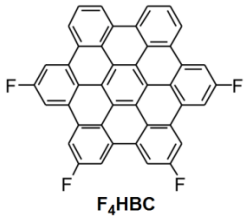

F$_4$HBC

Analogously to the doubly fluorinated **F$_2$HBC**, the related **F$_4$HBC** was obtained from **5b** (80 mg, 0.14 mmol), DDQ (0.21 g, 0.91 mmol), and trifluoromethanesulfonic acid (0.1 mL, 1.87 mmol) in 10 mL of DCM. The crude product was purified via sublimation to afford the target **F$_4$HBC** as a yellow solid in 11% yield (9 mg, 0.015 mmol).

MS (MALDI+, matrix: no matrix, Fig. S2): *m/z* = 593.759 ($[C_{42}H_{14}F_4]^+$); **Elemental analysis:** found C: 83.69%, H: 2.87% (calc. C: 84.84%, H: 2.37%).

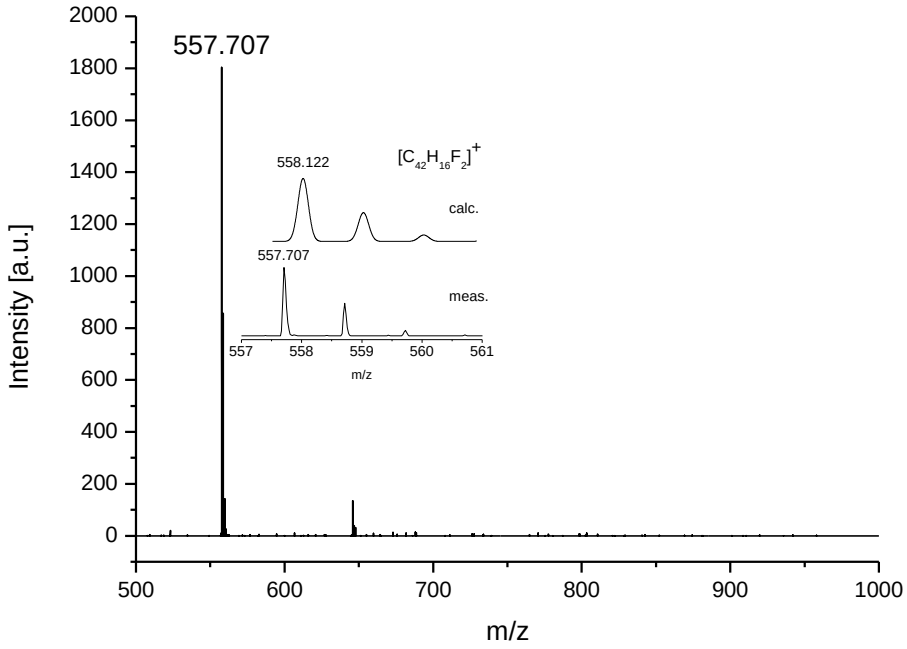

Fig. S1: MALDI-TOF mass spectrum of compound **F_2HBC**. The inset shows the comparison between simulated (top) and experimentally determined (bottom) isotopic distributions.

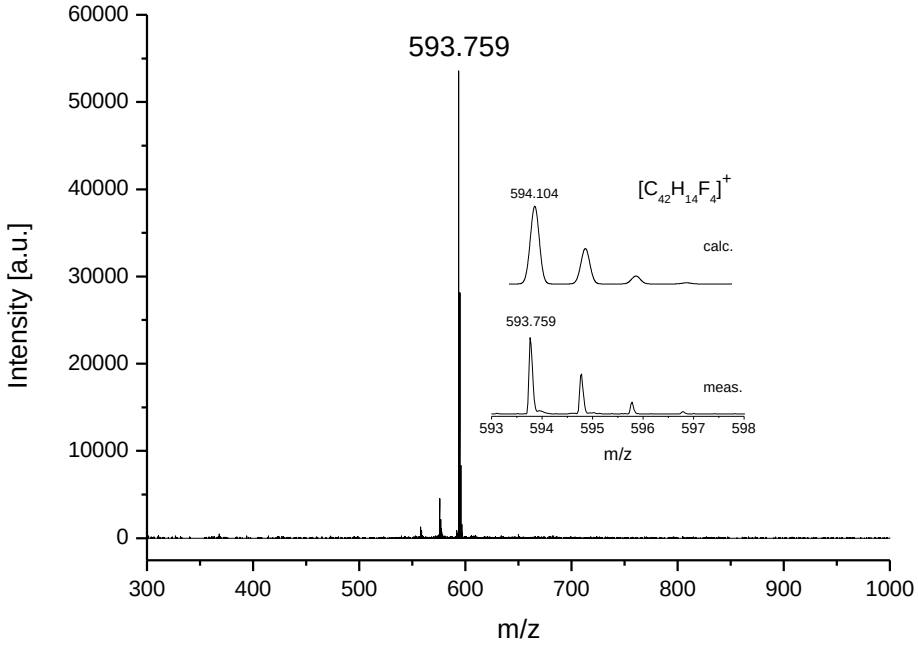

Fig. S2: MALDI-TOF mass spectrum of compound **F_4HBC**. The inset shows the comparison between simulated (top) and experimentally determined (bottom) isotopic distributions.

NEXAFS Dichroism Measurements

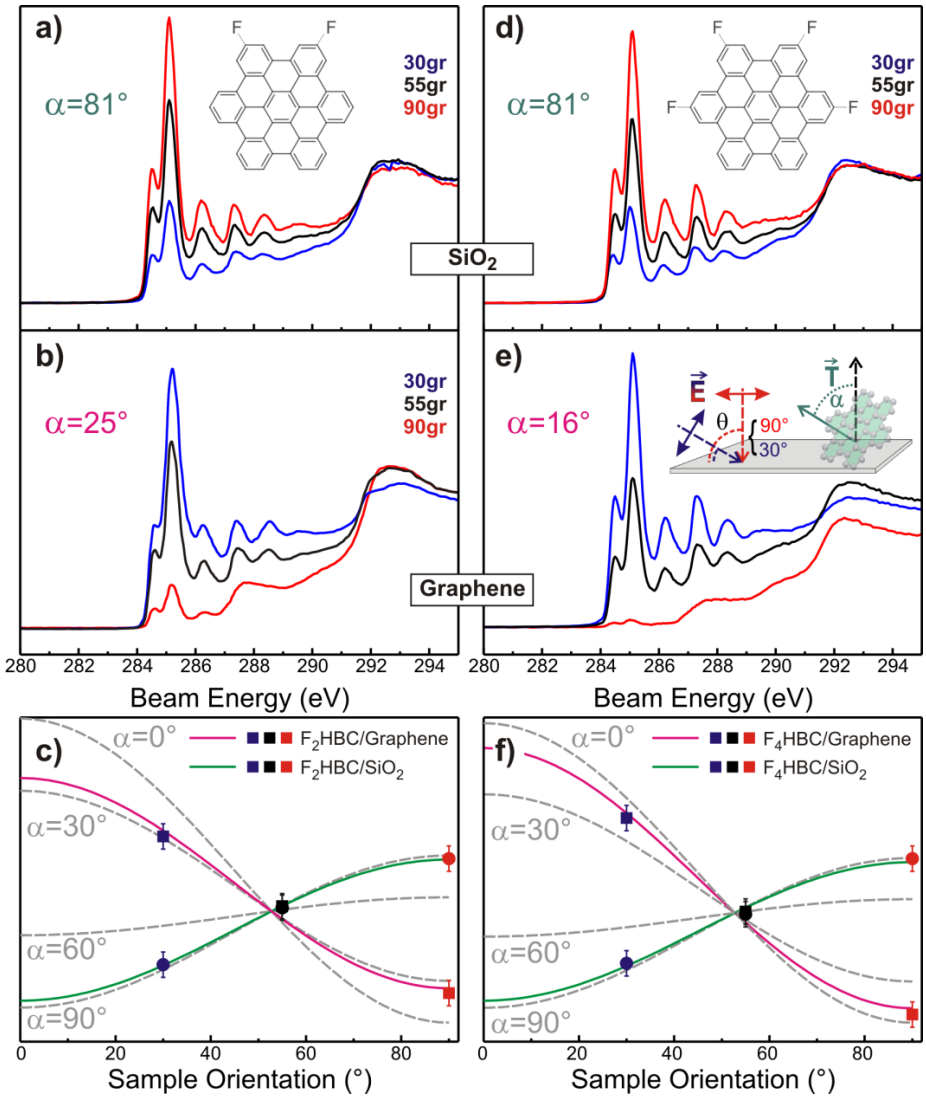

Fig. S3: C1s-NEXAFS dichroism measurements of a,b) F_2HBC and d,e) F_4HBC on SiO_2 (a,c) and graphene (b,d) substrates with sketch of experimental geometry in the inset of d). The inverse dichroisms correspond to upright molecular orientations on SiO_2 and recumbent configurations on graphite substrates as obtained from the quantitative evaluation shown in c) (F_2HBC) and f) (F_4HBC). In addition to the experimental points and fit results for graphene (squares, pink curve) and SiO_2 substrates (circles, green curve), dichroism curves corresponding to 0°, 30°, 60°, and 90° are presented.

The NEXAFS spectroscopy measurements also provide information on the molecular orientation of the molecules in processed thin films. This is because the absorption efficiency depends on the relative orientation between the X-ray beam polarization and the transition

dipole moment (TDM) orientation of the respective transitions. Therefore, measurements under different angles of incidence yield different absorption efficiencies which can be translated into the tilt of the molecular normal with respect to the sample normal (cf. inset in Fig. S3e).[3]

We have analyzed the molecular orientation by fitting the average TDM orientation a to the intensity dependence for π* transitions for adsorbates of at least threefold-symmetry (with molecular twist γ=0°):[3]

$$I_{\pi^*} \propto P\cos^2(\theta)\left(\frac{3\cos^2(\alpha)}{2}-\frac{1}{2}\right)+\frac{\sin^2(\alpha)}{2},$$

where θ is the relative orientation between the transition dipole moment (TDM) of the excitation and the polarization of the synchrotron light and P is the polarization factor of the beamline (0.91).

For both fluorinated derivatives, thin films prepared on SiO_2 substrates exhibit dichroisms which correspond to TDM orientations of α=81°. Since the respective TDMs are known to be oriented perpendicular to the molecular plane, such a dichroism corresponds to molecules in an upright configuration as similarly observed for thin films of non-fluorinated HBC on SiO_2.[4] On graphene, however, an inverse dichroism is found, revealing that the molecules adopt a lying configuration on these substrates, again in perfect congruence with the situation found for the parent HBC. All dichroism measurements are in perfect agreement with the XRD analysis presented in the main paper, which has equivalently revealed upright molecular alignments on SiO_2 and lying molecular geometries on graphene. The observed deviations from an idealized TDM orientation of 0° for the latter case can be explained by defect-induced upright growth, which is also observed in the XRD experiments.

References

[1] Y. Kikuzawa, T. Mori and H. Takeuchi, *Org. Lett.* 2007, **9**, 4817.

[2] D. J. Jones, B. Purushothaman, S. Ji, A. B. Holmes, and W. W. H. Wong, *Chem. Commun.* 2012, **48**, 8066.

[3] Stöhr, J. *NEXAFS Spectroscopy*; Gomer, R. Ed.; Springer: Berlin, Germany, 1992.

[4] P. Beyer, T. Breuer, S. Ndiaye, A. Zykov, A. Viertel, M. Gensler, J. P. Rabe, S. Hecht, G. Witte and S. Kowarik, *ACS Appl. Mater. Interfaces*, 2014, **6**, 21484-21493.

5.6 Characterization of orientational order in π-conjugated molecular thin films by NEXAFS

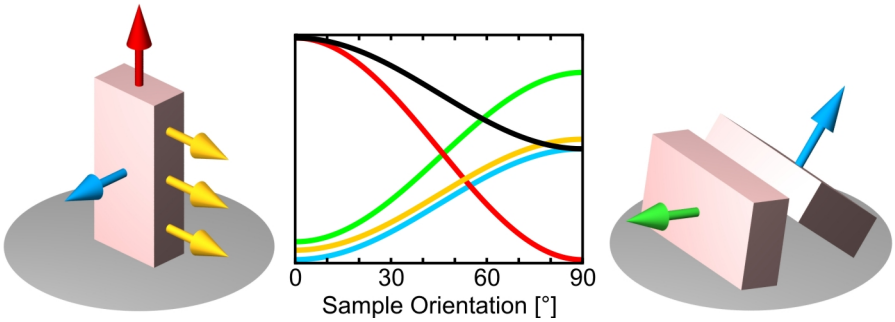

5.6.1 Inhaltsangabe

Enabled by the improved availability of synchrotron facilities, near-edge X-ray absorption fine structure(NEXAFS) spectroscopy has become a widely used technique, especially due to its tunable, potentially veryhigh, surface-sensitivity and its capability of analyzing the electronic structure of unoccupied orbitals. Inthis article we describe the fundamentals and technical requirements for NEXAFS spectroscopy with special focus on its application to the structural characterization of organic thin films. Based on prominentexamples we discuss typical experimental applications of this technique and their characteristics compared to complementary methods. Since the evaluation of NEXAFS measurements is not straight-forwardand allows for objectionable misinterpretations, we discuss numerous parasitic and often unattendedeffects which complicate the reliable analysis of NEXAFS spectra. Especially for the case of orientationdeterminations by means of NEXAFS using dichroisms analyses, the effects of molecular geometry andcrystal packing motifs are elucidated in detail to provide a comprehensive picture on potential obstacleswhich often occur during the study of organic thin films.

5.6.2 Eigenleistung

Der vorliegende Artikel hat Reviewcharakter und umfasst eine Zusammenstellung physikalischer Prinzipien sowie eine Vorstellung der Messmethode und der Auswertung winkelabhängiger NEXAFS-Daten im Zusammenhang mit π-konjugierten molekularen Dünnfilmen. Die Auswahl der relevanten Themen erfolgte durch intensive Beratung mit allen Autoren. Folgende Abschnitte des Artikels wurden dabei von mir maßgeblich durch die Auswahl anschaulicher Beispiele, die graphische Aufbereitung der Inhalte, sowie entsprechende Textabschnitte gestaltet: *Fundamental excitation processes* sowie *Experimental requirements*. Dabei ist die Auswahl des Benzol-Pyrazin-Vergleichs als besonders anschauliches Beispiel, sowie die Erläuterungen zu den Orbitaltypen anhand von Orbitaldarstellun-

gen auf Basis eigener Rechnungen hervorzuheben. Entsprechend wurden alle Abbildungen dieser Abschnitte von mir entworfen. Ebenso wurde der Abschnitt *Dichroism* entscheidend von mir geprägt. Für die Darstellung des Dichroismus in einem zweidimensionalen Falschfarbenbild, wurde von mir, basierend auf einer Idee von Tobias Breuer, ein entsprechende Messung geplant, durchgeführt und ausgewertet. Zudem stammt die Idee und Umsetzung der möglichst illustrativen Präsentation des Zusammenhangs von Molekülorientierung und Dichroismus in Form von dreidimensionalen Quadern von mir. Des Weiteren ist die genaue Trennung der einzelnen Beiträge zu diesem Projekt aufgrund der engen Zusammenarbeit schwierig. Ebenso wie meine Kollegen zu den von mir genannten Abschnitte mit Vorschlägen und Hilfestellungen beigetragen haben, wurden von mir andere Bereiche mitgeprägt. So stammen z.B. die Daten zur Tiefenprofilierung aus einer von mir durchgeführten und aufbereiteten Messung, und zu dem Abschnitt über die azimuthale Orientierung habe ich eine Teilabbildung im Stil der bereits erwähnten Quaderdarstellung beigetragen. Der Hauptteil der Textarbeit, insbesondere das Vereinheitlichen der verschiedenen Beiträge, wurde von Tobias Breuer vor genommen.

Journal of Electron Spectroscopy and Related Phenomena 204 (2015) 102–115

Contents lists available at ScienceDirect

Journal of Electron Spectroscopy and Related Phenomena

journal homepage: www.elsevier.com/locate/elspec

Characterization of orientational order in π-conjugated molecular thin films by NEXAFS

Tobias Breuer*, Michael Klues, Gregor Witte

Fachbereich Physik, Philipps-Universität Marburg, 35032 Marburg, Germany

ARTICLE INFO

Article history:
Available online 1 August 2015

Keywords:
NEXAFS spectroscopy
Organic thin films
Photoelectron spectroscopy
Pentacene
Organic semiconductors
Surface sensitivity

ABSTRACT

Enabled by the improved availability of synchrotron facilities, near-edge X-ray absorption fine structure (NEXAFS) spectroscopy has become a widely used technique, especially due to its tunable, potentially very high, surface-sensitivity and its capability of analyzing the electronic structure of unoccupied orbitals. In this article we describe the fundamentals and technical requirements for NEXAFS spectroscopy with special focus on its application to the structural characterization of organic thin films. Based on prominent examples we discuss typical experimental applications of this technique and their characteristics compared to complementary methods. Since the evaluation of NEXAFS measurements is not straight-forward and allows for objectionable misinterpretations, we discuss numerous parasitic and often unattended effects which complicate the reliable analysis of NEXAFS spectra. Especially for the case of orientation determinations by means of NEXAFS using dichroisms analyses, the effects of molecular geometry and crystal packing motifs are elucidated in detail to provide a comprehensive picture on potential obstacles which often occur during the study of organic thin films.

1. Introduction

A detailed knowledge of the geometrical alignment of molecules at surfaces and interfaces is of key importance to derive a microscopic understanding of surface processes involved for example in heterogeneous catalysis or surface functionalization. More recently, the interest in structural information and orientational ordering in molecular thin films has been renewed by the emerging field of organic electronics [1] based on π-conjugated molecular materials. While many of these materials form crystalline films, their physical properties are highly anisotropic. For example due to the shape anisotropy of the molecular entities a pronounced anisotropy is obtained for the charge carrier mobility [2] which has been attributed to pronounced differences in the orbital overlap of neighboring molecules along the various crystallographic directions [3]. Also light absorption properties of molecules as well as exciton dynamics are anisotropic and depend sensitively on the direction of illumination relative to the molecular axes [4,5]. Of particular importance is the control of the molecular orientation within the first layer on inorganic substrates because this layer serves as seed for subsequent growth of oriented molecular films and also influences the alignment of the electronic energy levels at the interface [6,7].

Classical surface science techniques such as scanning tunneling microscopy (STM) or low energy electron diffraction (LEED) are very successful in determining the lateral structure of molecular adsorbate films [8], while the normal incidence X-ray standing waves (NIXSW) technique allows the determination of vertical spacing in extremely thin films [9,10]. Though STM allows for the imaging of individual molecules with unprecedented resolution, this technique requires rather smooth samples with sufficient conductivity and is thus mostly limited to the characterization of films with thicknesses of very few monolayers deposited on conductive substrates. Similarly, also LEED requires conducting substrates and furthermore adequate long range periodic ordering within the adlayers. All these techniques, however, do not provide a quantitative determination of the molecular tilt angle.

In the case of crystalline films rather detailed structural information including the molecular packing motif and orientation can be derived from X-ray diffraction measurements, while this analysis becomes quite challenging for film thicknesses of only few monolayers. Meanwhile a structural characterization of crystalline films by means of grazing incidence X-ray diffraction (GIXD) has become possible even for monolayer thickness by the virtue of high brilliance of modern synchrotron radiation sources and sensitive 2D detectors [11–13]. Though structural information on molecular adsorbate structures can also be derived from photoelectron

* Corresponding author. Tel.: +49 64212824158.
E-mail address: tobias.breuer@physik.uni-marburg.de (T. Breuer).

http://dx.doi.org/10.1016/j.elspec.2015.07.011
0368-2048/

diffraction (XPD), this technique is rather elaborate as it requires sophisticated modeling and is mostly restricted to (sub)monolayer films adsorbed on crystalline substrates [14]. Alternatively, vibrational spectroscopy such as infrared spectroscopy (IRS) has been used to determine molecular orientations by comparing the intensity of characteristic vibrations occurring in oriented films and samples with isotropic orientation (i.e. pellets) [15]. Despite the apparent simplicity a reliable quantitative analysis requires an elaborate treatment of reference samples [16] as well as accurate theoretical calculations of the vibrational spectrum in order to correctly assign the characteristic modes, a task which can be challenging in case of extended π-conjugated molecules [17].

An important analytical method in this context is near-edge X-ray absorption fine structure (NEXAFS) spectroscopy sometimes also referred to as X-ray absorption near-edge structure spectroscopy (XANES) which is particularly sensitive to study the electronic structure of unoccupied molecular orbitals and electronic bands of solids [18].

The probed transitions from occupied core levels into empty or partially filled electronic states are element specific and highly sensitive to the local bonding and coordination, which can be utilized to study the local electronic structure of adsorbed molecules [19,20]. Since corresponding transitions from core levels into unoccupied molecular orbitals are governed by dipole selection rules they also allow to determine the molecular orientation by analyzing the dichroism of characteristic absorption peaks (so called fine structure) near the core shell ionization edge, that occurs when the incidence angle and polarization direction of the linearly polarized synchrotron beam are varied. This structural analysis is particular advantageous as it does not require any crystalline ordering within the molecular films like in the case of X-ray diffraction or LEED analyses and can also be applied to samples with noticeable roughness. Moreover, due to the high brightness of modern synchrotron sources such measurements can be readily carried out for adsorbates even at submonolayer coverage. Particular beneficial for this high sensitivity is the low background signal for such high energetic transitions in typical detection modes (details are given in Section 4) while in UV-photoemission spectroscopy the signatures from molecular levels are frequently superimposed by a large background signal from secondary electrons of the substrate. For the analysis of molecular films NEXAFS measurements are mostly performed at the *K*-edge of the light elements which have binding energies below 1 keV, such as carbon (285 eV), nitrogen (400 eV), oxygen (535 eV), or fluorine (685 eV). Since these experiments require a tunable monochromatic incident beam in the soft X-ray range with considerable photon flux they are carried out at synchrotron facilities within ultrahigh vacuum sample environments, required for the detection process (cf. Section 3), which are nowadays available at many beamlines.

Another advantage of NEXAFS is the high sensitivity to distinguish the chemical nature of intramolecular bonds. The C1s binding energy of saturated and aromatic hydrocarbons (i.e. C—C and C=C bonds) differs by about 0.1 eV only [21], so that a reliable identification on the basis of X-ray photoemission (XPS) data where the binding energy of the initial state is measured, is rather challenging. By contrast, NEXAFS spectroscopy is also sensitive to the energetic position of the final states. As a consequence, the pronounced difference in energy of unoccupied σ* and π* orbitals related to single and double bonds causes signatures in the belonging NEXAFS spectra which enable a clear distinction. This possibility allows furthermore the use of NEXAFS signatures as characteristic fingerprints for the chemical identification of polymers [22].

Due to the multitude of available synchrotron facilities worldwide modern synchrotron based analysis techniques such as NEXAFS are nowadays widely used, while in former times when NEXAFS was developed it was used by a small group of experts in the field only. The most comprehensive description of the fundamental aspects of this technique and its technical implementations is given in the book of Stöhr [18] which mostly treats the analysis of small molecules. Since then (and particularly driven by the recent success of organic electronics) NEXAFS has often been used for the characterization of films composed of extended π-conjugated molecules which reveal distinctly more complex NEXAFS signatures than simple aromatic molecules like benzene.

Here we give a short overview of the application of NEXAFS to characterize the orientational order in molecular films with particular emphasis on π-conjugated molecular materials aiming to avoid possible misinterpretations caused by an oversimplified view of this technique. The fundamental basics of NEXAFS, its technical instrumentation and its application to organic film analysis have been thoroughly described in previous reviews [23–27] so that these aspects are mentioned only briefly here.

2. Fundamental excitation processes

To illustrate the excitation mechanism yielding NEXAFS spectra we consider in the beginning one of the simplest aromatic hydrocarbons, namely benzene (C_6H_6). In this molecule the valence electrons of the carbon atoms exhibit a sp^2-hybridization which enables the formation of σ-bonds with hydrogen and the neighboring carbon atoms. In addition, the p_z-orbitals which are aligned perpendicular to the ring plane overlap efficiently, hence yielding a system of π-bonds spread over the whole carbon ring. Absorption of X-ray photons of which energy exceeds the binding energy (also denoted as ionization potential) of the core levels (i.e. C1s levels in case of hydrocarbons) causes a photoionization process and the emission of electrons which are detected energy-resolved in X-ray photoemission experiments (XPS). By contrast, upon continuous tuning of the incident energy of soft X-rays resonant excitations from core levels into unoccupied molecular states become possible and result in distinct peaks (resonances) in the X-ray absorption spectrum at energies well below the ionization potential. For energies larger than the ionization potential the absorption spectrum reveals a characteristic edge jump since the before mentioned photoemission process becomes energetically possible. In aromatic molecular systems the lowest unoccupied molecular orbitals (LUMO, LUMO + 1 etc.) have π symmetry and excitations into these final orbitals are denoted as π*-resonances. At higher energy also excitations into σ*-orbitals (so called σ*-resonances) appear. A characteristic signature of the various NEXAFS resonances is their spectral width. The width is not only influenced by the vibrational fine-structure which may lead to asymmetric peak broadening [28], but also by the different lifetimes of the individual resonances. The low energetic π*-resonances are energetically well separated while the large number of σ*-states in extended hydrocarbons forms a quasi-continuum of states with rather short lifetime. Therefore, π*-resonances appear generally sharper than σ*-resonances which often also have comparably low oscillator strength. The different absorption channels contributing to the integrated absorption spectrum are shown schematically in Fig. 1a) for the C1s edge of benzene. Remarkably, additional rather broad but distinct resonances also appear in the NEXAFS spectrum for photon energies exceeding the ionization potential. They are attributed to excitations into quasi-bound σ*-states which are stabilized by an effective centrifugal barrier due to high angular momentum components. According to their very short lifetime these resonances have a spectral width of several eV. In the following we will discuss the NEXAFS signature in more detail at the example of benzene.

First, we note that all initial states are energetically degenerated i.e. all 6 carbon atoms have the same C1s binding energy (because they are chemically equivalent). In a simple ground state

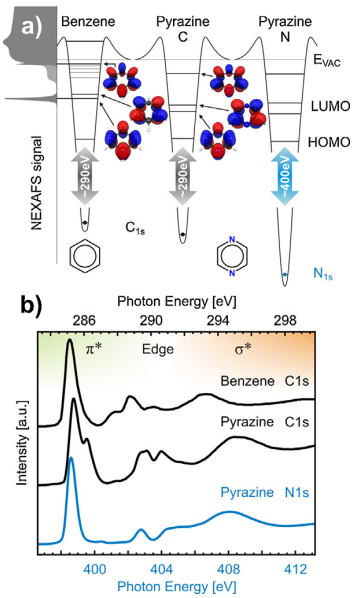

Fig. 1. (a) energy schemes showing the relevant molecular energy levels with consideration of relaxation effects as calculated using the StoBe code [29] for benzene and pyrazine. In the case of pyrazine, the carbon and nitrogen core levels are given as initial state, (b) NEXAFS spectra of solid benzene (C1s) [30] and pyrazine multilayer films (C1s and N1s) prepared by vapor dosing onto substrates held at cryogenic temperature. The photon energies of the C1s and N1s spectra are shifted with respect to the energy differences in the core levels [21].

calculation also the two lowest unoccupied orbitals, i.e. LUMO and LUMO + 1, appear degenerated. This circumstance has allowed a rather simple interpretation of the NEXAFS spectra of benzene since essentially only one prominent π*-resonance is observed (cf. Fig. 1b), which is also the case for simple benzene-derivatives [31] and graphite [32]. In such a simplified treatment the effect of electronic relaxation is not considered. As a result of the core hole formation, the electronic configuration of the molecule changes, which modulates the orbital shape as well as the energy of the respective transitions. An appropriate treatment of such electronic relaxation effects, however, shows that the mentioned degeneracy is lifted as a consequence of the symmetry break due to the presence of the core hole. However, the oscillator strength for transitions into the belonging LUMO + 1 state vanishes because the nodal plane of this final state runs through the excitation center, so that this transition is not visible in the spectra and the leading π*-resonance solely reflects excitations into the LUMO orbital. A similar situation occurs also for oligo-phenylenes [33], of which NEXAFS signature resembles that of benzene or graphite [32] despite their structural differences yielding essentially one distinct π*-resonance while higher resonances coincide with the adsorption edge and a continuum of σ*-states. A careful analysis yields, however, another π*-resonance for benzene which appears below the ionization edge and can be assigned to a LUMO + 8 orbital. For clarity, only the π*-orbitals are shown in the corresponding energy diagram in Fig. 1a). This circumstance may mistakenly lead to the oversimplification that these molecular materials have only one π*-resonance.

Generally, the degeneracy of molecular levels is also lifted for molecules with reduced symmetry. This is caused either by the shape anisotropy of the molecules (most linear polycyclic aromatic hydrocarbons (PAHs) are rod-shaped), or by introducing heteroatomic substituents or functional side groups and leads to the appearance of additional resonances in the NEXAFS spectra. This effect is illustrated by comparing the C1s NEXAFS spectra of benzene and pyrazine ($C_4H_4N_2$). In the latter molecule two diametrical C-H units of benzene are replaced by N atoms yielding an isoelectronic π-conjugated molecule. As shown in the corresponding energy diagram (cf. Fig. 1a) the energy of all unoccupied molecular orbitals of pyrazine is lowered compared to benzene, while the energy of the highest occupied molecular level (HOMO) remains nearly unaffected. Interestingly, also the C1s binding energy of pyrazine is lowered, yielding almost the same excitation energy for the lowest π*-resonance of both molecules whereas the C1s binding energies obtained by XPS reveal a characteristic difference (so called chemical shift). In contrast to benzene, also the transition into the LUMO + 1 final state has sufficient oscillator strength because the nodal plane of the corresponding orbital runs through the nitrogen atoms so that the excitation can be observed (cf. experimental spectra in Fig. 1b). Interestingly, this lifting of the degeneracy due to break of symmetry is already reproduced in a simple ground state calculation, i.e. without consideration of a core hole (own result, not shown).

The presence of heteroatoms enables also the acquisition of NEXAFS spectra at other edges, such as the nitrogen *K*-edge in the case of pyrazine. Though the energy regions of N1s and C1s NEXAFS spectra are distinctly different because of the higher N1s binding energy, the spectral signatures can be well compared in this case since both excitation processes have quasi the same molecular final states (if electronic relaxation is not considered). Fig. 1b compares the N1s and C1s NEXAFS spectra of pyrazine which exhibit great similarity since the energetically lowest and third-lowest excitations as well as the σ*-related resonances at higher energies are found with similar intensity and at equal energy positions with respect to the core level energies. Interestingly, however, the second π*-resonance is absent in the N1s NEXAFS spectrum. Like in the case of benzene this excitation corresponds to an excitation into the LUMO + 1 orbital which, however, has no oscillator strength because the nodal plane of this orbital runs through the nitrogen excitation centers as explained above.

As mentioned before, the low energetic leading π*-resonances are well separated and thus appear as sharp features in the spectrum. By contrast, the numerous σ*-resonances form a quasi-continuum because of the high number of accessible final states. Note that already a simple molecule like benzene has about 20 possible final states below the ionization potential. Together with their large spectral width a clear assignment of these σ*-resonances is rather difficult. However, by analyzing the geometry of the belonging final orbitals, characteristic features can be obtained which are illustrated for the case of benzene in Fig. 2). Below the ionization potential most σ*-orbitals exhibit a characteristic nodal plane between the C and H atoms and thus can be attributed to σ*-(C—H) resonances. Another characteristic is the large spatial expansion of these orbitals. Compared to the LUMO orbital which has π-symmetry (cf. Fig. 2a) the σ*(C—H) orbitals are distinctly large and are often denoted as Rydberg states in analogy to weakly bound atomic states[1]. By contrast, most orbitals that belong to σ*-resonances above the ionization potential exhibit characteristic nodal planes between the C—C and C—H bonds (cf. Fig. 2c).

Since the energy of σ*-resonances depends critically on the bond geometry they can be used to characterize effective bond lengths and molecular distortions (further information on this topic can be found in [18]). In connection with NEXAFS studies of large π-conjugated molecules a distinct shift of σ*-resonances was also

[1] Regarding the exact nature of Rydberg-states in molecules, different definitions have been proposed [28,34]. Depending on the applied definition, one can also identify orbitals below the ionization potential which can be considered as (normal) valence orbitals with Rydberg-state admixture. However, this differentiation is frequently unattended in the literature and resonances are labeled as Rydberg-states.

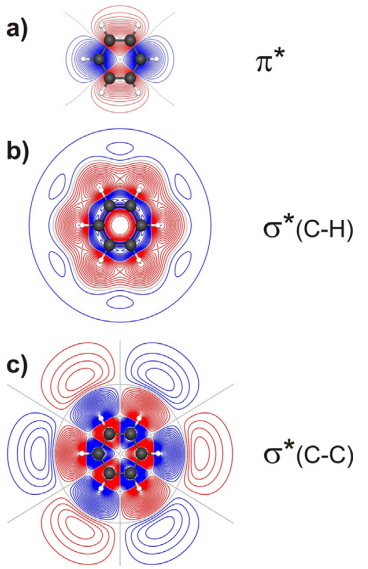

Fig. 2. Cuts through different ground state LUMO orbitals of benzene, 0.5 Å below the molecular plane: (a) LUMO, (b) LUMO + 9, (c) LUMO + 18 all visualized with same electron density cutoff. Note that the σ*-resonances are spatially rather extended, which explains their frequent denotation as Rydberg states (see text).

observed when comparing the C1s NEXAFS signatures of pentacene in van-der-Waals-stabilized multilayer films and monolayer films that are chemisorbed on a metal surface [35].

The discussed simple examples already show that several aspects need to be taken into consideration in order to explain the basis of NEXAFS spectra. Though a detailed understanding and assignment of all NEXAFS resonances in general requires rather precise knowledge of the electronic molecular structure, a quantitative analysis such as an orientation determination (which will be discussed in Section 6) can still be performed for planar π-conjugated hydrocarbons. This is possible because the low energetic C1s NEXAFS resonances have π* character which have a characteristic transition dipole moment (TDM) that is oriented perpendicular to the aromatic ring plane [36].

Aiming at a more detailed understanding of the NEXAFS signature, however, a thorough theoretical analysis is required. In the meantime various theoretical approaches and computer codes to calculate NEXAFS spectra have been developed which can also handle large aromatic hydrocarbons. These approaches differ essentially regarding the method to evaluate the electronic structure of the system under consideration. Today either density–functional theory (DFT) codes, implemented e.g. in StoBe [29], deMon2k [37], FDMNES [38], or ADF [39], codes based on quantum chemical ab initio methods, implemented e.g. in CASSCF STOCKHOLM [40], or codes applying Green function methods, implemented e.g. in FEFF9 [41], are used. These theoretical approaches allow nowadays to compute NEXAFS signatures also of rather extended π-conjugated molecules [42,43]. In an elaborate treatment not only the unoccupied molecular orbitals are calculated but also the impact of the generated core hole on the wave functions of the final molecular state (so called electronic relaxation) needs to be taken into consideration. Such a core hole screening not only leads to shifts in the energetic position (and possibly order of appearance) but also affects the oscillator strength of individual resonances. These effects have recently been analyzed in detail by the example of anthracene [44].

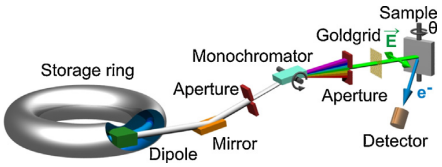

Fig. 3. Scheme of a dipole beamline showing the essential optical and detection elements for NEXAFS measurements.

3. Experimental requirements

Up to now the NEXAFS principle was discussed generally as absorption of X-ray photons due to excitations of core electrons into unoccupied final states. In fact, the absorption is not measured directly in the experiment, since the high absorption coefficient of most material for soft X-rays limits transmission measurements to elaborately prepared samples of limited thickness which are detached from the supporting substrate[2] [46]. Therefore, a closer look on the technical details of a standard NEXAFS setup is given in the following section.

Since NEXAFS spectroscopy requires a continuous photon spectrum in the X-ray region, which laboratory X-ray sources cannot provide, these measurements can only be carried out at synchrotron radiation sources. The actual origin of the radiation used for experiments is an insertion device (undulator or wiggler) or a bending magnet placed in the electron storage ring. Though undulators provide X-ray beams of much higher intensity and brilliance than for example dipole magnets do, the high photon flux in turn can be detrimental, since radiation damage can be a severe problem, especially for organic compounds [47,48]. The physical basis of the synchrotron radiation is the emission of electromagnetic radiation (Bremsstrahlung) when electrons experience an angular acceleration. In addition to its continuous energy spectrum the radiation is linearly polarized. Although linear polarization is not generally required for NEXAFS measurements, it is mandatory to determine molecular orientations, which will be discussed later (cf. Section 6).

Inside the evacuated beamline the X-rays are deflected onto a monochromator grating allowing to select a desired energetic region of the radiation by tilting the grating (cf. scheme in Fig. 3). Note that also X-ray photons whose frequency corresponds to a higher order harmonic of the fundamental beam may satisfy the slit-grating geometry. As a result, the beam is not perfectly monochromatic which complicates the evaluation of the measured spectra as discussed for a similar case in Section 4. A crucial aspect for the overall performance of carbon edge NEXAFS experiments is the cleanliness of the optical components. Whenever the beam strikes the surface of such optical elements, absorption occurs leading to element specific absorption lines in the beam spectrum. The combination of this energy dependent change in intensity and the energy dependent transmission of the optical elements is denoted as "beamline transmission", which has to be considered to quantitatively evaluate measured spectra. A description of the required data processing as it has been applied in all presented cases throughout this work, unless otherwise stated, is given e.g. in Ref. [49] and discussed in more detail in [24]. The beamline transmission is often rather low around the carbon absorption edge (C1s) since spurious

[2] The half-value thickness (HVT) in carbon of soft x-rays with an energy of 300 eV amounts to about 67 nm. Therefore, the carbon-containing films themselves can be easily transmitted for reasonable sample thicknesses. Since the supporting substrates themselves are typically rather thick (e.g. 100 μm thick Si-wafer), the transmittivity through the substrate is virtually zero (HVT_{Si} = 93 nm, $I(100\,\mu m)/I_0 = 2.8E-324$) [45].

carbon containing surface contaminations are difficult to impede. As a consequence, the beam intensity around the carbon *K*-edge can drop significantly. For other elements like nitrogen this aspect is not as critical. Therefore, NEXAFS measurements at e.g. the N1s and F1s absorption edge can be easily conducted at all beamlines, while C1s measurements require particularly pristine beamlines with low carbon contamination level. In many beamlines a fine goldgrid is placed directly in front of the analysis chamber. By measuring the photocurrent of this grid, it can be used as fluxmonitor to observe the temporal stability of the beam intensity and adjust the optical components of the beamline. Furthermore, this photocurrent exhibits a distinct signal in the C1s region which corresponds to inevitable carbon contaminations which are adsorbed on the grid. This signal can be used to cross-calibrate the energy of the acquired spectra [24].

Finally, the X-ray beam reaches the sample and is absorbed. As already mentioned, the absorption process is usually not measured directly. Instead, different detection modes are used, which are all based on the detection of secondary processes to quantify the absorption. If the photon energy fits to the difference between the core level and an unoccupied final state the photon can be absorbed and a core hole is created. Subsequently, this core hole will be refilled by an electron from a higher energetic level. This relaxation process is the basis of all NEXAFS detection modes. Upon relaxation, the energy difference can be either emitted as a fluorescence photon or transferred to a neighboring electron which leaves the sample as so called Auger electron. For heavy atoms fluorescence is the most probable process and allows to measure the intensity of emitted photons. In the case of light elements like carbon, nitrogen or oxygen, which are the major elements in organic molecules, Auger processes are most likely to occur. Therefore, electrons, respectively, currents have to be detected. The electron currents can be detected either by detecting the sample current ("total electron yield") or by counting electrons with kinetic energies above a certain threshold ("partial electron yield") or within a definable energy windows ("Auger electron yield") using channelplate detectors in combination with a retarding field or an electron analyzer, respectively. These detection modes and their specific advantages and disadvantages are discussed in more detail in Sections 4 and 5. If NEXAFS measurements shall be used to determine molecular orientations in so-called dichroic measurement, the sample needs to be rotatable. By rotation of the sample along an axis perpendicular to the plane spanned by the wavevector of the linearly-polarized beam and the electric field vector, the angle between the field vector and the surface can be chosen (angle θ in Fig. 3, further details in Section 6). Furthermore for some samples it is of interest to vary the direction of the electrical field vector relative to the azimuthal directions of the surface. Therefore some manipulators are also capable of azimuthal rotations along the surface normal, enabling azimuthally resolved measurements which will be discussed in Section 8.

If not stated otherwise, all spectra presented in this work have been acquired at the HE-SGM dipole beamline at BESSY II, Berlin. A detailed description of the experimental setup there is given in Ref. [26].

4. NEXAFS spectra

With larger size of the studied molecules also the complexity of the absorption spectra increases. As presented in Fig. 4a), in the experimental C1s NEXAFS spectrum of the PAH pentacene (PEN, $C_{22}H_{14}$) in its gas phase six separate peaks in the π^*-related region (282–288 eV) can be identified. The differences in energy of these excitations result from final state effects (LUMO vs. LUMO + 1) as well as initial state effects due to the six non-equivalent

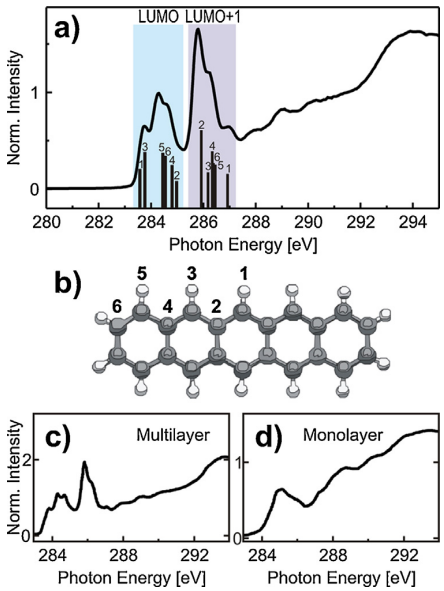

Fig. 4. (a) Gas phase C1s NEXAFS spectrum of pentacene (PEN) with assignment of different final states (LUMO and LUMO + 1) and calculated energies of transitions from different initial state levels of non-equivalent carbon atoms (data reprinted with permission from [50]) denoted in (b). (c) C1s NEXAFS spectrum of PEN multilayer, (d) monolayer on Au(1 1 1) [49].

carbon atoms (cf. Fig. 4b). Theoretical calculations from Alagia et al. [50] have indeed shown that the resonances at lower energies (shaded in light blue in Fig. 4a) can be attributed to excitations into the PEN LUMO, while the resonances in the energetic region of 285–287 eV correspond to excitations into the second lowest unoccupied molecular orbital of PEN. Upon closer inspection they have furthermore stated that the apparent six resonances exhibit a sub-structure and actually all twelve different combinations of final and initial states related to the differently coordinated carbon atoms C_1–C_6 (cf. Fig. 4b) result in energetic shifts, some of which are strong enough to allow their separation in the experiment, while others cannot be directly observed.

Like in this case, absorption signatures are typically calculated on a single-molecule-basis. This approach is justified since for van-der-Waals-bound solids the intermolecular interaction is rather weak and therefore does not affect the absorption spectra which is further supported by the finding that gas-phase spectra are typically perfectly equivalent to those of molecular solids [50,51]. Such equivalence between the gas phase and the solid state, however, does not hold true in all cases. Once the molecules experience strong interaction with their surrounding like neighboring molecules in charge-transfer complexes [52] or with the supporting substrate, their electronic structure can be strongly modified which results in severe changes in the absorption spectra. This is especially true for molecular monolayers chemisorbed on metal substrates [35,53–55]. One example is presented in Fig. 4c and d), where C1s NEXAFS spectra of PEN multilayer and monolayer films on a Au(1 1 1) substrate are compared [49]. While the multilayer spectrum perfectly resembles the gas phase spectrum as discussed before, the monolayer spectrum is broadened out and the original resonances can no longer be identified. By that means, NEXAFS spectroscopy is also sensitive to the chemical vicinity and enables to precisely discriminate between monolayer and multilayer films [35].

As stated in the previous section, typically secondary electrons are detected to quantify the X-ray absorption. Now, we will discuss

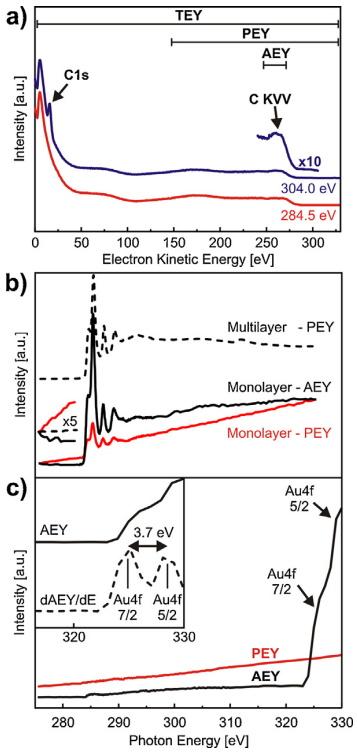

Fig. 5. (a) Photoelectron spectrum (XPS) of PEN multilayer grown on a SiO_2 substrate and recorded at E_{Exc} = 284.5 eV (red) and E_{Exc} = 304 eV (blue) with denotation of different detection modes, (b) C1s NEXAFS spectra of CuPc monolayer on Au(1 1 1) detected in AEY (black) and PEY (red) compared to multilayer spectrum (dashed), (c) comparison of PEY and AEY C1s NEXAFS spectra of a clean gold substrate with strong signal contributions from core electrons in AEY. (For interpretation of the references to color in this figure legend, the reader is referred to the web version of this article.)

the energetic spectrum of these electrons and compare the different signal detection modes.

In Fig. 5a photoelectron spectra of a PEN multilayer film deposited on a SiO_2 substrate measured at different excitation energies (284.5 eV and 304.0 eV) are presented. At low kinetic energy, a strong distinct peak is found, which corresponds to electrons that have experienced several inelastic scattering processes. At higher energies, also signals from elastically or non-scattered electrons are observed, e.g. the carbon KVV Auger electrons at an energy of about 263 eV [56]. As the probability to leave the sample without experiencing scattering processes decays exponentially with increasing film thickness, the majority of the non-scattered electrons is emitted from molecules of the top-most layers. This circumstance can be utilized to control the probe depth of NEXAFS measurements: detecting only elastically and non-scattered electrons results in highest surface sensitivity, while counting all electrons regardless of their energy also probes deeper layers. Based on these reflections three prominent different data acquisition modes have been developed: The total electron yield (TEY), the partial electron yield (PEY) and the Auger electron yield (AEY). In the TEY mode the total number of emitted electrons is measured by monitoring the sample bias current to compensate for the emitted electrons. In the PEY mode, electrons with low kinetic energy (e.g. below 150 eV) are suppressed using a negative retarding field in front of a channelplate detector. By that means only electrons with comparably high energy are collected, while electrons from deeper layers are mostly blocked. Finally, precise energetic windows can be defined for the detected electrons using an energy analyzer. This energetic window is in many cases set around the kinetic energy of the Auger electrons which are emitted during the molecular relaxation. Therefore, this detection mode is denoted as Auger electron yield (AEY). Clearly, the probe depths of the mentioned detection modes follow $d_{TEY} > d_{PEY} > d_{AEY}$.

Despite their elegance and the advantage of high surface-sensitivity the PEY mode and AEY mode can cause some complications in the signal interpretation compared to the TEY mode. For example, direct emissions of core level electrons (e.g. Au $4f_{7/2}$ at E_B = 84.0 eV [21]) can mistakenly occur throughout the whole – or even worse – parts of the spectrum. One result of such a circumstance is presented in Fig. 5b) for the case of copper phthalocyanine films measured in PEY with a retarding field of −150 eV. While for multilayer films (dashed line) the signal below the absorption edge is rather constant, a distinct rise of the signal is found for monolayer films (solid red line), which appears surprising at first sight since there are no final states available in which the molecules could be excited at that energy. The reason becomes clear by considering the core level energy of the gold substrate. The binding energies of the Au $4f_{7/2}$ and Au $4f_{5/2}$ states are 84.0 eV and 87.68 eV, respectively. Upon excitation by a photon beam with an energy of 270 eV to 330 eV these emitted electrons have kinetic energies of 186 eV–246 eV (Au $4f_{7/2}$) and can therefore pass the retarding field in front of the detector. This means that they always contribute to the PEY signal and their absolute contribution depends on the respective photoelectron cross-sections (Scofield-factors) and the transmission of the beamline optics. Since both of these factors are energy-dependent, the contribution does not result in a constant background, but causes a modulation of the acquired spectrum, which can complicate the quantitative analysis as required for orientation determination (see Section 6). In the present case, the beamline transmission increases with higher energy which leads to the observed signal increase. At higher film thicknesses the substrate core level emission-related signal is strongly attenuated which results in only negligible contribution to the PEY signal (dashed line in Fig. 5b), hence leading to a constant pre-edge signal. Also in the AEY spectra of the monolayer the signal below the absorption edge remains constant (solid black line). This is due to the different detection window in the AEY compared to the PEY, in this case chosen as 250 eV to 270 eV. Since the highest kinetic energy of the emitted core level electrons is 246 eV, they do not contribute to this signal in the given case.

Another very strong effect on the spectra that should be obviated for usable spectra is presented in Fig. 5c). Here, spectra of a bare gold substrate acquired in PEY and AEY are shown. In this case, the detection windows in the AEY acquisition was chosen as 240 eV to 260 eV. Therefore, the kinetic energy of the emitted gold core level electrons is sufficient to enter the detection window at energies of 240 eV + 84 eV = 324 eV (Au $4f_{7/2}$) and 240 eV + 87.7 eV = 327.7 eV (Au $4f_{5/2}$). Indeed, at these energies, strong additional signal contributions are observed in the AEY, which can be directly identified as the Au 4f core levels by analyzing the signal derivative (cf. inset in Fig. 5c). As expected, such edges in the NEXAFS spectrum do not occur for the PEY, where instead the aforementioned monotonous signal increase is found as result from the core level electrons. These examples show that the detection mode always has to be chosen under consideration of all contributing signals, especially the energy and intensity of core level emissions.

An additional complication may occur, when substrates are used which yield NEXAFS signals themselves. This is for example the case if C1s NEXAFS investigations are performed on samples prepared on graphite substrates. Similarly to the adsorbates, the C1s electrons in graphite can be efficiently excited into the present unoccupied orbitals. As a result, distinct signals in the π^*- and σ^*-related regions are observed, which may overlap with the molecular

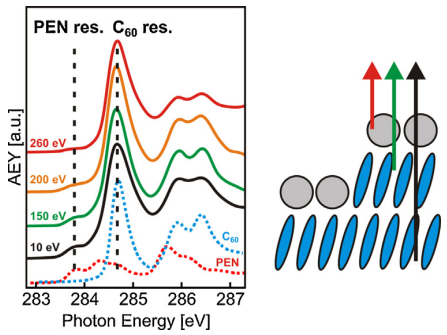

Fig. 6. C1s NEXAFS spectra recorded at different (electron) detection energies. At high detection energies (red) only the top C_{60} layer contributes to the signal while at lower energy also inelastically scattered electrons from the buried PEN layer reach the detector. (For interpretation of the references to color in this figure legend, the reader is referred to the web version of this article.)

spectrum. Due to the high surface sensitivity of NEXAFS spectroscopy in AEY and PEY acquisition (see below), this aggravates the analysis of such molecular films especially in the low coverage regime and for films which exhibit distinct islanding [57,58].

5. Surface sensitivity

By excluding the presence of such unwanted parasitic effects, the different detection modes can also be utilized to enable further insights: choosing adequate kinetic energies of the detected electrons allows to precisely control the probe depth and therefore conduct depth-profiling measurements. One example is presented in Fig. 6, where C1s NEXAFS spectra of a molecular heterostructure of pentacene and Buckminster–Fullerene (C_{60}) are shown. In this case, a layered structure with homogeneous interface has been achieved by depositing a small amount of C_{60} ($d_{nom} \sim 2$ nm) onto a PEN multilayer film at low substrate temperature [59]. In that series, C1s NEXAFS spectra have been recorded for different electron kinetic energies (E_{kin}) using small energetic windows around E_{kin} in the AEY mode. Measurements at high E_{kin} reveal only features resulting from the C_{60} molecules on top. With decreasing E_{kin} also fractions of the PEN spectrum (denoted by black arrows) become visible, thus allowing to also collect information from deeper layers. Upon separation of both signals, the separate evaluation of the signals from the top layer and deeper layers is enabled. This high surface sensitivity can be used to determine molecular orientations at the interface of organic heterostructures to investigate potential intermixing at the interface and the stability of the molecular orientation in films of different thickness. In a recent work by Schuettfort et al., this approach has been used to compare the molecular orientation in polymer films at the surface (using AEY) and near-surface regions (using PEY) and furthermore in the bulk by combining these results with NEXAFS transmission measurements [46]. In multilayered films it can furthermore be utilized to exclusively investigate the orientation of the molecules in the topmost layer while suppressing parasitic contributions from deeper layers as demonstrated for the case of pentacene layer deposition on top of C_{60}/pentacene heterostructures [59].

6. Dichroism

In general, the probability for an excitation of an electron from an initial state into a final state is given by Fermi's golden rule [18]:

$$I \propto \left| \left\langle \Psi_{\text{final}} \left| \mathbf{E} \cdot \mathbf{p} \right| \Psi_{\text{initial}} \right\rangle \right|^2 \rho_f(E) \tag{1}$$

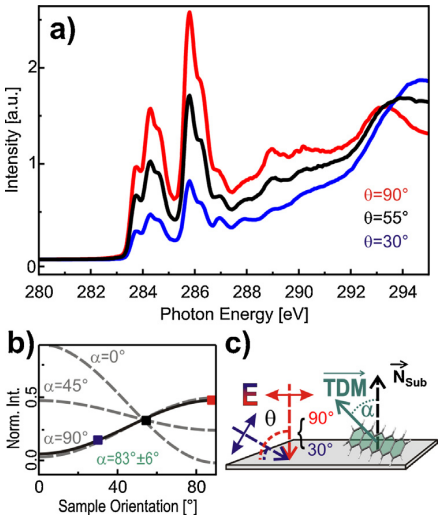

Fig. 7. (a) C1s NEXAFS spectra of PEN multilayer on SiO_2 substrate recorded at different sample orientations, (b) evaluation of dichroism, (c) scheme of experimental geometry and TDM orientation.

where **E** denotes the electric field vector, **p** the dipole transition operator and $\rho_f(E)$ the density of final states. For linearly polarized light, this simplifies to

$$I \propto \left| \mathbf{E} \cdot \mathbf{TDM} \right|^2 \tag{2}$$

where $\mathbf{TDM} = \left\langle \Psi_{final} \left| \mathbf{p} \right| \Psi_{initial} \right\rangle$ is called the transition dipole moment. For initial states with spherical symmetry and vector-type final states[3], as the case for transitions into π^*-orbitals in linear PAHs, the TDM lies parallel to the direction of the final state orbital. Therefore, the absorption strength is determined by the relative orientation between the *E*-field vector and the TDM. The exact dependence for samples with threefold or higher symmetry amounts to

$$I_{\pi^*} \propto P \cos^2\theta \left(\cos^2\alpha + \frac{1}{2P} \tan^2\theta \sin^2\alpha \right) \tag{3}$$

where P is the degree of polarization, α the angle between the TDM and the substrate surface normal and θ the sample orientation (angle between the substrate surface normal ($\mathbf{N_{Sub}}$) and the *E*-field vector, cf. Fig. 7c). Therefore, comparing the absorption signals obtained at different sample orientations enables deriving the TDM orientation, α, which gives insight into the orientation of the molecules on the surface. This is possible since the TDM orientation lies perpendicular to the aromatic molecular plane (cf. Fig. 7c) for π^*-excitations in PAHs [18], though this correlation may be slightly altered for strongly chemisorbed monolayer films [60]. In Fig. 7a, normalized C1s NEXAFS spectra of PEN multilayer films grown on SiO_2 surfaces recorded at different sample orientations are compared. Clearly, highest intensity is observed under normal incidence ($\theta = 90°$), while comparably weak signals are detected under grazing incidence ($\theta = 30°$). Fitting Eq. (3) in α then allows to derive the effective orientation of the TDM in the sample. As shown

[3] Vector-type orbitals embrace those orbitals, which can be described by one vector direction to account for the direction of the maximum orbital amplitude. Therefore, an isolated orbital that is not spherically symmetric can always be considered as vector-type. If, however, equivalent orbitals with similar binding energy and transition probability are available (e.g. σ^* (C—H)-orbitals in PAHs like pentacene), such a description is no longer possible. Therefore, such orbitals, which exhibit different spatial orientations are described as planar orbitals, if these directions at least span a common plane [16].

in Fig. 7b this yields $\alpha = 83^\circ \pm 6^\circ$ for this film, which corresponds well to the value of 86° in the crystalline $(0\,0\,1)_{PEN,TF}$-orientation derived from X-ray diffraction measurements [61,62].

In the aforementioned case the accuracy of the determined value for α is estimated as ±6°. Generally, the errors in α are non-constant and even slightly asymmetric since the dependence of the determined molecular orientation on the individual resonance intensities is strongly nonlinear (this can be seen very nicely in the dichroism plots in Fig. 13, right-hand side. As a result of the mentioned nonlinearity, the equidistant curves for α are only slightly separated for $\alpha = 0^\circ$ and $\alpha = 10^\circ$, but strongly separated for $\alpha = 40^\circ$ and $\alpha = 50^\circ$). The effect becomes clear by depicting an example: in the case of an assumed effective TDM orientation of 83° with primary uncertainties of the measured intensities of 5%, the resulting minimal and maximal values for α are $\alpha_{min} = 79.1^\circ$ and $\alpha_{max} = 90^\circ$. Equivalent primary uncertainties at a TDM orientation of 55° result in a clearly smaller splitting of these values ($\alpha_{min} = 53.2^\circ$, $\alpha_{max} = 56.8^\circ$). Therefore, molecular inclinations in the range of 30° to 70° can be determined more precisely than those corresponding either to strongly inclined (>70°) or rather recumbent (<30°) arrangements. The identification of the exact molecular orientation is further complicated by the fact that the determined orientations result from effective averaging over different orientations within the analyzed material. In the NEXAFS analysis all molecules contribute to the derived value of α, regardless whether the film is crystalline or amorphous. This constitutes an important advantage over diffraction-techniques like X-ray diffraction (XRD) or low energy electron diffraction (LEED), where only crystalline regions can be analyzed. However, one has to keep in mind that the derived value for α cannot be directly translated into actual molecular orientations without additional information from complementary experiments. In the case of the discussed PEN molecules for example, the TDM is oriented perpendicular to the molecular plane. As a consequence, the dichroism analysis allows to determine the orientation α between the molecular plane normal ($\mathbf{N_{Mol}}$) and the surface plane normal ($\mathbf{N_{Sub}}$, cf. Fig. 7c). However, it is not sensitive to rotations along $\mathbf{N_{Mol}}$. As a consequence, molecules with $\mathbf{N_{Mol}}$ perpendicular to $\mathbf{N_{Sub}}$ exhibit exactly the same dichroism for π*-resonances, regardless of the orientation of their long axis and it cannot be distinguished between molecules with their long axis and their short axis parallel to the surface (cf. Fig. 11a and b).

Like in the example presented in Fig. 7, in most experiments dichroisms are determined by recording spectra at three or four different sample orientations. In that cases obviously the significance of the derived values is reduced by the limited data basis. To enhance the statistics, in Fig. 8a quasi-continuous dichroism of a pentacene multilayer is presented, where 30 individual NEXAFS spectra have been recorded under different sample orientations and were stitched together to a two-dimensional visualization. In this representation horizontal and vertical cuts reveal interesting details: While horizontal cuts allow to extract the individual NEXAFS spectra, vertical cuts enable the direct evaluation of the dichroisms as determined at the given energy position. For example, a cut at 286 eV yields a dichroism similar to the one determined before. The very good agreement of all data points and their obtained small variance shows that such a dichroism analysis is rather stable and the corresponding error bars are indeed comparably small.

As discussed before, the resonances found at energies below 288 eV are attributed to π*-excitations. At higher energies, also σ*-type excitations contribute to the signal. Since the corresponding TDMs of the latter molecular orbitals are oriented within the molecular plane and therefore perpendicular to the TDMs of the π*-related orbitals, one might expect an inverted dichroism. Indeed, the observed dichroism is qualitatively inverted compared to that

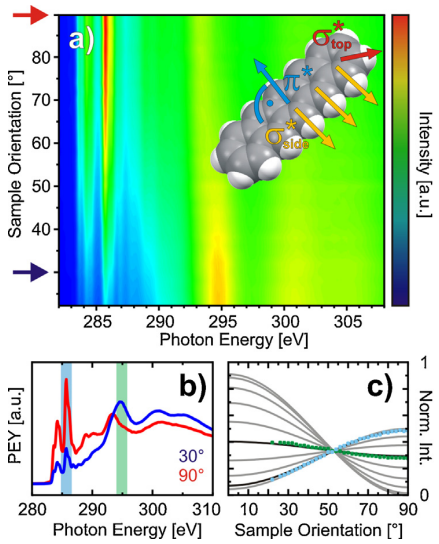

Fig. 8. (a) Quasi-continuous C1s NEXAFS measurement of PEN/SiO_2 multilayer film, (b) spectra recorded at 30° (blue) and 90° (red). Marked area denotes the energy at which the dichroisms are continuously evaluated in (c). (For interpretation of the references to color in this figure legend, the reader is referred to the web version of this article.)

of the π*-excitations. However, a quantitative analysis yields a strongly reduced dichroism corresponding to an effective TDM orientation of about 50°, which is far from being the complement to 83°. Though this seems contradictory at first glance, it can be easily understood by considering the nature of that excitation process.

Though all σ*-type orbitals are oriented in the molecular plane, the orientation of the individual TDMs inside the plane is strongly different. For example, some of them are oriented along the C—H bonds facing to the molecular side, while others point to the top of the molecule (cf. green and red arrows in Fig. 8a, molecular scheme). Since these states exhibit short lifetimes, they are rather broad in energy and therefore cannot be perfectly separated from one another. As a consequence, the observed dichroism results from contributions of numerous resonances, all with different individual dichroisms. Due to the typically high number of such excitations and their broad peak shape the dichroism analysis for these resonances is severely complicated. If two resonances exhibit similar oscillator strength but slightly different energy and different spatial orientation, this may result in apparent energetic "shifts" of resonances, since the individual strength of overlapping resonances varies with the angle of incidence. This effect can for example be seen in Fig. 8b) and the continuous measurement presented in panel a), where the strongest σ*-related peak seems to shift in energy upon changes of the sample orientation. Several examples which further explain this effect are presented schematically in Fig. 9. As mentioned before, all π*-related excitations feature TDMs with parallel orientation and therefore equivalent dichroism despite their difference in energy and oscillator strength. In panel c) a plate-like molecule is sketched with such a π*-related excitation with TDM oriented perpendicular to the molecular plane (blue) and two σ*-related excitations pointing to the side (orange) and top (red) of the molecule. As shown in panel d) for equivalent oscillator strengths, for such a molecular orientation both σ*-related resonances exhibit opposite dichroisms and their sum (black curve) exhibits a reduced dichroism. In the case of a higher number of resonances pointing to the side of the molecule (Fig. 9 e), the integral dichroism of the σ*-related resonances is even inverted and therefore qualitatively equivalent to that of the π*-related excitations.

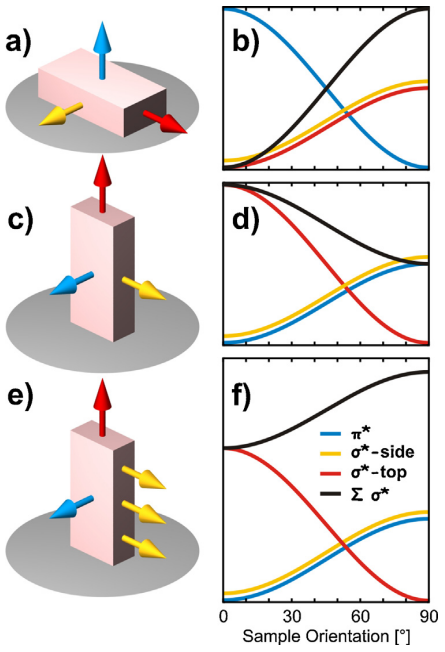

Fig. 9. Scheme of different TDM orientations corresponding to π*-(blue) and σ*-related (orange, red) transitions in plate-like molecules with corresponding dichroisms for given mol. orientation. The orange spectra (σ*-side) are slightly shifted for clarity. (For interpretation of the references to color in this figure legend, the reader is referred to the web version of this article.)

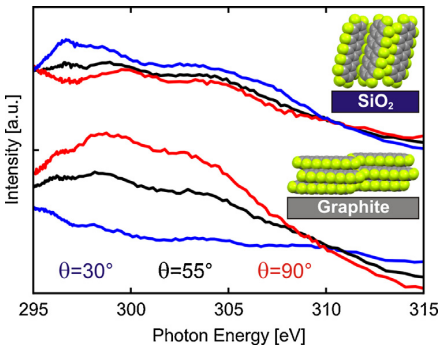

Fig. 10. C1s NEXAFS spectra showing a magnification of the σ*-region of perfluoropentacene thin films in different molecular orientation: uprightly-oriented molecules on SiO_2, flat-lying molecules on graphite. The spectra of PFP/graphite are shifted from the PFP/SiO_2 spectra for clarity.

If the molecule lies flat on the surface, however, all the TDMs of σ*-related excitations lie parallel with respect to the experimental geometry. In such a case, the dichroisms of the side-facing and top-facing excitations are indeed equivalent and inverse to that of the π*-related resonance.

Experimental proof for this interpretation is provided in Fig. 10. Here, the dichroism of the σ*-related excitations is compared for multilayer films of perfluoropentacene ($C_{22}F_{14}$, PFP) in different molecular orientation. While in an upright configuration as found in PFP films on SiO_2 the intensity of the σ*-resonances is virtually constant (dichroism some-where in between the cases presented in Fig. 9c and e, for a full spectrum of PFP multilayers on SiO_2 see [63]), a strong dichroism is observed for

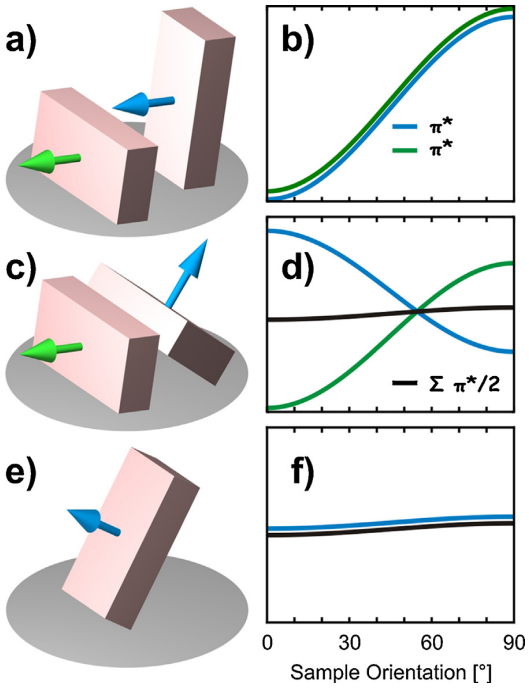

Fig. 11. Interrelation of dichroism of π* resonances and molecular orientation of planar π-conjugated molecules. (a and b) Dichroism of upright and tilted molecules (green curve slightly shifted for clarity), (c and d) effective TDM-orientation in a herringbone arrangement for lying molecules, (e and f) dichroism of molecules with tilt angle of 56° compared to the effective dichroism shown in (d) (blue curve slightly shifted for clarity). Arrows denote the orientation of the TDMs related to π*-excitation. (For interpretation of the references to color in this figure legend, the reader is referred to the web version of this article.)

flat-lying molecules on graphite substrates (cf. lower set of curves in Fig. 10).

7. Impact of crystal packing motif on dichroism analysis

The quantitative interpretation of NEXAFS spectra is further complicated when the molecular packing motifs within the unit cell have to be considered. In molecular crystals and crystalline films, where the unit cell contains molecules which are not translationally equivalent, the TDM orientations of these molecules can be non-parallel. As discussed before, this is unproblematic for π*-related excitations in PAHs if the molecules are only rotated along the axis normal to the aromatic plane since in this case the relative orientation of the TDM remains unchanged (cf. Fig. 11a and b). For other configurations in the unit cell, however, the situation becomes more complex. This is illustrated at the example of a herringbone packing motif which is adopted in the bulk crystal structure of many PAHs. Especially when the long axes of the molecules in the unit cell are oriented parallel or nearly parallel to the surface (generally referred to as lying or recumbent orientations) the individual TDMs of both molecules lead to distinctly different dichroisms for both molecules in the unit cell. One such example is presented in Fig. 11c. Though both molecules are aligned with their long axis parallel to the substrate, the individual TDMs are oriented with 80° (green) and 40° (blue) relative to the substrate normal, leading to an effective TDM of about 56° (cf. black curve in Fig. 11d). As mentioned before, it is extremely important to use complementary techniques in such cases to discriminate between molecules in “herringbone-lying” configurations and geometries

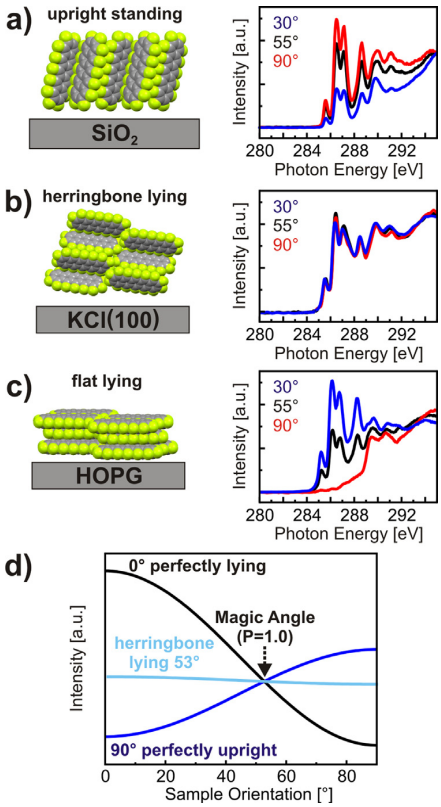

Fig. 12. Dichroism of π* resonances of PFP films in (a) upright orientation, (b) herringbone-lying orientation and (c) planar configuration with (d) corresponding dichroism curves.

where the molecules are tilted along their long axis by 56°, which yield the exact same dichroism (Fig. 11e and f).

In selected cases, this interrelation can be used to draw conclusions about the bulk structure of the investigated compound. Like pentacene also its perfluorinated compound PFP exhibits a herringbone packing-motif in its crystalline bulk structure. Therefore, in "herringbone-lying" arrangements like the $(1\,0\,2)_{PFP}$-orientation which can be prepared in films deposited onto potassium chloride substrates [4], a quantitative analysis of the TDM yields a value of $\alpha = 53°$, although the long molecular axis lies nearly perfectly parallel to the surface (cf. Fig. 12). In contrast, for films prepared on graphite substrates virtually no π*-related peaks are observed under normal incidence and the derived TDM orientation amounts to $\alpha = 10°$ (Fig. 12c). As discussed before, such a dichroism cannot occur in a herringbone arrangement, especially since the herringbone angle between both PFP molecules in the molecules is nearly perfectly perpendicular. In such a configuration one molecule which lies perfectly flat on the surface would always be accompanied by one counterpart that is tilted by 90°. Therefore, the lowest observable effective TDM orientation is $\alpha = 45°$. To further quantify the significance of this observation, the ratios between the intensities observed at sample orientations of $\theta = 30°$ and $\theta = 90°$ for a given effective TDM orientation can be calculated. As consequence of the lowest possible effective TDM orientation of $\alpha = 45°$ the highest observable ratio between $I(30°)$ and $I(90°)$ amounts to 1.68. In the mentioned case of PFP/graphite films, the observed ratio however was 40.1, further proving the reliability of this evaluation. Supporting XRD measurements have furthermore allowed to determine the actual packing motif in these thin films, showing that indeed the molecules adopt a planar packing motif, which is compatible with the observed TDM orientation [57]. If the relative orientation of both molecules in the unit cell (i.e. their herringbone angle) is known to remain unchanged, the observed effective TDM orientation can also be disentangled by considering the contributions of both molecules. In such cases, the actual molecular tilt can be precisely determined despite the presence of a herringbone arrangement in the bulk structure as described in Section 9 for the case of monolayer films [64].

These examples show that despite their comparably high absolute errors in orientation determination, NEXAFS can be used to precisely differentiate between different polymorphisms, especially between herringbone and planar arrangements [57,59].

8. Samples with lower symmetry

In Section 6 we have constrained the discussion to samples with threefold or higher symmetry since this is the most common case found e.g. for (1 1 1)-oriented metal surfaces or isotropic substrates like SiO_2 (note that isotropic substrates are interpreted as ∞-fold). For samples prepared on substrates with such high symmetry, the azimuthal dependence in the decisive Eq. (4) is averaged out. Consequently, the absorption intensity is independent of the azimuthal sample orientation φ (angle between TDM projection onto the surface and E-field vector, cf. inset of Fig. 13), which therefore can be ignored both in the experiment and the data analysis. However, for samples with lower symmetry, this does not hold true. In the most general case, the absorption probability for π*-excitations is given by

$$I_{\pi*} = P\left(\cos^2\theta\ \cos^2\alpha + \sin^2\theta\ \sin^2\alpha\ \cos^2\varphi + \sin\alpha\ \cos\alpha\ \sin\theta\ \cos\theta\ \cos\varphi\right) + \sin^2\alpha\ \sin^2\varphi \quad (4)$$

which simplifies to

$$I_{\pi*} = P\left(\cos^2\theta\ \cos^2\alpha + \sin^2\theta\ \sin^2\alpha\ \cos^2\varphi\right) + \sin^2\alpha\ \sin^2\varphi \quad (5)$$

for samples with twofold symmetry, since the terms containing $\cos\varphi$ are averaged out (in the case of threefold and higher symmetry, also the terms containing $\cos^2\varphi$ are averaged out, leading to Eq. (3)).

In such cases, the simple dichroism plots as presented in Fig. 7b) cannot be applied. The correct dichroism plots for all substrate symmetries are presented in Fig. 13. Apparently, some fundamental principles of the NEXAFS evaluation are modified in these cases. First, not all of the possible dichroism curves are monotonous. For substrates without symmetry (1-fold substrates, such as single-crystals of compounds with triclinic lattices) at $\varphi = 0°$ all TDM orientations relative to the surface normal (α) lead to non-monotonous curves as for example observed for the adsorption of self-assembled hexadecanethiol monolayers on In $P(1\,1\,0)$ [65]. Since in these cases two parameters (φ and α) instead of one (α) have to be determined, a higher number of spectra is required in order to obtain precise information on the molecular orientation. The second important difference refers to the so-called magic angle. For substrates with threefold or higher symmetry the intensity at $\theta_{magic} = \tan^{-1}\left(\sqrt{2P}\right)$ is independent of the TDM orientation α. Therefore, spectra acquired at this angle of incidence are not modulated by dichroism effects and reveal the actual oscillator heights of all resonances, similar to powder spectra in X-ray diffraction. For perfect polarization of the X-ray light ($P = 1$), θ_{magic} amounts to 54.74°, which is the reason why many NEXAFS spectra are acquired at 55°. We note, however, that this value is significantly different for non-perfect polarizations. For $P = 0.85$ e.g. it amounts to 52.5°. Consequently, all dichroism curves for samples with threefold or higher

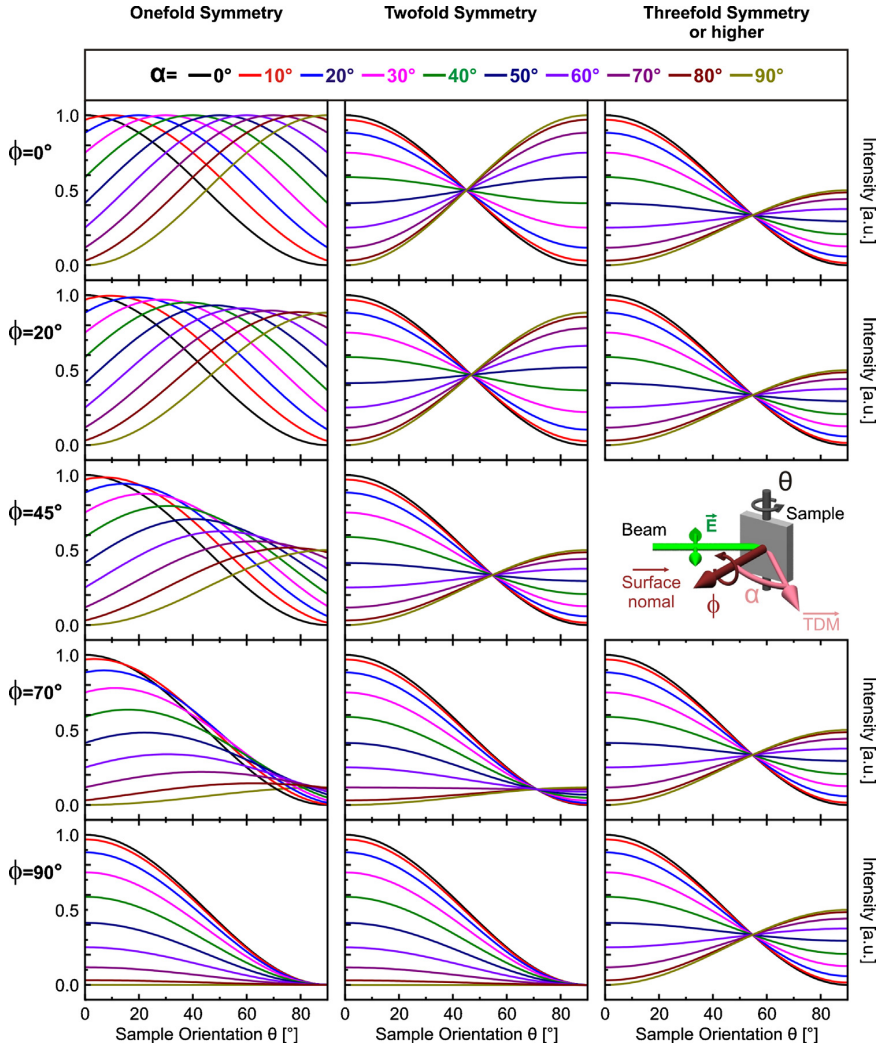

Fig. 13. Dichroism plots showing the dependency of the intensity of π^*-type NEXAFS resonances for different substrate symmetries and different azimuthal orientation with scheme defining the relevant angles. Note that in systems of threefold and higher symmetry, the dichroisms are independent of the azimuthal orientation.

symmetry cross at this point. In the case of twofold-symmetry, however, the value of the magic angle depends on φ and amounts to $\theta_{\text{magic}} = \tan^{-1}\left(1/\cos\varphi\right)$ for $P = 1$. Finally, for substrates with one-fold symmetry there is no magic angle. The curves do not cross in one point except from the case of $\varphi = 90^\circ$ at $\theta = 90^\circ$ (this is where no absorption occurs at all, since the *E*-vector and all TDMs are perfectly perpendicular). All these considerations are valid for vector-type orbitals. In the case of plane-type orbitals, a similar situation is found, which is, however, further complicated due to the mixture of different TDM orientations at a given energy. We note that frequently e.g. σ^*-related excitations in the C1s region of linear PAHs are interpreted as plane-type (see footnote 3), while, however, also isolated σ^*-resonances may feature a distinct spatial orientation and therefore be of vector-type as in the subsequently discussed example.

This azimuthal dependence in turn allows to determine the lateral alignment of molecules on a substrate. If measurements under different azimuthal angles at fixed θ do not yield the same spectra, this directly proves that the molecules are laterally not randomly oriented but exhibit a preferential azimuthal alignment. Such an analysis has e.g. been conducted by Kiguchi et al. [66], where the lateral alignment of α-sexithienyl (6T) in lying molecular orientation on Cu(1 1 0) and Ag(1 1 0) surfaces has been studied by azimuthally resolved NEXAFS measurements at the sulfur K-edge (cf. scheme in Fig. 14a). As presented in Fig. 14b), the intensity of the σ^*- resonance related to σ^*(S—C)-bonds measured under normal incidence depends strongly on the relative orientation between the electric field vector and the azimuthal surface directions. Since the maximal intensity is observed for **E||Cu[0 0 1]** (Fig. 14c) and the respective TDM is known to lie parallel to the long axis of the molecules, this allowed to conclude that the 6T molecules align with their long axis along this azimuth.

9. Structural characterization in complex monolayer films

A further important application of NEXAFS spectroscopy is the analysis of monolayer structures. Especially in the case of self-assembled monolayers (SAMs) which potentially combine simple preparation with manifold tuning possibilities of surface characteristics [67] NEXAFS provides an important route to characterize orientational order in such systems [68]. Because of their ease of preparation by means of immersion organothiol SAMs adsorbed

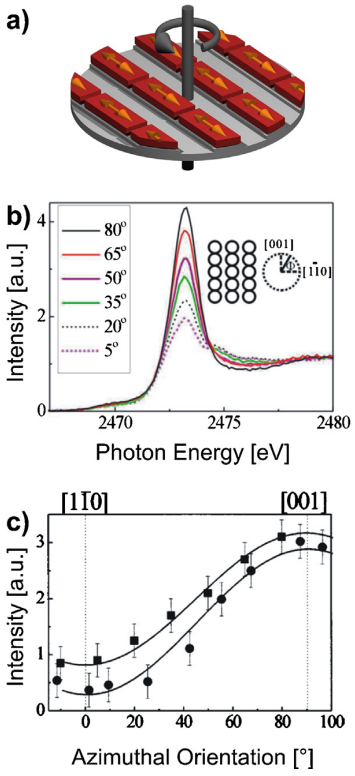

Fig. 14. (a) Scheme of azimuthal NEXAFS measurements, (b) series of S1s NEXAFS spectra of 6T molecules on Cu(1 1 0) recorded under normal incidence ($\theta = 90°$) with different *E*-field vector orientations (E || Cu [1–10] at 0°, E || Cu [0 0 1] at 90°), (c) azimuthal dependence (squares) (circles correspond to the equivalent adsorption of 6T on Ag(1 1 0)). Figure reprinted with permission from [66].

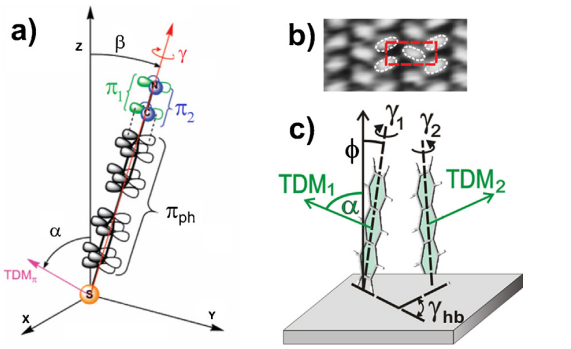

Fig. 15. (a) Scheme of alkanethiol with denotation of angles α (TDM orientation), β (tilt angle) and γ (twist angle) (figure reprinted with permission from [73]). (c) The relative orientation of the transition dipole moments in aromatic films with a herringbone arrangement [64] together with (b) high resolution STM data directly showing the herringbone arrangement [78].

on gold substrates have become model systems to understand the ordering mechanism and molecular structure in such monolayers. In the early stages aliphatic SAMs with alkane backbones have been considered. Because of the absence of π^* orbitals in alkyl chains the dichroism of σ^*-resonances is analyzed to determine the molecular orientation. For this analysis either σ^*(C—C) signatures are used which are subsumed to an average resonance with belonging TDM along the molecular axis or the energetically lower lying σ^*(C—H) resonance (commonly also referred to as Rydberg resonance R*) is considered of which average TDM is orientated perpendicular to the chain axis. [69,70] Because of the energetic width of the σ^* NEXAFS signature (caused by the multitude of underlying resonances, cf. discussion in Section 6) and the superimposed background signal of the absorption edge this analysis is less accurate. More recently, SAMs featuring aromatic backbones have become the focus of interest because they have rigid backbones and exhibit interesting electronic properties enabling potential applications in the field of organic electronics. In these systems the distinct π^*-resonances can be used to determine their orientational order [71]. A closer inspection, however, reveals that the orientation of the molecular backbone relative to the surface normal (β) cannot be determined directly from the determined TDM orientation (α) but also depends on the molecular twist angle (γ) (i.e. rotation around the long axis, cf. Fig. 15). As these angles are interrelated via [72]

$$\cos\alpha = \sin\beta \quad \cos\gamma. \tag{6}$$

assumptions have to be made for one of both parameters, e.g. from the twist angle found in bulk crystals, to allow the determination of the other parameter [71]. An alternative strategy allowing to evaluate both values independently is based on the use of chemical markers and their specific orientation which has been demonstrated for cyano-terminated oligophenyl-SAMs [73]. For that case the orientation of the phenyl rings (α_{ph}) was derived from the dichroism of the π_{ph}^* resonances obtained in C1s NEXAFS measurements, while N-edge NEXAFS measurements were employed to determine the orientation of the marker from the dichroism of the π_3^* resonance corresponding to π-orbitals of the CN bond with belonging TDM within the ring plane (cf. Fig. 15a). A similar approach has also been applied to determine the orientation and twist of SAMs consisting of azobenzene-based photoswitches which change their orientation upon light illumination [74].

Another complication becomes apparent if one compares the molecular structure of *para*-oligophenylenes in their gas and crystalline phases, as they show a distinctly different internal twist of the phenyl rings (also referred to as dihedral twist or torsion). While this additional degree of freedom has not been considered in the before mentioned analyses, theoretical studies have predicted that this internal twist also effects the packing and structure of SAMs [75]. In fact by using nitrogen substituents as chemical marker and replacing the outer phenyl ring of biphenyl and terphenyl backbones of the SAMs by a pyridine unit, the internal twist between phenyl and the pyridine rings has been determined from the dichroism of π^* resonance obtained in the C1s and N1s NEXAFS data. Comparing the experimental data with theoretical simulations of the NEXAFS signature showed that actually a dihedral twist of about 18° is adopted in the SAMs, thus emphasizing the importance of its consideration for a detailed geometrical analysis of SAMs [26,76]. In a later study, this approach was also applied to symmetrically substituted dicarbonitrile-*para*-oligophenyls in order to characterize the twisting of *para*-oligophenyl mono- and multilayer films grown on a Ag(1 1 1) surface [77].

Similar to the case of the before discussed crystalline PAH films (cf. Section 7), also SAMs with fully conjugated backbones such as napthalenethiols or anthracenethiols can adopt a herringbone packing motif (cf. Fig. 15c). This in turn also affects the analysis of NEXAFS data to derive the molecular tilt angle because it leads to an additional averaging over all molecules within the unit cell. An experimental challenge is the determination of the herringbone angle in such SAMs because it may differ from the packing motif adopted in the crystalline phase of the aromatic moiety (e.g. the acene) due to the constraint of the underlying gold lattice [64]. For the case of SAMs with anthracene backbone it has been possible to determine this herringbone angle γ_{hb} directly by means of high resolution STM (cf. Fig. 15b) [78] which enabled the determination

of the tilt angle (ϕ) of the backbone with respect to the sample normal [64].

In some cases the orientation of separate building blocks within a molecular entity can even be determined independently. The well-known organic semiconductor rubrene, for example, consists of a tetracene backbone and four phenyl rings which are attached at the long sides of this backbone. Since the relative orientation of the phenyl rings and the tetracene backbone strongly influences the structural and electronic properties of rubrene, the precise analysis of the individual orientations is mandatory. Since backbone and phenyl rings are not conjugated but form individual aromatic sub-systems, the molecular NEXAFS spectrum can be sufficiently described as superposition of tetracene and benzene spectra [79]. Therefore, the dichroism of the π^* resonances of both entities can be separately evaluated which enables the determination of the individual orientations of both aromatic subunits [80]. The same approach is applied to porphyrines to independently determine the configuration of the individual phenyl rings as well as the carbon macrocycle. Enabled by the exclusive localization of selected molecular orbitals to either the macrocycle or the phenyl rings in the molecular rim and their sufficient energetic separation, their dichroisms can individually be evaluated [81,82].

A similar problem is encountered in the case of non-planar molecules like diamondoids, where the complex cage-like structure of the molecules further complicates the quantitative evaluation of the molecular orientation. In that case, numerous σ^*-related excitations, all with different TDM orientations, contribute to the spectra. As discussed in Section 6 for the case of plate-like molecules, this strongly aggravates the corresponding analyses. A possible framework allowing the determination of the molecular tilt and twist SAMs with such complex structure has been proposed by Willey et al. [83]. For the case of adamantane-thiol SAMs they have simulated NEXAFS dichroisms for all possible combinations of molecular tilt and twist and compared these to the experimental data, which has allowed to derive plausible values for the tilt and twist angles.

10. Summary

In this article we have summarized the fundamental processes and the important technical details of NEXAFS spectroscopy, especially when applied to characterize organic thin films. This technique allows to precisely monitor the structure and chemical configuration of organic thin films. Utilizing the angular dependence of the absorption probability enables precise insights into the molecular orientation in such films, both in the monolayer and multilayer regime. However, such analyses are complicated by the high number of – potentially overlapping – resonances with different TDM orientations and effects of packing motifs in the solid state, which therefore requires their sufficient consideration during data evaluation.

The most important characteristics that NEXAFS features compared to other methods for structural characterization are its sensitivity to amorphous as well as crystalline regions, its tunable, potentially very high surface sensitivity and its averaging over mesoscopic sample regions, determined by the beam dimensions and the acceptance angle of the detector system. Though not discussed in detail in the present article, also the latter characteristic is rather important. Since all exposed molecules contribute equally, incoherently to the NEXAFS signal, it always has to be considered in the data interpretation that the determined orientations are effective values. Though not exactly averages over all occurring orientations in the sample – due to the nonlinearity of Eqs. (3) and (4) in α—the derived geometry of the molecules is determined by the superposition of all contributing signals. Therefore, it cannot be discriminated whether all molecules share the same orientation α or whether two or more distinct orientations with different relative occupation have added up to this effective value. One example is presented in Fig. 16: on the left hand side a molecular arrangement is sketched, where an equivalent number of molecules has adopted a perfectly upright and a lying configuration. The individual dichroisms of both these regions add up to an effective value of $\alpha = 45^\circ$, a result which is obviously also perfectly compatible with a molecular arrangement where all molecules exhibit a tilt of their long axis with respect to the surface by this value. Due to this ambiguity in the orientation determination the results derived from dichroism analyses always have to be cross-verified by supporting experiments using other techniques like scanning probe microscopy and X-ray diffraction. This is particular critical for films of π-conjugated molecules, which frequently exhibit a pronounced dewetting yielding different molecular orientations at the interface and in subsequent layers [35].

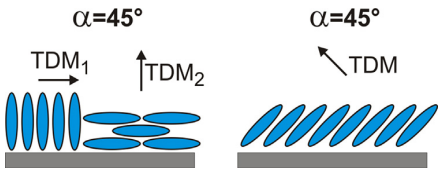

Fig. 16. Scheme of two different molecular arrangements, both leading to effective molecular orientations of $\alpha = 45^\circ$ determined by dichroisms analysis.

Furthermore, many cases have been reported, in which regions with different molecular orientations coexist in one sample, often as function of external preparation parameters like film thickness, substrate temperature, deposition rate or substrate quality [84,85]. For example in the case of diindenoperylene thin films grown on ITO surfaces a co-existence of molecules in an upright and lying orientation has been found [86]. Since the relative amount of both phases changes as function of temperature, the determined effective orientation α will also change continuously with temperature. Solely based on a NEXAFS analysis, this situation might be misinterpreted as continuous variation of the actual molecular tilt angle relative to the substrate, though the observed behavior is simply a result of the superimposing contributions from both phases.

However, this ambiguity can also be clarified directly by using the NEXAFS process. If the beam and detection spot can be focused to a small area and scanned across the sample, NEXAFS measurements with spatial resolution, also denoted as photo electron emission microscopy (PEEM) are enabled [87–89]. Since spatial resolutions below 30 nm can be reached, regions with different molecular orientation can be precisely identified and separately evaluated.

Acknowledgements

We acknowledge support by the Deutsche Forschungsgemeinschaft (Grant SFB 1083, TP A2) and the Helmholtz-Zentrum Berlin (electron storage ring BESSY II) for provision of synchrotron radiation at beamline HE-SGM.

References

[1] S.R. Forrest, M.E. Thompson, Chem. Rev. 107 (2007) 923–1386.
[2] N. Karl, Synth. Met. 133–134 (2003) 649–657.
[3] J. Cornil, J.P. Calbert, J.L. Brédas, J. Am. Chem. Soc. 123 (2001) 1250–1251.
[4] T. Breuer, G. Witte, Phys. Rev. B: Condens. Matter 83 (2011) 155428.
[5] K. Kolata, T. Breuer, G. Witte, S. Chatterjee, ACS Nano 8 (2014) 7377–7383.
[6] N. Koch, ChemPhysChem 8 (2007) 1438–1455.
[7] W. Chen, D.C. Qi, Y.L. Huang, H. Huang, Y.Z. Wang, S. Chen, X.Y. Gao, A.T.S. Wee, J. Phys. Chem., C 29 (2009) 12832–12839.
[8] A. Fasolino, A. Selloni, A. Shkrebtii, Landolt-Börnstein—24: Physics of Solid Surfaces—Structure, Springer-Verlag, Heidelberg, 1993.

[9] M. Krämer, A. von Bohlen, C. Sternemann, M. Paulus, R. Hergenröder, Appl. Surf. Sci. 253 (2007) 3533–3542.
[10] J. Zegenhagen, Surface structure analysis with X-ray standing waves, in: G. Bracco, D. Holst (Eds.), Surface Science Techniques, Springer-Verlag, Heidelberg, 2013.
[11] S.E. Fritz, S.M. Martin, C.D. Frisbee, M.D. Ward, M.F. Toney, J. Am. Chem. Soc. 126 (2004) 4084–4085.
[12] S.C.B. Mannsfeld, A. Virkar, C. Reese, M.F. Toney, Z. Bao, Adv. Mater. 21 (2009) 2294–2298.
[13] O. Sakata, M. Nakamura, Grazing incidence X-ray diffraction, in: G. Bracco, D. Holst (Eds.), Surface Science Techniques, Springer-Verlag, Heidelberg, 2013.
[14] D.P. Woodruff, Surf. Sci. Rep. 62 (2007) 1–38.
[15] A.N. Parikh, D.L. Allara, J. Chem. Phys. 96 (1992) 927.
[16] R. Arnold, A. Terfort, C. Wöll, Langmuir 17 (2001) 4980–4989.
[17] T. Breuer, M.A. Celik, P. Jakob, R. Tonner, G. Witte, J. Phys. Chem., C 116 (2012) 14491–14503.
[18] J. Stöhr, NEXAFS Spectroscopy, Springer-Verlag, Berlin, 1992.
[19] K. Weiss, S. Gebert, M. Wühn, H. Wadephol, C. Wöll, J. Vac. Sci. Technol., A 16 (1998) 1017.
[20] L. Triguero, Y. Luo, L. Pettersson, H. Ågren, P. Väterlein, M. Weinelt, A. Föhlisch, J. Hasselström, O. Karis, A. Nilsson, Phys. Rev. B: Condens. Matter 59 (1999) 5189–5200.
[21] C.D. Wagner, Handbook of X-ray Photoelectron Spectroscopy, Perkin-Elmer Corporation, Eden Prairie, 1979.
[22] S.G. Urquhart, A.P. Hitchcok, A.P. Smith, H.W. Ade, W. Lidy, E.G. Rightor, G.E. Mitchell, J. Electron. Spectrosc. Relat. Phenom. 100 (1999) 119–135.
[23] G. Hähner, Chem. Soc. Rev. 35 (2006) 1244–1255.
[24] B. Watts, L. Thomsen, P. Dastoor, J. Electron. Spectrosc. Relat. Phenom. 151 (2006) 105–120.
[25] D.C. Qi, W. Chen, A.T.S. Wee, NEXAFS studies of molecular orientation at molecule-substrate interfaces, in: N. Koch, N. Ueno, A.T.S. Wee (Eds.), The Molecule–Metal Interface, Wiley-VCH, Berlin, 2013.
[26] A. Nefedov, C. Wöll, Advanced applications of NEXAFS spectroscopy for functionalized surfaces, in: G. Bracco, D. Holst (Eds.), Surface Science Techniques, Springer-Verlag, Heidelberg, 2013.
[27] J. Chen, Surf. Sci. Rep. 30 (1997) 1–152.
[28] R. Püttner, C. Kolczewski, M. Martins, A.S. Schlachter, G. Snell, M. Sant'Anna, J. Viefhaus, K. Hermann, G. Kaindl, Chem. Phys. Lett. 393 (2004) 361–366.
[29] K. Hermann, L.G.M. Pettersson, M.E. Casida, C. Daul, A. Goursot, A. Koester, E. Proynov, A. St-Amant, Contributing authors:, D.R. Salahub, V. Carravetta, H. Duarte, C. Friedrich, N. Godbout, J. Guan, C. Jamorski, M. Leboeuf, M. Leetmaa, M. Nyberg, S. Patchkovskii, L. Pedocchi, F. Sim, L. Triguero, A. Vela, StoBe-deMon version 3.2 (2013) http://www.fhi-berlin.mpg.de/KHsoftware/StoBe/index.html
[30] M.J. Kong, A.V. Teplyakov, J.G. Lyuibovitsky, S.F. Bent, Surf. Sci. 411 (1998) 286–293.
[31] C. Schmidt, A. Witt, G. Witte, J. Phys. Chem., A 115 (2011) 7234–7241.
[32] Y.H. Tang, T.K. Sham, Y.F. Hu, C.S. Lee, S.T. Lee, Chem. Phys. Lett. 366 (2002) 636–641.
[33] G. Koller, S. Berkebile, J.R. Krenn, G. Tzvetkov, G. Hlawacek, O. Lengyel, F.P. Netzer, C. Teichert, R. Resel, M.G. Ramsey, Adv. Mater. 16 (2004) 2159–2162.
[34] P.S. Bagus, K. Weiss, A. Schertel, Ch. Wöll, W. Braun, C. Hellwig, C. Jung, Chem. Phys. Lett. 248 (1996) 129–135.
[35] D. Käfer, G. Witte, Chem. Phys. Lett. 442 (2007) 376–383.
[36] H. Ågren, O. Vahtras, V. Carravetta, Chem. Phys. 196 (1996) 47–58.
[37] A.M. Köster, G. Geudtner, P. Calaminici, M.E. Casida, R. Dominguez, R. Flores-Moreno, G.U. Gamboa, A. Goursot, T. Heine, A. Ipatov, F. Janetzko, J.M. del Campo, J.U. Reveles, A. Vela, B. Zuniga-Gutierrez, D.R. Salahub, deMon2k Version 4, 2013 http://www.demon-software.com
[38] Y. Joly, Phys. Rev. B: Condens. Matter 63 (2001) 125120.
[39] ADF2013, SCM, Theoretical Chemistry, Vrije Universiteit, Amsterdam, The Netherlands, http://www.scm.com.
[40] L.G.M. Pettersson, H. Ågren, O. Vahtras, V. Carravetta, J. Chem. Phys. 103 (1995) 8713.
[41] J.J. Rehr, J.J. Kas, F.D. Vila, M.P. Prange, K. Jorissen, Phys. Chem. Chem. Phys. 12 (2010) 5503–5513.
[42] R. De Francesco, M. Stener, G. Fronzoni, J. Phys. Chem., A 116 (2012) 2885–2894.
[43] G. Fratesi, V. Lanzilotto, L. Floreano, G.P. Brivio, J. Phys. Chem., C 117 (2013) 6632–6638.
[44] M. Klues, K. Hermann, G. Witte, J. Chem. Phys. 140 (2014) 14302.
[45] B.L. Henke, E.M. Gullikson, J.C. Davis, At. Data Nucl. Data Tables 54 (1993) 181–342.
[46] T. Schuettfort, L. Thomsen, C.R. McNeill, J. Am. Chem. Soc. 135 (2013) 1092–1101.
[47] J. Wang, C. Morin, L. Li, A.P. Hitchcok, A. Schöll, A. Doran, J. Electron. Spectrosc. Relat. Phenom. 170 (2009) 25–36.
[48] P. Feulner, T. Niedermayer, K. Eberle, R. Schneider, D. Menzel, A. Baumer, E. Schmich, A. Shaporenko, Y. Tai, M. Zharnikov, Phys. Rev. Lett. 93 (2004) 178302.
[49] D. Käfer, L. Ruppel, G. Witte, Phys. Rev. B: Condens. Matter 75 (2007) 085309.
[50] M. Alagia, C. Baldacchini, M.G. Betti, F. Bussolotti, V. Carravetta, U. Ekström, C. Mariani, S. Stranges, J. Chem. Phys. 122 (2005) 124305.
[51] J.A. Horsley, J. Stöhr, A.P. Hitchcock, D.C. Newbury, A.L. Johnson, F. Sette, J. Chem. Phys. 83 (1985) 6099.
[52] J. Fraxedas, Y.J. Lee, I. Jiménez, R. Gago, R.M. Nieminen, P. Ordejón, E. Canadell, Phys. Rev. B: Condens. Matter 68 (200) 195115.
[53] Y. Zou, L. Kilian, A. Schöll, T. Schmidt, R. Fink, E. Umbach, Surf. Sci. 600 (2006) 1240–1251.
[54] C. Schmidt, T. Breuer, S. Wippermann, W.G. Schmidt, G. Witte, J. Phys. Chem., C 116 (2012) 24098–24106.
[55] K. Weiss, S. Gebert, M. Wühn, H. Wadepohl, C. Wöll, J. Vac. Sci. Technol., A 16 (1998) 1017.
[56] M. Smith, L. Levenson, Phys. Rev. B: Condens. Matter 16 (1977) 2973–2977.
[57] I. Salzmann, A. Moser, M. Oehzelt, T. Breuer, X. Feng, Z.-Y. Juang, D. Nabok, R.G. Della Valle, S. Duhm, G. Heimel, A. Brillante, E. Venuti, I. Bilotti, C. Christodoulou, J. Frisch, P. Puschnig, C. Draxl, G. Witte, K. Müllen, N. Koch, ACS Nano 6 (2012) 10874–10883.
[58] P. Beyer, T. Breuer, S. Ndiaye, A. Zykov, A. Viertel, M. Gensler, J.P. Rabe, S. Hecht, G. Witte, S. Kowarik, ACS Appl. Mater. Interfaces 6 (2014) 21484–21493.
[59] T. Breuer, G. Witte, ACS Appl. Mater. Interfaces 5 (2013) 9740–9745.
[60] C. Mainka, P.S. Bagus, A. Schertel, T. Strunskus, M. Grunze, C. Wöll, Surf. Sci. 341 (1995) 1055–1060.
[61] I.P.M.W. Bouchoms, A. Schoonveld, J. Vrijmoeth, T.M. Klapjwijk, Synth. Met. 104 (1999) 175–178.
[62] S. Schiefer, M. Huth, A. Dobrinevski, B. Nickel, J. Am. Chem. Soc. 129 (2007) 10316–10317.
[63] M. Marks, C. Schmidt, C.H. Schwalb, T. Breuer, G. Witte, U. Höfer, J. Phys. Chem., C 116 (2012) 1904–1911.
[64] D. Käfer, G. Witte, P. Cyganik, A. Terfort, C. Wöll, J. Am. Chem. Soc. 128 (2006) 1723–1732.
[65] D. Zerulla, T. Chassé, J. Electron. Spectrosc. Relat. Phenom. 172 (2009) 78–87.
[66] M. Kiguchi, S. Entani, K. Saiki, G. Yoshikawa, Appl. Phys. Lett. 84 (2004) 3444.
[67] J.C. Love, L.A. Estroff, J.K. Kriebel, R.G. Nuzzo, G.M. Whitesides, Chem. Rev. 105 (2005) 1103.
[68] M. Zharnikov, M. Grunze, J. Phys. Condens. Matter 13 (2001) 11333–11365.
[69] M. Himmelhaus, I. Gauss, M. Buck, F. Eisert, C. Wöll, M. Grunze, J. Electr. Spectrosc. Relat. Phenom. 92 (1998) 139–149.
[70] G. Hähner, M. Kinzler, C. Thummler, C. Wöll, M. Grunze, J. Vac. Sci. Technol. A10 (1992) 2758.
[71] S. Frey, V. Stadler, K. Heister, W. Eck, M. Zharnikov, M. Grunze, B. Zeysing, A. Terfort, Langmuir 17 (2001) 2408–2415.
[72] H.-T. Rong, S. Frey, Y.-J. Yang, M. Zharnikov, M. Buck, M. Wühn, C. Wöll, G. Helmchen, Langmuir 17 (2001) 1582–1593.
[73] N. Ballav, B. Schüpbach, O. Dethloff, P. Feulner, A. Terfort, M. Zharnikov, J. Am. Chem. Soc. 129 (2007) 15416–15417.
[74] D. Brete, D. Przyrembel, C. Eickhoff, R. Carley, W. Freyer, K. Reuter, C. Gahl, M. Weinelt, J. Phys. Condens. Matter. 24 (2012) 394015.
[75] G. Heimel, L. Romaner, J.L. Bredas, E. Zojer, Langmuir 24 (2008) 474–482.
[76] J. Liu, B. Schüpbach, A. Bashir, O. Shekhah, A. Nefedov, M. Kind, A. Terfort, C. Wöll, Phys. Chem. Chem. Phys. 12 (2010) 4459–4472.
[77] F. Klappenberger, D. Kühne, M. Marschall, S. Neppl, W. Krenner, A. Nefedov, T. Strunskus, K. Fink, C. Wöll, S. Klyatskaya, O. Fuhr, M. Ruben, J.V. Barth, Adv. Funct. Mater. 21 (2011) 1631–1642.
[78] A. Bashir, D. Käfer, J. Müller, C. Wöll, A. Terfort, G. Witte, Angew. Chem. Int. Ed. 47 (2008) 5250.
[79] D. Käfer, L. Ruppel, G. Witte, Ch. Wöll, Phys. Rev. Lett. 95 (2005) 166602.
[80] L. Wang, S. Chen, L. Liu, D. Qi, X. Gao, J. Subbiah, S. Swaminathan, A.T.S. Wee, J. Appl. Phys. 102 (2007) 063504.
[81] K. Diller, F. Klappenberger, M. Marschall, K. Hermann, A. Nefedov, Ch. Wöll, J.V. Barth, J. Chem. Phys. 136 (2012) 014705.
[82] K. Diller, F. Klappenberger, F. Allegretti, A.C. Papageorgiou, S. Fischer, D.A. Duncan, R.J. Maurer, J.A. Lloyd, S.C. Oh, K. Reuter, J.V. Barth, J. Chem. Phys. 141 (2014) 144703.
[83] T.M. Willey, J.D. Fabbri, J.R.I. Lee, P.R. Schreiber, A.A. Fokin, B.A. Tkachenko, N.A. Fokina, J.E.P. Dahl, R.M.K. Carlson, A.L. Vance, W. Yang, L.J. Terminello, T. van Buuren, N.A. Melosh, J. Am. Chem. Soc. 130 (2008) 10536–10544.
[84] G. Witte, C. Wöll, J. Mater. Res. 7 (2004) 1889–1916.
[85] F. Schreiber, Phys. Status Solidi, A 6 (2004) 1037–1054.
[86] A. Hinderhofer, T. Hosokai, C. Frank, J. Novák, A. Gerlach, F. Schreiber, J. Phys. Chem., C 115 (2011) 16155–16160.
[87] M.B. Casu, B.-E. Schuster, I. Biswas, C. Raisch, H. Marchetto, T. Schmidt, T. Chassé, Adv. Mater. 33 (2010) 3740–3744.
[88] Y.J. Hsu, W.S. Hu, D.H. Wei, Y.S. Wu, Y.T. Tao, J. Electron. Spectrosc. Relat. Phenom. 144–147 (2005) 401–404.
[89] H. Ade, X. Zhang, S. Cameron, C. Costello, J. Kirz, S. Williams, Science 5084 (1992) 972–975.

5.7 Analysis of the near-edge X-ray-absorption fine-structure of anthracene: A combined theoretical and experimental study

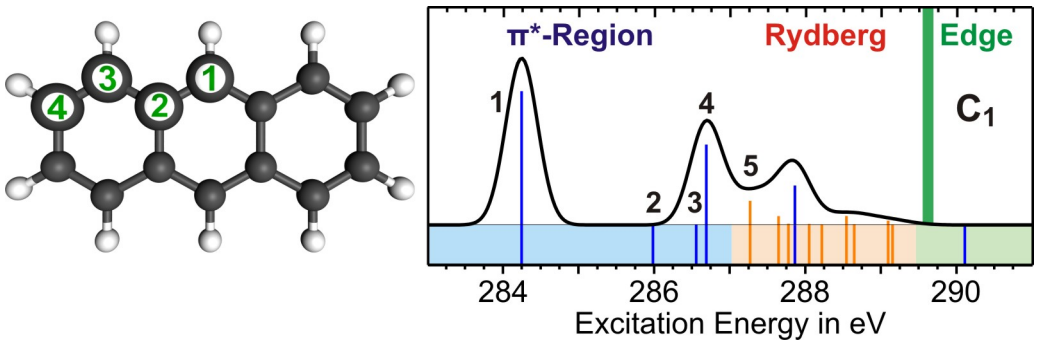

5.7.1 Inhaltsangabe

The near-edge fine structure of the carbon K-edge absorption spectrum of anthracene was measured and theoretically analyzed by density functional theory calculations implemented in the StoBe code. It is demonstrated that the consideration of electronic relaxation of excited states around localized core holes yields a significant improvement of the calculated excitation energies and reproduces the experimentally observed fine structure well. The detailed analysis of excitation spectra calculated for each symmetry inequivalent excitation center allows in particular to examine the influence of chemical shifts and core hole effects on the excitation energies. Moreover, the visualization of final states explains the large variations in the oscillator strength of various transitions as well as the nature of Rydberg-states that exhibit a notable density of states below the ionization potentials.

5.7.2 Eigenleistung

Sämtliche Experimente und Rechnungen, die in diesem Artikel vorgestellt werden, wurden von mit geplant, durchgeführt und ausgewertet. Ebenso erfolgte die graphische Aufbereitung der Ergebnisse durch mich. Hervorzuheben sind in diesem Zusammenhang die Bemühung um eine anschauliche Darstellung der π- und σ-Anteile in den berechneten Spektren. Außerdem wurden die Arbeitsschritte des verwendeten Programms (StoBe) zuvor nicht zusammenfassend in der Literatur dargestellt, worauf ich im methodischen Teil des Artikels besonderes Augenmerk gelegt habe. Details zu den Rechnungen wurden in den entsprechenden Textpassagen durch Klaus Hermann beigesteuert. Gregor Witte war bei der Interpretation der Daten, der Entwicklung des Gesamtkonzeptes der Veröffentlichung, sowie dem Verfassen des Textes beratend und unterstützend beteiligt.

THE JOURNAL OF CHEMICAL PHYSICS **140**, 014302 (2014)

Analysis of the near-edge X-ray-absorption fine-structure of anthracene: A combined theoretical and experimental study

Michael Klues,[1] Klaus Hermann,[2,a)] and Gregor Witte[1,b)]
[1]*Molekulare Festkörperphysik, Philipps-Universität Marburg, Germany*
[2]*Inorganic Chemistry Department, Fritz-Haber-Institut der Max-Planck-Gesellschaft, Berlin, Germany*

(Received 20 October 2013; accepted 10 December 2013; published online 2 January 2014)

The near-edge fine structure of the carbon K-edge absorption spectrum of anthracene was measured and theoretically analyzed by density functional theory calculations implemented in the StoBe code. It is demonstrated that the consideration of electronic relaxation of excited states around localized core holes yields a significant improvement of the calculated excitation energies and reproduces the experimentally observed fine structure well. The detailed analysis of excitation spectra calculated for each symmetry inequivalent excitation center allows in particular to examine the influence of chemical shifts and core hole effects on the excitation energies. Moreover, the visualization of final states explains the large variations in the oscillator strength of various transitions as well as the nature of Rydberg-states that exhibit a notable density of states below the ionization potentials. © *2014 AIP Publishing LLC*. [http://dx.doi.org/10.1063/1.4855215]

INTRODUCTION

Near edge X-ray absorption spectroscopy (NEXAFS) is a sensitive method to study the electronic structure of unoccupied orbitals and bands in molecules and solids.[1] The probed transitions from core levels into empty or partially filled electronic states are element specific and very sensitive to the local bonding environment and coordination. Besides the characterization of molecular materials it has been extensively utilized to study properties of transition metal oxides, nitrides, carbides, and sulfides.[2] NEXAFS has also become an important surface sensitive technique for studying the local electronic structure of adsorbed molecules.[3–5] Since corresponding transitions from core levels into unoccupied molecular orbitals are governed by dipole selection rules they also allow to determine the molecular orientation by analyzing the dichroism which occurs when the incidence angle and polarization direction of the linearly polarized synchrotron beam are varied. This structural analysis is particular advantageous as it does not require any crystalline ordering within the molecular films like in the case of X-ray diffraction analysis. Moreover, due to the high brightness of modern synchrotron sources such measurements can be readily carried out for adsorbates even at submonolayer coverage. The recent development in the field of organic electronics has led to a renewed interest in NEXAFS spectroscopy as an important tool to characterize the growth and structure of π-conjugated molecular materials.[6–14] Though the large lifetime of excitations into unoccupied π-orbitals in such materials give rise to rather sharp and distinct π^*-resonances in the corresponding NEXAFS spectra, a precise assignment and identification of these signatures is required in order to fully exploit the potential of NEXAFS-based analyses. One approach to rationalize the resonances in NEXAFS spectra is based on tracing them back to characteristic signatures occurring in (small) aromatic molecules which are considered as building blocks of larger molecules and polymer materials. In fact, this building block principle has been successfully applied to polymers or oligomers where sub-molecular units are electronically decoupled, e.g., by single C–C bonds.[15–18] However, this approach is not applicable to larger fully conjugated aromatic molecules which, instead, exhibit a number of additional π^*-resonances according to the size of the aromatic electron system.[19–21] This situation bears resemblance to the vibrational spectra of extended aromatic molecules, where collective, almost phononic vibrations appear instead of localized modes that are commonly used to identify functional units by fingerprints.[22]

At present various theoretical approaches and computer codes to calculate NEXAFS spectra have become available which can also handle large aromatic hydrocarbons. These approaches differ essentially by the method to evaluate the electronic structure of the system under consideration. Here density functional theory (DFT) codes, implemented, e.g., in StoBe,[23] deMon2k,[24] or ADF,[25] codes based on quantum chemical *ab initio* methods, implemented, e.g., in CASSCF STOCKHOLM,[26] or codes applying Green function methods, implemented, e.g., in FEFF9,[27] are used.

It has been demonstrated that in many cases obtaining molecular NEXAFS signatures based on total densities of unoccupied states (DOUS) only is not fully conclusive.[21] The reason for this is the missing consideration of initial state effects which are due to differences in the C1s binding energies of differently coordinated carbon atoms within the molecule. Further, the impact of the various core hole locations on the wave function of the final states (i.e., electronic relaxation) and the influence of corresponding transition matrix elements can become important. Despite recent developments of modeling molecular NEXAFS spectra the number of detailed

a)Electronic mail: hermann@FHI-Berlin.MPG.de
b)Electronic mail: gregor.witte@physik.uni-marburg.de

comparative studies is still very limited. Owing to technical challenges, experimental gas phase NEXAFS spectra which enable a direct comparison with calculations have been available only for very few aromatic molecules (including naphthalene and pentacene[28,29]) and accurate calculations are restricted to single molecules because of their complexity. On the other hand, NEXAFS measurements of molecular multilayer films showed that the electronic structure of molecules in van der Waals bound solids remains largely unchanged[30] if compared with that of corresponding free molecules. This justifies comparisons of experimental NEXAFS spectra of the solids with those calculated for single free molecules. Note that, due to the intra-molecular nature of the X-ray absorption process in NEXAFS, the energy scale of measured spectra is not affected by surface potentials and work functions such as in the case of photoelectron spectroscopy. In contrast, significant geometric and electronic distortions occurring for chemisorbed molecules may yield significantly changed NEXAFS signatures for monolayer films in contact with metal substrates.[3,10,31,32]

Approximations used in the theoretical treatment of electron correlation and relaxation as well as the choice of basis sets can affect calculated NEXAFS spectra such that they have to be shifted by several eV to match corresponding experimental data.[28,29] This can be overcome by appropriately choosing final state orbitals based on the transition potential approximation[33] together with a rather precise calculation of ionization energies to yield theoretical spectra which compare well with experimental data without requiring energetic corrections. These strategies, implemented in the DFT package StoBe,[23] have been successfully applied, for example, to describe the electronic structure and NEXAFS spectra of different C_6-ring-containing molecules.[34] Here the similar coordination of the different carbon atoms as well as the limited size and high symmetry of such single ring hydrocarbons lead to rather small energy differences in the NEXAFS resonances. Therefore, larger aromatic systems with distinct shape anisotropy are required to compare and validate the theoretical approach.

In this work we have examined carbon K-edge NEXAFS spectra of anthracene ($C_{14}H_{10}$) which is a polycyclic aromatic hydrocarbon consisting of three fused benzene rings (cf. Fig. 4(a)). Surprisingly, no high-resolution NEXAFS data (neither for gas-phase nor for solids) have been published so far for this acene. Only low-resolution NEXAFS spectra were reported for thin films adsorbed on Ag(111) and TiO_2(110) which in both cases reveal no distinct fine structure.[35,36] To provide high resolution reference data without intensity variations of individual resonances due to orientational effects and to exclude electronic distortions owing to chemical interaction with the supporting substrate the present NEXAFS data were acquired for powder samples and are compared with calculated spectra. The spectra are further compared with previous NEXAFS experiments carried out for long-range ordered and highly oriented anthracene-based self-assembled monolayers (SAMs)[37] which reveal the influence of the anchoring unit on the NEXAFS signature of the aromatic backbone and also enable an experimental identification of π^*-resonances based on their dichroism. Interestingly, inner-shell electron energy loss spectroscopy (ISEELS) data have been obtained in a previous inelastic electron scattering experiment for gaseous anthracene which had also been simulated in the framework of detailed quantum chemical calculations.[38] Since for large electron impact energies such electronic excitation processes become similar to NEXAFS this enables an additional comparison. The aim of the present study is, on one hand, to validate the accuracy of the StoBe-based parameter-free calculations of NEXAFS spectra of larger aromatic molecules and, on the other hand, to illustrate relaxation effects and explain pronounced variations of the oscillator strength for the individual NEXAFS resonances which is particular important for extended π-conjugated systems.

METHODOLOGY

Experimental details

Since the low sublimation enthalpy and resulting high vapor pressure of anthracene hampers the preparation of thin films by evaporation from Knudsen cells samples were prepared by reaming thin films of high purity anthracene (ACROS organics, purity 99%) onto a scarified copper plate which was rapidly cooled below 150 K after loading the sample holder into the UHV-chamber. The carbon K-edge NEXAFS measurements were carried out at the HE-SGM dipole beamline of the synchrotron storage ring facility BESSY II in Berlin (Germany). A retarding field analyzer with a suppressor field of 60 eV was used for partial electron yield (PEY) detection of secondary electrons as a function of the photon energy of the linearly polarized incident synchrotron light (polarization factor 91%). The exit slit of the grating monochromator was chosen such that a spectral width of the incident light was 300 meV achieved. The absolute energy scale of the NEXAFS spectra was calibrated by simultaneously recording the photocurrent from a carbon coated gold grid in the incident beam which exhibits a sharp resonance at 284.9 eV as cross-calibrated by means of a graphite sample. The raw NEXAFS data have been normalized with respect to the incident photon flux and considering the energy dependent transmission characteristic of the monochromator grating.

Computational approach

The work flow describing all individual steps of the present DFT calculations of carbon edge NEXAFS spectra based on the StoBe package[23] is depicted in Fig. 1. In the first step the molecular structure of the free anthracene molecule is optimized using the gradient-corrected revised Perdew-Burke-Ernzerhof (RPBE) functional[39,40] and all-electron triple-zeta valence plus polarization basis sets (TZVP).[41] The same functional and basis sets are also used in all further steps. This first step yields, apart from the equilibrium geometry, also information about the electronic ground state of the molecule. While in the geometry optimizations all carbon atoms are described by identical all-electron basis sets the following calculations of ionized and core excited states use basis sets which differ between the respective excitation carbon and the other spectator carbon centers. For the

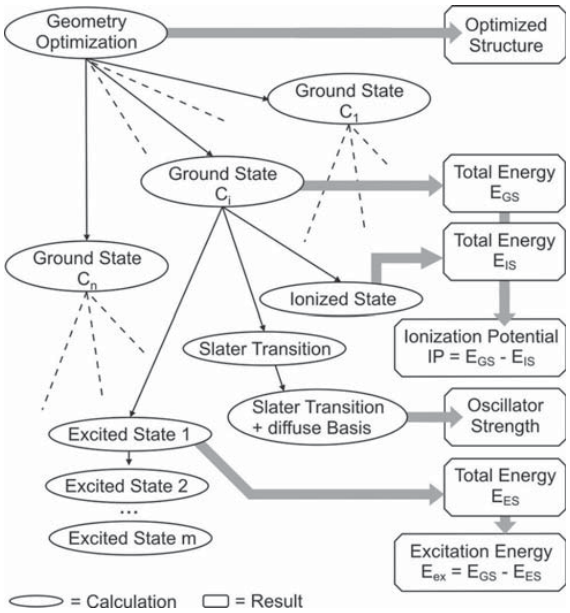

FIG. 1. Schematic flowchart of DFT-based calculations of carbon K-edge NEXAFS spectra carried out within the StoBe-package (for details see text). The angular boxes on the right-hand side represent the results of the individual steps of the iterations. C_i denotes the position of core hole excitation among the symmetry non-equivalent carbon positions, while m indicates the number of excited state which has to be considered for every center C_i.

excitation carbon a basis set of IGLO-III quality[42] is applied to adequately describe inner shell relaxation effects while the other carbon centers are accounted for by effective core potentials (ECPs) for the 1s shell and [3s3p1d] valence basis sets to avoid 1s core orbital mixing.[43,44]

Anthracene includes four types of carbon atoms (C_i) which are non-equivalent by symmetry and exposed to a slightly different chemical environment as indicated in Fig. 4(a). Thus, the above choice of basis sets is used in four different calculations of ground and C 1s hole states which yield corresponding total energies $E_{GS}(C_i)$ and $E_{IS}(C_i)$ where the difference $IP_i = E_{IS}(C_i) - E_{GS}(C_i)$ defines the fully relaxed ionization potential (ΔSCF value) of the corresponding carbon atom C_i, $i = 1, \ldots, 4$. The resulting IP values are corrected further by a shift of 0.4 eV to higher energies to account for relativistic effects.[45]

In the next step we consider carbon 1s core excitations into unoccupied final state orbitals where the latter are determined, for each of the four different carbon species, in one self-consistent calculation based on the transition potential approximation.[33] In this approach the electronic structure of the molecule is evaluated self-consistently where the corresponding C 1s orbital is occupied by only half an electron to account for electronic relaxation during the excitation process. The resulting unoccupied orbitals are then used as approximate final state orbitals in the evaluation of dipole transitions from the C 1s core orbital with transition moments determining the spectral oscillator strengths and Kohn-Sham eigenvalue differences yielding approximate excitation energies to describe the theoretical NEXAFS spectrum in a first approximation. In order to account for transitions into diffuse Rydberg states and final states beyond ionization the basis set at the carbon excitation center is augmented by a large set, [19s19p19d], of diffuse basis functions following a double basis set technique.[20,46] The NEXAFS spectrum for each non-equivalent carbon atom obtained so far needs to be improved further. First, the C 1s ionization potential obtained within the transition potential framework, which is identical with that obtained by Slater's transition state method,[47] includes only limited electronic relaxation. Thus, its value is larger by about 1 eV compared with the fully relaxed ΔSCF result. This can be corrected by applying a rigid shift to the NEXAFS spectrum obtained by the transition potential approximation which compensates the difference. Second, more reliable excitation energies can be obtained by explicit self-consistent calculations of excited states with the electron of a C 1s core orbital transferred to an unoccupied orbital of the ground state. Then the difference of the total energy of the excited state and that of the ground state determines the fully relaxed excitation energy, analogous to the ΔSCF procedure described above. For the present anthracene molecule this evaluation has been performed for the lowest fifteen excitations starting from the 1s core orbital of each of the four non-equivalent carbon atoms. For better convergence of the self-consistent calculations, virtual orbitals below the highest occupied orbital of higher excited states are restricted from orbital rotations by applying appropriate supersymmetry constraints. The improved excitation energy spectrum is then complemented with the corresponding dipole transition moment from the transition potential calculations to arrive at a final theoretical NEXAFS spectrum. To account for the finite experimental resolution and to enable a comparison with measured NEXAFS spectra the calculated transition energies are convoluted by Gaussians of full-width-at-half-maximum (FWHM) amounting to 0.5 eV for π^*-type and 0.7 eV for σ^*- or Rydberg-type resonances based on empirical values from experiment. Visualization of orbitals was performed with MacMolPlt.[48]

It should be noted that the computational scheme discussed above and shown schematically in Fig. 1 describes the internal work flow inside the StoBe code where most details can be hidden in corresponding script files, a common practice in electronic structure codes. Alternative methods have been developed to compute core excitation spectra where different theoretical approaches have been applied. This includes, apart from the present time-independent DFT treatment, computational schemes using the time-dependent DFT method[49] as implemented, e.g., in the computer codes ABINIT[50] or ORCA.[51] Further, many-body perturbation techniques solving Bethe-Salpeter equations[52] have been proposed and implemented, e.g., in the OCEAN code of the FEFF package[27,53] or the EXC code.[54]

RESULTS

Experimental C1s NEXAFS-spectra of anthracene

The experimental carbon K-edge NEXAFS data of anthracene are summarized in Fig. 2. Characteristic signatures are two intense and sharp peaks at 284.5 eV and 285.8 eV

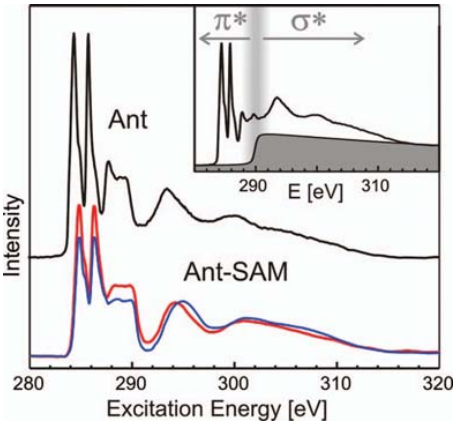

FIG. 2. C K-edge NEXAFS spectra of anthracene powder (black curve) and an anthraceneselenolate-SAM on Au(111) after subtracting a K-edge. The used K-edge as well as a raw spectrum before edge subtraction are shown in the inset. A notable dichroism occurs for the SAM yielding intensity variations of the π^* resonances for different photon polarization (red curve: perpendicular incidence, blue curve: grazing incidence).

accompanied by low intensity shoulders at higher energy, somewhat broader and partially overlapping peaks between 287.5 and 290 eV as well as substantially broader peaks around 294 and 300 eV. Based on their width and energetic positions relative to the ionization threshold (which typically amounts to about 290 eV for conjugated hydrocarbons[29]) the sharp peaks can be assigned to excitations into unoccupied π^* orbitals while the latter broad peaks are attributed to excitations into σ^* orbitals.[55] To facilitate comparison with calculated absorption spectra and in particular to identify the origin of spectral signatures around the ionization threshold, the additional electron signal due to Auger deexcitation of core holes created by photoemission (so called *absorption edge*) has been subtracted. As described in Ref. 1 this edge can be modeled analytically by assuming that the electron emission rate is determined essentially by the lifetime of the core hole. Considering a Lorentzian line shape for the core level excitation this yields an expression for the step edge in form of an *arc tangent* function.[56,57] More precisely, the edge is actually a superposition of several overlapping step functions, since every non-equivalent carbon atom within the molecule has a slightly different ionization potential which makes the exact position of the absorption edge and its shape hard to quantify in experiment. Therefore, the adsorption edge shown in the inset of Fig. 2 was constructed from the ionization potentials calculated for the symmetry non-equivalent carbon atoms (see below) taking into account their multiplicity and using an empirical peak width of 0.5 eV.

Due to the isotropic molecular orientation in powders the intensity of individual NEXAFS resonances is independent on the orientation of the electrical field vector **E** of the incident synchrotron light, hence, offering an ideal reference system to examine the free molecule NEXAFS signature. In contrast, NEXAFS spectra of oriented films of π-conjugated molecules exhibit a noticeable dichroism of π^* resonances which enables a quantitative characterization of molecular orientation.[6–11] This approach exploits the fact that the intensity of π^* resonances depends on the relative orientation of **E** according to $I(\pi^*) \propto |\mathbf{E} \cdot \mathbf{T}|^2$, where **T** denotes the transition dipole moment which is oriented normal to the ring plane of aromatic molecules.[1] In a previous study it has been shown that aromatic SAMs with anthracene backbones can be prepared with remarkable long-range ordering when selenolates are used as anchoring groups.[37] Therefore, the corresponding NEXAFS data of an anthraceneselenolate SAM are included for comparison in Fig. 2. Interestingly, the SAM reveals virtually the same NEXAFS signature as the anthracene powder which reflects the electronic decoupling of the aromatic backbone and the anchoring unit. However, a noticeable dichroism is found for resonances with energies below 290 eV (red curve: perpendicular beam incidence, blue curve: grazing incidence, $\theta = 30^\circ$) which reflects a distinct directional ordering. The quantitative analysis of the dichroism obtained in spectra taken at different angles of incidence of the synchrotron light yields an average angle of **T** relative to the surface normal of $\theta = 59^\circ$ (for details of the analysis see Ref. 37). In order to determine the orientation of the anthracene backbone also the herringbone packing motif within the film has to be taken into account. Employing the analysis shown in Ref. 58 this yields, altogether, an angle of 33° between the anthracene backbone plane and the surface normal.

Calculated NEXAFS-spectra

As depicted in Fig. 3 the total NEXAFS spectrum of anthracene calculated by the transition potential method is already in close agreement with the experimental data. Characteristic features such as the intense resonance doublet in the pre-edge region as well as broad resonances at energies higher than the absorption edge, corresponding to excitations into antibonding σ^*(C-C) orbitals, are reproduced reasonably. However, a closer look also reveals differences. The calculated energies of the leading peaks are too high and their intensity ratio is not correctly reproduced. Moreover, the experimental data exhibit shoulders in the high energy flank of these peaks which are missing in the calculations as well as the intensity around 289 eV. Since the excited molecular states at high energies are inherently difficult to calculate, and according to their very short lifetime yield only extremely broad signals, we will focus on the low-energy part of the NEXAFS spectrum below the ionization potential. Furthermore this energy region is of special interest because the corresponding states are sensitive to chemical changes and can be used for dichroitic measurements.

As discussed above, the theoretical NEXAFS spectra can be improved beyond the transition potential approximation by explicitly evaluating core excited final states of the molecule. As a result, Figs. 4(b)–4(e) show partial NEXAFS spectra for the four different carbon atoms C_1 to C_4 in anthracene where the lowest fifteen excited states have been considered. In these spectra the vertical lines indicate the excitation energies determined from total energies of the fully relaxed excited final and corresponding ground states. Lines which extend above the color bar reflect excitations with

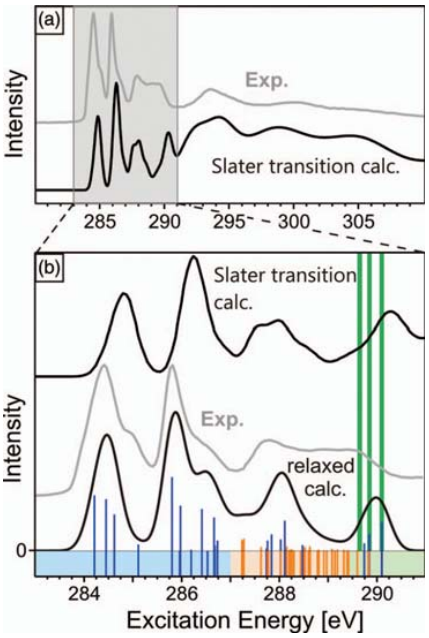

FIG. 3. Comparison of experimental and theoretical data with different levels of approximation. (a) Full spectrum resulting from slater transition potential calculations compared with experimental data. (b) Magnification of the pre-edge region showing also the result of a weighted superposition of the partial NEXAFS spectra (cf. Fig. 4) according to the multiplicity of the excitation centers including full electronic relaxation, as well as the corresponding region of the slater transition potential result.

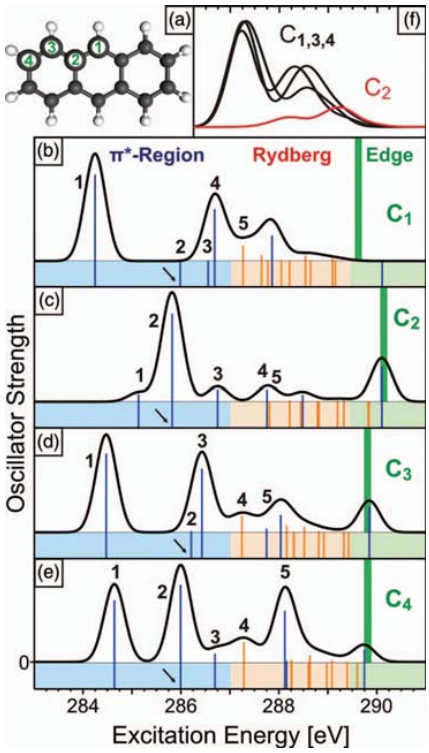

FIG. 4. Summary of calculated C 1s NEXAFS spectra of anthracene. (a) Structure of anthracene. Numbered carbon atoms were used as excitation centers for calculations; (b)–(e) Partial NEXAFS spectra calculated for each symmetry non-equivalent carbon center ($C_1 - C_4$) including full electronic relaxation (see text). The color code denotes the character of the corresponding final states (blue: π^* orbitals, orange: Rydberg states) while the green bars indicate the ionization potentials of the symmetry non-equivalent carbon centers sketched in (a). Small arrows point at excitations which are treated in Fig. 5. Note that the oscillator strengths of the various partial spectra are not to scale; (f) compilation of the partial NEXAFS spectra of (b)–(e) for excitations in the Rydberg region (see text).

relatively large transition moments with their lengths characterizing the moment size while those completely inside the color bar describe transitions of negligible moments. In addition, the painting of the color bar denotes the different character of the final state orbitals where blue and orange refer to π^*-orbitals and Rydberg-orbitals, respectively. The thick vertical green lines indicate the ionization thresholds of the different carbon atoms in the molecule exhibiting only small variations (*chemical shifts*) of less than or equal to 0.5 eV, see also Table I. Finally, the continuous curves in Figs. 4(b)–4(e) describe the corresponding discrete energy spectra convoluted by Gaussian broadening to give an experimental appearance, see above.

Common to all partial NEXAFS spectra, calculated for the different symmetry non-equivalent carbon atoms, are several less intense peaks at energies 0–3 eV below ionization threshold which are assigned to excitations into Rydberg-type final state orbitals (orange bars) which are spatially extended and of anti-bonding σ(C–H) character. These excitations are energetically well separated from more intense excitations (blue bars) at lower energy. The energetically lowest unoccupied orbitals above the LUMO of aromatic molecules are found to be almost always π-type which is also true for anthracene. Thus, the blue energy region of the spectrum is characterized by excitations into π-type orbitals (π^*-region). The partial NEXAFS spectra of the different carbon atoms can be superimposed according to their multiplicity to yield a total NEXAFS spectrum of the molecule to be compared with the measured spectrum after edge subtraction as shown in Fig. 3(b)).

TABLE I. Calculated ionization potentials (IP in eV) of the four symmetry non-equivalent carbon atoms in anthracene (cf. Fig. 4(a)).

	C_1	C_2	C_3	C_4
IP (eV)	289.6	290.1	289.8	289.8

DISCUSSION

Obviously, the calculated total NEXAFS spectrum, see Fig. 3(b), agrees quite closely with the experimental data. All fine structures are well reproduced and the energetic position of the resonances agree within 0.3 eV. Moreover, the theoretical analysis provides detailed insight into the character of the different excitations which can explain the size of their oscillator strengths.

The calculated partial excitation spectra shown in Figs. 4(b)–4(e) reveal, depending on the transitions, very

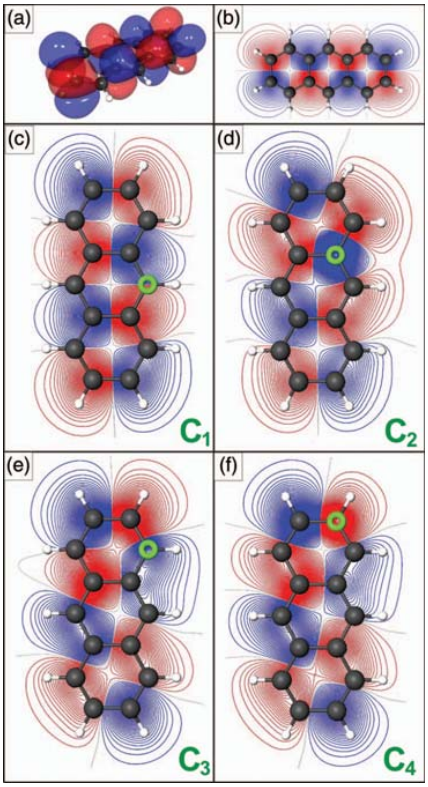

FIG. 5. Visualization of the LUMO+1 orbital in anthracene. (a) Iso-surface and (b) contour plot calculated for the ground state. The contour plane refers to a cut 0.5 Å below the plane through the atom centers. Positive and negative orbital values are shown in blue and red, respectively; (c), (d), (e), (f) Contour plot as in (b) but calculated for the excited final state with holes at C_1, C_2, C_3, or C_4. The contour lines in (c)–(f) refer to identical values and corresponding excitation centers are labeled by green toruses.

different oscillator strengths which can be understood by the symmetry of the corresponding final state orbitals. This is illustrated in Fig. 5 for carbon core excitations into the second lowest unoccupied (LUMO+1) final state orbital (indicated by arrows in Figs. 4(b)–4(e)) starting from the different carbon atoms. The LUMO+1 orbital of the anthracene ground state, see Figs. 5(a) and 5(b), is of π^*-type and described by an anti-bonding arrangement of C 2p orbitals perpendicular to the molecular plane and located at the inner eight carbon centers. This includes centers C_2, C_4 but excludes C_1, C_3. The orbitals of the core excited states corresponding to LUMO+1, see Figs. 5(c)–5(f), are somewhat distorted due to the core hole but still resemble that of the ground state. Thus, dipole transition matrix elements of the C 1s with corresponding final state LUMO+1 orbitals involve integration over products of the dipole operator with C 1s and 2p contributions at the respective carbon center which yield finite values for matrix elements at the inner eight carbon centers, such as C_2, C_4. In contrast, matrix elements at the outer six carbon centers, such as C_1, C_3, assume very small values. As a consequence, the oscillator strengths of the corresponding transitions are large for excitations at C_2, C_4 but small at C_1, C_3 as evidenced in Figs. 4(b)–4(e).

The dependence of the partial NEXAFS spectra on the shape of final state orbitals is also evident for core excitations involving rather extended Rydberg-type final state orbitals as shown in Fig. 4(f). While the partial spectra belonging to transitions from excitation centers C_1, C_3, and C_4 (black) yield nearly the same energy dependence of the spectral intensity the excitation spectrum for center C_2 (red) is rather different which is explained by the binding environment of the C_2 atom. Compared with the other carbon atoms, C_2 does not include a neighboring hydrogen to form a local C–H bond. However, Rydberg-type orbitals in anthracene are characterized by sizeable σ^*(C–H) contributions from carbon centers other than C_2. This is illustrated in Fig. 6 which compares the LUMO+4 Rydberg orbital of the ground state, Fig. 6(a), with corresponding orbitals of the core excited states, Figs. 6(b) and 6(c), containing holes at the carbon centers C_1 and C_2, respectively. Obviously, the final state orbital of the C_1 core

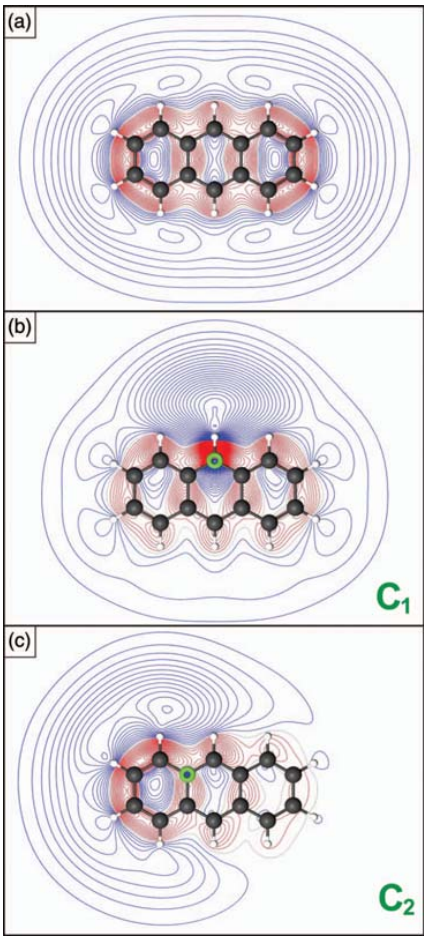

FIG. 6. Visualization of the LUMO+4 orbital in anthracene. (a) Contour plot calculated for the ground state along the molecular plane. Positive and negative orbital values are shown in blue and red, respectively. (b), (c) Contour plot as in (a) but calculated for the excited final state with a C_1 and C_2 hole. The contour lines in (a)–(c) refer to identical values, also used in Fig. 5, and corresponding excitation centers are labelled by green toruses. The final state orbitals of (b) and (c) correspond to excitations no. 5 in Figs. 4(b) and 5(c).

excitation, Fig. 6(b), shows a density near the C_1 center (due anti-bonding C–H contributions) which is larger than the respective orbital of the C_2 core excitation near the C_2 center. As a consequence, the dipole transition moment of the excitation no. 5 is larger in the C_1 than the C_2 derived partial NEXAFS spectrum which is confirmed in Figs. 4(b) and 4(c).

The carbon K-edge NEXAFS spectrum of anthracene has been calculated earlier by Ågren *et al.*[19] using the static exchange approach. While the general characteristics observed in the experimental data were roughly reproduced relative peak intensities were not well described. In particular, the calculated positions of the leading π^* resonances differ from the experiment by about 1.5 eV. The comparison of the experimental with the present theoretical spectra at different levels of approximation, transition potential vs. fully relaxed final state spectra, see Figs. 3(a) and 3(b), may explain these discrepancies. Our results suggest that electronic relaxation in the final states due to the changed coulomb potential caused by the core hole is a key element to obtain precise excitation spectra. As shown in Fig. 5 core hole screening can lead to noticeable distortion of the final state orbitals shifting nodal planes which affect the transition matrix elements. Further, low-lying excitation energies in the fully relaxed spectrum, Fig. 3(b), are shifted by about 1 eV when compared to the transition potential spectrum, Fig. 3(a), where the shift values vary by up to 0.5 eV for different excitations.

Core hole screening can also affect the energetic order of excitations in the spectrum depending on the excitation center. This is illustrated by a comparison of the fully relaxed partial NEXAFS spectrum for the C_1 center, Fig. 4(b), with that for the C_3 center, Fig. 4(d). While the C_1 derived spectrum includes four π^*-type excitations in the low-energy region before excitations to Rydberg final states appear, the C_3 derived spectrum offers only three with the energy regions of π^*- and Rydberg-type excitations overlapping. This substantiates the importance of core hole screening which influences the NEXAFS spectra differently depending on the location and chemical environment of the excitation center. It is consistent with earlier work by Oji *et al.*[21] and may challenge the validity of a constant energetic shift used in the static exchange approach.[19,29]

The analysis of the partial NEXAFS spectra calculated for different carbon excitation centers allows also to estimate the influence of site specific initial state effects due to chemical binding. A comparison of the IP values of the four different carbon atoms in anthracene, cp. Table I, reveals minor variations with the largest value referring to atom C_2. The latter seems plausible since C_2 has three carbon and no hydrogen neighbor while C_1, C_3, and C_4 all have two carbon and one hydrogen neighbor. Considering that the electronegativity of carbon is slightly higher than for hydrogen, this yields a somewhat reduced electron density at C_2 if compared with the other C_i species. Thus, there is a smaller shielding of the core charge in the initial state for C_2 which suggests a larger ionization energy. On the other hand, the IP value of C_2 is larger than that for C_1 by 0.5 eV, see Table I, while the first core hole excitation energies of the two atoms differ by 0.9 eV, see Table II. This indicates that only part of the difference in the excitation energies can be attributed to initial state effects.

TABLE II. Lowest five excitation energies calculated for the four symmetry non-equivalent carbon atoms in anthracene. All energies are given in eV.

Excitation	C_1	C_2	C_3	C_4
1	284.2	285.1	284.5	284.6
2	286.0	285.8	286.2	286.0
3	286.5	286.7	286.4	286.7
4	286.7	287.8	287.2	287.3
5	287.3	287.8	287.7	288.1

Together with the appearance of several pronounced π^* resonances within the same partial NEXAFS spectrum (involving the same carbon core hole), it demonstrates that the leading π^* doublet structure of anthracene cannot be attributed exclusively to core excitations at different carbon atoms into a LUMO-based final state as suggested earlier.[19]

Since the lowest unoccupied molecular orbitals of aromatic molecules are usually of π character the leading NEXAFS resonances are often attributed to excitations into π-type LUMO, LUMO+1, etc. orbitals where orbitals of the molecular ground state are considered. This simplified picture ignores, however, substantial variations in the dipole transition moments which sometimes lead to vanishing oscillator strength as discussed for the second π^* resonance in the partial NEXAFS spectra (cf. Figs. 4(b)–4(e)). This demonstrates that an assignment of molecular orbitals to final states of excitation solely based on the order of the respective subresonance is not possible and instead requires a detailed theoretical analysis.

Though we find quite good overall agreement of the calculated total NEXAFS spectrum of anthracene with measured data, as shown in Fig. 3, there are still some small deviations. The most prominent difference between theory and experiment is the missing shoulder in the high energy flank of the lowest excitation peak. In previous experiments additional fine structures have been observed in high resolution NEXAFS spectra which were identified as coupling of the electronic transitions to various vibronic excitations.[59,60] Since StoBe does not tread vibrations such excitations are not included in the final results. These features have been observed in gas phase C K-edge NEXAFS spectra of small aromatic hydrocarbons such as naphthalene or in O K-edge NEXAFS spectra of substituted aromatic molecules, which suggests an efficient coupling to C=O stretching mode, while they have not been observed in any C K-edge NEXAFS data of condensed aromatic molecules until now. Moreover, since such vibronic excitations appear as satellites of several NEXAFS resonances in the spectra it appears unlikely that the single extra shoulder occurring in the high energy flank of the lowest excitation peak results from a vibrational excitation. More likely the calculation underestimates the intensity of the underlying excitation. Nevertheless vibrations may explain further deviations. In addition, there is missing intensity in the energy region between 288 eV and 290 eV characterizing Rydberg excitations. The origin of these differences can be manifold. First, in the present theoretical study we evaluate fully relaxed excitation energies whereas for the dipole transition moments, determining spectral intensities, we restrict

ourselves to values obtained in the transition potential approximation which accounts only for limited electronic relaxation. This can be improved by calculating electron transition moments with fully relaxed final state wave functions. Second, basis set influences in the description of the molecular Rydberg-type orbitals and their consequences for corresponding excitations may have to be examined in detail. Third, multi-electron excitations ignored by the present theoretical description cannot be fully excluded in the experiment. Studies along these lines are currently under way.

CONCLUSIONS

The present combined theoretical and experimental study shows that carbon K-edge NEXAFS spectra of π-conjugated molecules can be calculated rather precisely when taking into account relaxation effects of final states caused by excitations from localized hole states. The approach implemented in the StoBe package has been validated for the anthracene molecule where an agreement between the measured and calculated peak positions of about 0.3 eV is found. The high accuracy in the calculation of ionization potentials of the different carbon atoms within the molecule allows, in particular, a reliable modeling of the absorption edge which can be subtracted from the measured spectra in order to identify further resonances that are overlapping with the edge jump. Such refined analyses are particularly useful for aromatic molecules containing heteroatoms where initial and final state effects become even more important. In that case several energetically well separated edges occur leading to sizeable overlap of some NEXAFS resonances with the edges. The ability to appropriately analyse NEXAFS signatures will also be of importance for future experiments on multinary molecular systems where an accurate understanding of the individual components is required to examine possible intermolecular coupling.

ACKNOWLEDGMENTS

We acknowledge the Helmholtz-Zentrum Berlin Electron storage ring BESSY II for providing synchrotron radiation at beam line HE-SGM and for financial support.

[1]J. Stöhr, *NEXAFS Spectroscopy* (Springer, Berlin, 1992).
[2]J. G. Chen, Surf. Sci. Rep. **30**, 1–152 (1997).
[3]K. Weiss, S. Gebert, M. Wühn, H. Wadepohl, and C. Wöll, J. Vac. Sci. Technol. A **16**, 1017–1022 (1998).
[4]L. Triguero, Y. Luo, L. G. M. Pettersson, H. Ågren, P. Väterlein, M. Weinelt, A. Fröhlisch, J. Hasselström, O. Karis, and A. Nilsson, Phys. Rev. B **59**, 5189–5200 (1999).
[5]G. Hähner, Chem. Soc. Rev. **35**, 1244–1255 (2006).
[6]E. Umbach, K. Glockler, and M. Sokolowski, Surf. Sci. **402**, 20–31 (1998).
[7]S. Frey, V. Stadler, K. Heister, W. Eck, M. Zharnikov, M. Grunze, B. Zeysing, and A. Terfort, Langmuir **17**, 2408–2415 (2001).
[8]S. Kera, M. B. Casu, K. R. Bauchspiess, D. Batchelor, T. Schmidt, and E. Umbach, Surf. Sci. **600**, 1077–1084 (2006).
[9]H. Peisert, I. Biswas, L. Zhang, M. Knupfer, M. Hanack, D. Dini, D. Batchelor, and T. Chasse, Surf. Sci. **600**, 4024–4029 (2006).
[10]D. Käfer and G. Witte, Chem. Phys. Lett. **442**, 376–383 (2007).
[11]W. Chen, D. C. Qi, Y. L. Huang, H. Huang, Y. Z. Wang, S. Chen, X. Y. Gao, and A. T. S. Wee, J. Phys. Chem. C **113**, 12832–12839 (2009).
[12]E. Voloshina, R. Ovcharenko, A. Shulakov, and Y. Dedkov, J. Chem. Phys. **138**, 154706 (2013).
[13]R. De Francesco, M. Stener, and G. Fronzoni, J. Phys. Chem. A **116**, 2885–2894 (2012).
[14]T. Hemraj-Benny, S. Banerjee, S. Sambasivan, M. Balasubramanian, D. A. Fischer, G. Eres, A. A. Puretzky, D. B. Geohegan, D. H. Lowndes, W. Han, J. A. Misewich, and S. S. Wong, Small **2**, 26–35 (2006).
[15]S. G. Urquhart, A. P. Hitchcock, A. P. Smith, H. W. Ade, W. Lidy, E. G. Rightor, and G. E. Mitchell, J. Electron Spectrosc. Relat. Phenom. **100**, 119–135 (1999).
[16]L. G. M. Pettersson, H. Ågren, B. L. Schürmann, A. Lippitz, and W. E. S. Unger, Int. J. Quantum Chem. B **63**, 749–765 (1997).
[17]W. E. S. Unger, A. Lippitz, C. Wöll, and W. Heckmann, Fresenius' J. Anal. Chem. **358**, 89–92 (1997).
[18]D. Käfer, L. Ruppel, G. Witte, and C. Wöll, Phys. Rev. Lett. **95**, 166602 (2005).
[19]H. Ågren, O. Vahtras, and V. Carravetta, Chem. Phys. **196**, 47–58 (1995).
[20]H. Ågren, V. Carravetta, O. Vahtras, and L. G. M. Pettersson, Theor. Chem. Acc. **97**, 14–40 (1997).
[21]H. Oji, R. Mitsumoto, E. Ito, H. Ishii, and Y. Ouchi, J. Chem. Phys. **109**, 10409 (1998).
[22]T. Breuer, M. A. Celik, P. Jakob, R. Tonner, and G. Witte, J. Phys. Chem. C **116**, 22652 (2012).
[23]K. Hermann, L. G. M. Pettersson, M. E. Casida, C. Daul, A. Goursot, A. Koester, E. Proynov, A. St-Amant, D. R. Salahub; Contributing authors: V. Carravetta, H. Duarte, C. Friedrich, N. Godbout, J. Guan, C. Jamorski, M. Leboeuf, M. Leetmaa, M. Nyberg, S. Patchkovskii, L. Pedocchi, F. Sim, L. Triguero, and A. Vela, StoBe-deMon version 3.2 (2013).
[24]A. M. Köster, G. Geudtner, P. Calaminici, M. E. Casida, R. Dominguez, R. Flores-Moreno, G. U. Gamboa, A. Goursot, T. Heine, A. Ipatov, F. Janetzko, J. M. del Campo, J. U. Reveles, A. Vela, B. Zuniga-Gutierrez, and D. R. Salahub, deMon2k version 4 (2013).
[25]See http://www.scm.com for ADF2013, SCM, Theoretical Chemistry, Vrije Universiteit, Amsterdam, The Netherlands.
[26]L. G. M. Pettersson, H. Ågren, O. Vahtras, and V. Carravetta, J. Chem. Phys. **103**, 8713 (1995).
[27]J. J. Rehr, J. J. Kas, F. D. Vila, M. P. Prange, and K. Jorissen, Phys. Chem. Chem. Phys. **12**, 5503–5513 (2010).
[28]E. Hollauer, E. dos Santos Prucole, M. L. M. Rocco, A. D. P. Netto, A. Schöll, and R. Fink, J. Braz. Chem. Soc. **16**, 31–36 (2005).
[29]M. Alagia, C. Baldacchini, M. G. Betti, F. Bussolotti, V. Caravetta, U. Ekström, C. Mariani, and S. Stranges, J. Chem. Phys. **122**, 124305 (2005).
[30]D. Käfer, L. Ruppel, and G. Witte, Phys. Rev. B **75**, 085309 (2007).
[31]J. Hasselström, O. Karis, M. Weinelt, N. Wassdahl, A. Nilsson, M. Nyberg, L. G. M. Pettersson, M. G. Samant, and J. Stöhr, Surf. Sci. **407**, 221–236 (1998).
[32]D. C. Qui, W. Chen, and A. T. S. Wee, in *The Molecule-Metal Interface*, edited by N. Koch, N. Ueno, and A. T. S. Wee (Wiley-VCH, 2013).
[33]L. Triguero, L. G. M. Pettersson, and H. Ågren, Phys. Rev. B **58**, 8097–8110 (1998).
[34]C. Kolczewski, R. Püttner, M. Martins, A. S. Schlachter, and G. Snell, J. Chem. Phys. **124**, 034302 (2006).
[35]S. Reiß, H. Krumm, A. Niklewski, V. Staemmler, and C. Wöll, J. Chem. Phys. **116**, 7704 (2002).
[36]P. Yannoulis, K. H. Frank, and E. E. Koch, Surf. Sci. **241**, 325–334 (1991).
[37]A. Bashir, D. Käfer, J. Müller, C. Wöll, A. Terfort, and G. Witte, Angew. Chem. **47**, 5250 (2008).
[38]M. L. Gordon, D. Tulumello, G. Cooper, A. P. Hitchcock, P. Glatzel, O. C. Mullins, S. P. Cramer, and U. Bergmann, J. Phys. Chem. A **107**, 8512–8520 (2003).
[39]B. Hammer, L. B. Hansen, and J. K. Norskov, Phys. Rev. B **59**, 7413–7421 (1999).
[40]J. P. Perdew, K. Burke, and M. Ernzerhof, Phys. Rev. Lett. **77**, 3865–3868 (1996).
[41]N. Godbout, D. R. Salahub, J. Andzelm, and E. Wimmer, Can. J. Chem. **70**, 560 (1992).
[42]W. Kutzelnigg, U. Fleischer, and M. Schindler, *NMR-Basic Principles and Progress* (Springer, Heidelberg, 1990).
[43]M. Nyberg, Ph.D. thesis, Stockholm University, 2000.
[44]L. G. M. Pettersson, U. Wahlgren, and O. J. Gropen, J. Chem. Phys. **86**, 2176–2184 (1987).
[45]L. Triguero, O. Plashkevych, L. G. M. Pettersson, and H. Ågren, J. Electron Spectrosc. Relat. Phenom. **104**, 195 (1999).
[46]H. Ågren, V. Carravetta, O. Vahtras, and L. G. M. Pettersson, Chem. Phys. Lett. **222**, 75–81 (1994).
[47]J. C. Slater and K. H. Johnson, Phys. Rev. B **5**, 844 (1972).

[48]B. M. Bode and M. S. Gordon, J. Mol. Graphics Modell. **16**, 133–138 (1998).
[49]M. E. Casida, in *Recent Development and Applications of Modern Density Functional Theory*, edited by J. M. Seminario (Elsevier, Amsterdam, 1996), p. 391.
[50]X. Gonze *et al.*, Comput. Phys. Commun. **180**, 2582 (2009).
[51]F. Neese, Wiley Interdiscip. Rev. Comput. Mol. Phys. **2**, 73 (2012).
[52]G. Onida, L. Reining, and A. Rubio, Rev. Mod. Phys. **74**, 601 (2002).
[53]J. J. Rehr, J. J. Kas, M. P. Prange, A. P. Sorini, Y. Takimoto, and F. D. Vila, C. R. Phys. **10**, 548–559 (2009).
[54]L. Reining, V. Olevano, F. Sottile, S. Albrecht, and G. Onida, see http://www.bethe-salpeter.org.
[55]T. Ohta, K. Seki, T. Yokoyama, I. Morisada, and K. Edamatsu, Phys. Scr. **41**, 150 (1990).
[56]As shown in Ref. 1 the measured absorption edge can be modeled by the expression: $I_{edge} = H[\frac{1}{2} + \frac{1}{\pi}\arctan(\frac{E-IP}{\Gamma/2})] \times \exp(-d(E - IP - \Gamma))$, where H, E, IP, and Γ denote the edge jump intensity, photon energy, ionization, potential and spectral resolution, respectively. The second factor accounts for the energy dependent photoionization cross section for photon energies larger than the ionization potential.[57]
[57]B. L. Henke, E. M. Gullikson, and J. C. Davis, At. Data Nucl. Data Tables **54**, 181 (1993).
[58]D. Käfer, G. Witte, P. Cyganik, A. Terfort, and Ch. Wöll, J. Am. Chem. Soc. **128**, 1723 (2006).
[59]D. Hübner, F. Holch, M. L. M. Rocco, K. C. Prince, S. Stranges, A. Schöll, E. Umbach, and R. Fink, Chem. Phys. Lett. **415**, 188 (2005).
[60]N. Schmidt, T. Clark, S. G. Urquhart, and R. H. Fink, J. Chem. Phys. **135**, 144301 (2011).

5.8 Understanding the F 1s NEXAFS Dichroism in Fluorinated Organic Semiconductors

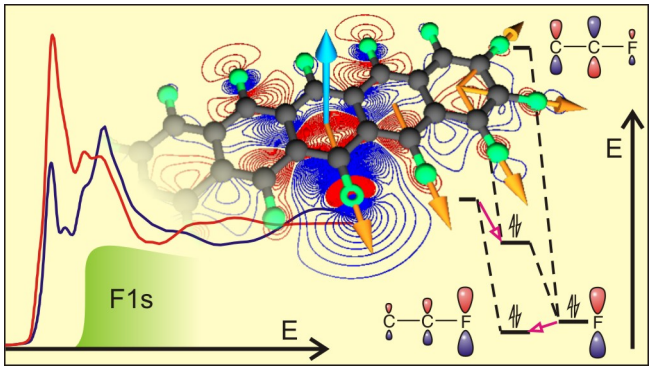

5.8.1 Inhaltsangabe

The analysis of NEXAFS spectra acquired at the absorption edge of heteroatoms like fluorine, nitrogen, or oxygen enables the determination of the molecular orientation of individual compounds even in multinary structures. Such an analysis requires detailed knowledge about the nature of the corresponding electronic excitations, especially because 1s-π^* and 1s-σ^* excitations frequently feature disparate transition dipole moments in planar molecules. Unlike intuitively assumed, the resulting dichroisms of both excitation types in planar systems are, however, not necessarily inverted. Instead, both the structure of the molecules and their alignment on the substrate determine the actual dichroisms. In this study, the NEXAFS signature and dichroisms of thin films of the organic n-type semiconductor perfluoropentacene (PFP) in different crystalline orientations at the carbon and fluorine absorption K-edge are thoroughly analyzed. For lying molecular orientations, an inverted dichroism at the fluorine K-edge compared to the carbon K-edge is found. In contrast, for upright molecular configurations the dichroisms at both absorption edges are similar. With the help of density functional theory methods, this behavior is explained by the different nature of the excitations. While at the carbon K-edge 1s-π^* excitations are most prominent, 1s-σ^*-related signals are dominant at the fluorine K-edge. Computations of the NEXAFS signatures and corresponding excitations at different levels of theory are compared with particular focus on electronic relaxation. Energetic positions and oscillator strengths, especially for resonances of σ^*-type, depend strongly on the theoretical approach whereas the π^*-related signals are barely affected by the methods applied in the present work. Similar effects were also found for the analysis of the smaller perfluoronaphthalene and are explained by the different relaxation effects for 1s-σ^*- and 1s-π^*-type excitations. As the investigated acenes are representative model systems for π-conjugated molecular semiconductors, the present findings are important for the understanding of

the electronic properties and the application of NEXAFS for structural analysis in such materials.

5.8.2 Eigenleistung

Alle NEXAFS-Messungen am Perfluoropentacen wurden von mir geplant, vorbereitet und in Zusammenarbeit mit Martin Oehzelt durchgeführt. Weitere experimentelle Ergebnisse in diesem Artikel wurden teilweise in Zusammenarbeit mit Tobias Breuer gewonnen. Sämtliche Berechnungen von NEXAFS-Spektren, die auf dem Programmpaket StoBe basieren, wurden von mir geplant und durchgeführt. Auf diesen Ergebnissen baut die Berechnung der Oszillatorstärken für angeregte Zustände auf, die von Paul Jerabek und Robert Berger vorgenommen wurde. Ebenso stammt die Interpretation der Bindungssituation im Rahmen der Hückeltheorie von diesen beiden Autoren. Die Betrachtung des Dichroismus, die unter anderem wiederum auf den Ergebnissen der vorgenannten Kollegen basiert, wurde vollständig von mir vorgenommen. Alle vorgenannten Kollegen haben zu ihren Teilgebieten Textpassagen geliefert, die von mir in den Gesamtkontext eingepasst wurden, wobei Gregor Witte, ebenso wie bei der Interpretation der Daten, unterstützend tätig war. Klaus Hermann und Robert Berger haben Vorschläge und Anmerkungen zum gesamten Artikel beigetragen.

THE JOURNAL OF PHYSICAL CHEMISTRY C

Article

pubs.acs.org/JPCC

Understanding the F 1s NEXAFS Dichroism in Fluorinated Organic Semiconductors

M. Klues,[†] P. Jerabek,[‡] T. Breuer,[†] M. Oehzelt,[§] K. Hermann,[∥] R. Berger,*[,‡] and G. Witte*[,†]

[†]Fachbereich Physik and [‡]Fachbereich Chemie, Philipps-Universität Marburg, 35032 Marburg, Germany

[§]Helmholtz Zentrum für Materialien und Energie GmbH, Hahn-Meitner-Platz 1, 14109 Berlin, Germany

[∥]Department of Inorganic Chemistry, Fritz-Haber-Institut der Max-Planck-Gesellschaft, 14195 Berlin, Germany

Supporting Information

ABSTRACT: The analysis of NEXAFS spectra acquired at the absorption edge of heteroatoms like fluorine, nitrogen, or oxygen enables the determination of the molecular orientation of individual compounds even in multinary structures. Such an analysis requires detailed knowledge about the nature of the corresponding electronic excitations, especially because 1s-π^* and 1s-σ^* excitations frequently feature disparate transition dipole moments in planar molecules. Unlike intuitively assumed, the resulting dichroisms of both excitation types in planar systems are, however, not necessarily inverted. Instead, both the structure of the molecules and their alignment on the substrate determine the actual dichroisms. In this study, the NEXAFS signature and dichroisms of thin films of the organic n-type semiconductor perfluoropentacene (PFP) in different crystalline orientations at the carbon and fluorine absorption K-edge are thoroughly analyzed. For lying molecular orientations, an inverted dichroism at the fluorine K-edge compared to the carbon K-edge is found. In contrast, for upright molecular configurations the dichroisms at both absorption edges are similar. With the help of density functional theory methods, this behavior is explained by the different nature of the excitations. While at the carbon K-edge 1s-π^* excitations are most prominent, 1s-σ^*-related signals are dominant at the fluorine K-edge. Computations of the NEXAFS signatures and corresponding excitations at different levels of theory are compared with particular focus on electronic relaxation. Energetic positions and oscillator strengths, especially for resonances of σ^*-type, depend strongly on the theoretical approach whereas the π^*-related signals are barely affected by the methods applied in the present work. Similar effects were also found for the analysis of the smaller perfluoronaphthalene and are explained by the different relaxation effects for 1s-σ^*- and 1s-π^*-type excitations. As the investigated acenes are representative model systems for π-conjugated molecular semiconductors, the present findings are important for the understanding of the electronic properties and the application of NEXAFS for structural analysis in such materials.

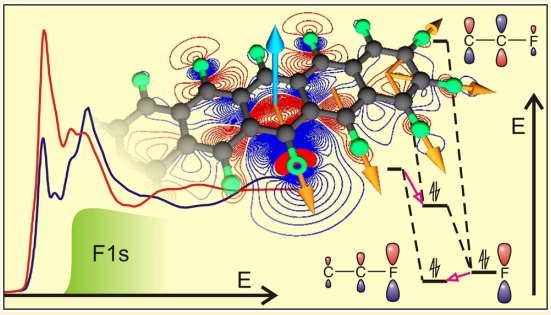

INTRODUCTION

Near-edge X-ray absorption spectroscopy (NEXAFS) is a powerful method to characterize electronic states of molecular materials. In molecules composed of light elements the corresponding transitions from occupied core levels into unoccupied molecular orbitals are governed by electronic dipole selection rules. Therefore, they allow one to determine the molecular orientation by analyzing the linear dichroism which occurs when the angle of incidence, and thus the polarization direction of the linearly polarized synchrotron beam relative to the sample normal is varied.[1−4] This structural analysis is particularly advantageous as it does not require any crystalline ordering within the molecular films like in the case of X-ray diffraction analysis and is also applicable in the submonolayer regime. Besides the linear dichroism discussed in this study, also circular dichroism can occur due to chirality of molecules.[5−8] However, such effects are more challenging to measure, because the circular dichroism is typically orders of magnitude smaller than the linear one.[9]

In the course of the recent success of organic electronics NEXAFS spectroscopy has become an important technique to characterize the growth and structure of molecular films of π-conjugated systems. For this purpose usually the (linear) dichroism of carbon K-edge NEXAFS spectra is analyzed because the electronic transition dipole moment for excitations from 1s core orbitals into unoccupied π^* orbitals of such polycyclic aromatic hydrocarbons is oriented perpendicular to the aromatic ring plane.[10,11] However, the application of this method to multinary heterostructures is frequently hampered by overlapping NEXAFS signatures and requires a precise

Received: April 21, 2016
Revised: May 25, 2016
Published: May 25, 2016

DOI: 10.1021/acs.jpcc.6b04048
J. Phys. Chem. C 2016, 120, 12693−12705

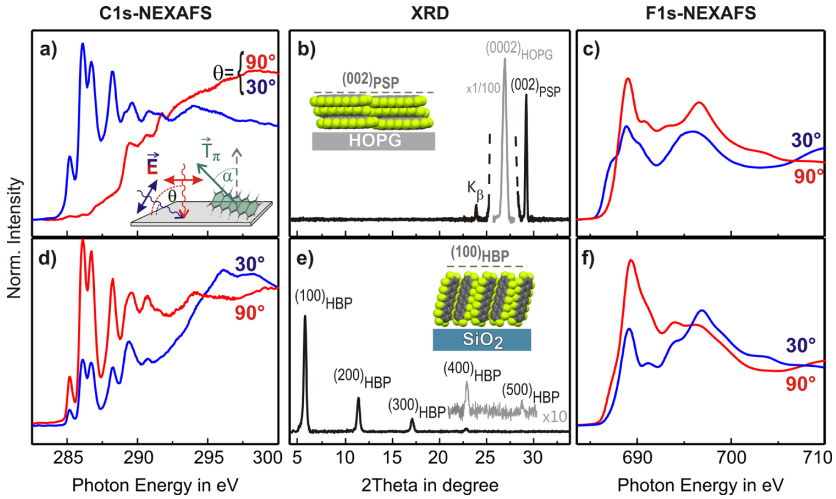

Figure 1. Structural characterization of PFP mutilayer films (d = 50 nm) grown on HOPG (a–c) and SiO_2 (d–f) substrates. (a, d) C 1s-NEXAFS spectra recorded at different angles of incidence (red: 90°; blue: 30°) with sketch of experimental geometry. (b, e) Specular X-ray diffraction patterns recorded in Bragg–Brentano geometry of PFP/HOPG and PFP/SiO_2 with corresponding molecular arrangements. (c, f) F 1s-NEXAFS spectra.

knowledge of the respective resonances. One strategy to overcome this challenge is the study of heterosubstituted hydrocarbons by analyzing the X-ray absorption spectra associated with such heteroatoms. For example, for phthalocyanines nitrogen K-edge NEXAFS spectra can be used to independently determine the orientation of one compound of the heterostructure.[12]

An interesting chemical modification of molecular materials provides fluorination.[13,14] It does not only suppress oxidation, hence enhancing chemical stability of the organic compounds, but also allows for the realization of molecular n-type semiconductors as demonstrated e.g. for perfluorinated acenes.[15] Although fluorine K-edge NEXAFS spectra can be acquired avoiding parasitic signals due to possible contaminations on optical elements, which is a typical issue for carbon K-edge NEXAFS,[16] a clear identification of the occurring resonances is challenging.

Early assignments of fluorine K-edge excitations of perfluorinated naphthalene (PFN) were derived from inner shell electron energy loss (ISEEL) data which feature similar excitations as NEXAFS. Based on accompanying Hückel calculations of the electronic structure, the resonances were mainly assigned to π^* resonances.[17] However, in contrast to heterosubstitution of aromatic molecules where the heteroatom is part of the aromatic ring system, like e.g. for pyrrolic nitrogen in phthalocyanines, a rather different situation occurs upon fluorination. This leads to the question whether the unoccupied π^* orbitals of the aromatic backbone are also partially extended to the F atoms to yield sufficient oscillator strength for π^* resonances to become observable. Indeed, this early assignment was later challenged by photon stimulated ion desorption measurements of perfluorinated copper phthalocyanine (PFCuPc) where both fluorine K-edge NEXAFS spectra and partial ion yield mass spectra were measured. This experiment revealed the appearance of F^+ ions at photon energies of the prominent NEXAFS resonance. It was interpreted as a resonant cleavage of C–F bonds, hence suggesting a possible σ^*(C–F) character of the resonance.[18] In a previous study of PFCuPc and perfluorinated pentacene (PFP) inversed dichroisms have been reported for the carbon and fluorine K-edge NEXAFS signatures.[19] Moreover, the accompanying theoretical analysis of the fluorine NEXAFS spectra, carried out within the framework of the transition potential method, has actually yielded a mixed π^*/σ^* character, which in turn hampers a quantitative analysis of the F 1s dichroism in pure and mixed systems.[19,20]

In their study Oteyza et al. used monolayer films of PFCuPc and PFP adsorbed on noble metals.[19] While this approach provides planar adsorption geometries in general, it remains *a priori* unclear whether the NEXAFS signature is affected by electronic adsorbate-substrate coupling. For example, for the adsorption of pentacene on Au(111) and Ag(111) surfaces a substantial change of the NEXAFS resonances was found,[21,22] reflecting notable electronic substrate coupling. Moreover, our previous study also revealed substantial radiation-induced damages of PFP as well as substrate-induced partial defluorination that occurs even on noble metals[23] which challenges the reliability of such measurements.

In this study, we want to elucidate the nature of F 1s NEXAFS resonances and their dichroism in more detail. Therefore, we have performed F 1s NEXAFS measurements on well-defined multilayer films of PFP with controlled molecular orientation. By analyzing PFP multilayer films grown on SiO_2 and on highly ordered pyrolytic graphite (HOPG), we exclude electronic substrate interaction and obtain well-defined diverse molecular orientations on both substrates: upright-standing molecules in the case of SiO_2[24] and a flat-lying arrangement on HOPG[25] as verified by C 1s NEXAFS and X-ray diffraction (XRD) measurements. By this means, the dichroisms could be analyzed in detail for different molecular configurations (cf. visualization in Figure 1). Our refined density functional theoretical (DFT) analysis is capable of identifying the individual resonances contributing to the F 1s NEXAFS spectrum with appropriate consideration of relaxation effects. Apart from excitation energies, we determine transition dipole moments for relaxed final states within a self-consistent field (ΔSCF) approach. This analysis was also applied to perfluoronaphthalene (PFN) to verify the approach for a smaller and

DOI: 10.1021/acs.jpcc.6b04048
J. Phys. Chem. C 2016, 120, 12693–12705

computationally less expensive test system. Finally, with this piece of information also the experimentally observed dichroism of PFP in upright and lying orientation can be well reproduced by generalizing the excitation scheme and considering the individual spatial arrangement of all C−F bonds within the molecule.

METHODOLOGY

Experimental Details. PFP ($C_{22}F_{14}$, Kanto Denka Kogoyo Co. LTD, purity >99%) films were grown under high vacuum conditions by molecular beam deposition onto Si wafers covered with a native oxide layer as well as HOPG substrates (SPI supplies, mosaicity <0.4°). Atomically smooth graphite surfaces were prepared via exfoliation in air. After loading into the vacuum system, all substrates were heated to 500 K to remove residual contaminations, and subsequently all PFP films were grown at room temperature. For comparison also PFN ($C_{10}F_8$, Sigma-Aldrich, purity 96%) films were studied. As its low sublimation enthalpy hampers preparation by evaporation from Knudsen cells, PFN films were prepared by exposing an oxidized copper plate, which was cooled to temperatures below 200 K, to PFN vapor dosed from a glass capillary through a leak valve. Because of the low sublimation enthalpy of PFN, the corresponding thin films rapidly evaporate already at room temperature and hence require sample cooling and renewed film preparation for the individual measurements.

The crystalline structure and orientation of the molecular films were analyzed by means of X-ray diffraction (Bruker AXS Discover D8) using monochromatized Cu Kα radiation and a LynxEye silicon strip detector.

The NEXAFS measurements were performed at the HE-SGM dipole beamline of the synchrotron storage ring BESSY II in Berlin (Germany) providing linearly polarized light (P = 0.91)[26] and resolving powers of E/dE = 2500 at the carbon K-edge and E/dE = 1500 at the fluorine K-edge, respectively. The NEXAFS spectra were recorded in partial electron-yield mode using a channel-plate detector with a retarding field of −150 V. Additional F 1s NEXAFS measurements for PFP films were performed at the SurICat beamline (BESSY II, Berlin) which features a higher energy resolution (P = 0.95, E/dE = 6000 at 400 eV). In this case, the total electron yield was detected by recording the sample current. For all molecular films NEXAFS spectra were acquired at different angles of incidence ranging between grazing incidence (θ = 30°) and normal incidence (90°, cf. inset of Figure 1a), and the observed linear dichroism was analyzed after flux normalization and considering the transmission of the monochromator.[27] As shown in our previous work[28] and the present theoretical analysis (see below), the carbon K-edge NEXAFS spectra of PFP are governed by distinct resonances that can be identified as excitations of C 1s electrons into unoccupied molecular π^* orbitals. For electronic transition dipole moments belonging to 1s-π^* excitations occurring in aromatic molecules, a surface of 3-fold symmetry, and use of linearly polarized light, the measured intensity variation of this transition, referred to as "vector type" in ref 1, can be expressed as

$$I_{vec} \propto \frac{1}{2}(P\cos^2\theta(3\cos^2\alpha - 1) + \sin^2\alpha) \quad (1)$$

with α referring to the angle between the normal of the aromatic ring plane and the surface normal as indicated in Figure 1a. As the electronic transition dipole moment, $\vec{T}$, for such excitations is oriented normal to the ring plane, the average molecular orientation relative to the sample surface, α, can be derived from a quantitative analysis of the dichroism observed at different angles of incidence θ.

To provide a calibration of the absolute energy scale of the carbon K-edge NEXAFS spectra, the photocurrent from a carbon-coated gold grid in the incident beam was recorded simultaneously which reveals a characteristic absorption peak at a photon energy of 284.9 eV.[27] Because of nonlinearities and hysteresis effects of the monochromator, the energy calibration from the carbon K-edge region cannot reliably be used for measurements at the fluorine K-edge. Therefore, additional reference points were used to provide an accurate energy calibration of the F 1s NEXAFS spectra. One approach is based on XPS measurements of a bare Au(111) single crystal. By choosing a photon energy which is in the energy range used for F 1s NEXAFS measurements and comparing the measured energy position of the Au 4f doublet in consideration of the work function of the detector and the known binding energy of this doublet,[29] the used photon energy was acquired. In addition, F 1s NEXAFS spectra of potassium hexafluorotitanate (K_2TiF_6, abcr GmbH, purity 98%) powder reamed on a roughened copper plate were measured. Previous work has shown that these spectra exhibit two discrete and sharp resonances, arising from d-type final states of the TiF_6^{2-} ion (see Supporting Information). The first resonance is known to be located at 683.9 eV,[30,31] which can be used for calibration. Both methods comply with each other within 0.3 eV, thus providing a reliable energy calibration.

Computational Approach. The NEXAFS calculations within this work were carried out utilizing the StoBe code.[32] Structure energy minimization, electronic ground state calculations, and the evaluation of ionized and electronically excited states were performed with the gradient-corrected revised Perdew−Burke−Ernzerhof (RPBE) functional[33,34] and all-electron Gaussian basis sets of valence triple-ζ plus polarization quality.[35] In the StoBe code core holes are kept localized, thus allowing to distinguish between various excitation centers and to compute partial NEXAFS spectra for every symmetry nonequivalent excitation center. For this purpose, the 1s electrons of all other atoms of the same element are described by effective core potentials (ECPs), whereas the valence electrons are represented by a [3s3p1d] valence basis set, so that a mixing between the corresponding core orbitals is prevented.[36,37] The 1s electrons of the excitation center are represented by an IGLO-III basis set[38] to provide additional flexibility for the description of core hole relaxation. In a final step during the transition potential calculations the basis was augmented by a [19s19p19d] basis set of diffuse functions within a double basis set technique, to improve the representation of diffuse molecular states.[39,40] In the present study NEXAFS spectra were calculated using two different approaches. Using the transition potential approximation[11,41] provides already a rather good description of NEXAFS spectra at low computational cost. This method is often an efficient compromise in representing the excitation, accompanying relaxation and dynamical correlation effects, whereas the related static exchange approximation[5,6] does not account for electron correlation and time-dependent DFT approaches[7,8] show large overall shifts, which have been ascribed to underlying self-interaction errors in the core orbitals. Because relaxation effects turned out to be of special interest for this study, the ΔSCF method was applied for the calculation of improved excitation energies. To account for these effects in the F 1s excitations, the

DOI: 10.1021/acs.jpcc.6b04048
J. Phys. Chem. C 2016, 120, 12693−12705

individual core excitations of the different fluorine atoms were computed by individually converging the electronic ground states and the particular electronically excited states (about four F 1s-π^* and two F 1s-σ^* type states for each symmetry nonequivalent F atom) of the fluorinated acenes in an (unrestricted) SCF procedure. For that purpose, the StoBe code—at the same level of theory as for the transition potential approach—has been utilized. A detailed description of such refined theoretical treatments and their computational implementation can be found in our previous work.[42] However, the StoBe code does not compute the corresponding electronic transition dipole moments between nonorthogonal Slater determinants, and the output is consequently lacking the oscillator strengths.

The overlap integrals and electric transition dipole moments between two converged, nonorthogonal Slater determinants Ψ_a and Ψ_b, which represent for instance in an approximate single-determinant description the electronic ground state and an electronically excited state of a molecule, have thus been calculated separately in this work.

According to the widely used Slater−Condon rules,[43] the matrix element $\langle\Psi_{a,e}|\vec{\mu}_e|\Psi_{b,e}\rangle$ of the electronic electric dipole moment[44] operator for two Slater determinants that differ in the occupation of one orbital only is simply given by the matrix element between the two differing molecular orbitals (MOs) $\langle\psi_i^{(a)}|\vec{\mu}_e|\psi_j^{(b)}\rangle$, assuming all other MOs are orthonormalized. As this assumption is not necessarily true, our code uses the more general Löwdin rules[45] for the evaluation of matrix elements of the electronic electric dipole moment operator between nonorthogonal Slater determinants:

$$\langle\Psi_{a,e}|\vec{\mu}_e|\Psi_{b,e}\rangle = \sum_{i,j=1}^{Occ} \langle\psi_i^{(a)}|\vec{\mu}_e|\psi_j^{(b)}\rangle D(i|j) \tag{2}$$

According to eq 2, every matrix element $\langle\psi_i^{(a)}|\vec{\mu}_e|\psi_j^{(b)}\rangle$ has to be multiplied with the corresponding cofactor $D(i|j)$ which is obtained via the minor $M(i|j)$ (i.e., the determinant of the overlap matrix $\mathbf{S}^{(a,b)}$ with elements $S_{ij}^{(a,b)} = \langle\psi_i^{(a)}|\psi_j^{(b)}\rangle$ from which the ith row and the jth column were deleted) multiplied with the factor $(-1)^{i+j}$. In addition to the electronic dipole moment operator $\vec{\mu}_e$, the nuclear electronic dipole moment operator $\vec{\mu}_n$ has to be considered to calculate the total electric (transition) dipole moment for a fixed nuclear arrangement as

$$\vec{\mathbf{T}} = \langle\Psi_{a,e}|\vec{\mu}|\Psi_{b,e}\rangle = \langle\Psi_{a,e}|\vec{\mu}_e|\Psi_{b,e}\rangle + \vec{\mu}_n\langle\Psi_{a,e}|\Psi_{b,e}\rangle \tag{3}$$

The term $\langle\Psi_{a,e}|\Psi_{b,e}\rangle$ corresponds to the overlap of the electronic wave functions and can be calculated as the determinant $\det(\mathbf{S}^{(a,b)})$ of the overlap matrix $\mathbf{S}^{(a,b)}$ between the MOs that are occupied in the two Slater determinants.

It is important to note that the ΔSCF method is only well applicable for the energetically lowest electronic state of a given symmetry. For higher excitations, the overlap between determinants of excited states can become non-negligible.[46−48] In these cases, the particular electronic states are likely to mix, and therefore the nonlinear description has to be waived in favor of a linearly optimized variation method involving multiple Slater determinants.[49]

Finally, to enable a comparison with experimental NEXAFS data, all transitions calculated for the nonequivalent excitation centers within the molecule have to be summed up by considering their multiplicity. Moreover, to account for the finite experimental resolution and natural peak width (due to the excitation lifetime), the calculated transition energies (E_{ex}) are convoluted by Gaussian functions

$$I(E,\theta) = \sum_i f_i I_{vec}(\theta)\frac{1}{\sigma_i} e^{-(E-E_{ex})^2/2\sigma_i^2} \tag{4}$$

where different standard deviations σ_i were utilized to describe transitions into π^*- and σ^*-type orbitals. The carbon K-edge NEXAFS signatures are best described by values of $\sigma_i(\pi^*)$ = 0.21 eV (yielding a full width at half-maximum (FWHM) of 0.49 eV) and $\sigma_i(\sigma^*)$ = 0.30 eV (FWHM: 0.71 eV), which are in close agreement with values observed before for non-fluorinated acenes.[21,42] In contrast, the fluorine K-edge NEXAFS spectra of the fluorinated acenes reveal distinctly broader resonances. In that case the best agreement with experimental data was obtained when using values of $\sigma_i(\pi^*)$ = 0.40 eV (FWHM: 0.94 eV) and $\sigma_i(\sigma^*)$ = 0.80 eV (FWHM: 1.88 eV) for the convolution (as shown below). To check whether the peak width of the main F 1s signature of fluorinated acenes is limited by the energy resolution in this spectral range, additional F 1s NEXAFS measurements were recorded for K_2TiF_6. This compound exhibits sharp NEXAFS resonances[30,31] which could be well resolved with a fwhm of about 1 eV (see Supporting Information), hence showing that the widths of the main F-edge NEXAFS signatures of PFP and PFN are not limited by the instrumental resolution.

The X-ray absorption signal is related to the oscillator strength f which can be calculated from $\vec{\mathbf{T}}$, the Bohr radius a_0, and the excitation energy E_{ex} given in hartree (E_h) according to[50]

$$f = \frac{2}{3}(E_{ex}/E_h)|\vec{\mathbf{T}}/(ea_0)|^2 \tag{5}$$

Together with the oscillator strength the amplitude is also scaled by I_{vec}, which is defined in eq 1 and introduces dichroic effects. Neglecting this term leads to spectra which can be directly compared with experimental data of amorphous samples or data recorded under the so-called magic angle (ca. 55°), where orientational effects are suppressed in the NEXAFS spectra.[51]

Computation of NEXAFS Dichroism. To compare the computed NEXAFS excitations with the experimental angle-resolved measurements, also dichroism curves of the F 1s-NEXAFS signatures have been simulated. For that purpose, the 25 energetically lowest excitations were evaluated, yielding in total 88 transitions. The corresponding molecular transition vectors $\vec{\mathbf{T}}_i$ have to be transformed into orientations adopted in the relevant crystallographic configurations [$(100)_{HBP}$ orientation for PFP films grown on SiO_2, $(001)_{PSP}$ for those on graphite; cf. Figure 1] considering the molecular packing motifs. Note that this also requires an appropriate transformation from the internal molecular coordinates into the Cartesian coordinate system applied in the StoBe code. This allows determining the relative angle of the $\vec{\mathbf{T}}_i$ vectors with respect to the surface normal, which then enables the calculation of the dichroism for every $\vec{\mathbf{T}}_i$. Summation over all excitations with appropriate weighting by the individual oscillator strengths then yields the total dichroism curves for a single molecule and summation over all molecules in the unit cell (Z = 2 for both polymorphs) finally yields the effective dichroism of the oriented thin films.[51] We note that due to the particular symmetry of the present samples this treatment can be simplified further since it is sufficient to consider only one

DOI: 10.1021/acs.jpcc.6b04048
J. Phys. Chem. C 2016, 120, 12693−12705

molecule per unit cell. In the π-stacked polymorph all PFP molecules lie perfectly parallel to the graphite surface and thus exhibit the same dichroism. Though the packing motif in PFP films formed on SiO_2 is more complex due to the molecular herringbone arrangement of the bulk polymorph, the description can be simplified again because the (100)-oriented PFP film features a screw displacement parallel to the surface normal. Consequently, both molecules within the unit cell exhibit the same orientation relative to the surface normal.

RESULTS AND DISCUSSION

A. Experimental Comparison of PFP C 1s and F 1s Dichroism. To provide structurally well-defined model systems with uniform molecular orientation and also exclude additional electronic substrate interaction, PFP multilayer films grown on HOPG and on SiO_2 have been examined. As demonstrated previously, PFP films on HOPG adopt a new polymorph where the molecules are arranged in a slip-stacked parallel, flat-lying orientation, denoted as "π-stacked polymorph" (PSP).[25] In contrast, PFP molecules on SiO_2 grow in an upright orientation[24] adopting a herringbone polymorph (HBP) as in the bulk crystal structure[15] which parallels the situation of the non-fluorinated pentacene.[52] The structural characterization based on X-ray diffraction and NEXAFS spectroscopy is summarized for PFP/HOPG in Figure 1a–c and PFP/SiO_2 in Figure 1d–f. For PFP/HOPG the corresponding X-ray diffractogram reveals only one film related $(002)_{PSP}$ peak (corresponding to an interlayer spacing of 3.07 Å) besides the dominating $(0002)_{HOPG}$ peak of the graphite substrate which is accompanied by a weak satellite due to weak K_β contributions. In a previous study it was found that on defective graphite substrates PFP also forms domains with molecules in upright orientation.[53] From the absence of additional diffraction peaks at lower angles the presence of domains with such disturbing orientation can be safely ruled out for the investigated sample, hence demonstrating the high structural quality of the present films. The corresponding C 1s NEXAFS spectra reveal a rich fine structure due to a multitude of transitions between core levels of the various carbon atoms and the large number of accessible unoccupied molecular orbitals. As depicted in Figure 1a, the C 1s NEXAFS spectra exhibit a distinct dichroism with largest intensity for grazing incidence (blue curve) and almost vanishing resonances at normal incidence (red curve), hence again reflecting the pronounced orientational order within the film. The peaks found at lower energy correspond to excitations of C 1s electrons into unoccupied π^* orbitals whose transition dipole moments (indicated as $\vec{T}_\pi$ in the inset in Figure 1a) are oriented perpendicular to the molecular plane of PFP (cf. theoretical analysis below). Because of incomplete wetting of the HOPG substrate by the PFP films, residual contributions from NEXAFS signals of the graphite substrate are found in the C 1s spectra, which also experience a distinct dichroism. To still allow a quantitative analysis of the PFP dichroism in these films without the disturbing dichroic substrate signal,[54] the contributions of the HOPG surface have been subtracted, weighted according to HOPG specific resonances. More information on this procedure can be found in refs 25 and 55 and the Supporting Information. For the quantitative analysis of the dichroism the leading three resonances (at energies below 287.5 eV) have been used to rule out misinterpretations caused by overlapping σ^* resonances. The corresponding analysis yields a molecular tilt angle of less than $10 \pm 6°$, which agrees favorably with the previous GIXRD-RSM analysis.[25] The apparent deviation from perfectly flat oriented molecules can be explained by the existence of defects on the HOPG surface and in the PFP films. Note that NEXAFS is not restricted to crystalline regions but also probes amorphous regions and thus provides an average molecular tilt angle, whereas the X-ray diffraction analysis is sensitive to crystalline regions only.[51] During the measurements particular care was taken to avoid protracted exposure times during acquisition of the NEXAFS spectra in order to exclude radiation damages. Such radiation damages have been reported to strongly affect the NEXAFS signature of PFP because additional resonances are formed upon intense X-ray illumination, probably corresponding to cross-linking of the individual molecules.[23]

By contrast, the corresponding F 1s NEXAFS signature which is displayed in Figure 1c is less detailed and reveals two rather broad resonances at around 689 and 696 eV, which are accompanied by weaker signals in their flanks. These resonances also exhibit a dichroism which is, however, distinctly weaker and inverted compared to the leading carbon K-edge NEXAFS signature of PFP in lying molecular orientation. Though the general NEXAFS characteristics are in close agreement with data reported earlier for PFP monolayers on Au(111) and Ag(111),[19] we observe some clear differences. At higher photon energies the signals in the σ^* region appear less pronounced in their data which could indicate a broadening of these resonances. As our study deals with van der Waals bound multilayer films modifications of the PFP spectra by interactions with the substrate can be safely ruled out. In the earlier study,[19] however, monolayer films adsorbed on metal substrates are investigated, which might have experienced considerable additional substrate interaction and therefore changes of their electronic structure. More striking, however, is an overall energetic shift of all resonances in their F 1s NEXAFS spectra by about 1 eV, which indicates a deviating energy calibration. As detailed in the experimental section, we have combined different independent approaches to calibrate the photon energy in our experiment, which assures the validity of the presented energy scales.

A complementary molecular orientation prevails in PFP films that are grown on SiO_2. In this case the molecules form (100) oriented films where molecules are oriented uprightly.[24] This ordering is well corroborated by the X-ray data presented in Figure 1e showing exclusively the (n00) peaks of the PFP–HBP phase,[56] thus proving that no competing molecular arrangements are present in the sample. The corresponding C 1s NEXAFS data (see Figure 1d) reveal a distinct dichroism which is inverted compared to that of PFP films on HOPG. The quantitative analysis of the dichroism based on the intensity of the leading π^* resonances yields a molecular tilt angle of 77°, which agrees favorably with the molecular orientation of 76° with respect to the (100) plane derived from the PFP crystal structure.[56] Interestingly, the leading resonance of the F 1s NEXAFS signature reveals the same dichroism as the π^* resonances of the C 1s NEXAFS spectra and is most intense for perpendicular incidence (i.e., $\vec{E}$ vector parallel to surface); i.e., the C 1s and F 1s dichroisms are not inverted. Only a shoulder of the second resonance at about 697 eV exhibits an inverted dichroism, hence showing a more complex behavior than postulated by Oteyza et al.[19]

B. Computation of PFP C 1s NEXAFS Spectra. In order to gain a deeper understanding of the observed NEXAFS signatures, they have been theoretically analyzed by means of

DOI: 10.1021/acs.jpcc.6b04048
J. Phys. Chem. C 2016, 120, 12693–12705

DFT. To qualify our approach, we have first calculated the C 1s NEXAFS signature of PFP in the framework of the transition potential method. Figure 2 shows a comparison of computed

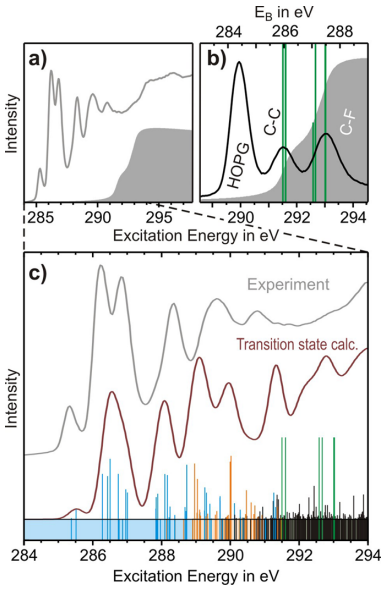

Figure 2. Comparison of experimental and theoretical data of PFP: (a) C 1s NEXAFS spectrum recorded at θ = 55°, together with a calculated carbon K absorption edge. (b) Fine structure of this edge related to the calculated ionization energies for the symmetry nonequivalent carbon atoms (indicated by green lines), further compared with a corresponding XP-spectrum of PFP on HOPG. Note: energy scales of the absorption and emission processes are shifted relative to each other (for details see text). (c) Experimental C 1s NEXAFS spectrum compared to computational results based on the transition state method. Underlying bars indicate individual excitations. Blue and orange bars denote excitations into π^* and σ^* orbitals, respectively, whereas black bars indicate unassigned resonances and green bars denote the ionization edges.

and experimental data. The computation of the fundamental absorption edge beneath the experimental spectrum as presented in Figure 2a corresponds nicely to the various binding energies derived from XPS experiments as shown in Figure 2b. To omit orientational effects, we have considered a NEXAFS spectrum that was acquired at the magic angle of $\theta \approx$ 55° where dichroism effects are negligible.[51] The calculated NEXAFS spectrum (cf. Figure 2c) was obtained by first computing electronic transitions from C 1s hole states into unoccupied molecular orbitals for each symmetry nonequivalent excitation centers C*i* (so-called partial NEXAFS spectra, see also Supporting Information) and subsequently superimposing them under consideration of the multiplicity of the respective carbon atoms C1−C6 (cf. Figure 3a).

The differing ionization energies of symmetry nonequivalent carbon atoms caused by their different chemical surrounding (*chemical shift*) not only affect the excitation energy of individual NEXAFS resonances (commonly referred to as *initial state effect*) but also lead to the presence of more than one fundamental carbon absorption edge. This is illustrated in Figure 2a, which shows the adsorption edge of PFP computed from the various ionization energies by using an analytical

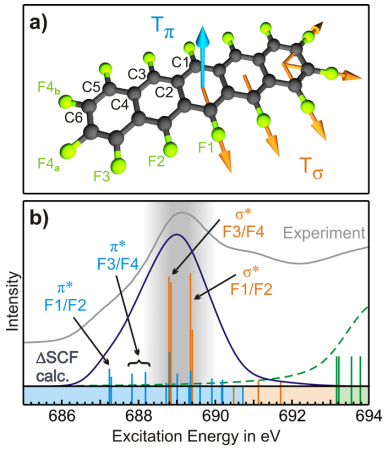

Figure 3. (a) Structure of a PFP molecule. All symmetry nonequivalent excitation centers are labeled, shown together with vectors indicating the directions of electric transition dipole moments (with arbitrarily chosen phases). (b) Comparison of an experimental F 1s NEXAFS spectrum of PFP on SiO_2 (recorded at the magic angle) with the result of the ΔSCF calculations (computed results shifted by 1.2 eV; for details see text). To classify the character of the underlying individual excitations, the same color code is used as in Figure 2.

model for the shape of an adsorption edge as described previously.[1,42] To qualify the calculated ionization energies and their energetic shifts, they are further compared with high-resolution X-ray photoemission (XPS) data of PFP films on HOPG. As shown in Figure 2b, the XP spectrum reveals, besides the C 1s peak of the graphite substrate, which was used for provision of an accurate energy scaling (E_B = 284.4 eV[57]), essentially two carbon signals at binding energies of 286.0 and 287.5 eV. The relative intensity and energetic separation is well reproduced by the calculated ionization energies yielding energies around 291.5 eV for carbon atoms (C2 and C4, cf. Figure 3a) not bound to fluorine and between 292.5 and 293 eV for the other carbon atoms. Note that in Figure 2b two different energy scales are used: the NEXAFS data are referred to the excitation energy, i.e., the photon energy, because the electron binding energy of free atoms or molecules is referenced to the vacuum level, whereas the binding energy of the emitted photoelectrons from solids is referenced to the Fermi level (E_B = 0 eV). Therefore, the difference of both energy scales arises from the work function and yields a value of 5.5 eV for the PFP/HOPG system. We note that this value agrees well with work functions reported for films of other fluorinated organic compounds on graphite.[58]

In addition to the energy of the various NEXAFS resonances, the theoretical analysis also provides detailed information on the oscillator strength and character of such excitations. Throughout this study the calculated excitation energies are denoted by vertical lines (see e.g. Figure 2c). Lines that extend above the bottom color bar reflect excitations with appreciable electronic transition dipole moments. For these lines, the lengths of the bars characterize the respective oscillator strengths. The lines where the bars lie below the separation line describe transitions of negligible intensity. In addition, the coloring of the bar denotes the different character of the transition: blue bars refer to excitations into π^* orbitals, whereas orange bars indicate σ^* orbitals. The latter are often

DOI: 10.1021/acs.jpcc.6b04048
J. Phys. Chem. C 2016, 120, 12693−12705

referred to as Rydberg orbitals when located right below the ionization energy.[42] The vertical green lines indicate the ionization thresholds of the different carbon atoms in the molecule. Finally, the discrete excitations have been convoluted by Gauss functions to obtain continuous curves which can be compared with experimental data.

Though the calculated C 1s NEXAFS spectrum generally reproduces the experimentally observed signature quite well, some small variations occur such as e.g. the splitting of the intense resonance around 286.5 eV and the exact position of resonances at energies above 289 eV. As demonstrated previously for anthracene, the theoretical description of NEXAFS spectra can be significantly improved by considering the full electronic relaxation in the excited states.[42] As such a treatment is computationally very demanding for extended molecules like PFP, it has only been performed for the F 1s NEXAFS spectra discussed in detail in the next section.

C. Computation of PFP F 1s NEXAFS Spectra. In Figure 3, a comparison of experimental and calculated F 1s NEXAFS spectra of a PFP multilayer film is presented. To exclude the influence of orientational order on the intensity of the individual resonances, again a spectrum is considered that was acquired at the magic angle. As excited molecular states at high energies (near the ionization potential) and the oscillator strength of related transitions are difficult to calculate accurately, we have restricted our theoretical analysis to excitations below 691.5 eV in the comparison with the main signature of the fluorine NEXAFS spectrum. We note, however, that due to the densely lying states near the ionization potentials (indicated by green lines in Figure 3b) as well as the fluorine K absorption edge, additional intensity occurs at higher excitation energies. For the theoretical analysis at first partial F 1s NEXAFS spectra were computed for every nonequivalent excitation center (F1−F4, cf. Figure 3a) and then superimposed according to their multiplicity. To account for the Coulomb interaction between the excited electron and the core hole, also the electronic relaxation is considered by evaluating self-consistent final states for the lowest 5−7 excitations. Although the overall NEXAFS signature is well reproduced, the calculated F 1s NEXAFS spectra systematically underestimate the excitation energies.

In order to still enable a detailed analysis of the underlying resonances, the calculated F 1s NEXAFS spectra were shifted by +1.20 eV to match the leading resonance around 689 eV (gray shaded region in Figure 3b). We note that a similar shift of 1.17 eV is found when comparing the respective differences between the C 1s and F 1s binding energies (ΔE = 402.0 eV and ΔE = 400.4 eV) measured by XPS (see Figure S4) and the calculated ionization potentials of carbon and fluorine (400.67 and 399.40 eV, cf. Figures 2b and 3b), hence providing an *a posteriori* justification.

This analysis shows in particular that the most intense features of the F 1s NEXAFS spectra of PFP correspond to F 1s-σ^* excitations which also explains their large peak width. In addition, resonances of π^* character are found at lower energies with comparably low oscillator strength. These results are perfectly in line with the experimental observations and explain the inverted dichroisms of the resonances in the F 1s spectra for PFP molecules in lying configuration. The deviating behavior for films with upright molecular orientation will be explained in section E.

The detailed analysis of the partial NEXAFS spectra (see Figure S5) shows that for all excitation centers the lowest energy excitations with observable intensity are F 1s → π^* transitions (at energies below 688.5 eV) whereas the most intense (typically larger by a factor of 5) excitation occurring at around 689 eV corresponds to a F 1s → σ^* transition. Interestingly, these excitations behave quite differently when considering relaxation effects. This effect is evident, for example, for the excitation center F1 in Figure 4 where the

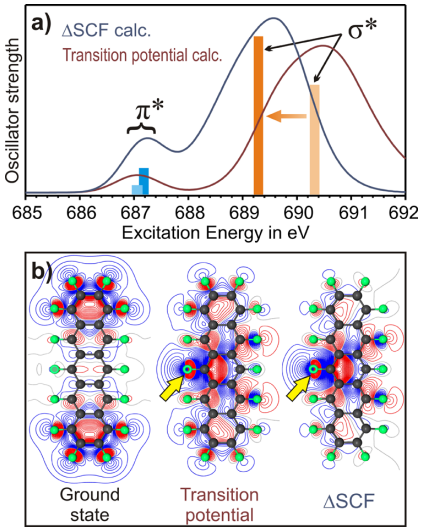

Figure 4. (a) Comparison of computed partial F 1s NEXAFS spectra of excitation center F1 performed by the Slater transition potential method and a fully relaxed ΔSCF calculation showing the influence of electronic relaxation on the position and intensity of underlying resonances. For clarity, only the lowest energetic π^* and σ^* resonances are marked by color bars. (b) Visualization of the corresponding final σ^* orbital as contour plots for both levels of theory as well as the corresponding unoccupied orbital (i.e., ground state) referring to plane through the atom centers. Positive and negative orbital values are shown in blue and red, respectively, whereas the hole at the F1 excitation center is labeled by a green torus (indicated by yellow arrow).

results of a fully relaxed ΔSCF calculation and the transition potential method are compared. Most notably, the leading σ^* resonances shift to considerably lower energies (by more than 1 eV), whereas the energy positions of the π^* resonances remain virtually constant (cf. Figure 4a).

This finding may be explained by the fact that the final molecular orbitals of the F 1s-σ^* excitations contain contributions from the 2s atomic fluorine orbitals that are for symmetry reasons rather sensitive to the effective core hole potential which is described differently in the various theoretical approaches. Within the fully relaxed ΔSCF calculation a complete electron is transferred from the core orbital into the formerly unoccupied orbital. For the first σ^* resonance of an excited F atom, this orbital interacts strongly with the positive potential of the nearby full core hole (FCH), and therefore the orbital energy is reduced by considerable amount. The transition potential approach uses a half core hole (HCH), and in contrast to the fully relaxed calculations, all empty orbitals interact with a less positive core hole potential. This yields a less attractive interaction as well as a reduced relaxation and results in a higher energy for the respective first σ^*

DOI: 10.1021/acs.jpcc.6b04048
J. Phys. Chem. C 2016, 120, 12693−12705

resonance. This is visualized in Figure 4b where the final orbital for the lowest 1s-σ^* excitation of atom F1 is displayed in the middle and on the right-hand side for the different theoretical approaches. Without consideration of relaxation effects, i.e., in the electronic ground state, no directly comparable orbital is found. (To roughly compare the orbital shape, also the lowest-lying 1s-σ^* state in the electronic ground state is shown that features nonzero density at the F1 atom.) The example on the left-hand side shows an almost negligible electron density at fluorine atoms F1 and F2, while by contrast, for both the Slater transition potential and the ΔSCF treatments of the relaxation process, a similar and notable redistribution is found for these atoms, indicating strong mixing of σ^*-orbitals. Though only small differences are seen, a more distinct localization around the excitation center in the ΔSCF calculation is found. Because of participation of 2s atomic orbitals in σ^* molecular orbitals, one may expect relaxation to be typically more pronounced than for π^* orbitals, which rationalizes the distinct energetic shift of the σ^* resonances. For excitations of F 1s-π^* character, the corresponding 2p atomic orbitals that contribute to the final π^* MO are expected to be less susceptible to changes of the effective core hole potential than 2s orbitals. Therefore, the differences in charge at the excitation centers do not have such a strong effect as for the σ^* resonances. A comparison with the corresponding unoccupied molecular orbital calculated for the electronic ground state (cf. Figure 4b) shows in particular that the commonly used first-order "frozen orbital" approximation is rather inadequate to describe the 1s-σ^* excitation. This also suggests that a proper account of relaxation effects may play a decisive role in the theoretical analysis of the so-called perfluoro effects discussed in ref 17. We note further that besides the energetic shift, also the relative intensity of the resonances is affected. This emphasizes the importance of an accurate description of relaxation effects as well as the appropriate calculation of the oscillator strength. A closer inspection of the final orbital that is shown in Figure 4b reveals distinct differences for the various descriptions especially in the periphery of the excitation center. Unfortunately, a quantitative determination of the oscillator strength for relaxed states is complicated by the nonorthogonality of the molecular orbitals which are used to describe the electronic ground state and the core hole excited state. However, we have performed the corresponding calculations by utilizing the Löwdin rules which were implemented in our analysis. As significant overlap between energetically higher lying multielectron wave functions with energetically lower ones is an indicator for limited applicability of this ΔSCF type of approach for the former states, also the scalar product between each electronic state for the respective F1−F4 excitations has been calculated (cf. Supporting Information). Most of the excited Slater determinants obtained in individual SCF procedures exhibit only a low level of nonorthogonality with each other, but some of them show a significant overlap (e.g., 0.352 between π_4 and π_6 for F2 and 0.813 between σ_2 and σ_3 for F3 excitations). As a consequence, they should be considered as not well described by the ΔSCF method, which is expected for higher excited states. This problem could in principle be tackled within a configuration interaction (CI) procedure by solving the generalized eigenvalue problem emerging from these nonorthogonal Slater determinants. The transition dipole moments would then be computed between the resulting orthogonal states. This was, however, not attempted in the present DFT-based framework.

D. Electronic Signature and Dichroism of Perfluoronaphthalene (PFN). To validate our present analysis and investigate whether the observed correlations also hold true for similar molecules, we have examined the NEXAFS signature of a smaller fluorinated acene, perfluoronaphthalene (PFN). Its smaller size reduces the computational effort and, furthermore, enables a comparison with earlier inner-shell electron energy loss spectroscopy (ISEELS) data which reveal essentially the same excitation mechanism as NEXAFS.[17] For this purpose PFN films were studied that had been prepared on an oxidized copper substrate. Corresponding XRD data (see Figure S3) confirm a bulk-crystalline texture of the films and reveal a predominant (001) orientation, where the molecules adopt an upright configuration.[59] The corresponding C 1s NEXAFS spectra (cf. Figure 5a) exhibit a characteristic energetic shift

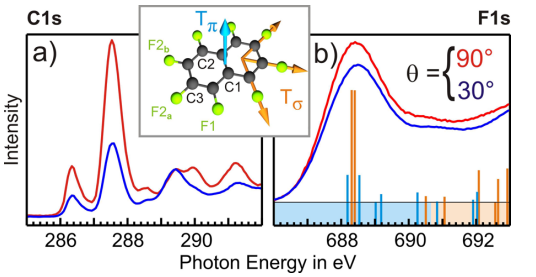

Figure 5. Summary of NEXAFS data of crystalline PFN films grown on an oxidic substrate that were recorded at different angles of incidence (red: 90°; blue: 30°) for (a) the C 1s region and (b) the F 1s region. Moreover, the latter is compared with ΔSCF calculations considering also relaxation effects. The inset shows the structure of PFN together with a labeling of symmetry nonequivalent atoms and vectors indicating electronic transition dipole moments of the various excitations.

compared to the non-fluorinated naphthalene due to the typical chemical shift as similarly observed for perfluoropentacene. The angle-dependent measurements reveal a distinct dichroism with strongest absorption for normal incidence, as in line with the upright molecular orientation adopted in such (001)-planes. As shown in Figure 5b, the corresponding F 1s NEXAFS spectra exhibit a strongly reduced, yet qualitatively akin dichroism. In principle, these observations are rather similar to those made for PFP/SiO_2. An important difference is, however, present. Although for both PFP and PFN in upright molecular orientation, the dichroism observed at the F 1s edge is reduced compared to the C 1s dichroism, this reduction is clearly stronger for PFN. As will be explained in detail in section E, this is a direct result of the different aspect ratios of PFP and PFN.

The corresponding theoretical analysis yields the same behavior as found before for PFP: the most prominent features at the F 1s absorption edge correspond to σ^* resonances of the fluorine atoms which are energetically almost degenerate. Again, they also overlap with π^* resonances, which feature clearly reduced oscillator strength. Notably, the best agreement with the results of the ΔSCF calculation is obtained when again applying a constant energy shift of 1.2 eV (cf. Figure 5b). Moreover, a comparison with corresponding Slater transition potential calculations shows a distinct relaxation toward lower energy only for the low energetic σ^* resonances whereas the π^* resonances are only slightly affected (see Supporting

DOI: 10.1021/acs.jpcc.6b04048
J. Phys. Chem. C 2016, 120, 12693−12705

Information), similar to the aforementioned case of PFP. This assignment of the resonances is well corroborated by the observed dichroism which has not been possible on the basis of ISEELS data. Remarkably, the energetic positions of the NEXAFS signatures are in excellent agreement with the previous ISEELS measurements which confirms in particular our energy calibration for the F 1s NEXAFS measurements.

In summary, the observations made for PFN are perfectly consistent with the findings for PFP and verify that the interpretations of the PFP NEXAFS spectra are solid and appear rather general.

E. Quantitative Computation of PFP Dichroisms and Qualitative Explanation. So far, the nature of the resonances has been discussed and the different dichroisms have been explained qualitatively. In addition, we have applied an approach to quantitatively compute the expected dichroisms of the individual resonances as well as the integral dichroisms for different molecular orientations. The refined ΔSCF calculations provide, besides the character of the individual resonances, also a description of the electronic transition dipole moments and the corresponding oscillator strengths. The latter information can be used to compute expected dichroisms for the differently oriented PFP films, of which structure is precisely known from the X-ray structure analysis (cf. Figure 1). Based on the knowledge of the crystal polymorphs and molecular orientations adopted in the molecular films, the electronic transition dipole moments (and the related oscillator strength) for electronic transitions from all excitation centers into final molecular orbitals have been summed up. Afterward, the vectorial projection onto the $\vec{E}$ vector of the incoming synchrotron radiation was calculated as described before. We note that although in general all molecules within the crystalline unit cell have to be taken into account, the particular sample symmetry requires a consideration of one molecule only (cf. Methodology section).

As depicted in Figure 6a,b the overall dichroisms of the F 1s NEXAFS signatures are well reproduced for PFP in lying as well as upright molecular orientation. Whereas the dichroism of the low energetic shoulder around 687 eV proceeds similar to that of the leading π^* resonances in the C 1s NEXAFS signature (cf. Figure 1a,d), a more complex situation is found for the most intense F 1s NEXAFS signature at about 689 eV. Besides the difficulty of partially overlapping π^* resonances (cf. Figure 3b) also the most intense lowest energetic σ^* resonances clearly contribute to different degrees to the weak dichroism. This can be explained by the respective geometrical position of the related excitation centers.[51] This is illustrated for the contributions of the σ^* resonances for the excitation centers F3 and F4 in Figure 6. In the case of graphite all PFP molecules lie perfectly flat on the surface so that the σ^*-related TDMs are oriented parallel to the surface plane though being azimuthally statistically distributed. The π^*-related TDMs, in contrast, are oriented perpendicular to the surface, hence leading to an inverted dichrosim as depicted in Figure 6c. A quite different situation is found for the uprightly oriented PFP molecules on SiO_2 yielding a lower symmetry compared to an isolated single molecule. According to the orientation of the individual C−F bonds of PFP molecules within the film, the projection of the σ^*-related TDMs onto the surface normal is no longer degenerate. Consequently, the TDMs corresponding to the excitation centers at the long axis ends of the molecules (cf. F4 in Figure 3a) exhibit distinctly different direction and dichroism than those at the short axis ends (F1−F3) (cf. Figure 6d). A

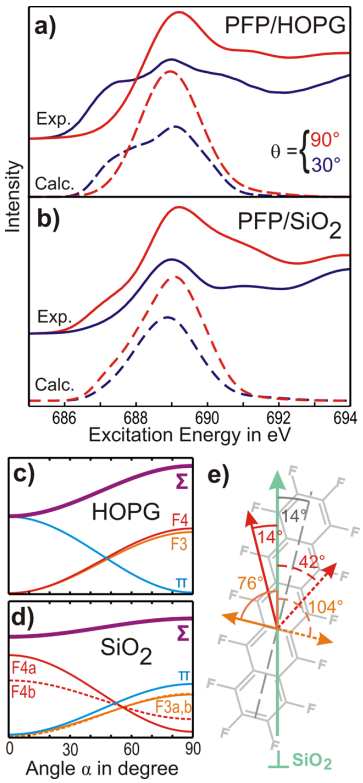

Figure 6. Comparison of dichroism of measured (solid lines) and calculated (dashed lines) F 1s NEXAFS spectra of highly oriented, crystalline PFP films on (a) HOPG and (b) SiO_2. Panels c and d depict the resulting dichroism of the lowest energy σ^*- and π^*-type resonances that were calculated according to the molecular packing of PFP on HOPG and SiO_2. The relative orientation of a PFP molecule on SiO_2 together with angles between transition dipole moments for σ^* resonances of atoms F3a, F3b, F4a, and F4b, and the surface normal is shown in (e).

closer inspection shows further that due to the molecular tilt even the σ^*-related TDMs for atoms F4a and F4b at the long axis end are differently oriented relative to the surface normal (cf. Figure 6e) and reveal a somewhat different dichroism. Because the observed dichroism results from the superposition of the individual dichroisms of each excitation center, it is easy to understand that the integral dichroism is reduced compared to the C 1s dichroism due to the unequal individual dichroisms. These considerations explain also the even stronger differences between the F 1s and the C 1s dichroism in uprightly oriented PFN films compared to the case of PFP. Because the relative amount of excitation centers at the short and long axis ends is different for PFP (10:4) and PFN (4:4, cf. Figure 5), the resulting dichroism at the F 1s edge is more distinct for PFP than for PFN.

While the refined ΔSCF calculations provide a detailed description of the origin and magnitude of the individual NEXAFS resonances, a qualitative description is already achieved by the linear-combination-of-atomic-orbitals (LCAO) method in the frame of Hückel theory,[1] as depicted in Figure 7. In particular, this provides a simple explanation for the appearance of weak π^* resonances in the F 1s NEXAFS

DOI: 10.1021/acs.jpcc.6b04048
J. Phys. Chem. C 2016, 120, 12693−12705

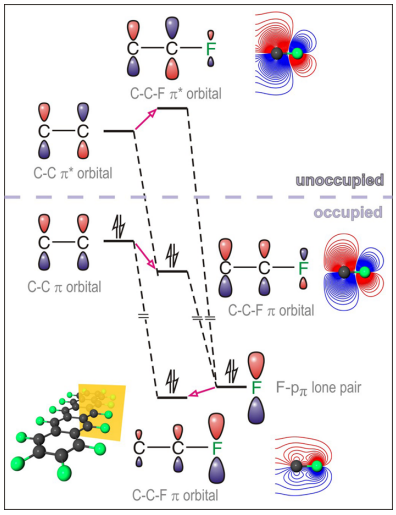

Figure 7. Generalized MO diagram of the π interaction between fluorine and the π system of an aromatic carbon backbone together with calculated contour plots showing the C1−F1 plane (indicated in the lower left inset) for selected orbitals. Note that the energy scale is broken.

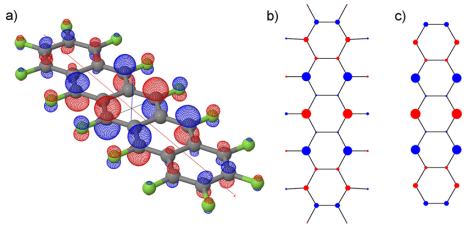

Figure 8. Representative molecular orbitals. Shown is the lowest unoccupied molecular orbital (LUMO) in the electronic ground state as obtained from (a) ground state Kohn−Sham DFT calculations for PFP, (b) Hückel molecular orbital theory for PFP, and (c) Hückel molecular orbital theory for pentacene. (a) shows contour surfaces for a given isovalue of the molecular orbital with the indicated axis arrangement of the molecule, whereas (b) and (c) give a schematic top-view representation of the LCAO-MO coefficient at the various centers of the π system. The radius of the circles is proportional to the absolute value of the LCAO-MO coefficient, whereas relative signs are indicated by filled red or blue circles. The molecular structure in (b) and (c) is just shown to illustrate the chosen topology.

spectra despite the large spatial separation of the fluorine excitation center and the aromatic carbon backbone.

An inspection of the π- and π*-type Kohn−Sham orbitals as obtained from DFT calculations for PFP in its electronic ground state shows that the orbital shapes resemble the Hückel MOs (cf. Figure 8 for a specific example and Supporting Information for more details). The unoccupied π* Hückel MOs LUMO (lowest unoccupied molecular orbital, orbital ϕ_{26}, in the Hückel calculations for PFP), LUMO+1 (orbital ϕ_{27} in the Hückel calculations), etc., have commonly large coefficients from the linear expansion of MOs in terms of atomic orbitals (LCAO-MO coefficient) on the C and significantly smaller ones on the F atoms. These π*-type MOs arise essentially from an antibonding combination of the π* orbitals of the carbon backbone with $2p_\pi$ lone pairs of F atoms (cf. Figures 3 and 4).

As the 2p atomic orbitals (AO) of F are much lower in energy than the 2p AOs of C, the size of the coefficient at the various F atoms depends essentially on the coefficient at the adjacent C atom. The carbon backbone part of these MOs, in turn, resembles essentially the π* orbitals of the parent pentacene molecule (cf. Supporting Information for corresponding energy diagrams, symmetry assignments, and molecular orbitals of PFP and pentacene), so that the LCAO-MO coefficients at both the C and F atoms in the relevant π* orbitals are readily estimated from simple Hückel theory. Matrix elements $\langle\psi_i^{(a)}|\vec{\mu}_e|1s\rangle$ of the electronic transition dipole moment between a localized 1s orbital and a molecular orbital $\psi_i^{(a)}$ are to a good approximation governed by the LCAO-MO coefficients of the 2p AOs only at the center of the 1s orbital, which thus determine both the intensity of a given transition and its polarization dependence. Consequently, the most intense transitions can be those into unoccupied PFP ground state MOs which possess coefficients with large absolute value at the excited F or C atom (cf. Figures 3 and 4). This explains the difference in intensity for the π* resonances between C 1s and F 1s NEXAFS: essentially only the degree to which an unoccupied MO extends on the particular excitation center plays a role with respect to the magnitude of the electronic transition dipole moment. In PFP, the π* MOs have large coefficients at the C atoms and, therefore intense resonances in C 1s NEXAFS, whereas only small coefficients are present at F atoms leading to comparatively weak π* resonances in F 1s NEXAFS as shown in the schematic MO-diagram in Figure 7. The intensity of the latter resonances is mostly determined by the LCAO-MO coefficient of fluorine $2p_\pi$ of the given excitation center to the respective π*-type MO, which can either be obtained from explicit DFT calculations or, as mentioned above, be estimated from simple Hückel theory. The MOs of the relevant σ* resonances are the antibonding C−F orbitals of the respective F excitation center and exhibit a close proximity to the core orbitals leading to the most intense transitions in the F 1s NEXAFS spectra.

The presence of energetically low π* resonances in the F 1s NEXAFS spectra of fluorinated acenes is thus due to transitions from F 1s core levels into F $2p_\pi$ orbitals which are part of the π system and are aligned also perpendicular to the ring plane. As the isolated F 2p lone pair orbitals are fully occupied (cf. Figure 7), these transitions become only possible, because the π interactions with the carbon backbone lead to electron density leakage from the fluorine F $2p_\pi$ orbitals into the carbon framework, and the resulting fractional hole at the fluorine atom becomes dispersed over various unoccupied molecular orbitals. In a simplified picture these transitions can thus be considered as quasi intra-atomic excitations within the fluorine atoms being dispersed over various molecular orbitals. This given explanation for the occurrence of π* resonances in the F 1s NEXAFS spectra appears rather general for fluorinated π-conjugated aromatic molecules where fluorination typically happens at the periphery. We note further that the contribution of the F 2p lone pair orbitals to the molecular π system also leads to a larger extension of the aromatic π system for perfluorinated aromatic hydrocarbons in comparison to their non-fluorinated sibblings. This is illustrated impressively in Figure 9 where the accumulated electron density of the π orbitals is compared for PFP and PEN. In view of the importance of the spatial distribution and overlap of π orbitals for charge transport in molecular semiconductors,[60,61] such an

DOI: 10.1021/acs.jpcc.6b04048
J. Phys. Chem. C 2016, 120, 12693−12705

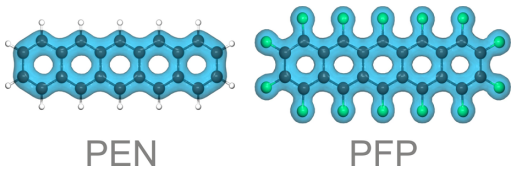

Figure 9. Spatial distribution of the accumulated electron density of all π orbitals within the electronic ground state of pentacene (PEN) and perfluoropentacene (PFP).

extension could be beneficial as it leads to a reduced distance of the orbitals of neighboring molecules along the molecular plane directions, whereas in most previous studies of organic semiconductors only the vertical stacking distance is considered.[62]

CONCLUSION

The present analysis clearly shows that although transition dipole moments for excitations into π^* and σ^* orbitals of planar aromatic molecules are oriented perpendicular to each other, the dichroism of σ^* resonances in F 1s NEXAFS spectra is not necessarily inverted to that observed in the π^* resonances in C 1s NEXAFS spectra. Instead, a detailed consideration of the molecular structure of the sample is required. For fluorinated acenes such as PFP or PFN, an inversion of F 1s-σ^* transitions only takes place for lying molecular orientations, whereas in upright configurations the observed angular dependence is nearly equal to that found at the C 1s edge. We demonstrate that a quantitative understanding of the σ^*-related dichroisms requires an appropriate consideration not only of the molecular packing motif but also of the individual orientations of the corresponding transition dipole moments within the molecules. Furthermore, we have shown that relaxation effects are important to accurately describe the energies and related oscillator strengths of the resonances. The underlying relaxations effects are not fully described by the transition potential approach and instead require refined ΔSCF calculations. Even though σ^* resonances turned out to be most prominent for fluorine K-edge NEXAFS, detailed inspection of the spectra furthermore identified also π^* resonances showing the same dichroism as observed at the carbon K-edge. This is caused by mixing of F_{2p} lone pair orbitals with the π system which leads to an alignment perpendicular to the molecular backbone. Consequently, the π^* excitations at the fluorine edge can be interpreted as quasi-intraatomic excitations. Moreover, this demonstrates that perfluorination yields a notable increase of the electronic molecular π system, which is expected to be beneficial for charge transport in such materials. Since the investigated acenes are representative model systems for π-conjugated molecular semiconductors, the present findings are important for the understanding of the electronic properties and the application of NEXAFS for structural analysis in such materials.

ASSOCIATED CONTENT

Supporting Information

The Supporting Information is available free of charge on the ACS Publications website at DOI: 10.1021/acs.jpcc.6b04048.

Additional NEXAFS data, calculated partial NEXAFS spectra, structural characterization of PFN films, Hückel analysis of PFP, and details of the Löwdin analysis (PDF)

AUTHOR INFORMATION

Corresponding Authors

*E-mail gregor.witte@physik.uni-marburg.de; Tel +49 6421 28-21384 (G.W.).

*E-mail robert.berger@uni-marburg.de; Tel +49 6421 28-25687 (R.B.)

Notes

The authors declare no competing financial interest.

ACKNOWLEDGMENTS

We acknowledge the Helmholtz-Zentrum Berlin-Electron storage ring BESSY II for providing synchrotron radiation at beamlines HE-SGM and SurICat and financial support provided by the German Science Foundation (DFG) through the collaborative research center "Structure and Dynamics of Internal Interfaces" (SFB 1083, TP A2 and B8).

REFERENCES

(1) Stöhr, J. *NEXAFS Spectroscopy*; Springer: Berlin, Germany, 1992.
(2) Taborski, J.; Vaterlein, P.; Dietz, H.; Zimmermann, U.; Umbach, E. NEXAFS Investigations on Ordered Adsorbate Layers of Large Aromatic Molecules. *J. Electron Spectrosc. Relat. Phenom.* **1995**, *75*, 129−147.
(3) Lamberti, C. The Use of Synchrotron Radiation Techniques in the Characterization of Strained Semiconductor Heterostructures and Thin Films. *Surf. Sci. Rep.* **2004**, *53*, 1−197.
(4) Hähner, G. Near Edge X-ray Absorption Fine Structure Spectroscopy as a Tool to Probe Electronic and Structural Properties of Thin Organic Films and Liquids. *Chem. Soc. Rev.* **2006**, *35*, 1244−1255.
(5) Carravetta, V.; Plachkevytch, O.; Vahtras, O.; Ågren, H. Ordinary and Rotary Intensities for X-ray Absorption at the C-1s Edge of Organic Chiral Molecules: Propylene Oxide and Trans-1,2-dimethylcyclopropane. *Chem. Phys. Lett.* **1997**, *275*, 70−78.
(6) Plashkevych, O.; Carravetta, V.; Vahtras, O.; Ågren, H. Theoretical Study of X-ray Circular Dichroism of Amino Acids. *Chem. Phys.* **1998**, *232*, 49−62.
(7) Jiemchooroj, A.; Ekström, U.; Norman, P. Near-edge X-ray Absorption and Natural Circular Dichroism Spectra of L-alanine: A Theoretical Study Based on the Complex Polarization Propagator Approach. *J. Chem. Phys.* **2007**, *127*, 165104.
(8) Jiemchooroj, A.; Norman, P. X-ray Absorption and Natural Circular Dichroism Spectra of C_{84}: A Theoretical Study using the Complex Polarization Propagator Approach. *J. Chem. Phys.* **2008**, *128*, 234304.
(9) Otero, E.; Urquhart, S. Nitrogen 1s Near-Edge X-ray Absorption Fine Structure Spectroscopy of Amino Acids: Resolving Zwitterionic Effects. *J. Phys. Chem. A* **2006**, *110*, 12121−12128.
(10) Ågren, H.; Vahtras, O.; Carravetta, V. Photoabsorption in Polyacenes: Model Molecules for Graphite. *Chem. Phys.* **1995**, *196*, 47−58.
(11) Fratesi, G.; Lanzilotto, V.; Floreano, L.; Brivio, G. P. Azimuthal Dichroism in Near-Edge X-ray Absorption Fine Structure Spectra of Planar Molecules. *J. Phys. Chem. C* **2013**, *117*, 6632−6638.
(12) Chen, W.; Qi, D. C.; Huang, Y. L.; Huang, H.; Wang, Y. Z.; Chen, S.; Gao, X. Y.; Wee, A. T. S. Molecular Orientation Dependent Energy Level Alignment at Organic-Organic Heterojunction Interfaces. *J. Phys. Chem. C* **2009**, *113*, 12832−12839.
(13) Subramanian, S.; Park, S. K.; Parkin, S. R.; Podzorov, V.; Jackson, T. N.; Anthony, J. E. Chromophore Fluorination Enhances Crystallization and Stability of Soluble Anthradithiophene Semiconductors. *J. Am. Chem. Soc.* **2008**, *130*, 2706.
(14) Tang, M. L.; Bao, Z. A. Halogenated Materials as Organic Semiconductors. *Chem. Mater.* **2011**, *23*, 446−455.
(15) Sakamoto, Y.; Suzuki, T.; Kobayashi, M.; Gao, Y.; Fukai, Y.; Inoue, Y.; Sato, F.; Tokito, S. Perfluoropentacene: High-Performance

DOI: 10.1021/acs.jpcc.6b04048
J. Phys. Chem. C 2016, 120, 12693−12705

p-n Junctions and Complementary Circuits with Pentacene. *J. Am. Chem. Soc.* **2004**, *126*, 8138−8140.
(16) Boller, K.; Haelbich, R. P.; Hogrefe, H.; Jark, W.; Kunz, C. Investigation of Carbon Contamination of Mirror Surfaces Exposed to Synchrotron Radiation. *Nucl. Instrum. Methods Phys. Res.* **1983**, *208*, 273−279.
(17) Robin, M. B.; Ishii, I.; McLaren, R.; Hitchcock, A. P. Fluorination Effects on the Inner-Shell Spectra of unsaturated Molecules. *J. Electron Spectrosc. Relat. Phenom.* **1988**, *47*, 53−92.
(18) Okudaira, K. K.; Setoyama, H.; Yagi, H.; Mase, K.; Kera, S.; Kahn, A.; Ueno, N. Study of Excited States of Fluorinated Copper Phtahlocyanine by Inner Shell Excitation. *J. Electron Spectrosc. Relat. Phenom.* **2004**, *137*−*140*, 137−140.
(19) de Oteyza, D. G.; Sakko, A.; El-Sayed, A.; Goiri, E.; Floreano, L.; Cossaro, A.; Garcia-Lastra, J. M.; Rubio, A.; Ortega, J. E. Inversed Linear Dichroism in F K-edge NEXAFS Spectra of Fluorinated Planar Aromatic Molecules. *Phys. Rev. B: Condens. Matter Mater. Phys.* **2012**, *86*, 075469.
(20) Broch, K.; Bürker, C.; Dieterle, J.; Krause, S.; Gerlach, A.; Schreiber, F. Impact of Molecular Tilt Angle on the Absorption Spectra of Pentacene:Perfluoropentacene Blends. *Phys. Status Solidi RRL* **2013**, *7*, 1084−1088.
(21) Käfer, D.; Ruppel, L.; Witte, G. Growth of Pentacene on Clean and Modified Gold Surfaces. *Phys. Rev. B: Condens. Matter Mater. Phys.* **2007**, *75*, 085309.
(22) Käfer, D.; Witte, G. Evolution of Pentacene Films on Ag(111): Growth beyond the First Monolayer. *Chem. Phys. Lett.* **2007**, *442*, 376−383.
(23) Schmidt, C.; Breuer, T.; Wippermann, S.; Schmidt, W. G.; Witte, G. Substrate Induced Thermal Decomposition of Perfluoro-Pentacene Thin Films on the Coinage Metals. *J. Phys. Chem. C* **2012**, *116*, 24098−24106.
(24) Kowarik, S.; Gerlach, A.; Hinderhofer, A.; Milita, S.; Borgatti, F.; Zontone, F.; Suzuki, T.; Biscarini, F.; Schreiber, F. Structure Morphology, and Growth Dynamics of Perfluoro-Pentacene Thin Films. *Phys. Status Solidi RRL* **2008**, *2*, 120−122.
(25) Salzmann, I.; Moser, A.; Oehzelt, M.; Breuer, T.; Feng, X.; Juang, Z. Y.; Nabok, D.; Della Valle, R. G.; Duhm, S.; Heimel, G.; et al. Epitaxial Growth of π-Stacked Perfluoropentacene on Graphene-Coated Quartz. *ACS Nano* **2012**, *6*, 10874−10883.
(26) Here the degree of polarization is defined as $|E_{\parallel}|^2/(|E_{\parallel}|^2 + |E_{\perp}|^2)$ as given in ref 1.
(27) Watts, B.; Thomsen, L.; Dastoor, P. C. Methods in Carbon K-edge NEXAFS: Experiment and Analysis. *J. Electron Spectrosc. Relat. Phenom.* **2006**, *151*, 105−120.
(28) Marks, M.; Schmidt, C.; Schwalb, C. H.; Breuer, T.; Witte, G.; Höfer, U. Temperature Dependent Structural Phase Transition at the Perfluoropentacene/Ag(111) Interface. *J. Phys. Chem. C* **2012**, *116*, 1904−1911.
(29) Wagner, C. D; Muilenberg, G. E. *Handbook of X-ray Photoelectron Spectroscopy*; Perkin-Elmer Corporation: Eden Prairie, MN, 1979.
(30) Vinogradov, A. S.; Fedoseenko, S. I.; Krasnikov, S. A.; Preobrajenski, A. B.; Sivkov, V. N.; Vyalikh, D. V.; Molodtsov, S. L.; Adamchuk, V. K.; Laubschat, C.; Kaindl, G. Low-lying Unoccupied Electronic States in 3d Transition-metal Fluorides Probed by NEXAFS at the F1s Threshold. *Phys. Rev. B: Condens. Matter Mater. Phys.* **2005**, *71*, 045127.
(31) Vinogradov, A. S.; Dukhnyakov, A. Y.; Ipatov, V. M.; Onopko, D. E.; Pavlychev, A. A.; Titov, S. A. Fine Structure of X-ray Absorption Spectra of the $(TiF_6)^{2-}$ Radical. *Sov. Phys. Solid State* **1982**, *24*, 803−806.
(32) Hermann, K.; Pettersson, L. G. M.; Casida, M. E.; Daul, C.; Goursot, A.; Koester, A.; Proynov, E.; St-Amant, A.; Salahub, D. R.; Carravetta, V.; et al. StoBe-deMon version 3.2, 2013.
(33) Hammer, B.; Hansen, L.; Nø rskov, J. Improved Adsorption Energetics within Density-Functional Theory using Revised Perdew-Burke-Ernzerhof Functionals. *Phys. Rev. B: Condens. Matter Mater. Phys.* **1999**, *59*, 7413−7421.
(34) Perdew, J. P.; Burke, K.; Ernzerhof, M. Generalized Gradient Approximation Made Simple. *Phys. Rev. Lett.* **1996**, *77*, 3865−3868.
(35) Godbout, N.; Salahub, D. R.; Andzelm, J.; Wimmer, E. Optimization of Gaussian-type Basis Sets for Local Spin Density Functional Calculations. Part I. Boron through Neon, Optimization Technique and Validation. *Can. J. Chem.* **1992**, *70*, 560−571.
(36) Nyberg, M. Probing Adsorbate-surface Chemical Bonds using Ab Initio Techniques combined with X-ray Spectroscopy. Ph.D. Thesis, Stockholm University, Sweden, 2000.
(37) Pettersson, L. G. M.; Wahlgren, U.; Gropen, O. Effective Core Potential Parameters for First- and Second-row Atoms. *J. Chem. Phys.* **1987**, *86*, 2176−2184.
(38) Kutzelnigg, W.; Fleischer, U.; Schindler, M. The IGLO-Method: Ab-initio Calculation and Interpretation of NMR Chemical Shifts and Magnetic Susceptibilities. In *NMR-Basic Principles and Progress*; Springer: Heidelberg, 1990; pp 165−262.
(39) Ågren, H.; Carravetta, V.; Vahtras, O.; Pettersson, L. G. M. Direct, Atomic Orbital Static Exchange Calculations of Photo-absorption Spectra of Large Molecules and Clusters. *Chem. Phys. Lett.* **1994**, *222*, 75−81.
(40) Ågren, H.; Carravetta, V.; Vahtras, O.; Pettersson, L. G. M. Direct SCF Direct Static-Exchange Calculations of Electronic Spectra. *Theor. Chem. Acc.* **1997**, *97*, 14−40.
(41) Triguero, L.; Pettersson, L. G. M.; Ågren, H. Calculations of Near-Edge X-ray-Absorption Spectra of Gas-phase and Chemisorbed Molecules by means of Density-Functional and Transition-Potential Theory. *Phys. Rev. B: Condens. Matter Mater. Phys.* **1998**, *58*, 8097−8110.
(42) Klues, M.; Hermann, K.; Witte, G. Analysis of the Near-Edge X-ray-Absorption Fine-Structure of Anthracene: A combined Theoretical and Experimental Study. *J. Chem. Phys.* **2014**, *140*, 014302.
(43) Condon, E. U. The Theory of Complex Spectra. *Phys. Rev.* **1930**, *36*, 1121.
(44) In the following, quantities characterized as electronic dipole moments will be denoted by "dipole moments" for the sake of brevity.
(45) Löwdin, P.-O. Quantum Theory of Many-Particle Systems. I. Physical Interpretations by Means of Density Matrices, Natural Spin-Orbitals, and Convergence Problems in the Method of Configurational Interaction. *Phys. Rev.* **1955**, *97*, 1474−1489.
(46) Davidson, E. R. Single-Configuration Calculations on Excited States of Helium. *J. Chem. Phys.* **1964**, *41*, 656−658.
(47) Davidson, E. R. Single-Configuration Calculations on Excited States of Helium. II. *J. Chem. Phys.* **1965**, *42*, 4199−4200.
(48) Gilbert, A. T. B.; Besley, N. A.; Gill, P. M. W. Self-Consistent Field Calculations of Excited States using the Maximum Overlap Method (MOM). *J. Phys. Chem. A* **2008**, *112*, 13164−13171.
(49) Helgaker, T.; Jørgensen, P.; Olsen, J. *Molecular Electronic-Structure Theory*; Wiley: Chichester, 2000.
(50) Hilborn, R. C. Einstein Coefficients, Cross Sections, f Values, Dipole Moments, and all that. *Am. J. Phys.* **1982**, *50*, 982.
(51) Breuer, T.; Klues, M.; Witte, G. Characterization of Orientational Order in π-conjugated Molecular Thin Films by NEXAFS. *J. Electron Spectrosc. Relat. Phenom.* **2015**, *204*, 102−115.
(52) Bouchoms, I. P. M.; Schoonveld, W. A.; Vrijmoeth, J.; Klapwijk, T. M. Morphology Identification of the Thin Film Phases of Vacuum Evaporated Pentacene on SiO_2 Substrates. *Synth. Met.* **1999**, *104*, 175−178.
(53) Breuer, T.; Salzmann, I.; Götzen, J.; Oehzelt, M.; Morherr, A.; Koch, N.; Witte, G. Interrelation between Substrate Roughness and Thin-Film Structure of Functionalized Acenes on Graphite. *Cryst. Growth Des.* **2011**, *11*, 4996−5001.
(54) Rosenberg, R.; Love, P.; Rehn, V. Polarizationdependent C(K) Near-Edge X-ray-Absorption Fine Structure of Graphite. *Phys. Rev. B: Condens. Matter Mater. Phys.* **1986**, *33*, 4034−4037.
(55) Götzen, J.; Käfer, D.; Wöll, C.; Witte, G. Growth and Structure of Pentacene Films on Graphite: Weak Adhesion as a Key for Epitaxial Film Growth. *Phys. Rev. B: Condens. Matter Mater. Phys.* **2010**, *81*, 085440.

DOI: 10.1021/acs.jpcc.6b04048
J. Phys. Chem. C 2016, 120, 12693−12705

(56) We note that like in the case of pentacene also a thin film phase of PFP has been reported,[63] which features slightly modified structure parameters compared to the bulk phase.[15] However, whereas these deviations are strong in the case of pentacene, they are only very small for PFP (e.g., $\Delta a/a$ = 1.6%, $\Delta b/b$ = 0.4%, $\Delta c/c$ = 0.2%) so that we assume the molecular tilt angle to be hardly affected. Furthermore, to our knowledge there is no crystal structure of the thin film phase published up to now, which also includes atom coordinates.
(57) Díaz, J.; Paolicelli, G.; Ferrer, S.; Comin, F. Separation of the sp3 and sp2 Components in the C1s Photoemission Spectra of Amorphous Carbon Films. *Phys. Rev. B: Condens. Matter Mater. Phys.* **1996**, *54*, 8064−8069.
(58) Christodoulou, C.; Giannakopoulos, A.; Nardi, M. V.; Ligorio, G.; Oehzelt, M.; Chen, L.; Pasquali, L.; Timpel, M.; Giglia, A.; Nannarone, S.; et al. Tuning the Work Function of Graphene-on-Quartz with a High Weight Molecular Acceptor. *J. Phys. Chem. C* **2014**, *118*, 4784−4790.
(59) Akhmed, N. A. Study of Crystalline-Structure of Octafluoronaphthalene. *Zh. Strukt. Khim.*. **1973**, *14*, 532.
(60) Hutchison, G. R.; Ratner, M. A.; Marks, T. J. Intermolecular Charge Transfer between Heterocyclic Oligomers. Effects of Heteroatom and Molecular Packing on Hopping Transport in Organic Semiconductors. *J. Am. Chem. Soc.* **2005**, *127*, 16866−16881.
(61) Yang, X.; Wang, L.; Wang, C.; Long, W.; Shuai, Z. Influences of Crystal Structures and Molecular Sizes on the Charge Mobility of Organic Semiconductors: Oligothiophenes. *Chem. Mater.* **2008**, *20*, 3205−3211.
(62) Minari, T.; Seto, M.; Nemoto, T.; Isoda, S.; Tsukagoshi, K.; Aoyagi, Y. Molecular-Packing-Enhanced Charge Transport in Organic Field-effect Transistors based on Semiconducting Porphyrin Crystals. *Appl. Phys. Lett.* **2007**, *91*, 123501.
(63) Salzmann, I.; Duhm, S.; Heimel, G.; Rabe, J. P.; Koch, N.; Oehzelt, M.; Sakamoto, Y.; Suzuki, T. Structural Order in Perfluoropentacene Thin Films and Heterostructures with Pentacene. *Langmuir* **2008**, *24*, 7294−7298.

DOI: 10.1021/acs.jpcc.6b04048
J. Phys. Chem. C 2016, 120, 12693−12705

Auszüge aus den *Supporting Information* zum Artikel:

M. Klues, P. Jerabek, T. Breuer, M. Oehzelt, K. Hermann, R. Berger und G. Witte, J. Phys. Chem. C 120 (2016), 12693-12705. DOI: 10.1021/acs.jpcc.6b04048

S1 Experimental results

S1.1 C1s background subtraction

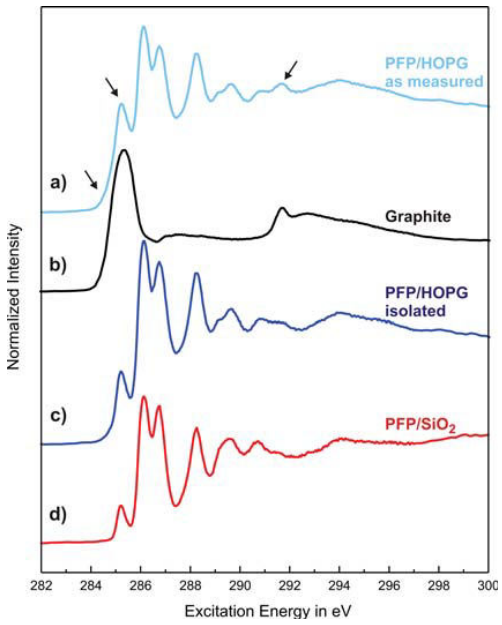

Figure S1: Flow chart of data processing to subtract the C1s NEXAFS signal of the graphite substrate: a) initial NEXAFS spectrum for a 10nm PFP film on HOPG and b) a bare graphite surface. The pure PFP spectrum in c) obtained after weighted subtraction of b) from a) shows the same spectral signature as d) a PFP film grown on SiO_2.

In contrast to SiO_2 substrates the graphite substrate also causes a distinct C1s signal in the NEXAFS measurements which is observed since the PFP films do not cover the HOPG surface completely. This signal also experiences a strong dichroism and corroborates the reliable analysis of the dichroism of the molecular adlayer. Therefore, a weighted subtraction of the substrate signal is required to remove residual contributions from the substrate as shown in Fig. S1. For this purpose the characteristic σ^*-resonance of graphite at 292 eV is used to determine the corresponding weighting factor. As shown in Fig.

S1, this allows reliably isolating the signature of the adlayer and subsequently analyzing the corresponding dichroism. Further details on this approach are provided in [6] and [10].

S1.2 F1s NEXAFS spectra of PFP and K_2TiF_6

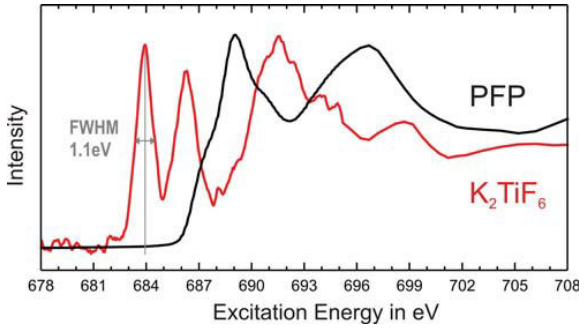

Figure S2: F1s NEXAFS spectra of PFP and K_2TiF_6.

K_2TiF_6 shows two leading, sharp d-type resonances. For these peaks a FWHM of 1.1 eV is observed, meaning that the predicted FWHM of 1.88 eV for σ-resonances is not given by resolution limitations of the beamline. Furthermore the literature known position of these peaks was used for energy calibration [11][12].

S1.3 Perfluoronaphthalene XRD

Perfluoronaphthalene thin films were prepared by freezing molecules from gas phase onto a cooled SiO_2 substrate. The PFN thin film is unstable under ambient conditions and desorbs in about a hour depending on initial thickness. Therefore XRD-measurements needed to be done quiet fast, explaining the low signal to noise ratio. Never the less several crystallographic orientations can be observed as depicted in Fig S3. Below the miller indices the relative signal strength compared to the most intense reflex (11-3) is given, which can be calculated from the literature known crystal structure of PFN [20]. As the (002)-plane has a more than fifty times smaller diffraction strength than the (11-3)-, (012)- or (11-2)-plane but shows nearly the same intensity in Fig.S3 it can be concluded, that the thin film is mainly oriented in (002) direction.

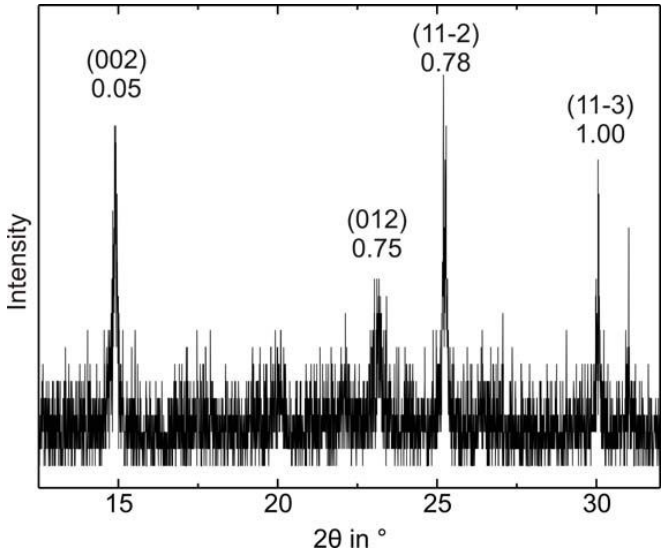

Figure S3: Diffractogram of Perfluoronaphthalene thin film. Reflexes are labeled corresponding to [20].

S1.4 Perfluoropentacene XPS

In Fig.S4 the energy difference between F1s and C1s-signals of perfluoropentacene measured by x-ray photoemission can be seen. Using the calculated ionisation potentials for the various excitation centres similar differences for the StoBe-results can be obtained, yielding values of 400.67 eV and 399.40 eV. Both numbers are smaller then the experimental differences by around 1 eV. Since the calculated ionisation potentials for the case of carbon are accurate within 0.3 eV, the deviation must be due to errors in the calculations for F1s-excitation centres. Averaging leads to a shift between calculated and experimental energy differences of about 1.17 eV. This justifies the empirical shift of 1.2 eV, which was necessary to compare the calculated and experimental NEXAFS-spectra.

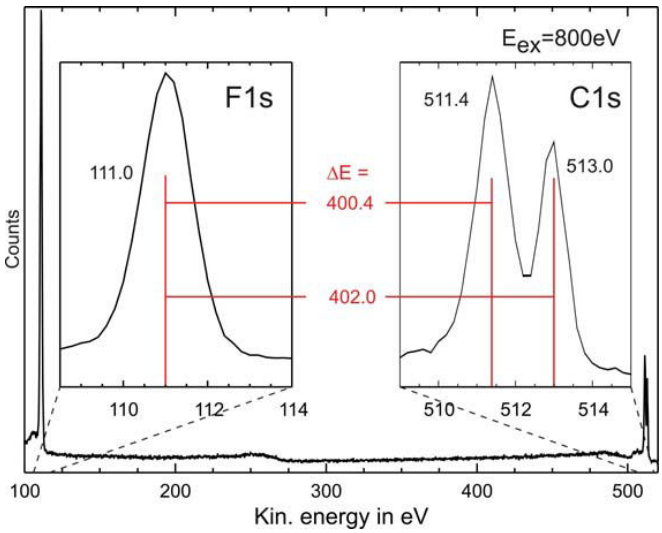

Figure S4: X-ray photoemission spectrum of Perfluoropentacene. Insets show magnifications of the F1s- and C1s-region. In red the energy differences of these peaks are given.

S2 Theoretical results

S2.1 Perfluoropentacene

S2.1.1 Partial F1s NEXAFS spectra of Perfluoropentacene

The StoBe-code calculates partial NEXAFS spectra for all symmetry inequivalent excitation centres. To compare the calculation with experimental data a total spectrum is calculated by summing up the partial ones. Therefore the multiplicity needs to be considered. All excitation centres can be found four times in a perfluoropentacene molecule except the F1-centre, which is represented only two times. Therefore the F1-spectrum has only half of the intensity of the spectra from the other centres within the full spectrum.

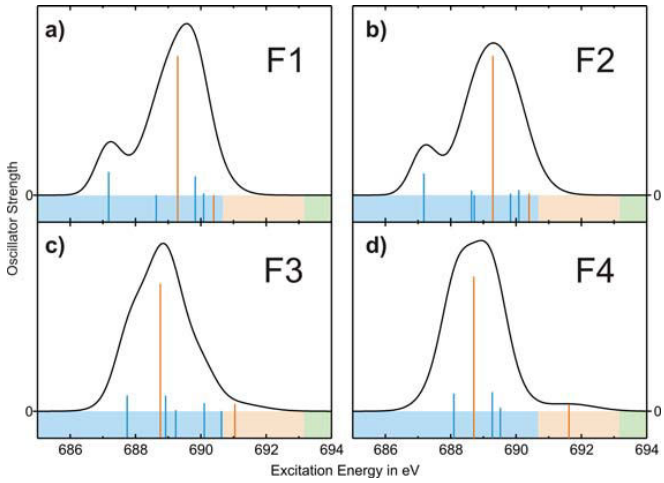

Figure S5: Partial F1s NEXAFS spectra for all symmetry inequivalent excitation centres of perfluoropentacene. π-resonances are depicted as blue bars, while σ-resonances are given in orange.

S2.1.2 Molecular orbitals

The figures in this subsection show select Kohn–Sham molecular orbitals as obtained for perfluoropentacene with the def2-SVP basis set and the PBE density functional as implemented in the program package Turbomole 6.6 [23],[24], utilizing the RI approximation [23]–[25]. The Kohn–Sham molecular orbitals

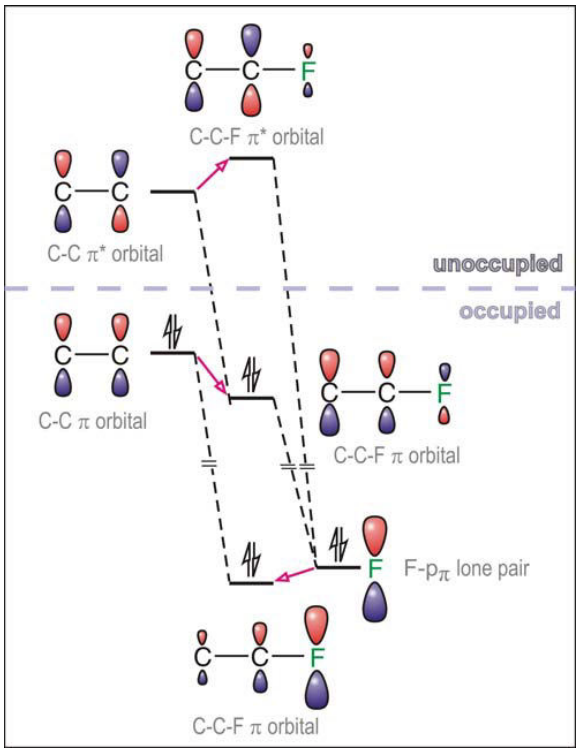

Figure S13: Generalized MO-diagram of the π-interaction between fluorine and the π-system of an aromatic carbon backbone.

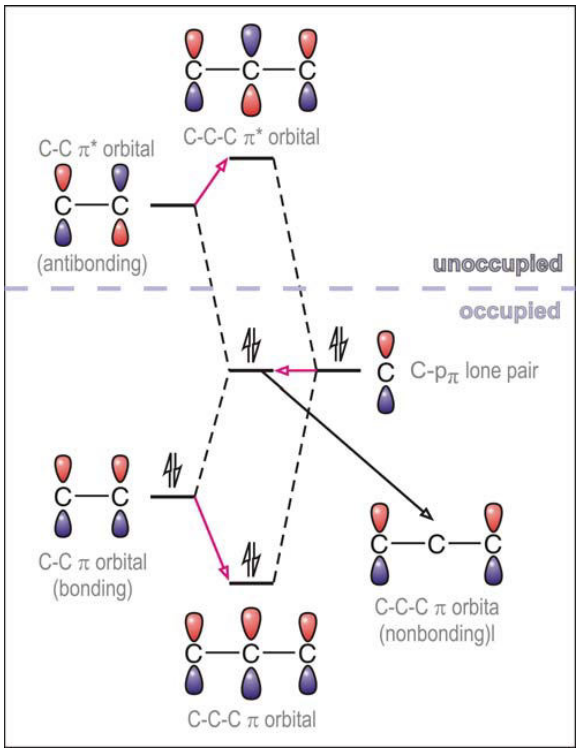

Figure S14: Generalized MO-diagram of the π-interaction between carbon and the π-system in an allyl molecule.

5.9 Crystalline Packing Motifs in Pentacene-like Organic Semiconductors

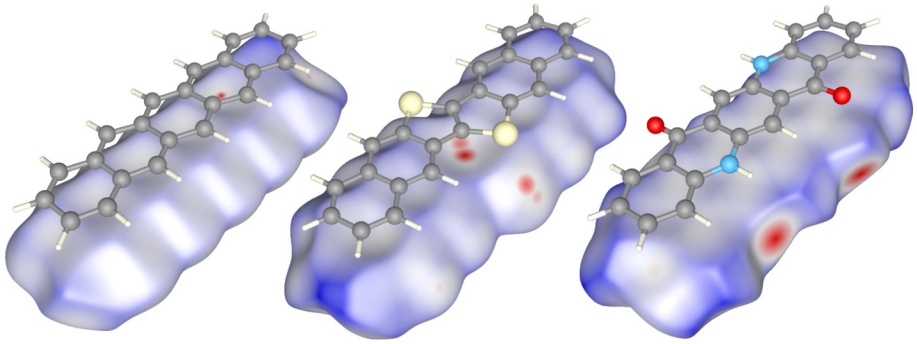

Artikel in Vorbereitung zur Veröffentlichung in *CrystEngComm*.

5.9.1 Inhaltsangabe

In terms of the charge transport properties of organic semiconductors, crystal structures emerge as a crucial parameter, which cannot be accurately predicted or controlled so far. For that reason, this comparative study will observe the qualitative connections between packing motifs and interactions using Hirshfeld analysis, electrostatic contour plots and simple geometric deliberations. The key idea to reduce the complexity of this subject is a proficient selection of pentacenelike semiconductor molecules with a comparable molecule geometry. This way, steric effects can be ruled out for the comparison while the electrostatic parts of the vdW-forces tip the scales on the packing motifes, and thus simple MEPs can be used for qualitative assertions. Additionally, the selection includes many extraordinarily performant semiconductors, which makes the observation especially interesting from the viewpoint of organic electronics. During the study, a charge distribution with a coherent sign of the potential along the edges of the molecules emerges as favourable for Herringbone motives. Moreover, the Hirshfeld analysis showcases the importance of atom sizes in regard to contact points between neighbouring molecules. This considered, future developments in this field could put their focus less on achieving a more and more narrow π-π-stacking, but rather on the implementation of individual, strong contact points.

5.9.2 Eigenleistung

Die Auswahl an Molekülen und damit die Grundidee des vorliegenden Artikels wurde in Zusammenarbeit mit Gregor Witte entwickelt. Sämtliche DFT-Rechnungen zu den Moleküleigenschaften wurden ebenso wie die Hirshfeldanalysen von mit durchgeführt. Die Interpretation der Daten, sowie das Erstellen des Manuskriptes erfolgte durch mich mit Unterstützung durch Gregor Witte.

Journal Name

ARTICLE

Crystalline Packing Motifs in Pentacen-like Organic Semiconductors

Received 00th January 20xx,
Accepted 00th January 20xx

DOI: 10.1039/x0xx00000x

www.rsc.org/

M. Klues,[a] and G. Witte[a]

In terms of the charge transport properties of organic semiconductors, crystal structures emerge as a crucial parameter, which cannot be accurately predicted or controlled so far. For that reason, this comparative study will observe the qualitative connections between packing motifs and interactions using Hirshfeld analysis, electrostatic contour plots and simple geometric deliberations. The key idea to reduce the complexity of this subject is a proficient selection of pentacenelike semiconductor molecules with a comparable molecule geometry. This way, steric effects can be ruled out for the comparison while the electrostatic parts of the vdW-forces tip the scales on the packing motifes, and thus simple MEPs can be used for qualitative assertions. Additionally, the selection includes many extraordinarily performant semiconductors, which makes the observation especially interesting from the viewpoint of organic electronics. During the study, a charge distribution with a coherent sign of the potential along the edges of the molecules emerges as favourable for Herringbone motives. Moreover, the Hirshfeld analysis showcases the importance of atom sizes in regard to contact points between neighbouring molecules. This considered, future developments in this field could put their focus less on achieving a more and more narrow π-π-stacking, but rather on the implementation of individual, strong contact points.

Introduction

A multitude of organic semiconductors have been examined for their applicability in electronic components such as field-effect transistors and solar cells during the past years. In particular some model systems stood out due to their exceptional properties and are being used for in-depth analyses of the underlying physical processes ever since. In the following, the model molecule of interest will be pentacene (PEN), which forms solids with an above-average carrier mobility.[1] More importantly, the outstanding processability allows for a controlled preparation of specific samples, most commonly thin films, which are used in further specialized experiments.[2] Based on such a model system it is a common strategy to use chemical modification in order to alter specific properties of the molecule. The focus usually is on electronic energy levels (most commonly HOMO- and LUMO-levels),[3] which bear great significance for electronic processes. Fluorination for example will turn the p-type semiconductor PEN into the n-type semiconductor perfluoropentacene (PFP),[4] while a gradual variation of energy levels can be reached by nitrogen substitution within the aromatic ring system.[5] In fact, the construction kit of chemistry allows for a plethora of possible compounds, with the result that a molecule's properties can be altered almost at will.[6] However, the physical properties of a solid are not exclusively determined by their molecular components, but are a result of the interactions of those components, which causes them to form a crystal structure. This structure is especially important for the electronic properties of an organic material, since the coupling of the molecules in terms of an overlap of the involved orbitals is crucial to the charge transport. For that reason, in the context of conjugated molecules such as PEN, the π-π-interaction often becomes a topic of discussion.[7] Unfortunately, even the seemingly tiniest chemical modification can have huge impact on the resulting crystalline structure. For instance, one can think of a new material with optimal energy level alignment for a given purpose, but lacking the positive or even necessary properties of the original material due to a massively altered crystal structure.

To this day the packing motives of organic materials cannot be predicted precisely among other reasons due to the small scale of their intermolecular interactions.[8] Therefore, the development of new semiconductors requires comparative studies that classify the known structures, work out the decisive interactions and relate them to the properties of the single molecules. In order to enable general statements, the characterisation of crystal structures should be based on their defining interactions rather than the geometrical structure. One method satisfying this precondition is a Hirshfeld-analysis, or more precisely the fingerprint of the structure which is based on such an analysis.[9] These plots contain information about interactions in the form of bond length and can even be compared quantitatively via a correlation of pictures.[10] Here we will apply such an analysis to a selection of pentacene-like molecules, such as the above-mentioned azaacenes,

[a] *Fachbereich Physik, Philipps-Universität Marburg, 35032 Marburg, Germany*

†Electronic Supplementary Information (ESI) available: Details on correlation coefficients, packing coefficients, polarizabilities, quadrupolmoments and close contacts are given, as well as an visualization of packing motifs for all structures are given. See DOI: 10.1039/x0xx00000x

fluorinated molecules as well as oxidised pentacenes and hybrid forms of these categories. An exception to this ensemble of organic semiconductors is constituted by dinaphthothienothiophene (DNTT), which cannot be related to PEN directly, but fits the selection nonetheless, due to its outstanding performance in devices[11] and its geometrical resemblance: All molecules can be conceived as almost rectangular cuboids with the dimension of a PEN-molecule, which, in good approximation, also holds true for DNTT. This way, steric effects due to bulky side groups can be eliminated and the defining interactions of the partially strongly differing crystal structures emerge more clearly.

Setting

The Molecular Ensemble

The molecules shown here have been compiled following three aspects: Geometrical resemblance to pentacene, general relevance for the subject area of organic semiconductors, and most notable difference in interaction. The first point forms the central idea of this comparative study, since the close geometric resemblance highlights the significance of their interactions. A simple gedankenexperiment helps illustrate this point further: If one ignores the exact chemical composition of the molecules, their measurements are almost identical. In terms of a closed packed structure they should therefore show similar packing motives, which however does not hold true in practice. So which properties of the molecules are the actual cause of the different crystal structures?

In terms of the second aspect, this compilation gains relevance for the subject area of organic semiconductors. PEN itself, just as well as its relatives PFP, dihydrodiazapentacene (DHDAP),[12] DNTT and quinacridone (QUA),[13] possess an above-average applicability for electronic components. Are there any parallels in the packing motives explaining these similarities? Additionally, diazapentacene (DAP),[14] pentacenquinon (QUI) and pentacentetron (TET) do not appear to be this performant

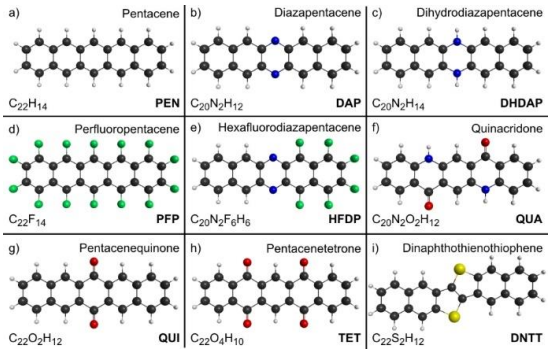

Figure 1: Structures of all molecules under consideration. Given are the names, molecular formulas and the corresponding shortcut used throughout this article. Note: Optimized geometries are depicted to underline the geometric resemblance of all molecules.

and are attributed for the degradation of said components, such as the PEN oxidation product QUI.[15] Why do these close relatives exhibit such a wide difference in behaviour?

Moreover, the assortment should cover as many interactions as possible. While the structure of most materials is determined by quadrupole momenta and particularly van der Waals interactions, the structure of QUA is determined by hydrogen bonds, and hexafluordiazapentacene (HFDP) provides with a motive dominated by static dipole moments.[16]

Organic compounds are known for their ability to crystallise into a variety of different polymorphisms, which is also known for some of the molecules examined here. However, the Hirshfeld analysis requires an exact crystal structure with all of the atom coordinates, which is why we will narrow it down to the polymorphisms of PEN, PFP and QUA as they are known in literature, and apart from these only one structure is established. For PEN, the two bulk-structures Campbellphase[17] and Siegrist-phase[18] willl be observed as well as the thin-film phase, which is especially relevant for thin-film applications.[19] With the α-, β- and γ-phase of QUA,[20] there will be also three structures up for discussion, while PFP will only be represented by two polymorphisms, bulk-phase[21] and π-stacked phase.[22] DAP‡, DHDAP, HFDP, QUI, TET and DNTT all have just one known structure at the present time.[14,12,16,23-25]

Computational Approach

All of the aforementioned structures were subject to a Hirshfeld analysis via „CrystalExplorer".[26] The method has already been introduced in detail, [9] so here is just a rundown of the underlying idea: During the analysis, the electron density of the molecule and its surroundings in the crystal gets converged. Based on this density, a weighting function which assigns the fraction of the molecule's density to the associated points can be generated. The corresponding Hirshfeld volume is then the sum of all parts with a proportion ≥ 0.5 and the Hirshfeld surface is defined as the surface of this volume or the sum of all points with a weighting function value of 0.5. The fingerprint plots shown here base upon such a surface, by plotting the distance to the nearest exterior atom outside the volume d_e against the distance of the nearest neighbor interior d_i for every surface point. A colour code is used to point out the occurrence of particular spacing couples, where red marks a frequent and blue a rare occurrence.

In order to fully realize a crystal structure via fingerprint plots, one generally needs to treat all molecules within the unit cell. As a result, a structure can have multiple plots. Only QUA-α and TET possess primitive unit cells and are thereby represented in a trivial way by just one plot. The symmetry groups of most of the other structures display symmetry operations such as screw axes, allowing to determine all molecular positions from only one molecule. That case requires the observation of just one fingerprint plot for the whole structure as well. This however does not hold true for the three PEN-structures, the DHDAP and the π-stacked polymorph of PFP, since they posses P-1 symmetry and two molecules within the unit cell respectively. Since the fingerprint plots are supposed to work as a measure to compare the structures to each other, it would be preferable

for these cases to also have a single representative plot. For that purpose, the distributions of both molecules were added up and a plot was created for their sum. As long as the d_i-d_e-couples indirectly decode interactions via bond lengths, these sum plots provide a depiction of all existing interactions within the crystal, and can be compared to the other fingerprints, for which the same holds true for symmetry reasons.

In order to compare the fingerprints quantitatively, correlation coefficients (mean of Spearman and Pearson) were calculated via Python standard routines using fingerprints with a grid of 15x15 bins and a scale of 0 to 3 Å.[27] This procedure is based on a method introduced by Parkin et al.[10] The presentation of the correlation data in terms of a dendrogram has been implemented via Python as well, using the UPGMA method. All further molecular properties like quadrupolmoments and polarizabilities were determined using the US-GAMESS code.[28,29] DFT-calculations were performed with B3LYP/6311G(d,p) and started with a structure optimization for each. To depict the electron density, an isovalue of 0.002 au was chosen, leading to volumina reflecting the approximate size of the molecule within the crystal, which are therefore comparable to the Hirshfeldvolumina.[30] Molecular electrostatic potentials (MEP) were generated using Molekel.[31]

Results

Fig. 2 shows fingerprints for all structures with features labeled by the underlying contact pairs. An appropriate attribution can be accomplished easily via Crystal Explorer, since it can create plots which only show those bins in color that can be ascribed to a specific atom couple.[32] The second line of fig. 2 shows four examples of this approach. The objective now is to compare the fingerprints with one another and sort them into groups according to their resemblance, which corresponds to sorting them by similar intermolecular interactions. In addition to a qualitative comparison based on their visual appearance one can also gather similarities quantitatively by using correlations. The results of the calculations mentioned above have been summarized in fig. 3 using a dendrogram. This results in collections that shall be observed more closely in the following.

Herringbone

The first collection in the dendrogram (green) consists of the five structures that have their plots depicted in the first two rows of fig. 2. Within the three PEN structures as well as with DHDAP and DNTT, C-H-contacts emerge clearly, taking the form of two "wings" in the plots. H-H contacts are to be found as well, showing a diffused spacing distribution, as is shown in the subplot. The N-H contacts within the DHDAP structure fail to create a difference worth mentioning since they coincide with the C-H intervals. While the similarities of the five plots can be recognized intuitively, the correlation helps with narrowing down their deviations. Within the collection, the DNTT structure showcases the smallest resemblance, which can be attributed to the C-S interaction that becomes visible on the diagonal of the picture. Upon observing the molecules of the crystal, all five structures display a typical "face on edge" Herringbone motiv of which there is an example in fig. 4a).

Perfluorination

The next collection (purple) consists of only two structures, but with great difference in their molecular packing. While PFP-bulk displays a "face on edge" motive (fig. 4c) just like the structures from the first collection, the molecules of PFP-π are stacked parallel, which is often called "pi- or slipped stacked" (example fig. 4b). Despite their difference, the fingerprint plots of these two closely resemble each other in the third row of fig. 2. Both display C-F contacts in the form of side-on "wings" in the same way as the C-H characteristics of the hydrocarbons mentioned above. Furthermore though, C-C contacts can be seen on the picture diagonal in both cases. The F-F interactions are remarkable, as they, other than the H-H contacts of the Herringbone collection, display distinctive characteristics that partly position themselves along the picture diagonal as well. Especially the red areas, i.e. distance couples of high accumulation, can be attributed to the F-F contacts.

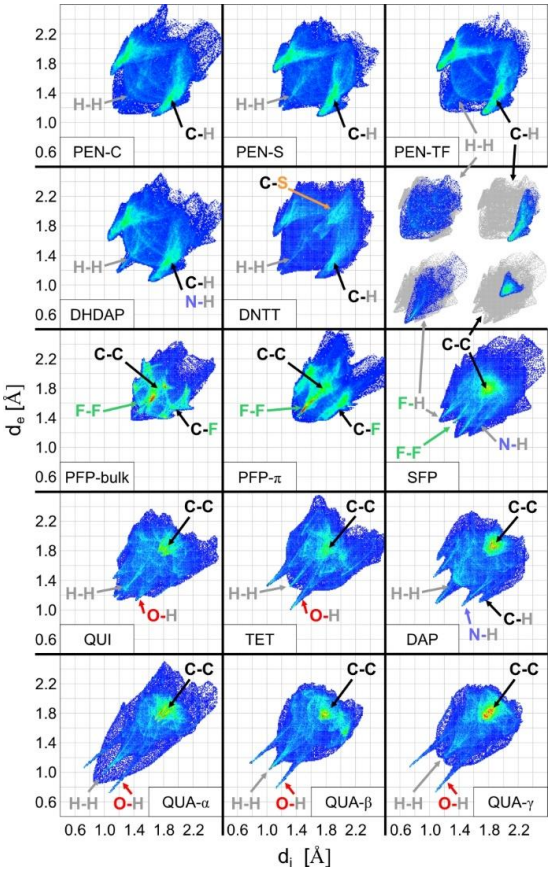

Figure 2: Fingerprintplots for all crystal structures. Striking features are labelled with the corresponding interaction type. Small Fingerprints in the second row show examples for Interaction identification via colouring of specific parts of the plots. Red regions denote high occurrence of d_i-d_e-couples.

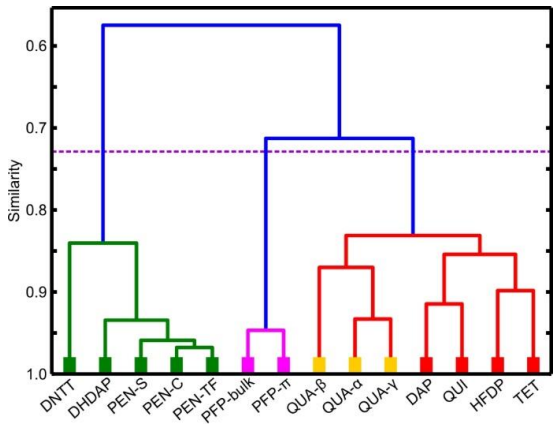

Figure 3: Dendrogram of correlations between fingerprints of all crystal structures.

Directed interactions

The last seven structures are compiled in the third collection (red). Two features strike the eye for all associated plots in the lower part of fig. 2: All structures feature C-C contacts, and in the lower left quadrant they display sharp, needle-like extensions of varying size. These characteristics often indicate a relatively strong interaction between two specific atoms, which is why we speak of them as directed interactions. For QUI, TET and the three QUA structures this shows most clearly in the O-H contacts. They also have H-H features like DAP, and other than in the Herringbone motifs they display characteristic patterns. Since DAP and HFDP do not contain any oxygen, the "needle extensions" go back to N-H, C-H and F-H contacts, while HFDP displays F-F features that behave analogously to the H-H parts of the other structures in this collection. Looking at the packing, QUI, TET and QUA-α have a slipped-stacked motive, with QUI slightly stepping out of line with slight contortions of the molecules against each other. QUA-β displays slipped-stacking as well, if only within the layers parallel to the (001)-level. These layers are twisted against each other, which is why we have no parallelism. DAP, HFDP and QUA-γ display a third distinct packing motif, with molecules aligned in parallel stacks, but the neighboring stacks are twisted against each other and thus adjoin on their longitudinal edges which results in two molecules having just one point of contact (see fig. 4c). This kind of packing will be entitled “criss-cross” motive according to the work of Paulus et al.[20] HFDP shows an additional feature with molecules alternately turned by 180° within the stacks, which can be attributed to the static dipole moment of 5.2D along the longitudinal axis.

Discussion

What is the nature of the interactions between those contact points mentioned above? To determine this, we shall first take a look at the possible kinds of interaction. In the context of conjugated organic molecules it is common to mention van der Waals forces as the driving attractive interaction, which, however, are a hypernym for multiple forces. These include electrostatic interactions (Keesom interactions), which are caused by the permanent multipoles of the molecules; induced forces, which are based on the polarizability of the molecules (Debye interactions); and dispersive forces (London dispersion), which are the result of spontaneous polarization. Induced effects make the smallest contribution to the total energy amount[8,33] and seem to have only a subsidiary influence on the packing motives since the essential aspects can be allocated to the other forces in the following. London dispersion however constitutes the major energetic part. Its value can be estimated using a formalism including the α-polarizability squared.[34] In general, since polarizability is a tensorial variable, there can be varying anisotropies among different molecules, resulting in divergent packing motifs. In this case however the main axle elements of the compounds mainly display similar relations (see SI), so this cannot be the explanation for differing packing motifs such as for PEN and DAP (see fig. 4). The close resemblance in polarizability is in fact a result of the specific selection of sample molecules, since its value substantially depends on the amount of electrons and the overall size of the system. Solely molecules containing oxygen show significantly lower results, which can be attributed to a loss of conjugation. As the London dispersion turns out weaker in these cases, other interactions take on greater significance for the specific structures. So following this line of argumentation we are left with electrostatic interactions to make up the most relevant fraction of van der Waals forces in order to explain the crystal structures of the molecules qualitatively. With the exception of HFDP, there are no molecules with a static dipole moment, so quadrupole moments are essential here. An intuitive assumption can hardly be gained solely on the basis of numeric values for quadrupole moments (see SI), which is why fig.5 displays electrostatic contour plots of the molecules. At this point a critical sidenote needs to be mentioned: Naturally all calculations concerning polarisability, quadrupole moments and MEPs are based on the consideration of individual gas-phase molecules and do not consider the surroundings within the crystal. Only the fingerprint plots contain implicit information about the bound state. However, the exact calculation of a crystal and in particular the prediction of its structure are still in development and furthermore are very elaborate. That is why simpler criteria are still necessary in order to achieve a qualitative understanding of the binding situation as well as to develop guidelines for the synthesis of new compounds. By comparing the molecular properties to their fingerprints, the former shall be tested on their significance for the structure in order to see whether trends emerge.

Apart from the already mentioned van der Waals forces there is another attractive force: Local dipolar interactions with covalent character. Basically, those are variable pronounced hydrogen bonds which can occur whenever there are electron lone pairs in contact with an electron deficient atom of the neighboring molecule. All forces mentioned so far are mainly of an attractive nature and therefore counteract the Pauli

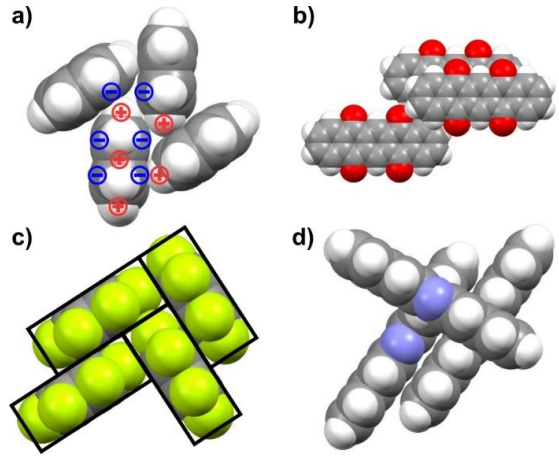

Figure 4: Examples for typical packing motives. a) Herringbone structure of PEN with charge distribution, b) Sliped Stacked motiv of TET, c) Herringbone of PFP-bulk with rectangles highlighting the orthogonal arrangement d) criss-cross structure of DAP

repulsion, which will always gain the upper hand for sufficiently short distances.

Backround of Herringbonemotives

For the interactions of polycyclic aromatic hydrocarbons, Hunter and Sanders[7] have constructed a simple model based on the assumption of a sandwich-like charge distribution with a positive core. Fig.4a) depicts exemplary the charge distribution for PEN. The idea is also supported by the MEPs in Fig.5a-d). All molecules with Herringbone structures have uniform sign of charge along their edges as well as the corresponding antipole in the middle of the molecule, more specifically located above and below the molecular plane. By combining positive and negative charges the typical "face on edge" motif is formed automatically. In the fingerprint plots, this becomes manifest in the form of C-H-contacts, which is however not an atom-specific interaction, but is attributed to the overall charge distribution of the molecule. This becomes clear in the case of DHDAP where the N-H-contact is identical to the C-H-contacts. H-H-interactions are repulsive in this way, which explains the appearance of huge distances in the plots. This pairing occurs especially on the head ends, since the Herringbone motif leads to layers with the ends of the molecules on their top- and underside. In turn, the layers here are in contact with each other. At the same time, the associated crystallographic plane is the preferred one for grows of the organic material on many other materials, since the corresponding surface energy is very low due to the electrostatic repulsion.[41] Nevertheless, those areas can apparently be defining for the structure. Observing the fingerprint plots of the three PEN polymorphisms, their only difference seems to lie in the blue background caused by the H-H-contacts. For instance, regarding the thin-film phase, which only occurs for thin films, a more upright alignment of the molecules can be assumed to favor an energetically more convenient substrate-H-interaction mediated by the ends of the molecules.

Impact of Fluorination

Within the second collection mentioned above (fig.3 purple) another Herringbone structure can be found, which is the PFP bulk-phase. In fact, everything discussed in the last section fully holds true for this case as well, since the fluorination only switches the sign of charge compared to PEN (see fig.5c), but this does not challenge the argumentation. Still, the fingerprints show some characteristics that do not appear in the plots of the first collection (green). The most interesting feature in this context is corresponding to F-F-contacts. An accumulation of di-de distance pairings within the plots (green-red areas) indicates an equilibrium distance, i.e. a minimum in the sum of all concerned interaction potentials. F-F interactions are not intrinsically attractive, so the characteristics in these plots suggest other forces pushing the molecules together to a point where the Pauli repulsion becomes relevant over the F-F contact. The simple reason why this occurs for fluorine but not for the hydrogen in the foregoing cases is the size of the atoms. This becomes clear at once by comparing fig.4a) and 4c). The space-filled depiction, using atomic radii inspired by van der Waals radii, shows fluorine atoms with about the same size as carbon atoms. This actually leads directly to an explanatory approach for the orthogonal packing motive within the PFP-crystal: The PFP molecules can be seen as rectangular "bricks", as it is indicated with rectangles in fig.4c). Molecules with a fringe of hydrogen atoms however taper off at the edge. For close packing such a compound, a right angle between the molecules can never be the best choice, but in case of the "PFP bricks" it constitutes the optimum. This interpretation is supported by packing coefficients as determined by the definition of Kitaigorodskii[35]. In applying van der Waals radii as they are also provided by the CrystalExplorer program[36,37], typical coefficients of approximately 0.7 emerge for all structures. Solely the two PFP structures are packed more compact with values of about 0.8, while the partly fluorinated HFDP ranges in between them with 7.5. Considering the molecular volume of PFP as a rectangular block also allows for some insight into the second packing motif of PFP. Apart from the Herringbone motif, Hunter and Sanders described a parallel arrangement of molecules, which are slightly shifted against each other, i.e. a slipped stacked motif, to be attractive as well. In the case of PFP this results from the Herringbone structure via turning every second molecule by 90°. Due to the simple "brick geometry" of the molecules, the emerging packing motif is still space-filling. For instance, this does not hold true for PEN. Its bent edges would contact each other leading to cavities in the structure. This would increase the C-H distances and the attractive interaction would be weakened, while the C-F distances of PFP remain largely unchanged. In fact, no slipped stacked growth is known for PEN and it cannot be induced with a suitable substrate either.

Strong local interactions

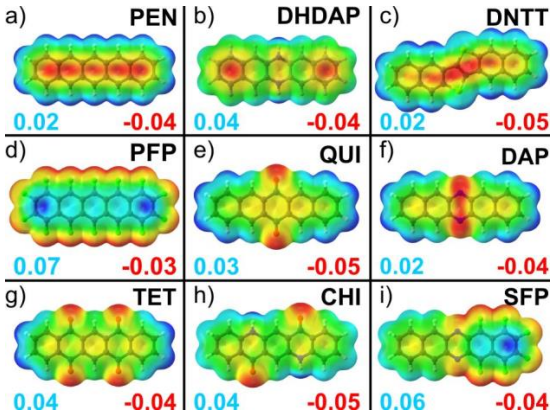

Figure 5: MEPs of all molecules. An Isovalue of 0.002au enables comparability to Hirschfeldvolumina. Red and blue numbers denote minimum and maximum values of the electrostatic potential in au.

The foregoing argumentations are all based on a layered allocation of the charges within the molecule. However this can change drastically due to the implementation of heteroatoms. DAP is an impressive example for such an effect. The nitrogen atoms change the potential compared to PEN only at two positions (fig.5f), but a completely different structure emerges (fig.4d). This structure is called “criss-cross” motif. The change of charge signs seems to be crucial, as DHDAP shows a change in the potential as well, but qualitatively the charge distribution is unaffected. Therefore DHDAP also forms a Herringbone motif. However, a face-on-edge structure cannot be electrostatically advantageous for DAP, as the qualitative change in the potential of the molecule's fringe leads to partial repulsion within the interaction with the carbon skeleton of the neighbouring molecule. For that reason, all molecules with a comparable potential display either a criss-cross or a slipped-stacked motif, enabling the realization of attractive contacts. The effects on packing motives using nitrogen substitution in aromatic hydrocarbons have been described in more detail by K.E. Maly.[38] However, the leading, purely electrostatic argument does not completely fit the binding situation in this. Within the crystal structures under consideration in this study, atoms with lone pairs such as N, O or F are usually in contact with hydrogens, which allows for hydrogen bonds to emerge. These can vary greatly in their strength.[39] Since the length of the bond is an indicator for its strength, some insight on this can be gained using the fingerprint plots. The stronger the bond, the shorter will be the distance, and the corresponding contact adopts a needle-like shape in the plot. The row QUI-TET-QUA constitutes a good example for this effect. QUI appears to have an exceptionally weak bond. Despite exhibiting a higher molecular mass than PEN, it sublimes at a lower temperature, so the weak additional hydrogen bonds do not outweigh the unfavourable electrostatics. QUI also does not form a perfect slipped stacked motif. Thus, the bonds are not strong enough to compensate interfering steric effects from the bigger oxygen atoms. All this already does not hold true for TET anymore and the O-H distances are 0.2Å shorter than in the case of QUI. Still, the distance of 2.3Å is rather long, with an accordingly weak hydrogen bond. Only the three QUA structures show typical strong hydrogen bonds with distances below 1.9Å. In fact, QUA constitutes an example for a strong feedback of intermolecular interaction with intramolecular characteristics. The strong hydrogen bond weakens the C-O bond within the molecule, which allows the molecule to gain conjugation thus causing energy levels to shift. This immediately becomes clear from a differing colour impression of the solution and the solid state of this substance, even though this effect is moreover mainly caused by excitons.[13,40] Structures displaying "needles" in their fingerprints are thus influenced by local interactions, and in the case of strong hydrogen bonds, as they appear in QUA, they are even dominated. That makes QUA a prototypical example for a new class of semiconductor molecules introducing hydrogen bonds for structure control. Concerning the matter of assessing hydrogen bonds using fingerprints, another critical sidenote needs to be mentioned: The plots are only as accurate as the underlying structure data. The position of hydrogens however can only be reliably determined via neutron diffraction. Since this kind of data is rarely available, the exact position of hydrogen atoms often is not determined in detail. This is crucial for the assessment of strong hydrogen bonds since the bond length between the involved hydrogen and its molecule can be effected noticeable. However, qualitative statements about trends as they have been made here are uninvolved, as this effect only scales at a range of 0.1Å. The last property that needs to be discussed are the C-C contacts that all structures of this collection have in common. Especially for semiconductor molecules this trait is often mentioned, as it implies an overlap of the π-systems, which in turn facilitates the charge transport. In this context it is often referred to π-π-interactions, which however should not be understood as an attractive interaction. Primarily, C-C contacts are repulsive. Only on close observation, modelling the whole electronic system of the neighbour molecules, an additional interaction emerges: the so-called "charge penetration effect", which is based on electron density of the π–system extending into the core areas of the neighbouring molecules.[8] Therefor π-π interactions emerge as a side-effect of other attractive, stronger interactions. In general for high charge carrier motilities short C-C distances are advantageous, but evidently it is not a unique characteristic. Sutton et al.[8] show that, even under these convenient circumstances, the relative shift of two molecules towards each other is a significant factor for the electronic coupling, since it is influenced by the exact spatial extent of the involved orbitals. Moreover some of the most performant substances such as PEN, DHDAP and DNTT within the assortment shown here, exhibit no π-π interactions at all. In return another contact could bear great significance. Fig.6 shows the Hirshfeld surfaces of PEN-C, DNTT and QUA-γ. The colour code is a result of di and de values related to the vdW-radii of the corresponding atoms.

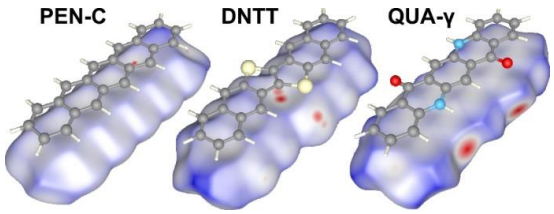

Figure 6: Hirschfeldsurfaces for PEN-C, DNTT and QUA-γ. Red areas denote regions of electronic overlap with neighbouring molecules. Molecular structures are translated 3.3Å perpendicular to original position.

Red areas mark zones with a sum of d-values smaller than what can be anticipated from the sum of vdW-radii, while blue areas indicate the opposite. Hence, red indicates regions where neighbouring molecule draw very close, and thus a strengthened orbital overlap is to be expected. Here, QUA with its clearly visible contact points of the hydrogen bonds constitutes a conclusive example. Now, comparing the surfaces of PEN and DNTT, two contact points in the middle of the DNTT molecule stand out. Those trace back to C-S contacts and are obviously much more pronounced than a corresponding C-H analogon of the PEN. Considering that overlap integrals depend on the distance in a highly nonlinear fashion and furthermore that sulfur is a direct component of the conjugated system in the case of DNTT (different to hydrogen within PEN), this is an explanatory approach for the outstanding conduction properties of DNTT.

Conclusions

For future advancements in both the understanding of physical relations within solids as well as the specific development of new semiconductors, it will still be necessary to work out their defining properties and create guidelines using comparative studies like. Therefor it is reasonable to reduce the complexity by conducting comparisons with an intelligent choice of molecules. By observing molecules with an almost identical geometry, steric effects could be ruled out as far as possible. Additionally, electrostatic forces, made accessible qualitatively via MEPs, were identified as the key interaction regarding the structure, since the London attraction is largely the same for all molecules in this study. The following correlations were elaborated via fingerprints, electrostatic contours and consideration of the atom sizes:

1. A Herringbone motif requires a uniform sign of charge for the electrostatic potential on the edges of the molecule.

2. Conversely, already two (or probably even one) interferences within the uniform potential of the edge cause a slipped-stacked or criss-cross packing.

3. With simple geometric deliberations, the size of atoms in the sense of vdW radii allows for insights about the structures, explaining the right angles in the packing motifs of PFP.

4. Huge heteroatoms like sulfur in DNTT generate contact points with neighboring molecules which might be beneficial for the electronic properties of the material.

Based on these observations, a possible synthesis strategy respectively a search criterion for new semiconductors emerges: By considering the potential at the edges of a polycyclic, aromatic molecule, a Herringbone motif can specifically be aimed for. Moreover, well-positioned, relatively huge heteroatoms such as sulfur, phosphorus and selenium can be used to create a strengthened overlap for enhanced transport properties.

Acknowledgements

The acknowledgements come at the end of an article after the conclusions and before the notes and references.

Notes and references

‡ To our knowledge the crystal structure of DAP is already discussed in literature[14] but cannot be found in any database up to the publication date of this article. Thanks to Prof. Dr. Qian Miao for providing these data.

1 H. Klauk, M. Halik, U. Zschieschang, G. Schmid and W. Radlik, *J. Appl. Phys.*, 2002, **92**, 5259.
2 R. Ruiz, D. Choudhary, B. Nickel, T. Toccoli, K.C. Chang, A.C. Mayer, P. Clancy, J.M. Blakely, R.L. Headrick, S. Iannotta and G. Malliaras, *Chem. Mater.*, 2004, **16**, 4497.
3 S. Braun, W.R. Salaneck and M. Fahlman, *Adv. Mater.*, 2009, **21**, 1450.
4 Y. Inoue, Y. Sakamoto, T. Suzuki, M. Kobayashi, Y. Gao and S. Tokito, *JJAP*, 2005, **44**, 3663.
5 Z. Liang, Q. Tang, R. Mao, D. Liu, J. Xu and Q. Miao, *Adv. Mater.*, 2011, **23**, 5514.
6 B.M. Medina, J.E. Anthony and J. Gierschner, *ChemPhysChem*, 2008, **9**, 1519.
7 C.A. Hunter and J.K.M. Sanders, *J. Am. Chem. Soc.*, 1990, **112**, 5525.
8 C. Sutton, C. Risko and J.L. Brédas, *Chem. Mater.*, 2015, **28**, 1.
9 M. A. Spackman and D. Jayatilaka, *CrystEngComm*, 2009, **11**, 19.
10 A. Parkin, G. Barr, W. Dong, C. J. Gilmore, D. Jayatilaka, J.J. MacKinnon, M.A. Spackman and C.C. Wilson, *CrystEngComm*, 2007, **9**, 648.
11 S. Haas, Y. Takahashi, K. Takimiya and T. Hasegawa, *Appl. Phys. Lett.*, 2009, **95**, 22111.
12 Q. Tang, D. Zhang, S. Wang, N. Ke, J. Xu, J.C. Yu, and Q. Miao, *Chem. Mater.*, 2009, **21**, 1400.
13 E.D. Głowacki, L. Leonat, M. Irimia-Vladu, R. Schwödiauer, M. Ullah, H. Sitter, S. Bauer and N.S. Sariciftci, *Appl. Phys. Lett.*, 2012, **101**, 23305.
14 Q. Miao, *SYNLETT*, 2012, **23**, 326.
15 S.H. Han, J.H. Kim, S.M. Cho, M.H. Oh, S.H. Lee, D.J. Choo and J. Jang, *Appl. Phys.* Lett., 2006, **88**, 73519.
16 J. Schwaben, N. Münster, M. Klues, T. Breuer, P. Hofmann, K. Harms, G. Witte and U. Koert, *Chem. Eur. J.*, 2015, **21**, 13758.
17 R.B. Campbell and J.M. Robertson, *Acta Cryst.*, 1962, **15**, 289.
18 T. Siegrist, C. Kloc, J.H. Schön, B. Batlogg, R.C. Haddon, S. Berg and G.A. Thomas, *Angew. Chem. Int. Ed.*, 2001, **40**, 1732.
19 S. Schiefer, M. Huth, A. Dobrinevski and B. Nickel, *J. Am. Chem. Soc.*, 2007, **129**, 10316.
20 E.F. Paulus, F.J.J. Leusen, and M.U. Schmidt, *CrystEngComm*, 2007, **9**, 131.

21 Y. Sakamoto, T. Suzuki, M. Kobayashi, Y. Gao, Y. Fukai, Y. Inoue, F. Sato and S. Tokito, J. Am. Chem. Soc., 2004, 126, 8138.
22 I. Salzmann, A. Moser, M. Oehzelt, T. Breuer, X. Feng, Z.Y. Juang, D. Nabok, R.G. Della Valle, S. Duhm, G. Heimel, A. Brillante, E. Venuti, I. Bilotti, C. Christodoulou, J. Frisch, P. Puschnig, C. Draxl, G. Witte, K. Müllen and N. Koch, *ACS Nano*, 2012, **6**, 10874.
23 A.V. Dzyabchenko, V.E. Zavodnik and V.K. Belsky, *Acta Cryst. B*, 1979, **35**, 2250.
24 D. Käfer, M. El Helou, C. Gemel and G. Witte, *Cryst. Growth Des.*, 2008, **8**, 3053.
25 T. Yamamoto and K. Takimiya, *J. Am. Chem. Soc*., 2007, **129**, 2224.
26 S.K. Wolff, D.J. Grimwood, J.J. McKinnon, M.J. Turner, D. Jayatilaka, M.A. Spackman, Crystal Explorer ver. 3.1, University of Western Australia, Perth, Australia 2013.
27 Python Software Foundation. Python Language Reference, version 2.7.6. Available at http://www.python.org
28 M.W. Schmidt, K.K. Baldridge, J.A. Boatz, S.T. Elbert, M.S. Gordon, J.H. Jensen, S. Koseki, N. Matsunaga, K.A. Nguyen, S. Su, T.L. Windus, M. Dupuis and J.A. Montgomery, *J. Comput. Chem.*, 1993, **14**, 1347.
29 M.S. Gordon and M.W. Schmidt in *Theory and Applications of Computational Chemistry: the first forty years*, ed. C.E. Dykstra, G. Frenking, K.S. Kim, G.E. Scuseria, Elsevier, Amsterdam, 2005, *Advances in electronic structure theory: GAMESS a decade later*, 1167-1189.
30 R.F.W. Bader, M.T. Carroll, J.R. Cheeseman and C. Chang, J. Am. Chem. Soc., 1987, **109**, 7968.
31 U. Varetto, Molekel 5.4
32 J.J. McKinnon, J. Dylan and M. A. Spackman, *Chem. Commun.*, 2007, **37**, 3814.
33 J.D. Dunitz and A. Gavezzotti, *Chem. Soc. Rev.*, 2009, **38**, 2622.
34 F. London, *Trans. Faraday Soc.*, 1937, **33**, 8.
35 A.I. Kitaigorodskii, *Acta. Cryst.*, 1965, **18**, 585.
36 A. Bondi, *J. Phys. Chem.*, 1964, **68**, 441.
37 R.S. Rowland and R. Taylor, *J. Phys. Chem.*, 1996, **100**, 7384.
38 K.E. Maly, *Cryst. Growth Des.*, 2011, **11**, 5628.
39 T. Steiner, *Angew. Chem. Int. Ed.*, 2002, **41**, 48.
40 E.D. Głowacki, M. Irimia-Vladu, M. Kaltenbrunner, J. Gąsiorowski, M.S. White, U. Monkowius, G. Romanazzi, G.P. Suranna, P. Mastrorilli, T. Sekitani, S. Bauer, T. Someya, L. Torsi and N.S. Sariciftci, *Adv. Mater.*, 2013, **25**, 1563.
41 D. Nabok, P. Puschnig and C. Ambrosch-Draxl, *Phys. Rev. B*, 2008, **77**, 245316.
42 M.A. Spackman and J.J. MacKinnon, *CrystEngComm*, 2002, **4**, 378.

Please do not adjust margins

Supporting Information

Crystalline Packing Motifs in Pentacene-like Organic Semiconductors

Michael Klues and Gregor Witte*

Fachbereich Physik, Philipps-Universität Marburg, Renthof 7, 35032 Marburg, Germany.
E-Mail: gregor.witte@physik.uni-marburg.de

Table of Contents

Abbreviations. All abbreviation used within the supporting information are listed below and are in accordance with the notation used in the article.

Molecules:

DAP	Diazapentacene
DHDAP	Dihydrodiazapentacene
DNTT	Dinaphthothienothiophene
HFDP	Hexafluorodiazapentacene
PEN	Pentacene
PFP	Perfluoropentacene
QUA	Quinacridone
QUI	Pentacenequinone
TET	Pentacenetetrone

Polymorphisms:

PEN-C	Pentacene Campbell Phase
PEN-S	Pentacene Siegrist Phase
PEN-TF	Pentacene Thin Film Phase
PFP-bulk	Perfluoropentacene Bulk Phase
PFP-π	Perfluoropentacene π-stacked Phase
QUA-α	Quinacridone α-Phase
QUA-β	Quinacridone β-Phase
QUA-γ	Quinacridone γ-Phase

Correlation Coefficients. All correlation coefficients have been calculated according to the definition of Spearman and Pearson [1] for fingerprints with 15x15 bins and a scale of 0 to 3Å. Calculations were performed using python standard routines. [2]

Table ST1: Correlation coefficients for fingerprints of all crystal structures.

	DAP	DHDAP	DNTT	PEN-C	PEN-S	PEN-TF	PFP-bulk	PFP-π	QUA-α	QUA-β	QUA-γ	QUI	HFDP	TET
DAP	1.0	0.65	0.7	0.66	0.66	0.62	0.61	0.62	0.82	0.8	0.85	0.91	0.82	0.79
DHDAP		1.0	0.77	0.94	0.96	0.91	0.53	0.5	0.44	0.57	0.45	0.6	0.56	0.55
DNTT			1.0	0.87	0.84	0.88	0.61	0.61	0.58	0.61	0.59	0.69	0.66	0.7
PEN-C				1.0	0.96	0.97	0.56	0.5	0.46	0.62	0.51	0.64	0.59	0.61
PEN-S					1.0	0.96	0.56	0.52	0.48	0.61	0.51	0.63	0.59	0.59
PEN-TF						1.0	0.53	0.51	0.48	0.6	0.48	0.6	0.57	0.58
PFP-bulk							1.0	0.95	0.71	0.67	0.64	0.72	0.85	0.82
PFP-π								1.0	0.69	0.64	0.63	0.73	0.84	0.82
QUA-α									1.0	0.87	0.93	0.87	0.84	0.82
QUA-β										1.0	0.87	0.86	0.8	0.79
QUA-γ											1.0	0.88	0.82	0.8
QUI												1.0	0.89	0.91
HFDP													1.0	0.9
TET														1.0

[1] A. Parkin, G. Barr, W. Dong, C. J. Gilmore, D. Jayatilaka, J.J. MacKinnon, M.A. Spackman and C.C. Wilson, *CrystEngComm*, 2007, **9**, 648.
[2] Python Software Foundation. Python Language Reference, version 2.7.6. Available at http://www.python.org

vdW-Volumes and Packing Coefficients: Van der Waals volumes V_{vdW} of molecules were calculated assuming spheres at all atomic positions with element specific vdW-radii and merging of all spheres. Following radii which are also used within the Crystal Explorer program [1] were applied throughout this work: H=1.09 Å; C=1.70 Å; N=1.55 Å; O=1.52 Å; F=1.47 Å. [2,3] For comparison the Hirshfeld volume V_H as computed with the Crystal Explorer is also listed. V_H is systematically larger than V_{vdW} but should exhibit the same trends. Packing coefficients C were calculated according to Kitaigorodskii [4] as $C = \frac{z \cdot V_{vdW}}{V_{cell}}$, where z denotes the number of molecules in the unit cell and V_{cell} is the unit cell volume.

Table ST2: Hirschfeld volumes V_H, molecular vdW volumes V_{vdW}, number of molecules z in the unit cell, unit cell volume V_{cell}, packing coefficient C.

	V_H (Å^3)	V_{vdW} (Å^3)	z	V_{cell} (Å^3)	C
PEN-C	339	245	2	692.38	0.71
PEN-S	338	244	2	685.49	0.71
PEN-TF	342	241	2	696.95	0.69
PFP-bulk	393	323	2	797.01	0.81
PFP-π	404	323	2	819.99	0.79
DNTT	376	269	2	767.71	0.70
QUA-α	340	251	1	347.27	0.72
QUA-β	331	249	2	674.50	0.74
QUA-γ	344	248	2	700.63	0.71
QUI	353	254	2	718.19	0.71
TET	373	267	1	379.41	0.70
DHDAP	327	236	2	667.85	0.71
DAP	327	240	2	667.78	0.72
HFDP	352	270	4	1433.75	0.75

[1] http://hirshfeldsurface.net
[2] A. Bondi, *J. Phys. Chem.*, 1964, **68**, 441.
[3] R.S. Rowland and R. Taylor, *J. Phys. Chem.*, 1996, **100**, 7384.
[4] A.I. Kitaigorodskii, *Acta. Cryst.*, 1965, **18**, 585.

Computing Molecular Properties: All properties were calculated with the US-GAMESS code [1], using DFT with the B3LYP functional and a 6311G(d,p) basis set. Molecules were at first geometry optimized by considering their symmetry before calculation of their polarizabilities and quadrupole moments. The precision of polarizability calculations was improved by decreasing convergence criteria, primitive cutoff factors as well as integral cutoffs. Energy and dipole derived polarizabilities are found to be equal for all molecules up to the fourth significant digit. Molecules were placed parallel to the xy-plane with their symmetry center at the origin, so that the z-axis is perpendicular to the molecular plane. The long axis of the molecules is oriented along the x-direction and therefore the short axis of the molecules is parallel to the y-axis. DNTT is an exception since in this case a long axis is not clearly defined. Here the long axis of the naphthalene subunits was oriented in x-direction. Due to symmetry reasons this orientation directly yields diagonal polarizability and quadrupole tensors for all molecules except DNTT and QUA. In these cases the tensor was diagonalized to provide better comparability. For the polarizability tensors this is a minor manipulation since diagonalization can be obtained by a rotation around the z-axis of less than 5 degrees in both cases, while for the quadrupole tensor rotations of 12 degrees for DNTT and 30 degrees for QUA are needed.

Polarizability:

Table ST3: α-polarizability of all molecules.

	xx (au)	yy (au)	zz (au)
PEN	612	244	87
PFP	640	257	88
HFDP	604	233	86
DAP	603	229	85
DHDAP	574	224	87
QUI	521	244	87
TET	440	264	88
QUA (diag.)	472	249	88
DNTT (diag.)	631	270	97

Quadrupole Moments:

Table ST4: calculated quadrupole moments of all molecules. Values are given in Buckinghams.

	xx	yy	zz
PEN	14.65	11.89	-26.54
PFP	-11.02	-16.5	27.52
HFDP	28.2	-20.29	-7.92
DAP	31.99	-5.1	-26.88
DHDAP	-7.48	26.95	-19.47
QUI	48.92	-22.66	-26.25
TET	63.31	-46	-17.3
QUA (diag.)	53.04	-33.9	-19.14
DNTT (diag.)	-30.1	5.66	24.35

[1] http://www.msg.ameslab.gov/gamess

Atomic Distances: Fingerprint plots are also used to determine distances between neighbouring atoms. Therefore only d_i-d_e pairs of a special atom pair will be coloured in the plot, allowing to identify the smallest sum of a d_i-d_e pair. This approach yields the same values as directly measuring close contacts between two neighbouring atoms, since the corresponding connecting line needs to intersect the Hirshfeld surface, which necessarily yields a d_i-d_e pair for this smallest distance. Note that this definition is also applied to the C-C contacts. Therefore, the presented values don`t implicitly represent the molecular plane distance, which should be systematically smaller than the given numbers, but are nevertheless quite close to the plane distances.

Table ST5: Close contact distances for different atom pairs.

	C-H (Å)	N-H (Å)	O-H (Å)	C-F (Å)	C-C (Å)
PEN-C	2.73				
PEN-S	2.82				
PEN-TF	2.81				
DNTT	2.73				
DAP	2.76	2.48			3.50
DHDAP	2.65	2.68			
HFDP		2.68		3.04	3.32
QUI			2.53		3.50
TET			2.31		3.36
QUA-α			1.78		3.38
QUA-β			1.90		3.40
QUA-γ			1.81		3.43
PFP-bulk				3.10	3.22
PFP-π				2.96	3.18

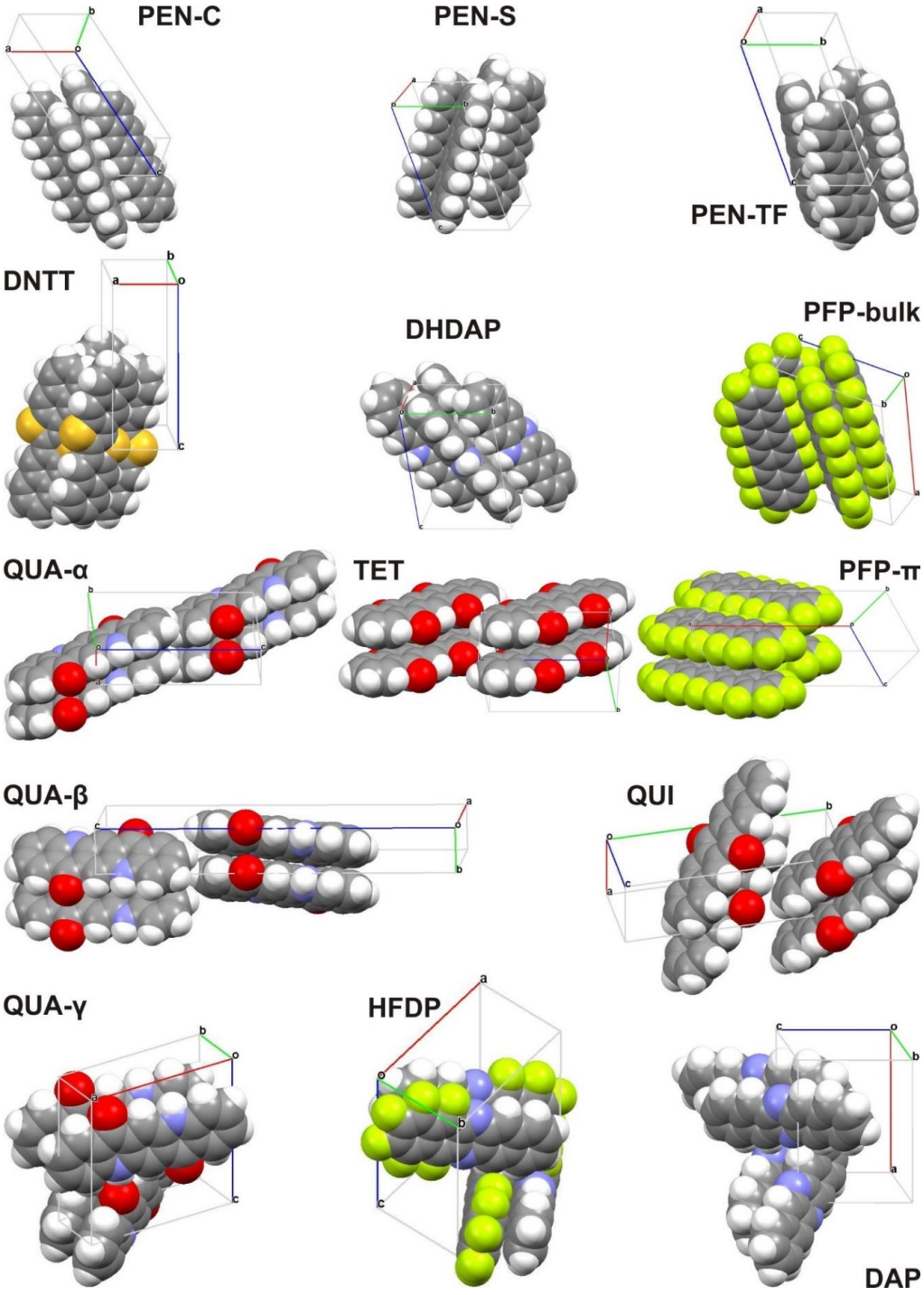

Figure S1: Visualization of packing motifs for all considered crystal structures together with the unit cells.

Danksagung

> Science is like sex: Sometimes something useful comes out, but that is not the reason we are doing it.
>
> *Richard Feynman*

Der eifrige Leser dieses Werkes hat sich bis zu diesen Zeilen durch über 200 Seiten Text und Abbildungen gearbeitet. Dass im Laufe meiner Promotion doch so viel - mehr oder weniger - Berichtenswertes zusammen gekommen ist, ist aber nicht allein mein Verdienst. Den aufmerksamen unter den eifrigen Lesern wird ein Name aufgefallen sein, der in jeder Autorenliste meiner Veröffentlichungen auftaucht: Gregor Witte. Bei ihm möchte ich mich für die jahrelange Unterstützung und Zusammenarbeit bedanken, die er als Doktorvater in mich und damit auch diese Arbeit gesteckt hat. Aber nicht nur seine fachliche Kompetenz, von der ich in ungezählten Gesprächen profitiert habe, sowie die vielen Anregungen und Ideen, die er stets parat hat, haben mich voran gebracht. Bisweilen war es auch sein Gespür für die richtige Herausforderung zum richtigen Zeitpunkt, das mich motiviert hat, den nächsten Schritt zu tun.
Ebenfalls bedanken möchte ich mich bei meinem Zweitgutachter und Kooperationspartner Robert Berger. Die Perspektive eines theoretischen Chemikers, mit der er auf viele meiner Probleme geschaut hat, lieferte nicht selten verblüffend einfache Antworten, für die ich mich bedanken möchte. Ich kann nur hoffen, dass es kein allzu schlechtes Licht auf mich wirft, dass ich auf manche dieser Ideen wohl niemals selbst gekommen wäre.
Weiterhin möchte ich mich bei allen anderen Kooperationspartner bedanken, mit denen zusammen die verschiedenen Veröffentlichungen entstanden sind. Hervorzuheben sind hier Paul Jerabek und Jonas Schwaben, mit denen die intensive Zusammenarbeit besonders viel Freude bereitet hat.
Ein weiterer Name, der ebenfalls in vielen Autorenlisten fällt, ist Tobias Breuer. Seine Bürotür steht allen Kollegen stets offen und ich bin ungezählte Male auf der Suche nach Rat und Unterstützung hindurch geschritten. Der Gang hat sich stets gelohnt und viele Projekte wären ohne ihn so nicht zustande gekommen. Dafür gebührt ihm ein großes Dankeschön.
Tobias ist jedoch nicht der einzige Kollege, der mich in den vergangenen Jahren unterstützt hat. In vorderster Front stehen da auch meine Büronachbarn Michael Kothe und Paul Rotter. Während Michael ein treuer Mitstreiter und Leidensgenosse (je nach dem...) auf so mancher Expedition ans BESSY war, hat Paul durch seine verblüffende Computerkompetenz so manche meiner Rechnungen erst möglich gemacht. Abseits davon muss ich mich aber auch für ein inspirierendes, verständnisvolles, unterstützendes und im allgemeinen einfach gutes Büroklima bedanken. (Und nein, mit „Büroklima“ meine ich nicht die schneidfähige Atmosphäre aus Rechnerabluft und angereicherten Aromastoffen.)
Allen anderen Kollegen aus der AG Molekulare Festkörperphysik möchte ich ebenfalls für ihre Unterstützung, das gute Arbeitsklima und ihre Geduld danken. Schließlich weiß ich, dass ich besonders vormittags, bevor wir unseren gemeinsamen Mensaausflug unternommen haben, den ich nicht nur wegen des Mittagessens, sondern besonders auch wegen der Gesellschaft so schätze,

ein schwieriger Zeitgenosse sein kann. Besonders hervorheben möchte ich hier Peter Oßwald, den Feinmechanikermeister unserer Arbeitsgruppe. Mit ihm zu planen, zu konstruieren und gelegentlich auch handfest zu schrauben war mir stets eine besondere Freude und ich denke, dass die klangvollen Titel unserer gemeinsamen Projekte, wie z.B. „Halter-42“ und „(G) lovebox“, die Qualität unserer Arbeit am besten beschreiben. Stellvertretend geht mit dem Dank an Peter auch ein Kompliment an die Kollegen aus der feinmechanischen Werkstatt. Es ist beinahe unmöglich, einen Entwurf zu zeichnen, den sie nicht in die Realität umsetzen könnten und gelingt es einem doch, ist dies nur ein sicheres Anzeichen dafür, dass es eine einfachere Lösung gibt, auf die man nicht selten direkt aufmerksam gemacht wird. Ebenso möchte ich mich beim Elektroniklabor bedanken, für das stellvertretend Carsten Schindler zu nennen ist. Solange das Problem einen Stecker oder zumindest eine Batterie hat, helfen Besuche dort immer weiter und sind zudem stets lehrreich. Grundsätzlich gilt: Defekte Elektronik ist erst dann kaputt, wenn die E-Werkstatt sie nicht reparieren kann und meiner Erfahrung nach bezeichnet „kaputt“ in diesem Sinne einen kaum erreichbaren Zustand der Zerstörung.
Darüber hinaus gilt mein Dank auch dem Helmholtz Zentrum Berlin, das mich und meine Arbeit durch viele Messzeiten, also in Form von Synchrotronstrahlung, unterstützt hat. Außerdem gebührt auch der Deutschen Forschungsgemeinschaft ein Dankschön, die über den Sonderforschungsbereich 1083 unter anderem auch mich und meine Arbeit finanziert hat.
Aber auch abseits der Physik gibt es viele Menschen, denen ich ein Dankeschön schulde. Schon bei meinen Lehrern (Ohne die ich ebenfalls nicht soweit gekommen wäre: Dankeschön!) konnte ich zu Schulzeiten keinen Enthusiasmus für meinen Gebrauch oder vielmehr Nichtgebrauch der deutschen Rechtschreibung und Grammatik wecken. Daran hat sich bis heute wenig geändert, sodass ich allen Beteiligten fürs Korrekturlesen danken möchte. Besonders sind dabei Elisabeth Seide und Katharina von Hippel zu nennen, die darüber hinaus auch zum großen Kreis meiner Freunde und Bekannten gehören, die mich außerhalb des Büros oder Labors begleitet haben. Besonders der Ausgleich, den ich gemeinsam mit guten Freunden durch die Pfadfinderei in Gruppenstunden und Zeltlagern gefunden habe, hat mich auch durch die schwierigen Phasen dieser Arbeit gebracht.
Last but not least wie es so schön heißt, möchte ich mich auch bei meiner Familie und ganz besonders bei meinen Eltern Maria und Gerhard Klues bedanken. Der stete Rückhalt, den sie mir auf meinem Weg nun schon seit Jahren geben, hat es mir überhaupt erst ermöglicht, so weit zu kommen.

Danke!

Literaturverzeichnis

[1] Breuer T., Celik M.A., Jakob P., Tonner R. and Witte G.: Vibrational Davydov Splittings and Collective Mode Polarizations in Oriented Organic Semiconductor Crystals, in: *The Journal of Physical Chemistry C* 116 (2012), 14491-14503. DOI: 10.1021/jp304080g

[2] Kallmann H. and Pope M.: Bulk Conductivity in Organic Crystals, in: *Nature* 186 (1960), 31-33. DOI: 10.1038/186031a0

[3] Shirakawa H., Louis E., MacDiarmid A.G., Chiang C.K. and Heeger A.J.: Synthesis of electrically conducting organic polymers: halogen derivatives of polyacetylene, $(CH)_x$, in: *Journal of the Chemical Society, Chemical Communications* 16 (1977), 578. DOI: 10.1039/c39770000578

[4] Hasegawa T. and Takeya J.: Organic field-effect transistors using single crystals, in: *Science and Technology of Advanced Materials* 10 (2009), 024314. DOI: 10.1088/1468-6996/10/2/024314

[5] Forrest S.R.: The path to ubiquitous and low-cost organic electronic appliances on plastic, in: *Nature* 428 (2004), 911-918. DOI: 10.1038/nature02498

[6] Cullen D.K. and Smith D.H.: Elektrischer Anschluss ans Nervensystem, in: *Spektrum der Wissenschaft* 4 (2013). Weblink (27.10.2016): www.spektrum.de/news/elektrischer-anschluss-ans-nervensystem/1186735

[7] Carvelli M., van Reenen A., Janssen R.A.J., Loebl H.P. and Coehoorn R.: Exciton formation and light emission near the organic–organic interface in small-molecule based double-layer OLEDs, in: *Organic Electronics* 13 (2012), 2605-2614. DOI: 10.1016/j.orgel.2012.07.035

[8] Haibo W. and Donghang Y.: Organic heterostructures in organic field-effect transistors, in: *NPG Asia Materials* 2 (2010), 69-78. DOI: 10.1038/asiamat.2010.44

[9] Oehzelt M., Akaike K., Koch N. and Heimel, G.: Energy-level alignment at organic heterointerfaces, in: *Science Advances* 1 (2015), e1501127. DOI: 10.1126/sciadv.1501127

[10] Braun S., Salaneck W.R. and Fahlman M.: Energy-Level Alignment at Organic/Metal and Organic/Organic Interfaces, in: *Advanced Materials* 21 (2009), 1450-1472. DOI: 10.1002/adma.200802893

[11] Greiner M.T. and Lu Z.-H.: Thin-film metal oxides in organic semiconductor devices: their electronic structures, work functions and interfaces, in: *NPG Asia Materials* 5 (2013), e55. DOI: 10.1038/am.2013.29

[12] Schmidt C., Witt A. and Witte G.: Tailoring the Cu(100) Work Function by Substituted Benzenethiolate Self-Assembled Monolayers, in: *The Journal of Physical Chemistry A* 115 (2011), 7234-7241. DOI: 10.1021/jp200328r

[13] Schultz T., Schlesinger R., Niederhausen J., Henneberger F., Sadofev S., Blumstengel S., Vollmer A., Bussolotti F., Yang J.-P., Kera S., Parvez K., Ueno N., Müllen K. and Koch N.: Tuning the work function of GaN with organic molecular acceptors, in: *Physical Review B* 93 (2016), 125309. DOI: 10.1103/PhysRevB.93.125309

[14] Brédas J.-L., Beljonne D., Coropceanu V. and Cornil J.: Charge-Transfer and Energy-Transfer Processes in π-Conjugated Oligomers and Polymers: A Molecular Picture, in: *Chemical Reviews* 104 (2004), 4971-5004. DOI: 10.1021/cr040084k

[15] Coropceanu V., Cornil J., da Silva Filho D.A., Olivier Y., Silbey R. and Brédas J.-L.: Charge Transport in Organic Semiconductors, in: *Chemical Reviews* 107 (2007), 926-952. DOI: 10.1021/cr050140x

[16] Coropceanu V., Li H., Winget P., Zhu L. and Brédas J.-L.: Electronic-Structure Theory of Organic Semiconductors: Charge-Transport Parameters and Metal/Organic Interfaces, in: *Annual Review of Materials Research* 43 (2013), 63-87. DOI: 10.1146/annurev-matsci-071312-121630

[17] Schmidt C., Breuer T., Wippermann S., Schmidt W.G. and Witte G.: Substrate Induced Thermal Decomposition of Perfluoro-Pentacene Thin Films on the Coinage Metals, in: *The Journal of Physical Chemistry C* 116 (2012), 24098-24106. DOI: 10.1021/jp307316r

[18] Dürr A.C., Schreiber F., Kelsch M., Carstanjen H.D. and Dosch H.: Morphology and Thermal Stability of Metal Contacts on Crystalline Organic Thin Films, in: *Advanced Materials* 14 (2002), 961-963. DOI: 10.1002/1521-4095(20020705)14:13/14<961::AID-ADMA961>3.0.CO;2-X

[19] Breuer T., Karthäuser A. and Witte G.: Effects of Molecular Orientation in Acceptor-Donor Interfaces between Pentacene and C 60 and Diels-Alder Adduct Formation at the Molecular Interface, in: *Advanced Materials Interfaces* 3 (2016), 1500452. DOI: 10.1002/admi.201500452

[20] Ruiz R., Choudhary D., Nickel B., Toccoli T., Chang K.-C., Mayer A., Clancy P., Blakely J.M., Headrick R.L., Iannotta S. and Malliaras G.G.: Pentacene Thin Film Growth, in: *Chemistry of Materials* 16 (2004), 4497-4508. DOI: 10.1021/cm049563q

[21] Breuer T. and Witte G.: Diffusion-Controlled Growth of Molecular Heterostructures: Fabrication of Two-, One-, and Zero-Dimensional C_{60} Nanostructures on Pentacene Substrates, in: *ACS Applied Materials & Interfaces* 5 (2013), 9740-9745. DOI: 10.1021/am402868s

[22] Breuer T. and Witte G.: Epitaxial growth of perfluoropentacene films with predefined molecular orientation: A route for single-crystal optical studies, in: *Physical Review B* 83 (2011), 155428. DOI: 10.1103/PhysRevB.83.155428

[23] Haas S., Batlogg B., Besnard C., Schiltz M., Kloc C. and Siegrist T.: Large Negative Thermal Expansion in Pentacene due to Steric Hindrance, in: *Physical Review B* 76 (2007), 205203. DOI: 10.1103/PhysRevB.76.205203

[24] Tanner D., Jacobsen C., Garito A. and Heeger A.: Infrared studies of the energy gap in tetrathiofulvalene-tetracyanoquinodimethane (TTF-TCNQ), in: *Physical Review B* 13 (1976), 3381-3404. DOI: 10.1103/PhysRevB.13.3381

[25] Breuer T., Salzmann I., Götzen J., Oehzelt M., Morherr A., Koch N. and Witte G.: Interrelation between Substrate Roughness and Thin-Film Structure of Functionalized Acenes on Graphite, in: *Crystal Growth & Design* 11 (2011), 4996-5001. DOI: 10.1021/cg200894y

[26] CrystalExplorer (Version 3.1), Wolff S.K., Grimwood D.J., McKinnon J.J., Turner M.J., Jayatilaka D. and Spackman M.A., University of Western Australia, 2012. Webadresse (1.11.2016): http://crystalexplorer.scb.uwa.edu.au/index.html

[27] Guerra F.C., Handgraaf J.W., Baerends E.J. and Bickelhaupt F.M.: Voronoi deformation density (VDD) charges: Assessment of the Mulliken, Bader, Hirshfeld, Weinhold, and VDD methods for charge analysis, in: *Journal of Computational Chemistry* 25 (2004), 189-210. DOI: 10.1002/jcc.10351

[28] Spackman M.A. and Jayatilaka D.: Hirshfeld surface analysis, in: *CrystEngComm* 11 (2009), 19-32. DOI: 10.1039/b818330a

[29] Hirshfeld F.L.: Bonded-atom fragments for describing molecular charge densities, in: *Theoretica Chimica Acta* 44 (1977), 129-138. DOI: 10.1007/BF00549096

[30] Bader R.F.W., Carroll M.T., Cheeseman J.R. and Chang C.: Properties of atoms in molecules: atomic volumes, in: *Journal of the American Chemical Society* 109 (1987), 7968-7979. DOI: 10.1021/ja00260a006

[31] Fabbiani F.A., Byrne L.T., McKinnon J.J. and Spackman M.A.: Solvent inclusion in the structural voids of form II carbamazepine: single-crystal X-ray diffraction, NMR spectroscopy and Hirshfeld surface analysis, in: *CrystEngComm* 9 (2007), 728. DOI: 10.1039/B708303N

[32] Mercury Webadresse (1.11.2016): http://www.ccdc.cam.ac.uk/solutions/csd-system/components/mercury/

[33] Mitchell A.S. and Spackman M.A.: Molecular surfaces from the promolecule: A comparison with Hartree–Fock *ab initio* electron density surfaces, in: *Journal of Computational Chemistry* 21 (2000), 933-942. DOI: 10.1002/1096-987X(200008)21:11<933::AID-JCC3>3.0.CO;2-F

[34] Koga T., Kanayama K., Watanabe S. and Thakkar A.J.: Analytical Hartree–Fock wave functions subject to cusp and asymptotic constraints: He to Xe, Li^+ to Cs^+, H^- to I^-, in: *International Journal of Quantum Chemistry* 71 (1998), 491-497. DOI: 10.1002/(SICI)1097-461X(1999)71:6<491::AID-QUA6>3.0.CO;2-T

[35] Bondi A.: Van der Waals Volumes and Radii, in: *The Journal of Physical Chemistry* 68 (1964), 441-451. DOI: 10.1021/j100785a001

[36] Rowland R.S. and Taylor R.: Intermolecular Nonbonded Contact Distances in Organic Crystal Structures: Comparison with Distances Expected from van der Waals Radii, in: *The Journal of Physical Chemistry* 100 (1996), 7384-7391. DOI: 10.1021/jp953141+

[37] Paulus E.F., Leusen F.J.J. and Schmidt M.U.: Crystal structures of quinacridones, in: *CrystEngComm* 9 (2007), 131-143. DOI: 10.1039/b613059c

[38] Khalid W., El Helou M., Murböck T., Yue Z. Montenegro J.M., Schubert K., Göbel G., Lisdat F., Witte G. and Parak W.J.: Immobilization of Quantum Dots *via* Conjugated Self-Assembled Monolayers and Their Application as a Light-Controlled Sensor for the Detection of Hydrogen Peroxide, in: *ACS Nano* 5 (2001), 9870-9876. DOI: 10.1021/nn2035582

[39] Stöhr, J.: NEXAFS Spectroscopy. Berlin Heidelberg: Springer, 1992. ISBN 3-540-54422-4

[40] Watts B., Thomsen L. and Dastoor P.C.: Methods in carbon K-edge NEXAFS: Experiment and analysis, in: *Journal of Electron Spectroscopy and Related Phenomena* 151 (2006), 105-120. DOI: 10.1016/j.elspec.2005.11.006

[41] Schmidt, C.: Eigenschaften fluorierter Aromaten an Metall/Organik-Grenzflaechen. Dissertation. Universität Marburg, 2012.

[42] Breuer T., Klues M. and Witte G.: Characterization of orientational order in π-conjugated molecular thin films by NEXAFS, in: *Journal of Electron Spectroscopy and Related Phenomena* 204 (2015), 102-115. DOI: 10.1016/j.elspec.2015.07.011

[43] Wagner, C.D.: Handbook of X-ray Photoelectron Spectroscopy. Eden Prairie: Perkin-Elmer Corporation, 1979.

[44] Kong M.J., Teplyakov A.V., Andrew V., Lyubovitsky J.G. and Bent S.F.: NEXAFS studies of adsorption of benzene on Si(100)-2x1, in: *Surface Science* 411 (1998), 286-293. DOI: 10.1016/S0039-6028(98)00336-7

[45] Klues M., Hermann K. and Witte G.: Analysis of the near-edge X-ray-absorption fine-structure of anthracene: A combined theoretical and experimental study, in: *The Journal of Chemical Physics* 140 (2014), 014302. DOI: 10.1063/1.4855215

[46] Zagorodskikh S., Zhaunerchyk V., Mucke M., Eland J.H.D., Squibb R.J., Karlsson L., Linusson P. and Feifel R.: Single-photon double and triple ionization of acetaldehyde (ethanal)studied by multi-electron coincidence spectroscopy, in: *Chemical Physics* 463 (2015), 159-168. DOI: 10.1016/j.chemphys.2015.10.006

[47] Schmidt M.W., Baldridge K.K., Boatz J.A., Elbert S.T., Gordon M.S., Jensen J.H., Koseki S., Matsunaga N., Nguyen K.A., Su S., Windus T.L., Dupuis M. and Montgomery J.A.: General atomic and molecular electronic structure system, in: *Journal of Computational Chemistry* 14 (1993), 1347-1363. DOI: 10.1002/jcc.540141112

[48] Gordon M.S. and Schmidt M.W.: Theory and Applications of Computational Chemistry: the first forty years. *Advances in electronic structure theory: GAMESS a decade later.* Amsterdam: Elsevier, 2005.

[49] GAMESS-Dokumentation.
Weblink (6.11.2016): http://www.msg.ameslab.gov/GAMESS/documentation.html

[50] Jensen F.: Introduction to Computational Chemistry. Weinheim: Wiley, 2006. ISBN: 978-0-470-01186-7

[51] Sousa S.F., Fernandes P.A. and Ramos M.J.: General Performance of Density Functionals, in: *Journal of Physical Chemistry A* 111 (2007), 10439-10452. DOI: 10.1021/jp0734474

[52] Bode B.M. and Gordon M.S.: MacMolPlt: A graphical user interface for GAMESS , in: *Journal of Molecular Graphics and Modelling* 16 (1998), 133-138. DOI: 10.1016/S1093-3263(99)00002-9

[53] Varetto U.: Molekel 5.4. Weblink (6.11.2016): https://ugovaretto.github.io/molekel

[54] StoBe-deMon version 3.3 (2014), Hermann K. and Pettersson L.G.M., Casida M.E., Daul C., Goursot A., Koester A., Proynov E., St-Amant A. and Salahub D.R. Contributing authors: Carravetta V., Duarte H., Friedrich C., Godbout N., Gruber M., Guan J., Jamorski C., Leboeuf M., Leetmaa M., Nyberg M., Patchkovskii S., Pedocchi L., Sim F., Triguero L. and Vela A.

[55] Klues M.: Präparation und Charakterisierung von Diazaacen-Dünnfilmen. Masterarbeit. Universität Marburg 2012.

[56] Godbout N., Salahub D.R., Andzelm J. and Wimmer E.: Optimization of Gaussian-type basis sets for local spin density functional calculations. Part I. Boron through neon, optimization technique and validation, in *Canadian Journal of Chemistry* 70 (1992), 560-571. DOI: 10.1139/v92-079

[57] Kutzelnigg W., Fleischer U. and Schindler M.: NMR-Basic Principles and Progress. Heidelberg: Springer, 1990.

[58] Pettersson L.G.M., Wahlgren U. and Gropen O.: Effective core potential parameters for first- and second-row atoms, in *The Journal of Chemical Physics* 86 (1987), 2176. DOI: 10.1063/1.452115

[59] Slater J.C. and Johnson K.H.: Self-Consistent-Field Xα Cluster Method for Polyatomic Molecules and Solids, in *Physical Review B* 5 (1972), 844. DOI: 10.1103/PhysRevB.5.844

[60] Triguero L., Plashkevych O., Pettersson L.G.M. and Ågren H.: Separate state vs. transition state Kohn-Sham calculations of X-ray photoelectron binding energies and chemical shifts, in *Journal of Electron Spectroscopy and Related Phenomena* 104 (1999), 195-207. DOI: 10.1016/S0368-2048(99)00008-0

[61] Anthony J.E.: Functionalized Acenes and Heteroacenes for Organic Electronics, in *Chemical Reviews* 106 (2006), 5028-5048. DOI: 10.1021/cr050966z

[62] Anthony J.E.: The Larger Acenes: Versatile Organic Semiconductors, in *Angewandte Chemie International Edition* 47 (2008), 452-483. DOI: 10.1002/anie.200604045

[63] Campbell R.B., Robertson J.M. and Trotter J.: The crystal structure of hexacene, and a revision of the crystallographic data for tetracene, in *Acta Crystallographica* 15 (1962), 289-290. DOI: 10.1107/S0365110X62000699

[64] Siegrist T., Besnard C., Haas S., Schlitz M., Pattison P., Chernyshov D., Batlogg D. and Kloc C.: A Polymorph Lost and Found: The High-Temperature Crystal Structure of Pentacene, in *Advanced Materials* 19 (2007), 2079-2082. DOI: 10.1002/adma.200602072

[65] Schiefer S., Huth M., Dobrinevski A. and Nickel B.: Determination of the Crystal Structure of Substrate-Induced Pentacene Polymorphs in Fiber Structured Thin Films, in *Journal of the American Chemical Society* 129 (2007), 10316-10317. DOI: 10.1021/ja0730516

[66] Sakamoto Y., Suzuki T., Kobayashi M., Gao Y., Fukai Y., Inoue Y., Sato F. and Tokito S.: Perfluoropentacene: High-Performance p-n Junctions and Complementary Circuits with Pentacene, in *Journal of the American Chemical Society* 126 (2004), 8138-8140. DOI: 10.1021/ja0476258

[67] Salzmann I., Moser A., Oehzelt M., Breuer T., Feng X., Juang Z.Y., Nabok D., Della Valle R.G., Duhm S., Heimel G., Brillante A., Venuti E., Bilotti I., Christodoulou C., Frisch J., Puschnig P., Draxl C., Witte G., Müllen K. and Koch N.: Epitaxial Growth of π-Stacked Perfluoropentacene on Graphene-Coated Quartz, in *ACS Nano* 6 (2012), 10874-10883. DOI: 10.1021/nn3042607

[68] Schwaben J., Münster N., Breuer T., Klues M., Harms K., Witte G. and Koert U.: Synthesis and Solid-State Structures of 6,13-Bis(trifluoromethyl)- and 6,13-Dialkoxypentacene, in *European Journal of Organic Chemistry* (2013), 1639-1643. DOI: 10.1002/ejoc.201201714

[69] Schwaben J., Münster N., Klues M., Breuer T., Hofmann P., Harms K., Witte G. and Koert U.: Efficient Syntheses of Novel Fluoro-Substituted Pentacenes and Azapentacenes: Molecular and Solid-State Properties, in *Chemistry A European Journal* 21 (2015), 13758-13771. DOI: 10.1002/chem.201501399

[70] Anthony J.E., Brooks J.S., Eaton D.L. and Parkin S.R.: Functionalized Pentacene: Improved Electronic Properties from Control of Solid-State Order, in *Journal of the American Chemical Society* 123 (2001), 9482-9483. DOI: 10.1021/ja0162459

[71] Bässler H.: Localized states and electronic transport in single component organic solids with diagonal disorder, in *physica status solidi b* 107 (1981), 9-54. DOI: 10.1002/pssb.2221070102

[72] Takeya J., Yamagishi M., Tominari Y., Hirahara R., Nakazawa Y., Nishikawa T., Kawase T., Shimoda T. and Ogawa S.: Very high-mobility organic single-crystal transistors with in-crystal conduction channels , in *Applied Physical Letters* 90 (2007), 102120. DOI: 10.1063/1.2711393

[73] Bowen E.J. and Steadman F.: The Photo-oxidation of Rubrene , in *Journal of the Chemical Society* (1934), 1098-1101. DOI: 10.1039/JR9340001098

[74] Käfer D., Ruppel L., Witte G. and Wöll C.: Role of Molecular Conformations in Rubrene Thin Film Growth , in *Physical Review Letters* 95 (2005), 166602. DOI: 10.1103/PhysRevLett.95.166602

[75] Vijayalakshmi S., Föhlisch A., Kirchmann P.S., Hennies A. Pietzsch A., Nagasono M. and Wurth W.: Bond polarization and image-potential screening in adsorbed C_6F_6 on Cu(111), in *Surface Science* 600 (2006), 4972-4977. DOI: 10.1016/j.susc.2006.08.017

[76] Anger F., Scholz R., Gerlach A. and Schreiber F.: Vibrational Modes and Changing Molecular Conformation of Perfluororubrene in Thin Films and Solution, in *The Journal of Chemical Physics* 142 (2015), 224703. DOI: 10.1063/1.4922052

[77] Wu J., Wojciech P. and Müllen K.: Graphenes as Potential Material for Electronics, in *Chemical Reviews* 107 (2007), 718-747. DOI: 10.1021/cr068010r

[78] Goddard R., Haenel M.W., Herndon W.C., Krueger C. and Zander M.: Crystallization of Large Planar Polycyclic Aromatic Hydrocarbons: The Molecular and Crystal Structures of Hexabenzo [bc, ef, hi, kl, no, qr] coronene and Benzo [1, 2, 3-bc: 4, 5, 6-b'c'] dicoronene, in *Journal of the American Chemical Society* 117 (1995), 30-41. DOI: 10.1021/ja00106a004

[79] Mukai K., Harada M., Kikuzawa Y., Mori T. and Sugiyama J.: Electrochemical Properties of Hexa-*peri*-hexabenzocoronene in Nonaqueous Lithium Cell, in *Electrochemical and Solid-State Letters* 14 (2011), A52-A55. DOI: 10.1149/1.3541056

[80] Botoshansky M., Herbstein F.H. and Kapon M.: Towards a Complete Description of a Polymorphic Crystal: The Example of Perylene; Redetermination of the Structures of the (Z = 2 and 4) Polymorphs, in *Helvetica Chimica Acta* 86 (2003), 1113-1128. DOI: 10.1002/hlca.200390097

[81] Parkin A., Barr G., Dong W., Gilmore C.J., Jayatilaka D., McKinnon J.J., Spackman M.A. and Wilson C.C.: Comparing entire crystal structures: structural genetic fingerprinting, in *CrystEngComm* 9 (2007), 648. DOI: 10.1039/b704177b

[82] London F.: The general theory of molecular forces, in *Transactions of the Faraday Society* 33 (1937), 8b. DOI: 10.1039/TF937330008B

[83] Sutton C., Risko C. and Brédas J.-L.: Noncovalent Intermolecular Interactions in Organic Electronic Materials: Implications for the Molecular Packing vs Electronic Properties of Acenes, in *Chemistry of Materials* 28 (2016), 3-16. DOI: 10.1021/acs.chemmater.5b03266

[84] Haas S., Takahashi Y., Takimiya K. and Hasegawa T.: High-performance dinaphtho-thieno-thiophene single crystal field-effect transistors, in *Applied Physics Letters* 95 (2009), 022111. DOI: 10.1063/1.3183509

[85] Alagia M., Baldacchini C., Baldacchini B., Maria G., Bussolotti F., Carravetta V., Ekström U., Mariani C. and Stranges S.: Core-shell photoabsorption and photoelectron spectra of gas-phase pentacene: Experiment and theory, in *The Journal of Chemical Physics* 122 (2005), 124305. DOI: 10.1063/1.1864852

[86] Oteyza D.G., Sakko A., El-Sayed A., Goiri E., Floreano L., Cossaro A., Garcia-Lastra J.M., Rubio A. and Ortega J.E.: Inversed linear dichroism in F K-edge NEXAFS spectra of fluorinated planar aromatic molecules, in *Physical Review B* 89 (2012), 075469. DOI: 10.1103/PhysRevB.86.075469

[87] Kowarik S., Gerlach A., Hinderhofer A., Milita S., Borgatti F., Zontone F., Suzuki T., Biscarini F. and Schreiber F.: Structure, morphology, and growth dynamics of perfluoro-pentacene thin films, in *Rapid Research Letters* 2 (2008), 120-122. DOI: 10.1002/pssr.200802052

[88] Löwdin P.-O.: Quantum Theory of Many-Particle Systems. I. Physical Interpretations by Means of Density Matrices, Natural Spin-Orbitals, and Convergence Problems in the Method of Configurational Interaction, in *Physical Review* 97 (1955), 1474. DOI: 10.1103/PhysRev.97.1474

[89] Robin M.B., Ishii I., McLaren R. and Hitchcock A.P.: Fluorination effects on the inner-shell spectra of unsaturated molecules, in *Journal of Electron Spectroscopy and Related Phenomena* 47 (1988), 53-92. DOI: 10.1016/0368-2048(88)85005-9

Abbildungsverzeichnis

Wissenschaftlicher Werdegang

Michael Klues

geb. am 21. Nov. 1986 in Lingen (Ems)

1993	-	06/1997	Ludwig-Schriever-Grundschule Lünne
08/1997	-	06/2006	Franziskusgymnasium Lingen, *Allgemeine Hochschulreife*
10/2007	-	07/2010	Philipps Universtiät Marburg, *B. Sc. Physik* Bachelorarbeit am Fachbereich Physik, Prof. Dr. Witte
10/2010	-	10/2012	Philipps Universität Marburg, *M. Sc. Physik* Masterarbeit am Fachbereich Physik, Prof. Dr. Witte
11/2012	-	12/2016	Philipps Universität Maburg, *Dr. rer. nat.* Wissenschaftlicher Mitarbeiter und Doktorand in der Arbeitsgruppe Molekulare Festkörperphysik Doktorvater: Prof. Dr. Gregor Witte